



Australian
National
University



THÈSE / UNIVERSITÉ DE RENNES 1
sous le sceau de l'Université Européenne de Bretagne

En Cotutelle internationale avec
The Australian National University, Australie

pour le grade de
DOCTEUR DE L'UNIVERSITÉ DE RENNES 1
Mention : Chimie

Ecole doctorale Sciences de la Matière

présentée par

Nicolas Ripoché

Préparée à l'unité de recherche UMR 6226
Institut des Sciences Chimiques de Rennes
UFR Sciences de Propriétés de la Matière

Triphenylmethylium- Based Multitopic Two-Photon Absorbers: Synthesis and Characterization

**Thèse soutenue à Rennes
le 20 Novembre 2015**

devant le jury composé de :

Mireille BLANCHARD-DESCE

Directeur de recherche CNRS (Université de
Bordeaux 1) / *rapporteur*

Todd B. MARDER

Professeur (University of Würzburg) / *rapporteur*

Olivier MONGIN

Maître de conférences (Université de Rennes 1) /
examineur

Marie P. CIFUENTES

Professeur associé (Australian National University) /
examineur

Frédéric PAUL

Directeur de recherche CNRS (Université de
Rennes 1) / *directeur de thèse*

Mark G. HUMPHREY

Professeur (Australian National University) / *co-
directeur de thèse*

Contents

Summary.....	iv
Acknowledgements.....	vi
Abbreviations.....	viii
Introduction: Triphenylmethane-based derivatives for third-order nonlinear optics	1
Chapter I: All-organic triphenylmethane-based derivatives.....	59
Chapter II: Organometallic derivatives of malachite green.....	99
Chapter III: Organometallic derivatives of crystal violet	155
General conclusion	189
Experimental.....	197

Summary

Triphenylmethane dyes have attracted considerable attention since the beginning of the 20th century. They have first drawn the interest of the scientific community for their remarkable dyeing and medicinal properties. This interest led in turn to the publication of a vast pool of synthetic publications and comparatively much fewer theoretical studies. Unfortunately, this interest decreased in the 1970s, possibly due to a lack of proper understanding of their electronic structure and difficulties in modeling it. The recent advances in lasers and in nonlinear optics (NLO) have renewed this interest by opening new ways of investigation and delineating new potential uses for these dyes. The work reported in this thesis focus on two triphenylmethane-based dyes; Malachite Green (**MG**⁺) and Crystal Violet (**CV**⁺). Selected organic and organometallic derivatives have been targeted for investigation of their third-order NLO properties.

In the introduction, NLO theory is presented with a focus on third-order properties, NLO phenomena and the relevant experimental techniques. Selected examples of third-order NLO-active molecules are then described in order to illustrate the general design criteria commonly adopted for third-order NLO-active molecules and to emphasize the interest in incorporating a metal center in this type of structure. The potential of **MG**⁺- and **CV**⁺-based structures to behave as two-photon absorbers (TPA) is highlighted, followed by a review of the scientific work in this field. Finally, the aims of this thesis are given at the end of the introduction, along with a work plan.

The first chapter presents the synthesis and characterization of relevant fully organic derivatives of **MG**⁺ and **CV**⁺. The introduction of 9-anthracenyl or 2-fluorenyl groups as “two-photon antennas” as well as the use of a rigidified fluorenum structure or the enlargement of the π -manifold and their impact on the linear and nonlinear optical properties are then discussed.

The introduction of ferrocenyl and iron/ruthenium alkynyl complexes as substituents is presented in the second chapter, followed by a description of the targeted **MG**⁺-based derivatives. We show by cyclic voltammetry that the use of these redox-active synthons affords access to additional reversible redox states that have been studied by spectroelectrochemistry. The physicochemical behavior as a function of the oxidation state of these compounds is discussed after a description of their synthesis and characterization. Perspectives for electroswitching their NLO response are discussed.

The final chapter is focused on related octupolar **CV**⁺-based derivatives in which the organometallic substituents replace or reinforce the donor power of the peripheral amino substituents. The increase in symmetry of their structure is responsible for various modifications of their properties, which are studied and discussed in the same way as in the previous chapters. Again, after presenting their synthesis and extensive characterization, perspectives to obtain efficient nonlinear electrophores from these new organometallic dyes are discussed.

Acknowledgments

The work presented here has been undertaken cooperatively between the "Organometallic Chemistry and Molecular Materials" group of the Australian National University and the "Functional Organometallic Systems" group at the University of Rennes 1. This PhD has been made possible thanks to the financial support from "Region Bretagne" and the Australian Research Council-funded scholarships; they are both greatly acknowledged for their support.

Foremost, I would like to thank my supervisors, Dr. Frédéric Paul and Prof. Mark G. Humphrey, for having offered me the opportunity to carry out this PhD in their respective groups as well as their excellent guidance and encouragement throughout these three years. Assoc. Prof. Marie Cifuentes is also greatly thanked for her support as well as the help provided while moving to Australia.

Thanks to Thierry Roisnel, Vincent Dorcet and Dr. Graeme Moxey for running the X-ray diffraction analyses on the crystals in this work. I am also greatly indebted to Dr. Mahbod Morshedi for all his help in chemistry and wise advice during my time in Australia. Many thanks also to Dr. Guillaume Grelaud and Dr. Gilles Argouarch for the initial impulse they gave me and to Prof. Marek Samoc and Dr. Katarzyna Matczyszyn for their warm welcome and their help with Z-scan measurements during the few weeks I spent in Poland. Thanks also to Dr. Anissa Amar and Prof. Abdou Boucekkine for the DFT calculations they have performed on my compounds. I also want to thank Dr. Christine Paul, Dr. Carole Daiguebonne, Dr. Philippe Gall and Laurence Lohezic for trusting and helping me for this first experience of teaching at the INSA of Rennes.

I am also thankful to Dr. Mireille Blanchard-Desce, Prof. Todd B. Marder and Dr. Olivier Mongin for reviewing this manuscript and comprising my evaluation panel.

This work involved quite a lot of people from both universities, and even if working in two different environments is not always that easy, they have facilitated the realization of this project in the best possible conditions for me. In this respect, I would like to thank the different members of both groups with whom I have had the pleasure to work: Dr. Ayham Thome, Amédée Triadon, Dr. Alison Barnes, Dr. Areej Merhi, Dr. Dandan Yao, Xu Zhang, Seyfallah Abid; and Dr. Adam Barlow, Dr. Prue Guest, Richard Dexter, Dr. Caterina Gruenwaldt, Suzannah Streatfield, Junhong (Nate) Fu, Anthony Nolan, Aradhana Dissanayake, Noor Aisyah Ahmad Shah, Huajian Zhao, Xinwei Yang and

Fazira Ilyana binte Abdul Razak. I am also thankful to Cécile Valter for making the various glassware, Alison Scott and Cécile Peron for the support they gave me while doing the paperwork involved in this PhD and to Gwenaël Colombel, the "man in blue", who always knows how to share his joy of living.

Finally, I want to thanks my family and friends from France and Australia who have always been supportive during these three years, and their presence throughout these three years despite the distance.

Abbreviations

°: degree

λ_{max} : wavelength of maximum absorption (nm)

{¹H}: complete proton decoupling (NMR)

Å: angström

δ: chemical shift (NMR, in ppm), bond bending / deformation (IR)

ε: molar absorption coefficient (M⁻¹cm⁻¹)

ν: bond stretching (IR)

Ag / AgCl: silver / silver chloride reference electrode

AcOH: acetic acid

Anth: anthracene

AnthC₂: alkynyl anthracene

Ar: aryl

ASAP: atmospheric solids analysis probe

br: broad

Bt: benzotriazole

C₂: alkyne

C_α: carbon atom directly coordinated to a metal

C_β: first carbon bonded to the C_α

C_γ: first carbon bonded to the C_β

Cp: η⁵-cyclopentadienyl (C₅H₅)

Cp*: η⁵-pentamethylcyclopentadienyl (C₅Me₅)

CT: charge transfer

CV⁺: crystal violet

CV: cyclic voltammetry

d: doublet

dd: doublet of doublets

DBU: 1,8-diazabicyclo[5.4.0]undec-7-ene

DCM: dichloromethane

DIPA: diisopropylamine

DFWM: degenerate four waves mixing

DMSO: dimethylsulfoxide

dppe: 1,2-bis(diphenylphosphino)ethane

dt: doublet of triplets

DPV: differential pulse voltammetry

EI: electron impact

ESA: excited state absorption

ESI: electrospray ionization

Et: ethyl group (C₂H₅)

[Fe]: Fe (η⁵-C₅Me₅)(κ²-dppe)

Fc: ferrocenyl

FcH: ferrocene

FcH⁺: ferrocenium

Flu: 1, 2-dibutylfluorene

fs: femto-second (10⁻¹⁵ s)

GS: ground state

ESA: excited state absorption

h: hour

high vacuum: pressure less than 10⁻² mbar (oil pump vacuum)

HOMO: highest occupied molecular orbital

IC: intersystem crossing

IR: infrared

i_{pa}/i_{pc}: ratio of peak currents

J: coupling constant

LDA: lithium diisopropylamine

LMCT: ligand to metal charge transfer

LUMO: lowest unoccupied molecular orbital

Me: methyl

MeOH: methanol

MLCT: metal to ligand charge transfer

m: multiplet (NMR), medium (IR)

mg: milligram	THF: tetrahydrofuran
min: minute	UV-Vis: ultraviolet-visible
m/z: mass to charge ratio	V: volt
MG⁺: malachite green	vs.: versus
NIR: near-infrared	v/v: volume-to-volume ratio
nm: nanometers	w: weak
NMR: nuclear magnetic resonance	w/w: weight-to-weight ratio
NLO: nonlinear optics	
OTTLE: optically transparent thin layer electrochemical cell	
PPP-MO: Pariser-Parr-Pople molecular orbital	
Ph: phenyl	
ppm: parts per million	
quant.: quantitative	
R_f: retention factor	
[Ru]: <i>trans</i> - Ru (Cl)(κ ² -dppe) ₂	
RSA: reverse saturable absorption	
rpm: revolutions per minute	
TFA : trifluoroacetic Acid	
Tol: toluene	
s: singlet	
S: strong	
SCE: saturated calomel electrode	
SA: saturable absorption	
sept: septuplet	
sh: shoulder	
t: triplet	
T: temperature	
THG: third-harmonic generation	
TLC: thin layer chromatography	
TMSa: trimethylsilylacetylene	
TMS: trimethylsilyl	
TPMs: triphenylmethane dyes	
TPA/2PA: two-photon absorption	
TPEF/2PEF: two-photon excited fluorescence	

Introduction:

**Triphenylmethane-based derivatives for
third-order nonlinear optics**

Introduction

Triphenylmethane-based derivatives for third-order nonlinear optics

Contents

1. Nonlinear optics: general comments	5
1.1. NLO theory	5
1.2. Third-order NLO phenomena	6
1.2.1. Two-photon absorption	7
1.2.2. Saturable absorption and reverse saturable absorption	10
1.3. Experimental techniques for measuring two-photon absorption	11
1.3.1. Two-photon excited fluorescence	12
1.3.2. Z-scan	13
1.4. Third-order NLO materials for TPA or SA/RSA	16
1.4.1. Structure and nature of the materials	16
1.4.2. Examples of third-order NLO active materials with high TPA cross-sections	18
2. Triphenylmethane dyes	24
2.1. General comments	24
2.2. Solvolysis	26
2.3. Remarkable optical properties	27
2.4. Nomenclature and examples	28
3. TPMs: synthesis and physico-chemical properties	31
3.1. Synthesis	31
3.2. Photophysics of TPMs	33
3.2.1. Electronic absorptions	33
3.2.2. Relaxation processes	37
3.3. Photochemistry	41
4. Literature review of the cubic NLO properties of TPMs	42
4.1. THG and DFWM measurements	43

4.2. Z-scan measurements	44
4.3. TPEF measurements	45
4.4. Synopsis	46
5. Objectives	47
5.1. Organic derivatives	47
5.2. Organometallic derivatives	49
6. Conclusion	52
References	54

1. Nonlinear optics: general comments

1.1. NLO theory

The invention of lasers has brought to science a new area of research and has allowed the observation of multiple and advanced phenomena. Nonlinear optical (NLO) behaviour is one of them and is observed when an intense beam of light, such as that generated by lasers, interacts with matter. The resulting beam is then modified in a nonlinear fashion. Its phase, frequency, amplitude, polarization, path or other propagation characteristics are no longer effectively proportional to the incident beam as is the case for less intense light sources. The optimisation of these properties leads to the development of materials with unique properties that can be used in several fields such as optical communication, optical computing, data storage, imaging, microfabrication and medicine.^[1] Their development is linked to the increasing demand for more and more efficient optical information transfer, the need for faster communications, and the progress in healthcare. While most of the actual commercial applications in optical processing result from bulk inorganic solids/glasses or polymers, research in this field also focuses more and more on single molecules or nano-sized objects as these may give rise to more efficient and more compact molecular-based devices. Use of multiphoton applications in health care is an even more recent domain where there is plenty of room for improvement. This necessitates a better understanding of the associated phenomena and their properties at the molecular level.

For a molecular chemist it is often better to consider NLO properties at the molecular scale. Light, as described by classical Maxwell theory, is an electromagnetic field associated with an electric field \mathbf{E} . When directed toward a material, the light interacts with the polarizable electrons of the material's molecules. This disturbs the molecules' electric fields and therefore induces a dipole moment μ at the molecular level. As long as the intensity of the field of \mathbf{E} does not reach values similar to those within the molecule, \mathbf{E} is proportional to μ . However, when the light reaches a high enough intensity, the properties of the material change from the classic (leading to well-known linear optical properties for the material) to nonlinear, implying new properties and relations. This can be described by the following power series (**Equation1**):

$$\mu = \mu_0 + \alpha E + \beta E^2 + \gamma E^3 + \dots \quad (1)$$

μ_0 : static dipole moment

α : linear polarizability

β : quadratic hyperpolarizability (second-order polarizability)

γ : cubic hyperpolarizability (third-order polarizability)

Summing the induced dipole moments of the molecules in the material leads to a polarization equation that describes the macroscopic response (**Equation 2**).

$$\mathbf{P} = \mathbf{P}_0 + \chi^{(1)}\mathbf{E} + \chi^{(2)}\mathbf{E}^2 + \chi^{(3)}\mathbf{E}^3 + \dots \quad (2)$$

\mathbf{P} : induced polarization

\mathbf{P}_0 : permanent polarization

$\chi^{(1)}$: linear susceptibility

$\chi^{(2)}$ and $\chi^{(3)}$: quadratic and cubic susceptibilities

These two equations (**Equation 1** and **2**) can be mathematically developed and each term can be linked to specific NLO effects. Relationships between the molecular structure and a given NLO effect can be obtained. Hitherto, NLO effects have been comprehensively described for the second-order, β or $\chi^{(2)}$, but the cubic effects, and beyond, are much more complicated to develop and model.^[2] As a result, structure/property relationships and rules are not always available to predict the best structural modifications to enhance a specific third-order (or higher) NLO property.^[3–8] However, for these higher-order NLO effects some empirical rules have been established that provide a solid base for the design of active molecules.

The following work is focused on the third-order properties, as given by $\chi^{(3)}$, the cubic susceptibilities on a macroscopic scale, themselves related to γ , the molecular cubic hyperpolarizability. In particular, we will be more concerned during this work with processes involving absorptive NLO properties, *i.e.* the phenomena affecting the actual absorption of photons by the molecules, as opposed to the refractive properties, concerning the modifications of the light path through the matter and its characteristics.

1.2. Third-order NLO phenomena

It is important to note that third-order NLO phenomena exist in every molecule, compared to second-order phenomena for which particular symmetries nullify the nonlinear effects, specifically in centro symmetric molecules. Third-order effects are negligible in many materials, but some molecules are more active than others, and it is possible to tune them by changing the molecular structure.

Moreover, the third-order effects are wavelength- and time-dependent and, as mentioned previously, will result from changes in the refractive or absorptive properties of the medium. At the molecular scale, refractive and absorptive properties are usually differentiated by developing the complex number γ (**Equation 3**) with the real and imaginary parts being responsible for the different effects.

$$\gamma = \sqrt{\gamma_{\text{Re}}^2 + \gamma_{\text{Im}}^2} \quad (3)$$

The real term γ_{Re} generates phenomena related to nonlinear modifications of the refractive properties whereas the imaginary term γ_{Im} is responsible for absorptive modifications. γ_{Re} leads to effects such as the optical Kerr effect, frequency tripling or four-wave mixing.^[9,10] These ultra fast modifications of the refractive properties are mostly used to manipulate optical data or create a laser source with selected wavelengths. On the other hand, the imaginary part induces slower effects such as two-photon absorption (TPA), saturable absorption (SA) or reverse saturable absorption (RSA). The sign of γ_{Im} also has its importance: if $\gamma_{\text{Im}} > 0$, TPA or RSA phenomena are occurring and if $\gamma_{\text{Im}} < 0$, SA occurs. These different absorptive properties and their applications are described in more detail in the next paragraphs.

1.2.1. Two-photon absorption

Two-photon absorption (TPA or 2PA) corresponds to the simultaneous absorption of two photons through a virtual state.^[11] A simplified Jablonski diagram illustrates this phenomenon in **Figure 1**. The phenomenon can be viewed as the absorption of a first photon to reach a "virtual" state, which in turn can absorb a second photon to reach the real excited state. Two TPA processes are observed: one corresponds to the degenerate case with the absorption of two photons of the same energy (**a**) and the second to a cascade of photons of different energies (**b**).^[12] The former effect requires a monochromatic laser beam at the correct energy, while the second process requires a polychromatic intense light source coming from different sources.

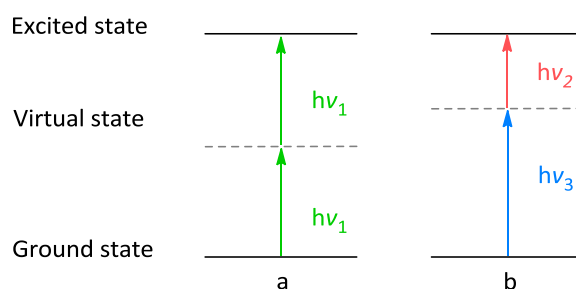


Figure 1: TPA of photons of same (a) and different (b) energies

This representation is only a model as the virtual states do not have a real existence, and thus the two photons need to be absorbed at exactly the same time. In a more practical way, the two photons usually stem from the same laser source at the half energy, double the wavelength, of the energy gap that would populate the excited state via one-photon absorption. This requires a high enough density of photons and a correct phase matching between them for the TPA phenomenon to occur.

These requirements on photons result in a remarkable spatial localization of this phenomenon: the density of photon is only high enough at the focal point of the laser beam for the TPA to occur. Therefore it is possible to obtain a very good spatial resolution in the volume. Compared to the one-photon absorption process, the photons used for TPA are also less damaging as, at double the wavelength, they have a much lower energy but induce the same effect in the material (associated with the population of the excited state). This is of great interest, especially regarding the medicinal applications, since a beam of lower energy also has a deeper penetration power under the skin while inducing less collateral cell damage. Furthermore, the high spatial resolution of the phenomenon helps to target specific tissues, as for instance in the case of photodynamic therapy. It also helps to achieve better resolution and three-dimensional view when imaging is sought for diagnostic or specific treatment.

Another field also benefits from these advantages: microfabrication (**Figure 2**). The spatial resolution allowing the polymerization, thanks to TPA sensitizers, in nano- to micro-scale sized areas. These important technological applications explain the huge interest around TPA-active molecules in the past few years. The applications listed above are the most common but several other important ones resulting from the TPA phenomenon can be found in the literature.^[13,14]

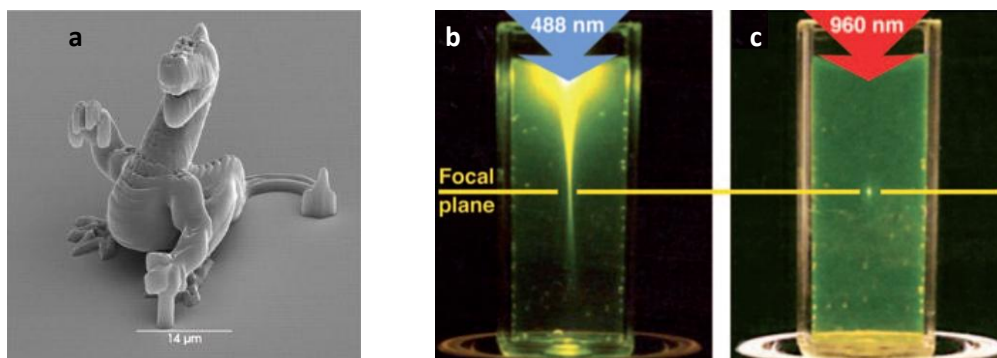


Figure 2: Example of use of TPA for microfabrication (a).^[15] Illustration of the spatial resolution of the TPA phenomenon by comparing two-photon fluorescence (c) with classic (one-photon) fluorescence (b) ^[16]

The intensity of the TPA phenomenon is usually described by its cross-section σ_{TPA} (**Equation 4**) which can be either expressed in cm^4/GW or more conveniently in Goeppert-Mayer units in honor of its discoverer ($1 \text{ GM} = 10^{-50} \cdot \text{cm}^4 \cdot \text{s} \cdot \text{photon}^{-1} \cdot \text{molecule}^{-1}$).^[17]

$$\sigma_{\text{TPA}} = \frac{4\pi^2 \hbar \omega^2}{n^2 c^2 N} \text{Im}[\chi^{(3)}] = \frac{4\pi^2 \hbar \omega^2}{n^2 c^2} \text{Im}[\gamma] \quad (4)$$

\hbar : Planck's constant h divided by 2π

ω : frequency of photons in Hz

n : refractive index

c : speed of light in a vacuum

N : number density of molecules

Another number is also used: the nonlinear absorption coefficient, often abbreviated as β (not to be confused with the molecular quadratic hyperpolarizability). When the only nonlinear absorption phenomenon experienced by a sample at a given wavelength is TPA, the latter can be derived as shown in **Equations 5** and **6**. The dependency on λ is worth noting. This implies that when comparison between molecules is sought for a given family of compounds, TPA measurements should be carried out at the same wavelength, but this is not always simple since $\chi^{(3)}$ is also wavelength dependent. When the nonlinear absorption of a sample involves other phenomena such as SA or RSA in addition to TPA (see below), **Equation 5** can also be used to extract a β value, but an “effective” TPA coefficient in this case because it results from the convolution of all absorptive nonlinear optical phenomena taking place in the sample. To limit the contribution of these other (and temporally slower) effects on $\chi^{(3)}$, the latter should be determined on an ultrashort timescale (e.g. using Z-scan with fs laser pulses).

$$\beta = \frac{3\pi}{\epsilon_0 n^2 c \lambda} \text{Im}[\chi^{(3)}] \quad (5)$$

$$\beta = \frac{\sigma_{\text{TPA}} N}{\hbar \omega} \quad (6)$$

λ : wavelength in nm

These two quantities σ_{TPA} and β are the most commonly used to report TPA efficiency for molecules in the literature. While β describes the material's behavior on a macroscopic scale, σ_{TPA} is used at the molecular level. Depending on the technique used for measuring TPA and provided its the sole nonlinear phenomenon experienced by the sample at a given wavelength, γ_{im} or $\chi_{\text{im}}^{(3)}$ can also be found as alternative measures of TPA since values of σ_{TPA} or β can be extrapolated from them.

1.2.2. Saturable absorption and reverse saturable absorption

In the same way as TPA, SA and RSA also imply the absorption of two photons. The main difference is that they are absorbed one after another *via* a process called excited-state absorption (ESA) (**Figure3**). This is a stepwise process where the first photon is absorbed, generating the first excited state (not a virtual state as in TPA), and then a second photon is absorbed from this excited state to generate the second excited state which has different physicochemical properties.

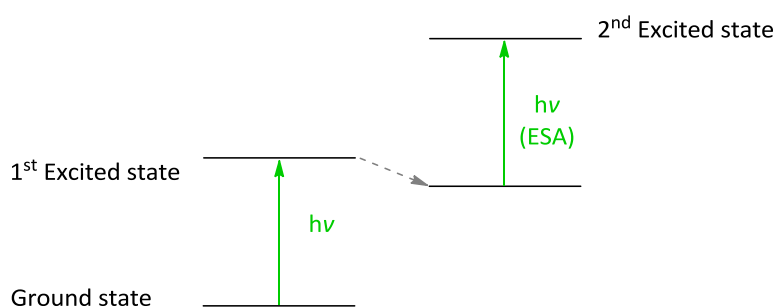


Figure 3: Saturable absorption or reverse saturable absorption

Since the second excited state has different properties to the ground state, it can induce a "photodarkening" for RSA or a "photobleaching" for SA.^[18] For RSA, the excited state has greater absorptivity (or cross-section) than the ground state and as a result the transmission of the medium will decrease when the photon density increases. In contrast, for SA the excited state has a lower

absorptivity (or cross-section) than the ground-state and the transmission will increase when the photon density increases. These phenomena can lead to applications such as optical limiting or optical bleaching.^[19] Optical limiting is mostly used to protect devices, apparatus and sensors or even humans from high light intensities. Albeit slower than purely refractive third-order NLO effects such as the Kerr effect, these effects might also be used for all-optical computing since they will give rise to "gating" effects for light concentrated by a pump beam in a pump-probe configuration.^[20] Technology where light is used as a signal is attracting more and more attention, since it allows a faster processing of data than classic electronic circuits triggered by current pulses.

As mentioned in the previous section, TPA, RSA and SA have different response times, RSA and SA being slower than TPA (which is nearly instantaneous) as they necessitate the population of an intermediate (real) excited state. Hence, time-resolved measurements can be used to determine the contribution of each effect to the third-order NLO response of a given sample experiencing nonlinear absorption at a selected wavelength. Depending on the targeted applications, it is important to ensure that these processes are not interfering with each other or in some cases that their effects are contributing additively. Each one of these phenomena possesses interesting properties that can be used in different technological applications.

1.3. Experimental techniques for measuring two-photon absorption

The vast number of third-order, and more generally NLO, effects has also given rise to several techniques for measuring them and various set-ups are encountered depending on the desired properties. Most of these techniques have already been reviewed and summarized in the previously mentioned references.^[17,18,21,22] They do not always give access to the values of the real or imaginary parts of the complex numbers γ or $\chi^{(3)}$. The most useful techniques for measuring TPA of organic and organometallic molecules are two-photon excited fluorescence (TPEF) and Z-scan. The first one uses a set-up that is similar to a normal fluorescence spectrometer but it necessitates a more intense laser source to observe TPA. In contrast, the Z-scan technique does not require the sample to be luminescent but is often less accurate, due to the possible existence of other nonlinear absorption processes contributing to the imaginary parts of $\chi_{\text{im}}^{(3)}$. Z-scan nevertheless gives access to the imaginary and real parts of the cubic hyperpolarizability, and was therefore the preferred technique to determine γ_{im} for the weakly fluorescent compounds of the present work. Note also that other techniques such as degenerate four-wave mixing (DWFM) or third-harmonic generation (THG) allow one to measure the overall cubic NLO response of a sample. These will not be detailed here since they

do not provide any specific estimate of the two-photon processes in the NLO response. Alternatively, the evaluation of nonlinear absorption processes can be derived from optical-limiting measurements or pump-probe measurements (conducted on different timescales); with respect to two-photon processes, these techniques are usually more suited to study slower effects than TPA, and will therefore also not be detailed here.

It is noteworthy that it can be very difficult to compare the NLO data obtained with different systems and in different laboratories, even when care is taken to translate them into a uniform set of units. This is the result of the strong wavelength- and pulse duration- dependence of the measured NLO responses, due to the vast number of underlying physical processes. Moreover, due to practical reasons, every set-up and laser are different and can also induce slight specific modifications which should be taken into account (when identified). Finally, the measurements are always calibrated using reference materials, but a given reference can be different from one group to another and often several $\chi^{(3)}$ values can be found in the literature for a single reference, as is the case of silica which is often used as a reference for Z-scan measurements.^[23]

Nevertheless, nowadays, the increasing amount of data in the field of nonlinear optics is giving a more and more reliable picture of the performances of various molecules or materials, even if some "old" measurements still have to be considered carefully. In addition, the actual lasers allow a finer wavelength tuning and generate more stable pulses from nanosecond to femtosecond, free from residual noise. As a result, the reported values are becoming increasingly accurate and reliable.

1.3.1. Two-photon excited fluorescence

TPEF is similar to the one-photon equivalent: after being excited to one of its excited states the molecule decays in a non-radiative way to its first excited state (**Figure 4**). This is known as Kasha's rule^[24] and most compounds follow this empirical rule. Then, if the decay back to the ground state proceeds *via* a radiative process, fluorescence can be observed. TPEF measures the global efficiency of this radiative process $\sigma_{\text{TPA}} \cdot \phi$, with ϕ being the fluorescence quantum yield. The latter needs to be measured by preliminary studies if not already known.^[7]

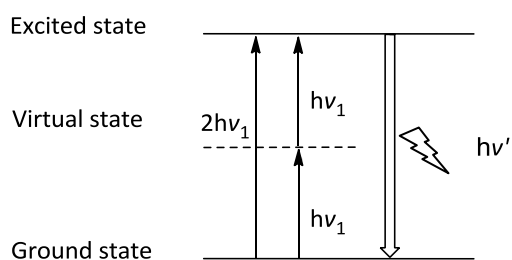


Figure 4: one and two photon fluorescence

The experimental set-up employs a classical fluorimeter (**Figure 5**), with a specific source to irradiate the sample at the desired wavelength with short pulses to ensure the detection of a single phenomenon. The detection is most of the time perpendicular to the incident light. The TPA cross-section σ_{TPA} is then obtained with good accuracy (a few percent error in the best cases) compared to other methods. The main drawback of TPEF is that it requires fluorescent compounds. Moreover, this technique does not give access to other contributions (RSA, SA, nonlinear refractive effects) to the third-order response ($\chi^{(3)}$ or γ) of a given sample.

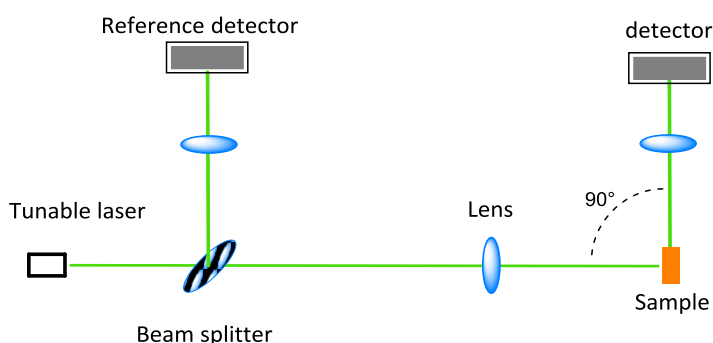


Figure 5: Typical set-up for TPEF

1.3.2. Z-scan

The Z-scan technique is also a relatively simple and convenient method for studying the cubic NLO response of a sample. It allows the separate measurement of the nonlinear refractive and absorptive properties of non-fluorescent samples. Since most of the organometallic species are not fluorescent, Z-scan is probably the most universal technique for studying these molecules. **Figure 6** shows a representation of a Z-scan set up. An incident laser beam is focused on a focal plane ($z=0$). Then, the sample is moved along this z -axis, perpendicular to the focal plane. The data corresponding to the transmission of the medium are measured *via* closed- and open-aperture detectors. The former allows the measurement of the refractive properties by measuring the shift in the focal point, and the second measures the absorptive properties, by monitoring the changes in light intensity while the sample is moving. **Figure 6** also shows the typical profile of the data obtained from the open-aperture

experiment. In **a**, as the sample moves toward $z=0$, the light absorption increases, and TPA results in a decrease in the light transmission. In **b**, the previously discussed “photobleaching” occurs: the closer to the focal point the better the transmission is. In the same way for **c**, when a certain point is reached the “photodarkening” process happens and the excited states absorb light. After mathematical treatment and comparison with the reference beam and the reference material, one obtains both the real and the imaginary parts of γ or $\chi^{(3)}$.

Note that other types of Z-scan setups have been developed these last years. For instance, instead of having a moving sample, some set-ups present a tunable lens allowing the focal point to be directly moved without any mechanical movement.^[25] Alternatively, double-beam Z-scan setups have been developed.^[26] Such set-ups can drastically increase the speed of measurements or allow diverse manipulations to be performed on the sample, like electrochemistry, while doing the measurements at the same time. In this thesis we have focused on measuring the effective TPA cross-sections. The measurement also gives the refractive part, but the latter has not been made available at the time this part was written, due to the longer corrections required to treat the raw data.

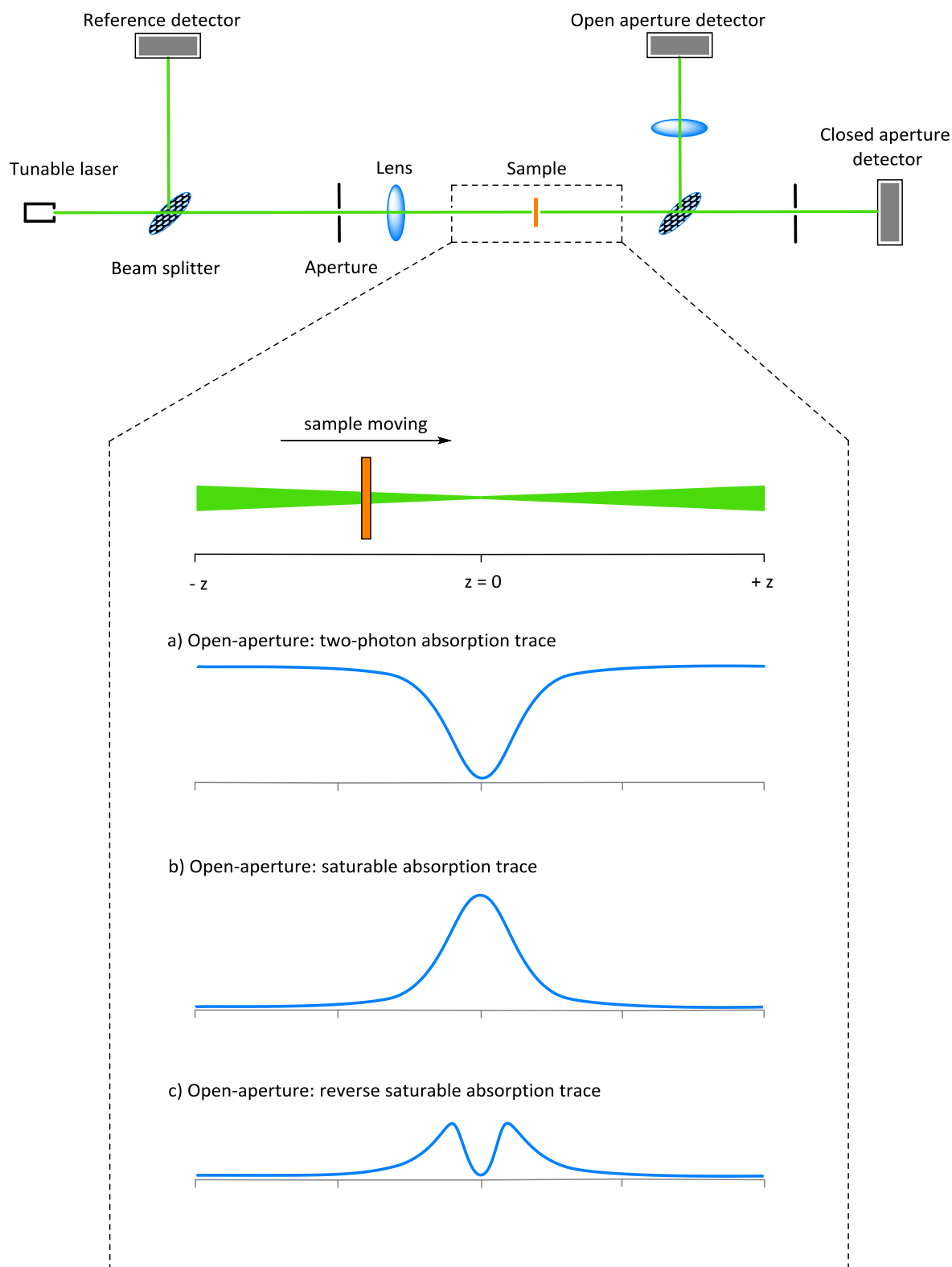


Figure 6: Example of a Z-scan set up and traces obtained for absorptive properties showing light transmission as a function of the z-axis location

1.4. Third-order NLO materials for TPA or SA/RSA

1.4.1. Structure and nature of the materials

As mentioned previously, third-order NLO properties are more complex than second-order properties. From a computational perspective, due to the large number of effects and electronic levels involved,^[27] modelling is challenging, in spite of progress this past decade. Theoretical computations of cubic NLO effects are increasingly used to understand/predict the influence of structural modifications on NLO effects, but primarily for small- to medium-sized organic molecules.^[16,17,21] In spite of recent progress in calculations and theory, structure-activity relationships are still not well-established for all types of molecules for a given NLO process. So far, only a few general criteria have been empirically observed to enhance the overall cubic NLO effects, as given by γ or $\chi^{(3)}$. First, the more active molecules usually possess an extended π -system and a multipolar structure with an alternation of electron-donating and -withdrawing groups. The disposition of donor or acceptor groups also has an important role and often the NLO response will improve when the symmetry of the molecule increases, going from dipolar to quadrupolar to octupolar (**Figure 7**).

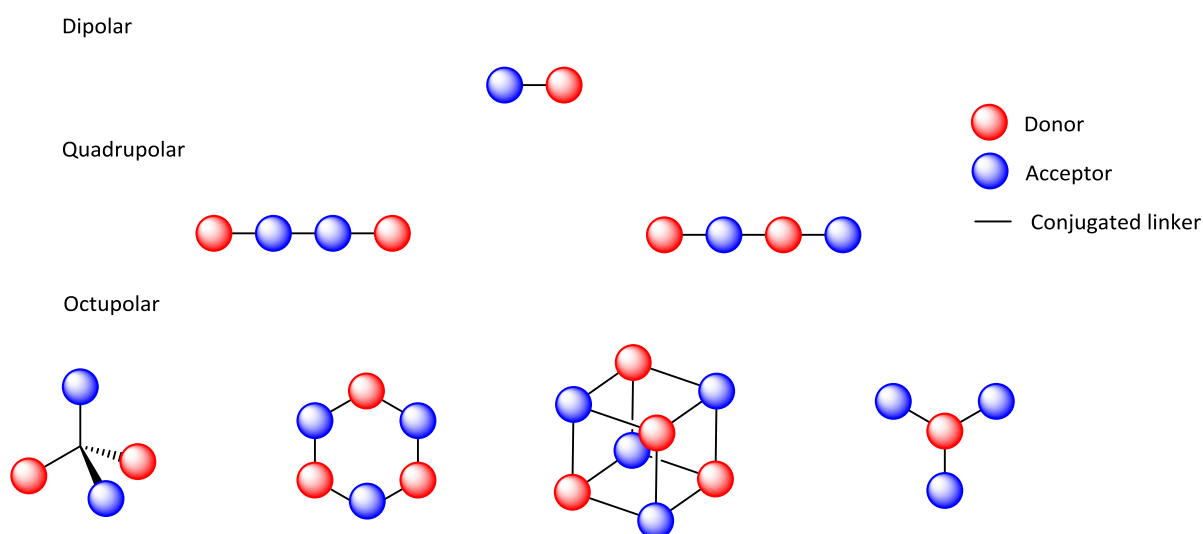


Figure 7: Examples of multipolar structures

As a result, the disposition in space, and the number, the conjugation and the distance between electron-donating and electron-withdrawing groups are crucial factors in the design of highly active third-order materials. The electron-donating and electron-releasing groups can be either inorganic, organic or organometallic. As these groups possess different effective electronegativities and interact differently with the spacers between them, some modifications and combinations are not

similarly effective for all geometries/structures and fine tuning is often required, depending on the exact molecular structure sought.

Among the donors, several types have been used: dialkyl- and diaryl-amino and oxygen-based groups are the most common. The more donating the group is, the more active the compound is, and as a first approach, NLO activity can be correlated to the Hammett coefficient values. However, among amines, an exception is worth mentioning: arylamines, for which the number of π -electrons counterbalances their weaker donating power compared to dialkylamines. In terms of acceptors, similar observations can be made based on the Hammett coefficients. The most commonly used acceptors are the nitro, cyano/malonitrile, sulfonyl, triflyl or organoboryl groups (**Chart 1**).^[4,7,11,28–30]

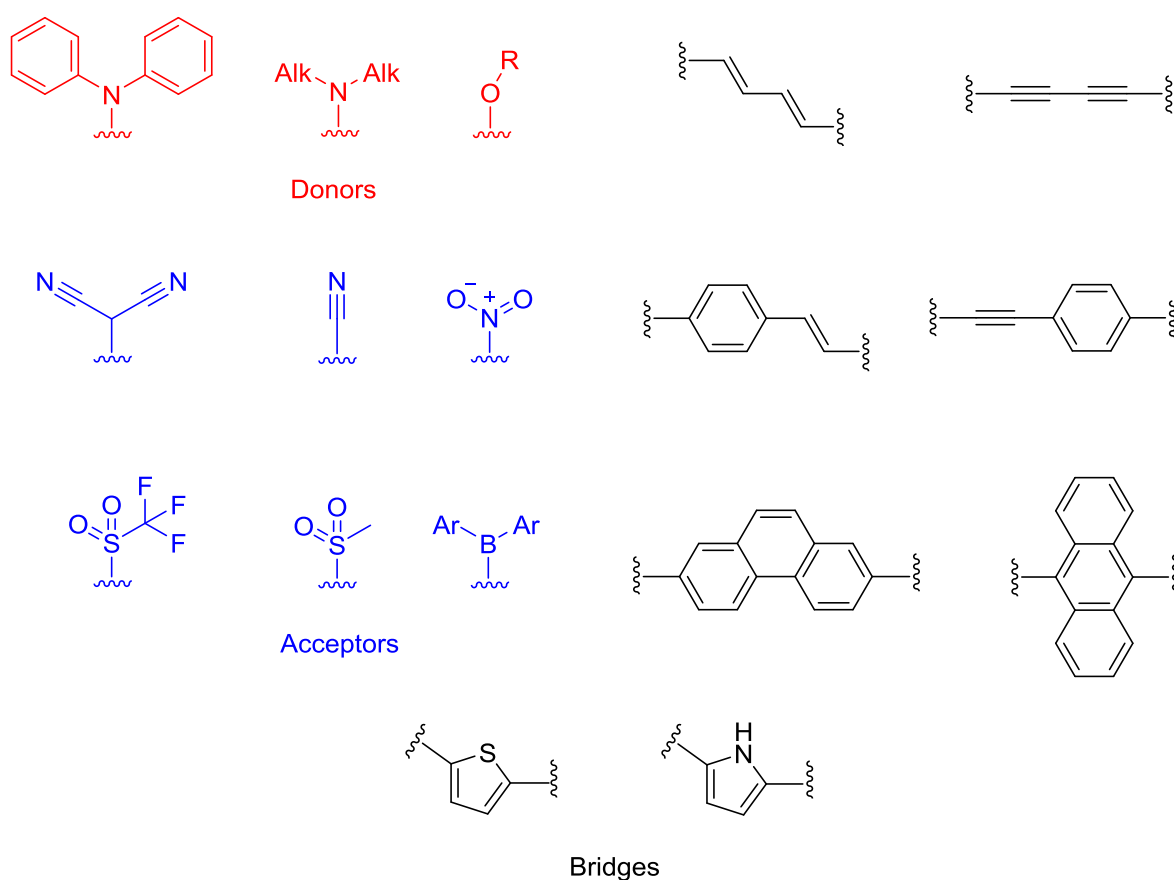


Chart 1: Examples of classic donors, acceptors or bridging units

An optimal electronic coupling between these groups through the bridge is also necessary to facilitate the electronic interaction between donors and acceptors. So far, phenylene-vinylene or ethynyl/phenyl-ethynyl are the most popular hydrocarbon bridges as they provide an effective π -conjugation pathway for most donor/acceptor couples. Extended π -conjugated bridges like anthracene or phenanthrene and aromatic heterocycles like thiophene or pyrrole are also commonly encountered in the design of molecules with large NLO properties. However, as mentioned above, depending on the targeted structure, fine tuning is required to properly select the best combination of D/bridge/A to

optimize the desired NLO response. The stability of the bridging unit and its length are additional criteria, since chemical stability and "volume efficiency" are often required for applications. Also, while increasing the number of bridging units, the number of π -electrons also increases, requiring the system to remain planar to ensure an optimal electronic communication. All these issues have to be taken into consideration, making the design of the best molecular structure a difficult task.^[4,12,17,23,28,31]

1.4.2. Examples of third-order NLO active materials with high TPA cross-sections

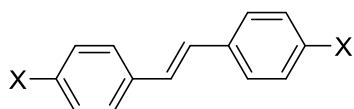
The literature contains extensive lists of cubic hyperpolarizability values because every material is third-order NLO active, regardless of its symmetry and composition, including bulk materials, molecules in solution, and doped glasses. With the complexity introduced by the existence of different phenomena, and the variety of experimental setups and conventions used to extract the relevant parameters, it is sometimes challenging to make reliable comparisons between the third-order NLO properties of molecules. Some values for classic materials can be found in the *Handbook of Nonlinear Optics* written by Sutherland.^[21] Some relevant and didactic examples of two-photon absorbers will be described in the following paragraphs to provide an illustration of typical molecules of interest and their associated σ_{TPA} values.

Inorganic materials were the first to be tested as they are in general robust, transparent and available in crystalline form. Their main drawbacks are a slow response time, small structural diversity, and difficulty in synthesizing them in a monocrystalline form. Their NLO activity is usually high and originates mostly from electronic effects, but also, in many cases, from distortions of the crystal lattice. The most popular inorganic salts used for third-order nonlinear optics are semiconductors such as gallium arsenide (GaAs) or cadmium sulfide (CdS), which find applications as saturable absorbers.^[32] Their crystal-growing technology is well developed, allowing for their easy incorporation in various devices. Inorganic crystals are, for the moment, the only available materials commercially used for various applications in nonlinear optics, despite the fact that they are not as versatile as organic or organometallic materials. As multiphoton absorbers, their NLO activity does not originate exclusively from TPA, unlike the examples given below.

1.4.2.1. Organic compounds

Organic molecules have fast NLO responses and can be easily synthesized with considerable structural variation fortuning the properties. Their NLO responses originate from electronic effects and

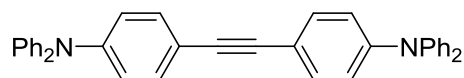
are usually essentially instantaneous. Due to the large number of donors/acceptors and geometrical variations, as discussed previously, it is difficult to give a comprehensive overview of all active structures. **Chart 2** illustrates some examples of organic materials designed for TPA such as **1-3** and **6-7**. In line with the general guidelines previously mentioned, they show an increase of the TPA cross-sections when increasingly electron-releasing donors are incorporated; from methoxy to alkylamine and then to arylamine. Moreover, increasing the length of the π -system by incorporating a fluorene unit within the molecular spacer (e.g. proceeding from **2** to **7**) also drastically increases the TPA cross-section. Finally, compounds **8** and **9** illustrate the fact that peripheral donors are much more effective than acceptors (by an order of magnitude) in quadrupolar structures built around a 2,7-fluorenyl core.



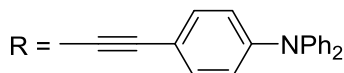
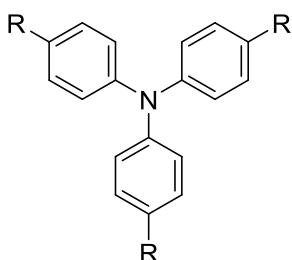
1 X = H, $\sigma_{\text{TPAmax}} = 12$ GM at 514 nm (fs-TPEF)^a

2 X = NBu₂, $\sigma_{\text{TPA}} = 110$ GM at 620 nm (fs-TPEF)^a

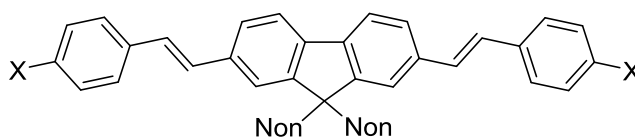
3 X = NPh₂, $\sigma_{\text{TPAmax}} = 340$ GM at 680 nm (fs-TPEF)^a



4 $\sigma_{\text{TPAmax}} = 420$ GM at 650 nm (Zscan)^b

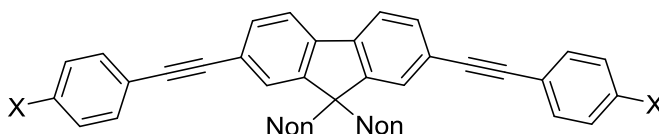


5 $\sigma_{\text{TPAmax}} = 1200$ GM at 650 nm (Zscan)^b



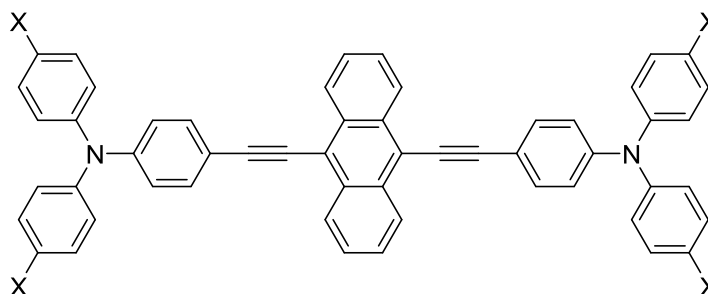
6 X = OMe, $\sigma_{\text{max}} = 110$ GM at 705 nm (fs-TPEF)^a

7 X = NBu₂, $\sigma_{\text{max}} = 1300$ GM at 740 nm (fs-TPEF)^a



8 X = NHex₂, $\sigma_{\text{max}} = 1200$ GM at 705 nm (fs-TPEF)^a

9 X = SO₂CF₃, $\sigma_{\text{max}} = 83$ GM at 705 nm (fs-TPEF)^a



10 X = OMe, $\sigma_{\text{TPAmax}} = 400$ GM at 842 nm (fs-TPEF)^c

11 X = Cl, $\sigma_{\text{TPAmax}} = 550$ GM at 809 nm (fs-TPEF)^c

Chart 2: Examples of organic TPA molecules. a: ^[16], b: ^[33], c: ^[34]

As spacers in these quadrupolar structures, vinylene and ethynylene bridges are similar: comparing compounds **3** and **4** or **7** and **8** illustrates this point as these compounds possess similar TPA cross-sections. Although the values of the double bond-containing compounds are expected to be higher, as double bonds are known to be more “conducting” than triple bonds, the latter having a less effective bond alternation because of π - π and π^* - π^* energy mismatches at the $C(sp^1)$ - $C(sp^2)$ connections, the optimization of NLO effects does not always obey such simplistic rules.^[35] Z-scan values often appear larger than values obtained by TPEF for a similar compound at a given wavelength,^[36] illustrating the difficulty in comparing results obtained by different kinds of measurements (e.g. **3** and **4**). Triple bonds possess better thermal stability, which makes them more likely to be used for applications involving thermal stability or high light intensity.

The influence of geometry, when progressing from quadrupoles to octupoles, can be illustrated with **4** and **5**. Although only a three-fold improvement is seen when progressing from **4** to **5**, **5** is nevertheless more compact than three equivalents of **4**, resulting in a better molecular performance for **5**. **Chart 3** shows the influence of the bridging unit’s length, because the TPA cross-sections increase with the number of π -electrons in the molecule. However, it is only true up to three phenylene ethynylene units, as the cross-section decreases with further lengthening due to decreasing electronic communication between the (donor) endgroups. The use of an anthracene spacer, similarly to 2,7 fluorenyl, tends to enhance TPA response due to the corresponding increase in the π -manifold.

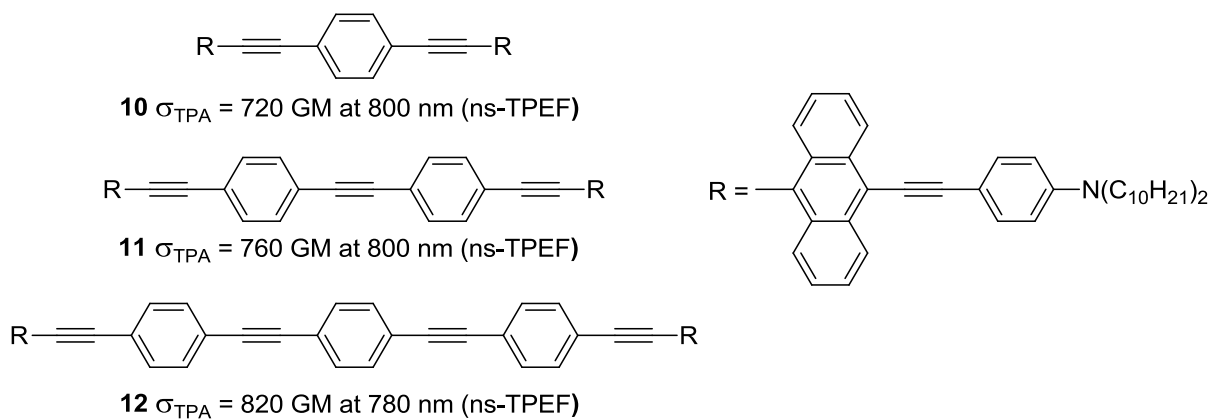


Chart 3: Effect of the increasing number of bridging units on the NLO response. a: ^[37]

1.4.2.2. Organometallic compounds

Similar observations can be made with organometallic molecules, which can be considered as hybrid structures between organic and inorganic. They often possess the synthetic versatility of organic compounds, the metal centres being considered as D or A, depending on their electronic structure. Literature data indicates that they tend to have higher NLO responses than the pure organics of comparable length as they possess more polarizable electrons. Selected examples can be seen in **Chart 4** with metal centres playing the role of donor substituent. Their molecular third-order NLO hyperpolarizabilities are reported in **Table 1**, but only the imaginary part (γ_{im}) should be taken in consideration for judging their TPA capability. Similar to organics, lengthening the π -system (**13** compared to **15** and **14** to **16**) and the change in symmetry lead to an increase in the NLO response (**17** and **18**, respectively, compared to **15** and **16**). Progressing from dipolar to octupolar results in a much larger than threefold improvement. Note also that a similar improvement is not seen for γ , illustrating that these structural variations impact the various NLO properties.

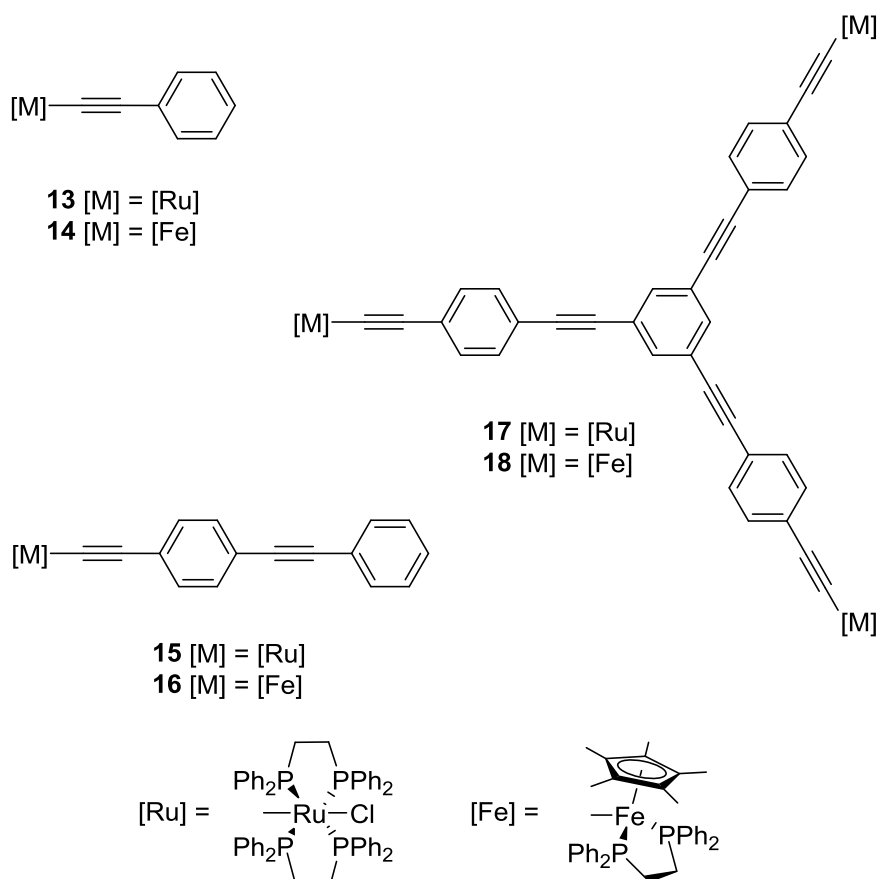


Chart 4: Examples of organometallic NLO-active compounds

Compounds	γ_{Re}	γ_{Im}	$ \gamma $	σ_{TPA}
13^a	-170 ± 40	71 ± 20	180 ± 45	17^{c}
14^b	110 ± 100	17 ± 10	110 ± 100	5.6 ± 3
15^a	-100 ± 100	450 ± 200	460 ± 200	110 ± 50
16^b	-1500 ± 1200	200 ± 40	1500 ± 1200	66 ± 15
17^b	-330 ± 100	2200 ± 500	2200 ± 600	530 ± 120
17^{3+ a}	13500 ± 3000	-4700 ± 500	14000 ± 3000	-1200 ± 100
18^b	-3300 ± 800	2800 ± 700	4300 ± 1100	920 ± 250
18^{3+ b}	-2000 ± 1000	-3300 ± 1000	3900 ± 1400	-1100 ± 330

Table 1: a: Measurements at 800 nm ^[38,39], b: Measurements at 695 nm ^[40], c: extrapolated from γ_{Im}

Metal centres can also be used as bridges, such as organoruthenium molecules recently used as nano-wires between gold electrodes.^[41–43] In addition, when they are electroactive, the metal centres of the molecule can be used as redox groups to switch on and off its NLO properties. Compounds **17³⁺** and **18³⁺** are good examples of oxidized compounds which possess different excited states than their neutral parents and thus have different NLO properties. Thus, their behaviour changes completely from the neutral state, in which they are two-photon absorbers, to saturable absorbers for the oxidized species, as evidenced by the change in sign of γ_{Im} .

Considering further the metal centres, there are other variations that can be considered such as changing the ancillary ligands or the metal itself. The change in the metal centre gives clear trends for second-order NLO properties, but related trends for third-order activities are still open to debate due to the lack of comparable data. The values suggest a positive trend going from gold to iron in the order $\text{Au} < \text{Ru} < \text{Ni} < \text{Fe}$, when γ values are compared.^[44–46] However, depending on the particular cubic NLO effect of interest, other trends might be found.^[45,47] For instance, comparing TPA for compounds **17** and **18** is not easy since the measurements have been carried out at a single wavelength regardless of the absorption maximum, which varies from ruthenium to iron. The ancillary ligand also has a significant impact on the cubic NLO properties. Thus, changing the coordination sphere leads to modifications of the NLO response as a function of the electron-withdrawing/releasing effects or depending on the number of polarizable electrons that the ligands bring. These effects have been reviewed several times by Coe or Humphrey and their coworkers.^[31,48,49] Compared to organic derivatives, the main drawback of organometallic derivatives, when air stable, is that they are often more absorbing in the UV-vis region, making them less transparent. This can be a problem for many NLO applications such as optical limiting.

1.4.2.3. Dendritic effects

Another category of molecules that is also of interest is dendrimers and polymers, as these architectures are closer to macroscopic size and thus to bulk materials. These structures usually possess a huge number of π -electrons and consequently exhibit third-order nonlinearities, which increase with generations and at a greater rate than expected based on the sum of their linear components.^[50–52] The cause of the phenomenon is not very well understood, but empirical results clearly reveal a more than ten-fold increase in the cubic NLO $\chi^{(3)}$ values for each generation for several types of organometallic dendrimers.^[50,53,54] In contrast, for organic dendrimers, the branching does not always have a positive effect: instead of cooperative (additive) enhancement, a weakening of the NLO response can sometimes be observed when progressing to the next generation. Symmetry breaking or interferences brought by the extra generation have been invoked to rationalize these observations.^[4,55]

1.4.2.4. Synopsis and new perspectives

To summarize, the more-active molecules for TPA also obey the general structural criteria delineated for cubic NLO effects which are to (i) possess an extended π -system, (ii) to be polarized with an overall quadrupolar (or octupolar) symmetry, and incorporating strong electron-donating and accepting groups at the periphery. The symmetry of the system is of great importance as this third-order NLO response follows most often an increasing trend from dipolar to quadrupolar to octupolar. The choice of the donors and acceptors as well as the bridging units has to be made in order to favour a good overlap between fragment orbitals, to ensure electronic communication. Finally, the chosen system has to be synthetically accessible. Evidently, depending on the targeted applications, additional considerations add to these general rules. As shown in the previous sections, organometallics also follow the same rules as organic molecules. The d^6 metals presented here can replace donors, due to their donating power but also can be used as bridging units. The synthetic versatility of metal alkynyl complexes allows for a great variety of compounds and structures, and is augmented by redox-switchability, with properties that can be tuned by varying the ancillary ligands at a metal centre in a given geometry. Finally, dendritic architectures open a further dimension in the quest for strong two-photon absorbers.

All these molecules and the related molecular materials possess advantages and drawbacks depending on the targeted application, and interest continues to grow, as evidenced with the increasing amount of data.^[11,16] Surprisingly, considering the number of molecular structures screened

so far, only a few papers have investigated the use of triphenylmethane (TPM)-based dyes, such as crystal violet (**CV**⁺), for their third-order NLO properties, in spite of the fact that this moiety (**Chart 5**) fulfils many of the structural criteria enumerated above (conjugated and multipolar structure, octupolar symmetry, etc.). In 1994,^[23] a computational contribution of Brédas and co-workers pointed out the huge potential for **CV**⁺ and related derivatives such as Malachite Green (**MG**⁺) to behave as remarkable two-photon absorbing materials in the NIR range, a spectral domain appealing both from the perspective of telecom-based and medicinal applications. However, despite the obvious promise of this type of compound and the numerous investigations concerned with the second-order NLO properties of **CV**⁺,^[27,56,57] little research has been devoted to investigate the two-photon absorption properties of TPM-based dyes. In the next paragraphs, we will now briefly outline the synthesis and physico-chemical properties of these fascinating molecules, followed by a review concerning the rare reports of their third-order NLO properties.

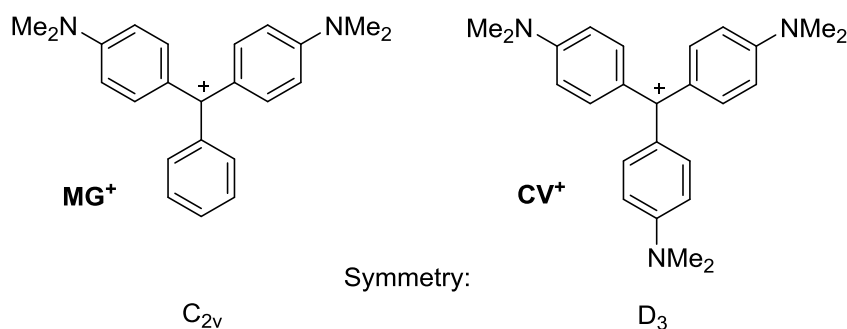


Chart 5: Crystal violet (**CV**⁺) and Malachite green (**MG**⁺)

2.Triphenylmethane dyes

2.1. General comments

Triphenylmethane (TPM) dyes and more generally triarylmethane (TAM) dyes form a large and diversified family of compounds, not so much for their structures as for their properties and applications (**Chart 6**). They were amongst the first organic commercial dyes to be used by the textile industry and they have also spread to fields like medicine, probing and even catalysis.^[58] Due to these widely diversified uses, TPM dyes are often found in waste waters. Given that some of these derivatives have been found to be carcinogenic and genotoxic, the accent in current research is directed at ways to detect and remove them from many industrial processes.^[59–62] However, as mentioned above they have generated increasing interest in the field of nonlinear optics, as their unique structure and properties make them good candidates, especially for applications based on third-order NLO properties.

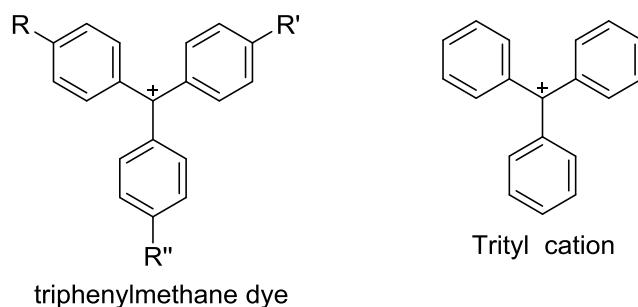
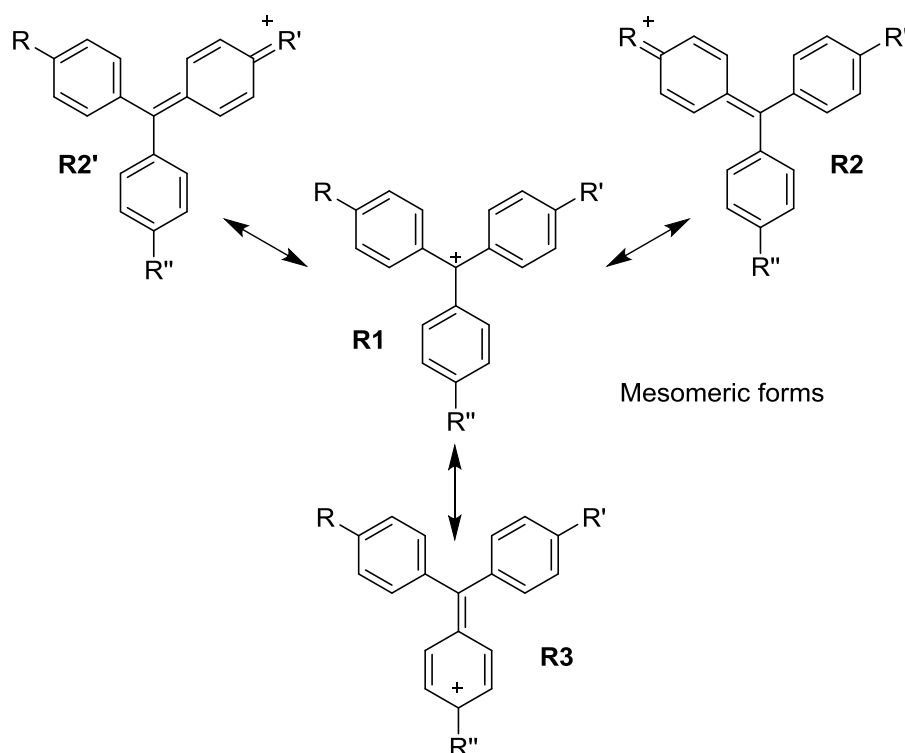


Chart 6: Examples of TPM-based carbocations

TPMs are related to the structure in **Chart 6**, a substituted tritylcation, the latter being the first isolated poly-aromatic carbocation (in 1901).^[63–65] Carbocations are usually poorly stable as they are strong electron-accepting groups and therefore highly electrophilic. For example, the trityl carbocation is air, moisture and light sensitive due to its high electrophilicity. Most of the carbocations used in chemistry are less stable. As a result, most often they are only considered as reaction intermediates which can only be isolated at low temperature.^[66] The instability of carbocations has been widely investigated and their use as reaction intermediates has allowed great progress in organic synthesis from academia to industry. Well-known reactions involving carbocations are, for example, polymerization processes or the formation of branched hydrocarbons, or more common reactions, like the pinacol rearrangement and Friedel-Crafts alkylation. For a full overview of the uses of carbocations in synthesis or catalysis, one can consult the recent review from Naredla *et al.* or the book from Olah and Prakash.^[67,68] Note that typical "non-stabilized" carbocations are far too reactive to be interesting in the context of this work, as the stability and robustness of TPMs is much higher. This stability is a prerequisite for "usable" compounds in solution under high laser intensities.

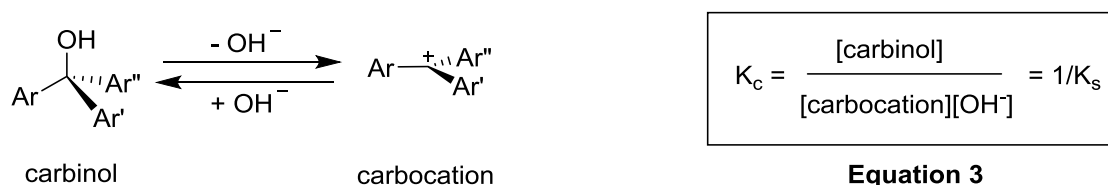
In TPM derivatives, the presence of the phenyl groups, sometimes supplemented by electron-releasing groups such as amines, as in **CV**⁺ or **MG**⁺, tremendously increases their stability. Thanks to charge delocalization, as exemplified by the different mesomeric forms of **Scheme 1**, such dyes can be manipulated, to some extent, as classical organic compounds. More generally, the stability of TPM-based dyes strongly depends on the number and π -donating power of the different R groups. Accordingly, each structural variation of the peripheral substituents will strongly influence their electronic structure, stability and properties, and can potentially lead to uses in widely different applications.



Scheme 1: CV^+ - or MG^+ -type carbocations and associated mesomeric forms

2.2. Solvolysis

In TPM-based dyes, peripheral donors are essential to stabilize the positive charge. This stabilization, due to charge delocalization, is crucial for obtaining long-lived carbocationic species, as these species are quite reactive. Their stability is often evaluated by the rate constant of solvolysis, generally by hydroxyl ions originating from traces of water (**Equation 3**).^[69,70] This reversible reaction takes place with water, under alkaline conditions or, for the less stabilized TPM-based dyes, in polar solvents like alcohols.^[71] As a result, TPM dyes can be used as pH indicators. For example, the ionization constant ($\text{p}K$) of MG^+ is 6.90 and this carbinol is 100% ionized at pH 4.0, 50% at pH 6.9, 25% at 7.4 and 0% at pH 10.1.^[72] This means that in most applications, in polar media at neutral pH, TPM dyes are actually mixtures of carbinols and carbocations. Formation of the carbinol is most often responsible for the colour fading, as the carbinol is most often colourless, no longer possessing a sp^3 -hybridized central carbon, and thereby reducing electron delocalization and shifting the electronic absorption into the UV range.



Scheme 2: Carbinol solvolysis equilibrium

2.3. Remarkable optical properties

With respect to the geometrical criteria favouring NLO properties listed above, the structures of **CV**⁺ and **MG**⁺, which combine a carbocation in the centre, one of the strongest acceptors, with several amino groups at the periphery, one of the strongest donor groups, though conjugated 1,4-phenylene bridges, should favour third-order NLO activity. In the case of **CV**⁺, where R = R' = R'', the octupolar geometry should also confer relatively strong quadratic NLO properties. **Chart 6** displays the symmetry of crystal violet **CV**⁺(C₃) and malachite green **MG**⁺(C₂), which will constitute the model reference compounds for this work. **CV**⁺ is comparable to functional triphenylboron derivatives in terms of electronic properties and NLO response. While these molecules are isoelectronic and isostructural, their chemistry is quite different; boron derivatives are quite sensitive and often require the use of bulky aromatic groups, such as mesityl, to ensure sufficient stability for NLO studies.^[29,30,73]

A characteristic feature of TPM-based carbocations is their strong absorption bands (~10⁻⁵ L mol⁻¹ cm⁻¹ around 600-700 nm) in the visible/NIR region, the primary reason why they have been used as dyes. Most of the measurements of TPM-based dyes have been carried out in solution and therefore potentially result in a mixture of carbinols and carbocations, if water is present and if the pH is not controlled (**Scheme 2**). Moreover, many measurements in the literature were carried out starting from the corresponding carbinol in concentrated acid solution, to form the desired carbocation *in situ*. The absorption spectrum of the resulting solutions exhibit an acid concentration dependency.^[74,75] When the pH is not controlled, these conditions do not always allow characterization of the TPM dyes to be performed since, in addition to carbinol, extra-protonation of amines leading to unstable polycarbocationic species can occur. Indeed, in highly acidic media some extra-protonated species are observed and undergo further reaction leading to rapid loss of colour of the media.^[76]

TPM-based dyes usually exhibit fast non-radiative deactivation leading to poor fluorescence in solution. This fluorescence deactivation effect has been extensively studied; it results from twisted intramolecular charge transfer (TICT) processes and can be counter-balanced when the aminophenyl rotational motions are restrained. Thus, some fluorescence can be restored at low temperature, in

very viscous media, or via chemical modifications to properly rigidified derivatives (such as, for instance, in rhodamine derivatives, as we shall see later on).

TPM-based dyes have been used in many other applications other than dyeing. Non-rigidified derivatives were sometime used as viscosity probes, and they form fluorescent aptamers with DNA or RNA, which makes them perfect candidates for imaging or *in vivo/vitro* visualization.^[77] Crystal violet **CV**⁺ and malachite green **MG**⁺, which possess good bio-compatibility, are probably the most popular choices for such applications. **CV**⁺ derivatives have also been extensively used in biology as coloured markers (for instance to differentiate Gram+ and Gram- cell types), while **MG**⁺ has been employed as an antiseptic agent.^[78,79] Another recent interest is TPA, as described below, and such dyes can generate TPA in the NIR region, a strategic wavelength range for telecommunications or in medical application. Finally, in line with their fast relaxation properties and multiphoton-absorption properties, TPM-based dyes have also been used for the generation and optical rectification of sub-picosecond laser pulses.^[58]

2.4. Nomenclature and examples

The relatively large presence of TPMs across many fields is not always noticed due to the various names that each derivative possesses in everyday life. Indeed, four different methods are used to name these dyes and several different commercial designations exist for the same TMP dye. This clearly does not help when it comes to list all the uses of a given chemical. The first two proposed nomenclatures derived from their colour or were related to their use as dyes, and are listed in the Colour Index^[80] or designated by their IUPAC name^[81]. The CAS Registry Number has allowed a standardization of names but the commercial names remain for most of them, and more than one name can still be found for a single TPM carbocationic derivative. **Table 2** lists some classical TPM dyes and their different names. The IUPAC name is not listed as it is quite lengthy and most often inconvenient to use, compared with the more common names or the CAS number which fully describes the molecule.^[82,83] For example, the IUPAC name for the chloride salt of crystal violet is tris(4-(dimethylamino)phenyl)methylium chloride, and for malachite green the IUPAC name is 4-[(4-dimethylaminophenyl)phenylmethylium]-*N,N*-dimethylaniline chloride.

#	C.I. generic name	C.I. constitution number	CAS registry number	Possible commercial name or usual names
CV⁺	Basic violet 3	C.I. 42555	548-62-9	Crystal violet, methyl violet 5BO
19	Basic violet 4	C.I. 42600	2390-59-2	Ethyl violet, ethyl violet AX
20	Basic violet 14	C.I. 42510	632-99-5	Magenta, fuchsine, fuchsin
21	Acid violet 19	C.I. 42685	3244-88-0	Acid fuchsine S, acid magenta, acid rubin
22	Acid green 9	C.I. 42100	4857-81-2	Brilliant acid green B, merantine green B, xylene fast green 6B
23	Basic green 1	C.I. 42040	633-03-4	Brilliant green, diamond green G, fast green JJO
MG⁺	Basic green 4	C.I. 42000	569-64-2	Malachite green, Victoria green B

Table 2: Examples of TPM and their different names

Chart 7 shows the chemical structures of the compounds in **Table 2**. In everyday life applications, TPM dyes can be found as their (so-called) “acid” or “basic” structures. The basic structure is zwitterionic and neutral, such as for **21** and **22**, while the acid structure corresponds to a pair of ions with the chromophore unit a cation, the counter anion being most of the time inorganic, such as for **CV⁺**, **MG⁺**, **19-20** and **23**.

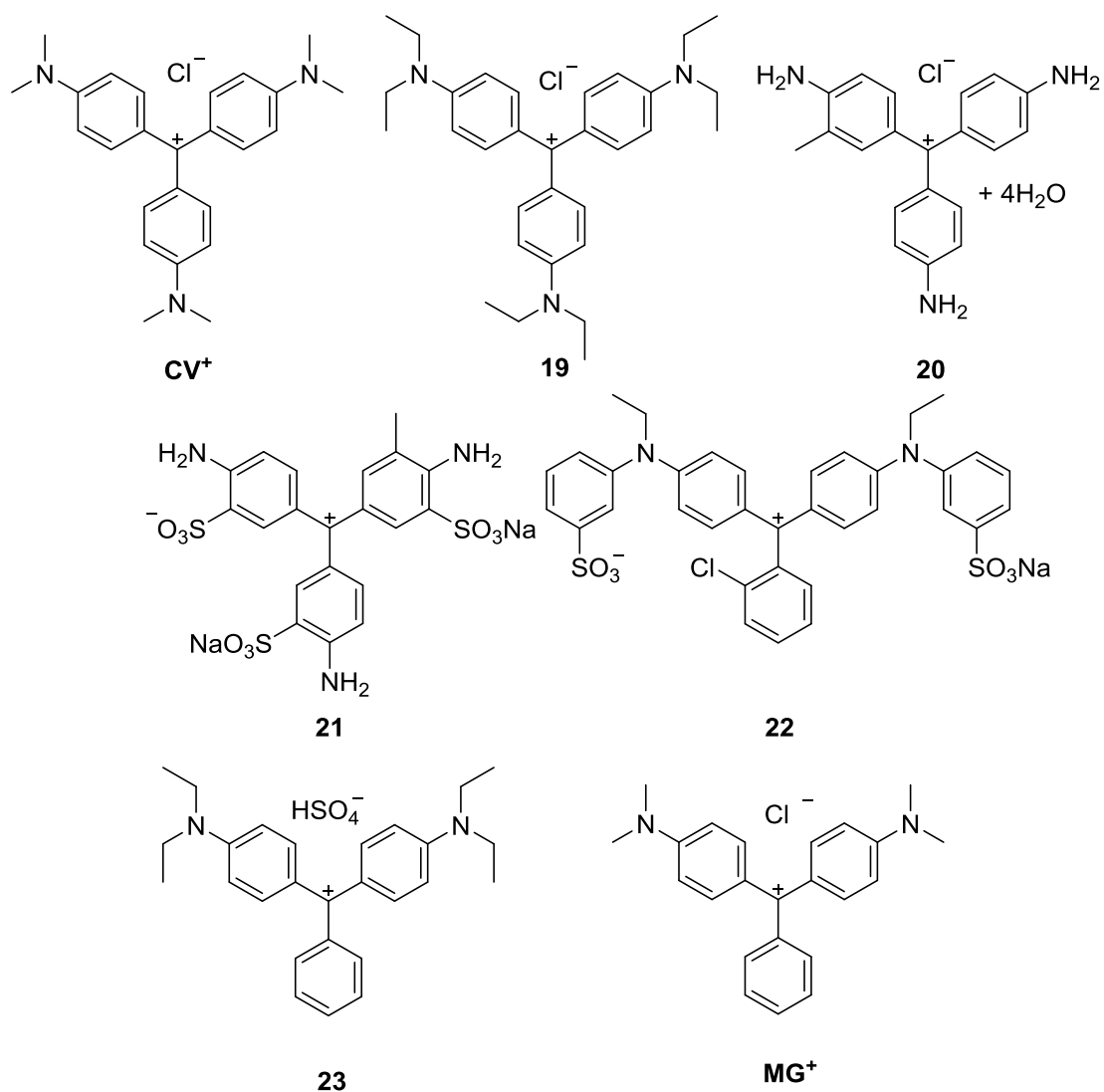


Chart 7: Selected examples of TPMs

Other related derivatives worth mentioning here, as they correspond to important TPM-dye precursors, are the leuco-TPMs and carbinols (**Chart 8**). Both species are neutral molecules possessing a coordinatively saturated central carbon atom. Leuco-TPMs have a hydrogen substituent on the central carbon whereas carbinols have a hydroxyl group. For **MG⁺**, for instance, **MG^H** and **MG^{OH}**, respectively, will correspond to the leuco-MG and to the corresponding carbinol.

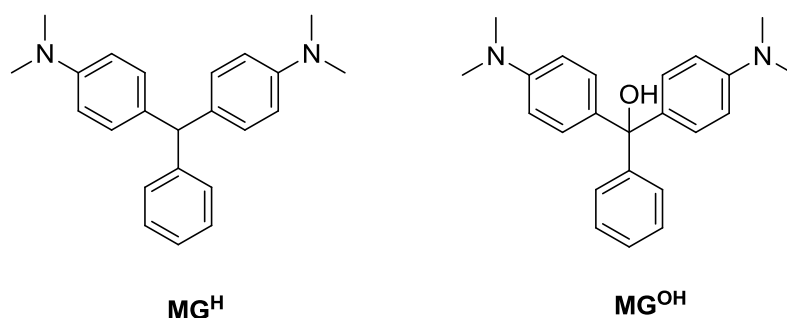
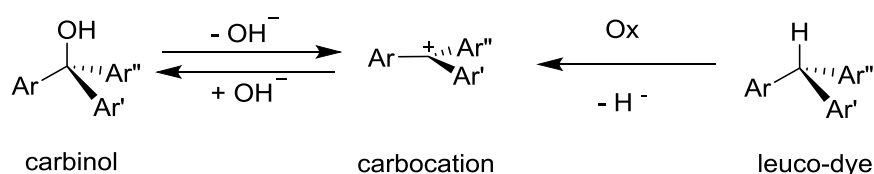


Chart 8: Leuco-dye and carbinol of MG^+

3. TPMs: synthesis and physico-chemical properties

3.1. Synthesis

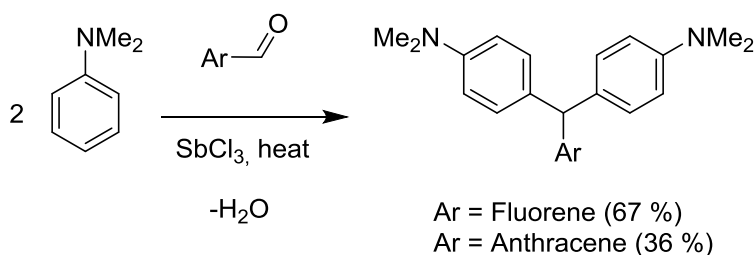
TPM dyes have been extensively used in the textile industry and biology, and consequently several pathways have been developed to synthesize these compounds. Depending on the symmetry of the dye and its functionalization, the synthetic pathways can vary, but all of them proceed through carbinol or leuco-dye intermediates (**Scheme 3**). These precursors lead to the desired carbocations by addition of oxidant, such as DDQ or PbO_2 , followed by acid for the leuco-derivatives, and by addition of protons (acidic solution) for the carbinols, as the hydroxyl group is very labile in e.g. MG^{OH} (**Chart 8**). Both synthetic approaches can in principle be used to access a given carbocation, but carbinols are far more sensitive when the peripheral substituent groups are strongly donating (e.g. amines). Leuco-dyes were extensively used in the early development of this chemistry^[84,85] but nowadays the preferred pathway proceeds through carbinol intermediates, since carbocations are easily generated from these species. In contrast, for leuco-dyes harsher oxidizing conditions are always required which most often results in lower yields. This is probably why the carbinol route is most often used when applications are targeted, as there can be high-purity requirements for the carbocationic species (see part 2.3).^[77,86]



Scheme 3: Carbocation formation from carbinol and leuco-dye

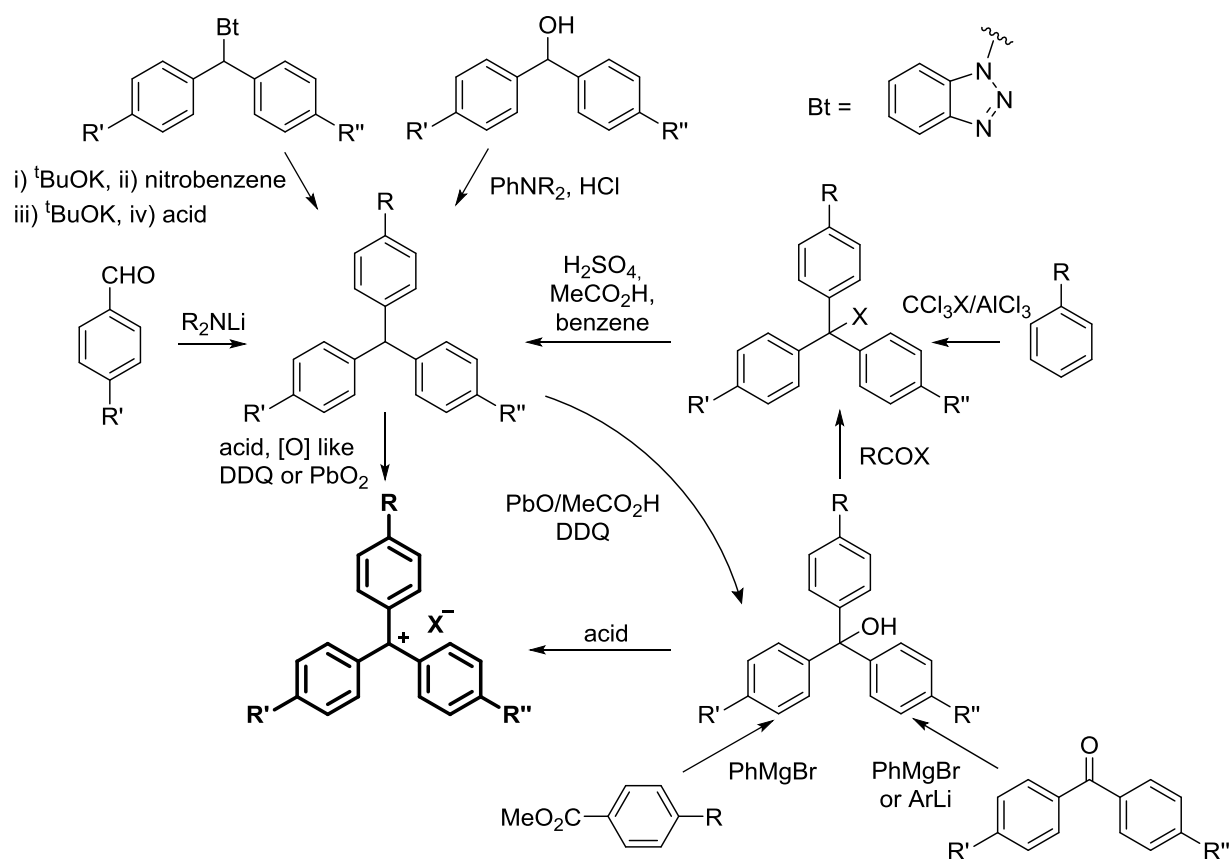
Scheme 5 summarizes the different routes that can be found for obtaining TPM-based carbocationic derivatives. Most of them can be extended to TAM-based derivatives. Carbinols are

usually formed by addition of a Grignard or lithiated reagent to a ketone, and have usually higher yields and allow more diversity than the corresponding leuco-based pathways.^[77,87] The latter are usually obtained by aromatic electrophilic substitution in acidic media. Quite recently, catalysts have greatly improved the range of the precursors that can be synthesized. Thus, Lewis acids like FeCl₃,^[88] ytterbium triflate,^{[89][90]} SbCl₃,^[91,92] or palladium catalysts^[93–95] facilitate the isolation of leuco dyes from a range of commercially available precursors, such as aromatic ketones (like benzophenone and its derivatives), under smoother reaction conditions. For instance, a remarkable tandem regioselective electrophilic aromatic substitution reaction is given in **Scheme 4**.



Scheme 4: Lewis acid-catalyzed synthesis of new leuco dyes

Other less common catalysts have been used for related reactions e.g. o-benzenedisulfonimide and a nickel catalyst combined with a chelating leaving group,^[96] or NbCl₅.^[97] Nickel catalysts have also been used to form enantio-enriched non-symmetrical leuco-dyes.^[98] Some aspect of this recent work can be found in the comprehensive review of S. Mondal *et al.* which focuses on diaryl- and triaryl-methanes.^[99] Alternatively, the use of diarylmethane precursors with new leaving groups such as, for instance, benzotriazole (Bt) has allowed the introduction of electron-withdrawing groups, like nitro groups, onto one of the phenyl rings of leuco dyes. However, for many of these new leuco dyes, conversion to the carbocation has not been attempted, and therefore no information is available regarding their propensity to behave as useful intermediates. For fully symmetrical (octupolar) TPM dyes, fully symmetric precursors are required. In this respect, reactions involving dimethyl carbonate, triethyl orthoformate or even chloroform with arene nucleophiles are often used.^[65,100]



Scheme 5: Common synthetic routes to TPM dyes

Thus, while the general synthetic routes to TPM-based dyes have not really changed since the early stages of industrial chemistry, significant progress and improvements have nevertheless been made in the range of precursors available and in the reaction procedures, driven by requirements from either the textile industry or biology. Many of these new derivatives have been studied for their photophysical properties. However, these studies have mostly been focused on linear optical properties, supplemented by some investigations into second-order NLO properties since the 1990s, but much remains to be done regarding their third-order NLO properties, as shown in the following paragraphs.

3.2. Photophysics of TPMs

3.1.1. Electronic absorptions

As mentioned before, one of the main characteristics of TPMs is their strong absorbance in the visible region. The high molecular extinction coefficients make them powerful dyes. The spectral features are directly related to their structure, substituents and to the environment of the dye, each of these factors inducing changes in extinction coefficient or wavelength. The modifications

induced by structural changes on the absorptive properties have been listed and rationalized mostly in an empirical way, as the excited-state manifold of TPM dyes is not fully understood.^[101] Their excitation and relaxation processes have been intensively debated for the last seventy years. Charge-transfer (CT) transitions from the peripheral electron-rich arms to the carbocationic centre are expected with this kind of structure. Depending on the overall symmetry, exclusion rules predict the existence of two distinct transitions at low energy in the D_3 case (as considered in this paper), one of them being allowed and doubly degenerate and the other forbidden, and three distinct ones in the C_2 case, one among them also being forbidden. However, for some derivatives, the forbidden band can sometime be weakly observed in D_3 symmetry and similar number of transitions might therefore be observed in each case.

Figure 8 shows the spectrum of MG^+ and CV^+ , our reference compounds for this work. They have an absorption maximum (λ_{max}) at lowest energy around 590 nm for CV^+ and 625 nm for MG^+ and exhibit rather intense bands (ϵ ca. $10^5 \text{ L.mol}^{-1}.\text{cm}^{-1}$). An important point to note is the shoulder appearing on the optical absorption bands for both compounds on their lowest energy side. Despite several theories, it still remains unclear which phenomenon is at the origin of these shoulders. This shoulder can either arise from a partially resolved vibronic structure or could result from another electronic transition overlapped with the main one. In the second case, this new transition might originate either from a conformer or from another closely related species generated from the pure starting compound, such as an adduct with itself (exciplex or excimer) or with the solvent. The hypothesis of a vibronic structure was rapidly eliminated since at low temperature the expected increase in resolution for the fine structure was not observed. Instead, the shoulder is decreasing, suggesting an independent species as the explanation. Also, the behaviour upon dilution was not supportive of the formation of a weakly bonded self-adduct (oligomer) in solution forming an exciplex as the origin of the second band.

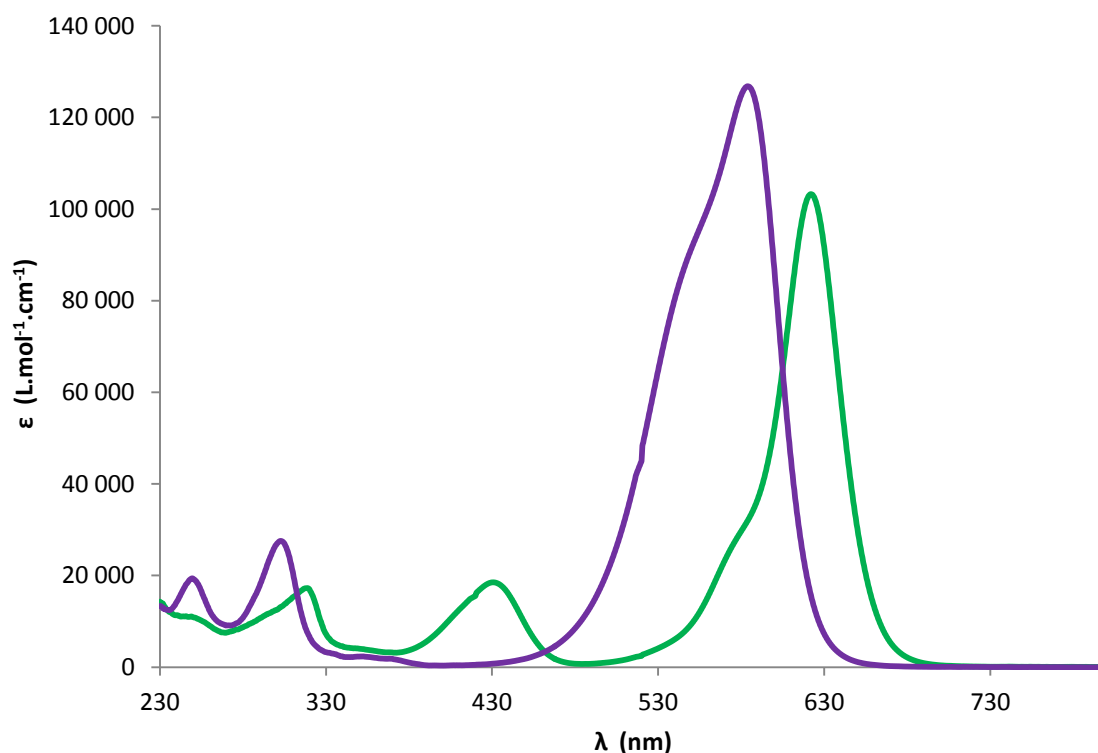


Figure 8: CV^+ (purple) and MG^+ (green) spectra in DCM

One of the first interpretations for this second species was proposed by Lewis and co-workers. According to these researchers there is an equilibrium between two rotational conformers, one with a propeller structure (D_3 symmetry) and the other with a less symmetric conformation (C_2 symmetry) (**A**; **Figure 9**).^[102] This was supported by the fact that the intensity of the shoulder diminishes at low temperature and in low polarity solvents, suggesting that an equilibrium was operative between the two species at the origin of the different peaks. However, up to the early 1990s, this C_2 conformer of CV^+ had never been observed and several calculations had demonstrated that such a distorted isomer would not lead to a stable species corresponding to a minimum in energy. Based on these statements, McHale proposed that the shoulder was due to a symmetry breaking-deformation (**B**; **Figure 9**) induced by the solvent, the dye itself or even the counter ion.^[58] The last-mentioned, interacting with one of the amino groups, was expected to lift the degeneracy of the degenerate S_1 excited state of the original octupolar structure.^[103] Note that, as mentioned above, a lowering of the symmetry of the absorbing species from D_3 to C_2 will change the number and energy of the first allowed transitions in the case of CV^+ . Maruyama later proposed that the shoulder on the low energy side of the transition stemmed from a "solvation isomer", featuring a solvent molecule "coordinated" to the central carbon atom (**C**; **Figure 9**) in rapid equilibrium (~ 500 fs at 295 K) with the non-coordinated species. This solvation isomer would have its central carbon out of plane with an overall C_3 symmetry due to the

solvent molecule interacting with the central carbocation. Unfortunately no experimental observations of such solvent adducts have ever been reported so far.^[104–106]

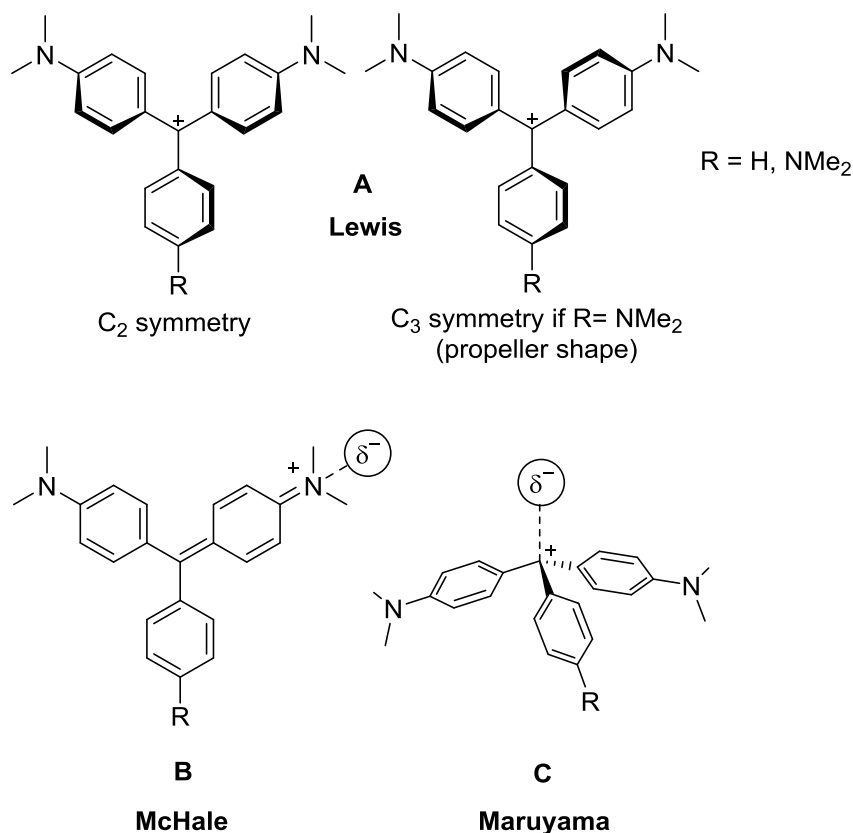


Figure 9: Envisaged structures for the second species at the origin of the shoulder on the first allowed absorption band of **CV**⁺

In 1999, Lovell and coworkers reviewed this topic and, with the help of new crystallographic data (co-crystallization of **CV**⁺ with phthalic acid) and additional calculations, proposed that any of these adducts (**B** and **C**) were indeed conceivable, but proposed that the latter forms in the excited state and not in the ground state (i.e. as excimers, but formed with the solvent), somewhat supporting Murayama's hypothesis.^[107] However, they could not definitively eliminate the possible existence of a less symmetrical adduct in the ground state similar to that proposed by McHale (**B**). In favour of the presence of these two species in solution was the fact that the calculated ground states were quasi iso-energetic ($\Delta G < 1 \text{ kcal mol}^{-1}$) and these species could therefore easily isomerize at room temperature.

While this contribution clarified the problem, it did not end the debate. Thus, more recently, Ghanadzadeh *et al.* in 2007, with measurements in liquid crystal matrices, obtained evidence that solute-solute interactions (ion pairing or dye aggregation) were influencing the main band and that anisotropic solvation had an even larger influence on the observed shoulder.^[108] In 2008, Loison and

co-workers carried out single molecule measurements and only observed a single band, strengthening the fact that the second absorption band indeed originates from a different species and not from a vibronic structure or a true excimer.^[109] This also eliminates the hypothesis of a spontaneous Jahn-Teller distortion, as the shoulder would still have been observed.^[110] Thus, the environment must be responsible for the shoulder and there is clear evidence that the appearance of the shoulder originates from intermolecular interactions as well as the broadening of the lowest energy peak. Furthermore, with new calculations following geometric optimizations, Loison and coworkers rehabilitated the hypothesis of an adduct with a molecule of water interacting with the central carbocation.^[109] While such a proposal found additional support in the very recent work of Macovez and co-workers,^[111] the existence of a less symmetrical structure for this adduct also found computational support from Terenzani and coworkers.^[57] It now seems that some consensus has been reached in the shoulder originating from a second species of lower symmetry formed in the medium due to interaction with either the counter-anion or solvent. However, whether this adduct has a structure closer to that proposed by McHale (structure **B**) or Mukayama (structure **C**) has not been definitively clarified.

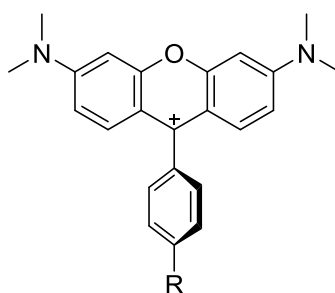
3.2.2. Relaxation processes

In parallel to the investigations related to the absorption spectra delineated above, the relaxation behaviour of TPMs was also extensively studied. **Figure 10** shows a general representation of TPM dye relaxation processes subsequent to excitation into their two singlet states at lowest energy. Different experiments were conducted throughout the twentieth century and different theories were proposed to rationalize these phenomena. Most TPM dyes present a fast (sub pico-second) non-radiative relaxation process and become fluorescent (and sometime) phosphorescent only in a viscous medium or/at low temperature, with a viscosity dependency from 0.33 % to 0.66 % and up to 35% fluorescence for some TPMs, which explains their use as sensors and probes.^[112] Rigidification of the system by the formation of dimers, aggregates or even incorporation in a matrix, has the same effect. It has also been proven that there is a solute concentration dependency of the fluorescence, *i.e.* the concentration of the dye influences its relaxation behaviour.^[113] This is not really surprising since TPMs are known to form aggregates at high concentrations, opening intermolecular non radiative deactivation pathways. Finally, chemical rigidification of the chromophore also partially restores their fluorescence.

In addition to their first excited state, TPM dyes can also fluoresce from a second allowed excited state S_2 , making TPMs some of the few organic molecules that are exceptions to Kasha's rule.^[114] Accordingly, for \mathbf{CV}^+ , two-photon fluorescence from $S_2 \rightarrow S_0$ has been observed.^[115] It is

interesting to note that for D_3 molecules like **CV**⁺ the first excited state is doubly degenerate, and hence the S_1/S_2 gap is lower in energy than in less symmetrical dyes such as **MG**⁺ due to stronger excitonic coupling. This difference favours radiative relaxation from the second excited state S_2 for **MG**⁺. However, this explanation based on energy differences in the GS has to be nuanced since for more symmetrical molecules, S_2 fluorescence might also be favoured by the symmetry lowering in the excited states, as mentioned in the previous paragraph.

In line with all these observations, the relaxation from the first excited state S_1 is believed to involve a conformational relaxation through an intermediate state S_x preceded by a fast solvent vibrational relaxation.^[116,117] The S_x state and the non-radiative relaxation pathway taken by the molecule were considered as corresponding to a twisted intramolecular charge transfer (TICT) state which corresponds to a distorted version of the first excited CT state S_1 . It is thought to be formed via the torsional motion of one of aminoaryl groups in the S_1 (or S_2) excited states, since both processes exhibit a viscosity dependency.^[118–122] The importance of charge transfer in these processes can be nicely illustrated by another recent investigation concerning the relaxation pathways of the dimethylamino derivatives of rhodamine (**Chart 9**). The aminorhodamine is not fluorescent unless protonated. It is believed that the protonation of the amine cuts down the charge transfer process to the phenyl ring upon excitation, which is responsible for the non-radiative relaxation, resulting in recovery of the fluorescence of the molecule. This constitutes another experimental evidence that the rapid non-radiative relaxation pathway of TPM dyes is initiated by an internal charge transfer to the amino group, dissipating the excited-state energy.^[123] Very recently, Li and co-workers investigated the relaxation times from S_1 for **MG**⁺ and its leuco and carbinol precursors via transient absorption,^[124] and proposed a detailed picture of the S_x intermediates (**Figure 10**) in line with such an interpretation.



R = H, rhodamine
R = NMe₂, aminorhodamine

Chart 9: Rhodamine and aminorhodamine

Older studies by Yoshizawa *et al.* have highlighted the fact that there is also a direct relaxation pathway from S_2 to S_0 .^[125] Researchers have discussed at length the possibility of conical intersection between either $S_2 \rightarrow S_1$ or $S_1 \rightarrow S_0$ ^[126] and even both at the same time^[127,128] involving the twist of the aminophenyls as the contributing vibrational motion. A recent paper from Laptanok *et al.* shows that $S_2 \rightarrow S_1$ and $S_1 \rightarrow S_0$ are dependent on the solvent viscosity, while relaxation from the Franck-Condon state corresponding to S_2 is viscosity independent for **MG**⁺. Thus, $S_2 \rightarrow S_0$ is the preferred relaxation pathway for that dye.^[129] This last observation has also been verified for other TPM dyes functionalized with bromides and hydroxyl groups.^[130] Finally, in some derivatives, S_2 was shown to undergo an unusual intersystem crossing (ISC) to T_2 and phosphorescence from this triplet state was also evidenced, revealing a fairly complex photochemistry.^[131]

The relaxation dynamics of TPM dyes are clearly complex and the current lack of experimental investigations on these compounds, as pointed out by Grabowski *et al.*, does not help in obtaining a comprehensive picture of the precise role of TICT for all derivatives.^[132] Nonetheless, the recent papers tend to agree on some points. The first excited state S_1 seems to relax via a conical insertion to an intermediate state S_1 that is a TICT state, which decays to the ground state by either simultaneous rotation of the substituted phenyls in a frontward or backward fashion or by rotation of only one substituted phenyl. The exact way the charge is spread around the molecule upon excitation is still not known. The higher excited state S_2 may also involve a conical insertion to S_1 , but it is probably not the preferred pathway. Regarding the luminescence of these compounds, it has been shown that rigidification of the system might favour the radiative decay of S_1 and increase their fluorescence quantum yield under ambient conditions. The excitation of S_2 and fluorescence from this state might also be observable in some cases.

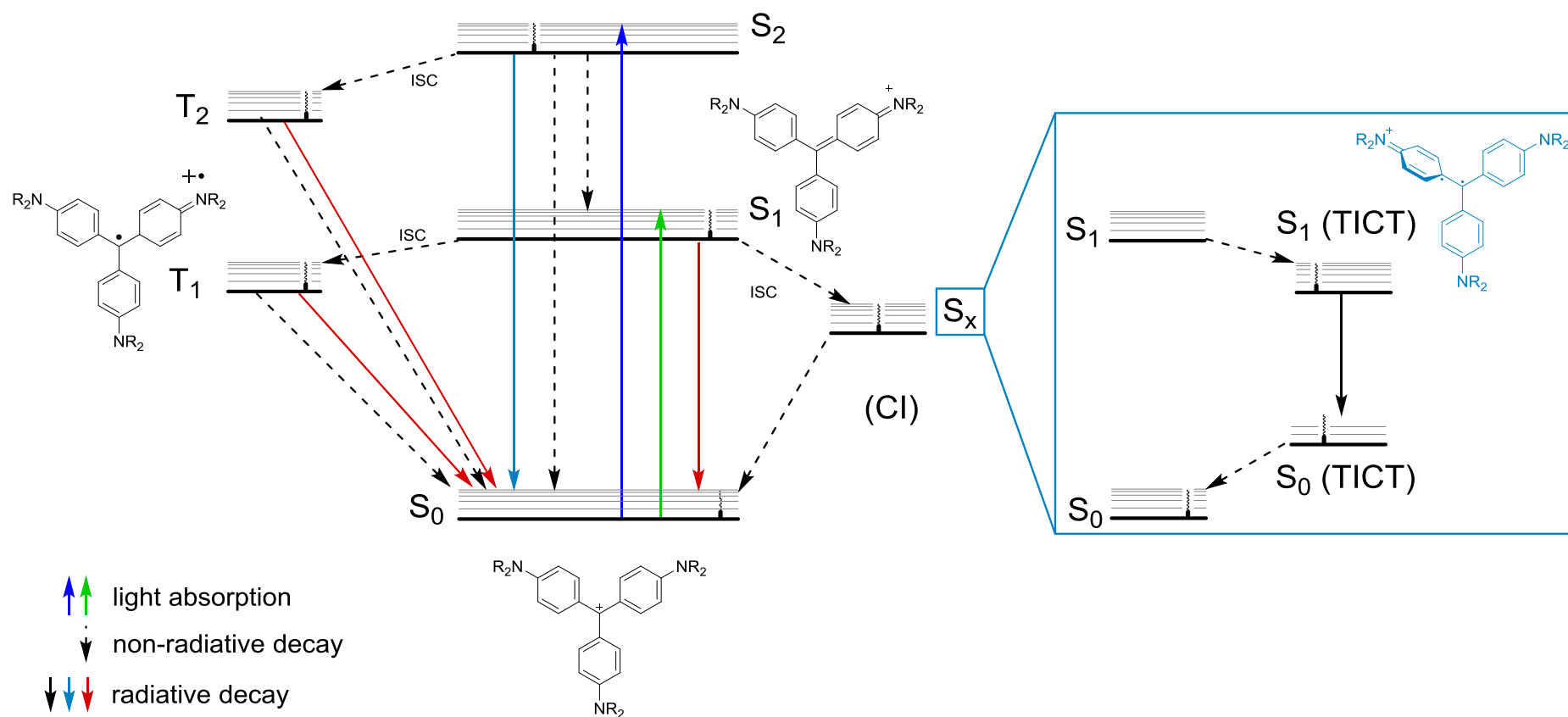
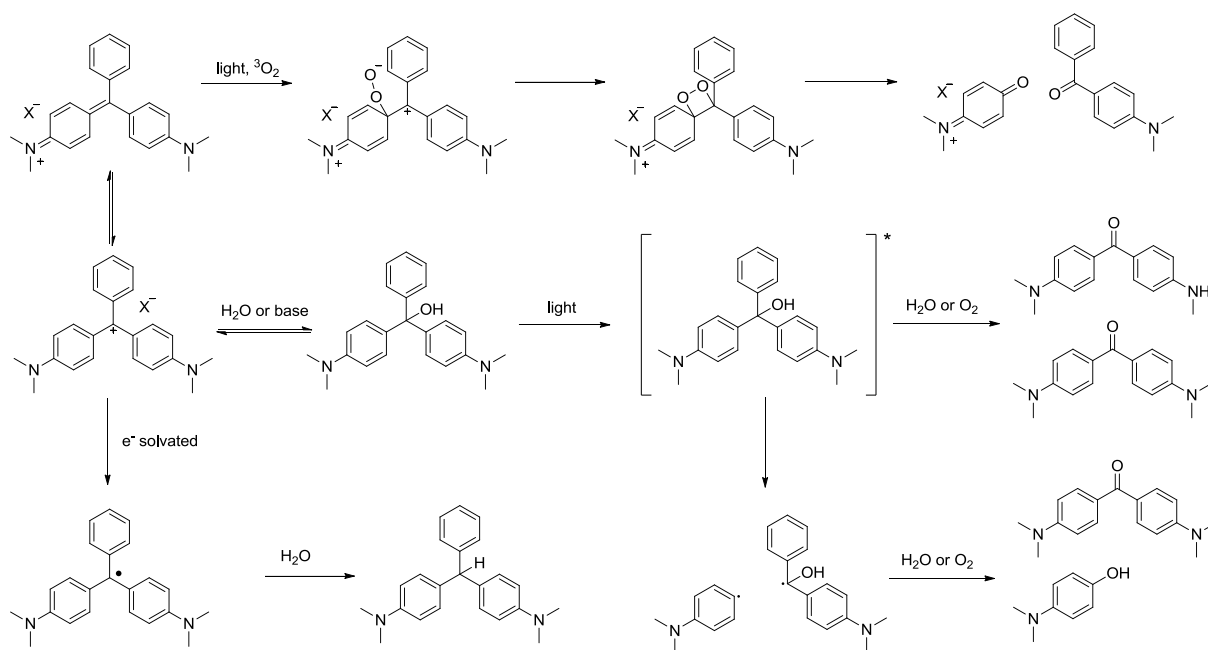


Figure 10: Commonly accepted excitation and relaxation pathways for symmetric (D_3) TPM dyes

3.3. Photochemistry

While much more stable than non-stabilized carbocations, TPM dyes can nevertheless decompose under various conditions. Driven by their use in the textile industry, these carbocationic species have been extensively studied in the context of dye fading, which was demonstrated to depend on the type of medium on which the dyes are deposited and on their exposure to light under different conditions.^[58] As previously mentioned, nucleophilic addition of H₂O in the ground state contributes to this phenomenon in polar media at neutral pH. However, it has also been shown that TPM dyes can undergo reactions when excited by light, or exposed to heat, oxygen and various chemicals. It was also stated that the rates of these detrimental photo-reactions, which are mostly irreversible, strongly depend on the stability of the carbocation in the ground state. A dependency on concentration has also been demonstrated, in line with the existence of self-reaction in the excited state.

Photo-oxidation and photo-reduction are commonly observed transformations with TPM dyes in powdered form, in solution or even when incorporated into a medium. Known side-reactions under light irradiation are N-dealkylation processes, conversion to ketones, radical formation and carbinol formation. These reactions are provoked by singlet oxygen or hydrogen donating solvents. They always lead to colour fading, as the resulting products are no longer charged. The central carbon of the former dye is now sp³-hybridized, cutting down any π -delocalization, resulting in a shift of the strong electronic absorption responsible for their characteristic colour into the UV range. The formation of singlet oxygen under light exposure has also been investigated but appears to be only a minor photochemical process compared to the afore mentioned ones. Indeed, most often, triphenylmethane dyes will behave as oxidizing agents in their excited state(s). This phenomenon also happens even under anaerobic conditions. It has been observed on protein substrates like wool. The active species is suggested to be the triplet state, based on photo-reduction of **CV**⁺ usually occurring with immobilized dyes on substrates, which have a greater propensity to decay via their excited triplet states due to motional restrictions limiting their relaxation via TICT states. **Scheme 6** gives an overall picture of these detrimental photochemical processes in the case of **MG**⁺.



Scheme 6: decomposition pathways for MG^+

4. Literature review of the cubic NLO properties of TPMs

TPM dyes have interesting structures with the potential for exhibiting cubic NLO properties, as they possess an octupolar or nearly-octupolar geometry, with three phenyl rings linked to a sp^2 carbocation, one of the best organic acceptor groups. This carbocation is stabilized by peripheral amino substituents, which are also good donor groups within a multipolar donor/acceptor layout of dipoles. However, as mentioned previously, their third-order nonlinearities have not been extensively investigated so far and the existing reports mostly relate to commercial derivatives.

Thus, Brédas *et al.* in 1994 were the first to mention TPMs and notably CV^+ as promising materials for third-order nonlinear optics. For this dye, they calculated a TPA value of 350 GM, which is comparable to that of C_{60} despite the fact that CV^+ possesses three times less π -electrons.^[23] As mentioned before, the diversity of setups and the various ways of measuring the NLO performance, allied to the scarcity of data concerning their NLO properties, did not allow a straightforward evaluation of their potential for various applications related at that time. Nevertheless, this investigation clearly revealed the interest of such compounds for third-order nonlinear optics. The following paragraph reviews the literature concerning third-order measurements conducted on TPM dyes. **Chart 10** displays the TPM dyes encountered for the diverse measurements.

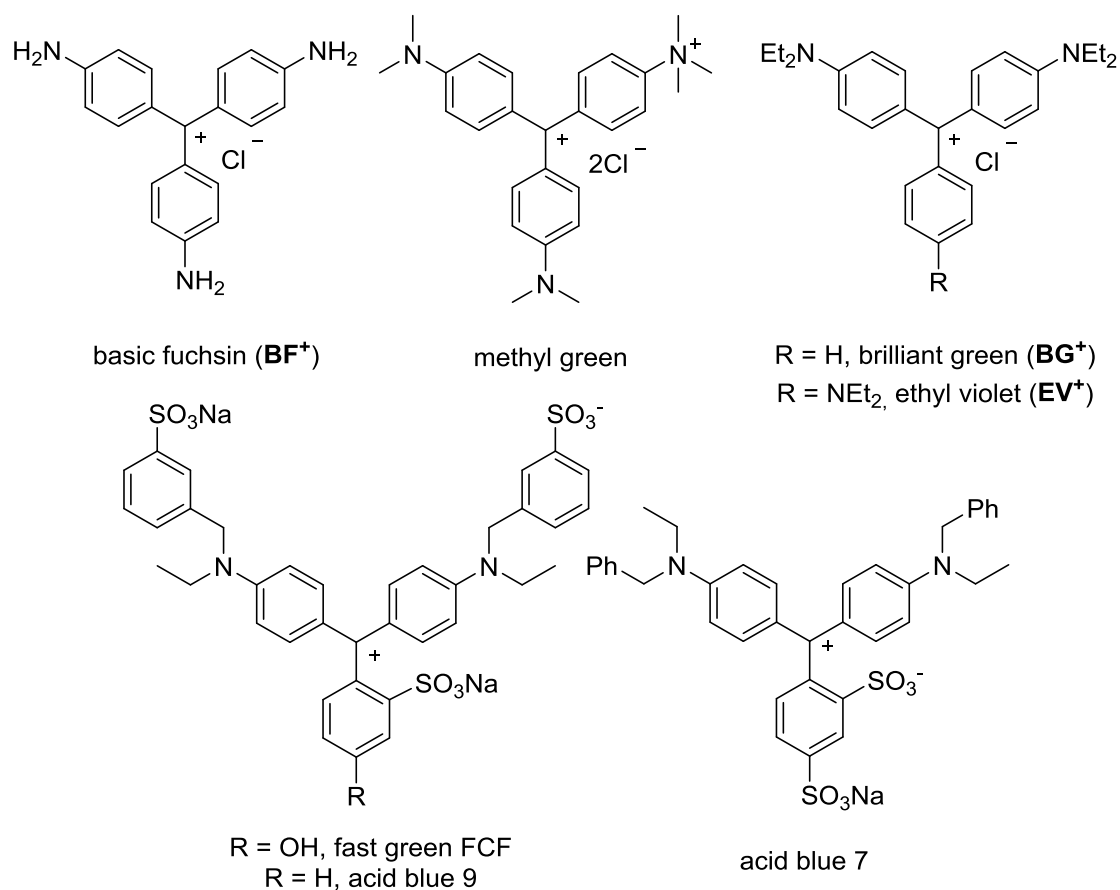


Chart 10: TPM dyes measured for their third-order NLO properties

4.1. THG and DFWM measurements

THG, Third Harmonic Generation, also called frequency tripling, is a phenomenon where the frequency and therefore the energy of the incoming beam is tripled by passing through the NLO-active material. Studies with doped films or polymer matrices containing TPM dyes have been commonly performed thanks to their easy fabrication.

Basic fuchsin BF^+ , CV^+ , MG^+ and ethyl violet (EV^+) have been measured in PMMA films [poly(methylmethacrylate)] with a proportion of 30 wt%. $\chi^{(3)}$ values of $\sim 10^{-12}$ esu were found for these films, comparing well with values obtained for organic NLO-phores of the same size previously tested following the same technique. The measurements were done with a tunable laser in the range of 900-1600 nm; however, the set-up used did not allow measurements below 900 nm where a major TPA band seems to exist.^[133,134]

Polymeric films of CV^+ and **24** (Chart 11) were next measured for their THG capability in the same polymer. Extrapolated molecular cubic hyperpolarizability (γ) values of 2×10^{-33} for CV^+ and of

30×10^{-33} esu for **24** were found at 1907 nm. At that time, the latter value was one of the highest reported values for γ at these frequencies. The UV-vis spectrum of **24** is quite similar to that of CV^+ (8 nm difference, the extended compound being slightly red-shifted) and possesses the same spectral characteristics, however, the values obtained are at different wavelengths, and the *in situ* protonation of one of the amine groups of **24** biases the results.^[135]

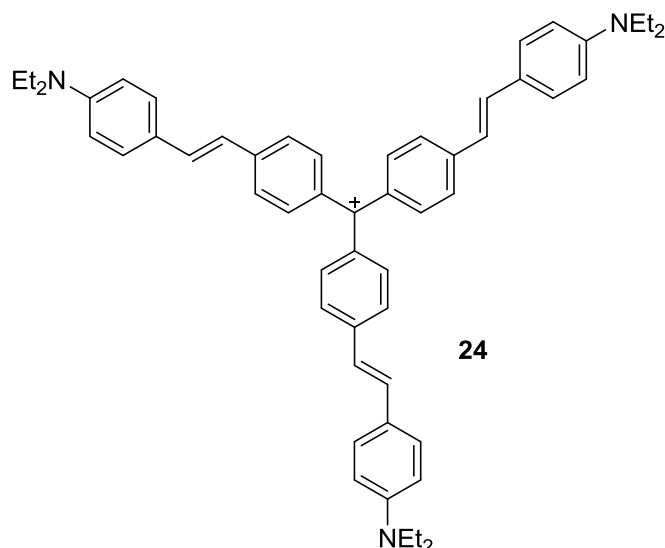


Chart 11: Extended crystal violet

Subsequently, Palanisamy *et al.* measured the third-order NLO coefficients of a series of TPM dyes that included acid blue 9,^[136] brilliant green (BG^+)^[137] and methyl green (**Chart 10**)^[138,139] in doped gelatine films using degenerate four-wave mixing (DFWM) at 633 nm. DFWM is a technique, where three laser beams from the same laser source are synchronized on a NLO material generating a fourth one with an intensity proportional to the square of $\chi^{(3)}$ and the intensities of the three incoming beams. $\chi^{(3)}$ values were not reported (nor was the concentration); only the percentage of phase conjugation being given. While revealing an interesting cubic NLO activity, these measurements are not very useful for a comparison to other molecules, since no relevant values were communicated.

4.2. Z-scan measurements

Palanisamy and coworkers have also done measurements on basic fuchsin (BF^+ ; **Chart 10**) in methanol solutions as well as in PMMA matrices using Z-scan at 532 nm. They reported $\chi^{(3)}$ values of 3.38×10^{-6} esu in solution and 3.53×10^{-5} esu in films, both at 0.4 mM.^[140] Under the same conditions, acid blue 7 (**Chart 10**) has been measured at 633 nm giving a $\chi^{(3)}$ value of 8.37×10^{-6} esu.^[141]

Solutions of fast green FCF (**Chart 10**) in water have also been measured by Z-scan in order to determine their optical limiting power, a phenomenon due to both ESA and TPA, and in gelatine films to determine their four-wave mixing capability at 632 nm. However, it is not clear which of the phenomena was dominant, and only output values were given for the measurements.^[142] The nonlinear refractive index of acid blue 9 (**Chart 10**) has also been measured using this technique and highly self-defocusing (negative value) power was evidenced.^[143] Even if no TPA values were measured here, there is a strong correlation between materials with high nonlinear indexes and their two-photon absorbing capabilities.^[144] Optical limiting properties of **BF**⁺ in PMMA^[145] and doped **MG**⁺ films at 532 nm^[146] have been also measured with this technique resulting in a modification of n_2 from $0.1 \times 10^{-8} \text{ cm}^2 \cdot \text{W}^{-1}$ to $3.2 \times 10^{-8} \text{ cm}^2 \cdot \text{W}^{-1}$ with concentrations increasing from 10^{-5} to $2 \times 10^{-4} \text{ mol/L}$ also proving their third-order nonlinear interest.

Two other groups have measured **BG**⁺ with the Z-scan technique in solution at 632.8 nm and found $\chi^{(3)}$ values of $1.16 \times 10^{-3} \text{ esu}$ in a water/ethanol solution at a concentration of 0.42 mmol/L^[147] and $4.10 \times 10^{-7} \text{ esu}$ at a concentration of 0.05 mmol/L in aqueous solution.^[148] When corrected for concentration, the values are very different, although similar set-ups were used here. These discrepancies seems too large for invoking nonlinear solvatochromism and might rather be explained by self-aggregation or photo-induced decomposition of the dye.

4.3. TPEF measurements

Subsequent to the review of Brédas *et al.* in 1994, the first experimental observation of TPA for **CV**⁺ was reported by Chui *et al.*, in 1998, who tried to find a way to suppress the corresponding fluorescence in order to perform HRS measurements of the hyperpolarizability of that compound at 1064 nm.^[149]

While TPA-induced fluorescence was mentioned in this work, the first measurement of TPA cross-sections for TPM dyes was only reported in 2002 on brilliant green (**BG**⁺; **Chart 10**) and **CV**⁺. A cross-section of 762 GM (at 840 nm) was found for **BG**⁺, which is very similar to that of **MG**⁺, and a cross-section of 1980 GM (at 752 nm) was found for **CV**⁺. Note that these TPA peaks occur at twice the wavelength of the second lowest energy transition for these TPM dyes. These values have been obtained by TPEF in glycerol and there is a rather good match with their calculated values: 2041 GM for **CV**⁺ and 852 GM for **BG**⁺.^[150] However, these values have to be taken carefully as these compounds have relatively low fluorescence quantum yields under ambient conditions (3.07 % for **CV**⁺ and 1.85 % for **BG**⁺) and very concentrated solutions were used to determine their TPA cross-

sections by TPEF, resulting in more than 40 % error on these measurements. Moreover, the calculated TPA cross-sections are also not very reliable for such large compounds. These initial results seem to be confirmed by a more recent paper by Brédas and co-workers in which the full visible spectral range is covered by TPA. These TPEF measurements have been supplemented by non-degenerate-TPEF measurements. This alternative technique suffers from the same problems previously encountered with **CV**⁺ and **BG**⁺ and pertaining to their low fluorescence yields. **BG**⁺ could not be measured using this technique.^[151] The calculated σ_{TPA} maximum values found are ca. 1700 GM for **BG**⁺ and 100 000 GM for **CV**⁺ values, quite far away from experimental values from Beljonne's paper. This full spectral range measurement has now revealed that the two lowest energy transitions were indeed active in TPA, but the lowest energy transition is far less active than the second-lowest one. In line with selection rules operative for octupolar molecules, the transition at lowest energy, which has the highest extinction coefficient, is the less active in the two-photon spectrum for both **CV**⁺ and **BG**⁺.

4.4. Synopsis

TPM-based dyes have proven to be active third-order NLO compounds. However, the few third-order NLO measurements reported for TPM dyes do not afford a complete picture of their potential for NLO-related applications, especially considering the absence of standardization between experimental measurements performed in the different studies, although promising results have been shown for two-photon absorption. These molecules are synthetically readily accessible, as demonstrated by the many derivatives commercially available, and they also present a great structural versatility owing to the great flexibility associated with their syntheses. However, their poor fluorescence complicates the study of their TPA capabilities by TPEF and has possibly discouraged more detailed investigations until now. This lack of data and interest is illustrated with the recent review of Pawlicki *et al.*^[16] which, albeit referencing the most studied/promising two-photon absorbers, completely overlooks Brédas and co-worker's seminal work on these compounds, without any mention of **MG**⁺/**CV**⁺ derivatives or even carbocationic TPM species.^[150,151] **MG**⁺ and **CV**⁺ derivatives possess a real potential as two-photon absorbers in the NIR range, and measuring the NLO spectral dependence of appropriate derivatives should lead to a better knowledge of their NLO properties. Considering organometallic derivatives of TPMs, the situation is even more extreme; while some have indeed been synthesized and shown to possess similar linear optical absorptions to purely organic derivatives, to the best of our knowledge they have not been probed for their cubic NLO activities.

5. Objectives

In order to determine structure-cubic NLO property relationships of TPM dyes, relevant modifications will be performed on the carbocationic core of **CV**⁺ or **MG**⁺ derivatives. Firstly, structural variations will be introduced in a series of organic compounds related to **MG**⁺ and their TPA properties will be measured by Z-scan. Secondly, selected organic donor group(s) will be replaced by organometallic synthons. Relative to organic donors, these redox-active groups should enhance the NLO response, but could also potentially allow switching of these NLO properties.^[31] As model cores, both **CV**⁺ and **MG**⁺-based structures have their advantages: the latter ones have less symmetrical structures and, albeit potentially less active than the latter ones, will allow determination of how a given structural modification on the third branch impacts the molecular properties, whereas **CV**⁺ based ones, requiring all modifications to be fully symmetrical, will probably give rise to the most active structures. These structural modifications will be implemented so that they do not lead to unstable carbocations. Overall, **MG**⁺-based derivatives will help to understand the influence of the third branch on the TPA cross-sections, whereas **CV**⁺-based derivatives will provide information on the symmetry of the system.

5.1. Organic derivatives

One essential factor for a TPA-active compound is to have an extended π -system. In **MG**⁺ or **CV**⁺, this latter is not extremely well developed. Hence, the first modification that was envisioned is to use diphenylamine instead of dimethylamine as donor group (**Figure 11**) for the reasons mentioned in paragraph 1.4.1., *i.e.* despite being less donating, arylamines are often more effective donors than dialkylamines for TPA. Then, the phenyl group constituting the third branch can, for example, be replaced by more extended aromatic fragments that might play the role of “antennas” towards light. Thus, anthracene or fluorene, which are already well known TPA absorbing groups, will be tested in this work.^[16] However, given that the bulkiness of the 9-anthracenyl fragment might disfavor planar conformations which are desirable to enhance the electronic π -communication within the three branches of the molecule, the insertion of an ethynyl linker between the carbocation and the third substituent will also be performed. This modification should in principle ensure planar conformations and the possibility of probing the influence of π -conjugation in these derivatives.

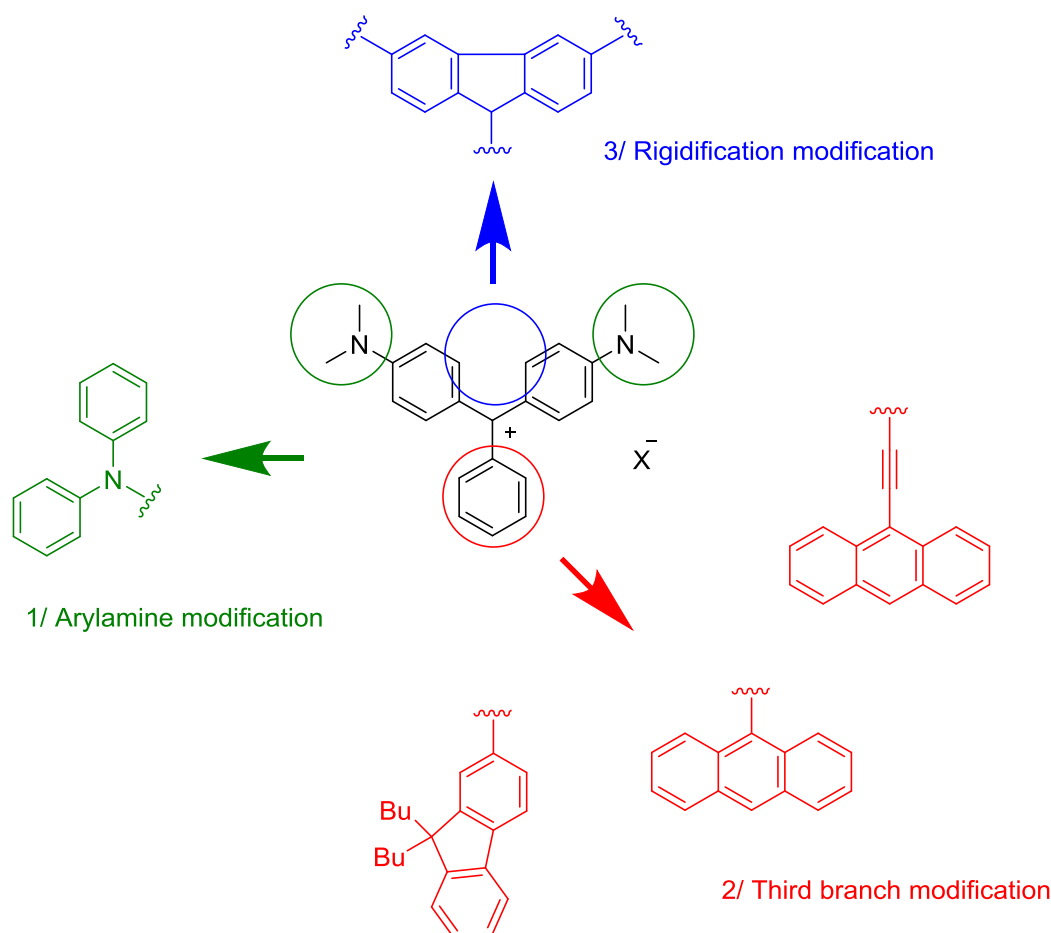


Figure 11: Envisaged modifications for MG^+

Finally, some rigidified compounds for which the two amine-substituted phenyl groups are linked in a co-planar conformation with the central carbocation have been targeted. We hope that this fluorene-like rigidification of the π -system will somewhat restrain the non-radiative relaxation and favour fluorescence. In this respect, and despite its interest, rigidification of the dialkylamino analogue has been removed for synthetic reasons and we have focused our efforts on the previous structural modification in order to obtain a first overview of the properties of these systems before envisioning further changes. All these structural modifications should bring a first insight into the cubic NLO properties and, more precisely, the TPA properties of TPMs of these carbocations. Enhancing their fluorescence would provide an alternative mean to measure their TPA cross-sections by TPEF and would extend their scope for various applications, such as imaging for instance.

For CV^+ , the replacement of dimethylamines by diphenylamines will lead to the compound shown in **Figure 12**. The other structural modifications tested on the third branch of MG^+ derivatives are not applicable here, since they would remove amino groups, resulting in less stable compounds, while a related rigidification of CV^+ would lead to a really constrained, and probably less stable, structure.

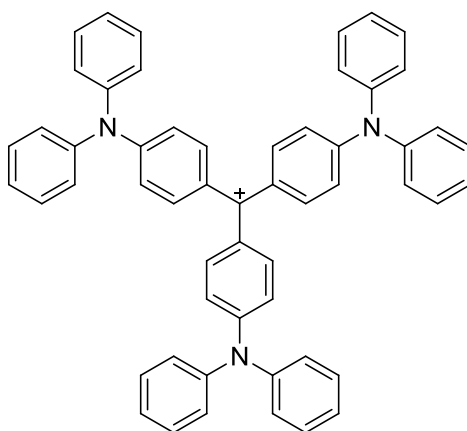


Figure 12: Envisaged modification for **CV⁺** derivative

5.2. Organometallic derivatives

In the same way, some organometallic derivatives will next be targeted where one or several amino groups will have been replaced by organometallic redox-active centres. These metallic cores have been chosen because of their potential NLO benefits, as well as their redox-switching properties. The organo-iron and organo-ruthenium alkynyl groups «Fe(η^5 -C₅Me₅)(κ^2 -dppe)C≡C» and «Ru(Cl)(κ^2 -dppe)₂C≡C» previously presented, as well as the ethynylferrocenyl unit were retained for these purposes (**Chart 12**). Indeed, several NLO-active derivatives have already been made using these synthons and show enhanced third-order NLO responses compared to related all-organic analogues, as well as remarkable redox-switching properties.^[31]

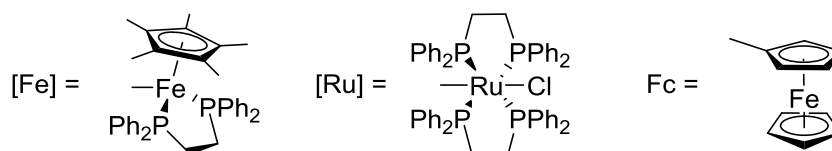


Chart 12: Selected organometallic synthons

All these organometallic derivatives are isolobal d⁶ group 8 metals in *O_h* or pseudo-*O_h* environments, even if their ancillary ligands are quite different and do not allow a straightforward comparison between them. Their diversity will allow assessment of a wide panel of modifications during this screening. First, they present distinct redox potential values (**Table 3**) and will allow

switching over a large potential range vs. SCE: [Fe] derivatives will most likely exhibit a negative oxidation potential, which results from the high electron density brought by the Cp*, whereas those of [Ru] and Fc should be nearly similar. However in Fc, the metal is not directly bonded to the alkyne, and therefore comparison between the latter set will allow assessment of the influence of having the alkynyl bridge directly connected to the metal centre.

Compound	$E_{1/2}$ (Fe ^{II} /Fe ^{III} or Ru ^{II} /Ru ^{III})
[Fe]Cl	-0.22 ^a
[Fe]C≡C-Ph	-0.11 ^a
[Ru]Cl	+0.60 ^b
[Ru]C≡C-Ph	+0.55 ^b
FcC≡C-H	+0.72 ^c
FcC≡C-Ph	+0.67 ^c

Table 3: a: CH₂Cl₂, [ⁿBu₄N][PF₆], 0.1 M, 20 °C relative to SCE calibrated with ferrocene at 0.460 V, Pt electrode, sweep rate 0.100 V.s⁻¹; ^[152] b: CH₂Cl₂, Pt auxiliary and working Ag/AgCl reference electrodes (FcH/FcH⁺) located at 0.56 V, ΔEp = 0.06 V; ^{[153][154]} c: CH₂Cl₂, [ⁿBu₄N][PF₆], 0.1 M, 20 °C. Pt. ^[155]

These potentials are also directly related to their stability in air. Thus organo-ruthenium alkynyl complexes or ethynylferrocenyl derivatives are stable in air whereas iron derivatives decompose quickly upon air exposure. Accordingly, ferrocenyl units have already been used in former work to overcome the organo-iron(II) instability and access air-stable derivatives.^[156] However, the reverse situation holds for the corresponding oxidized M(III) species, rendering the corresponding ethynyl ferrocenyl- and ruthenium alkynyl complexes more reactive than their relative organoiron counterparts.^[157]

In addition, ruthenium alkynyl complexes will offer the advantage of further possible functionalization *via* formation of bis-alkynyl derivatives, leading to larger π-conjugated molecules. In particular for *D*_{3h} systems, an extension of the system will lead to dendritic assemblies for which large NLO responses can be anticipated. A dendritic NLO effect for bis-alkynyl ruthenium complexes has been noted by Humphrey and coworkers, as mentioned in the precedent paragraphs.^[50]

In order to investigate the impact of these organometallic end-groups, we will first start with studying unsymmetrical **MG**⁺-based derivatives. The same approach as for the organic derivatives will be followed: first modification of the unsubstituted phenyl ring will be attempted (**Figure 13**). This

modification will allow incorporation of an "external" switching units on **MG**⁺. Two structural modifications will be attempted for each of these organometallic endgroups, either direct replacement of the phenyl ring by one of them, or attachment of these endgroups to the para-position of the phenyl ring. These systematic changes will permit assessment of the influence of the spacer between the metal centre and the carbocation on their properties. Subsequently, replacement of the dimethylamino groups by diphenylamino units will also be examined.

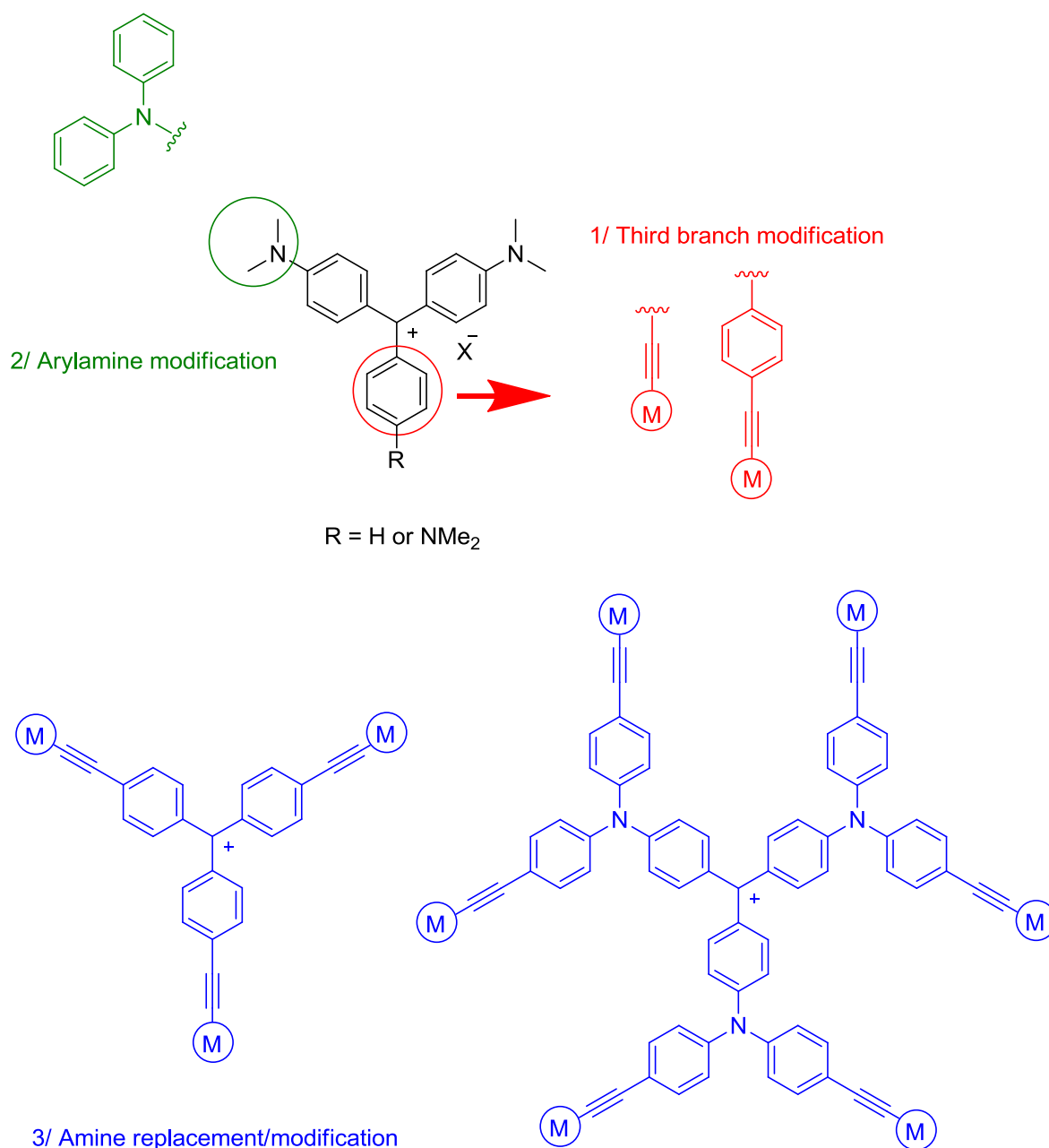


Figure 13: Envisaged modifications for organometallic derivatives

For the more symmetrical CV^+ core, again, only two modifications were envisioned: the first one consists of a direct replacement of all the amino donor groups by one of the organometallic donors previously tested, and the second one consists of appending this organometallic donor to the peripheral rings of diphenylamino-based derivatives, leading to a pseudo-dendritic species having six metal centres. While these organometallic substituents would interact directly with the carbocation in the first case, they would “tune” the donor power of the diphenylamino donors in the second case. Both families of compounds should exhibit redox-switchable NLO properties, since this time, oxidation will affect the donor power of all the peripheral groups, either directly (first compound targeted) or indirectly (second compound targeted).

6. Conclusion

Nonlinear optics is a growing field of research due to its multiple phenomena and numerous potential applications in various highly technological domains. It is believed that the development of nonlinear molecular devices will allow real progress to be made from medicine to data storage and data processing, with advantages and properties surpassing the current materials. TPA affords many appealing properties for various applications in these fields, such as a remarkable spatial resolution and the possible involvement of less energetic light beams. These have led to several applications such as imaging, micro-fabrication and optical computing. Since its theoretical prediction by Maria Goeppert-Mayer in 1931, much progress has been made and more effective two-photon absorbers are developed every year since the start of this century. Initiated with purely inorganic or organic compounds, the fundamental interest in this field is moving now to organometallic derivatives as these compounds might bring the best of both sides. For such investigations, the group 8 metal alkynyl complexes are good candidates that offer considerable scope for structural variations. The development of active TPM-based organometallics that permit redox-switching will involve understanding the interplay of complex electronic processes for which preliminary studies of model complexes will be required.

Accordingly, the work plan presented in here follows from results obtained by the groups of F. Paul and M. G. Humphrey who investigated the NLO properties of group 8 metal alkynyl complexes. Given the potential of the well known dyes crystal violet and malachite green as third-order NLO-phores, it is of interest to generate organometallic analogues of these compounds with improved cubic NLO responses. Consideration will be given to symmetry-related issues: some structures possess an octupolar geometry and may therefore be more active than others. Malachite

green with reduced symmetry is much more synthetically amenable to various modifications and constitutes a better model to understand the effect of a given particular structural modification.

The aim of the project will be, firstly, to confirm the potential of such TPM-based derivatives as TPA-absorbers from synthesis and study of a judicious series of organic compounds analogous to **CV**⁺ and **MG**⁺ and, secondly, to screen a series of related organometallic derivatives where the peripheral amino donor groups are selectively replaced by redox-active alkynyl complexes. The envisioned modifications of the organic core involve the replacement of dimethylamino donors as well as rigidification of the system and replacement of the phenyl ring by various π -conjugated units. Depending on the results obtained, organometallic derivatives consisting of " $\text{Fe}(\eta^5\text{-C}_5\text{Me}_5)(\kappa^2\text{-dppe})$ ", " $\text{Ru}(\text{Cl})(\kappa^2\text{-dppe})_2$ " or ferrocene end-groups will subsequently be developed and tested as two-photon absorbers, before studying the redox-switching properties of these systems.

Accordingly, the first chapter concerns the synthesis of organic derivatives of **MG**⁺ and **CV**⁺ featuring the previously discussed structural variations, their physico-chemical characterization, and the study of their TPA response *via* Z-scan studies.

The second chapter focuses on related organometallic derivatives with the introduction of one metal-alkynyl centre, either directly connected to the central carbon or *via* a phenyl linker. The synthesis and the spectral characterization of these compounds will be discussed as well as the influence of the metal oxidation on the spectral features.

Finally, the last chapter will deal with the synthesis and characterization of fully symmetric star-shaped organometallic derivatives based on **CV**⁺. In the same way, the synthesis of these polynuclear structures will be described as well as their spectral features. The effect of oxidation on their properties will be also discussed.

References

- [1] I. R. Whittall, A. M. McDonagh, M. G. Humphrey, M. Samoc, *Adv. Organomet. Chem.* **1999**, *43*, 349–405.
- [2] C. W. Spangler, M. He, E. G. Nickel, J. Laquindanum, L. R. Dalton, N. Tang, R. Hellwarth, *Mol. Cryst. Liq. Cryst. Sci. Technol. Sect. Mol. Cryst. Liq. Cryst.* **1994**, *240*, 17–23.
- [3] M. G. Kuzyk, K. D. Singer, G. I. Stegeman, *Adv. Opt. Photon.* **5** **2013**, 4–82.
- [4] F. Terenziani, C. Katan, E. Badaeva, S. Tretiak, M. Blanchard-Desce, *Adv. Mater.* **2008**, *20*, 4641–4678.
- [5] A. I. Ciuciu, D. Firmansyah, V. Hugues, M. Blanchard-Desce, D. T. Gryko, L. Flamigni, *J. Mater. Chem. C* **2014**, *2*, 4552–4565.
- [6] C. Katan, S. Tretiak, M. H. V. Werts, A. J. Bain, R. J. Marsh, N. Leonczek, N. Nicolaou, E. Badaeva, O. Mongin, M. Blanchard-Desce, *J. Phys. Chem. B* **2007**, *111*, 9468–9483.
- [7] O. Mongin, L. Porrès, M. Charlot, C. Katan, M. Blanchard-Desce, *Chem. – Eur. J.* **2007**, *13*, 1481–1498.
- [8] C. Sissa, V. Parthasarathy, D. Drouin-Kucma, M. H. V. Werts, M. Blanchard-Desce, F. Terenziani, *Phys. Chem. Chem. Phys.* **2010**, *12*, 11715–11727.
- [9] N. Bloembergen, *Nonlinear Optics: Lecture Note and Reprint Volume*, Benjamin, **1965**.
- [10] E. Garmire, in *Nonlinear Opt.* (Ed.: N. Kamanina), InTech, **2012**.
- [11] G. S. He, L.-S. Tan, Q. Zheng, P. N. Prasad, *Chem. Rev.* **2008**, *108*, 1245–1330.
- [12] M. Rumi, J. W. Perry, *Adv. Opt. Photonics* **2010**, *2*, 451.
- [13] F. Kajzar, J. Zyss, *Nonlinear optics and Quantum optics* **2012**, *43*, 31–95.
- [14] H.-B. Sun, S. Kawata, in *NMR • 3D Anal. • Photopolymerization*, Springer Berlin Heidelberg, **2006**, pp. 169–273.
- [15] A. Ostendorf, B. N. Chichkov, in *A New Approach to Micromachining* (Ed.: Laurin Publishing), Photonic Spectra **2006**.
- [16] M. Pawlicki, H. A. Collins, R. G. Denning, H. L. Anderson, *Angew. Chem. Int. Ed.* **2009**, *48*, 3244–3266.
- [17] Z. Hu, V. S. Khadka, W. Wang, D. W. Galipeau, X. Yan, *J. Mol. Model.* **2012**, *18*, 3657–3667.
- [18] D. S. Dudis, A. T. Yeates, D. Kost, *Adv. Mater.* **1994**, *6*, 248–251.
- [19] R. C. Hollins, *Curr. Opin. Solid State Mater. Sci.* **1999**, *4*, 189–196.
- [20] F. Z. Henari, *J. Opt. Pure Appl. Opt.* **2001**, *3*, 188–190.
- [21] R. L. Sutherland, *Handbook of Nonlinear Optics*, CRC Press, **2003**.
- [22] P. N. Butcher, D. Cotter, *The Elements of Nonlinear Optics*, Cambridge University Press, Cambridge, **1990**.
- [23] J. L. Bredas, C. Adant, P. Tackx, A. Persoons, B. M. Pierce, *Chem. Rev.* **1994**, *94*, 243–278.
- [24] M. Kasha, *Discuss. Faraday Soc.* **1950**, *9*, 14–19.
- [25] R. Kolkowski, M. Samoc, *J. Opt.* **2014**, *16*, 125202.
- [26] M. R. Ferdinandus, M. Reichert, T. R. Ensley, H. Hu, D. A. Fishman, S. Webster, D. J. Hagan, E. W. Van Stryland, *Opt. Mater. Express* **2012**, *2*, 1776.
- [27] J. Zyss, I. Ledoux, *Chem. Rev.* **1994**, *94*, 77–105.
- [28] M. Albota, D. Beljonne, J.-L. Brédas, J. E. Ehrlich, J.-Y. Fu, A. A. Heikal, S. E. Hess, T. Kogej, M. D. Levin, S. R. Marder, D. McCord-Maughon, J. W. Perry, H. Röckel, M. Rumi, G. Subramaniam, W. W. Webb, X.-L. Wu, C. Xu, *Science* **1998**, *281*, 1653–1656.
- [29] C. D. Entwistle, T. B. Marder, *Angew. Chem. Int. Ed.* **2002**, *41*, 2927–2931.
- [30] C. D. Entwistle, T. B. Marder, *Chem. Mater.* **2004**, *16*, 4574–4585.
- [31] G. Grelaud, M. P. Cifuentes, F. Paul, M. G. Humphrey, *J. Organomet. Chem.* **2014**, *751*, 181–200.
- [32] T. Kodaira, A. Watanabe, O. Ito, M. Matsuda, S. Tokura, M. Kira, S.-S. Nagano, K. Mochida, *Adv. Mater.* **1995**, *7*, 917–919.

- [33] Z. Fang, M. Samoc, R. D. Webster, A. Samoc, Y.-H. Lai, *Tetrahedron Lett.* **2012**, *53*, 4885–4888.
- [34] B. Strehmel, S. Amthor, J. Schelter, C. Lambert, *ChemPhysChem* **2005**, *6*, 893–896.
- [35] J. O. Morley, *Int. J. Quantum Chem.* **1993**, *46*, 19–26.
- [36] R. Signorini, C. Ferrante, D. Pedron, M. Zerbetto, E. Cecchetto, M. Slaviero, I. Fortunati, E. Collini, R. Bozio, A. Abbotto, L. Beverina, G. A. Pagani, *J. Phys. Chem. A* **2008**, *112*, 4224–4234.
- [37] W. J. Yang, C. H. Kim, M.-Y. Jeong, S. K. Lee, M. J. Piao, S.-J. Jeon, B. R. Cho, *Chem. Mater.* **2004**, *16*, 2783–2789.
- [38] S. K. Hurst, N. T. Lucas, M. P. Cifuentes, M. G. Humphrey, M. Samoc, B. Luther-Davies, I. Asselberghs, R. Van Boxel, A. Persoons, *J. Organomet. Chem.* **2001**, *633*, 114–124.
- [39] M. P. Cifuentes, C. E. Powell, M. G. Humphrey, G. A. Heath, M. Samoc, B. Luther-Davies, *J. Phys. Chem. A* **2001**, *105*, 9625–9627.
- [40] G. T. Dalton, M. P. Cifuentes, L. A. Watson, S. Petrie, R. Stranger, M. Samoc, M. G. Humphrey, *Inorg. Chem.* **2009**, *48*, 6534–6547.
- [41] S. Marqués-González, D. S. Yufit, J. A. K. Howard, S. Martín, H. M. Osorio, V. M. García-Suárez, R. J. Nichols, S. J. Higgins, P. Cea, P. J. Low, *Dalton Trans.* **2012**, *42*, 338–341.
- [42] E. Wuttke, Y.-M. Hervault, W. Polit, M. Linseis, P. Erler, S. Rigaut, R. F. Winter, *Organometallics* **2014**, *33*, 4672–4686.
- [43] S. Marqués-González, M. Parthey, D. S. Yufit, J. A. K. Howard, M. Kaupp, P. J. Low, *Organometallics* **2014**, *33*, 4947–4963.
- [44] I. R. Whittall, M. G. Humphrey, A. Persoons, S. Houbrechts, *Organometallics* **1996**, *15*, 1935–1941.
- [45] I. R. Whittall, M. P. Cifuentes, M. G. Humphrey, B. Luther-Davies, M. Samoc, S. Houbrechts, A. Persoons, G. A. Heath, D. Bogsányi, *Organometallics* **1997**, *16*, 2631–2637.
- [46] I. R. Whittall, M. P. Cifuentes, M. G. Humphrey, B. Luther-Davies, M. Samoc, S. Houbrechts, A. Persoons, G. A. Heath, D. C. R. Hockless, *J. Organomet. Chem.* **1997**, *549*, 127–137.
- [47] M. H. Garcia, M. P. Robalo, A. R. Dias, M. T. Duarte, W. Wenseleers, G. Aerts, E. Goovaerts, M. P. Cifuentes, S. Hurst, M. G. Humphrey, M. Samoc, B. Luther-Davies, *Organometallics* **2002**, *21*, 2107–2118.
- [48] B. J. Coe, *Coord. Chem. Rev.* **2013**, *257*, 1438–1458.
- [49] K. A. Green, M. P. Cifuentes, M. Samoc, M. G. Humphrey, *Coord. Chem. Rev.* **2011**, *255*, 2530–2541.
- [50] K. A. Green, M. P. Cifuentes, M. Samoc, M. G. Humphrey, *Coord. Chem. Rev.* **2011**, *255*, 2025–2038.
- [51] C. K. M. Chan, C.-H. Tao, K.-F. Li, K. M.-C. Wong, N. Zhu, K.-W. Cheah, V. W.-W. Yam, *Dalton Trans.* **2011**, *40*, 10670.
- [52] M. E. Thompson, P. E. Djurovich, S. Barlow, S. Marder, in *Comprehensive Organometallic Chemistry III* (Eds.: D.M.P. Mingos, R. H. Crabtree), Elsevier, Oxford, **2007**, pp. 101–194.
- [53] A. M. McDonagh, M. G. Humphrey, M. Samoc, B. Luther-Davies, *Organometallics* **1999**, *18*, 5195–5197.
- [54] K. A. Green, P. V. Simpson, T. C. Corkery, M. P. Cifuentes, M. Samoc, M. G. Humphrey, *Macromol. Rapid Commun.* **2012**, *33*, 620–620.
- [55] A.-M. Caminade, in *Dendrimers* (Eds.: A.-M. Caminade, C.-O. Turrin, R. Laurent, A. Ouali, B. Delavaux-Nicot), John Wiley & Sons, Chichester, **2011**, pp. 67–98.
- [56] G. Hennrich, I. Asselberghs, K. Clays, A. Persoons, *J. Org. Chem.* **2004**, *69*, 5077–5081.
- [57] J. Campo, A. Painelli, F. Terenziani, T. Van Regemorter, D. Beljonne, E. Goovaerts, W. Wenseleers, *J. Am. Chem. Soc.* **2010**, *132*, 16467–16478.
- [58] D. F. Duxbury, *Chem. Rev.* **1993**, *93*, 381–433.
- [59] N. Hidayah, F. Abu Bakar, N. A. Mahyudin, S. Faridah, M. S. Nur-Azura, M. Z. Zaman, *Int. Food Res. J.* **2013**, *20*, 1511–1519.
- [60] W. Azmi, R. K. Sani, U. C. Banerjee, *Enzyme Microb. Technol.* **1998**, *22*, 185–191.
- [61] S. Srivastava, R. Sinha, D. Roy, *Aquat. Toxicol. Amst. Neth.* **2004**, *66*, 319–329.
- [62] E. Sudova, J. Machova, Z. Svobodova, T. Vesely *Veterinarni Medicina* **2007**, *52*, 527–539.

- [63] S. Srivastava, R. Sinha, D. Roy, *Aquat. Toxicol. Amst. Neth.* **2004**, 66, 319–329.
- [64] F. Kehrman, F. Wentzel, *Berichte Dtsch. Chem. Ges.* **1901**, 34, 3815–3819.
- [65] M. S. Shchepinov, V. A. Korshun, *Chem. Soc. Rev.* **2003**, 32, 170–180.
- [66] V. G. Shubin, *Russ. Chem. Bull.* **2009**, 57, 761–767.
- [67] R. R. Naredla, D. A. Klumpp, *Chem. Rev.* **2013**, 113, 6905–6948.
- [68] G. A. Olah, G. K. S. Prakash, in *Carbocation Chemistry* (Ed.: Wiley-Blackwell), US, **2004**.
- [69] R. M. O’Ferrall, in *Adv. Phys. Org. Chem.* **2010**, 19–122.
- [70] P. G. Cozzi, F. Benfatti, *Angew. Chem. Int. Ed.* **2010**, 49, 256–259.
- [71] M. Wada, H. Mishima, T. Watanabe, S. Natsume, H. Konishi, K. Kirishima, S. Hayase, T. Erabi, *Bull. Chem. Soc. Jpn.* **1995**, 68, 243–249.
- [72] R. J. Goldacre, J. N. Phillips, *J. Chem. Soc. Resumed* **1949**, 1724–1732.
- [73] A. Vöge, D. Gabel, in *Boron Sci.*, (Ed: N. S. Hosmane), CRC Press, **2011**, pp. 295–318.
- [74] C. Arbez-Gindre, B. R. Steele, G. A. Heropoulos, C. G. Screttas, J.-E. Communal, W. J. Blau, I. Ledoux-Rak, *J. Organomet. Chem.* **2005**, 690, 1620–1626.
- [75] C. Villalonga-Barber, B. R. Steele, V. Kovač, M. Micha-Screttas, C. G. Screttas, *J. Organomet. Chem.* **2006**, 691, 2785–2792.
- [76] R. R. Naredla, C. Zheng, S. O. Nilsson Lill, D. A. Klumpp, *J. Am. Chem. Soc.* **2011**, 133, 13169–13175.
- [77] J. Lux, E. J. Peña, F. Bolze, M. Heinlein, J.-F. Nicoud, *ChemBioChem* **2012**, 13, 1206–1213.
- [78] T. J. Beveridge, *Biotech. Histochem.* **2001**, 76, 111–118.
- [79] A. M. Maley, J. L. Arbiser, *Exp. Dermatol.* **2013**, 22, 775–780.
- [80] E. Wich, *Color Res. Appl.* **1977**, 2, 77–80.
- [81] G. P. Moss, P. A. S. Smith, D. Tavernier, *Pure Appl. Chem.* **1995**, 67, 1307–1375.
- [82] W. Herbst, K. Hunger, G. Wilker, H. Ohleier, R. Winter, in *Ind. Org. Pigments*, Wiley-VCH Verlag GmbH & Co. KGaA, **2004**, pp. 637–645.
- [83] M. Clark, Ed. , in *Handbook of Textile and Industrial Dyeing*, Woodhead Publishing, **2011**, pp. i–iii.
- [84] E. R. Riegel, J. A. Kent, *Riegel’s Handbook of Industrial Chemistry*, Van Nostrand Reinhold, **1992**.
- [85] R. Muthyala, A. R. Katritzky, X. Lan, *Dyes & Pigments* **1994**, 25, 303–324.
- [86] L. Sanguinet, R. J. Twieg, G. Wiggers, G. Mao, K. D. Singer, R. G. Petschek, *Tetrahedron Lett.* **2005**, 46, 5121–5125.
- [87] A. Noack, A. Schröder, H. Hartmann, *Dyes & Pigments* **2003**, 57, 131–147.
- [88] Z. Li, Z. Duan, J. Kang, H. Wang, L. Yu, Y. Wu, *Tetrahedron* **2008**, 64, 1924–1930.
- [89] S. Genovese, F. Epifano, C. Pelucchini, M. Curini, *Eur. J. Org. Chem.* **2009**, 2009, 1132–1135.
- [90] A. S. Chaudhari, Y. S. Parab, V. Patil, N. Sekar, S. R. Shukla, *RSC Adv.* **2012**, 2, 12112–12117.
- [91] B. M. Babu, P. B. Thakur, V. M. Bangade, H. M. Meshram, *Tetrahedron Lett.* **2015**, 56, 766–771.
- [92] B. M. Babu, P. B. Thakur, N. Nageswara Rao, G. Santosh Kumar, H. M. Meshram, *Tetrahedron Lett.* **2014**, 55, 1868–1872.
- [93] S. Lin, X. Lu, *J. Org. Chem.* **2007**, 72, 9757–9760.
- [94] J.-Y. Yu, R. Kuwano, *Org. Lett.* **2008**, 10, 973–976.
- [95] S. Tabuchi, K. Hirano, T. Satoh, M. Miura, *J. Org. Chem.* **2014**, 79, 5401–5411.
- [96] M. Barbero, S. Cadamuro, S. Dughera, C. Magistris, P. Venturello, *Org. Biomol. Chem.* **2011**, 9, 8393–8399.
- [97] J.-T. Hou, J.-W. Gao, Z.-H. Zhang, *Monatshefte Für Chem. - Chem. Mon.* **2011**, 142, 495–499.
- [98] B. L. H. Taylor, M. R. Harris, E. R. Jarvo, *Angew. Chem. Int. Ed.* **2012**, 51, 7790–7793.
- [99] S. Mondal, G. Panda, *RSC Adv.* **2014**, 4, 28317–28358.
- [100] V. Nair, S. Thomas, S. C. Mathew, K. G. Abhilash, *Tetrahedron* **2006**, 62, 6731–6747.
- [101] J. Griffiths, K. J. Pender, *Dyes & Pigments* **1981**, 2, 37–48.
- [102] G. N. Lewis, T. T. Magel, D. Lipkin, *J. Am. Chem. Soc.* **1942**, 64, 1774–1782.
- [103] H. B. Lueck, J. L. McHale, W. D. Edwards, *J. Am. Chem. Soc.* **1992**, 114, 2342–2348.

- [104] M. Ishikawa, Y. Maruyama, *Chem. Phys. Lett.* **1994**, *219*, 416–420.
- [105] Y. Maruyama, M. Ishikawa, H. Satozono, *J. Am. Chem. Soc.* **1996**, *118*, 6257–6263.
- [106] Y. Maruyama, O. Magnin, H. Satozono, M. Ishikawa, *J. Phys. Chem. A* **1999**, *103*, 5629–5635.
- [107] S. Lovell, B. J. Marquardt, B. Kahr, *J. Chem. Soc. Perkin Trans. 2* **1999**, 2241–2247.
- [108] A. Ghanadzadeh, A. Zeini, A. Kashef, *J. Mol. Liq.* **2007**, *133*, 61–67.
- [109] C. Loison, R. Antoine, M. Broyer, P. Dugourd, J. Guthmuller, D. Simon, *Chem. – Eur. J.* **2008**, *14*, 7351–7357.
- [110] L. Angeloni, G. Smulevich, M. P. Marzocchi, *J. Mol. Struct.* **1980**, *61*, 331–336.
- [111] R. Macovez, N. Lopez, M. Mariano, M. Maymò, J. Martorell, *J. Phys. Chem. C* **2012**, *116*, 26784–26790.
- [112] P. Sen, S. Yamaguchi, T. Tahara, *Faraday Discuss.* **2010**, *145*, 411–428.
- [113] R. Miyata, Y. Kimura, M. Terazima, *Chem. Phys. Lett.* **2002**, *365*, 406–412.
- [114] T. Itoh, *Chem. Rev.* **2012**, *112*, 4541–4568.
- [115] Y. Rao, X. Guo, Y.-S. Tao, H. Wang, *J. Phys. Chem. A* **2004**, *108*, 7977–7982.
- [116] A. Mokhtari, A. Chebira, J. Chesnoy, *J. Opt. Soc. Am. B* **1990**, *7*, 1551.
- [117] M. J. Rosker, F. W. Wise, C. L. Tang, *Phys. Rev. Lett.* **1986**, *57*, 321–324.
- [118] Y. Nagasawa, Y. Ando, D. Kataoka, H. Matsuda, H. Miyasaka, T. Okada, *J. Phys. Chem. A* **2002**, *106*, 2024–2035.
- [119] A. C. Bhasikuttan, A. V. Sapre, T. Okada, *J. Phys. Chem. A* **2003**, *107*, 3030–3035.
- [120] Y. Kanematsu, H. Ozawa, I. Tanaka, S. Kinoshita, *J. Lumin.* **2000**, *87–89*, 917–919.
- [121] Y. Nagasawa, Y. Ando, T. Okada, *Chem. Phys. Lett.* **1999**, *312*, 161–168.
- [122] Y. Nagasawa, Y. Ando, T. Okada, *J. Chin. Chem. Soc.* **2000**, *47*, 699–704.
- [123] T. J. Sørensen, K. Kilså, B. W. Laursen, *Chem. – Eur. J.* **2015**, *21*, 8521–8529.
- [124] G. Li, D. Magana, R. B. Dyer, *J. Phys. Chem. B* **2012**, *116*, 12590–12596.
- [125] M. Yoshizawa, K. Suzuki, A. Kubo, S. Saikan, *Chem. Phys. Lett.* **1998**, *290*, 43–48.
- [126] S. Rafiq, R. Yadav, P. Sen, *J. Phys. Chem. B* **2010**, *114*, 13988–13994.
- [127] A. Nakayama, T. Taketsugu, *J. Phys. Chem. A* **2011**, *115*, 8808–8815.
- [128] B.-B. Xie, S.-H. Xia, L.-H. Liu, G. Cui, *J. Phys. Chem. A* **2015**, *119*, 5607–5617.
- [129] S. P. Liptonok, K. Addison, I. A. Heisler, S. R. Meech, *Chem. Phys. Lett.* **2014**, *607*, 43–46.
- [130] P. Singhal, H. N. Ghosh, *Phys. Chem. Chem. Phys.* **2014**, *16*, 16824–16831.
- [131] A. Janowski, J. Rzeszutarska, *J. Lumin.* **1980**, *21*, 409–416.
- [132] Z. R. Grabowski, K. Rotkiewicz, W. Rettig, *Chem. Rev.* **2003**, *103*, 3899–4032.
- [133] G. Ramos-Ortiz, S. Romero, J. L. Maldonado, O. Barbosa-García, M. A. Meneses-Nava, M. Romero, N. Farfán, *Rev. Mex. Fis.* **2006**, *52*, 527–533.
- [134] G. Ramos-Ortiz, J. L. Maldonado, M. A. Meneses-Nava, O. Barbosa-García, M. Olmos, M. Cha, *Opt. Mater.* **2007**, *29*, 636–641.
- [135] D. R. Greve, S. B. Schougaard, T. Geisler, J. C. Petersen, T. Bjørnholm, *Adv. Mater.* **1997**, *9*, 1113–1116.
- [136] T. Geethakrishnan, P. K. Palanisamy, *Pramana* **2006**, *66*, 473–478.
- [137] Q. M. Ali, P. K. Palanisamy, *Opt. Laser Technol.* **2007**, *39*, 1262–1268.
- [138] T. Geethakrishnan, P. K. Palanisamy, *Opt. - Int. J. Light Electron Opt.* **2006**, *117*, 282–286.
- [139] T. Geethakrishnan, P. K. Palanisamy, *Appl. Phys. B* **2005**, *82*, 169–172.
- [140] G. Vinitha, A. Ramalingam, P. K. Palanisamy, *Spectrochim. Acta. A. Mol. Biomol. Spectrosc.* **2007**, *68*, 1–5.
- [141] T. Geethakrishnan, P. K. Palanisamy, *Opt. Commun.* **2007**, *270*, 424–428.
- [142] K. Jamshidi-Ghaleh, S. Salmani, M. H. Majles Ara, *Opt. Commun.* **2007**, *271*, 551–554.
- [143] E. Koushki, A. Farzaneh, S. H. Mousavi, *Appl. Phys. B* **2010**, *99*, 565–570.
- [144] M. Sheik-Bahae, D. J. Hagan, E. W. Van Stryland, *Phys. Rev. Lett.* **1990**, *65*, 96–99.
- [145] R. K. H. Manshad, Q. M. A. Hassan, *Adv. Appl. Sci. Res.* **2012**, *3*, 3696–3702.
- [146] S. S. Hussain, A. H. Waleed, A. B. Hussain, *Adv. Appl. Sci. Res.* **2012**, *3*, 2940–2946.
- [147] I. Mamedbeili, H. Nasibov, *Laser Phys.* **2009**, *19*, 2002–2007.

- [148] R. K. Choubey, S. Medhekar, R. Kumar, S. Mukherjee, S. Kumar, *J. Mater. Sci. Mater. Electron.* **2014**, *25*, 1410–1415.
- [149] T. W. Chui, K. Y. Wong, *J. Chem. Phys.* **1998**, *109*, 1391–1396.
- [150] D. Beljonne, W. Wenseleers, E. Zojer, Z. Shuai, H. Vogel, S. J. K. Pond, J. W. Perry, S. R. Marder, J.-L. Brédas, *Adv. Funct. Mater.* **2002**, *12*, 631–641.
- [151] K. J. Thorley, J. M. Hales, H. Kim, S. Ohira, J.-L. Brédas, J. W. Perry, H. L. Anderson, *Chem. – Eur. J.* **2013**, *19*, 10370–10377.
- [152] F. Paul, C. Lapinte, *Coord. Chem. Rev.* **1998**, *178–180, Part 1*, 431–509.
- [153] N. Gauthier, C. Olivier, S. Rigaut, D. Touchard, T. Roisnel, M. G. Humphrey, F. Paul, *Organometallics* **2008**, *27*, 1063–1072.
- [154] C. E. Powell, M. P. Cifuentes, J. P. Morrall, R. Stranger, M. G. Humphrey, M. Samoc, B. Luther-Davies, G. A. Heath, *J. Am. Chem. Soc.* **2003**, *125*, 602–610.
- [155] L. Cuffe, R. D. A. Hudson, J. F. Gallagher, S. Jennings, C. J. McAdam, R. B. T. Connelly, A. R. Manning, B. H. Robinson, J. Simpson, *Organometallics* **2005**, *24*, 2051–2060.
- [156] G. Grelaud; PhD thesis, The Australian National University/Université de Rennes 1 **2012**.
- [157] N. Gauthier, N. Tchouar, F. Justaud, G. Argouarch, M. P. Cifuentes, L. Toupet, D. Touchard, J.-F. Halet, S. Rigaut, M. G. Humphrey, K. Costuas, F. Paul, *Organometallics* **2009**, *28*, 2253–2266.

Chapter I:

All-organic triphenylmethane-based derivatives

Chapter I

All-organic triphenylmethane-based derivatives

Contents

1. Introduction	62
1.2. Brief literature review	64
2. Synthesis	67
2.1. Synthesis of the precursors	68
2.2. Synthesis of the targeted TPM dyes.....	70
3. Characterization.....	72
3.1. IR spectroscopy	72
3.2. NMR spectroscopy	73
3.3. Molecular structures	77
3.4. UV-Visible spectroscopy.....	81
3.5. Theoretical work	86
4. Z-scan studies.....	91
5. Conclusion	95
References.....	96

1. Introduction

This chapter develops the synthesis of organic molecules based on the **MG⁺** and **CV⁺** architectures (**Chart 1**), their spectroscopic characterization and presents some of their linear and nonlinear optical features. The syntheses of the targeted derivatives are discussed in the light of the existing literature. The isolated derivatives are then characterized using classical methods: IR, NMR, and UV-Vis spectroscopies. Crystallographic data are subsequently presented: they are relevant for understanding charge delocalization within the compounds and the extent to which selected structural modifications influence this property. The structure's influence on the electronic properties is also discussed and the absorption spectra are examined with the help of DFT calculations carried out by Anissa Amar in the group of Prof. Abdou Boucekkine. The third-order NLO properties are measured by Z-scan to determine the TPA cross-sections of these derivatives and develop structure/property relationships.

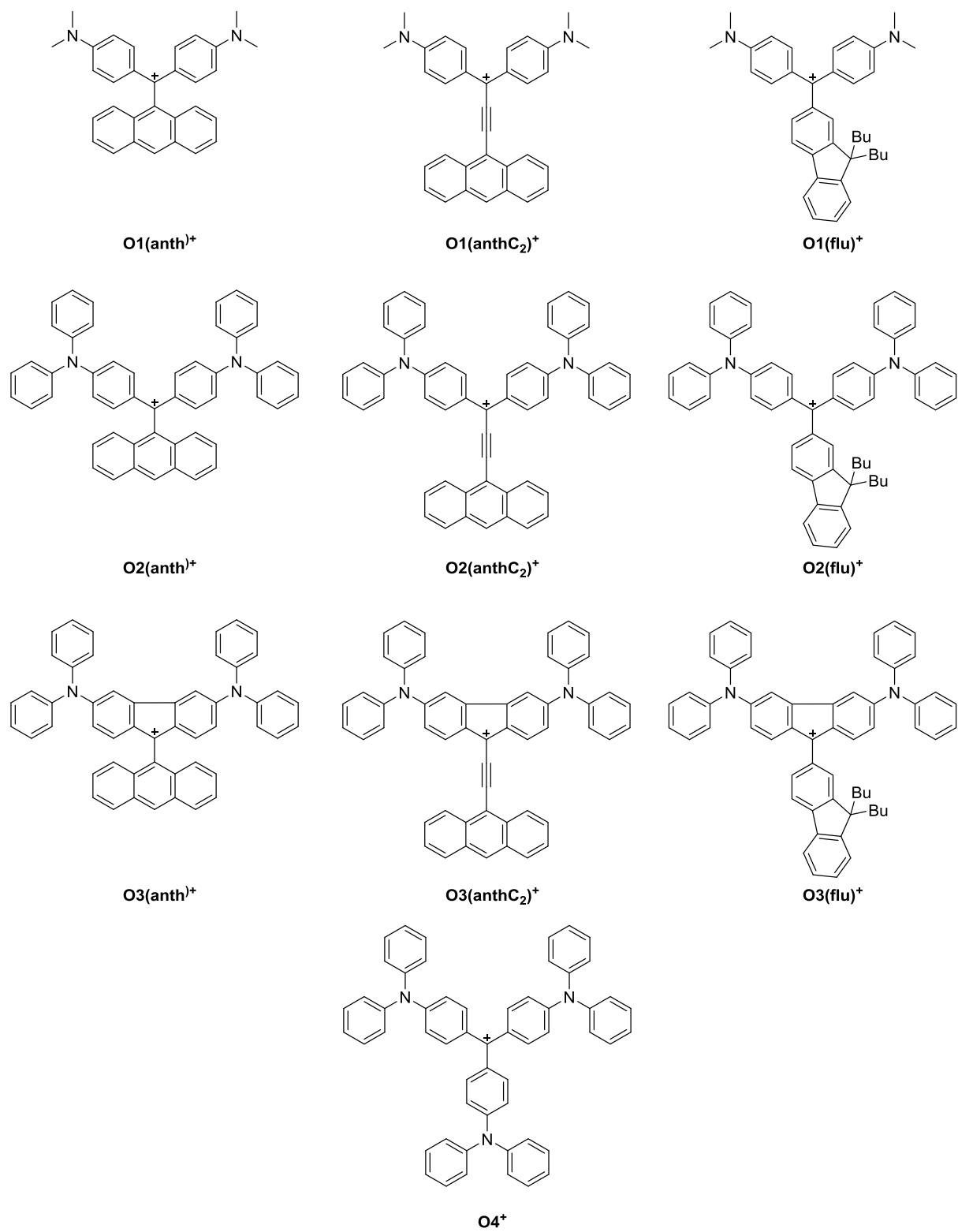


Chart 1: targeted **MG⁺** derivatives

1.2. Brief literature review

As mentioned previously, many TPM dyes have been used around the world for various applications, the most popular being **MG**⁺ and **CV**⁺. These interesting molecules have found widespread use in the dye industry and medicine. Initially, the nature of the low-energy absorptions at the origin of their deep color was not precisely known. At that time, with the exception of a few theoretical papers,^[1-5] synthetic screening was the method of choice for finding the best molecular structure for a given need. Hence, many TPM dyes were made, and their absorption maxima were determined and listed in tables, but until the 1980s, little additional insight into their electronic structure had been gleaned apart from structural leads to control color. Meanwhile, many synthetic routes to functional derivatives were developed. The following brief review summarizes the structural diversity achieved with TPM dyes.

Barker and co-workers synthesized several TPM-based derivatives to develop structure-property relationships to control color.^[6-11] They investigated the influence on the spectral features of these dyes of rigidification, steric effects and even extension of the π -manifold of **CV**⁺ and **MG**⁺. Similar work was undertaken by Hallas *et al.* on **MG**⁺ fluorine-containing derivatives (**Chart 2**).^[12] Previous studies have been summarized by Griffith and Pender, including calculations rationalizing the observed trends.^[1] For **MG**⁺ derivatives, the electronic perturbation induced by the extension of the π -system by replacing the unsubstituted phenyl ring by naphthalene (also known as Victoria Blue), fluorene or biphenyl groups is quite minor, as these structural changes only induce a small red-shift of the first and second (if any) absorption bands.^[13] Relative to **CV**⁺, this second band is always present in **MG**⁺ derivatives, as it results from symmetry lowering ($D_3 \rightarrow C_2$) induced by the removal of the amine substituent on the third phenyl ring. Likewise, it appears in the less symmetric **CV**⁺ derivatives **III_a** and **IV_a** and in rigidified derivatives such as **V_a**, **VI_a**. In addition to inducing the appearance of a second transition at low energy, this last structural modification has a drastic electronic effect, since it also induces a huge bathochromic shift of about 250 nm of both bands in the NIR.^[14] Their molecular extinction coefficients^[14] remain, however, quite similar to those observed for classical TPM dyes (*i.e.* around $10^5 \text{ L.mol}^{-1}.\text{cm}^{-1}$).

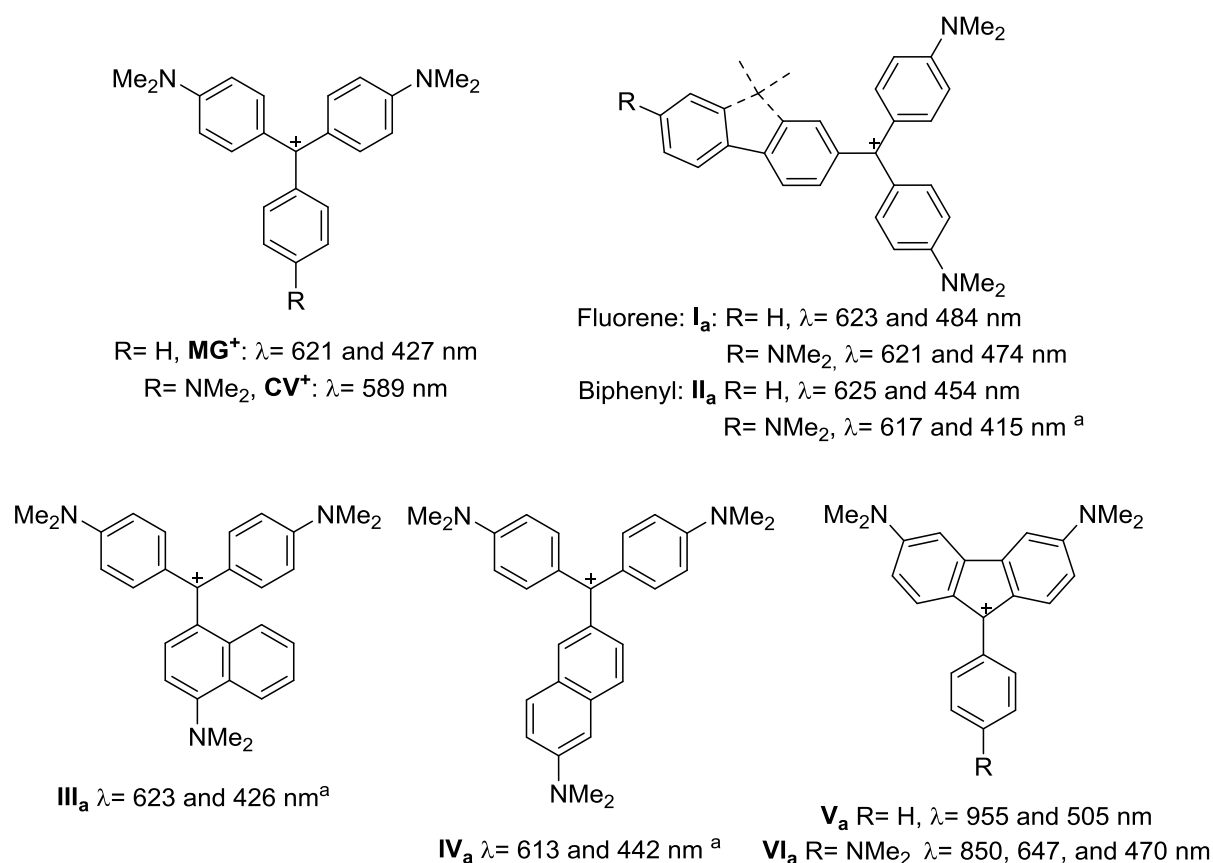
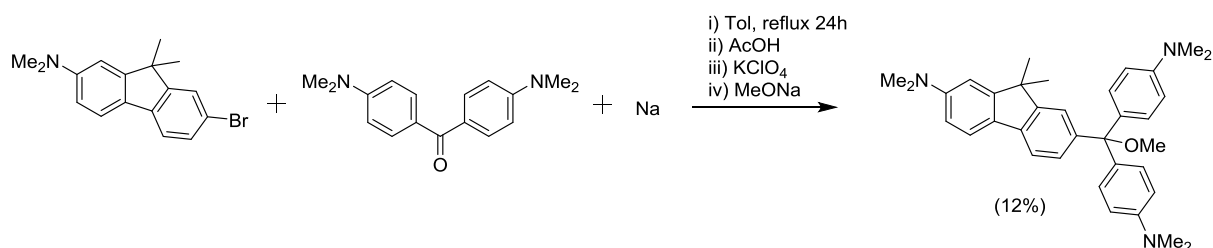


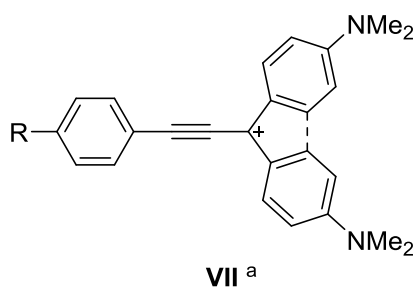
Chart 2: Compounds mentioned in references 1 to 8 in 98 % AcOH. a: EtOH + 1 eq. HCl.

These compounds were derived from Grignard reagents or sodium salts and ketones, to form carbinol or ether derivatives in a first step, as exemplified in **Scheme 1**, and then the carbocation was generated upon addition of acid (see also Introduction; section 3.1). Characterization consists largely of an elemental analysis and a melting point, which is rather poor, especially considering that some of these derivatives are not thermally stable and were reported to decompose over time. Furthermore, the UV-visible electronic absorptions reported for these carbocations have to be used carefully. Most measurements were on species generated *in situ*, often in highly acidic solutions, the actual concentration of mono-cationic dye not always being known. Accordingly, rapid fading of the solution was often observed during these measurements for the most reactive compounds, such as those possessing rigidified cores, ascribable to either re-formation of the starting carbinol or decomposition. The rigidified compounds are more sensitive to nucleophilic attack, possibly due to their planar structures which do not sterically shield the central carbocation.



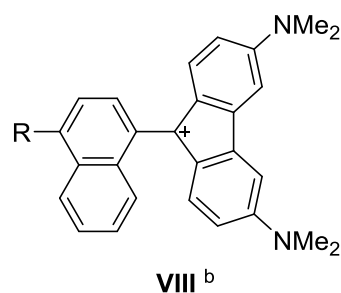
Scheme 1: Example of synthetic pathway used by Hallas *et al.*^[12]

More recently, Nakatsuji and coworkers,^[15-17] Guinot *et al.*,^[18,19] and Vidal *et al.*^[20] have also investigated the influence of the third branch in **MG**⁺- and related fluorenum-based derivatives by adding a triple/double bond or using naphthyl derivatives, respectively (**Chart 3**). Bathochromic shifts were observed in each case. An obvious explanation for this redshift is the extension of the π -system by the triple/double bond or by the naphthalene spacer. For fluorenum derivatives, the rigidification is clearly inappropriate to explain the bathochromic shift observed, relative to their non-rigidified analogues **VII**_b, considering that rhodamine (**Introduction, Chart 9**), the rigidified analogue of **MG**⁺, does not present a bathochromic shift compared to **MG**⁺ (550 nm in MeOH^[21] vs. 620 in DCM). Despite being reproduced by PPP-MO methods, the origin of this shift remains unclear.^[1,15-17] Transitions between selected vibronic components of a single transition were initially proposed to explain this result. Another explanation links the observation to the anti-aromaticity of this unit,^[22] resulting in a lowering of the HOMO-LUMO energy gap. Since then, no further work has been conducted on these derivatives and the exact origin of this large bathochromic shift relative to non-rigidified analogues remains an open question. The only studies on characterized carbocations of this type originate from Nakatsuji's group; the instability of these carbocationic species after isolation was reported, especially in protic solvents such as EtOH.



Rigidified: **VII_a** R= NMe₂, λ = 956, 718 nm
 R= OMe λ = 1025, 910, 579 nm
 R= Me, λ =1040, 920, 559 nm
 R= H, λ = 1052, 927, 551 nm
 R= Br λ = 1056, 931, 558 nm
 R= NO₂, λ = 1096, 961, 560 nm

Non-rigidified: **VII_b** R= NMe₂, λ = 663 nm
 R= OMe λ = 680, 530 nm
 R= H, λ = 688, 493 nm



R= H, λ = >900, 858, 535, 495 nm
 R= NMe₂, λ = 835, 701, 485, 450 nm
 R= N⁺NMe₂, λ = >900, 860, 525, 490 nm

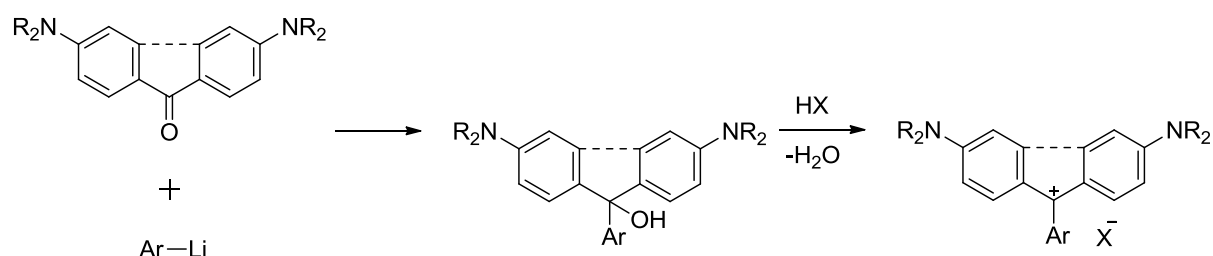
Chart 3: Extended version of fluorenyl carbocations. a: DCM, b: measured in 98% acetic acid

In conclusion, considerable care must be taken when examining results from *in situ* measurements, although such measurements provide a good database from which to analyze the impact of structural modifications on the electronic structures. Finally, some recent papers describe innovative and efficient catalyzed syntheses of leuco-TPMs featuring anthracenyl substituents.^[23] In principle, these species constitute synthetic precursors to TPM carbocations closely related to those presented in the previous chapter. The synthesis of the corresponding TPM dyes was not attempted, as no guarantee exists that these leuco-dyes constitute convenient precursors to the corresponding carbocations using an alternative synthetic route to that described here.

2. Synthesis

None of the targeted compounds were previously reported. Several targeted compounds of this work are, nevertheless, similar to existing species and will allow good comparison of spectral features. All the targeted molecules possess common synthons, and hence the most obvious way to access these TPM dyes was by a convergent synthesis. Lithiation is the first step for this convergent approach (**Scheme 2**). It is supposedly higher yielding compared to other approaches based on electrophilic aromatic substitution, in which many side-reactions can occur, and which involve the use of Lewis acid catalysts (zinc chloride, zeolites, sulfonic acid) or Brønsted acid catalysts (sulfuric acid, hydrochloric acid, methanesulfonic acid). The last reaction is the preferred pathway in industrial

chemistry, purity not being the main requirement for the use of these compounds as stains or dyes. While the quality of industrial processes has improved, they do not usually provide the same degree of purity as approaches based on carbanions. Among these, the use of lithium reagents has been preferentially used in the recent literature to access the carbinols.^[24,25] These species can be quite reactive and the purification of such compounds can be difficult, as mentioned by Costero *et al.*, who employed this high reactivity to make sensors for chemical warfare such as nerve stimulants (e.g. Sarin and related phosphonate derivatives). The sensing mechanism involves phosphorylation of the carbinolhydroxyl group followed by a dephosphatization reaction induced by the electron-donor amino groups, forming the carbocationic dye.^[26] This illustrates well the carbinols's reactivity. Precautions have therefore to be taken when manipulating these derivatives in order to avoid decomposition.



Scheme 2: Pathway employed for synthesis of the targeted TPM dyes with a rigidified core

The carbinol intermediates will then be dehydrated upon addition of acid to form the desired carbocations. As discussed in the introduction (section 3.2), this step will depend on the donating power of the *para*-substituents on the peripheral phenyl rings and on their number (2 or 3). Quantitative use of acid should lead to the monocationic species, which will be isolated as their inorganic salts, avoiding the problem raised by *in situ* measurements where large excess of acid might partly generate extraprotonated species.

2.1. Synthesis of the precursors

The desired ketone precursors have been described in the literature or are commercially available (**Chart 4**). Benzophenone substituted with dimethylamino groups is known as Michler's ketone **28** and is prepared using the Friedel-Crafts acylation of dimethylaniline using triphosgene.^[27]

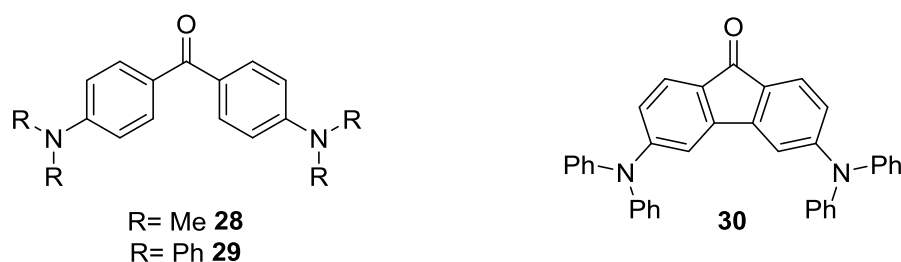
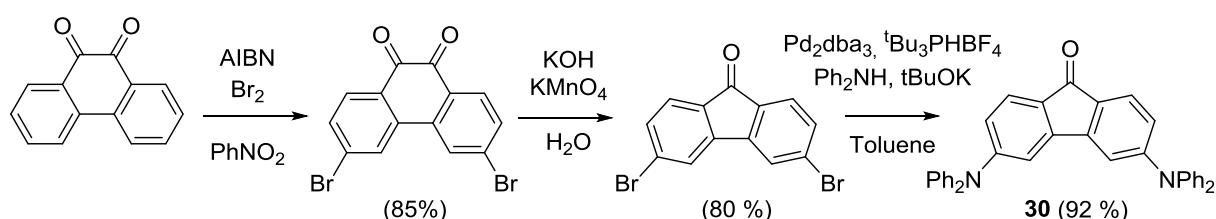


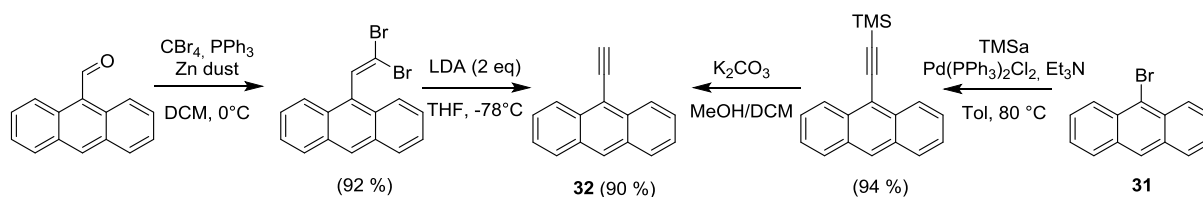
Chart 4: Ketone starting materials

The corresponding ketone with diphenylamino groups **29** is prepared from the corresponding dibromo precursor and diphenylamine using an Ullmann coupling reaction to form quantitatively the desired product, following an experimental protocol proposed by Moorthy *et al.*^[28] The rigidified compound requires more steps as the di-halogenation of fluorene always leads to substitutions at positions 2 and 7. The synthesis (**Scheme 3**) starts with the di-bromination of 9,10-phenanthrenedione, followed by decarboxylation and a Buchwald-Hartwig reaction in order to introduce the diphenylamino substituents.^[29,30] This last reaction was modified from the original procedure to form the catalyst *in situ*, thereby avoiding the use of pyrophoric tri(*tert*-butyl)phosphine.^[31,32]



Scheme 3: Synthesis of **30**

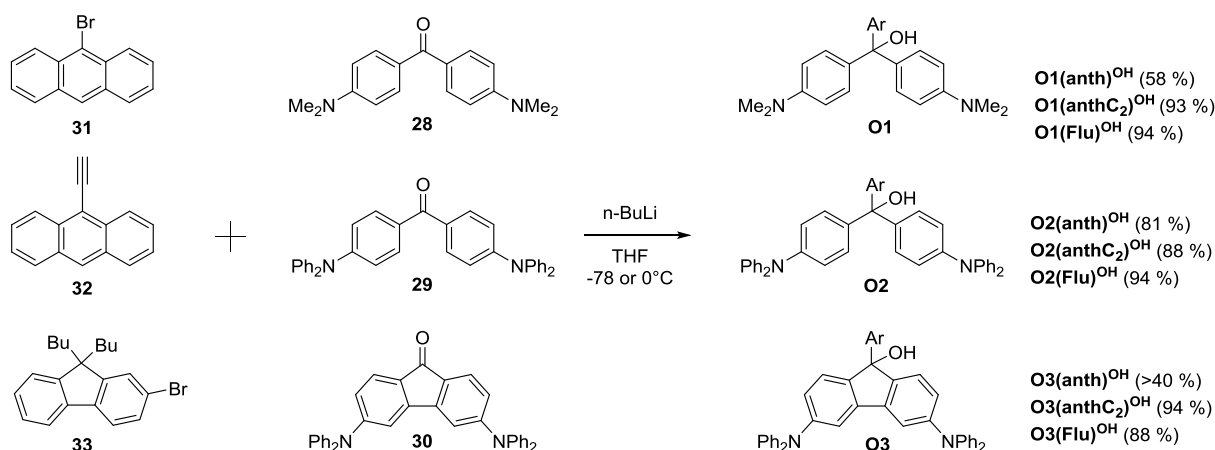
For the fluorenyl and anthracene synthons, 2-bromo-9,9-dibutylfluorene can be made by bromination followed by dibutylation of fluorene, following literature procedures,^[33] while 2-bromoanthracene is a commercially available precursor. 9-Ethynylantracene is known to be unstable and has to be used quickly after synthesis, to avoid polymerization upon light exposure. It can be made starting from 9-bromoanthracene; a Sonogashira cross-coupling reaction with trimethylsilylacetylene (TMSa) forms the protected version that is stable over time, and can be desilylated with K_2CO_3 in DCM/MeOH or TBAF. An alternative route, starting from anthracene carboxaldehyde, proceeds via a Corey-Fuchs reaction, forming first the stable dibromovinyl intermediate which is reacted with lithium diisopropylamide (LDA) to form the free alkyne for further reactions (**Scheme 4**). These routes afford similar yields and both were used because of the starting materials available in the laboratory.



Scheme 4: Synthesis of 9-ethynylantracene **32**

2.2. Synthesis of the targeted TPM dyes

To access the desired carbinols, the reactions followed classical lithiation conditions (THF at 0°C for free alkyne and -78°C for metal/halogen exchange reactions) followed by addition of the desired ketone in solution (**Scheme 5**). The difficulty arises in the purification and isolation of these compounds, as they are quite reactive and can decompose overtime and they dehydrate quickly on acidic or hot surfaces, if not handled with care. The use of triethylamine is necessary to neutralize silica while running chromatographic columns, and thereby avoid the formation of carbocationic species which would remain on the column and lead to loss of material. However, even on a neutralized column eluted with 1% triethylamine, the dimethylamino compounds are quite reactive and led to formation of deeply colored deposits on the chromatographic column.

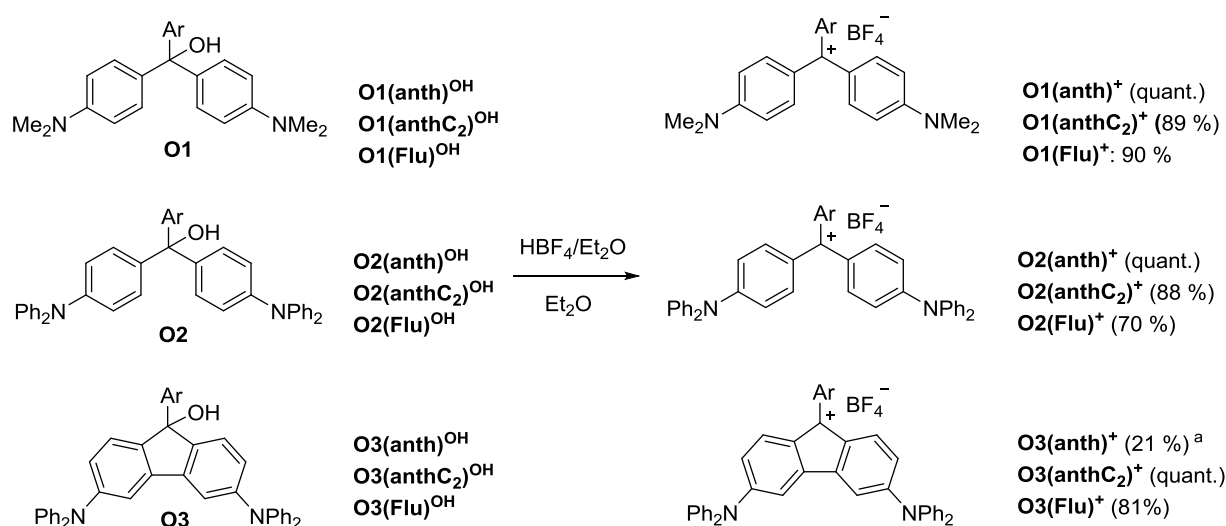


Scheme 5: Synthesis of organic carbinol derivatives **O1^{OH}-O3^{OH}**

The carbinols **O1^{OH}-O3^{OH}** were made in good yields except for **O3(anth)^{OH}**, which was observed but could not be purified and isolated as it decomposes too quickly (within an hour in solution). The steric constraints of the bulky anthracene exerted at the sp³ carbon probably explains the high reactivity of this particular carbinol. As observed by NMR, a competitive reaction takes place

over time, forming an unknown anthracene derivative. The reaction mixture therefore has to be purified quickly by flash column chromatography to remove the unreacted starting material, and the carbinol **O3(anth)^{OH}** must be used directly thereafter.

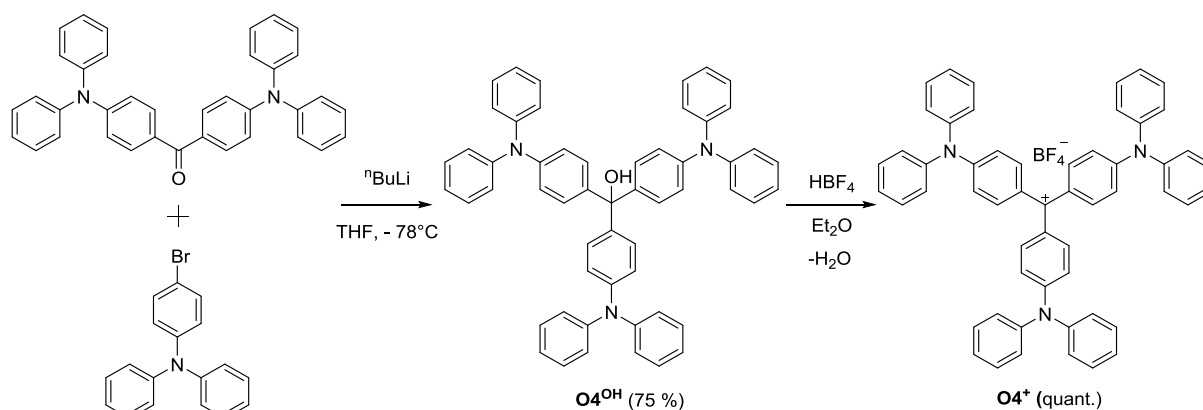
The isolated carbinols were then dissolved in Et₂O and the corresponding carbocations were formed upon addition of tetrafluoroboric acid (**Scheme 6**). The formation of the carbocations is quantitative and most of the tetrafluoroborate salts that are formed precipitate from solution. However, some of the extended derivatives, especially those containing fluorene groups and diphenylamino substituents, are soluble in Et₂O, in spite of their cationic character. Thus, these reaction media have to be filtered at low temperature to avoid losses. DCM has also been tried as a solvent for this last step, with a procedure similar to that used by Nakatsuji *et al.*^[15–17] but this workup always led to a mixture of products, probably due to the occurrence of side-reactions between the resulting carbocations in solution and HBF₄ or some impurities also present in the acidic solution (such as fluoride ions). The direct precipitation of these carbocations from Et₂O avoids such problems and was therefore adopted for all of these compounds. After filtration, the excess HBF₄ that can persist in the sample was washed away with Et₂O and the products were dissolved in DCM and re-precipitated with Et₂O to give fine colored powders.



Scheme 6: Formation of carbocationic species **O1⁺**-**O3⁺**. a: Overall yield from ketone precursor

In the same way, the **CV⁺** derivatives **O4^{OH}** and **O4⁺** have been synthesized following **Scheme 7** with an overall yield of 75 %. These derivatives can be found in the academic literature in

papers up to the 1980s,^[34,35] and in diverse recent patents,^[36,37] but there is a clear lack of spectroscopic characterization and obviously no NLO measurements have been carried out.



Scheme 7: Formation of the targeted **CV⁺** derivatives

The resulting **MG⁺**- and **CV⁺**-based carbocations were most often isolated as BF_4^- salts. These are air-stable salts that can be stored under normal conditions in vials for several months. However, some of these derivatives can be hydrophilic (as mentioned before) and it is better to avoid moisture when storing them for extended periods of time. They are also stable in solution over weeks in non-polar solvents and even in presence of small amounts of water. However, in polar solvents, there is a rapid fading of the color, most likely caused by re-formation of the starting carbinols. This fading can, however, easily be prevented by addition of a slight excess acid or by use of dry solvents under inert atmospheres.

3. Characterization

3.1. IR spectroscopy

IR spectroscopy can be used to follow structural changes depending on specific vibrational modes of the molecules. The disappearance of the hydroxyl group and the appearance of the counter anion, here a BF_4^- and characterized by an intense B-F stretching mode around 1100 cm^{-1} , are obvious from the spectra of the two compounds. Other typical vibrational modes are also observable such as the stretching of the triple bonds around 2130 cm^{-1} for the extended anthracenyl derivatives (**Table 1**). The other IR signatures are similar for carbinols and carbocations, with the amine $\nu_{\text{N-C}}$ modes located around 3200 cm^{-1} and $\nu_{\text{C=C}}$ modes of the π -system around 1564 cm^{-1} and 1350 cm^{-1} . For 9-ethynylantracenyl derivatives, the triple bond stretching ($-\text{C}\equiv\text{C}-$) is too weak to be observable

in the carbinols' case but is clearly noticeable in the corresponding carbocations, probably due to its increased polarization imposed by the conjugation with the nearby carbocationic center.

The variation between the three sets of compounds featuring the same diaminoaryl group are, however, too small to draw a sensible trend. This is also true for the O-H stretching modes of the carbinols at ca. 3300-3500 cm^{-1} which correspond to a non-labile hydrogen, due to their broadness and overlap with potential $\nu_{\text{O-H}}$ modes of water originating from traces of moisture in the samples.

carbinols	$\nu_{\text{O-H}}$	Carbocations	$\nu_{\text{B-F}}$	Functional groups
O1(anth)^{OH}	3446	O1(anth)⁺	1056	-
O1(anthC₂)^{OH}	3407	O1(anthC₂)⁺	1162	2140 (-C≡C-)
O1(flu)^{OH}	3455	O1(flu)⁺	1168	-
O2(anth)^{OH}	3530	O2(anth)⁺	1163	-
O2(anthC₂)^{OH}	3421	O2(anthC₂)⁺	1249	2135 (-C≡C-)
O2(flu)^{OH}	3449	O2(flu)⁺	1167	-
O3(anth)^{OH}	-	O3(anth)⁺	1257	-
O3(anthC₂)^{OH}	3406	O3(anthC₂)⁺	1169	2132 (-C≡C-)
O3(flu)^{OH}	3447	O3(flu)⁺	1279	-
O4^{OH}	3435	O4⁺	1172	-

Table 1: Stretching frequencies of carbinols and carbocations (cm^{-1} , ± 2) for samples in KBr pellets or as neat powders

3.2. NMR spectroscopy

All carbinols, their organic precursors and carbocationic derivatives have been characterized by ^1H and ^{13}C NMR. The spectroscopic details for the known precursors of these compounds have been reported and will not be presented here, but the carbinols (**O1^{OH}**-**O4^{OH}**) with the exception of **O3(anthC₂)^{OH}** and their corresponding carbocations (**O1⁺**-**O4⁺**) are new and their NMR data will be briefly presented in the following paragraphs.

The more significant features in the carbinols' ^1H NMR spectra are the peaks of the hydroxyl group in the range 4.5 - 6 ppm (**Table 2**), which are sharp for tertiary alcohols; this suggests that the basicity of the oxygen is high and the hydrogen is not very labile, confirming the energetic $\nu_{\text{O-H}}$

observed in the IR spectrum (**Table 1**). The other signals are unremarkable, with doublets for the AB system related to the desired aromatic ketonic group ($^3J_{\text{H-H}} = 8.9$ Hz for $-\text{NMe}_2$, $^3J_{\text{H-H}} = 8.7$ Hz for $-\text{NPh}_2$) and corresponding signals for the fluorenium group in compounds **O3**⁺. The use of acetone- d_6 as a solvent was favored since the carbinols were far more stable in this polar solvent than in CDCl_3 . The latter can be acidic, due to impurities, and leads to partial dehydration of the sample. Moreover, acetone also avoids signal overlap in the aromatic region and results in clearer spectral signatures for the compounds.

	O1(flu)^{OH}	O1(anth)^{OH}	O1(anthC₂)^{OH}	O2(flu)^{OH}	O2(anth)^{OH}	O2(anthC₂)^{OH}
δ (ppm)	4.75	4.72	5.62	5.30	5.41	6.10

	O3(flu)^{OH}	O3(anth)^{OH}	O3(anthC₂)^{OH}	O4^{OH}
δ (ppm)	5.20	5.35 ^a	6.00	5.19

Table 2: ^1H NMR chemical shifts of hydroxyl groups in acetone- d_6 . a: shift obtained from a reaction mixture

All hydroxyl groups give clear trends in their ^1H NMR signals. Considering the same third branch, they experience an overall downfield shift going from $-\text{NMe}_2$ to rigidified compounds and finally $-\text{NPh}_2$, the latter two families of compounds having rather close values. This shift (**Table 2**) can be linked to the electron density present at the hydrogen of the hydroxyl group, since dimethylamino groups are more electron-releasing than diphenylamino groups, therefore leading to an increased shielding effect. In the same way, the planar system helps electron donation and shields the hydroxyl group compared to the non-planarized diphenylamino analogues.

As exemplified in **Figure 1**, upon formation of the carbocations, the signal related to the hydroxyl groups disappears and shifts are apparent for the signals of the protons of the aromatic region. This observation is not surprising since the π -system gains planarity and conjugation in the carbocations. A clear shift is thus noticeable for the ^1H signals of the diamino groups and for the fluorenyl units, but it is less pronounced for other aromatic signals of the various samples. Certainly, the observed shifts also originate to some extent from the different solvents used for characterizing the carbocations. Given that acetone- d_6 proved to partially reform the carbinol due to traces of water present in this solvent, CD_2Cl_2 or CDCl_3 were preferred, depending on the carbocations' solubilities.

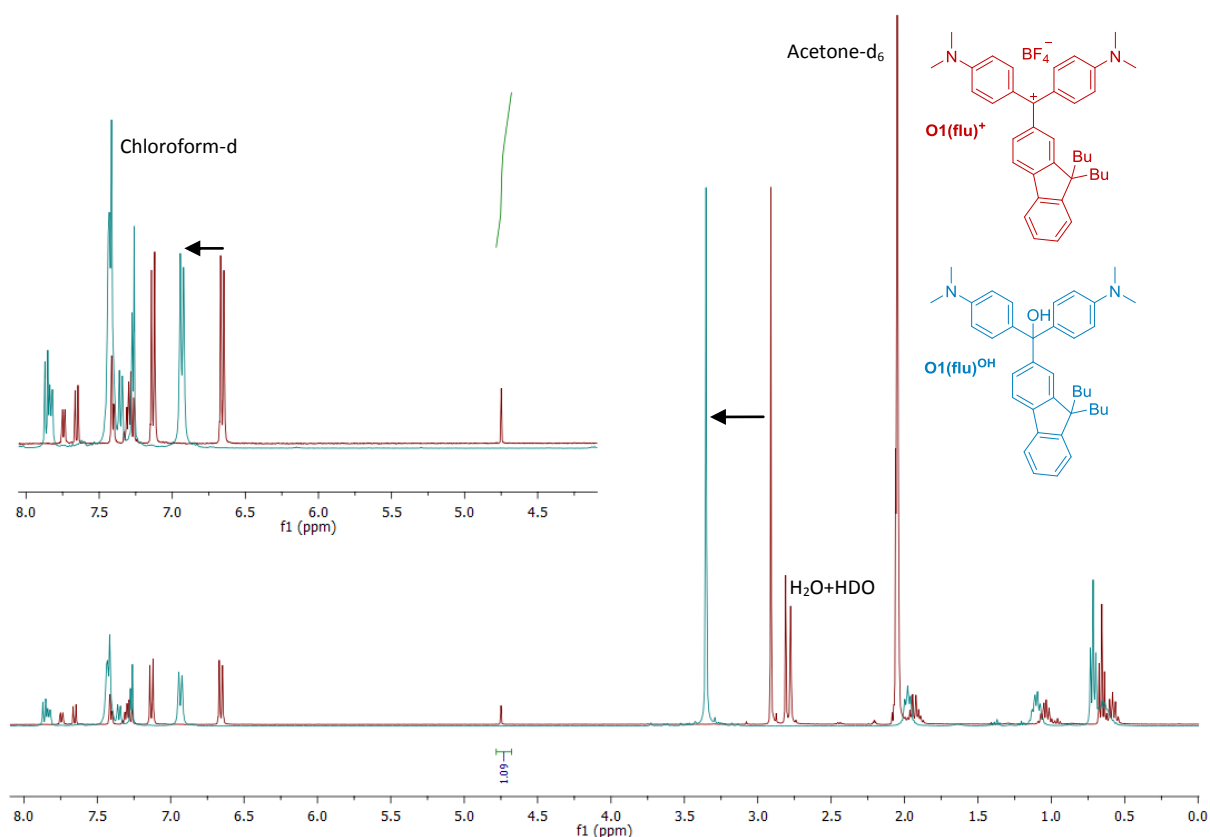


Figure 1: Overlaid ^1H NMR spectra of $\text{O1(flu)}^{\text{OH}}$ and O1(flu)^+

Because ^{13}C NMR shifts have been used to unravel the charge distribution in related carbocations,^[39-41] we had a closer look at the shift for this particular carbon atom for the various TPM dyes synthesized. For a given third branch, an upfield shift in the ^{13}C resonance of the C_α -carbon is observed when the electron-donating power of the amino substituents decreases (**Table 3**). The diphenylamine being less donating, it is less likely to induce shielding of the central carbocation, and the values of the shifts are higher than for the others. Furthermore, when compared to tritylcation (211.6 ppm), the shielding effect related to electron-donating groups is even more apparent. The same behavior is also observed for $(\text{O3}(\text{anth})^+)$, $(\text{O3}(\text{anthC}_2)^+)$, $(\text{O3}(\text{flu})^+)$ and their corresponding non-rigidified analogues in ^{13}C . Again, this difference in shift can be related to the fact that planar systems allow a better conjugation, resulting in the observed upfield shift. Conclusions from these data must be cautious, since in ^{13}C spectroscopy, the shifts are not solely related to the change in the atomic electron density but also to orbital effects, contrary to ^1H NMR. While the trends are similar, no proportionality could be found between the ^1H and the ^{13}C shifts, evidencing the presence of other contributing effects in the latter case.

$\delta^{13}\text{C}$ (ppm)	O1(anthC ₂) ^{OH}	O1(anth) ^{OH}	O1(flu) ^{OH}	O2(anthC ₂) ^{OH}	O2(anth) ^{OH}	O2(flu) ^{OH}
	107.31	83.88	82.02	105.97	83.87	82.14
	154.55	156.69	178.52	155.74	176.29	181.12
	O1(anthC ₂) ⁺	O1(anth) ⁺	O1(flu) ⁺	O2(anthC ₂) ⁺	O2(anth) ⁺	O2(flu) ⁺
$\delta^{13}\text{C}$ (ppm)	O3(anthC ₂) ^{OH}	O3(anth) ^{OH}	O3(flu) ^{OH}	O4 ^{OH}		
	103.87	/	83.76	81.56		
	150.28	158.12	172.73	179.26		
	O3(anthC ₂) ⁺	O3(anth) ⁺	O3(flu) ⁺	O4 ⁺		

Table 6: Comparison of ^{13}C NMR shifts of the C(OH) carbon atoms and carbocations for the various molecules synthesized

The shifts of the ^1H aromatic protons belonging to a given third branch in these **MG⁺** derivatives, when analyzed in terms of donating influence of the amino groups, do not lead to a clear trend. The electronic effect is not dominant here, as it is convoluted with another effect: the shifts are concentration dependent. This has never been mentioned in terms of spectroscopic studies in the literature, but it is not surprising considering that formation of π -stacked aggregates at concentrations above 10^{-4} M in solution is well known for these derivatives.^[42] Such a phenomenon certainly also influences the NMR shifts of the aromatic arm, as shown in **Figure 2**. Taking **O2(flu)⁺** as an example, the concentration-dependent shift observed for the ^1H signals in the aromatic region might be ascribed to such intermolecular interactions. The fact that there is no shift in the alkyl region suggests that there are no interactions between protons belonging to this part of the molecule or that such shifts are less sensitive to interactions.

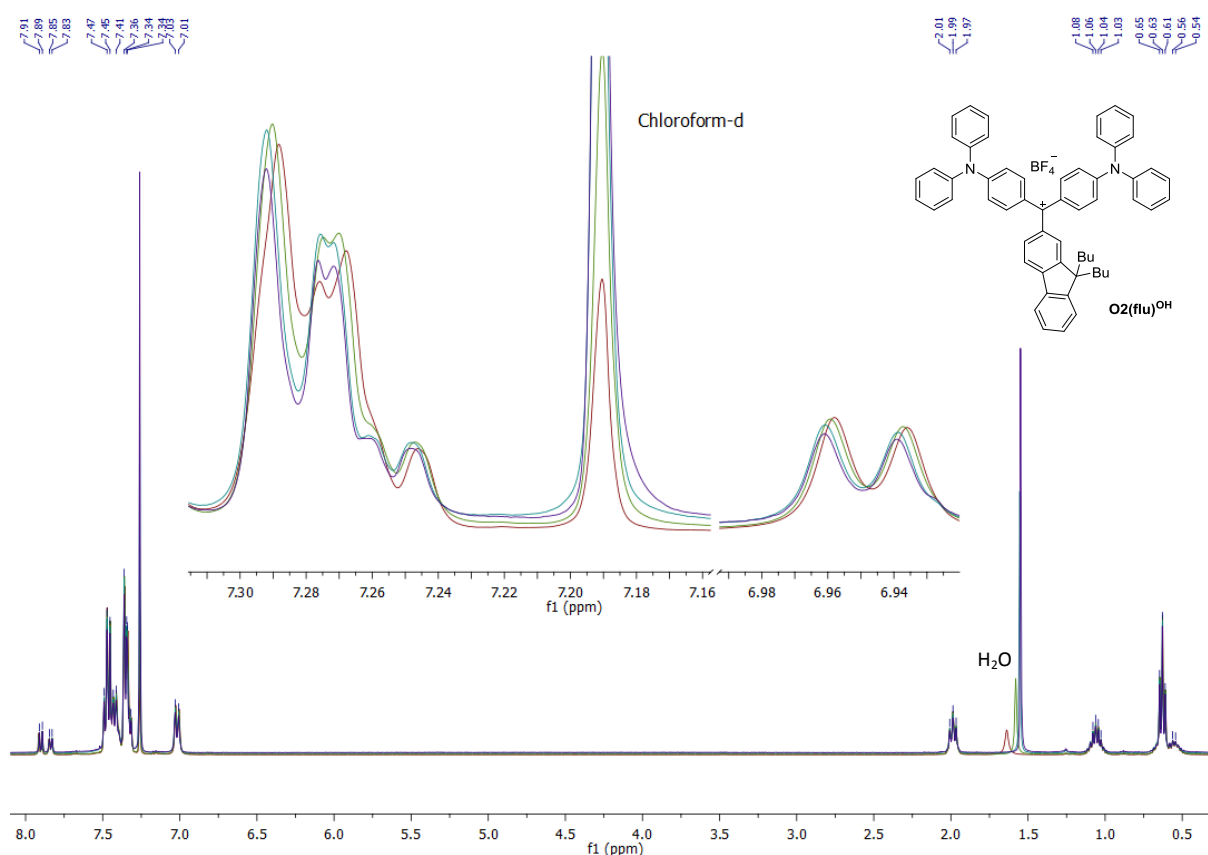


Figure 2: ^1H spectrum of **O2(flu)^{OH}** at four different concentrations ($5, 14, 20$ and $28 \cdot 10^{-3} \text{ mol.L}^{-1}$) in CDCl_3

3.3. Molecular structures

Except for **O1(flu)⁺** and **O2(flu)⁺**, the non-rigidified fluorene derivatives, crystals of all these compounds were obtained and proved to be suitable for X-ray studies. For **O1(flu)⁺** and **O2(flu)⁺**, the bulk of the butyl chains of the molecule probably complicated proper stacking during attempted crystallizations, an effect possibly compensated by the rigidified fluorenium in **O3(flu)⁺**. Most of these crystals are deeply colored with a shiny metallic glitter. For all derivatives, the asymmetric units are similar, as they mostly belong to monoclinic systems. More detailed crystallographic data can be found in the experimental part. **Figure 3** presents the adopted numeration scheme for the data in **Table 4**, which displays selected bond lengths as well as the torsion angle ϑ . The latter is defined by the angle between the plane containing the central carbon and the plane defined by the third arm, providing an indicator about its conjugation with the carbocation in the solid. The contribution of the mesomeric forms (**A**, **B** and **C**) in the GS can be estimated from the X-ray data. Even if form **C** appears

disfavored, it should induce a noticeable difference in the C1-C22 bond length compared to the typical $C(sp^3)-C(sp^3)$ distance. Reference bond lengths are given in the table for comparison.

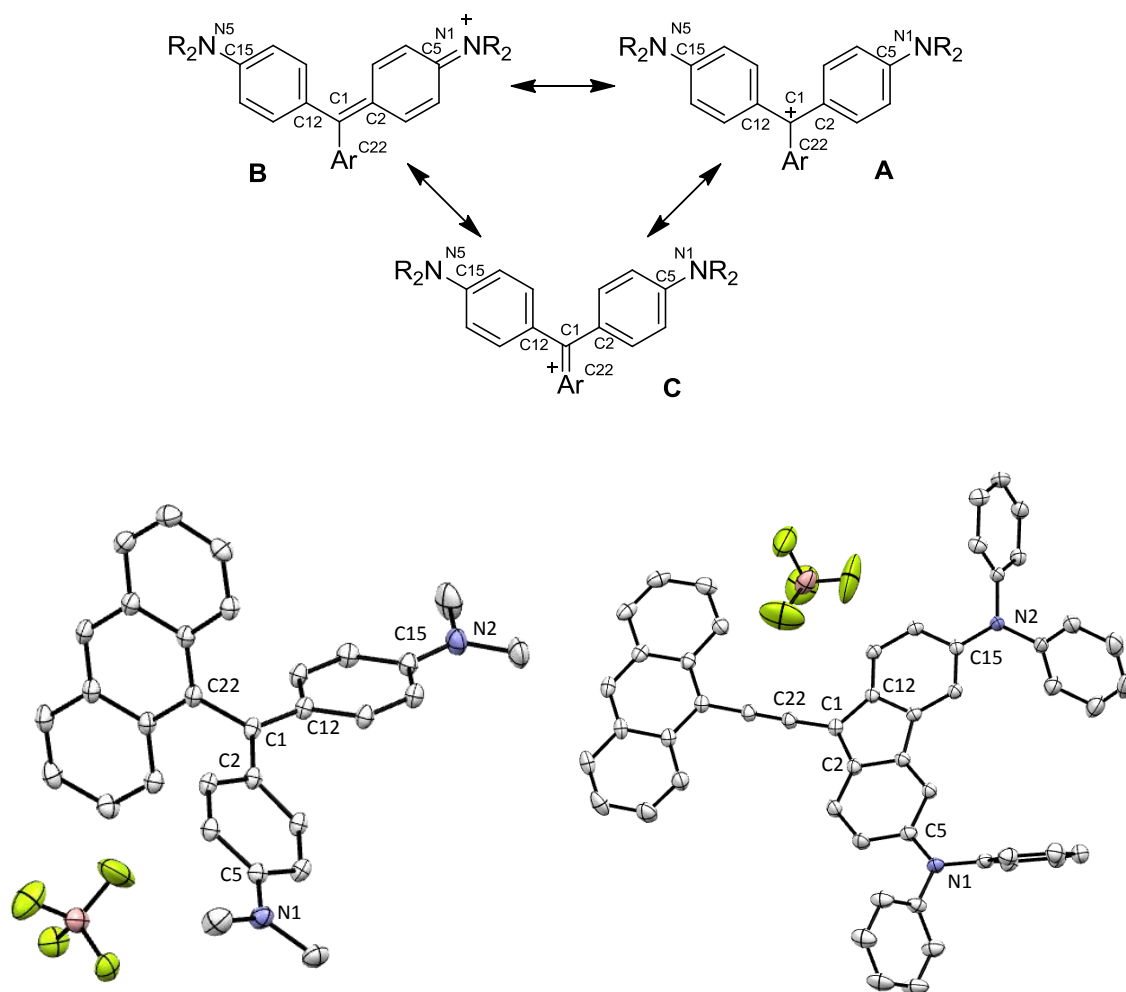


Figure 3: ORTEP views of **O1(anth)⁺** and **O1(anthC2)⁺** with their BF₄⁻ counter anions at 50 % probability (solved by Dr. Graeme Moxey). Hydrogen atoms and DCM have been omitted for clarity

In the solid state, the charge can be more localized on one side of the molecule due to interactions with the counter-anion. This can be appreciated by the difference in length between C1-C2 and C1-C12 as well as by the corresponding C-N bond lengths, and can be correlated to the distance between one of the nitrogen atoms and the counter anion; this is less noticeable for the aminophenyl derivatives, as the phenyl, possibly due to its steric bulk, prevents the counter anion interacting strongly with the nitrogen atoms. The conjugation with the central carbocation is apparent as the amine-carbon bond is shorter than a strict $C_{Ar}-N$ (planar) sp^2-sp^2 length, and hence possesses a double bond character. The same trend is also observed with the C1-C2 and C1-C12 bonds, which are shorter than typical Csp^2-Csp^2 bonds. According to these criteria, **O1(anth)⁺** and

O1(anthC₂)⁺ show much more conjugated structures than the other TPM dyes which crystallize with on average shorter bond lengths.

	C1-C2	C1-C12	Δ^a	C1-C22	C5-N1	C15-N2	Δ^a	Torsion angle ϑ^b
O1(anth)⁺	1.426(2)	1.414(2)	12	1.497(2)	1.343(2)	1.348(2)	5	-71.79 (1)
O2(anth)⁺	1.405(3)	1.448(3)	43	1.488(3)	1.351(3)	1.379(3)	28	76.45 (2)
O3(anth)⁺	1.400(5)	1.450(5)	50	1.477(5)	1.371(5)	1.396(5)	25	-69.52 (2)
O1(anthC₂)⁺	1.426(3)	1.433(3)	7	1.423(2)	1.341(3)	1.348(3)	7	-3.39 (3)
O2(anthC₂)⁺	1.436(3)	1.437(3)	1	1.412(2)	1.360(3)	1.378(3)	18	11.24 (2)
O3(anthC₂)⁺	1.425(3)	1.439(3)	14	1.392(3)	1.364(3)	1.374(3)	10	1.62 (2)
O3(flu)⁺	1.404(4)	1.466(5)	22	1.485(6)	1.348(5)	1.408(4)	60	-40.30 (5)
Typical bond length^c	C _{sp3} -C _{ar}	C _{sp2} -C _{ar}		C _{sp2} -C _{sp2}	C _{ar} -N(planar)			C _{sp2} =N
	1.513	1.483		1.460	1.371			1.279

Counter anion distance to	N1	N2	Δd^d	C1
O1(anth)⁺	7.053(2)	6.236(2)	0.83	4.950(2)
O2(anth)⁺	5.224(4)	5.312(4)	0.09	6.558(3)
O3(anth)⁺	7.103(6)	4.195(6)	2.9	6.033(6)
O1(anthC₂)⁺	4.043(3)	4.596(3)	5.55	7.484(3)
O2(anthC₂)⁺	5.279(3)	7.694(3)	2.4	9.062(3)
O3(anthC₂)⁺	6.532(4)	6.130(4)	0.4	7.379(4)
O3(flu)⁺	4.724(9)	7.533(9)	2.8	5.937(10)
O4⁺	5.713(8)	6.192(8)	0.48	5.824(8)

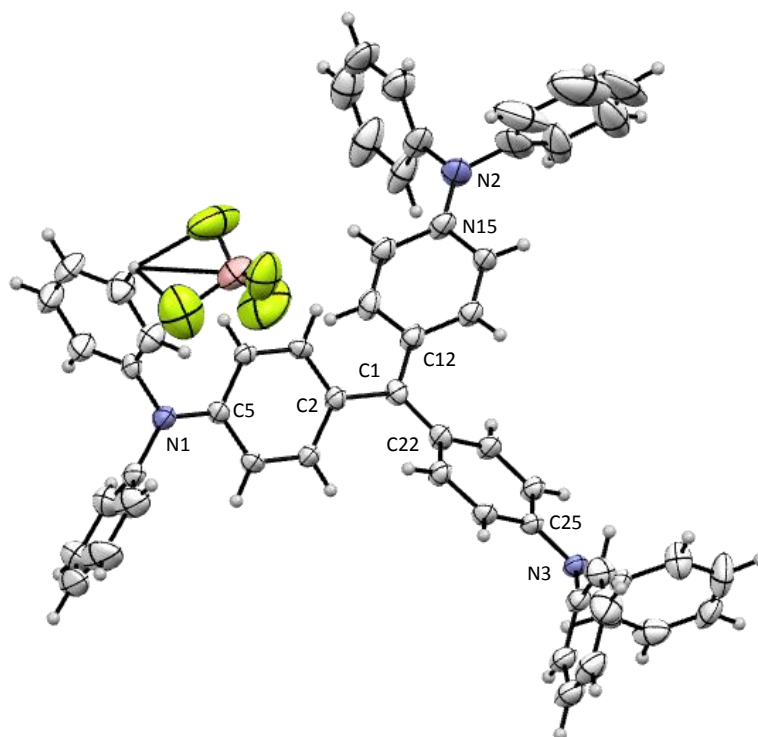
Table 4: Selected bond lengths and angles for the carbocations, errors in bracket. a: Difference between previous bond lengths in 10⁻³ Å. b See text for definition. c See ref.^[38] d: Difference between previous bond lengths in Å.

For all compounds, the C1-C22 bond is shorter than expected for a single aryl-carbon bond, showing that this aryl substituent is participating in charge delocalization, albeit less than the aminophenyl groups. This is particularly pronounced with the 9-ethynyl anthracene derivatives (**O1(anthC₂)⁺**, **O2(anthC₂)⁺**, **O3(anthC₂)⁺**), possibly because of the planarity of these systems with the inserted triple bond leading to relief of steric interactions. Comparison with the similar bonds in the anthracene derivatives (**O1(anth)⁺**, **O2(anth)⁺**, **O3(anth)⁺**) clearly reveals better π -conjugation of the third branch with the rest of the system in the former set of compounds.

While some of the derivatives have more localized positive charge on one of the amines (possibly due to counter anion interactions in the solid state), the other compounds reveal a complete conjugation supporting a more symmetrical structure, especially with the diarylamino

units. The third branch is also "communicating" with the rest of the system, but to a minor extent since the C⁺-C is close to the theoretical C_{sp2}-C_{Ar} bond length with the ethynyl systems being the more delocalized. The structures do not suggest a localized charge since they significantly differ from any of the three limiting forms (**A**, **B** or **C**); it is more likely that a form intermediate between **A** (carbocation) and **B** (iminium) exists.

In comparison, the only **CV**⁺ derivative crystallized does not possess marked dissymmetrical features, the central carbon being, as expected, planar like the other compounds and the three branches nearly equivalent and with a propeller shape to preserve the C₃ symmetry. A slightly more pronounced interaction of one of the branches can be observed, possibly due to interaction with the counter anion, as shown in **Figure 4**, and probably resulting from packing in the solid state. Also, in the conformation adopted by the molecules, the peripheral phenyls are twisted at 83° which limits the communication with the rest of the molecule. In solution, such a molecule most likely adopts a dynamic structure with a smaller average angle of the peripheral phenyls strengthening the electronic stabilization of the central carbocation (**Table 5**).



	C1-C2	C1-C12	C1-C22	C5-N1	C15-N2	C25-N3	Torsion peripheral phenyl	Torsion central phenyl
O4⁺	1.417(10)	1.450(10)	1.437(8)	1.379(9)	1.367(10)	1.370(8)	83.63 (1)	31.89 (7)

Table 5: Selected bond length in Å and angles in ° for **O4⁺**

In addition to structurally validating the targeted compounds, the X-ray crystallography studies confirm the geometries, especially for **O1(anth)⁺**, **O2(anth)⁺** and **O3(anth)⁺**, the anthracene derivatives. In these TPM dyes, the anthracenyl group is quasi-perpendicular to the rest of the molecule which severely limits electronic π -interaction with the rest of the molecule. In contrast, the 9-ethynylantracenyl group, at least in the solid state, is coplanar with the mean plane of the sp^2 carbocation, justifying a posteriori the extension of the system in order to increase the conjugation. The amino substituents are coplanar with the 1,4-phenylene rings, indicating charge delocalization. There is no evidence for an “out of the plane” distortion of the central carbon for the molecule in the solid state, such as for the solvent adducts hypothesized by Murayama.

3.4. UV-Visible spectroscopy

The spectra of carbinols and carbocations were recorded as solutions in DCM in the range 230 - 2000 nm. When compared to those of the corresponding carbocations, the absorption spectra of carbinol precursors reveal the absence of low-energy absorptions in line with the significant color difference between them. This provides a simple experimental means to ensure the purity of each solution. The sp^3 character of the carbinol disrupts the π -manifold, resulting in no charge-transfer process in the visible region. As a result the carbinols are slightly yellow due to absorbing mostly in the UV region due to $\pi - \pi^*$ and $n - \pi^*$ transitions of the aromatics. As soon as the carbocation is formed, a huge absorption in the visible region appears, resulting from the charge-transfer (CT) process taking place from the peripheral (4-arylamino and aryl) groups toward the central carbocation, as also revealed by theoretical calculations. The two transitions usually observed at lowest energy for **MG⁺** derivatives correspond to two different polarizations of this CT process. They are degenerate in the more symmetrical **CV⁺** derivatives, for which they correspond to the band at lowest energy.

Figure 5 displays a good illustration of the spectral difference between the CV^+ -based carbocations and carbinols O4^{OH} and O4^+ . The carbinol O4^{OH} absorbs in the UV range at wavelengths below 350 nm, while the carbocation possesses an intense band at 638 nm (CV^+ is at 586 nm) with a molecular extinction coefficient around $10^5 \cdot \text{L} \cdot \text{mol}^{-1} \cdot \text{cm}^{-1}$, similar to CV^+ . Note that O4^+ is shifted in a bathochromic way compared to CV^+ , illustrating the effect of arylamino substituents instead of alkylamino ones. From purely charge-transfer considerations, a weaker donor should increase the HOMO-LUMO gap and the band should be blue-shifted upon replacement of dimethylamino by diphenylamino substituents. However, the observed effect is the opposite. The effect of a lower donicity is possibly compensated by the bathochromic shift resulting from the overall extension of the conjugated π -system across the amine when progressing from dimethylamino to diphenylamino substituents. The other noticeable thing is that the shoulder on this transition in CV^+ seems to have disappeared, but given that the band is broader, such a shoulder might not be resolved and indeed be hidden beneath. Despite being forbidden for this fully symmetrical chromophore, the $S_0 \rightarrow S_3$ transition is also weakly observable near 410 nm for O4^+ .

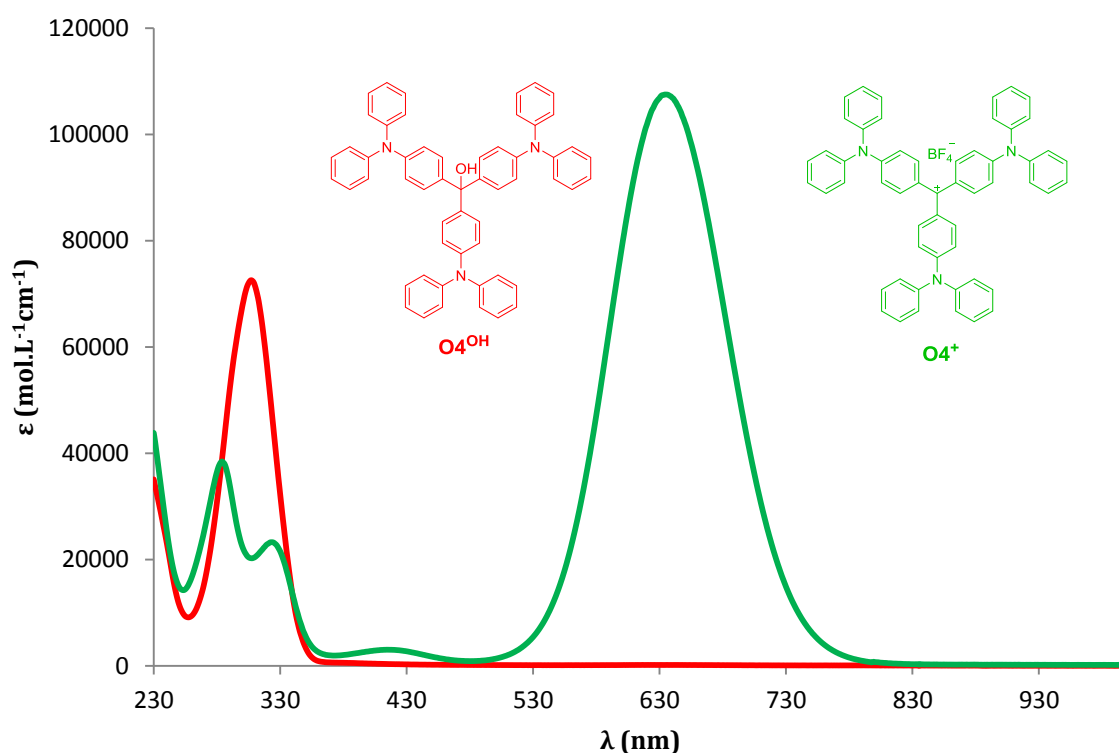


Figure 5: Spectra of O4^{OH} and $[\text{O4}^+][\text{BF}_4^-]$

Regarding the **MG**⁺ derivatives, the data can be analyzed in two ways, either by studying the influence of the third branch, or by studying the influence of the various diaminophenyl parts. **Table 6** displays the spectral features of these compounds. They all possess a characteristic set of two bands at low energy, with the first one between 620 and 702 nm for the non-rigidified derivatives (similar to **MG**⁺) and extinction coefficients around 10⁵·L·mol⁻¹·cm⁻¹. These absorption bands always possess a shoulder, which is barely noticeable for the diaminophenyl derivatives (series of compounds **O4**⁺). All these compounds also possess a second excited state around 450 nm, similar to **MG**⁺, the fluorene derivatives exhibiting a larger intensity for this second transition. These values are consistent with those reported in literature for similar derivatives, as listed in the previous paragraph.^[12] DFT calculations were conducted on model molecules by Dr. A. Amar and Prof. A. Boucekkine (University of Rennes 1) in order to help understand more precisely the origin of the different transitions observed for all these compounds. These results will be briefly presented in section 4.5.

Compound	O1(Anth) ⁺	O1(AnthC₂) ⁺	O1(fluo) ⁺	O2(Anth) ⁺	O2(AnthC₂) ⁺	O2(flu) ⁺
$\lambda_{S0 \rightarrow S1}$ (nm)	637	702	620	692	731	668
ϵ (10 ⁻⁵ ·L·mol ⁻¹ ·cm ⁻¹)	(1.06)	(1.17)	(1.30)	(0.91)	(1.25)	(0.89)
$\lambda_{S0 \rightarrow S2}$ (nm)	498	432	490	430	443	534
ϵ (10 ⁻⁵ ·L·mol ⁻¹ ·cm ⁻¹)	(0.16)	(0.13)	(0.48)	(0.09)	(0.09)	(0.48)
$\Delta\lambda$ (nm)	139	270	130	262	288	134
	O3(Anth) ⁺	O3(AnthC₂) ⁺	O3(flu) ⁺	O4 ⁺	CV ⁺	MG ⁺
$\lambda_{S0 \rightarrow S1}$ (nm)	1068	1141	1020	630	582	620
ϵ (10 ⁻⁵ ·L·mol ⁻¹ ·cm ⁻¹)	(0.25)	(0.13)	(0.33)	(10.6)	(1.26)	(1.02)
$\lambda_{S0 \rightarrow S2}$ (nm)	510	786	622	405 ^a	-	427
ϵ (10 ⁻⁵ ·L·mol ⁻¹ ·cm ⁻¹)	(0.13)	(0.32)	(0.54)	(0.03)	-	(0.18)
$\Delta\lambda$ (nm)	558	355	398	225	-	193

Table 9: Main absorption bands for **MG**⁺ and **CV**⁺-type carbocations. a: $\lambda_{S0 \rightarrow S3}$

The influence of the third branch is illustrated in **Figure 6** for the dimethylamino derivatives, but the same trend is observed with the other series. There is a bathochromic shift in proceeding from fluorenyl to anthracenyl to the 9-ethynylanthracenyl compounds. This apparently follows the number of electrons taking part in the conjugated π -system for each molecule. Indeed, **O1(anthC₂)**⁺ has thirty electrons, **O1(anth)**⁺ twenty-eight and **O1(flu)**⁺ twenty-six. Unexpectedly, this shows that despite the anthracenyl groups being nearly perpendicular to the π -system, the

electronic influence of this group is nevertheless felt by the carbocationic center, as revealed by its significant influence on the energy of the low-energy charge transfer process. Further evidence for such an influence comes from the comparison with Michler's hydrol blue (**Chart 4**), which has a reported absorption at 607.5 nm, at lower energy than the anthracene derivatives, showing that some interaction with the π -system is effective in the latter.^[43]

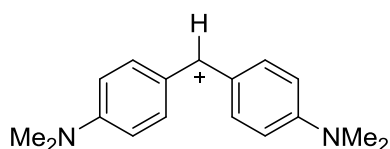


Chart 4: Michler's hydrol blue

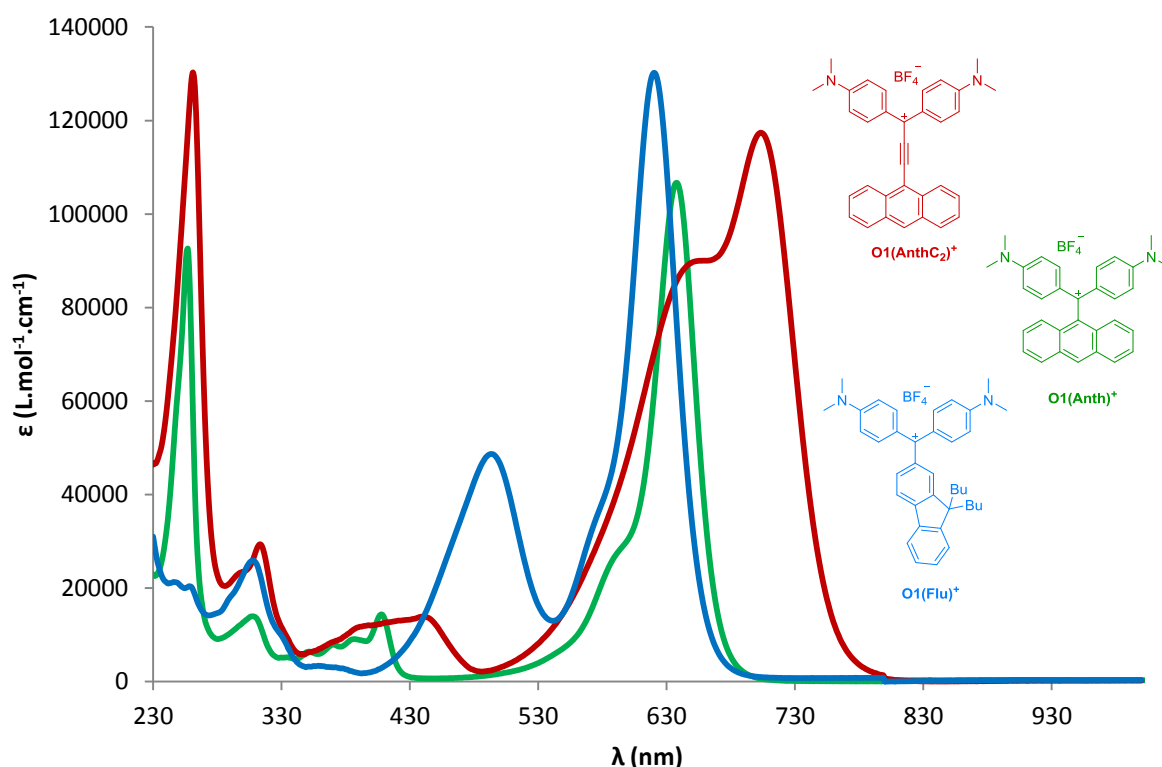


Figure 6: UV-vis spectra of $[O1(anthC_2)^+][BF_4^-]$, $[O1(anth)^+][BF_4^-]$ and $[O1(flu)^+][BF_4^-]$

The influence of the donor moiety for a given third branch, here fluorene, is displayed in **Figure 7**. Similar trends are also observed with anthracenyl and the 9-ethynylantracenyl derivatives. A bathochromic shift of 30 nm when proceeding from dimethylamino to diphenylamino substituents is observed. The intensity of each of the low-energy bands is similar and not greatly influenced by the changes in donor substituents, nor by the nature of the third branch. The case of rigid core derivatives is drastically different, as these absorptions experience a huge bathochromic shift to

appear around 1060 nm (in the NIR) for the absorption at lowest energy and near 630 nm for the second one. Furthermore, the low energy band is now less intense than the second one, and a vibronic progression seems to be present. Computational studies are needed to clarify the origin of this. The rigidification of the system maximizing the overlap between the π -manifolds of the two aminophenyl rings and the central carbocation is perhaps not the only origin of this important shift. It may also be partly due to the antiaromatic nature of the fluorenylium acceptor in this particular derivative which completely changes the system and therefore the absorptive properties.^[22] Indeed, rhodamines^[44] or other rigidified systems,^[45] do not experience a bathochromic shift compared to **MG**⁺ (Introduction, Chart 9), therefore the origin of such dramatically different spectral features cannot only be ascribed to the better π -overlap operative in the rigidified analogues.

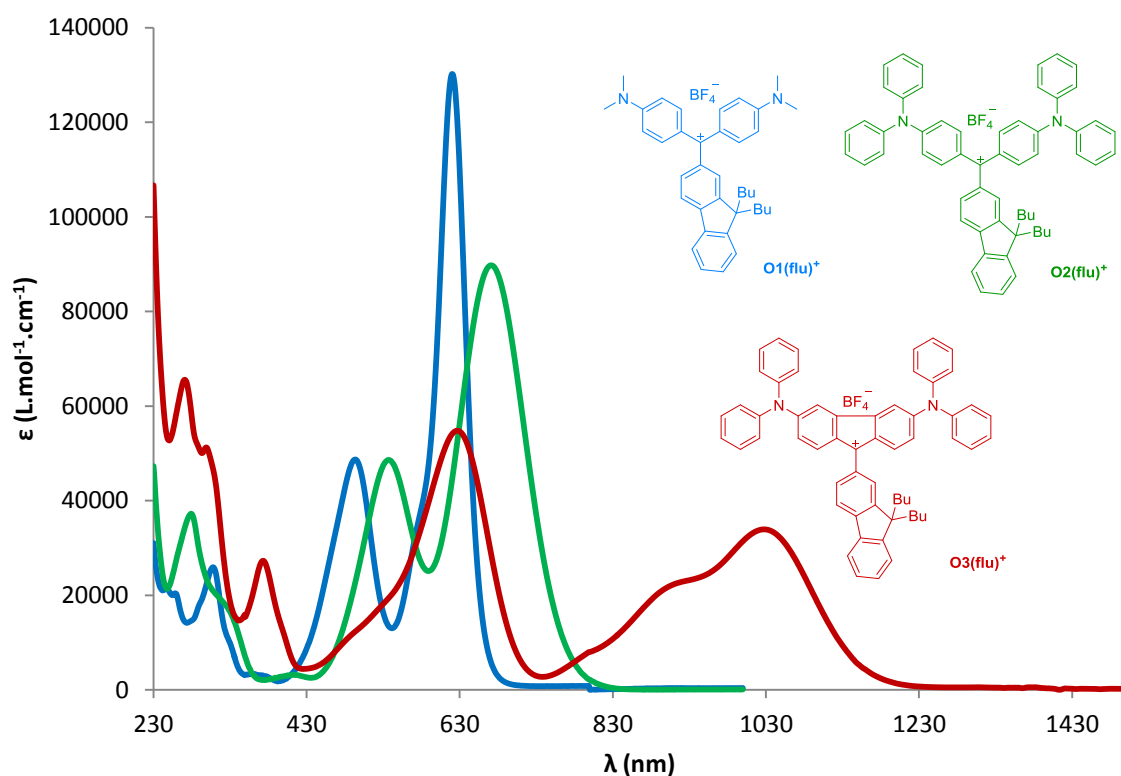


Figure 7: UV-Vis spectra of **[O1(flu)]⁺[BF₄⁻]**, **[O2(flu)]⁺[BF₄⁻]** and **[O3(flu)]⁺[BF₄⁻]**

In conclusion, the newly synthesized organic derivatives of **CV**⁺ and **MG**⁺ possess spectral features very similar to their parents, at least for the non-rigidified compounds. This is a good omen for the TPA measurements by Z-scan, since significant nonlinear properties can be expected for these derivatives. Moreover, for the other derivatives, the low-energy absorptions can be fine-tuned in energy either via a change of the donor amino substituents, as might have been expected, but also in quite a significant way by changing the nature of the third branch in the **MG**⁺-type derivatives. This is

more surprising given the poor overlap seen between this branch and the central carbocation in many derivatives. Another point to be mentioned is that **O2(anth)⁺**, **O2(anthC₂)⁺** and **O2(flu)⁺** are not fluorescent. Similar to the rhodamine derivatives cited in the Introduction (sect. 3.2.2.; **Chart 9**) for which rigidification of the central part (and protonation of the amine of the third branch) leads to faster radiative decays and induces some fluorescence at higher temperatures, such derivatives might be more fluorescent than their non-rigidified analogues.^[46] However, given the low energy of their first excited state, their fluorescence should take place at even lower energy and may not be simply detectable by sight. It will require a fluorimeter with infrared detector which was not available in Rennes or Canberra during this work.

3.5. Theoretical work

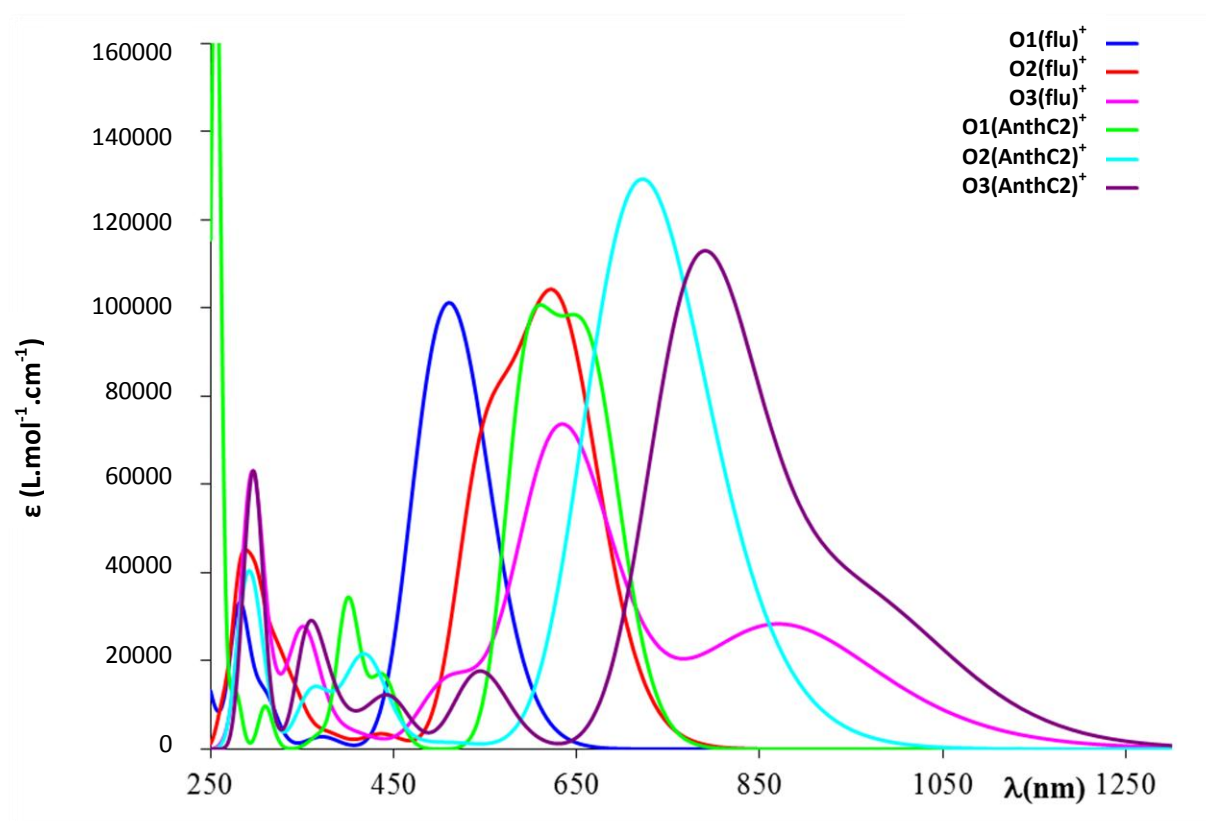


Figure 8: TD-DFT spectra computed for selected **MG⁺**-based derivatives

Modeling of selected **MG⁺** derivatives by DFT and calculation of their electronic absorption spectra by the TD-DFT method have been done by Dr. A. Amar and Prof. A. Boucekkine to provide additional insight into the nature of the transitions observed at lowest energy. As expected, for all

compounds, calculations reveal a large spread of the positive charge of the carbocation over the π -manifold in their ground state, in line with previous theoretical results.^[42,47] Their frontier molecular orbitals (MOs) are quite delocalized with a LUMO centered around the carbocationic center and HOMO mostly localized on the diaminophenyl part, while the HOMO-1 and HOMO-2 are also localized on the third aromatic branch, excluding the 9-ethynylantracenyl derivatives for which the nature of the HOMO and HOMO-1 is inverted relative to the other compounds (**Figure 8**). **Figure 9** displays the molecular orbitals of the three fluorene-containing derivatives as well as one of the anthracene-containing ones.

Overall, there is a rather good agreement between the theory and experiment for λ_{max} values, affording confidence in the molecular orbital interpretation of these transitions. Regarding the calculated energies for these transitions (**Table 7**), there are some discrepancies in the values found for the bands when compared to those experimentally observed, but the spectral trend is reproduced, *i.e.* diphenylamine has a bathochromic shift compared to dimethylamine and the rigidified compounds are even more red-shifted (**Figure 8**). In contrast, the molecular extinction coefficients are less accurately modeled, especially for the rigidified derivatives. The transitions involved are HOMO→LUMO and HOMO-1→LUMO, giving a strong CT character from the periphery to the center to the lowest energy transitions, in line with previous theoretical results.^[42,47,48] The first transition is a charge transfer localized on the amino-aryl/carbocation part of the molecule from the periphery to the carbocation. The second transition is a charge transfer from the third branch to the amines. These transitions appear inverted in the computations in the case of the 9-ethynylantracene derivatives, since the CT transition involving the non-donor substituted and the C^+ are at lower energy. Whether this is the case in the real molecules remains an open question considering the experimental intensities found which do not followed the computed ones. Nevertheless, this indicates that in 9-ethynylantracenyl derivatives both excited states must be very close, explaining the spectral overlap experimentally observed for these transitions in the case of the compounds **O1(anthC₂)⁺** and **O2(anthC₂)⁺**.

Obviously, the proper choice of the third branch in **MG⁺** derivatives allows fine tuning of the energy (and to some extent the intensity) of the lowest energy bands of these derivatives. Extension of the π -manifold leads to a bathochromic shift of the low energy bands, while incorporation of an alkyne spacer even leads to an inversion of the two charge-transfer states localized in the diphenyl-amino part and in the last branch of these systems. For the former set of compounds, the large influence of the nature of the third branch on the transition at lowest energy is mostly through the LUMO, while it influences the second transition through both the LUMO and HOMO-1. The reverse situation holds for the second set of compounds featuring the 9-ethynylantracenyl substituent.

HOMO-1	HOMO-2	HOMO	LUMO	LUMO+1	LUMO+2
O1(flu) ⁺					
O2(flu) ⁺					
O3(flu) ⁺					

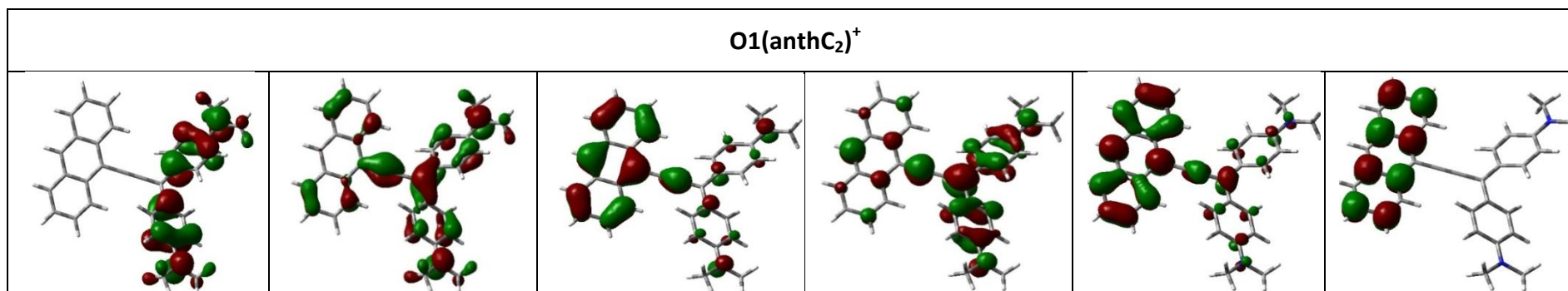


Figure 9: Molecular orbitals of selected MG⁺-based derivatives featuring either fluorenyl or 9-ethynylanthracenyl substituents as the third branch

	λ_{EXP}	λ_{max} (nm)	λ_{cal} (nm)	Oscillator strength	Main transitions (weight)
O1(Flu)⁺		281	281	0.2300	H-7->L+0(+59%) H-1->L+1(26%)
		371	371 (sh)	0.0305	H-2->L+0(+82%)
	628	510	528 488	0.9222 0.7600	H-0->L+0(+101%) H-1->L+0(+99%)
O2(Flu)⁺	280	288	300	0.2675	H-0->L+3(+66%) H-0->L+2(+23%)
	320	323	323 (sh)	0.1488	H-0->L+1(+97%)
	400	438	438	0.0388	H-2->L+0(+96%)
	530	553	551	0.7708	H-1->L+0(+98%)
	650	621	631	1.1050	H-0->L+0(+100%)
O3(Flu)⁺	380	296	297	0.2638	H-1->L+0(+48%) H-0->L+3(+22%)
	630	353	353	0.2950	H-0->L+1(+82%)
	780	513	513	0.2169	H-3->L+0(+94%)
	920	635	635	1.0133	H-1->L+0(+99%)
	1030	873	873	0.3887	H-0->L+0(+97%)
O1(AnthC₂)⁺		402	400	0.2503	H-1->L+1(+54%) H-3->L+0(45%)
		445	438	0.136	H-2->L+0(+77%) H-0->L+1(21%)
	630	610	599	0.7332	H-1->L+0(+101%)
	720	645	663	0.7050	H-0->L+0(+100%)
O3(AnthC₂)⁺		400	421	0.1678	H-0->L+1(+96%)
	730	724	728 717	0.8219 0.9686	H-1->L+0(+100%) H-0->L+0(+100%)
O3(AnthC₂)⁺	810	543	543	0.1506	H-3->L+0(+95%)
	1010	788	788	1.1773	H-1->L+0(+101%)
	1140	968	968	0.3292	H-0->L+0(+98%)

Table 10: Computed absorption wavelengths at the B3LYP/6-31G* level in DCM

4. Z-scan studies

Z-scan measurements have been performed very recently in collaboration with Dr. Katarzyna Matczyszyn and Prof. Marek Samoc at Wroclaw University of Technology (WUT) and preliminary TPA cross-section data are reported here, measured by open aperture measurements. These give a better understanding of the potential of these compounds to behave as two-photon absorbers. The Z-scan measurements were carried out with a femtosecond laser in the range 300 - 2000 nm. The measurements were carried out on isolated TPM dyes dissolved in a slightly acidified solution of DMSO. This solvent was chosen for solubility reasons and to avoid any photo-induced side reactions often observed between chlorinated solvents and the amines. The addition of acid was done in order to ensure stability over time of the desired carbocation and avoid any carbinol formation due to adventitious traces of water. The use of Z-scan can provide information on both real and imaginary parts of $\chi^{(3)}$ but only σ_{TPA} is described in this work. The rigidified compounds were not measured because their stability in the solvent turned out to be problematic in the strong laser beam used.

Nonetheless, all the compounds show relatively large third-order NLO responses. **Table 11** summarizes the maxima for the TPA cross-sections of these compounds, along with some figures of merit. Every compound of the series shows the same TPA behavior, the transition corresponding to the second lowest absorptive band being far more active than the transition at lower energy, in contrast to what was observed in the linear spectrum, but in line with previous theoretical predictions and experimental measurements.^[47-49] The higher intensity of the second TPA band can indeed be ascribed to a smaller detuning with the first absorption band leading to the observed improvement,^[48] a situation often encountered with octupolar chromophores.^[50] As a result, the TPA band is located between 800 nm and 1100 nm for the second absorption and around 1200 nm for that at lowest energy.

CV⁺ and **MG⁺** measured under similar conditions to the other compounds provide reference values permitting evaluation of the impact of the structural modifications on the cross-sections. **Figure 10** displays the linear absorption spectrum of **MG⁺** and its two-photon equivalent, where the two transitions are clearly apparent. These measurements constitute the first measurements of **MG⁺** and **CV⁺** using fs Z-scan at several wavelengths. For **CV⁺**, only the cross-section values corresponding to the one-photon allowed (i.e. TPA-forbidden) transition have been obtained, to avoid any interference with linear absorption, but it is legitimate to suppose that the $\sigma_{\text{TPA max}}$ of **CV⁺** is higher (> 230 GM) than the one found for **MG⁺** for this second TPA transition, based on symmetry considerations. Significantly lower cross-sections were found for these compounds in the present

studies than those reported by Beljonne *et al.* by TPEF (762 GM and 673 GM at respectively, 840 and 880 nm for **MG**⁺ and 1980 GM at 752 nm for **CV**⁺).^[47] This is somewhat surprising, since Z-scan is generally accepted as less accurate, and usually leads to higher cross-section values than TPEF. However, these TPEF measurements were of compounds with very low fluorescence quantum yields, so large concentrations had to be used, leading to experimental uncertainties as large as 40 % for **MG**⁺.^[47] Such a large experimental uncertainty is still insufficient to explain the discrepancy with our values. The good agreement found with computed cross-sections in the earlier report cannot be considered as conclusive given the large uncertainties of computed third-order NLO values. In this respect, this first cross section computed for **CV**⁺ (of 300 GM)^[51] is less relevant than the last values calculated (2041 GM).^[47] Whatever the reason for the differences, our values can be considered as lower bounds of the actual TPA activities, and the fair internal consistency between values obtained for different TPM derivatives allows us to discuss the impact of structural modifications among these derivatives.

Thus, among the **MG**⁺ derivatives, the more active compounds are the fluorenyl derivatives, notably the diphenylamine derivative **O2(flu)**⁺ (**Figure 11**). The figure of merit used (here with molecular mass) decreases due to the butyl chains, which are inert in terms of NLO merit. The fluorene derivatives tend also to be more photo-stable under the high laser fluence used. By comparison the anthracene derivatives seem to decompose slowly during the measurement, with the experimental setup used. This is not surprising, since anthracene derivatives can be quite photochemically unstable and the high light intensity probably results here in photochemical side-reactions. Figures of merit where these values have been divided by the molecular mass of the molecules are also provided in the Table.

The diphenylamino analogue of **CV**⁺, **O4**⁺, possesses a much larger cross-section (785 GM) than **CV**⁺. consistent with the use of diphenylamine as an electron-donating substituent favorably influencing the TPA cross-sections.

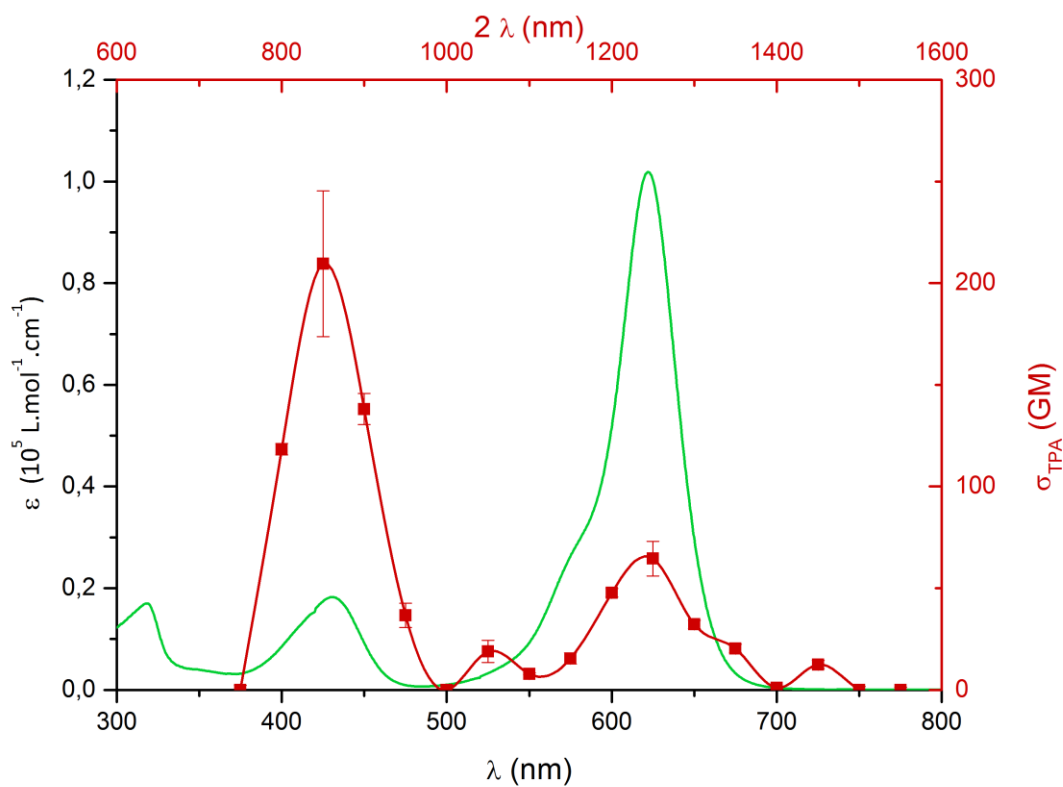


Figure 10: linear (green) and TPA (red) spectra of $[\text{MG}^+][\text{Cl}^-]$

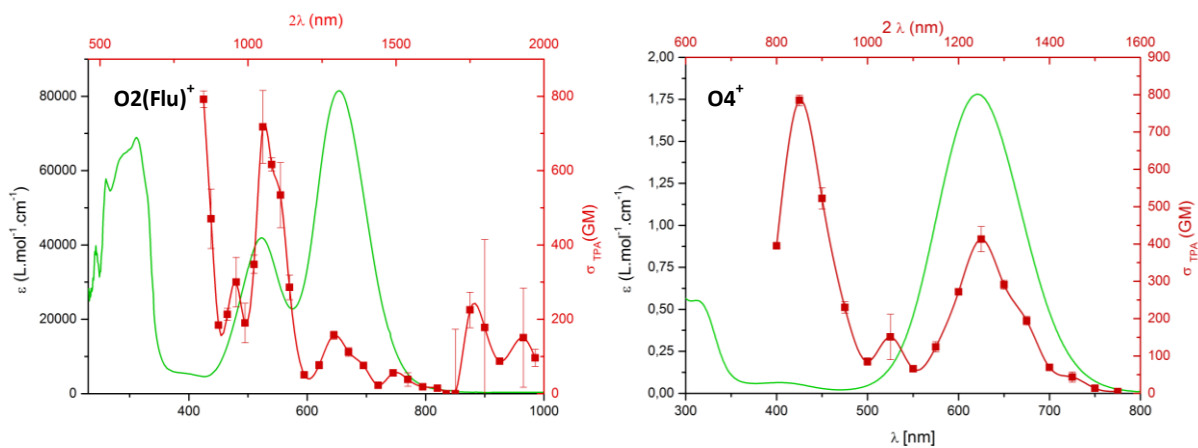


Figure 11: linear (green) and TPA (red) spectra of $[\text{O2(flu)}^+][\text{BF}_4^-]$ and $[\text{O4}^+][\text{BF}_4^-]$

	MG⁺	CV⁺	O1(anthC₂)⁺	O1(anth)⁺	O1(flu)⁺
λ (nm)	850	1283	900	800	1080
	1250		1300	1200	1290
σ_{TPA}(GM)^a	209 (36)	119 (8)	228 (6)	178 (3)	261 (8)
	64 (9)		161 (8)	75 (3)	40 (2)
Figure of merit (Mw)	0.50	0.29	0.42	0.34	0.42
	0.15		0.30	0.16	0.06
	O2(anthC₂)⁺	O2(anth)⁺	O2(flu)⁺	O4⁺	
λ (nm)	1100	950	1050	850	
	1400	1300	1290	1250	
σ_{TPA}(GM)^a	205 (10)	351 (57)	717 (97)	785 (15)	
	100 (5)	229 (58)	157 (10)	413 (33)	
Figure of merit (Mw)	0.26	0.46	0.83	0.94	
	0.13	0.30	0.18	0.50	

Table 11: TPA of the synthesized compounds in acidic DMSO. a: error in brackets

To sum up our observations, there is a clear positive effect of replacing the dimethylamino by diphenylamino substituents for generation of TP-absorbers. In line with our expectations, the values found here for the TPA cross-sections are hundreds of GM units, good for molecules of that size. Maximal TPA values occur at low energies, a remarkable feature of interest for several applications. There is nearly a two-fold increase when switching to the arylamino derivatives. For **MG⁺** derivatives, the extension of the π -system and resulting planarity when progressing between **O1(anthC₂)⁺** and **O1(anth)⁺** also results in an increase in the TPA cross-sections. Despite having less π -electrons than the other groups tested as "antennas" on the **MG⁺** derivatives, the fluorene leads to the most interesting derivatives, and possesses good photo-stability with the highest TPA cross-sections. The **CV⁺** derivative is more active than **MG⁺**. While it possesses an extended π -system, its octupolar symmetry is also at the origin of this performance relative to less symmetrical **MG⁺**-based derivatives. Re-measuring the rest of the series in a more suitable solvent (if any can be found) should afford further conclusions about the effect of the rigidification in these TPM-based systems.

5. Conclusion

The targeted all-organic TPM dyes have been synthesized following a convergent synthesis via the formation of carbinols formed subsequent to lithiation reactions. Upon addition of acid to these carbinol precursors, isolation of the desired carbocations was achieved in good yields. These species have been characterized with the usual methods, and in many cases by X-ray crystallography. Their structures were thus confirmed, and their geometries in the solid state provide key information on their electronic structure in the ground state (GS). Finally, their linear absorption spectra have been recorded. Their UV-vis spectra resemble that of **MG**⁺ (or of **CV**⁺ for **O4**⁺) with compounds exhibiting two (or one) main transitions at low energy in the NIR range.

Based on these data and on DFT calculations, the positive charge on these compounds appears strongly delocalized along the π -manifold between the diamino groups in the GS. The dominant VB mesomer imparts a carbocationic character to the central carbon while a comparably lower iminium character is distributed over the nitrogen atoms. The third branch has only a small impact on the electronic structure in the GS except when a triple bond is added. Despite this small impact of the third branch in the GS, its influence on the excited states is stronger, as extension of the π -system, with fluorene, anthracene or 9-ethynylanthracene, leads to a pronounced bathochromic effect on the corresponding absorption spectra. Replacement of the dimethylamino substituents by diphenylamino substituents followed by partial rigidification of the carbocationic system have an even more dramatic effect, especially in the latter case, which induces red-shifts of the lowest absorption up to 200 nm in the NIR region.

Finally, in line with our expectations, Z-scan measurements confirmed the potential of these compounds as two-photon absorbers with relatively large σ_{TPA} cross-sections for such small derivatives. Moreover, these TPA processes take place at quite low energies, a remarkable feature that can be interesting for several applications. A significant increase of the TPA-response with diphenylamine derivatives as well as fluorene has been observed. Fluorene-containing compounds also possess a better photo-stability under the laser fluence compared to the anthracene series, which partially decomposed in the experimental conditions. The octupolar derivative **O4**⁺ is the most active of the series, confirming the interest in this specific geometry.

References

- [1] J. Griffiths, K. J. Pender, *Dyes & Pigments* **1981**, 2, 37–48.
- [2] J. Fabian, H. Hartmann, *Light Absorption of Organic Colorants*, Springer, Berlin, Heidelberg, **1980**.
- [3] G. N. Lewis, J. Bigeleisen, *J. Am. Chem. Soc.* **1943**, 65, 2102–2106.
- [4] G. N. Lewis, T. T. Magel, D. Lipkin, *J. Am. Chem. Soc.* **1942**, 64, 1774–1782.
- [5] G. N. Lewis, M. Calvin, *Chem. Rev.* **1939**, 25, 273–328.
- [6] A. Barker, C. C. Barker, *J. Chem. Soc.* **1954**, 1307–1309.
- [7] C. C. Barker, G. Hallas, A. Stamp, *J. Chem. Soc.* **1960**, 3790–3800.
- [8] C. C. Barker, G. Hallas, *J. Chem. Soc.* **1961**, 2642–2644.
- [9] C. C. Barker, G. Hallas, *J. Chem. Soc.* **1961**, 1529–1531.
- [10] C. C. Barker, G. Hallas, *J. Chem. Soc. B Phys. Org.* **1969**, 1068–1071.
- [11] C. Aaron, C. C. Barker, *J. Chem. Soc. B Phys. Org.* **1971**, 319–324.
- [12] G. Hallas, J. D. Hepworth, D. R. Waring, *J. Chem. Soc. B Phys. Org.* **1970**, 975–979.
- [13] G. Hallas, K. N. Paskins, D. R. Waring, *J. Chem. Soc. Perkin Trans. 2* **1972**, 2281–2286.
- [14] D. A. Brown, M. J. S. Dewar, *J. Chem. Soc. Resumed* **1954**, 2134–2136.
- [15] S. Nakatsuji, H. Nakazumi, H. Fukuma, T. Yahiro, K. Nakashima, M. Iyoda, S. Akiyama, *J. Chem. Soc., Perkin 1*, **1991**, 1881–1886.
- [16] S. Nakatsuji, H. Nakazumi, H. Fukuma, T. Yahiro, K. Nakashima, M. Iyoda, S. Akiyama, *J. Chem. Soc. Chem. Commun.* **1990**, 489–491.
- [17] S. Nakatsuji, K. Nakashima, M. Iyoda, S. Akiyama, *Bull. Chem. Soc. Jpn* **1988**, 61, 2253–2255.
- [18] S. G. R. Guinot, J. D. Hepworth, M. Wainwright, *Dyes & Pigments* **1999**, 40, 151–156.
- [19] S. G. R. Guinot, J. D. Hepworth, M. Wainwright, *Dyes & Pigments* **2000**, 47, 129–142.
- [20] X. Vidal, J. R. Herance, J. Marquet, J. L. Bourdelande, J. Martorell, *Appl. Phys. Lett.* **2007**, 91, 081116.
- [21] J. E. Whitaker, P. L. Moore, R. P. Haugland, R. P. Haugland, *Biochem. Biophys. Res. Commun.* **1991**, 175, 387–393.
- [22] P. Costa, I. Trosien, M. Fernandez-Oliva, E. Sanchez-Garcia, W. Sander, *Angew. Chem.* **2015**, 127, 2694–2698.
- [23] G. R. Bardajee, Beilstein *J. Org. Chem.* **2011**, 7, 135–144.
- [24] A. Noack, A. Schröder, H. Hartmann, *Dyes & Pigments* **2003**, 57, 131–147.
- [25] J. Lux, E. J. Peña, F. Bolze, M. Heinlein, J.-F. Nicoud, *ChemBioChem* **2012**, 13, 1206–1213.
- [26] A. M. Costero, M. Parra, S. Gil, R. Gotor, R. Martínez-Mañez, F. Sancenón, S. Royo, *Eur. J. Org. Chem.* **2012**, 2012, 4937–4946.
- [27] M. J. Hannon, P. C. Mayers, P. C. Taylor, *Tetrahedron Lett.* **1998**, 39, 8509–8512.
- [28] J. N. Moorthy, A. L. Koner, S. Samanta, A. Roy, W. M. Nau, *Chem. – Eur. J.* **2009**, 15, 4289–4300.
- [29] J. Ipaktschi, R. Hosseinzadeh, P. Schlaf, E. Dreiseidler, R. Goddard, *Helv. Chim. Acta* **1998**, 81, 1821–1834.
- [30] B. Kobin, L. Grubert, S. Blumstengel, F. Henneberger, S. Hecht, *J. Mater. Chem.* **2012**, 22, 4383–4390.
- [31] Z. Q. Gao, P. F. Xia, P. K. Lo, B. X. Mi, H. L. Tam, M. S. Wong, K. W. Cheah, C. H. Chen, *Org. Electron.* **2009**, 10, 666–673.
- [32] M. R. Netherton, G. C. Fu, *Org. Lett.* **2001**, 3, 4295–4298.
- [33] M. Chandrasekharam, G. Rajkumar, C. S. Rao, T. Suresh, P. Y. Reddy, J.-H. Yum, M. K. Nazeeruddin, M. Graetzel, *Adv. Nat. Sci. Nanosci. Nanotechnol.* **2011**, 2, 035016.
- [34] D. Hellwinkel, H. Stahl, H. G. Gaa, *Angew. Chem.* **1987**, 99, 822–823.

- [35] D. Hellwinkel, H. Stahl, H. G. Gaa, R. Gottfried, *Phosphorus Sulfur Relat. Elem.* **1983**, *18*, 121–124.
- [36] M. S. Kim, H. Y. Oh, J. W. Kyung, S. K. Kim, J. M. Lee, Y. S. Han, C. G. Park, J. G. Yoon, *United States Patent Application: 0050037234 - Organic EL Device*, **A1**, 20050037234.
- [37] S. Egusa, *Semiconductor Luminescent Device Having Organic/inorganic Junction*. **1991**, EP0448268 (A2).
- [38] F. H. Allen, D. G. Watson, L. Brammer, A. G. Orpen, R. Taylor, in *Int. Tables Crystallogr.* (Ed.: E. Prince), International Union Of Crystallography, Chester, England, **2006**, pp. 790–811.
- [39] G. A. Olah, E. B. Baker, M. B. Comisarow, *J. Am. Chem. Soc.* **1964**, *86*, 1265–1265.
- [40] D. A. Forsyth, R. J. Spear, G. A. Olah, *J. Am. Chem. Soc.* **1976**, *98*, 2512–2518.
- [41] R. R. Naredla, C. Zheng, S. O. Nilsson Lill, D. A. Klumpp, *J. Am. Chem. Soc.* **2011**, *133*, 13169–13175.
- [42] S. Lovell, B. J. Marquardt, B. Kahr, *J. Chem. Soc. Perkin Trans. 2* **1999**, 2241–2247.
- [43] F. Dietz, N. Tyutyulkov, M. Rabinovitz, *J. Chem. Soc. Perkin Trans. 2* **1993**, 157–164.
- [44] T. J. Sørensen, K. Kilså, B. W. Laursen, *Chem. – Eur. J.* **2015**, *21*, 8521–8529.
- [45] T. Pastierik, P. Šebej, J. Medalová, P. Štacko, P. Klán, *J. Org. Chem.* **2014**, *79*, 3374–3382.
- [46] T. J. Sørensen, K. Kilså, B. W. Laursen, *Chem. – Eur. J.* **2015**, *21*, 8521–8529.
- [47] D. Beljonne, W. Wenseleers, E. Zojer, Z. Shuai, H. Vogel, S. J. K. Pond, J. W. Perry, S. R. Marder, J.-L. Brédas, *Adv. Funct. Mater.* **2002**, *12*, 631–641.
- [48] J. Campo, A. Painelli, F. Terenziani, T. Van Regemorter, D. Beljonne, E. Goovaerts, W. Wenseleers, *J. Am. Chem. Soc.* **2010**, *132*, 16467–16478.
- [49] K. J. Thorley, J. M. Hales, H. Kim, S. Ohira, J.-L. Brédas, J. W. Perry, H. L. Anderson, *Chem. – Eur. J.* **2013**, *19*, 10370–10377.
- [50] C. Katan, S. Tretiak, M. H. V. Werts, A. J. Bain, R. J. Marsh, N. Leonczek, N. Nicolaou, E. Badaeva, O. Mongin, M. Blanchard-Desce, *J. Phys. Chem. B* **2007**, *111*, 9468–9483.
- [51] J. L. Bredas, C. Adant, P. Tackx, A. Persoons, B. M. Pierce, *Chem. Rev.* **1994**, *94*, 243–278.

Chapter II:

Organometallic derivatives of malachite green

Chapter II

Organometallic derivatives of malachite green

Contents

1. Introduction	103
1.1. Literature review	105
1.1.1. Ferrocene derivatives	105
1.1.2. Metal alkynyl derivatives	108
1.1.3. Allenylidene derivatives	110
1.1.4. Other organometallic derivatives	112
2. Synthesis	113
2.1. Synthesis of organic precursors	115
2.2. Synthesis of ethynylferrocene derivatives	116
2.3. Synthesis of alkynyl complexes	117
3. Characterization	120
3.1. Ferrocene derivatives	121
3.1.1. IR spectroscopy	121
3.1.2. NMR spectroscopy	121
3.2. Organometallic derivatives	122
3.2.1. IR spectroscopy	122
3.2.2. NMR spectroscopy	124
3.3. X-ray crystallography	125
3.3.1. Carbinols	125
3.3.2. Metal allenylidene/metal alkynyl derivatives	126
3.3.3. Metal bis-alkynyl derivatives	128
3.3.4. Conclusion	129
3.4. UV-Vis spectroscopy	130
3.4.1. Ethynylferrocene derivatives	130
3.4.2. Metal allenylidene derivatives	133
3.4.3. Ruthenium alkynyl derivatives	134
3.4.4. Conclusion	136
3.5. Cyclic voltammetry	137

3.5.1. Ethynylferrocene derivatives.....	137
3.5.2. Metal alkynyl or allenylidene derivatives.....	139
3.5.3. Conclusion	142
3.6. Spectroelectrochemistry	143
3.6.1. MG^+ -based derivatives	144
3.6.2. Allenylidene derivatives	147
3.6.3. Conclusions on spectroelectrochemical studies	150
4. Conclusion	150
References.....	153

1. Introduction

This chapter describes the synthesis of several organometallic derivatives (**Chart 1**) based on $\text{MG}^+(\text{C}_2)$ architectures and is aimed at introducing a redox-active metal center on the branch that is not functionalized with an amino group. These modifications should lead to an enhancement of the third-order NLO properties and provide the opportunity to tune them, depending on the metal's oxidation state and on the wavelength of the incident light. A literature review focused on related organometallic complexes is presented first. The synthesis of the targeted molecules is then described, followed by their characterization using diverse analytical techniques: NMR, IR, and UV-Vis spectroscopies, and cyclic voltammetry. These data are then discussed and compared. The last-mentioned technique will reveal if the complexes undergo reversible redox processes and will provide useful information on their chemical stability in states featuring additional positive charge on the metal center. In order to investigate further the influence of the metal oxidation on the linear absorptive properties, some spectroelectrochemical studies were also conducted. Based on these studies, the possible influence of oxidation on the NLO properties will be briefly discussed.

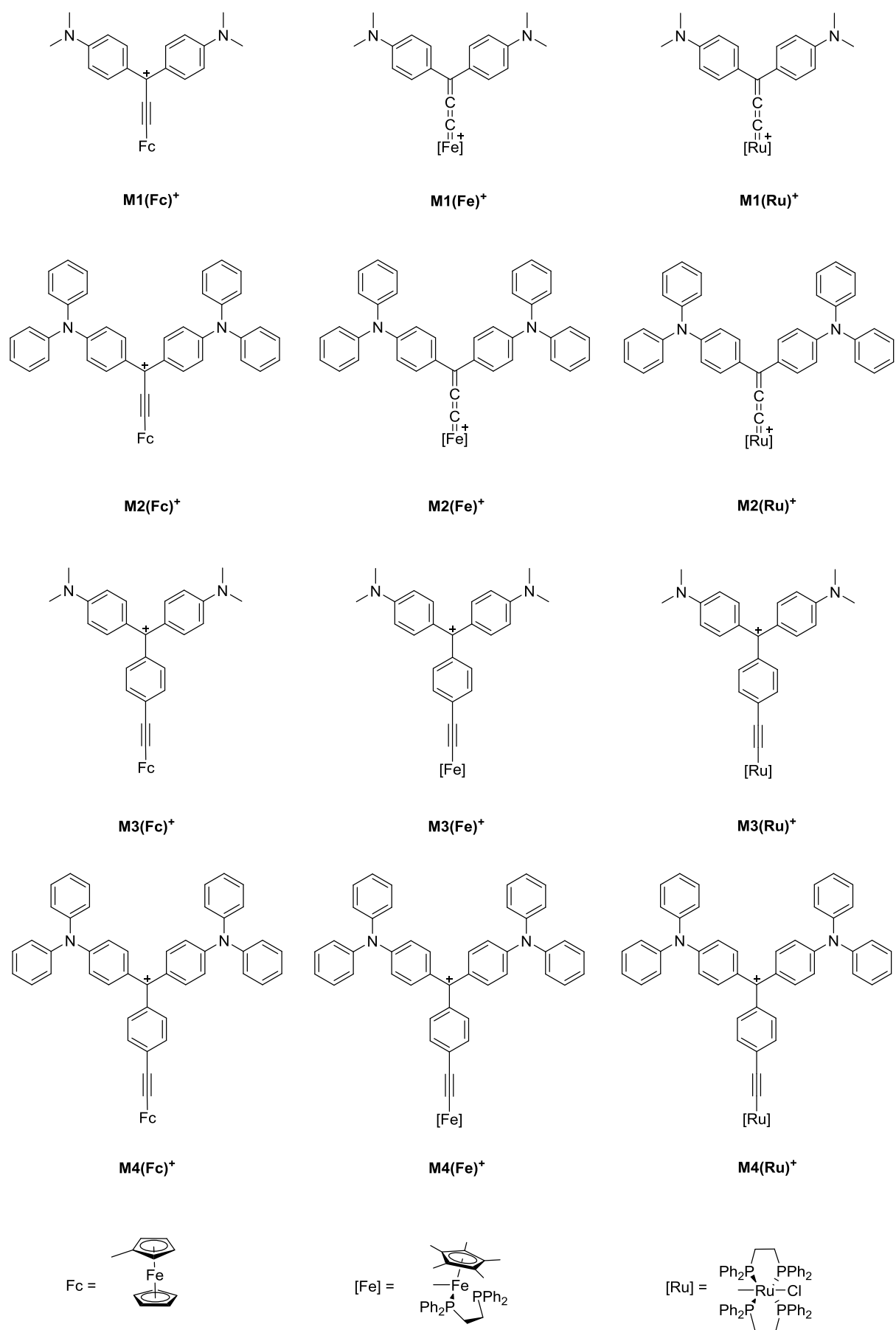


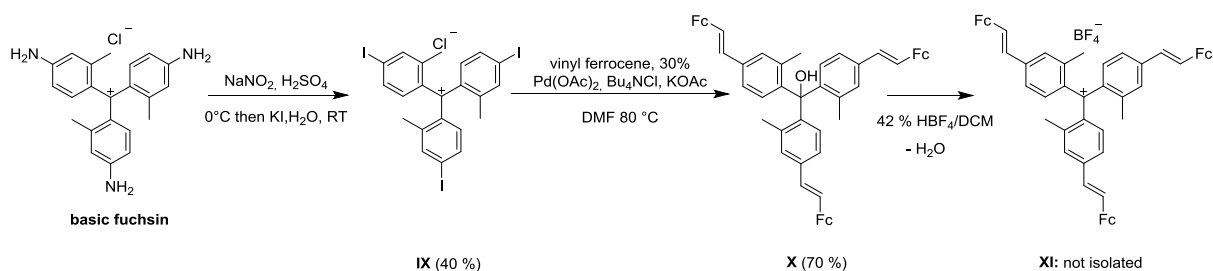
Chart 1: Targeted organometallic derivatives of **MG⁺**

1.1. Literature review

Redox-active organometallic TPM dyes are not often encountered among third-order NLO-active substances as their synthesis can be difficult and often leads to reactive/sensitive compounds. In the same way as for organics, these compounds can be accessed *via* their carbinol precursors, which must be synthesized first. The desired carbocations are then generated *in situ* from these precursors in acidic media. This part is mostly focused on the synthesis of such organometallic derivatives involving a d^6 transition metal and possessing a structure similar to \mathbf{MG}^+ and \mathbf{CV}^+ . These two structures are very close and their optical properties are often compared in the literature. Accordingly, the corresponding compounds featuring similar organometallic endgroups will be reviewed at the same time in the following sections.

1.1.1. Ferrocene derivatives

The most commonly used redox-active organometallic synthon is certainly ferrocenyl (Fc). It can be manipulated like an organic moiety as it is inert to most of the classic reactions and can usually sustain an aerobic work-up. It is oxidized at a potential near 0.5 V vs. SCE. **Chart 2** displays some derivatives built on the \mathbf{MG}^+ or \mathbf{CV}^+ cores that were reported in the literature. For instance, the symmetric complex **XI** made by Sengupta *et al.* on a \mathbf{CV}^+ core features vinyl ferrocene termini in place of the amino groups.^[1,2] The corresponding symmetrical halogenated \mathbf{CV}^+ derivative **IX** was firstly synthesized from commercial derivatives and vinyl ferrocene was then coupled to the halogenated positions *via* a Heck reaction (**Scheme 1**).



Scheme 1: Synthesis of **XI** starting from basic fuchsin

The carbocation **XI** was then formed *in situ* upon addition of HBF_4 but was not isolated. The UV-Vis spectrum reveals that the organometallic group acts as a mild donor explaining the intense absorption band observed at low energy ($\lambda = 1068 \text{ nm}$). The latter possesses a significant

bathochromic shift ($\Delta\lambda = 478$ nm) when compared to **CV**⁺. Similar non-symmetric derivatives were also reported. The series of compounds **XII** and **XIII** (**Chart 2**) have thus been synthesized by Arbez-Gindre and co-workers from organolithium precursors and the corresponding ketones.^[3] Again, none of these carbocations were isolated. They possess structures similar to either **CV**⁺(**XII**_c) or **MG**⁺ (**XII**_{a,b} and **XIII**_{a,b,c}). Accordingly, their UV-Vis characteristics resemble those of **CV**⁺ and **MG**⁺ but again feature huge bathochromic shifts of their low-energy absorptions. In addition, the first hyperpolarizabilities of **XII** and **XIII** have been measured by hyper-Rayleigh scattering (HRS), showing their interest as second-order NLO-phores with frequency-dependent β values up to 900×10^{-30} esu for **MG**⁺ derivatives and 1700×10^{-30} esu for **XII**_{a-c} derivatives (at 1.064 μ m). No third-order NLO properties were reported for these particular TPM dyes.

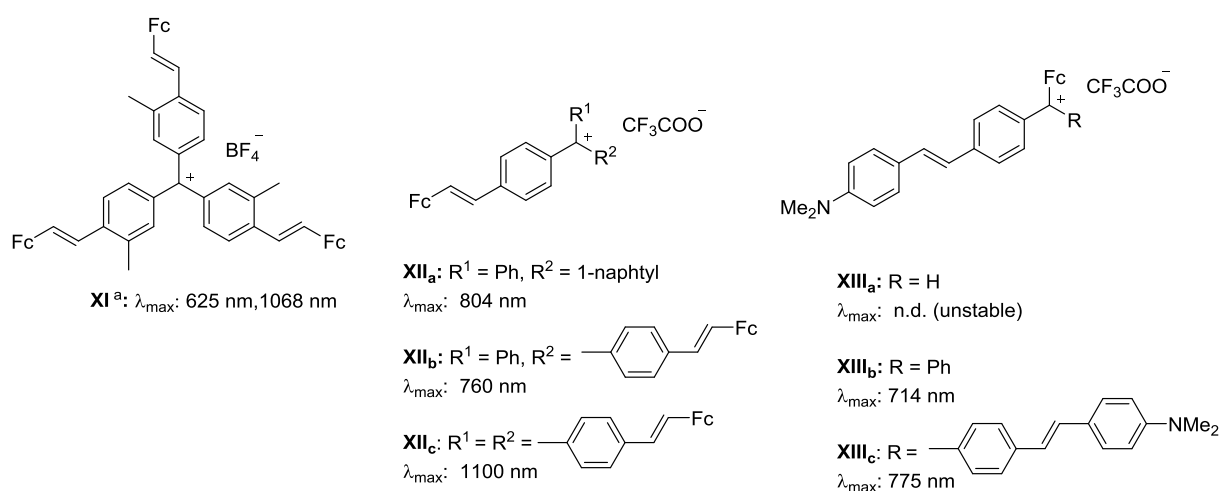


Chart 2: Ferrocene derivatives of **CV**⁺ and **MG**⁺ from Sengupta *et al.* and Arbez-Gindre and co-workers. a: HBF₄ (42%)/DCM, b: TFA (33-93%)

The same kind of ferrocene derivatives were subsequently used to form dendrimers by Villalonga-Barber *et al.* (**Chart 3**).^[4,5] Here also, the carbocations were generated *in situ* from the carbinol precursors in acidic media. The same problems related to their isolation, stability and characterization were noted, as some of them, such as **XIV**_a, only survived a few hours in solution. The spectra of these ferrocene derivatives, measured *in situ*, exhibit absorption bands in the NIR range, while the spectra of analogous purely organic dendrimers possess absorptions resembling those of **MG**⁺. This again illustrates the bathochromic shift induced at the low-energy band by the presence of ferrocenyl-based electron-releasing groups. The cyclic voltammetry of the precursor carbinol dendrimers has been performed, showing a quasi-reversible metal-centered Fe(II)/Fe(III) oxidation. In contrast, none of the carbocations has been subjected to electrochemical

investigations. Thus, the influence on the Fc^+/Fc redox interconversion on the linear optical properties of these dyes has not been quantified.

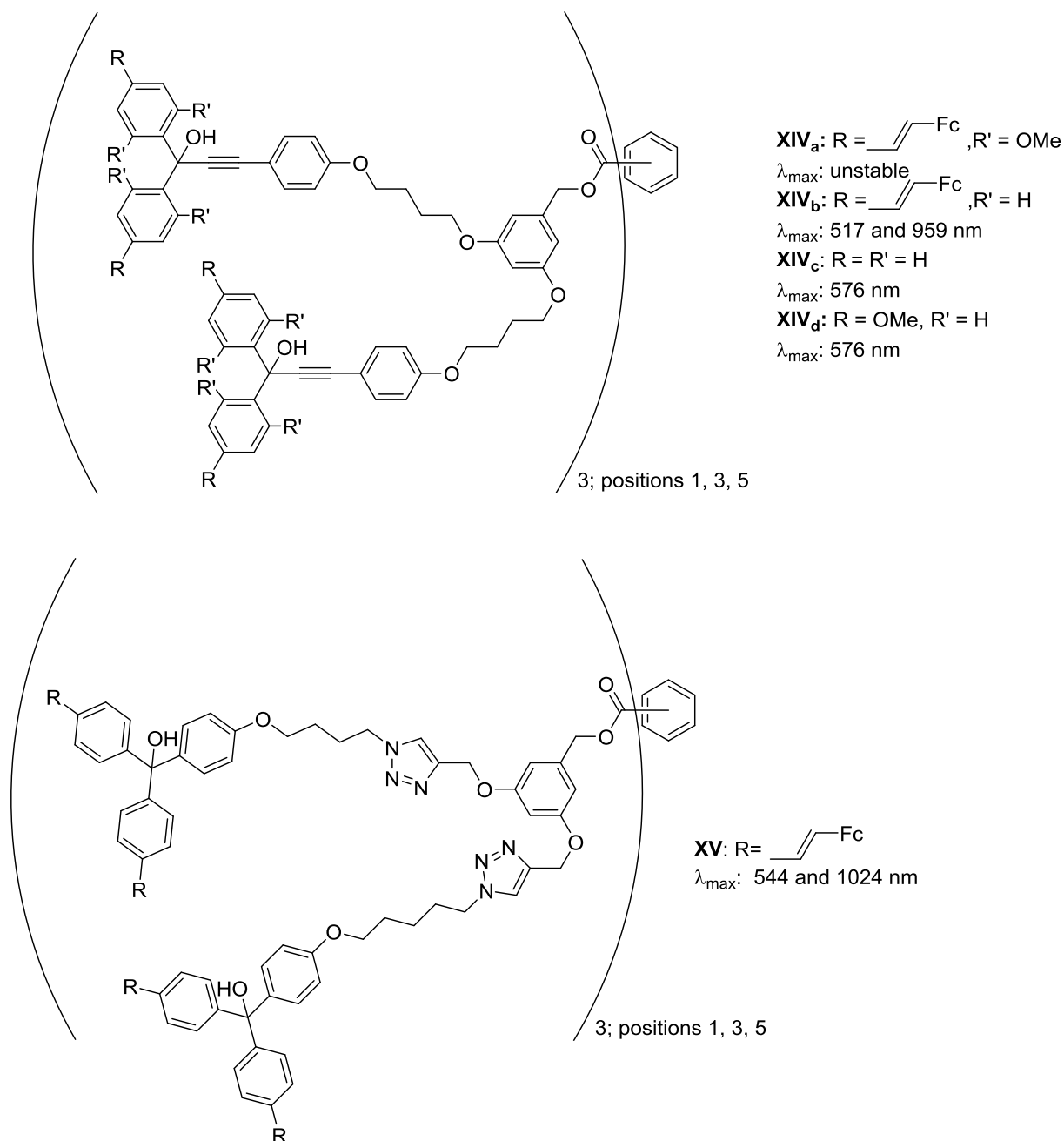


Chart 3: Dendrimers synthesized by Villalonga-Barber *et al.*

Two other groups studied related ferrocenyl carbocations. The derivatives **XVI-XVIII** (**Chart 4**) were obtained using the same lithiation-based synthetic approach as that used for **XII** and **XIII**. While **XVI** proved to be fairly unstable, with a lifetime of about 5 min (and could only be characterized by NMR spectroscopy at low temperature),^[6] **XVII** and **XVIII** were less reactive and could be

characterized *in situ* at room temperature.^[7] All these ferrocenyl-based carbocationic species formally possess a redox tautomer with a Fe^{II} 16-electron structure stabilized by the bridgehead carbon. Such a VB description reveals the allenylidene-type character of these derivatives (**A** and **B**, **Figure 1**).^[8] Despite not being directly related to TPM dyes, such a VB description helps one to understand the chemistry of these ferrocenyl carbocations, and shows how iron helps stabilize the positive charge. This also explains the large bathochromic shifts of the low-energy bands observed for these derivatives. No cyclic voltammetry has been reported for these systems. However, even if interesting as dyes, they are too unstable to be used for NLO-based applications. The use of dimethyl- or diphenylamino substituents, as in **M1** and **M2**, should help in stabilizing them and facilitate their isolation.

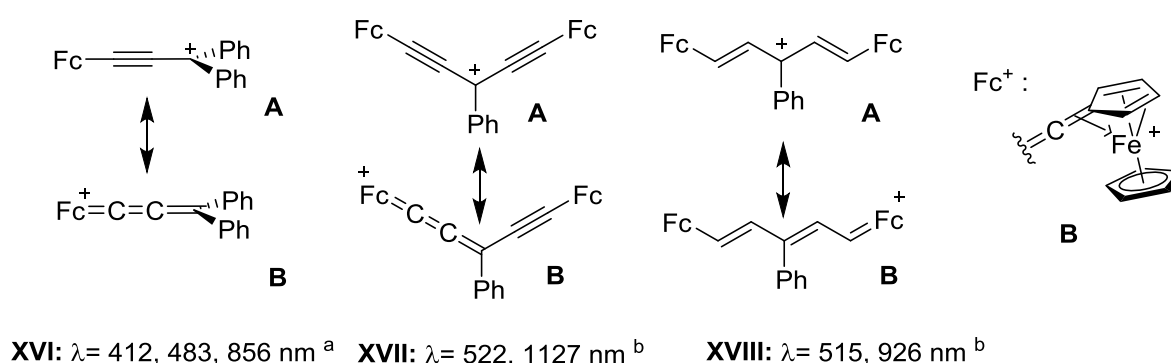


Figure 1: Ferrocenyl derivatives. a: DCM + HBF_4 , -70°C , b: *in situ* measurement with TFA

Ferrocenyl groups act as stabilizing electron-releasing groups in the examples above, as all these derivatives are significantly more stable than the (unsubstituted) tritylcation. All these compounds also possess NIR absorptions that are of interest for this project. Furthermore, their carbinol precursors can be reversibly oxidized, although no measurements on the carbocations have been reported thus far. Most of the carbocationic species are formed *in situ* and there is no simple way to measure them. Finally, it appears that no ethynyl ferrocene derivatives of MG^+ have been reported, although such species would certainly be more stable than species such as **XIV**.

1.1.2. Metal alkynyl derivatives

Derivatives of this kind, featuring group 8 (redox-active) metal alkynyl substituents in place of the ethynyl ferrocene groups, are even less frequent in the literature.

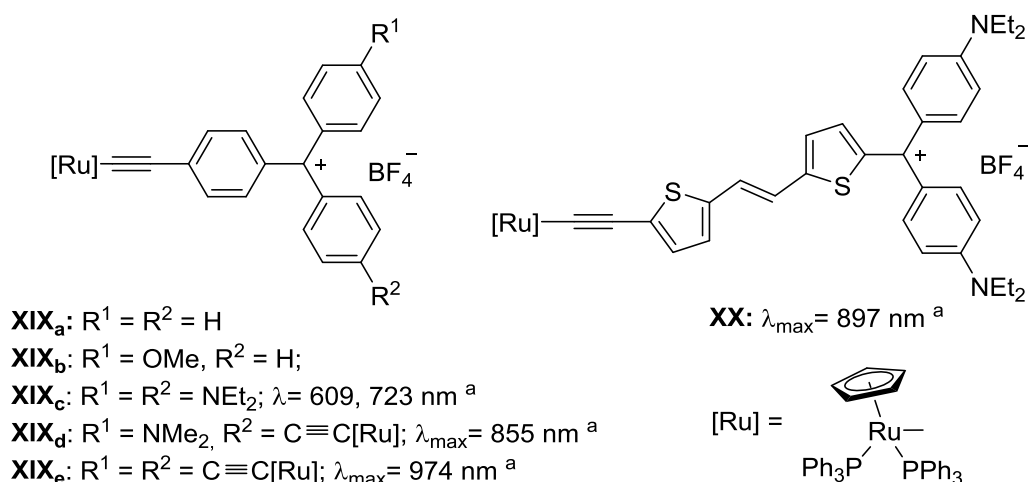
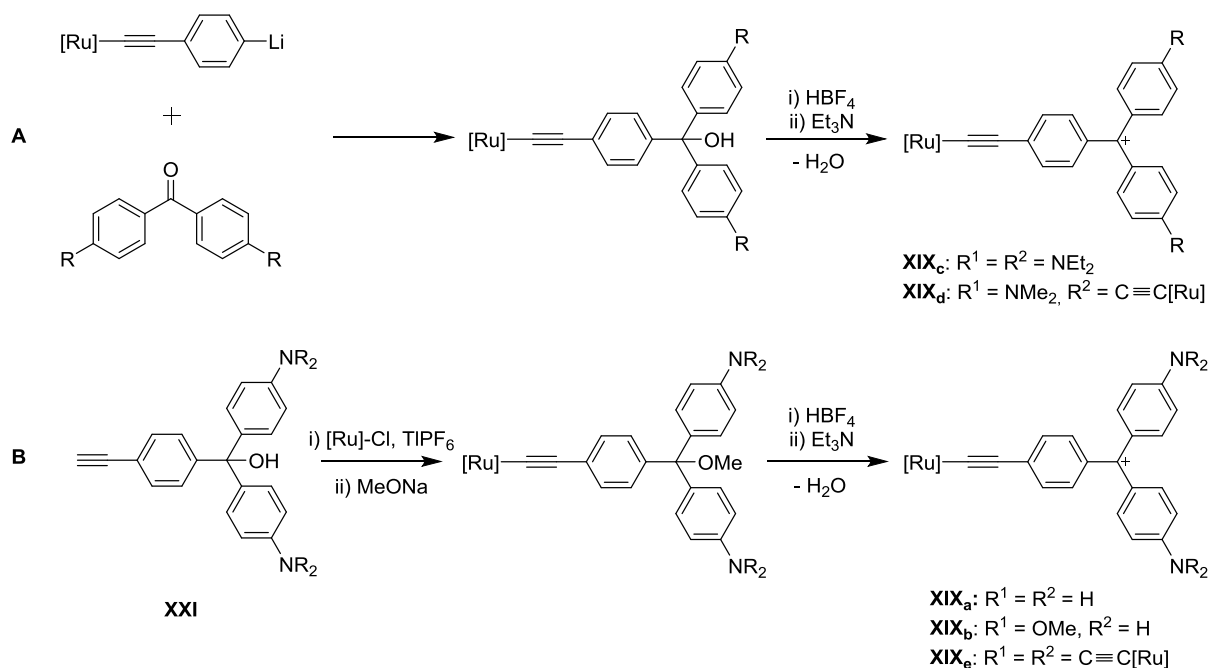


Chart 4: CV^+ and MG^+ organoruthenium derivatives. a: in DCM

The compounds **XIX** and **XX** (Chart 4) made by Wu *et al.* are the only ones of this kind reported thus far. They illustrate the gain of stability brought to the TPM carbocations by the use of more donating organometallic synthons than ferrocenyl, such as " $Ru(Cp)(PPh_3)_2$ ", which can also efficiently replace some of the dialkylamino groups in CV^+ -based structures.^[9] Thus, **XIX_a** and **XIX_b** are quite unstable (as we shall see later, **XIX_a** is a typical allenylidene complex), but as soon as additional dialkylamino groups are added at the *para* positions of the unsubstituted phenyl rings, the resulting compounds become sufficiently stable to survive under ambient conditions in air.

Two different pathways were used to obtain these complexes. The first route (**A**, Scheme 2) proceeds by synthesis of carbinols from lithio-precursors and ketone, followed by addition of HBf_4 . The acetylide is then formed by addition of Et_3N . However, due to the steric crowding around the metal centers limiting access of the base, as well as reactivity problems encountered with the resulting carbinols, a second route toward these compounds has been explored (**B**, Scheme 2). The latter proceeds by formation of the methoxy-substituted metal alkynyl precursor and formation of the desired metal acetylide carbocation, *via* a vinylidene intermediate. An internal dehydration process was observed during the first step (i), preventing clean isolation of the vinylidene intermediate. This alternative approach allows access to the desired carbocations in one step from the methoxy precursor upon addition of acid followed by Et_3N , and was preferred, most likely due to an easier purification of the products (**XIX_{a-e}**). This synthesis route was quite effective and the back formation of the carbinol was not observed. Curiously, this reaction was not much exploited for synthesis of related derivatives.

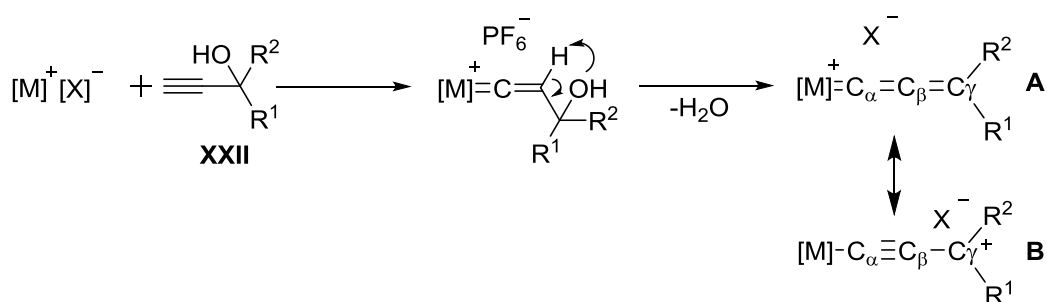


Scheme 2: Example of synthetic pathways to Ru(II) alkynyl-based TPM dyes

These new organometallic derivatives of TPM dyes were characterized by NMR, IR and UV-vis spectroscopies. The influence of charge delocalization was observed, notably in the ¹³C NMR spectra, with a characteristic upfield shift of the α -carbon atom of the alkynyl ligand compared to that of the corresponding phenylalkynyl complex. The UV-vis spectral features are similar to those of the corresponding organic TPMs, but again with large bathochromic shifts of the absorptions at lowest energy, due to the presence of alkynyl ruthenium(II) centers. Thus, the lowest energy band appears at 974 nm for **XIX_e** and at 897 nm for **XX**. These compounds clearly possess an interesting potential for NLO-based applications in the NIR range due to these intense absorptions in the visible-NIR region. However, neither the NLO properties nor their electrochemistry were investigated.

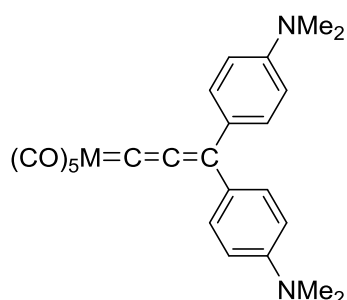
1.1.3. Allenylidene derivatives

Closely related derivatives of the "shorter" alkynyl derivatives (**M1** and **M2**) targeted in the present study have been known for a long time. These are diarylallenylidene complexes,^[10–12] cumulenenic species originally synthesized from the corresponding propargylic alcohols **XXII** *via* internal dehydration by Selegue in 1982 (**Scheme 3**).^[13]

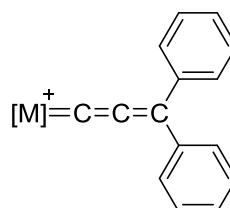


Scheme 3: Formation of a cumulene via Selegue's method

However, *para*-amino substituted derivatives of this type are rare and, except for chromium and tungsten non-redox-active examples developed by Fischer's group (**XXIII**; **Chart 5**),^[14,15] we are not aware of other examples.^[16] Albeit largely cumulenic, these species nevertheless possess a marked triple bond character (form **A** and **B**, **Scheme 3**) that is emphasized by the dimethylamino substituents, as shown by Fischer: the carbon C_γ was, in the latter case, more electrophilic than C_α, reactivity that was corroborated by crystallographic studies.



XXIII_a: M = Cr
 λ_{max} = 410, 560 and 686 nm
XXIII_b: M = W
 λ_{max} = n.d.



XXIV_a: M = Fe
 λ_{max} = n.d.
XXIV_b: M = Ru
 λ_{max} = 504 and 413 nm (MLCT)
 273 and 353 nm (LMCT)

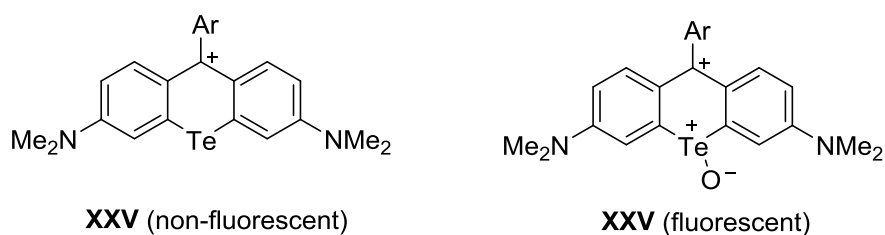
Chart 5: Chromium and tungsten derivatives synthesized by Fischer *et al.* and organoruthenium and iron cumulenes

The unsubstituted analogues (**XXIV_{a-b}**) of **M1** and **M2** are known.^[11,17] The low-energy transitions in their electronic spectra are mostly metal-to-ligand charge-transfer (MLCT) in nature. However, in derivatives such as **XXIII_a** the influence of the dimethylamino substituents on the low-energy transitions has not been investigated. Their electrochemistry has seldom been studied, the metal being difficult to oxidize reversibly due to its positive charge. Accordingly, the extant cyclic

voltammetric studies of organoruthenium derivatives such as **XXIV**, focus on their reduction, which involves two one-electron processes with only the first reduction being reversible (at -1.03 V, with the latter irreversible process at -2.11 V vs FcH⁺/FcH).

1.1.4. Other organometallic derivatives

Albeit non-redox active, organotellurium derivatives **XXV** (**Chart 6**) are also noteworthy. In these organometallic rhodamine-like structures, the rigidification of the system is achieved by complexation of a tellurium atom between two of the TPM rings (at their 2 and 2' positions).^[18] Remarkably, these compounds become fluorescent upon addition of water or oxygen to the tellurium, which deactivates any non-radiative pathways that were previously operative due to the presence of this metalloid. The rigidification of the TPM dye increases its reactivity towards nucleophilic reagents and leads to bonding between the central carbon and water or between oxygen and the tellurium. This coordination quenches the deactivation process that is detrimental to luminescence in the absence of water. Interestingly, the introduction of the metal at this position, in addition to inducing a rigidification of the TPM core, also induces a bathochromic shift of the lowest-energy transitions. As a result, the intense bands at lowest energy are located between 600 and 700 nm (λ_{max}) for these compounds whereas they appear at 550 nm for the corresponding dimethylamino-rhodamine analogue **XXVI** (rosamine).^[19,20]



Ar= Ph: $\lambda_{\text{max}} = 680 \text{ nm}^a$
 Ar= 2-MePh: $\lambda_{\text{max}} = 670 \text{ nm}^a$
 Ar= 2,4,6-Me₃Ph: $\lambda_{\text{max}} = 664 \text{ nm}^a$

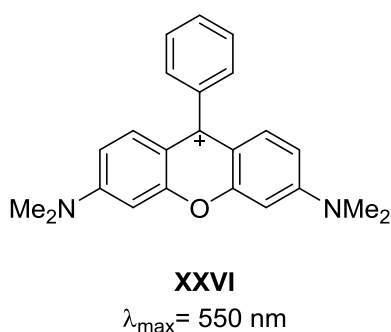


Chart 6: Organotellurium derivatives and rosamine. a: In phosphate buffer (0.012 M)

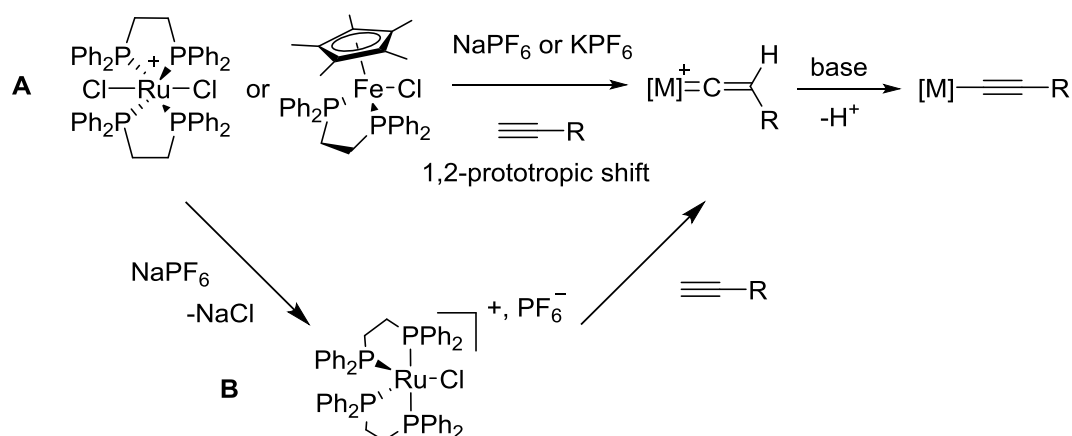
To the best of our knowledge, these are the only reports of synthesis and use of organometallic derivatives related to **MG**⁺ and **CV**⁺. Most of these compounds have not been extensively characterized, since many of them were generated *in situ* and not isolated. In this respect, apart from the numerous allenylidene derivatives reported so far suggesting that **M3-M4** will be viable targets, the work of Wu and coworkers is certainly the most complete and the closest to our ultimate aims. It supports expectations of the viability of the targeted molecules **M3-M4** and suggests promising linear and nonlinear optical properties in the cationic state for these organometallic TPM dyes.

2. Synthesis

Different syntheses were considered for **M1-M4** (Chart 1), which depend on the organometallic endgroup present.

Because the ferrocene derivatives are inert to most of the reactions, a procedure similar to that used for the organic compounds can be followed. These most often start by addition of a lithiated species to a ketone, followed by a dehydration triggered by addition of acid.

For the organoruthenium " $\text{Ru}(\text{Cl})(\kappa^2\text{-dppe})_2$ " and organoiron " $\text{Fe}(\eta^5\text{-C}_5\text{Me}_5)(\kappa^2\text{-dppe})$ " alkynyl-based derivatives, the strategy adopted was to introduce the metal at the end of the synthesis *via* a vinylidene intermediate, followed by deprotonation, to form the desired acetylide (Path **A**, **Scheme 4**).^[21] In these reactions, all the reactants can be combined to form vinylidene complexes *via* a chloride abstraction followed by a 1,2-prototropic shift.^[22] Moreover, in the case of ruthenium alkynyl complexes, the stable 5-coordinate precursor $[\text{Ru}(\text{Cl})(\kappa^2\text{-dppe})_2][\text{PF}_6]$ can also be used in place of $[\text{Ru}(\text{Cl})_2(\kappa^2\text{-dppe})_2]$ to speed up the synthesis and avoid the formation of bis-alkynyl complexes, as side-reactions occur when excess of alkyne is present (Path **B**). According to Wu's work and to the numerous publications on allenylidene complexes, the chemistry at these compounds must be carried out under air-free conditions, using Schlenk techniques, as the compounds can undergo rapid oxidation upon air exposure. Given that for the known organometallic TPM derivatives, the corresponding vinylidene complexes were seldom isolated, we will not attempt to isolate and characterize these species; they are often not stable for these particular derivatives and are prone to undergo nucleophilic attack or cleavage in the presence of oxygen, to form metal carbonyl complexes.

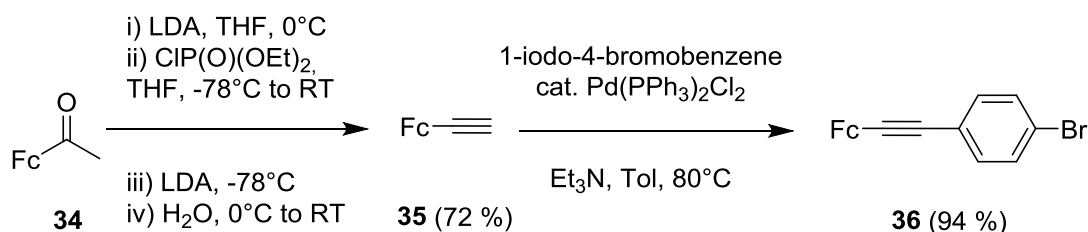


Scheme 4: Formation of organometallic acetylides

Characterization of the compounds of type **M1-M4**, especially employing X-ray structural studies, IR and NMR spectroscopies, will help to understand their electronic structure and charge delocalization in the ground state (GS). In particular, the cumulenlic character of the derivatives **M1-M2** might be somewhat depressed relative to classic allenylidene complexes of this kind characterized previously, due to the presence of the diamino groups which favor the build up of charge on the central carbon, as shown by Fischer and coworkers.^[14,15] The electrochemistry of these cationic species will then be investigated by cyclic voltammetry (CV), particular attention being paid to their linear optical properties in each of their stable redox states.

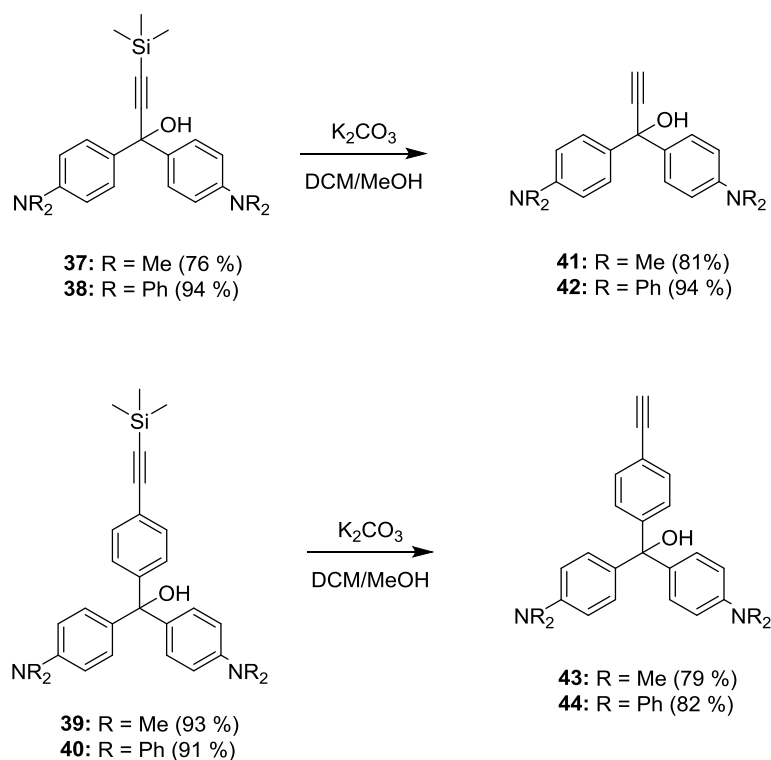
2.1. Synthesis of organic precursors

Ethynylferrocene **35** was synthesized from acetylferrocene **34** according to a modified procedure of Balavoine's group which converts a methyl ketone to a terminal acetylene (**Scheme 5**).^[23] Compound **35** constitutes a versatile precursor for various reactions such as lithiation or Sonogashira reactions. The latter was used to afford **36** by a cross-coupling.^[24,25]



Scheme 5: Synthesis of ethynyl ferrocene derivatives

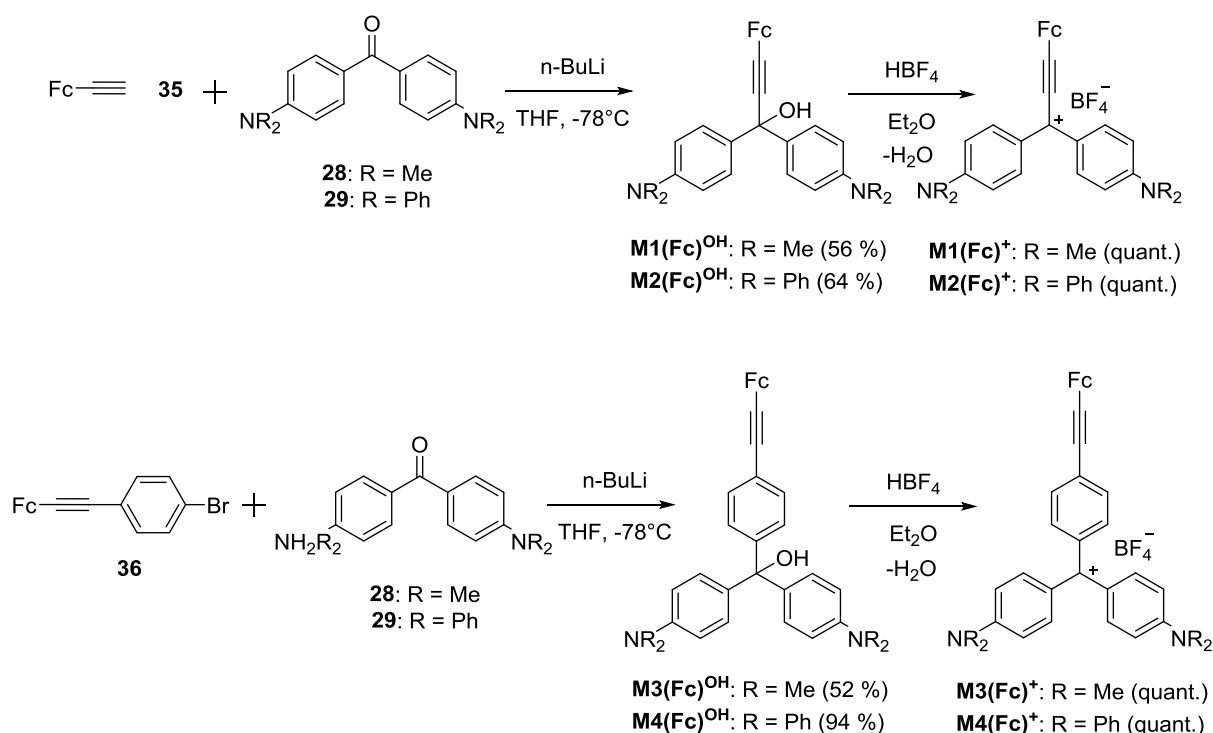
The corresponding propargylic alcohols **37-38** and the extended terminal alkyne **39-40** were then prepared. The trimethylsilyl-protected precursors **37-40** were synthesized using the usual lithiation-addition-dehydration procedure, preceded in the case of **39-40** by a Sonogashira cross-coupling reaction to install the alkyne on the phenyl ring. These species were subsequently deprotected with potassium carbonate in order to form the terminal alkynes **41-44**. Some of these derivatives are known in the literature, e.g. **41**^[26-28] or **42**^[29] (**Scheme 6**) but have not been fully characterized. Similar to the fully organic propargylic alcohols, they decompose quite easily when ionized, especially the deprotected ones, and their characterization has therefore to be performed immediately after their isolation. Accordingly, the present work has now allowed their more complete characterization. In these derivatives, the alkyne function is more activated towards nucleophiles than in other aromatic alkynes, and so their purity was always assessed before using them in the following steps.



Scheme 6: Deprotection of the organic alkynes

2.2. Synthesis of ethynylferrocene derivatives

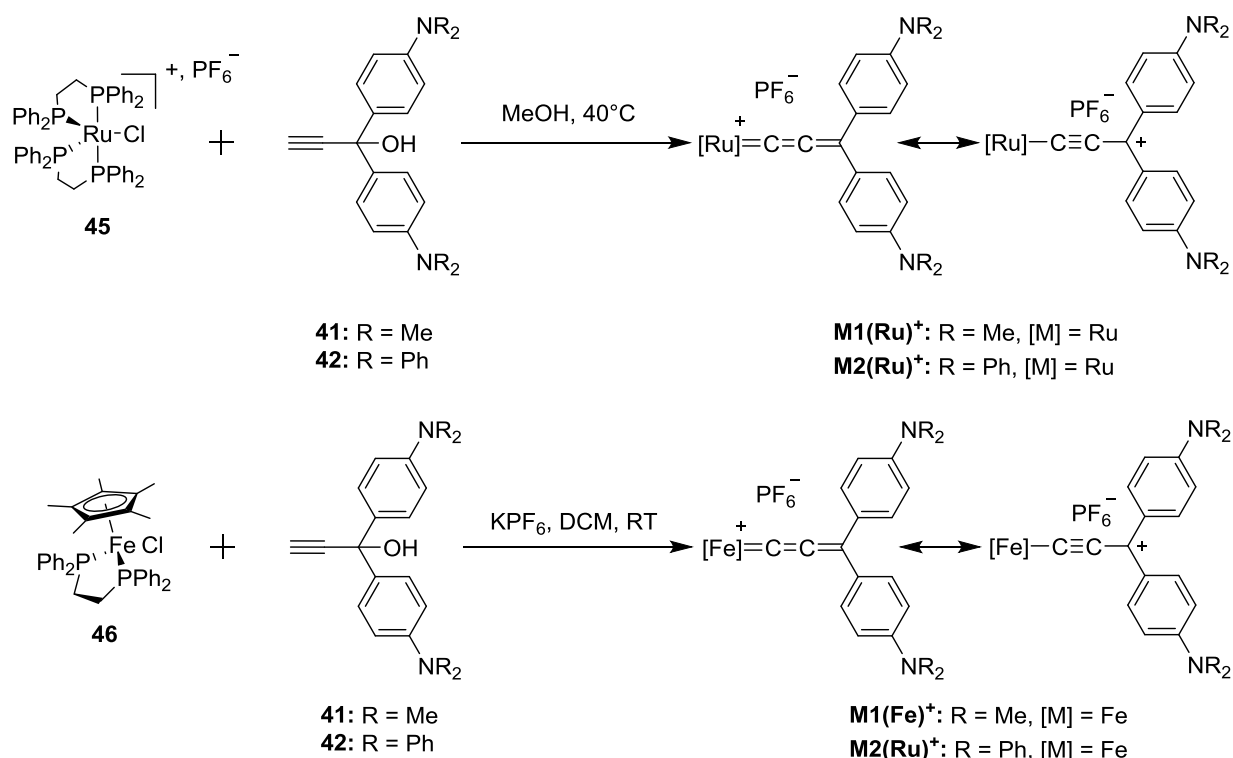
Lithiation of **35** and **36** and addition to the ketones **28** and **29** forms the desired carbinols **M1^{OH}**-**M4^{OH}**. Addition of HBF_4 then generates the desired ferrocenyl carbocations **M1⁺**-**M4⁺** (**Scheme 7**). The first of these reactions proceeds in moderate yields, mostly due to losses coming during purification of the carbinol precursors by column chromatography. The final step is quantitative as the desired products precipitate from solution as dark powders. For the first time with such ferrocenyl complexes, the corresponding carbocations were isolated and could be extensively characterized.



Scheme 7: Synthesis of ferrocenyl derivatives **M1-M4**

2.3. Synthesis of alkynyl complexes

Precursors **41-44** were reacted with the 5-coordinate ruthenium precursor **45** in DCM overnight at RT or with the organo-iron precursor **46** in the presence of the non-coordinating anion hexafluorophosphate as its potassium salt in MeOH at 40°C over 12 h (**Scheme 8**). The dark compounds obtained are reactive, especially in solution when exposed to air as has been reported for similar derivatives.^[16,30–32] Moreover, the starting complex and the carbonyl complex have similar solubilities due to their cationic nature, and it proved impossible to separate the desired product from this decomposition product. In the solid state, however, the alkynyl complexes appear sufficiently stable to allow their manipulation in air for short periods of time (<10 min). The yields of these compounds are variable, as their synthesis was undertaken on small scales using Schlenk techniques. The allenylidene complex is always the main compound present in the crude reaction mixture at the end of the reaction, losses mostly coming from work up and subsequent purifications. Overall, the isolated yields were always superior to 70 %.

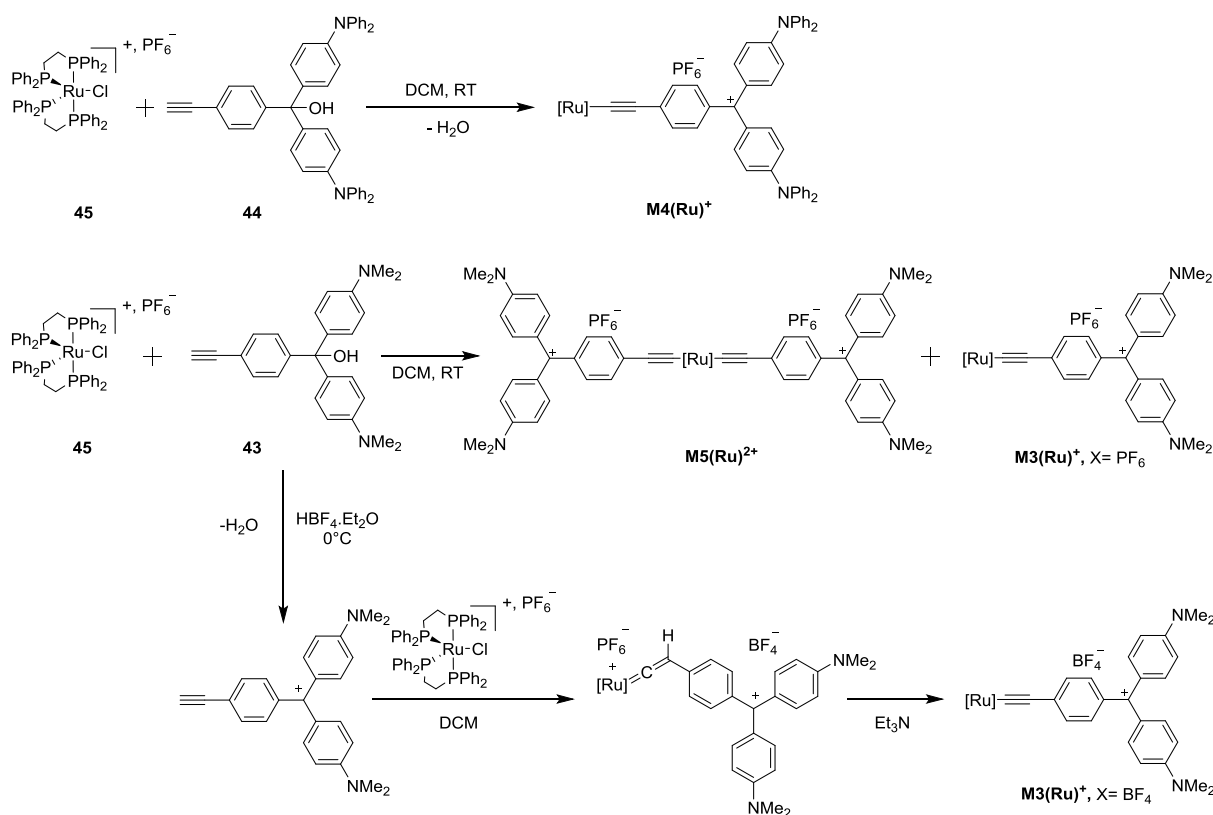


Scheme 8: Formation of the Ru(II) and Fe(II) alkynyl and allenylidene species **M1-M2**

In accordance with Wu's observations,^[9] the phenyl derivatives behave similarly to the allenylidene ones (**M1** and **M2**, **Scheme 3**), leading to direct formation of the alkynyl complexes with the ruthenium $\text{Ru}(\kappa^2\text{-dppe})_2\text{Cl}$ endgroup. While allenylidene complexes were proposed to be formed via an intramolecular deprotonation process, a similar but intermolecular dehydration process is favored here because of the comparably larger distance separating the carbon atoms being deprotonated and de-hydroxylated: another equivalent of precursor certainly acts as a base and relays the deprotonation process of the vinylidene. This was good news for us, since the synthesis of these alkynyl compounds was anticipated to be difficult due to the possible competitive formation of the vinylidene complex and of the desired carbocation.

However, although formed nearly selectively, the purification turned out to be more difficult than expected, especially for the ruthenium derivatives. Indeed, ruthenium bis-acetylides can be formed in presence of excess of base, as shown by Touchard and coworkers or Humphrey and coworkers.^[33,34] This subsequent reaction depends on the basicity of the propargylic precursor, itself related to the donating power of the amines. Thus, the activation reaction of the second alkyne is slower in the case of diphenylamine derivatives as they are less basic than dimethylamine ones, allowing for isolation of the mono-acetylide before extensive formation of the bis-acetylide has taken

place. In contrast, with analogous dimethylamino alkynes a mixture of **M3(Ru)⁺** and the bis-acetylide **M5(Ru)²⁺** was always obtained, regardless of experimental conditions employed (**Scheme 9**).

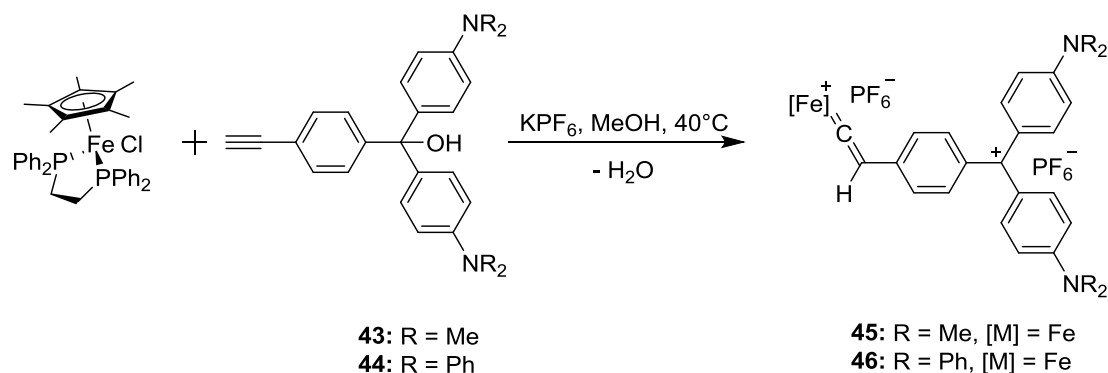


Scheme 9: Synthesis of Ru(II) alkynyl derivatives **M3(Ru)⁺**

A method to purify one of these two complexes (**M5(Ru)²⁺** and **M3(Ru)⁺**) was nevertheless found, based on their solubility: the bis-acetylide is insoluble in cold chloroform. Hence, it is possible to enrich the mixture in solution in **M3(Ru)⁺** by selectively precipitating compound **M5(Ru)²⁺**. However, this procedure is not practical from a quantitative point of view, since it takes time to isolate a pure sample of compound **M3(Ru)⁺**. A second route, which was more successful, involved generating the corresponding carbocation *in situ* at low temperature by direct reaction between the carbinol precursor **43** and the 5-coordinate ruthenium precursor **45** to form the vinylidene species. The vinylidene is then deprotonated upon addition of Et₃N to form the desired acetylide **M3(Ru)⁺**. The addition of NEt₃ did not result in the formation of the carbinol complex.

The corresponding iron derivatives (**Scheme 10**) were much more problematic to isolate. Possibly due to the larger basicity of the alkynyl complexes, the spontaneous dehydration observed with ruthenium did not occur, regardless of the alkyne used. Thus, vinylidenes (**45**: 85.35 ppm and **46**: 87.46 ppm) were predominantly formed, in addition to the desired carbocations. The reaction

can be monitored by following the disappearance of the hydroxyl group by ^1H NMR. Addition of a non-nucleophilic base, such as $^t\text{BuOK}$ or DBU, to this mixture of dicationic vinylidene-carbocations and carbocations always led to decomposition of these products and formation of several unidentified species. Due to time limitations, further work on these derivatives was stopped in order to concentrate on the other derivatives.



Scheme 10: attempts at formation of Fe(II)-alkynyl derivatives **M3(Fe)⁺** and **M4(Fe)⁺**

3. Characterization

All new organometallic species were characterized using the conventional techniques: IR and NMR spectroscopies and X-ray crystallography. The dicationic bis-acetylide complex **M5(Ru)²⁺** was also characterized similar to the other mono-alkynyl compounds; it possesses a multipolar structure and is expected to exhibit cubic NLO properties. The derivatives **M3(Fe)⁺** and **M4(Fe)⁺** could not be isolated. These characterization techniques provide insight into the electronic structure of the carbon-rich bridge of these compounds in the GS, especially for the allenylidene derivatives. These compounds were then subjected to cyclic voltammetry and UV-Vis spectroscopy to investigate their optical and redox properties. Their spectroelectrochemistry was finally recorded in order to afford insight into the possibility to use such molecules for NLO switching. Because of the structural differences between ethynyl ferrocene-based derivatives and metal-alkynyl based TPM dyes, these rather distinct families of complexes will be discussed separately.

3.1. Ferrocene derivatives

3.1.1. IR spectroscopy

The ferrocene C-H stretching band is at approximately the same frequency for carbinols or carbocations, evidencing the poor communication between the metallocene and the π -system. Although no difference in the ferrocene $\delta_{\text{C-H}}$ can be seen after formation of the TPM dye, the notable shift in the $\nu_{\text{C}\equiv\text{C}}$ of about 100 cm^{-1} is an evidence of its formation. It results from a large electronic interaction between the triple bond and the carbocationic carbon atom. Note that this stretching frequency is too high to correspond to a true allenylidene linkage, indicating that the alkynyl character certainly dominates in these conjugated species.

Compounds	$\nu_{\text{C}\equiv\text{C}}$	$\nu_{\text{B-F}}$	$\nu_{\text{O-H}}$	$\delta_{\text{C-H Fc}}$
M1(Fc)^{OH}	2222	-	3191	820
M2(Fc)^{OH}	2224	-	3574	822
M3(Fc)^{OH}	2206	-	3205	820
M4(Fc)^{OH}	2207	-	3446	826
M1(Fc)⁺	2144	1167	-	827
M2(Fc)⁺	2136	1173	-	838
M3(Fc)⁺	2198	1171	-	830
M4(Fc)⁺	2196	1173	-	833
36	2205	-	-	822

Table 1: IR signatures of ferrocene derivatives in cm^{-1} (± 2)

3.1.2. NMR spectroscopy

^1H NMR spectra of the carbinols are similar to those of the organic derivatives, *i.e.* resonances for the diphenylamine derivatives are less shielded than the dimethylamino analogues (**Table 2**). This is more obvious with the shift of the hydroxyl group (compounds **M1(Fc)^{OH}**-**M4(Fc)^{OH}**) but less noticeable for the ferrocene shifts which are similar through the series of carbinols. The sp^3 carbon atom of the carbinol reduces the electronic interaction with the two para-aminoaryl groups of the molecule.

Related trends are also apparent in the shifts of the carbocations (**M1(Fc)⁺**-**M4(Fc)⁺**): the dimethylamino resonances (**M1(Fc)⁺** and **M3(Fc)⁺**) are more shielded than those of the

diphenylamino (**M2(Fc)**⁺ and **M4(Fc)**⁺) derivatives. The extension of the π -system with the phenyl linker also has a screening effect and chemical shifts are decreased between **M1(Fc)**⁺ and **M3(Fc)**⁺; the same effect should be observed with **M2(Fc)**⁺ and **M4(Fc)**⁺ but the broadening of the signals of **M4(Fc)**⁺ does not allow this comparison to be made. This broadened ferrocenyl peak could originate from self-exchange with traces of oxidized molecules with their cationic parents or from the presence of aggregates in solution.

Compounds	δ -OH	δ -Fc
M1(Fc) ^{OH a}	5.33	4.48 (s, 2H), 4.24 (s, 7H)
M2(Fc) ^{OH b}	5.49	4.49 (t, $J = 1.8$ Hz, 2H), 4.27 – 4.23 (t, $J = 1.8$ Hz, 2H), 4.22 (s, 5H)
M3(Fc) ^{OH b}	4.79	4.54 – 4.46 (m, 2H), 4.30 – 4.27 (m, 2H), 4.24 (s, 5H)
M4(Fc) ^{OH b}	5.22	4.39 – 4.35 (m, 2H), 4.17 – 4.14 (m, 2H), 4.11 (s, 5H)
M1(Fc) ^{+ c}	-	4.79 (s, 2H), 4.70 (s, 2H), 4.37 (s, 5H)
M2(Fc) ^{+ d}	-	4.91 (s, 2H), 4.86 (s, 2H), 4.41 (s, 5H)
M3(Fc) ^{+ e}	-	4.59 (s, 2H), 4.35 (s, 2H), 4.29 (s, 5H)
M4(Fc) ^{+ d}	-	4.83 (broad s, 9H)

Table 2: Selected ¹H NMR shifts (in ppm) for ferrocene derivatives. a: CD₂Cl₂ (400 MHz), b: acetone-d₆ (400 MHz), c: CDCl₃ (800 MHz), e: CDCl₃ (300 MHz)

3.2. Organometallic derivatives

3.2.1. IR spectroscopy

Characteristic signatures of the carbinols and corresponding carbocations were observed, in particular those corresponding to the stretching motion of the cumulenenic carbon-carbon bond. Thus, very similar signatures can be found for the triple bond stretching mode for the various carbinol derivatives. In contrast, for the O-H stretching mode, the difference is noticeable between diphenylamino and dimethylamino analogues, this difference being larger for the former compounds. This illustrates again the observations already made in the previous chapter (**O1**⁺-**O4**⁺) with the organic compounds. For the various carbocations, more significant differences exist between the $\nu_{C\equiv C}$ or $\nu_{C=C=C}$ modes. For the organo-iron and organo-ruthenium complexes of **M1**⁺-**M4**⁺ type, the values are well below those expected for triple bonds (2100-2260 cm⁻¹), even for the extended derivatives **M3**⁺ and **M4**⁺ (**Table 3**). The "shorter" compounds **M1**⁺ and **M2**⁺ have characteristic values for allenylidene complexes of iron (**XXI_a**)^[17] or ruthenium (**XXI_b**).^[11]

[Fe] derivatives	$\nu_{C=C}$	ν_{p-F}	[Ru] derivatives	$\nu_{C=C}$	ν_{p-F}
M1(Fe)⁺	1927	841	M1(Ru)⁺	1942	842
M2(Fe)⁺	1911	836	M2(Ru)⁺	1921	836
XXIV_a	1896	n.d.	M3(Ru)⁺	2014 ^c	839
[Fe]-C≡C-Ph^a	2053	-	M4(Ru)⁺	1986	836
			M5(Ru)²⁺	2034	840
				2007	
			XXIV_b	1924	839
			[Ru]-C≡C-Ph^b	2067	-

Table 3: IR signatures (KBr, $\text{cm}^{-1}(\pm 2)$) of iron and ruthenium cumulenenic derivatives. a: See refs.^[30,35,36], b: See ref.^[21] c: Shoulder present on the $\nu_{C=C}$ band at *ca.* 2030 cm^{-1} (m), possibly originating from Fermi coupling.^[37]

The extended derivatives **M3⁺**-**M4⁺** also possess a strong cumulenenic character but are in the high frequency range for alkynyl compounds, supporting an intermediate character between the two limiting forms shown in **Figure 2**. In the same way as for organics, the dimethylamino derivative **M3(Ru)⁺**, featuring the most electron-donating amino groups, favors a better charge localization from the amines toward the carbocationic center, resulting in a larger acetylide character. Hence, the multiple C=C bond stretching is higher in **M3(Ru)⁺** and **M4(Ru)⁺** than in **M1(Ru)⁺** and **M2(Ru)⁺**. Based on these values, the cumulenenic character of the carbon-rich linkage ranks in the order **M2(Ru)⁺**>**M1(Ru)⁺**>**M4(Ru)⁺**>**M3(Ru)⁺**.

Finally, the bis-acetylide complex **M5(Ru)²⁺** shows two $\nu_{C=C}$ modes suggesting a local dissymmetry in the solid state between the two similar alkynyl ligands, the existence of some vibronic coupling between the two $\nu_{C=C}$ equivalent modes, or Fermi coupling with other modes.^[37] According to the energy of these modes, the complex has a lower cumulenenic structure than its mono-alkynyl counterpart **M3(Ru)⁺**.

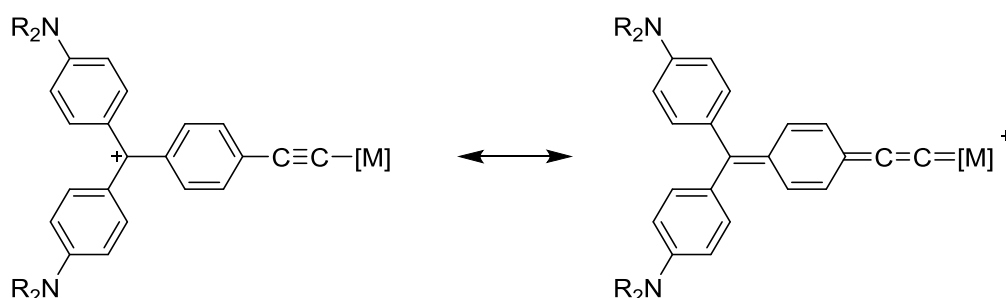


Figure 2: Limiting VB mesomers for compounds **M3⁺**-**M4⁺**

IR spectroscopy confirms that in the metal alkynyl-based dyes, the organometallic branch is (strongly) interacting with carbocationic center and takes part in the charge delocalization process, competing thereby with the dimethyl/diphenyl amino donors appended in *para*-positions of the phenylene rings on the carbocationic center. π -ligated ferrocenyl endgroups interact much less with the carbocationic center than do organoiron and organoruthenium alkynyl units, as expected from the direct σ -ligation of their metal center with the carbon-rich bridge in the latter complexes.

3.2.2. NMR spectroscopy

For organoiron and organoruthenium alkynyl complexes the ^{31}P chemical shifts confirm the observations from the IR relating to the bonding to the metal (**Table 4**). For allenylidene derivatives **M1**⁺-**M2**⁺, the shifts observed are below those expected for typical organoiron (100 ppm) or organoruthenium (49.44 ppm) acetylide complexes and above those for purely cumulenic species (92.1 ppm and 38.4 ppm, respectively), while confirming a structure with dominant cumulenic character. For extended derivatives **M3(Ru)**⁺-**M4(Ru)**⁺, the shifts are observed at comparatively lower fields compared to **M1(Ru)**⁺-**M2(Ru)**⁺ but still below those of classic acetylide complexes, in good accordance with the trend shown by $\nu_{\text{C}\equiv\text{C}}$ values.

[Fe] complex	^{31}P	[Ru] complex	^{31}P
M1(Fe) ^{+a}	95.1	M1(Ru) ^{+b}	40.9
M2(Fe) ^{+a}	93.6	M2(Ru) ^{+b}	40.3
45 ^a	85.3 ^c	M3(Ru) ^{+b}	47.6 (PF ₆) 48.4 (BF ₄)
46 ^a	87.4 ^c	M4(Ru) ^{+b}	47.3
XXIV _a ^f	92.1	M5(Ru) ^{+a}	52.0
[Fe]-C\equivC-Ph ^d	100.0	XXIV _b	38.4
		[Ru]-C\equivC-Ph ^e	49.4

Table 4: Selected ^{31}P NMR shifts (ppm) for organoruthenium and organoiron derivatives. a: 162 MHz, CD₂Cl₂. b: 162 MHz, CDCl₃. c: Vinylidene. d: See Refs.^[30,35,36] e: (121.50 MHz, CD₂Cl₂).^[21] f: (CDCl₃).^[17]

3.3. X-ray crystallography

Crystals of two extended carbinol precursors (**39** and **43**) as well as the shorter derivative (**M1**⁺) with each of the three organometallic endgroups and the bis-acetylide complexes (**M5(Ru)**²⁺) were obtained and proved to be suitable for X-ray studies.

3.3.1. Carbinols

Despite being less interesting, the structures of the carbinol precursors clearly reveal the sp³ character of the carbon atom linked to the hydroxyl group, with an angle close to 109.5° (**Figure 3**). The bonding parameters are not uncommon, as every value is close to the standard values, in spite of some hydrogen bonding interactions between the oxygen and one amine/hydroxyl group depending on the molecule. The structures of **39** and **43** also provide reference values for other carbinol derivatives.

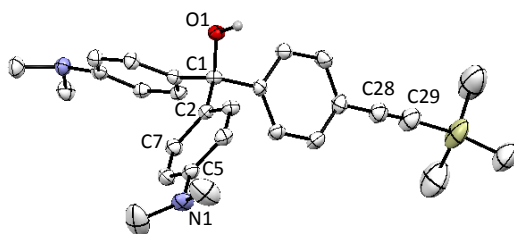


Figure 1: X-ray structure of **39** solved by Dr. Graeme Moxey

	O1-C1	O1-C1-C2	C1-C2	C5-N1	C2-C7	C28-C29
39	1.444(4)	105.61 (3)	1.540(5)	1.412(5)	1.386(5)	1.186(6)
43	1.469(4)	107.12 (3)	1.529(5)	1.397(6)	1.370(6)	1.048(8)
Ref^a	O-C _{sp3}	109.5	C _{sp3} -C _{Ar}	C _{Ar} -N(2)	C _{Ar} -C _{Ar}	C _{sp1} -C _{sp1}
	1.440		1.506	1.390	1.384	1.183

Table 5: Selected bond lengths (Å) and angles (°) for the carbinol precursors. a: See Ref.^[38]

3.3.2. Metal allenylidene/metal alkynyl derivatives

Among the three "shorter" derivatives crystallized, **M1(Fe)⁺** and **M1(Ru)⁺** can be compared to values reported in the literature for related cumulenenic species featuring the same organometallic endgroups (**Table 6** and **Figure 4**). The same dissymmetry in the bond lengths between the two arylamino groups, hence some charge localization in the solid state, is also observed as shown with the C_γ-C2 and the C_γ-C12 bond lengths. This is likely attributable to the spatial proximity of the PF₆⁻ or BF₄⁻ counter-anion to one of the amines, as illustrated by the differences (Δd) between the amine/anion distances.

	C _γ -C2	C _γ -C12	C _β -C _γ	C _α -C _β	M/Fc-C _α
[M1(Fc)⁺][BF₄]	1.419(9)	1.446(9)	1.435(9)	1.185(9)	1.444(9)
Fc-C≡C-Ph^a	-	-	1.440	1.192	1.429
[M1(Fe)⁺][PF₆]	1.438(6)	1.460(5)	1.389(5)	1.239(5)	1.826(3)
[XXIV_a][PF₆]^b	1.470	1.479	1.361	1.257	1.785
[Fe]-C≡C-Ph^d	-	-	1.430	1.210	1.894
[M1(Ru)⁺][PF₆]	1.460(10)	1.476(10)	1.387(10)	1.220(9)	1.941(6)
[XXIV_b][PF₆]^c	1.459	1.477	1.370	1.246	1.902
[Ru]-C≡C-Ph^e	-	-	1.445	1.198	2.007

	C5-N1	C15-N2	C2-C3	C3-C4	Δd ^f
[M1(Fc)⁺][BF₄]	1.339(10)	1.388(10)	1.425(10)	1.358(10)	0.385
Fc-C≡C-Ph^a	-	-	-	-	-
[M1(Fe)⁺][PF₆]	1.375(4)	1.375(3)	1.413(6)	1.370(7)	0.370
[XXIV_a][PF₆]^b	-	-	-	-	-
[Fe]-C≡C-Ph^d	-	-	-	-	-
[M1(Ru)⁺][PF₆]	1.364(10)	1.379(10)	1.364(10)	1.394(10)	0.249
[XXIV_b][PF₆]^c	-	-	-	-	-
[Ru]-C≡C-Ph^e	-	-	-	-	-

Table 6: Bond length in Å. a: See Ref.^[39] b: See Ref.^[17] c: See Ref.^[40] d: See Ref.^[30] e: See Refs.^[41,42] f: Difference between N1/N2 to closest counter anion

The cumulenenic character results from charge delocalization via mesomeric effects (**Figure 4**). As a consequence, the C_M-C_α and the $C_\beta-C_\gamma$ distances should be shorter than their typical bond length equivalents (such as found in **[XXIV_a][PF₆]** and **[XXIV_b][PF₆]** derivatives) and $C_\alpha-C_\beta$ should be longer than a typical C(sp)-C(sp) triple bond (such as found in **Fc-C \equiv C-Ph**, **[Fe]-C \equiv C-Ph** and **[Ru]-C \equiv C-Ph** derivatives). For an ideal cumulenenic structure all these bond lengths should be closer to the corresponding double bonds (such as found in the corresponding allenylidene complexes of ruthenium **XXIV_b** and iron **XXIV_a**). For the ferrocene derivative **M1(Fc)⁺** the difference with **Fc-C \equiv C-Ph** taken as a benchmark for an alkynyl complex is minor confirming the dominant alkynyl character of the bonding. In contrast, the bonding parameters of the two structures of **M1(Fe)⁺** and **M1(Ru)⁺** are much closer to those of the allenylidene complexes **XXIV_b** and **XXIV_a**, respectively, again revealing a less pronounced cumulenenic character. For **M1(Fe)⁺** and **M1(Ru)⁺**, this might be attributed to the presence of the dimethylamino substituents which are favoring the competitive charge delocalization between them and the carbocation, and therefore disfavoring its mesomeric interaction with the metal center (**B**; **Figure 4**). Accordingly, the middle bond of the cumulene is shorter. The comparably lower cumulenenic character of the ferrocenyl derivatives is attributable to the π -ligation of the metal center to the π manifold in these complexes, disfavoring mesomeric interactions with the carbocationic carbon in comparison to σ -ligated metal alkynyl endgroups.

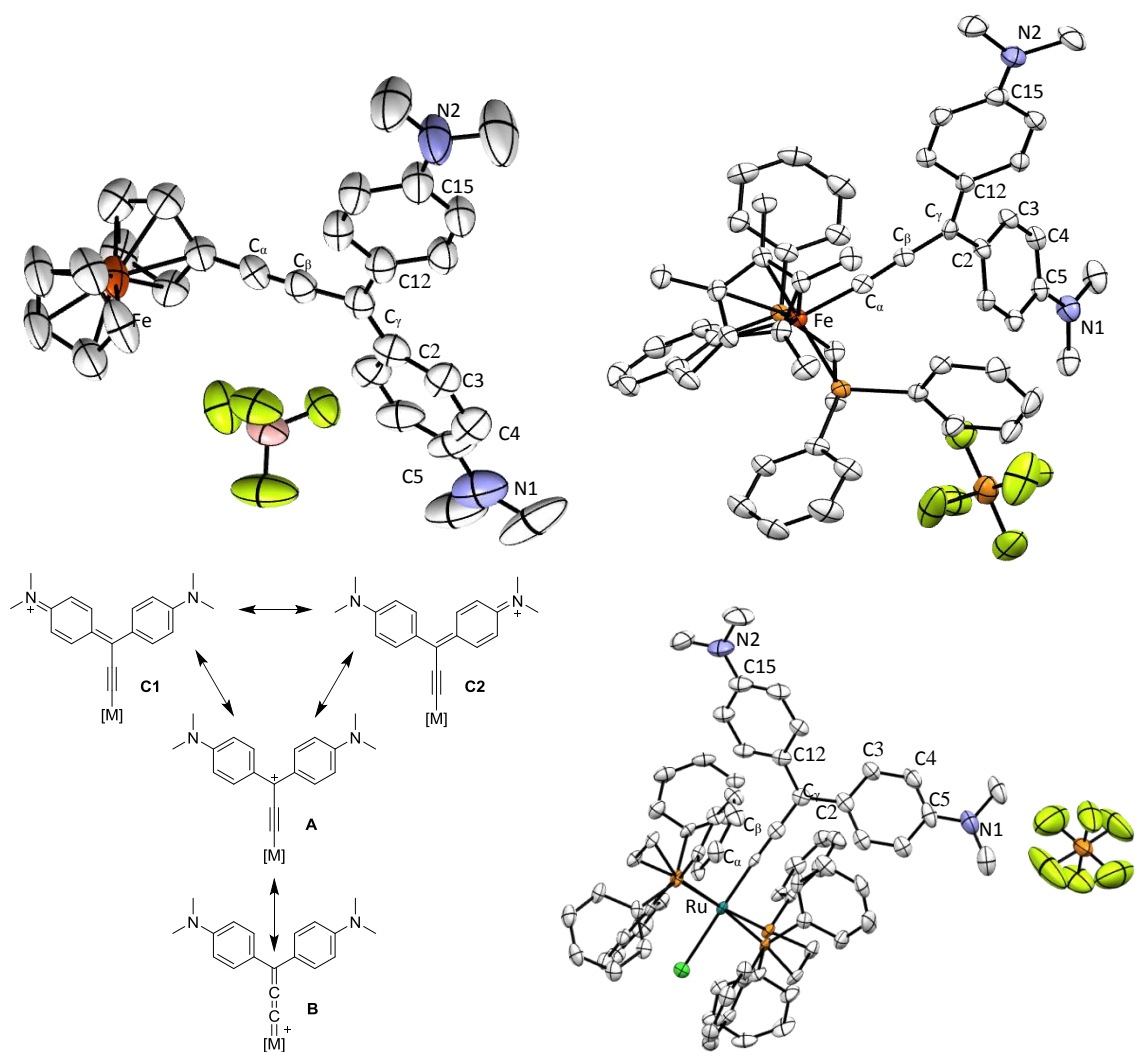


Figure 4: Structures and numeration of compounds $[M1(Fe)^+][BF_4]$, $[M1(Fe)^+][PF_6]$ (solved by Dr. Thierry Roisnel) and $[M1(Ru)^+][PF_6]$ (solved by Dr. Graeme Moxey). Insert: VB representation giving the various mesomeric forms

3.3.3. Metal bis-alkynyl derivatives

The solid-state structure of the bis-acetylide derivative $M5(Ru)^{2+}$ is also interesting as it provides information on extended metal-alkynyl derivatives such as $M3^+$ or $M4^+$ (Figure 5 and Table 7). The two acetylide ligands are equivalent in the crystal (as suggested by IR if no vibronic or Fermi coupling is considered). A closer examination of the bonding parameters reveals that the bond lengths do not correspond to a strong cumulenenic character and that the alkynyl character dominates. Thus, the stabilization of positive charge of the two carbocationic ligands seems to take place through the two amino substituents. Whether this is a solid state (averaging) effect or an actual molecular feature remains to be sorted out.

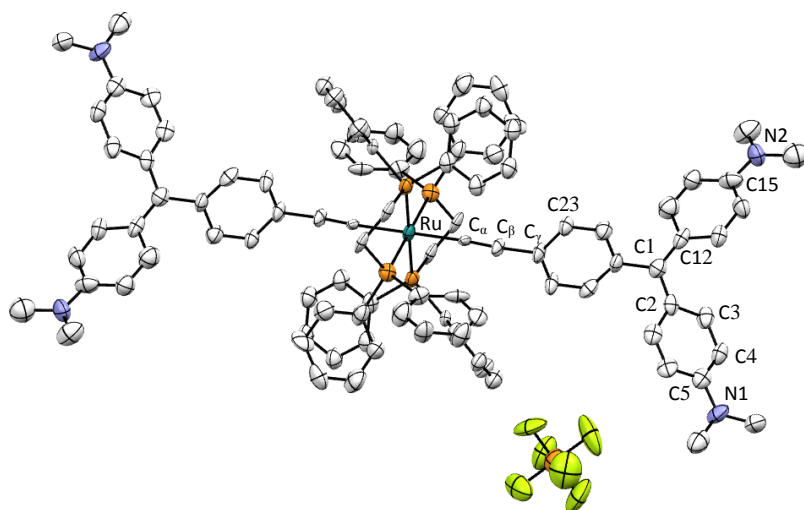


Figure 5: structure of bis-acetylide $[M5(Ru)^{2+}][PF_6^-]_2$ solved by Dr. Graeme Moxey

	C1-C2	C1-C12	C $_{\beta}$ -C $_{\gamma}$	C $_{\alpha}$ -C $_{\beta}$	Ru-C $_{\alpha}$	C5-N1	C15-N2	C $_{\gamma}$ -C23
$[M5(Ru)^{2+}][PF_6^-]_2$	1.391(2)	1.391(3)	1.494(2)	1.202(2)	2.020(2)	1.397(2)	1.403(3)	1.405(2)
$[Ru](-C\equiv C-Ph)_2^a$	-	-	1.449	1.207	2.064	-	-	1.399
			1.434	1.194	2.061			1.394

Table 7: Selected bond lengths (Å) for the X-ray structure of $[M5(Ru)^{2+}][PF_6^-]_2$. a: See Refs.^[42–44]

3.3.4. Conclusion

All these crystallographic studies confirm that most of the targeted organometallic dyes in the series $M1^+$ - $M4^+$ have indeed been isolated. Based on these structural data and consistent with the spectroscopic data summarized previously, it appears that these dyes exhibit a cationic charge delocalized over all of the structure, resulting in a carbon-rich unit with a structure intermediate between purely cumulenenic and poly-ynic in the ground state. While the shorter metal alkynyl derivatives $M1^+$ and $M2^+$ have a nearly typical allenylidene structure, the longer $M3^+$ and $M4^+$ derivatives with a 1,4-phenylene unit inserted into the carbon-rich bridge are closer to metal-alkynyl complexes. In strong contrast with $M1(Ru)^+$, compound $M5(Ru)^{2+}$ has a dominant bis-alkynyl character in its structure likely attributable to the presence of the additional 1,4-phenylene unit in the carbon-rich spacer separating the carbocation from the metal center; the aromaticity of this unit certainly mitigates against mesomeric effects. Furthermore, the counter-anion appears to favor an unsymmetrical charge distribution in the solid state for some of these derivatives, similarly to that seen with organic molecules. For the ferrocenyl complexes the same trend is also obeyed, except that all these derivatives present a dominant alkynyl character. Thus, depending on its connectivity

(σ vs. π), the metal center interacts differently with the carbocationic center through the π -manifold of the carbon-rich bridge. Its oxidation state should therefore have a significant impact on the optical properties, as we shall investigate hereafter.

3.4. UV-Vis spectroscopy

The electronic spectra of the compounds **M1**⁺-**M5**²⁺ were recorded in DCM in the range 230-1500 nm along with those of their carbinol precursors. The absorptions at lowest energy are summarized in **Table 8** and discussed hereafter. Ferrocene derivatives are described first, followed by cumulenic species and ruthenium-based **MG**⁺ derivatives at the end.

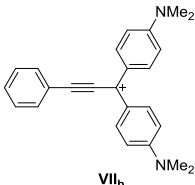
	M1(Fc) ⁺	M2(Fc) ⁺	M3(Fc) ⁺	M4(Fc) ⁺	M1(Fe) ⁺	M2(Fe) ⁺	M1(Ru) ⁺	M2(Ru) ⁺
λ (nm)	486	524	450	481	516	546	597	574
ϵ (10 ⁵ ·M ⁻¹ ·cm ⁻¹)	(0.15)	(0.20)	(0.22)	(0.19)	(0.45)	(0.32)	(0.59)	(0.65)
	667	720	626	681	660	660	692	621
	(0.59)	(0.65)	(0.94)	(0.66)	(0.35)	(0.30)	(0.5)	(0.76)
ΔE (10 ⁴ ·cm ⁻¹)	5.6	5.2	6.2	6.1	4.2	3.2	2.3	1.3
	M3(Ru) ⁺	M4(Ru) ⁺	M5(Ru) ²⁺	MG ⁺	VII_b			
λ (nm)	600	634	606	620	688			
ϵ (10 ⁵ ·M ⁻¹ ·cm ⁻¹)	(1.02)	(0.54)	(2.20)	(1.02)	(1.01)			
	748	854	752	427	493			
	(0.56)	(0.60)	(1.03)	(0.18)	(0.36)			
ΔE (10 ⁴ ·cm ⁻¹)	3.3	4.1	3.2	7.3	5.7			

Table 8: Spectral data for the two lowest-energy absorption bands of the organometallic dyes **M1**⁺-**M5**²⁺ and **MG**⁺ with ΔE corresponding to the difference in energy between the two main bands

3.4.1. Ethynylferrocene derivatives

The ferrocene carbinol precursors **M1(Fc)**^{OH}-**M4(Fc)**^{OH} have been measured under identical conditions and, in a similar fashion to the all-organic carbinols investigated in chapter I, their absorptions are mainly located in the UV region. Hence, to avoid repetition this part is not described but the corresponding data can be consulted in the experimental section. The UV-vis spectra of the ferrocene-based carbocations **M1(Fc)**⁺- **M4(Fc)**⁺ are displayed in **Figure 6**.

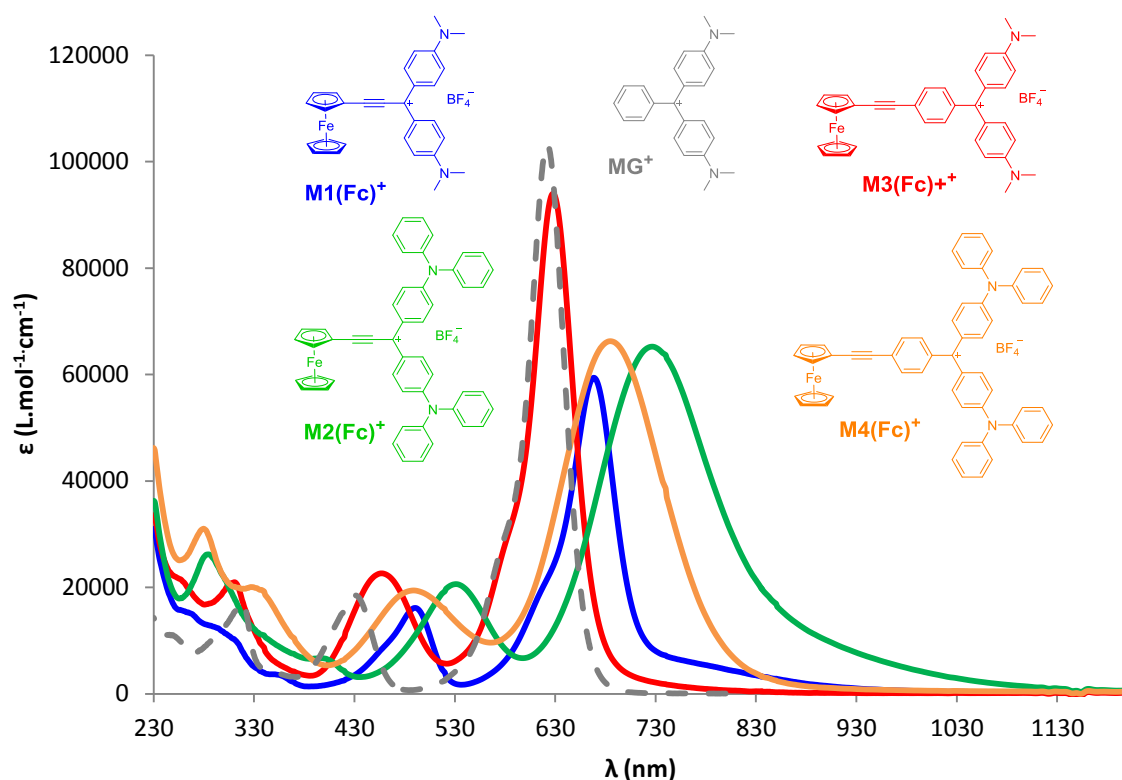


Figure 6: UV-vis spectra of the ferrocene-based carbocationic derivatives **[M1(Fc)⁺ - M4(Fc)⁺][BF₄⁻]** and **MG⁺**

The spectral features are similar to **MG⁺** with two main absorption bands. As discussed in the last two chapters from consideration of IR and NMR data, ferrocene interacts little with the rest of the system. From looking at **M3(Fc)⁺**, the closest derivatives to **MG⁺**, it is even more obvious: the two bands are really similar in wavelength (630 and 450 nm for **M3(Fc)⁺** and 621 and 430 nm for **MG⁺**). From the calculations described in the previous chapter, the lowest absorption (HOMO→LUMO) is primarily charge transfer in character from the diamino groups to the central carbon, while the second lowest band (HOMO-1→LUMO) corresponds to a dominant charge transfer from the third branch to the core. This can explain the larger shift experienced by the second band of this compound due to the presence of an ethynyl ferrocene substituent in the *para* position.

The direct replacement of the phenyl ring by an ethynylferrocene unit (**M1(Fc)⁺** and **M2(Fc)⁺**) has a more dramatic effect, with a red-shift of 30 nm of both bands compared to **MG⁺**, possibly corresponding to the increase in the π -system supporting the transitions when a triple bond is directly attached to the carbocation (**A**, **Figure 7**), as opposed to phenyl-extended derivatives for which the corresponding excited state (**B**) is comparably more energetic since the energetic cost of disruption of aromaticity in the phenyl ring compensates for the gain in delocalizing the charge.

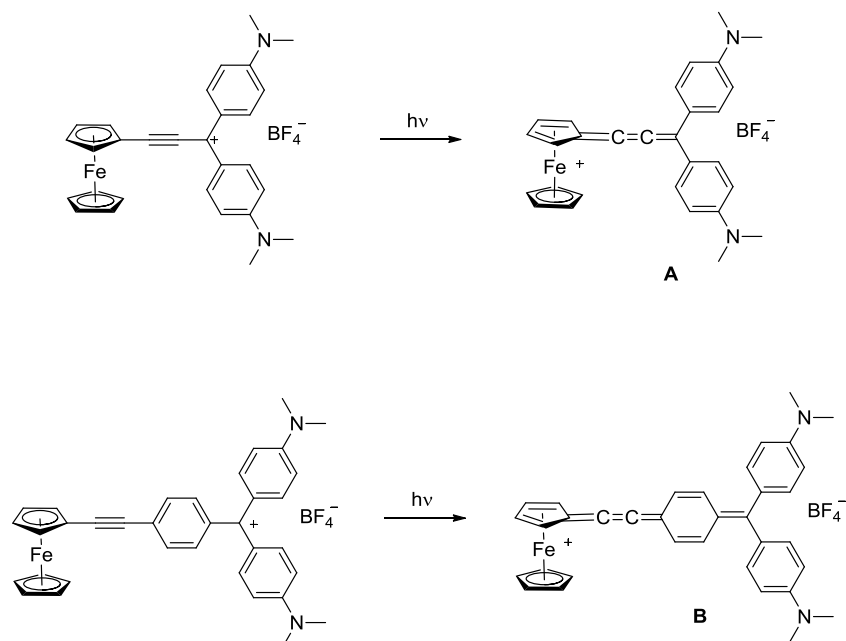


Figure 7: Dominant CT in the first excited state of **[M1(Fc)⁺][BF₄⁻]** and **[M3(Fc)⁺][BF₄⁻]**

Diphenylamino substituents, similar to observations with the organic analogues, induce a bathochromic shift of 30-60 nm on the lowest energy absorptions, this shift being slightly less pronounced for the second band. This indicates that both transitions involve charge transfer to the diaminophenyl fragments. The shift of the first band must therefore correspond to extension of the π manifold involved in the CT underlying the first absorption band. Moreover, diphenylamino substituents being less electron-donating than dimethylamino ones, the competitive charge transfer toward the third branch (**A** or **B**) is somewhat favored in the excited state, hence explaining the bathochromic shift observed for the second bands of **M2(Fc)⁺** and **M4(Fc)⁺**

Additional bands corresponding to transitions possessing a large metal-to-ligand charge-transfer (MLCT) character are also likely to exist, as the carbocation is electron deficient and ferrocene electron rich. However these transitions are probably weaker as the iron is poorly conjugated with the system and the bands are possibly present at higher energies, overlapped by the more intense ligand centered (LC) bands present in this spectral region.

3.4.2. Metal allenylidene derivatives

The spectra of the metal allenylidene species **M1**⁺-**M2**⁺ also possess intense visible absorption bands with extinction coefficients of ca. $5 \cdot 10^4 \text{ M}^{-1} \cdot \text{cm}^{-1}$ (**Table 8** and **Figure 8**). These intensities are slightly smaller than those of the corresponding absorptions in the related organic derivative **O1(AntC2)**⁺ discussed earlier (and used here as a reference compound) but represent the spectral signature of the carbocationic fragment. The lowest energy band for the Fe derivatives **M1(Fe)**⁺ and **M2(Fe)**⁺ appears at 660 nm for both, which suggests that this transition is somewhat decorrelated from the amino substituents and more likely dominated by a strong MLCT character. The second lowest energy band is red-shifted for the diphenylamine, as expected for a transition involving the amino substituents. As before, this shift possibly originates from the extended π -system. By analogy with the organics, and based on its larger intensity, it is tempting to attribute it to the CT transfer involving mostly the amino groups, which was previously located at lower energy than the other band dominated by the MLCT process. Therefore, in these compounds, the electronic transitions at lowest energy seem to have been energetically inverted relative to **MG**⁺, similar to what had been theoretically predicted for 9-ethynylanthracene derivatives such as **O1(AntC2)**⁺ (Chapter I-4.5). Accordingly, we tentatively propose that for the allenylidene complexes **M1(Fe)**⁺ and **M2(Fe)**⁺, the HOMO→LUMO band corresponds to a charge transfer process from the metal to the organic core (the MLCT) and the second-lowest-energy band to the HOMO-1→LUMO transition, with a dominant charge transfer character from the amine to the central carbon. Such an assignment would explain the larger half width and lower intensity of the first transition (more compatible with its metal-containing character) and correspond to the literature on related metal allenylidene complexes for which the moderate to intense electronic absorption at lowest energy was often attributed to a MLCT process.^[16]

For the ruthenium derivatives **M1(Ru)**⁺ and **M2(Ru)**⁺, two intense bands are also observed at low energies. These are closer in energy, and both bands seem to experience a bathochromic shift when progressing from the dimethylamino derivative (**M1(Ru)**⁺) to the diphenylamino one (**M2(Ru)**⁺). Consistent with the spectrum of **O1(AntC2)**⁺ used as reference, the lowest energy band possesses the highest extinction coefficient. Therefore, the suspected band inversion observed with **M1(Fe)**⁺ and **M2(Fe)**⁺ has probably not happened for these ruthenium species. The large overlap of these two bands in **M2(Ru)**⁺ dyes suggests, however, that the "inversion" limit, which depends on the electron releasing-power of the allenylidene branch (i.e. the metal center) compared to that of the branches featuring the amino substituents, may be close. Finally, for **M1(Ru)**⁺ and **M2(Ru)**⁺, two broad bands

of low intensity appear as shoulders on the most intense band in the visible range at ca. 700 nm and 800 nm, respectively. The origin of these absorptions, which resemble those observed in the ferrocenyl analogues **M1(Fc)⁺** and **M2(Fc)⁺**, is presently unknown. They might be tentatively attributed to MLCT processes but will necessitate theoretical calculations to be definitively assigned.

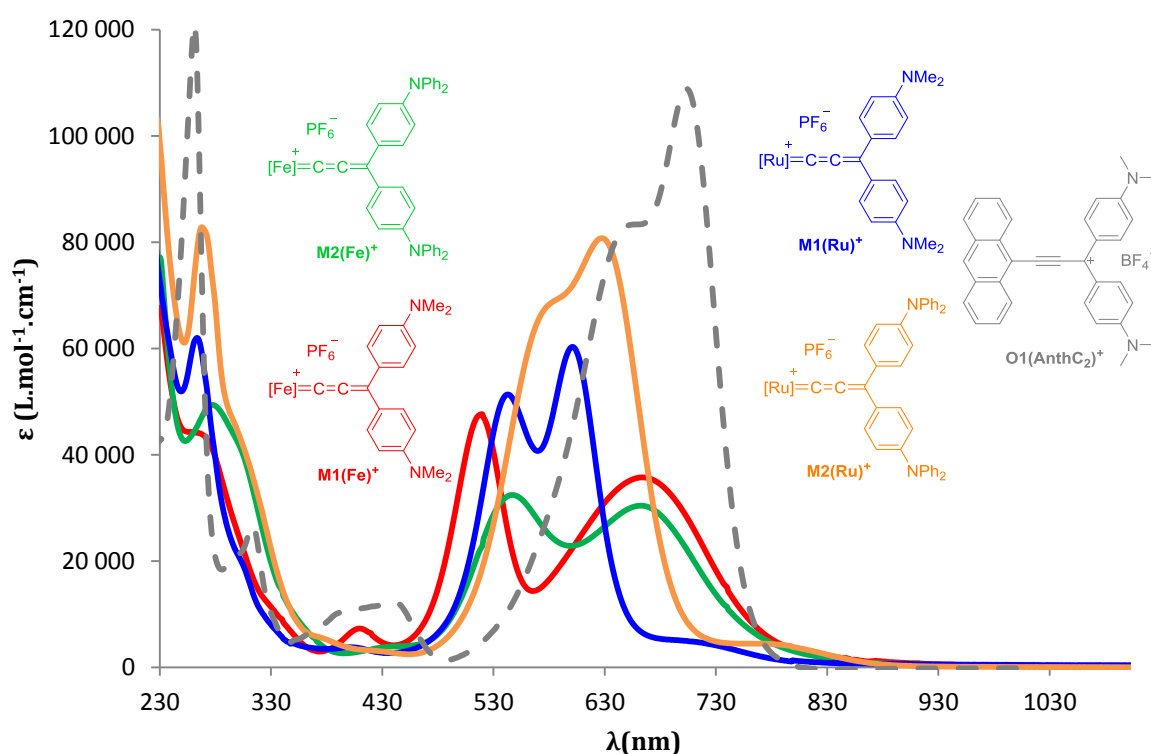


Figure 8: UV-vis spectra of the metal allenylidene derivatives ($[\text{PF}_6]^-$ salts) and $[\text{O1}(\text{AnthC}_2)]^+[\text{BF}_4]^-$

3.4.3. Ruthenium alkynyl derivatives

The UV-vis spectra of the ruthenium-alkynyl derivatives **M3(Ru)⁺**, **M4(Ru)⁺** and **M5(Ru)²⁺** (**Figure 9**) differ from that of **MG⁺**. Again, two comparably intense bands are present at low energy, but with inverted intensities. Upon progressing from **M3(Ru)⁺** to **M4(Ru)⁺**, both bands experience the usual bathochromic shift observed for diphenyl derivatives (100 nm for the lowest energy band and 60 nm for the second one). Again, based on its lower intensity and shape, we would propose that the broad transition at lowest energy corresponds to the CT transition within the TPM fragment (which possesses the largest MLCT character). Compared to **MG⁺**, for which the CT process originating from the electron-donating amino groups occurs at lower energy than that predominantly involving the phenyl substituent, it seems that the same phenomenon as observed for the iron-based allenylidene

species **M1(Fe)⁺** and **M2(Fe)⁺** is taking place here: both CT bands are inverted, that with the largest MLCT character now being found at lowest energy. Note, however, that contrary to what was observed for **M1(Fe)⁺** and **M2(Fe)⁺**, the low energy band remains influenced by a change in peripheral amino groups, in line with its admixed CT character. In addition, for **M3(Ru)⁺**, spectra of the two different salts with PF₆⁻ and BF₄⁻ counter ions have also been recorded. Upon comparison, no difference at all was observable, suggesting no interactions (ion-pair formation for instance) of these dyes with their counter ions in DCM, as expected for such non-coordinating and spectroscopically silent ions.

Apart for a very small red-shift and a rough doubling of the extinction coefficients of the two bands at low energy, the bis-acetylide derivative **M5(Ru)²⁺** has a spectrum nearly identical to that of **M4(Ru)⁺**. This might have been expected, given that this compound possesses two identical TPM-based chromophores (in contrast to **M4(Ru)⁺** which possesses one). Hence, it seems that the transitions of this dicationic compound are identical in nature to those observed for **M4(Ru)⁺**, which mainly consist of transitions involving the TPM fragment. Similar observations have already been made concerning the electronic absorption spectra of related mono- and bis-alkynyl ruthenium derivatives.^[45,46]

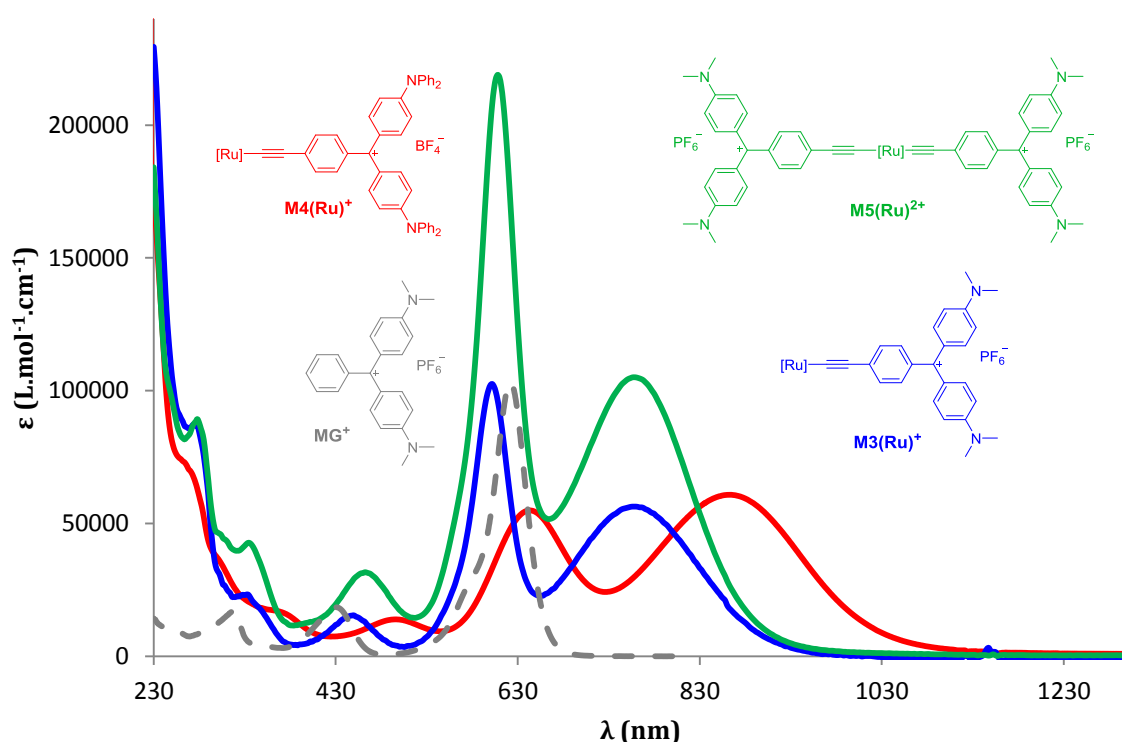


Figure 9: UV-vis spectra of the ruthenium alkynyl derivatives **[M3(Ru)⁺][PF₆⁻]**, **[M4(Ru)⁺][PF₆⁻]** and **[M5(Ru)²⁺][PF₆⁻]₂**

3.4.4. Conclusion

All these organometallic derivatives possess NIR absorption bands with intense extinction coefficients of comparable magnitudes (0.5 to $2 \times 10^5 \text{ M}^{-1}\cdot\text{cm}^{-1}$). The diphenylamino substituents always induce a red-shift for these bands, as previously seen for the purely organic **MG**⁺ derivatives studied in chapter I. When comparing organometallic endgroups with σ -bonded d⁶ transition metals (metal alkynyl derivatives) to organometallic endgroups with π -bonded d⁶ metal centers (ethynylferrocene derivatives) in these dyes, the red-shift of the absorptions appears always more pronounced in the former, albeit noticeable in both cases. This can be ascribed to a stronger electronic interaction with the d metal MOs in the first excited states for σ -bonded metals.

Then, among the metal alkynyl and metal allenylidene derivatives, depending on the nature of the metal center and the amino substituents present on the peripheral phenyl rings, different relative intensities (and half-widths) are observed for the two low lying transitions characteristic of the carbocationic fragment. We thus tentatively propose that an inversion of the low energy transitions observed in **MG**⁺ takes place for dyes featuring strongly electron-rich metal centers and comparably less electron-releasing peripheral amino substituents. For organometallic **MG**⁺-based dyes, such an inversion always places the CT transition with the largest metal-ligand character (i.e. polarized along the third branch) at lowest energy. It is interesting to note that larger bathochromic shifts have been obtained for alkynyl compounds than for their corresponding allenylidene counterparts (e.g. compare **M3(Ru)**⁺ and **M1(Ru)**⁺ or **M4(Ru)**⁺ and **M2(Ru)**⁺), and this is in spite of the fact that the metal center is more spatially remote from the central carbocation in the former dyes. TD-DFT calculations would be particularly helpful for shedding light on the nature of the low-lying transitions and to confirm our hypotheses.

Finally, the bis-alkynyl derivatives **M5(Ru)**²⁺ possesses a similar UV-vis spectrum to its mono alkynyl counterpart **M4(Ru)**⁺, with only a small bathochromic shift of 6 nm and a doubling of the extinction coefficients. Overall, the absorption properties of the organometallic derivatives synthesized so far are encouraging, as the spectra possess intense spectral features in the NIR range. Similar to organic derivatives, these first absorption bands, regardless of their MLCT character, should give rise to TPA activity deep into the NIR range.

3.5. Cyclic voltammetry

Cyclic voltammetry (CV) studies of the organometallic dyes **M1⁺-M5²⁺** provide information about the reversibility of a given redox process undergone by the complexes, notably about the metal-centered processes which are of major interest in this work aimed at identifying redox-switchable NLO-phores. CV also provides a better understanding of their electronic properties and can even reveal the existence of interactions between the various redox sites of these compounds in favourable cases. For instance, if there is some electronic interaction between the carbocationic sites and the metal centers in **M1⁺-M5²⁺**, the latter should be oxidized at higher potentials than in model compounds featuring only one of these redox sites (and vice versa).

3.5.1. Ethynylferrocene derivatives

Cyclic voltammograms of the complexes were recorded in DCM in the range -1.6 – 1.6 V. Ferrocene carbinols have also been measured (**Table 9**), **Figure 10** showing the cyclic voltammogram obtained for **M2(Fc)^{OH}**. All the other ferrocene carbinols display a similar voltammogram: a reversible oxidation process that occurs at 0.56 V and which can be attributed to the Fc⁺/Fc couple. Unsurprisingly, these values are close to that of the external reference used (FcH⁺/FcH). This proximity indicates the absence of strong intermolecular electronic interactions between the amines and the ferrocene through the sp³ carbon atom carrying the hydroxyl group. A second chemically irreversible process corresponds to the simultaneous oxidation of amines (and their stepwise reduction on the return sweep). This is not so surprising since the oxidation of alkyl^[47] and aryl^[48] amines are known to result in polymer formation. These detrimental processes must be considered if redox-switching is planned with these dyes, as they occur at potentials close to that corresponding to the ferrocenyl group.

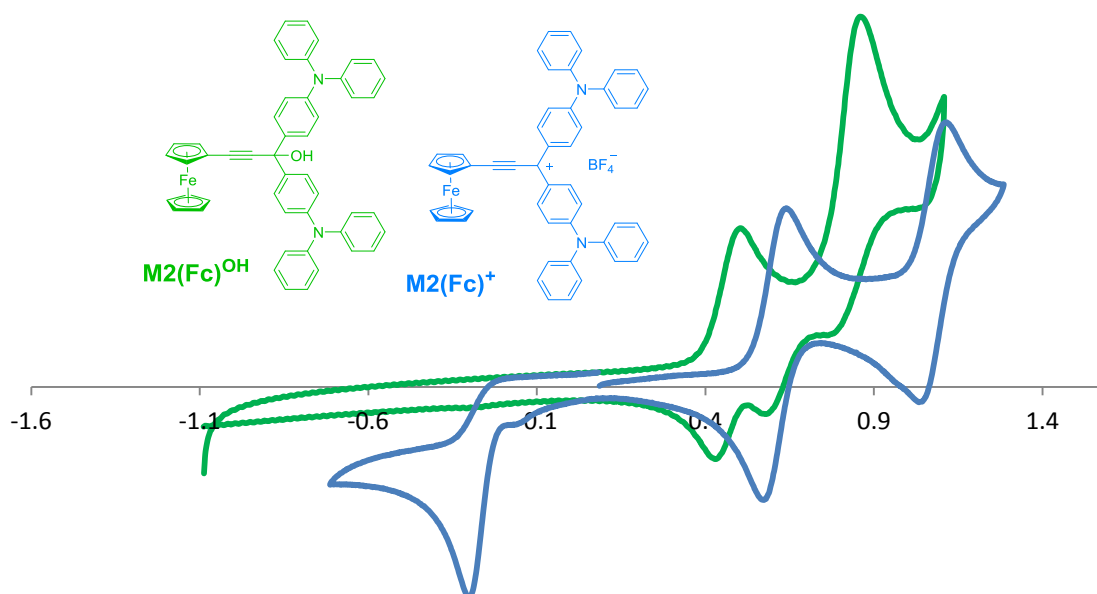


Figure 10: Cyclic voltammograms of $\text{M2(Fc)}^{\text{OH}}$ and $[\text{M2(Fc)}^+][\text{BF}_4^-]$ in DCM containing 0.10 M $[n\text{-Bu}_4\text{N}][\text{PF}_6]$ (Abscissa in V and ordinate in nA; $E_{1/2}$, $\Delta E_{1/2}$ and ΔE_p in V vs. SCE)

	Reduction (carbocation)	Oxidation(metal)			Oxidation (amine)
Complex	$E_{\text{pa}}(\text{V})^{\text{b}}$	$E_{1/2}(\text{V})$	$\Delta E_p(\text{V})$	$i_{\text{pc}}/i_{\text{pa}}$	$E_{\text{pc}}(\text{V})$
$\text{M1(Fc)}^{\text{OH}}$	-	0.55	0.06	0.98	0.83
$\text{M2(Fc)}^{\text{OH}}$	-	0.56	0.02	1.0	0.94
$\text{M3(Fc)}^{\text{OH}}$	-	0.52	0.08	0.98	0.74
$\text{M4(Fc)}^{\text{OH}}$	-	0.56	0.02	1.0	0.95
M1(Fc)^+	-0.35	0.59	0.04	1.0	1.02
M2(Fc)^+	-0.06	0.79	0.04	0.98	1.10
$\text{M3(Fc)}^{+ \text{a}}$	-0.40	0.55	0.04	0.90	1.28
$\text{M4(Fc)}^{+ \text{a}}$	-0.23	0.68	0.02	0.84	1.31

Table 9: Cyclic voltammetric data for $\text{M1(Fc)}^{\text{OH}}$ - $\text{M4(Fc)}^{\text{OH}}$ in DCM containing 0.10 M $[n\text{-Bu}_4\text{N}][\text{PF}_6]$ ($E_{1/2}$, $\Delta E_{1/2}$ and ΔE_p in V vs. SCE). a: Corrected values. b: Non reversible

The corresponding ethynylferrocene carbocations $\text{M1}^+ \text{--} \text{M4}^+$ were investigated next. The oxidation of the ferrocenyl unit is chemically reversible and occurs first, and is followed by that of the amino substituent. For M4(Fc)^+ , the metal oxidation potential is close to that corresponding to amine oxidation and both phenomena can take place simultaneously resulting in a poorly reversible process; hence, the voltage sweep has to be monitored carefully to ensure that only the metal is

oxidized when doing measurements. The ferrocenyl-based oxidations are observed at higher potentials than for the corresponding carbinol derivatives, due to its interaction with the carbocation. It is more shifted for **M1⁺-M2⁺** than for **M3⁺-M4⁺**, in line with a stronger electronic interaction in the former set of derivatives. Similar observations can be made regarding the oxidation potential of the amino sites. Comparison between the anodic shifts reveals that the electronic influence of the carbocationic site is larger for the amino substituents than for the ferrocenyl group, in line with a charge mostly delocalized between the terminal amino groups. Based on such considerations, diphenylamino substituents interact less with the carbocationic site than do dimethylamino groups. As a result, the ferrocenyl group is oxidized at a higher potential in **M2⁺** and **M4⁺**. Moreover, an irreversible wave corresponding to the formation of the corresponding radical cation is observed at cathodic potentials near -0.20 V. This attribution is indirectly confirmed by the observation of a related irreversible reduction event in the same potential range for most of the purely TPM dyes synthesized in chapter I.

3.5.2. Metal alkynyl or allenylidene derivatives

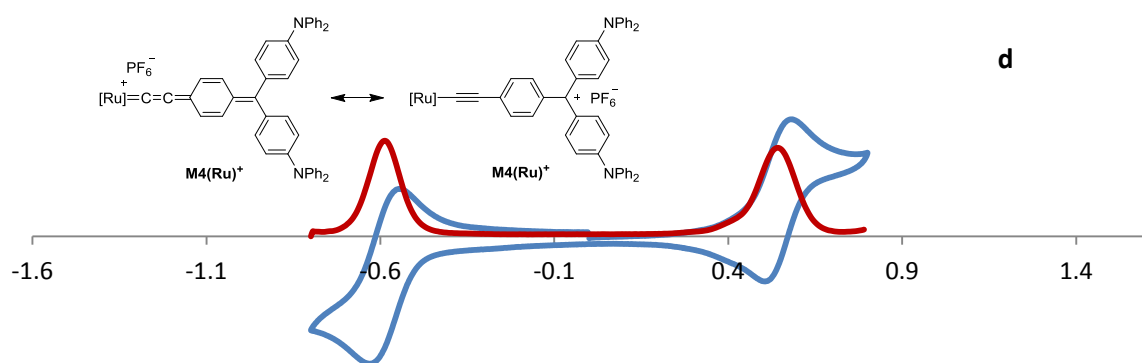
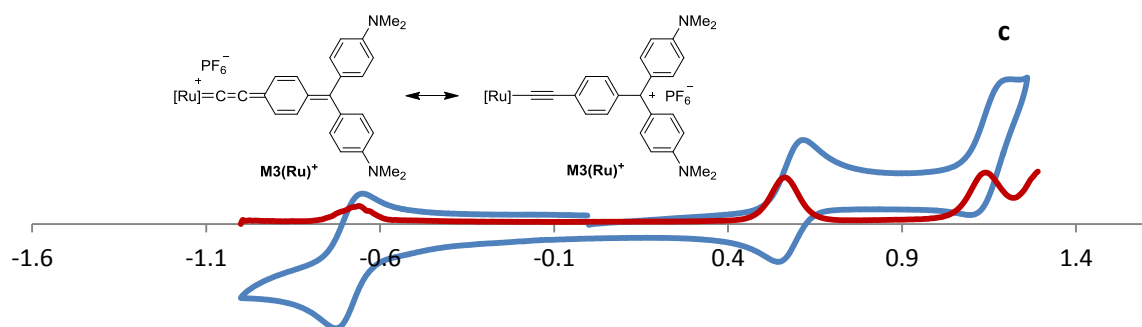
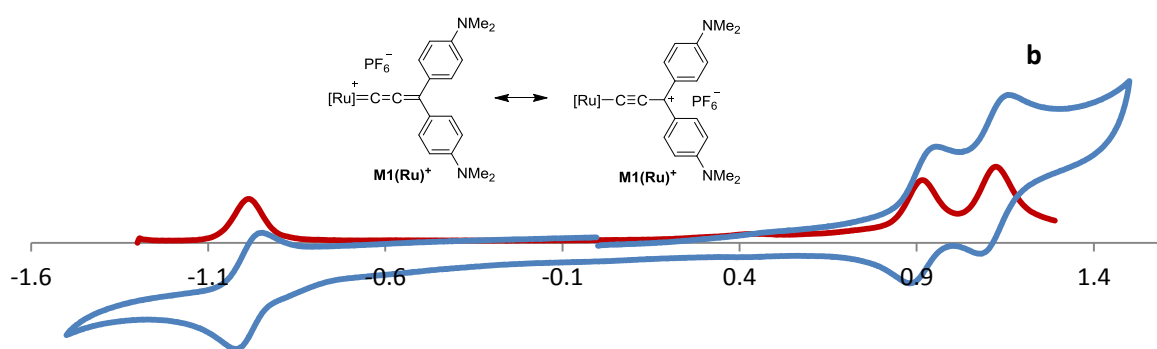
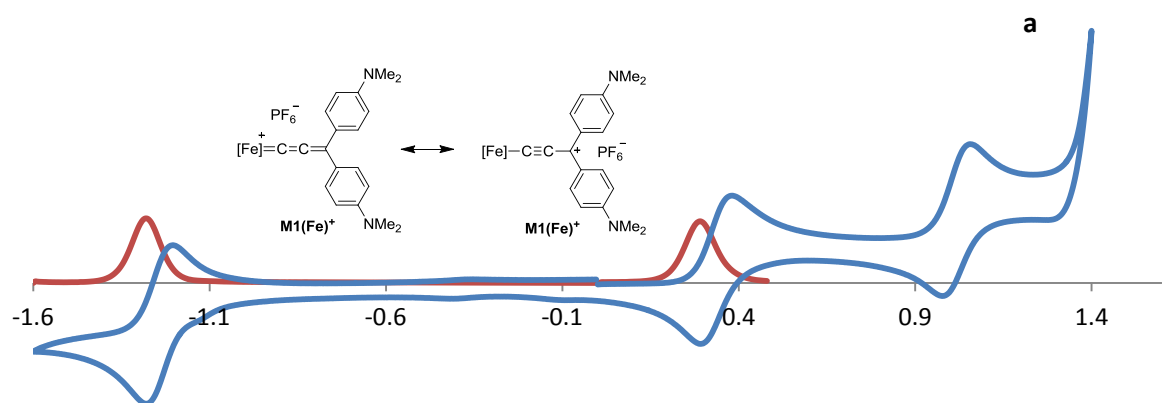
A qualitatively similar behavior is observed for the metal alkynyl or allenylidene derivatives **M1⁺-M4⁺**, as the σ -bonded organometallic endgroup allows the metal centers of these derivatives to have a better electronic communication with the rest of the system. **Figure 11** displays typical examples of cyclic voltammograms obtained for various dyes. Again, one reduction and two (or more) oxidation waves are observed.

The reduction wave near -1.1 V corresponds to the formation of a radical resulting from a one-electron exchange process (as indicated by differential pulse voltammetry DPV). DPV is a technique with improved sensitivity which also allows area integration resulting in a knowledge of the number of electrons involved in redox processes.^[42] Such a reduction is also observed for the ruthenium allenylidene species.^[11] The potentials of these processes has now been cathodically shifted from more than 0.5 V, relative to those observed for the corresponding ethynylferrocenyl derivatives, revealing the much larger electron-releasing power of the metal-alkynyl endgroups of **M1⁺**. In spite of their apparent chemical reversibility at 0.1 V/s, these reduction processes become chemically irreversible at lower scan rates and are of no practical interest for spectroelectrochemistry. Note also that the second reduction process corresponding to the addition of another electron and formation of the corresponding carbanion was never observed for any of these derivatives in the chemical window allowed by the solvent.

For **M1(Fe)⁺**, the first oxidation process (near 0.3 V) presumably corresponds to oxidation of the metal center, while the second oxidation corresponds to a stepwise oxidation of one amine, as observed for ferrocene derivatives. Albeit seemingly reversible at these scan rates, it becomes irreversible at lower sweep rates. Note that the metal-centered potential has been anodically shifted from ca. 0.4 V compared to that of the corresponding phenyl alkynyl complex^[30] due to the effect of the partial cationic charge delocalized from the carbocation. Similar features are observed in oxidation for **M1(Ru)⁺**, but the metal-centered oxidation now occurs at higher potentials (near 0.9 V), closer to the first oxidation of the amino substituent. Again, this corresponds to an anodic shift of ca. 0.4 V compared to that of the corresponding phenylalkynyl complex.^[45]

Similar cyclic voltammograms can be observed for the diphenylamino derivatives **M2(Fe)⁺** and **M2(Ru)⁺**, except that the irreversible amino substituent oxidation now occurs at higher potentials, a result of diphenylamino groups being less electron rich, to the extent that it is no longer observed in the potential window.

Similar features are also present in the voltammograms of the metal alkynyl derivatives **M3(Ru)⁺** and **M4(Ru)⁺** (c-d; **Figure 11**). The chemically pseudo-reversible reduction in the corresponding radical cation now takes place between -0.7 V and -0.5 V depending on the amino substituents present, while the Ru-centered oxidation takes place around 0.5-0.6 V, the potential being again a little higher for the diphenylamino derivative. Note that this potential range is much closer to that of the corresponding phenylalkynyl complex (0.55 V),^[45] in line with a much weaker interaction with the carbocation through the 4-phenylenethynylene spacer. In this respect, **M5(Ru)²⁺** (e; **Figure 11**) gives rise to a very similar voltammogram to **M4(Ru)⁺**, except that the metal-centered oxidation is slightly more anodic (+0.12 V) due to the presence of two positive charges on this bis-alkynyl derivative, and that the reduction of the two carbocationic TPM sites takes place in a stepwise fashion at $E^\circ_1 = -0.8$ V, in line with the existence of an electronic interaction between these electrochemical events.



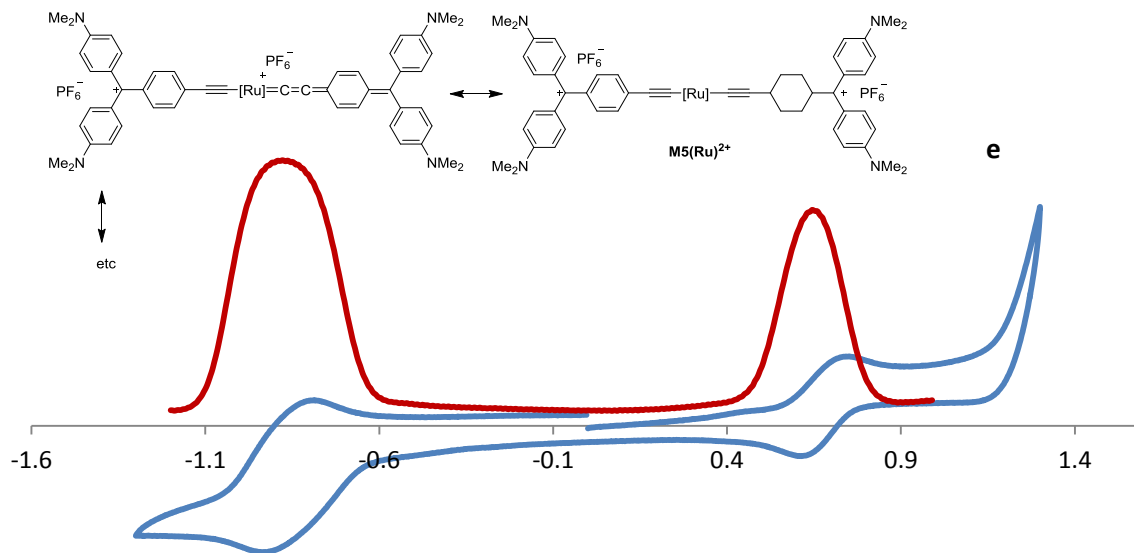


Figure 11: Cyclic voltammograms and differential pulse voltammograms of (a) $[\text{M1}(\text{Fe})^+][\text{PF}_6^-]$, (b) $[\text{M2}(\text{Ru})^+][\text{PF}_6^-]$, (c) $[\text{M3}(\text{Ru})^+][\text{PF}_6^-]$, (d) $[\text{M4}(\text{Ru})^+][\text{PF}_6^-]$, (e) $[\text{M5}(\text{Ru})^{2+}][\text{PF}_6^-]_2$ in DCM containing 0.10 M $[n\text{-Bu}_4\text{N}][\text{PF}_6]$ ($E_{1/2}$, $\Delta E_{1/2}$ and ΔE_p in V vs. Ag ; Abscissa in V and ordinate in nA)

Complex	$E_{1/2}$ reduction	$E_{1/2}$ oxidation	ΔE_p	i_{cp}/i_{pa}
$\text{M1}(\text{Fe})^+$	-1.27	0.34	0.05	1.05
$\text{M2}(\text{Fe})^+$	-1.16	0.48	0.05	1.02
$\text{M1}(\text{Ru})^+$	-0.98	0.92	0.04	0.98
$\text{M2}(\text{Ru})^+$	-0.75	1.06	0.06	0.82
$\text{M3}(\text{Ru})^+$	-0.66	0.58	0.04	1.00
$\text{M4}(\text{Ru})^+$	-0.57	0.54	0.04	1.00
$\text{M5}(\text{Ru})^{2+}$	-0.90	0.66	0.03	1.00

Table 10: Cyclic voltammetric data in DCM containing 0.10 M $[n\text{-Bu}_4\text{N}][\text{PF}_6]$ ($E_{1/2}$, $\Delta E_{1/2}$ and ΔE_p in V vs Ag^+/Ag)

3.5.3. Conclusion

For $\text{M1}^+-\text{M5}^{2+}$ the only chemically reversible waves amenable to electro-switching experiments in an OTTE cell correspond to the $\text{M}^{\text{II}}/\text{M}^{\text{III}}$ processes. Their oxidation potentials are listed in **Table 10**. Trends can be drawn based on the nature of the organometallic end group. The first observation is that all the oxidation potentials are anodically shifted toward higher values due to their interaction with the carbocationic part of the molecule. The observed order is $\text{Fc} < [\text{Fe}] < [\text{Ru}]$ for allenylidene species. This ordering is different from that observed for corresponding phenylethynyl or phenylalkynyl complexes $[\text{Fe}]\text{-C}\equiv\text{CPh}$ (-0.15 V) $< [\text{Ru}]\text{-C}\equiv\text{CPh}$ (+0.44 V) $\leq \text{Fc-C}\equiv\text{CPh}$ (+0.58 V; corrected value)^[30,45] because of the comparatively larger interaction occurring for the σ -bonded metals with the carbocationic center. In contrast, for the extended derivatives $\text{M3}^+-\text{M4}^+$, for which there is much less interaction, the ordering is the same: $[\text{Ru}] < [\text{Fc}]$. Thus, for ferrocene

derivatives, when the metal is not σ -bonded to the rest of the system, the oxidation potential is not significantly influenced by the nearby charge. In contrast, for Fe(II) and Ru(II) alkynyl endgroups, a non-negligible shift (hundreds of mV) is observed.

The remarkable feature of organometallic dyes such as **M1**⁺ or **M2**⁺ is that whereas the corresponding diphenylallenylidene complexes are very hard to oxidize^[16] and give rise to irreversible follow-up chemical events, introduction of dimethyl- or diphenylamino substituents at the *para*-positions of the peripheral phenyl rings cathodically shifts the metal-centered oxidation potential. In this respect, dimethylamino substituents in **M1(Fe)**⁺, **M1(Ru)**⁺ and **M3(Ru)**⁺ and to a lesser extent diphenylamino substituents in **M2(Ru)**⁺ and **M4(Ru)**⁺ are helping to stabilize the positive charge and remove it partially from the metal center. Thanks to these substituents, **M1**⁺ and **M2**⁺ present a chemically reversible oxidation, amenable to switching experiments in an OTTLE cell.

3.6. Spectroelectrochemistry

Spectroelectrochemistry is a technique coupling UV-Vis spectroscopic detection and a potentiostat: the cell is equipped with an electrode that can oxidize/reduce the compound *in situ*. This technique can be helpful for spectroscopically characterizing *in situ* redox isomers that cannot be chemically isolated due to their high reactivity. The setup used for this work also permits work at low temperature, which can be helpful for very sensitive species. The only requirement is that the redox isomers are sufficiently stable over a timescale allowing for their coulometric generation in the spectroelectrochemical (OTTLE) cell.

Spectroelectrochemistry of **M1**⁺-**M4**⁺ and **M5**²⁺ has thus been performed upon oxidizing the metal center. In order to ensure the reversibility of the process, reduction of the radical cation was continued until the spectrum matched that of the starting compound. Spectra presented here are an overlay of the oxidation and reduction process as sometimes the phenomena are too rapid to obtain proper isosbestic points. Depending on the compound's sensitivity, the measurements were carried out either at room temperature or at low temperature (-40°C). UV-Vis spectra of the oxidized metal center should enhance understanding of the electronic excited states of the oxidized species and give some indication about the absorptive nonlinear processes that might be operative.

3.6.1. MG⁺-based derivatives

Table 11 gives the changes in absorption bands between a given carbocation **M3⁺** or **M4⁺** and its oxidation product, the corresponding radical dication. Oxidation of the organometallic endgroup could potentially lead to dramatic spectral changes through umpolung of the π -manifold connected to the metal center, but this is apparently not the case. As observed with the ferrocene derivatives **M3(Fc)⁺** (**Figure 12**) and **M4(Fc)⁺** only slight bathochromic shifts (up to 16 nm) are seen, sometimes accompanied by a broadening of the absorption bands. Thus, the lower-energy transition shifts towards lower energy, while the other transition (presumed to possess a dominant MLCT character) experiences a hypsochromic shift. A new band also appears in the NIR. Considering its intensity, the latter possibly arises from a forbidden d-d transition centered on iron.

We have currently no definitive explanation for this poor electrochromism, but we believe that for the ferrocenyl derivatives, the explanation rests on the weak electronic interaction of the ferrocenyl group with the carbocationic system. Upon oxidation we switch the weakly electron-donating organometallic substituent to a weakly electron-withdrawing group, without significantly perturbing the carbocationic TPM chromophore. Stable **MG⁺** analogues functionalized in the para position of the phenylene ring with electron-withdrawing groups were only measured *in situ*, but the spectra of such dyes do not differ much from that of **MG⁺**.^[49] Additional bands might arise subsequent to oxidation, such as d-d transitions or LMCT bands, but for ferrocenium derivatives, these spectral features are usually quite weak,^[50–52] at least in comparison to the characteristic transitions of the TPM chromophore. As a result, only a very weak electrochromism is seen.

	M3(Fc)⁺	M3(Fc)²⁺	M4(Fc)⁺	M4(Fc)²⁺	MG⁺	
λ (nm)	450 626	446 635	481 681	505 705	427 620	
	M3(Ru)⁺	M3(Ru)²⁺	M4(Ru)⁺	M4(Ru)²⁺	M5(Ru)²⁺	M5(Ru)³⁺
λ (nm)	600 748	610 900 1220	634 854	663 933 1225	606 752	610 751 1170

Table 11: Wavelength changes in **MG⁺**-based organometallic derivatives upon metal oxidation.

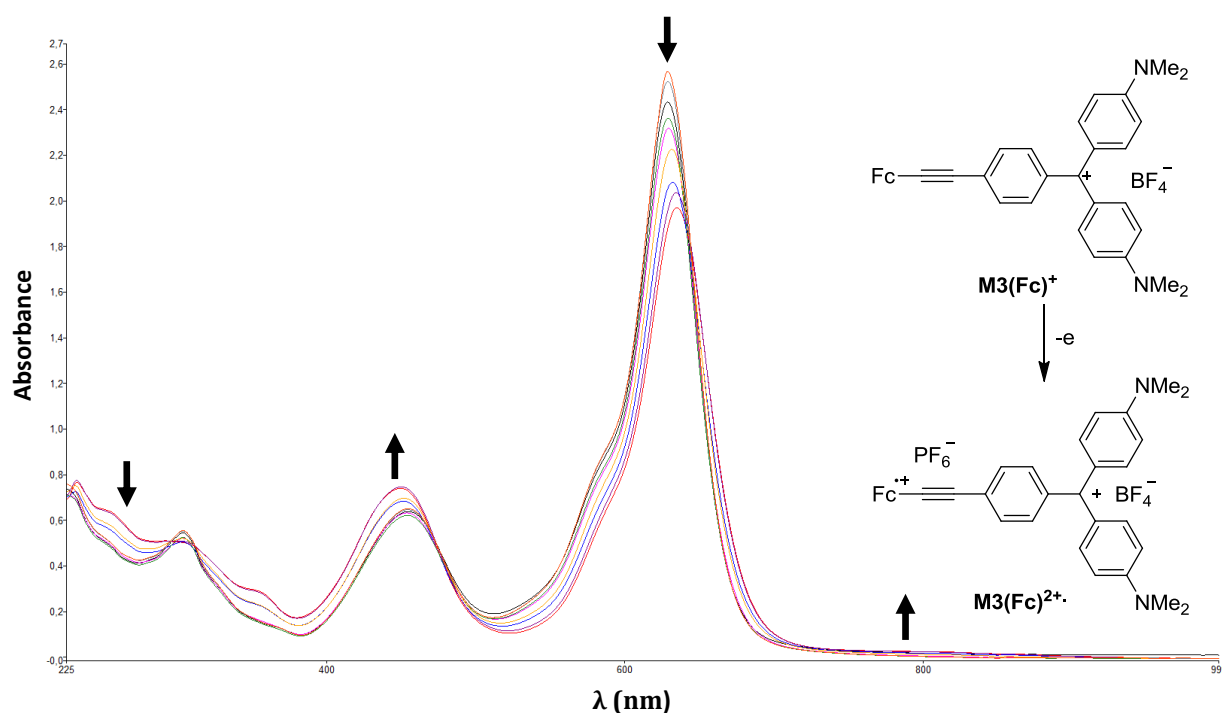


Figure 12: Spectral changes observed for **M3(Fc)⁺ [BF₄⁻]** upon oxidation

Similar observations pertaining to an overall weak electrochromism can also be made for the ruthenium alkynyl derivatives **M3(Ru)⁺**, **M4(Ru)⁺** and **M5(Ru)²⁺**, as shown with the example of **M3(Ru)⁺** (**Figure 13**). The spectra of the other compounds which are relatively similar. Again, oxidation of the metal center induces a decrease of the band previously attributed to the MLCT, while two new absorption bands appear in the NIR range.

The decrease of the low-energy absorption is in line with our tentative attribution as a band with a strong MLCT character. Accordingly, upon oxidation of the metal center, such a band should disappear or shift hypsochromically. The new but moderately intense band that appears near 900 nm might correspond to a MLCT process subsequent to oxidation, while its weak shoulder at low energy could correspond to a forbidden d-d process, similar to the one observed with the ferricinium derivative. While the electrochromism is now more pronounced than for ferrocene derivatives, as was to be expected for these organometallic groups interacting more with the TPM unit, it is nevertheless not strong. The linear optical spectrum is still dominated by the intense peak near 600 nm corresponding to the TPM chromophore in both redox states, which are apparently not much affected by the oxidative umpolung of the third branch.

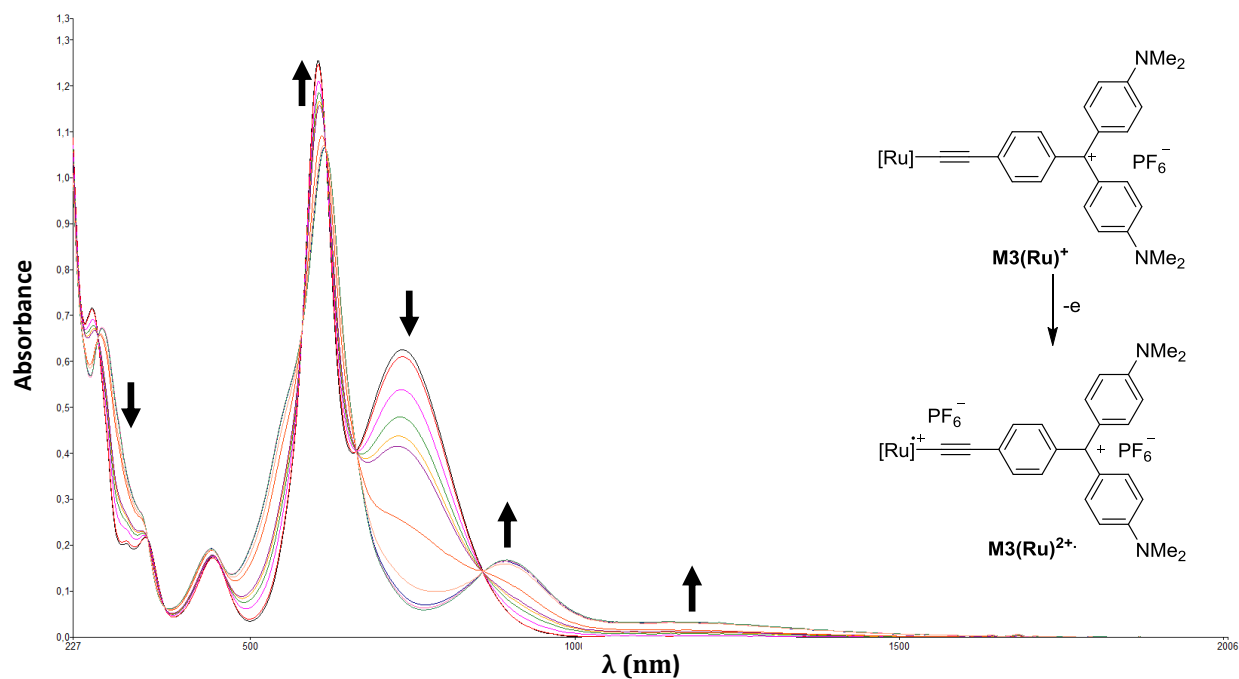


Figure 13: Spectral changes observed for $[M3(Ru)^+][PF_6^-]$ upon oxidation

For comparison, an overlay of all the mono-oxidized compounds can be found below on Figure 14.

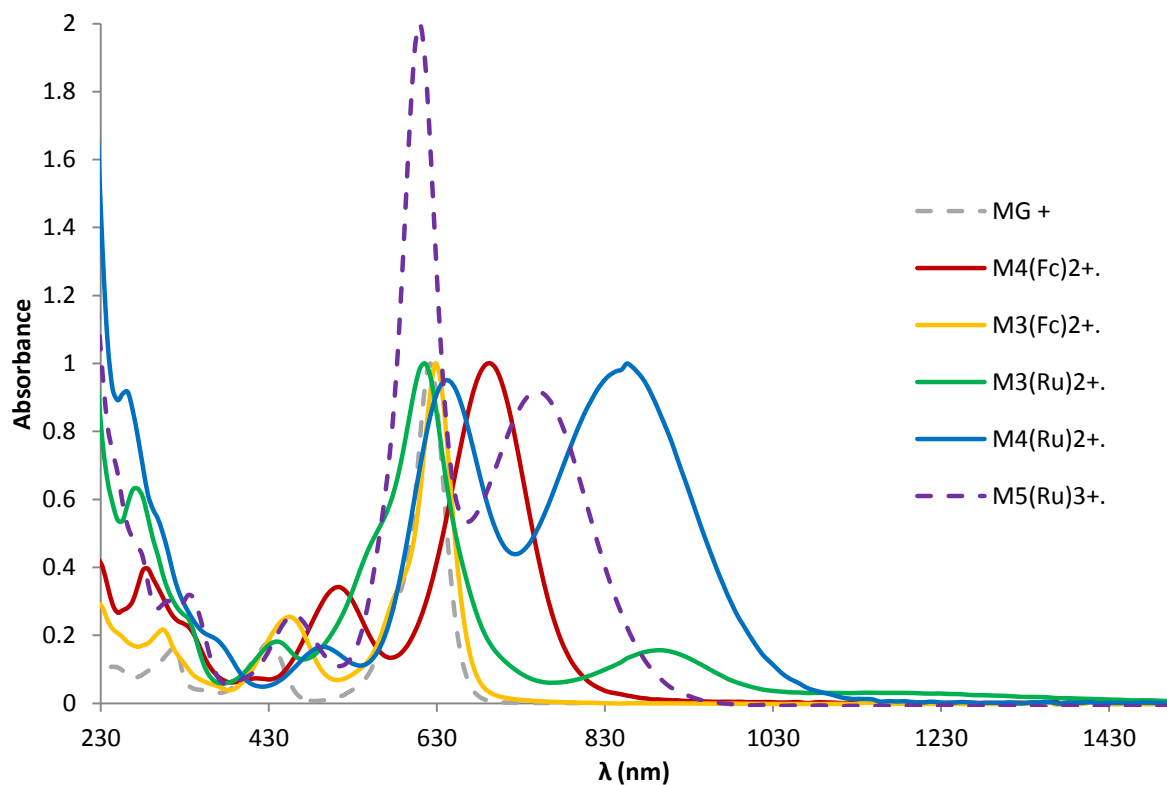


Figure 14: UV-Vis spectra of the mono-oxidized MG^+ -type derivatives against that of MG^+ . For comparison purpose the spectra have been normalized on the intense low-energy band excepted for $[M5(Ru)^{3+}][PF_6^-]$

3.6.2. Allenylidene derivatives

Table 12 gives the changes in absorption bands for the all the cumulenenic species/ethynyl ferrocene derivatives and their oxidized states but they are discussed separately.

3.6.2.1. Ethynylferrocene derivatives

Figure 15 displays the spectroelectrochemistry of **M1(Fc)⁺**. Upon oxidation the main band decreases and a new but weaker one appears at 712 nm (compared to 667 nm) along with a shoulder on its low energy side. The second band is far less affected by oxidation and exhibits only a slight bathochromic shift. The small band (appearing as a shoulder) in the NIR range also disappears. The presence of isosbestic points evidence the overall reversibility of the process, although a slight decomposition of the sample was also observed. The final spectrum strongly resembles that of **MG⁺**. Likewise to the proposal above for ferrocene derivative, we believe that the weak electrochromism observed results from the poor electronic interaction of the ferrocenyl substituent with the cationic center. Once oxidized, its electronic influence on the rest of the chromophore is shut down, leaving basically the equivalent of a Michler's blue analog (Chap. I; **Chart 4**) which still has a strong absorption in this spectral range. The remaining absorptions, more specific to the ferricinium chromophore, are indeed much weaker in comparison.

	M1(Fc)⁺	M1(Fc)²⁺	M2(Fc)⁺	M2(Fc)²⁺	MG⁺	
λ (nm)	486	488	524	524	427	
	667	712	720	784	620	
	M2(Fe)⁺	M2(Fe)²⁺	M1(Ru)⁺	M1(Ru)²⁺	M2(Ru)⁺	M2(Ru)²⁺
λ (nm)	427	662	597	633	574	574
	620	692 1160	692	1028	621	631 1500

Table 12: Wavelength changes in allenylidene-based derivatives upon metal oxidation

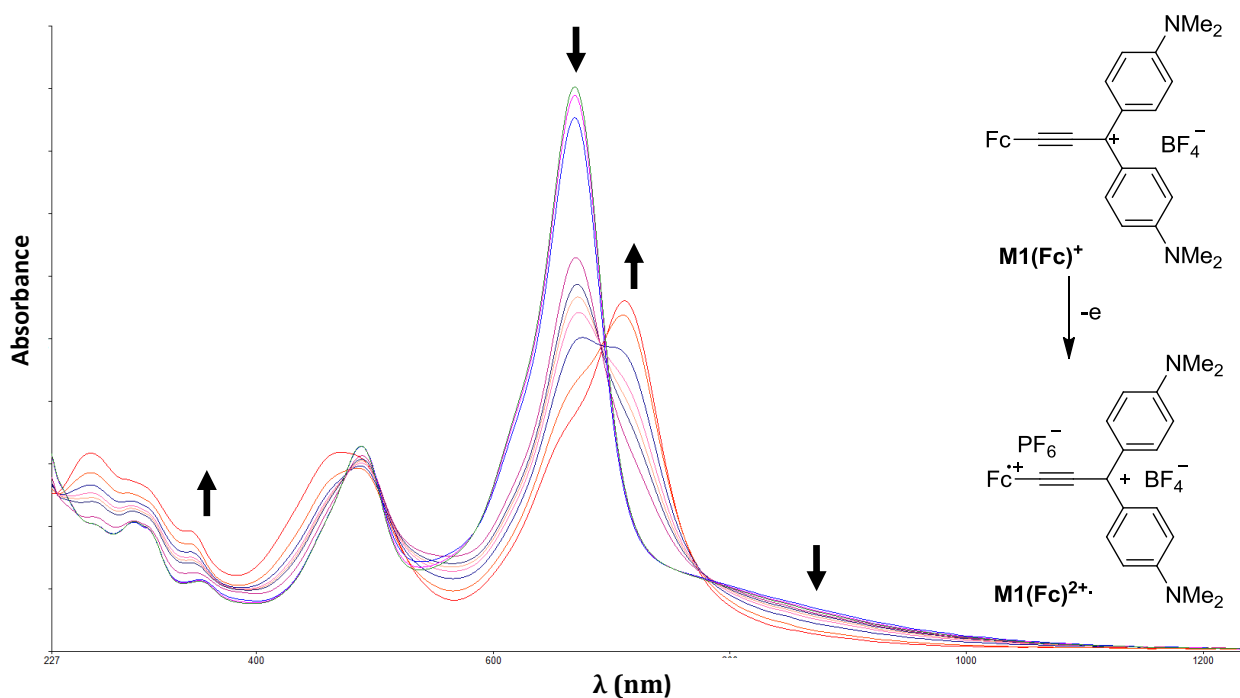


Figure 15: Spectral changes observed for $[M1(Fc)^+][PF_6^-]$ upon oxidation.

3.6.2.2. Metal allenylidene derivatives

A related spectroelectrochemical investigation for the metal allenylidene derivative $M1(Ru)^+$ is displayed in **Figure 16** (spectra for other related species can be found in the experimental section). As can be seen, the spectral changes taking place upon oxidation are similar to those observed for $M1(Fc)^+$, but they are slightly more marked, possibly in line with the larger electronic interaction between the metal center and the carbocationic site in these derivatives. A decrease of the second absorption band is observed, while a strengthening of the one at lowest energy takes place accompanied by a bathochromic shift. A small and broad band appears near 1050 nm in the NIR range as well as another band near 450 nm. The former band could correspond to a LMCT transition or to a partially allowed d-d transition. The appearance of this band is also observed in the other $M1^+$ and $M2^+$ derivatives, as shown in **Table 12**. Note that this time, the spectra of the oxidized species $M1(Ru)^{2+}$ does not resemble that of MG^+ , since only the band at high energy, near 630 nm, is present. Again this spectral feature, which resembles that reported for Michler's blue (607.5 nm),^[53] can be attributed to a CT band within the dimethylamino/carbocation part (in $M1(Ru)^+$).

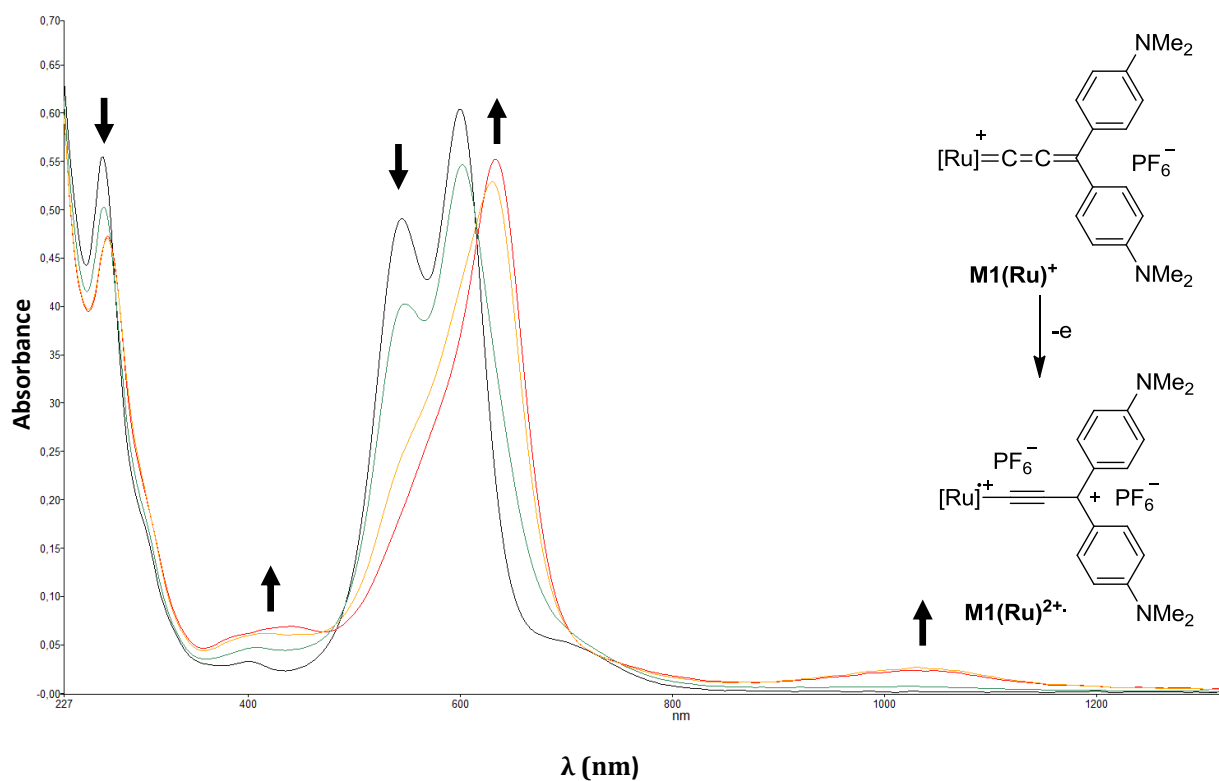


Figure 16: Spectral changes observed for $[M1(Ru)^+][PF_6^-]$ upon oxidation

For comparison, an overlay of all the mono-oxidized compounds can be found below on **Figure 17**.

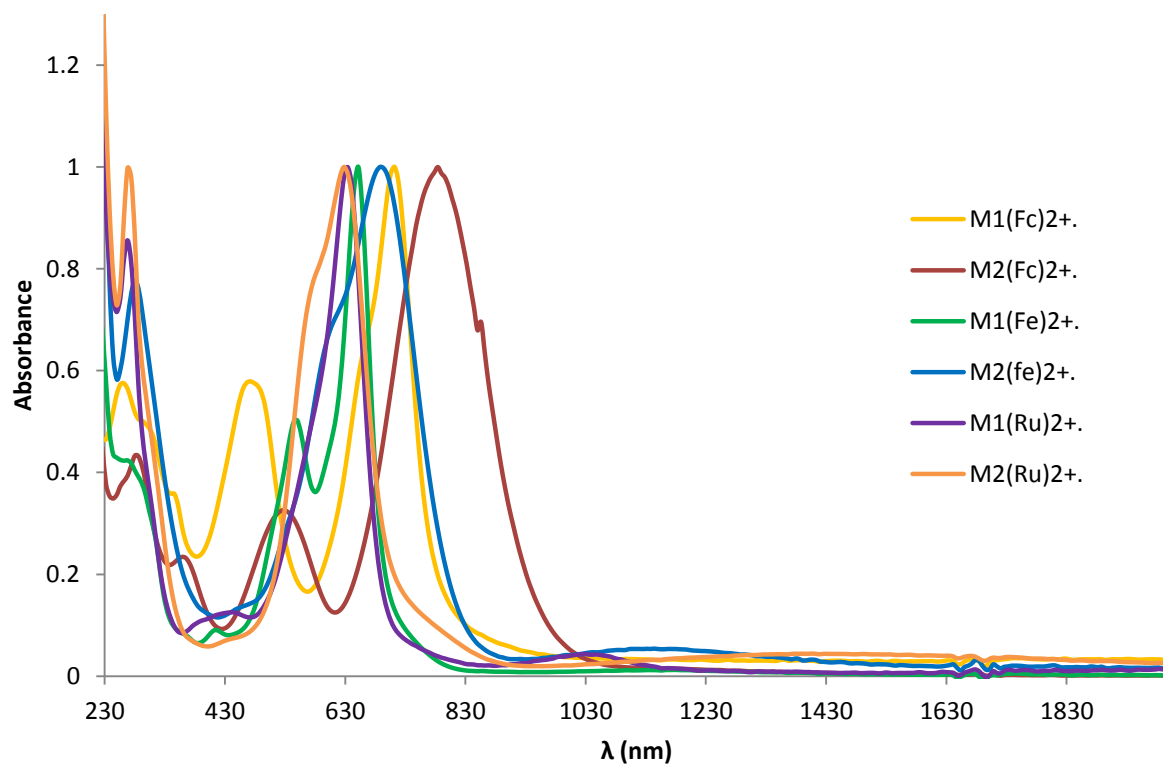


Figure 17: UV-Vis spectra of the mono-oxidized MG^+ -type derivatives against that of MG^+ . For comparison purpose the spectra have been normalized on the intense low-energy band.

3.6.3. Conclusions on spectroelectrochemical studies

Usually, spectra of metal-alkynyl or metal-allenylidene complexes are governed by MLCT or LMCT transitions at low energies. MLCT usually occurs in the neutral state as the metal center tends to be more electron-rich than the ligand, but in the oxidized state LMCT are often present. However, as we shall see, the interpretation of the data presented in this section is not trivial, especially in the absence of TD-DFT calculations, since TPM dyes have several low-energy bands originating from their carbocationic moiety which can combine with the MLCT/LMCT transitions previously mentioned and mostly affected by oxidation, complicating their identification.

In regard of their spectroelectrochemical behavior upon oxidation, the compounds **M1⁺-M5²⁺** can be separated in two different groups: cumulenenic derivatives (**M1⁺-M2⁺**) and TPM-based derivatives (**M3⁺-M5²⁺**). Thus, for each set of compounds, contrary to our expectations, only a moderate electrochromism was stated.

Not surprisingly, the largest spectral contrast between the two redox states probed is obtained each time with metal alkynyl derivatives, for which the electronic coupling with the organic core is stronger than for ethynylferrocenyl derivatives. For the cumulenenic derivatives, oxidation of the metal seems to sever the electronic interaction between the metal and the organic fragment, leaving an organic chromophore resembling Michler's blue and an appended radical cation exhibiting a weak LMCT or d-d transitions at lower energy, in the NIR range. The same situation prevails for the TPM derivatives, except that after oxidation the organic chromophore resembles **MG⁺**. In both cases, due to the spectral dominance of this organic chromophore in the visible range and to the small changes occasioned to its linear absorptions by oxidation, only a moderate linear electrochromism will result for many spectral regions in the visible range. However, for most of the metal alkynyl derivatives some spectral regions in the NIR range undergo important changes in absorption that might be exploited for inducing large nonlinear electrochromic effects.

4. Conclusion

The synthesis of most of the new organometallic derivatives of **MG⁺(M1⁺-M4⁺)** have been performed successfully. Two different synthetic routes were followed: one similar to that used for the organic derivatives was applied to the synthesis of ferrocene-containing dyes and another one, based on the intermediacy of alkyne or polyyne precursors was used for accessing the desired metal-

alkynyl-containing dyes. The latter synthetic route led sometimes to selectivity issues due to the high reactivity of the vinylidene compounds formed as intermediates. However, thanks to the development of purification procedures based on the solubility of these compounds, most of the targeted alkynyl complexes could be isolated, except for the iron alkynyl derivatives of **M3⁺-4⁺**, for which decomposition was observed. Apart from these two compounds, most of the targeted organometallic dyes were eventually isolated (including the new bis-alkynyl ruthenium derivative **M5(Ru)²⁺**).

The compounds **M1⁺-M5²⁺** were fully characterized using conventional methods and their electronic and structural features in the GS were discussed. Along with crystallographic studies and observations previously made on related organic molecules, it appears that these dyes exhibit a cationic charge delocalized all over their structure, resulting in a carbon-rich part with a structure intermediate between purely cumulenenic and polyyenic in the ground state. While the shorter metal alkynyl derivatives **M1⁺** and **M2⁺** have a nearly typical allenylidene structure, the longer **M3⁺** and **M4⁺** derivatives with a 1,4-phenylene unit inserted in the carbon-rich bridge are closer to metal-alkynyl complexes. The metal allenylidene derivatives **M1⁺-M2⁺** possess a more marked triple-bond character than the related diphenyl allenylidene complexes due to the presence of the para-amino substituents. Reciprocally, the TPM-based metal alkynyl derivatives **M3⁺-M4⁺** possess a more marked cumulenenic character than the related phenyl alkynyl complexes due to the presence of the carbocationic moiety. These structural features are comparatively less marked for the ethynylferrocenyl derivatives, because the d⁶ transition metal center is not σ -bonded to the rest of the system. Thus all the ethynylferrocene derivatives present a dominant alkynyl character. Depending on its connectivity (σ vs. π), the metal center is clearly interacting with the carbocationic center through the π -system of the carbon-rich bridge. Thus, cyclic voltammetry further confirmed that stronger interactions were operative between the metal center and the organic carbocationic core for organometallic substituents presenting a σ -bonded metal.

Concerning their optical properties, the presence of the organometallic endgroups induce strong bathochromic shifts on the intense low lying absorptions present in the visible range which are characteristic of the carbocationic chromophore. These shifts depend on the particular structure of each dye, an effect also perceptible for the ferrocenyl derivatives, but to a lesser extent than for the metal alkynyl or metal allenylidene species. This opens a way to tune structurally the linear spectra of these compounds in a given spectral range. Further progress will certainly result from the assignment of the various transitions observed, which is currently not possible in the absence of theoretical modelling. Furthermore, the intense absorptions of these organometallic dyes in the

visible range suggest that large nonlinear effects such as TPA might occur in the NIR range. Accordingly, their cubic nonlinear properties will be investigated soon by Z-scan.

Finally, concerning the possibility of redox-switching their optical properties, cyclic voltammetry reveals that these organometallic dyes can be either reduced to the corresponding neutral radicals or oxidized at their organometallic substituent, first, and then on their amino substituents. However, while some of these redox processes appeared chemically reversible at the electrode, only the metal-centered oxidation of the organometallic substituents turned out to be amenable to practical control of their redox state in an OTTLE cell for switching their linear optical properties. In this respect, spectroelectrochemical investigations afforded more information about the spectra of their mono-oxidized state. Contrary to our initial expectations, the linear spectra do not vary much upon oxidation of most of the derivatives. The origin of this behavior rests on the fact that the spectrum of these dyes is dominated in both redox states by the intense absorptions of the carbocationic part of the dye and the latter is not significantly affected by the metal-centered oxidation. Nevertheless, with selected metal alkynyl derivatives some spectral regions in the NIR range undergo important changes in absorption which might translate to large nonlinear electrochromic effects.^[54,55] The latter remain to be measured by Z-scan in an OTTLE cell .

References

- [1] S. Sengupta, S. K. Sadhukhan, *J. Mater. Chem.* **2000**, *10*, 1997–1999.
- [2] S. Sengupta, *Tetrahedron Lett.* **2003**, *44*, 307–310.
- [3] C. Arbez-Gindre, B. R. Steele, G. A. Heropoulos, C. G. Screttas, J.-E. Communal, W. J. Blau, I. Ledoux-Rak, *J. Organomet. Chem.* **2005**, *690*, 1620–1626.
- [4] C. Villalonga-Barber, B. R. Steele, V. Kovač, M. Micha-Screttas, C. G. Screttas, *J. Organomet. Chem.* **2006**, *691*, 2785–2792.
- [5] C. Villalonga-Barber, K. Vallianatou, S. Georgakopoulos, B. R. Steele, M. Micha-Screttas, E. Levin, N. G. Lemcoff, *Tetrahedron* **2013**, *69*, 3885–3895.
- [6] M. Ansorge, K. Polborn, T. J. J. Müller, *Eur. J. Inorg. Chem.* **2000**, *2000*, 2003–2009.
- [7] C. Arisandy, E. Fullam, S. Barlow, *J. Organomet. Chem.* **2006**, *691*, 3285–3292.
- [8] K. L. Rinehart, C. J. Michejda, P. A. Kittle, *J. Am. Chem. Soc.* **1959**, *81*, 3162–3163.
- [9] I.-Y. Wu, J. T. Lin, Y. S. Wen, *Organometallics* **1999**, *18*, 320–327.
- [10] S. Szafert, P. Haquette, S. B. Falloon, J. A. Gladysz, *J. Organomet. Chem.* **2000**, *604*, 52–58.
- [11] S. Rigaut, O. Maury, D. Touchard, P. H. Dixneuf, *Chem. Commun.* **2001**, 373–374.
- [12] R. W. Lass, P. Steinert, J. Wolf, H. Werner, *Chem. – Eur. J.* **1996**, *2*, 19–23.
- [13] J. P. Selegue, *Organometallics* **1982**, *1*, 217–218.
- [14] H. Fischer, D. Reindl, G. Roth, *Z. Für Naturforschung B* **1994**, *49*, 1207–1214.
- [15] B. Reichmann, M. Drexler, B. Weibert, N. Szesni, T. Strittmatter, H. Fischer, *Organometallics* **2011**, *30*, 1215–1223.
- [16] M. I. Bruce, *Chem. Rev.* **1998**, *98*, 2797–2858.
- [17] G. Argouarch, P. Thomino, F. Paul, L. Toupet, C. Lapinte, *C. R. Chim.* **2003**, *6*, 209–222.
- [18] M. W. Kryman, G. A. Schamerhorn, K. Yung, B. Sathyamoorthy, D. K. Sukumaran, T. Y. Ohulchanskyy, J. B. Benedict, M. R. Detty, *Organometallics* **2013**, *32*, 4321–4333.
- [19] I. C. S. Cardoso, A. L. Amorim, C. Queirós, S. C. Lopes, P. Gameiro, B. de Castro, M. Rangel, A. M. G. Silva, *Eur. J. Org. Chem.* **2012**, *2012*, 5810–5817.
- [20] J. E. Whitaker, P. L. Moore, R. P. Haugland, R. P. Haugland, *Biochem. Biophys. Res. Commun.* **1991**, *175*, 387–393.
- [21] D. Touchard, P. Haquette, S. Guesmi, L. Le Pichon, A. Daridor, L. Toupet, P. H. Dixneuf, *Organometallics* **1997**, *16*, 3640–3648.
- [22] J. Silvestre, R. Hoffmann, *Helv. Chim. Acta* **1985**, *68*, 1461–1506.
- [23] G. Doisneau, G. Balavoine, T. Fillebeen-Khan, *J. Organomet. Chem.* **1992**, *425*, 113–117.
- [24] T. M. Keller, S. B. Qadri, *Chem. Mater.* **2004**, *16*, 1091–1097.
- [25] V. N. Okulov, M. A. Dyadchenko, A. V. Churakov, E. V. Polunin, D. A. Lemenovskii, H. Yu, L. Wang, V. P. Dyadchenko, *Mendeleev Commun.* **2015**, *25*, 171–173.
- [26] S. Nakatsuji, K. Nakashima, M. Iyoda, S. Akiyama, *Bull. Chem. Soc. Jpn.* **1988**, *61*, 2253–2255.
- [27] Z. Wang, Q. Meng, Z. Zhang, D. Fu, W. Zhang, *Tetrahedron* **2011**, *67*, 2246–2250.
- [28] A. J. Curtis, C. D. Gabbutt, B. Mark Heron, C. Kilner, *Tetrahedron Lett.* **2011**, *52*, 708–710.
- [29] J. N. Moorthy, A. L. Koner, S. Samanta, A. Roy, W. M. Nau, *Chem. – Eur. J.* **2009**, *15*, 4289–4300.
- [30] R. Denis, L. Toupet, F. Paul, C. Lapinte, *Organometallics* **2000**, *19*, 4240–4251.
- [31] C. Bianchini, P. Innocenti, M. Peruzzini, A. Romerosa, F. Zanobini, *Organometallics* **1996**, *15*, 272–285.
- [32] F. Paul, C. Lapinte, *Coord. Chem. Rev.* **1998**, *178–180, Part 1*, 431–509.
- [33] D. Touchard, C. Morice, V. Cadierno, P. Haquette, L. Toupet, P. H. Dixneuf, *J. Chem. Soc. Chem. Commun.* **1994**, 859–860.
- [34] A. M. McDonagh, M. P. Cifuentes, I. R. Whittall, M. G. Humphrey, M. Samoc, B. Luther-Davies, D. C. R. Hockless, *J. Organomet. Chem.* **1996**, *526*, 99–103.
- [35] F. de Montigny, G. Argouarch, T. Roisnel, L. Toupet, C. Lapinte, S. C.-F. Lam, C.-H. Tao, V. W.-W. Yam, *Organometallics* **2008**, *27*, 1912–1923.

- [36] N. G. Connelly, M. P. Gamasa, J. Gimeno, C. Lapinte, E. Lastra, J. P. Maher, N. L. Narvor, A. L. Rieger, P. H. Rieger, *J. Chem. Soc. Dalton Trans.* **1993**, 2575–2578.
- [37] F. Paul, J.-Y. Mevellec, C. Lapinte, *J. Chem. Soc., Dalton Trans.* **2002**, 1783–1790.
- [38] F. H. Allen, D. G. Watson, L. Brammer, A. G. Orpen, R. Taylor, in *Int. Tables Crystallogr.* (Ed.: E. Prince), International Union Of Crystallography, Chester, England, **2006**, pp. 790–811.
- [39] M. Zora, C. Açıkgöz, T. A. Tumay, M. Odabaşoğlu, O. Büyükgüngör, *Acta Crystallogr.* **2006**, 62, m327–m330.
- [40] G. Grelaud; PhD Thesis, The Australian National University/Université de Rennes 1 **2012**.
- [41] M. A. Fox, J. E. Harris, S. Heider, V. Pérez-Gregorio, M. E. Zakrzewska, J. D. Farmer, D. S. Yufit, J. A. K. Howard, P. J. Low, *J. Organomet. Chem.* **2009**, 694, 2350–2358.
- [42] C. W. Faulkner, S. L. Ingham, M. S. Khan, J. Lewis, N. J. Long, P. R. Raithby, *J. Organomet. Chem.* **1994**, 482, 139–145.
- [43] S. Marqués-González, M. Parthey, D. S. Yufit, J. A. K. Howard, M. Kaupp, P. J. Low, *Organometallics* **2014**, 33, 4947–4963.
- [44] Z. Atherton, C. W. Faulkner, S. L. Ingham, A. K. Kakkar, M. S. Khan, J. Lewis, N. J. Long, P. R. Raithby, *J. Organomet. Chem.* **1993**, 462, 265–270.
- [45] C. E. Powell, M. P. Cifuentes, J. P. Morrall, R. Stranger, M. G. Humphrey, M. Samoc, B. Luther-Davies, G. A. Heath, *J. Am. Chem. Soc.* **2003**, 125, 602–610.
- [46] N. Gauthier, N. Tchouar, F. Justaud, G. Argouarch, M. P. Cifuentes, L. Toupet, D. Touchard, J.-F. Halet, S. Rigaut, M. G. Humphrey, et al., *Organometallics* **2009**, 28, 2253–2266.
- [47] A. Adenier, M. M. Chehimi, I. Gallardo, J. Pinson, N. Vilà, *Langmuir* **2004**, 20, 8243–8253.
- [48] K. Izutsu, *Electrochemistry in Nonaqueous Solutions*, John Wiley & Sons, New York, **2009**.
- [49] I. Brindle, A. M. Jones, *Dyes Pigments* **2000**, 47, 117–127.
- [50] Y. S. Sohn, D. N. Hendrickson, H. B. Gray, *J. Am. Chem. Soc.* **1970**, 92, 3233–3234.
- [51] D. M. Duggan, D. N. Hendrickson, *Inorg. Chem.* **1975**, 14, 955–970.
- [52] D. N. Hendrickson, Y. S. Sohn, D. M. Duggan, H. B. Gray, *J. Chem. Phys.* **1973**, 58, 4666–4675.
- [53] F. Dietz, N. Tyutyulkov, M. Rabinovitz, *J. Chem. Soc. Perkin Trans. 2* **1993**, 157–164.
- [54] M. P. Cifuentes, C. E. Powell, M. G. Humphrey, G. A. Heath, M. Samoc, B. Luther-Davies, *J. Phys. Chem. A* **2001**, 105, 9625–9627.
- [55] N. Gauthier, G. Argouarch, F. Paul, L. Toupet, A. Ladjarafi, K. Costuas, J.-F. Halet, M. Samoc, M. P. Cifuentes, T. C. Corkery, et al., *Chem. – Eur. J.* **2011**, 17, 5561–5577.

Chapter III:

Organometallic derivatives of crystal violet

Chapter III

Organometallic derivatives of crystal violet

Contents

1. Introduction	158
2. Synthesis and characterization	161
2.1. Direct replacement of amines to access molecular architectures such as S1	161
2.1.1. Ethynylferrocene derivatives.....	161
2.1.2. Metal alkynyl derivatives.....	164
2.2. Attempts to access molecular architectures such as S2	168
2.2.1. Common organic precursor.....	168
2.2.2. Ethynylferrocenyl derivatives.....	168
2.2.3. Metal alkynyl derivatives.....	171
3. Electronic and optical properties	174
3.1. UV-Vis spectroscopy.....	175
3.1.1. Trimetallic S1(Ru)⁺ compound.....	175
3.1.2. Hexametallic S2(Fc)⁺ compound.....	176
3.1.3. Conclusion	177
3.2. Cyclic voltammetry.....	178
3.2.1. Trimetallic S1(Ru)⁺ compound.....	178
3.2.2. Hexametallic S2(Fc)⁺ compound.....	179
3.2.3. Conclusion	181
3.3. Spectroelectrochemistry	182
3.3.1. Trimetallic S1(Ru)⁺ compound.....	182
3.3.2. Hexametallic S2(Fc)⁺ compound.....	183
3.3.3. Conclusion	184
4. Conclusion	185
References.....	187

1. Introduction

Following the encouraging results presented in the previous chapters, investigations on related CV^+ -based organometallic derivatives will now be undertaken. While maintaining the symmetric octupolar geometry that should increase the TPA cross-sections, electron-rich organometallic centers can be introduced either as a direct replacement of amino donors (**S1**, **Chart 1**) or by reinforcing the donating power of the diphenylamino donors by grafting the redox-active organometallic substituents in the *para* positions of the peripheral phenyl groups, leading to an extended version of CV^+ (**S2**). This dendritic structure should lead to even more active compounds in terms of third-order NLO response and also to larger σ_{TPA} cross-sections.

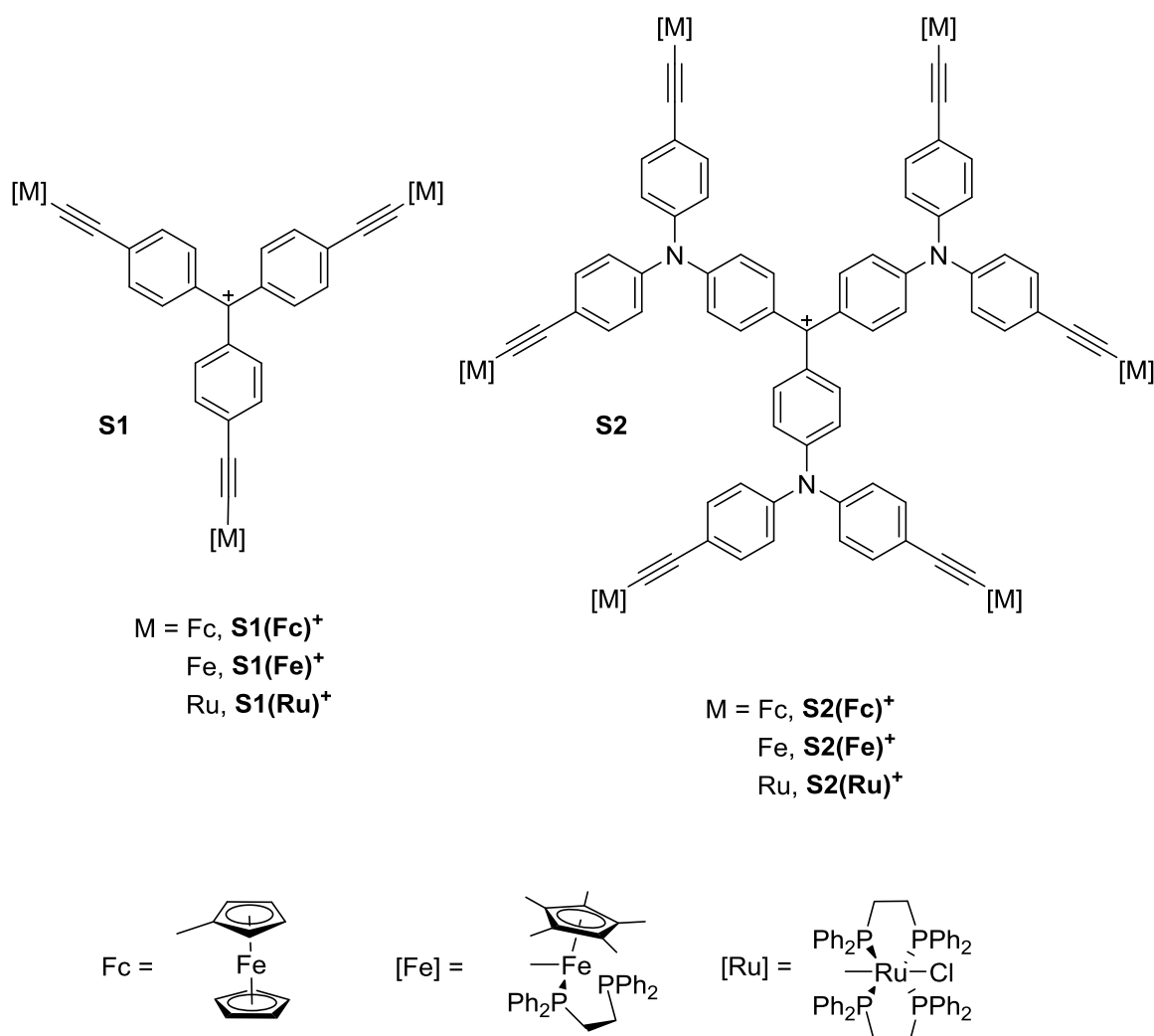
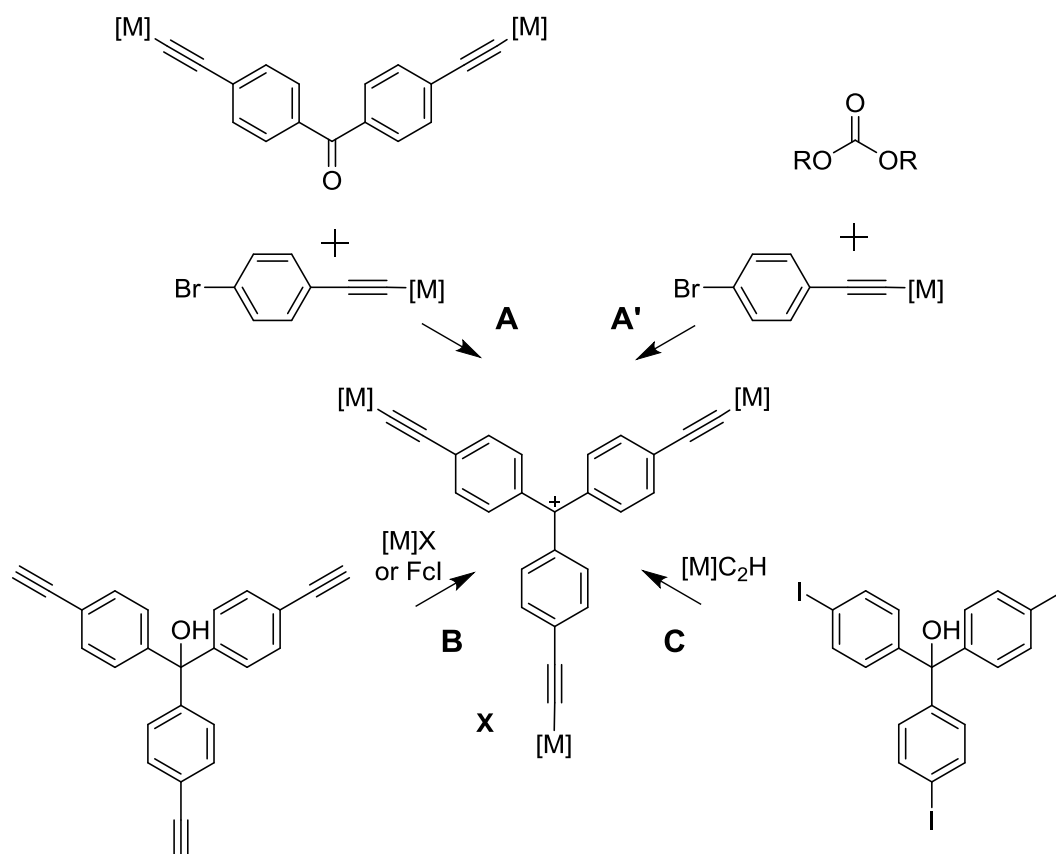


Chart 1: Targeted organometallic derivatives based on CV^+

This chapter is therefore mostly focused on the synthesis of these derivatives. As the previous chapter mentions, derivatives similar to **S1** have already been reported with either vinyl ferrocenyl endgroups or ruthenium alkynyl " $\text{Ru}(\text{Cp})(\text{PPh}_3)_2\text{C}\equiv\text{C}-$ " endgroups, so that molecules based on **S1** and its extended versions (**S2**) can be considered as synthetically accessible targets.

Several synthetic strategies can be envisaged to reach these derivatives. **Scheme 1** displays the different synthetic routes that might be envisioned for **S1**.

Paths **A** and **A'** depict two of the routes previously reported for accessing the organoruthenium species reported by Wu *et al.*^[1] This synthesis necessitates metal centers resistant to lithiation and able to support a subsequent classical aerobic work up, hence it is more likely to be used with air-stable species such as ethynylferrocene or ruthenium alkynyl complexes, given that iron alkynyl derivatives are air sensitive and will therefore present a greater challenge in work up. For alkynyl complexes, an attractive alternative is through the formation of an acetylide complex *via* alkyne activation and vinylidene formation/deprotection (route **B**), as used in the last chapter.^[2–4] With organic carbinols featuring three alkyne termini, a Sonogashira reaction involving iodoferrocene can also be envisioned to access the corresponding tris-ethynylferrocenyl derivatives.^[5,6] Route **C** is similar to route **B**, but with inverted halogen-based and alkynyl-based synthons. Hence, this reaction may be used with ethynylferrocene. Such an approach was used by Sengupta *et al.* with vinyl ferrocene to access an analogue of **S1** featuring alkene bridges via a Heck cross-coupling reaction.^[7,8] Route **C** might also be performed with " $\text{Fe}(\eta^5\text{-C}_5\text{Me}_5)(\kappa^2\text{-dppe})\text{-C}\equiv\text{C-H}$ " or related terminal alkynyl complexes used as the alkyne.^[9] Such a "metalla-Sonogashira" can be sometimes useful when synthetic problems are encountered in the more classic approach **B**.^[10–14] However, it is usually limited to smaller scale reactions and not applicable when strongly electron-donating substituents are appended to the halogenated aryl ring. Moreover, the " $[\text{M}]\text{C}\equiv\text{C-H}$ " reactant has to be prepared beforehand, usually from a more common $[\text{M}]\text{Cl}$ precursor (*e.g.* for $[\text{M}] = [\text{Fe}(\eta^5\text{-C}_5\text{Me}_5)(\kappa^2\text{-dppe})]$).



Scheme 1: Four possible synthetic routes to access CV^+ -based derivatives such as **S1**

For accessing larger derivatives such as **S2**, similar reactions might be envisioned to install the six peripheral organometallic groups based either (i) on nucleophilic reactions with ketones or carbonates using appropriately functionalized organometallic synthons or (ii) on alkyne activation reactions/Sonogashira cross-couplings protocols, from suitable central organic synthons peripherally functionalized with six halogen or six alkyne groups.

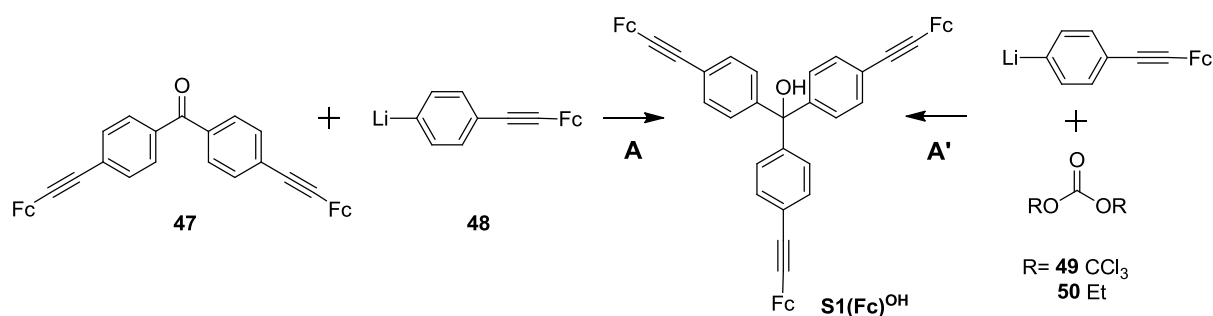
In the next paragraphs, the synthesis and structural characterization of these organometallic derivatives will be described. The first part will discuss the direct replacement of amines to reach derivatives such as **S1** and the second part will summarize the synthesis of larger amine-functionalized derivatives such as **S2**. The physical properties of the isolated compounds will then be described in a third part.

2. Synthesis and characterization

2.1. Direct replacement of amines to access molecular architectures such as S1

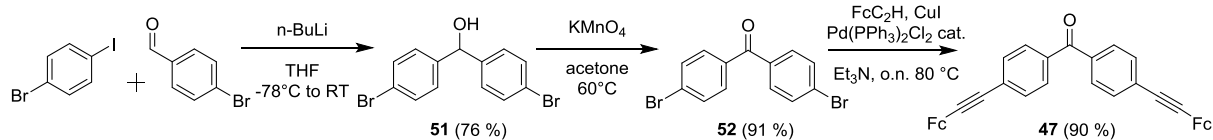
2.1.1. Ethynylferrocene derivatives

Ferrocene derivatives are inert chemically. Thus, any of the routes (**A**, **B** or **C**) proposed in **Scheme 1** are possible and might lead to the desired compounds. Because of the starting compounds available in the laboratory, route **A'** was tried first (**Scheme 2**) as it provided the shortest access to the desired carbinol derivative **S1(Fc)^{OH}**. However, reaction of the ethynylferrocene-functionalized lithioaryl base **48** with diethyl carbonate **50** or with triphosgene **49**^[15] led each time to an inseparable mixture of products in which only traces of the desired compounds could be detected (mass evidence).



Scheme 2: Synthetic routes tested for accessing ethynylferrocene carbinols

Route **A** was tested next. It required the formation of the dimetallated ketone precursor **47**. The latter was obtained *via* a Sonogashira cross-coupling reaction from **52**,^[16] itself prepared using a modified literature procedure from the 4-bromobenzaldehyde and para-bromiodobenzene (**Scheme 3**).^[17] The ketone **47** has a poor solubility in classical organic solvents, which explains the purification issues encountered and the recurrent presence of starting material when testing path **A'**. Crystals of the new ketone **47** were obtained, confirming its structure (**Figure 2**). The structural study reveals the expected bond lengths and angles for this type of derivative.



Scheme 3: Synthetic pathway for accessing the ketone derivative **47**

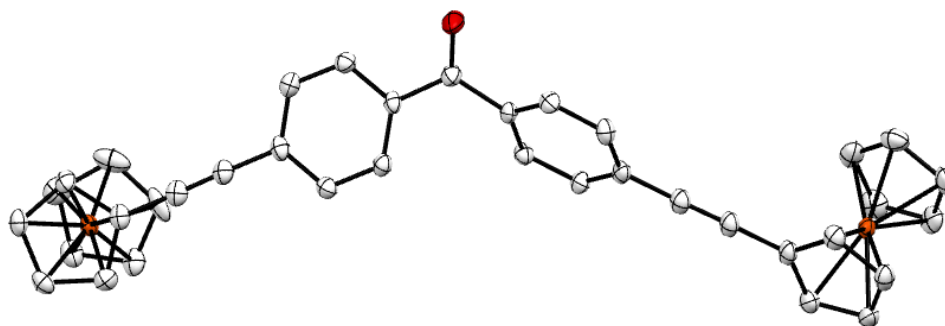


Figure 1: structure of **47** solved by Dr. Graeme Moxey

Subsequent reaction of the lithiated ferrocenyl derivative **48** with **47** formed the desired compound **S1(Fc)^{OH}** which was isolated in 20 % yield. This yield is low because of the poor solubility of **47** in THF or Et₂O, the two solvents tested for this lithiation reaction.

Crystals of **S1(Fc)^{OH}** were also obtained (**Figure 2**). For this carbinol compound, the bond lengths and angles are characteristic of a tetrahedral (sp³) central carbon and of three triple bonds in the *para* positions (**Table 1**). The C-O is also "normal" compared to literature value of 1.440 Å.^[18]

Complex	angle	C≡C	C-O	C1-C2	C=O
47	-	1.198(3)	-	1.493(3)	1.222(3)
S1(Fc)^{OH}	108.5	1.194(9)	1.442(5)	1.533(5)	-

Table 1: Selected bond lengths (Å) and angles (°) for **47** and for **S1(Fc)OH** (averaged over the three arms)

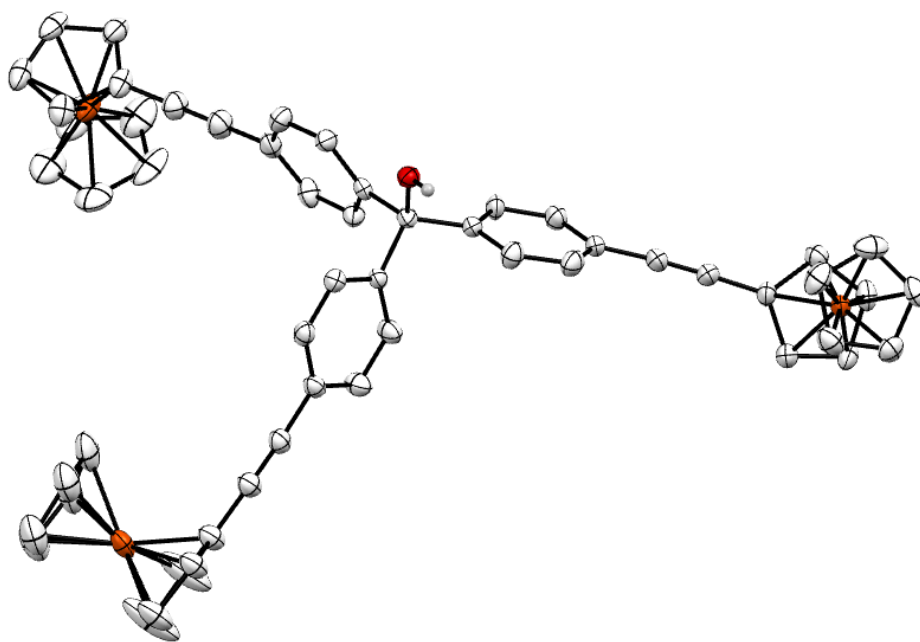


Figure 2: structure of **S1(Fc)**^{OH} solved by Dr. Graeme Moxey

Subsequent attempts to form **S1(Fc)**⁺, the corresponding carbocation have, however, been unsuccessful, even when using acids stronger than HBF₄ like trifluoroacetic or triflic acid. The solution of **S1(Fc)**^{OH} turns blue upon addition of excess acid, probably due to the formation of the expected carbocationic species, but the product rapidly decomposes within a couple of minutes even at low temperature. The resulting product remaining in solution does not possess any of the characteristic spectral data of the desired compound nor of the starting carbinol. No further optimization of its synthesis was thus attempted, because it was deemed that the targeted carbocation was insufficiently stable. Under such circumstances, rapid *in situ* measurements would be needed for further characterizing this unstable specie. Note that the analogous carbocation with vinyl ferrocene termini had also been reported to exhibit instability in solution.^[7,8,19,20]

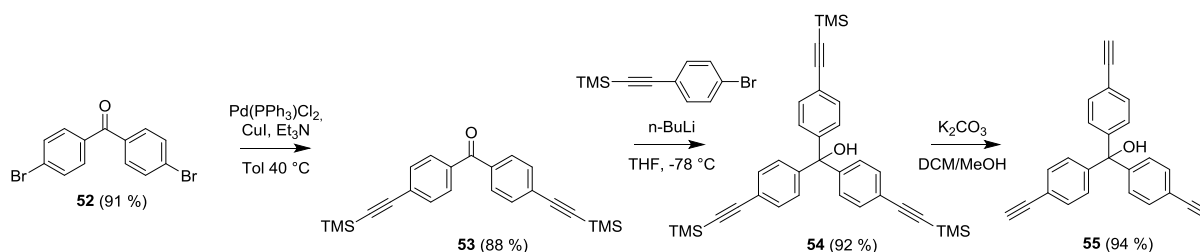
Characterization of precursors already reported can be found in the cited literature. New compounds have all been fully characterized with the usual techniques. The NMR shifts of the diverse ferrocene derivatives and precursors are not unusual, and can be found in the corresponding experimental procedure. **Table 2** displays the IR signatures of selected ethynylferrocenyl derivatives, such as **35** (1-bromo-4-ferrocenylethynylbenzene) in chapter II, as well as some of the precursors just described for comparison. For ethynylferrocene derivatives, the $\nu_{C\equiv C}$ values are normal and similar to previously discussed compounds featuring ethynylferrocene groups.

Complex	$\nu_{\text{O-H}}$	$\nu_{\text{C}\equiv\text{C}}$	$\delta_{\text{C-H Fc}}$	$\nu_{\text{C=O}}$
47	-	2199	838	1640
S1(Fc)^{OH}	3538	2205	825	-

Table 2: IR data ($\text{cm}^{-1} \pm 2$) for ethynylferrocene derivatives

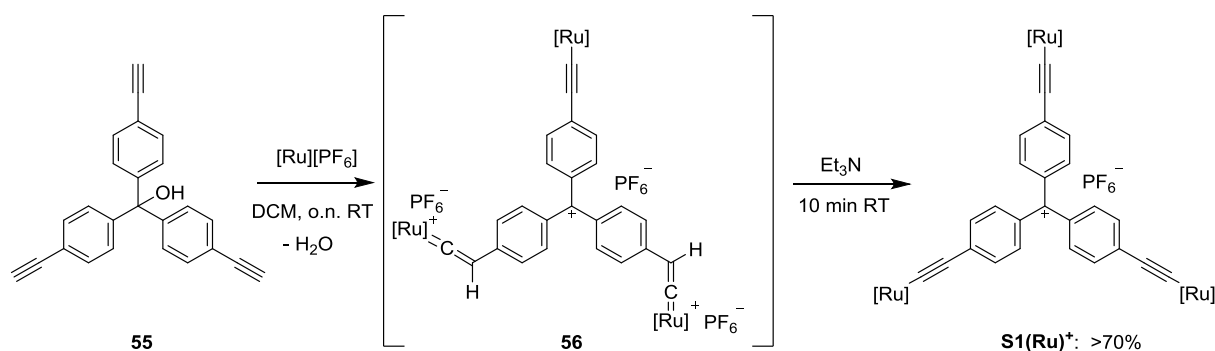
2.1.2. Metal alkynyl derivatives

For iron(II) and ruthenium(II) alkynyl-based derivatives, compound **55** was synthesized in four steps from **53** (Scheme 4). **55** has already been reported.^[21]



Scheme 4: Synthesis of the triyne precursor for accessing the targeted Fe(II) and Ru(II) alkynyl complexes

The organic triyne **55** was then reacted with the ruthenium 5-coordinate precursor **45** in DCM (Scheme 5). Surprisingly, spontaneous dehydration of the tris-vinylidene carbinol intermediate occurs, in spite of the absence of base or amino-donating groups, to form eventually the corresponding bis-vinylidene carbocationic complex **56** as the dominant species in solution. This compound was characterized by ^{31}P and ^1H NMR spectroscopies; a 1/2 ratio of acetylide/vinylidene in the ^{31}P NMR spectrum and concomitant disappearance of the carbinol signature in the ^1H NMR spectrum were observed. The two remaining vinylidene moieties were then deprotonated upon addition of base (Et_3N) to form the desired CV^+ analogue. Fortunately, the addition of Et_3N did not reform the carbinol species; such a reaction was also observed by Wu *et al.*^[1]



Scheme 5: Synthesis of the CV^+ analogue $[\text{S1(Ru)}^+][\text{PF}_6^-]$

Similar reactions starting from **55** were also undertaken with $[\text{Fe}(\eta^5\text{-C}_5\text{Me}_5)(\kappa^2\text{-dppe})\text{Cl}]$ to isolate the corresponding Fe(II) derivative, but these attempts were unsuccessful, failing even to form cleanly the corresponding tris-vinylidene complex.

These ruthenium alkynyl derivatives possess the expected IR signatures (**Table 3**). Their carbinol derivatives exhibit lower values for the alkynyl stretching modes, in line with the literature data.^[18,22] A much more marked decrease in the $\nu_{\text{C}\equiv\text{C}}$ mode(s) is apparent when converting the carbinol **55** to its carbocation S1(Ru)^+ , in line with a pronounced charge delocalization in the GS, and evidencing a larger cumulenenic character due to the three resonance forms (**Scheme 6**) than for the ethynylferrocene analogue. The $\nu_{\text{C}\equiv\text{C}}$ is also lower than for the related organoruthenium MG^+ -based derivatives M3(Ru)^+ and M4(Ru)^+ (**Chart 3**) studied in the previous chapter, suggesting more charge delocalization in the GS for the symmetric carbocation S1(Ru)^+ , or at least the existence of some vibronic coupling between the various $\nu_{\text{C}\equiv\text{C}}$ modes of each branch.

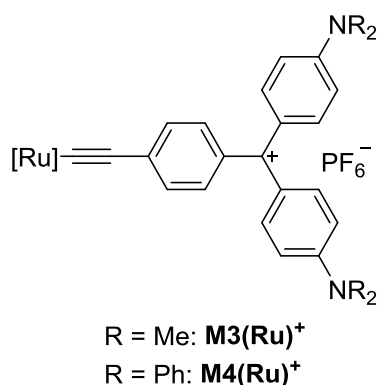


Chart 2: Organoruthenium compounds previously synthesized

Complex	$\nu_{\text{O-H}}$	$\nu_{\text{C}\equiv\text{C}}$	$\nu_{\text{C}\equiv\text{H}}$	$\nu_{\text{P-F}}$
54	3597	2159	-	-
55	3538	2116	3281	-
S1(Ru)⁺	-	1958	-	834
M3(Ru)⁺	-	2014	-	839
M4(Ru)⁺	-	1986	-	836

Table 3: IR data for selected Ru(II) alkynyl derivatives and their carbinol precursors ($\text{cm}^{-1} \pm 2$)

The cumulenic character is also observed by ^{31}P NMR, as the ruthenium derivative **S1(Ru)⁺** has a shift very close to those of **M3(Ru)⁺** and **M4(Ru)⁺**, confirming the strong charge delocalization along the three arms.

compounds	^{31}P (ppm)
S1(Ru)⁺	47.6
M3(Ru)⁺	47.6 (PF_6)
	48.4 (BF_4)
M4(Ru)⁺	47.4

Table 4: ^{31}P NMR data (ppm) of organoruthenium derivatives (162 MHz, CDCl_3)

Crystals of **S1(Ru)⁺** were eventually obtained (**Figure 3**) with a chloride counter ion. Unfortunately, the crystallographic dataset obtained for the **S1(Ru)⁺** crystals is not of sufficiently good quality to extract accurate values for the geometrical parameters, so a detailed discussion of the bonding within the molecule will not be supplied. Nevertheless, the connectivity of the molecule confirms that the desired target was obtained. The bond distances suggest a slightly dissymmetric structure for this compound in the solid state. Also, remarkably, the central triphenylene part of the molecule tends to adopt the most coplanar conformation achievable (the torsion angles of peripheral phenyl with mean plane of the carbocation are in between 20 and 40°), as expected from strong intermolecular π interactions (in line with the various mesomers **B₁-B₃** given in the VB **Scheme 6**) and intermolecular stacking interactions.

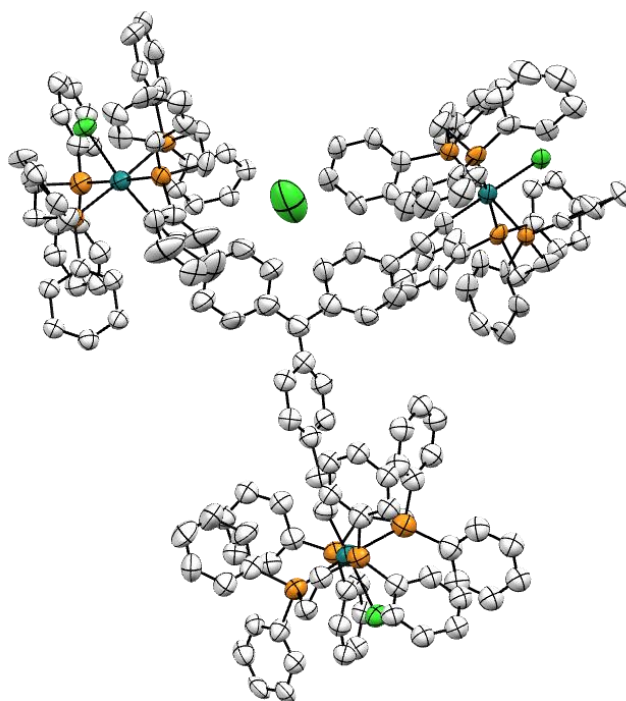
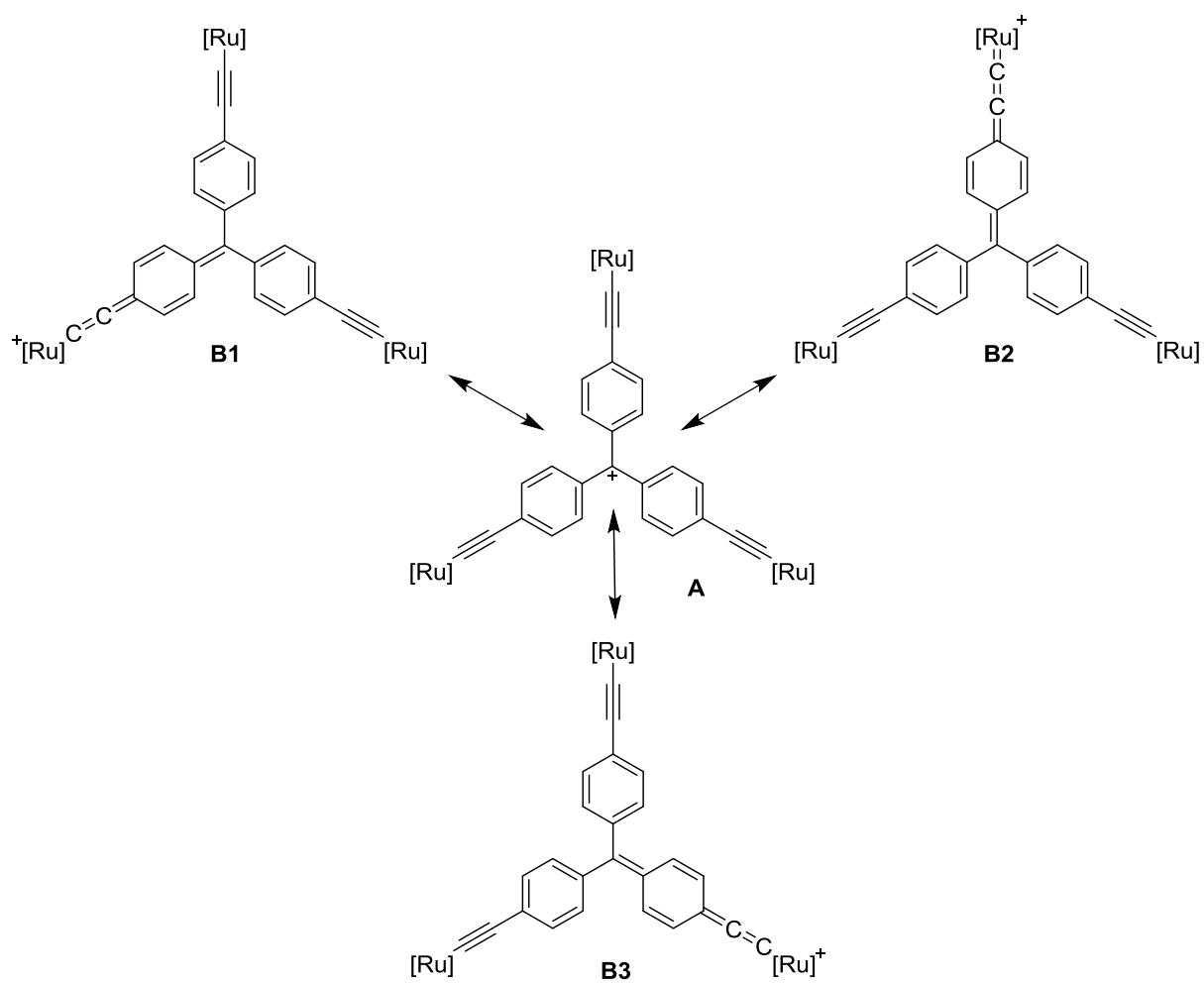
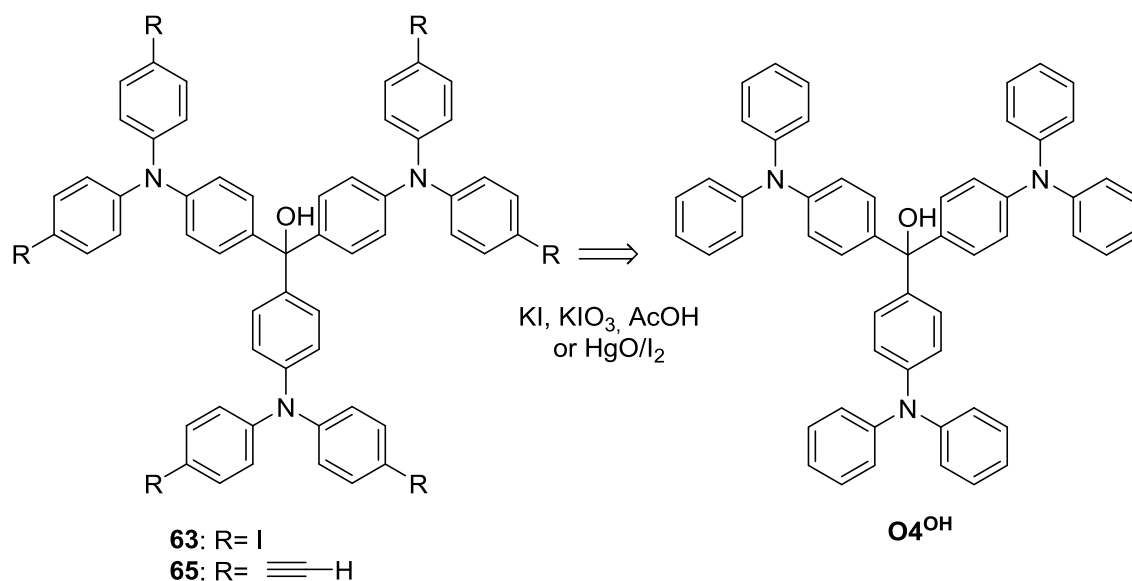


Figure 3: Structure of $[S1(Ru)^+][Cl^-]$ (connectivity only, Cl^- as a counter anion) obtained by Dr. Graeme Moxey

2.2. Attempts to access molecular architectures such as **S2**

2.2.1. Common organic precursor

Once the hexayne precursor **65** is isolated, the extended derivatives **S2** might then be simply synthesized following very similar synthetic procedures to those used for "shorter" derivatives **S1**. A starting material to access this key precursor, the compound **63**, was targeted first based on its synthetic versatility. The idea was to form this new hexa-halogenated species from **O4^{OH}**. Electrophilic aromatic halogenation chemistry always involves oxidizing or acidic conditions, while the central carbinol is really sensitive to these conditions, and so unsurprisingly the usual iodination conditions were unsuccessful, even with milder reagents such as HgO/I₂.^[23–25] Attempts to protect this site using several protecting groups (methoxy, benzyl, trialkylsilyl)^[26] for alcohol functions were performed but all were unsuccessful; the protecting groups tested were almost as sensitive as the carbinol itself under the halogenations reaction conditions tested.

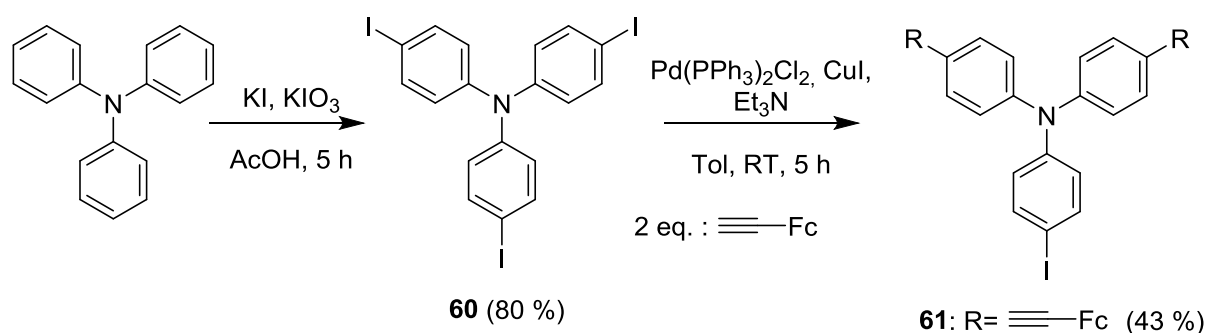


Scheme 7: First attempt at obtaining **63**

2.2.2. Ethynylferrocenyl derivatives

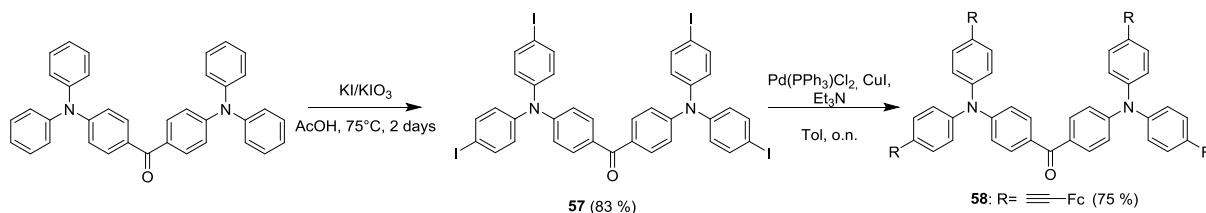
The second route envisioned to access the hexayne precursor did not proceed through this hexa-halogenated species, but was closer to strategy **A** in **Scheme 1**. It is given in **Scheme 8** and

permits direct access to the hexa-ferrocenyl species **52(Fc)^{OH}**. It starts with the addition of the lithiated derivative of triarylamine **61** to the substituted ketone **58**. This reaction requires first the isolation of the triphenylamine derivative **61** and of the ketone **57**. Triphenylamine derivatives are well known and the derivative **61** can be synthesized using well-known procedures starting from tri(4-iodophenyl)amine, itself obtained in one step from triphenylamine.^[25] From tri(4-iodophenyl)amine, bis-functionalization by ethynylferrocene was effected using a Sonogashira coupling reaction with the alkyne in sub-stoichiometric conditions (2/3 ratio) (**Scheme 8**).



Scheme 8: Synthesis of **60** and **61**

Despite lowering the yields, such an approach avoids the additional steps that would be required for achieving the symmetry-lowering at a triarylamine required to access this particular precursor in a more efficient synthetic approach. However, in terms of overall yield, the limiting reaction is that leading to the new tetra-iodo derivative **57**, which allows access to the required tetra-functional derivatives after further functionalization. **57** was obtained in good yields (83 %) following a literature report from 2004.^[27] From this compound, the synthesis of the corresponding tetra-ethynylferrocene analogue was achieved in good yields via Sonogashira cross-coupling reactions (**Scheme 9**).



Scheme 9: Synthesis of **57-58**

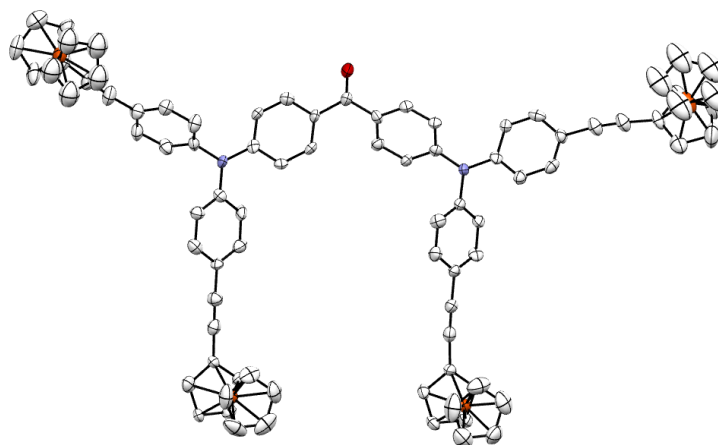
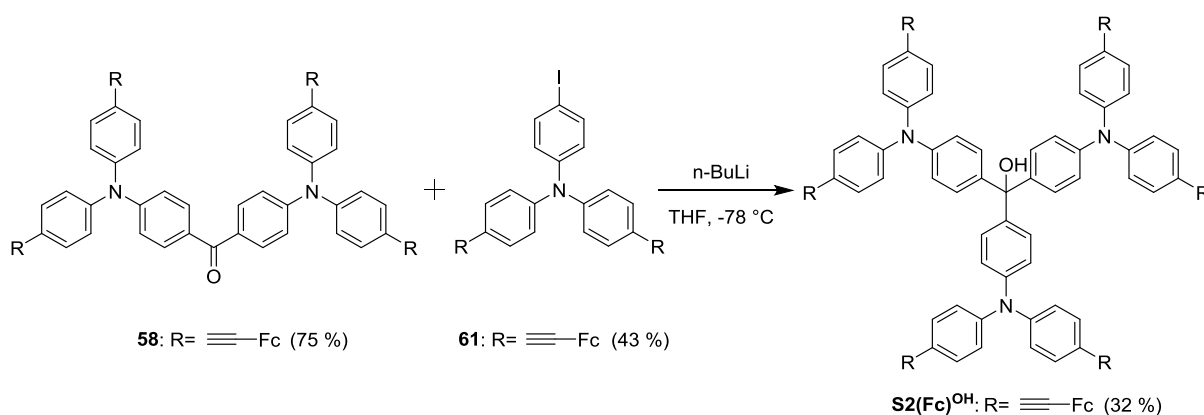


Figure 4: Structure of **59** solved by Dr. Thierry Roisnel

Crystals of **59** were obtained and definitively established the identity of the molecule (**Figure 4**). Further crystallographic details can be consulted in the corresponding experimental part, as no specific structural features are worth highlighting.



Scheme 10: Synthesis of the C_3 -symmetric carbinol intermediates

Subsequent to the lithiation of the functional derivatives **61** with butyllithium at low temperature, addition of the corresponding functional ketone **58** was performed. The reaction proceeded successfully allowing isolation of the targeted symmetric compounds **S2(Fc)^{OH}** in good yields (**Scheme III-10**). However, the isolated yield of the hexa-ferrocenyl derivative was lower than expected (32%) because of solubility and purification reasons. **Table 2** displays characteristic IR signatures of some of these ethynylferrocenyl derivatives. Similar to the other ethynylferrocenyl compounds previously isolated, the values of the characteristic stretching modes are close to the various precursors (**58**, **61** and **S2(Fc)^{OH}**) and the final compounds, indicating the poor interaction between the ethynylferrocenyl group and the rest of the molecule in these compounds.

Complex	$\nu_{\text{O-H}}$	$\nu_{\text{C}\equiv\text{C}}$	$\delta_{\text{C-H Fc}}$	$\nu_{\text{C=O}}$	$\nu_{\text{B-F}}$
M4(Fc)^{OH}	3446	2207	826	-	-
M4(Fc)⁺	-	2196	833	-	1174
58	-	2204	821	1646	-
61	-	2209	817	-	-
S2(Fc)^{OH}	3563	2206	819	-	-
S2(Fc)⁺	-	2204	820	-	1172

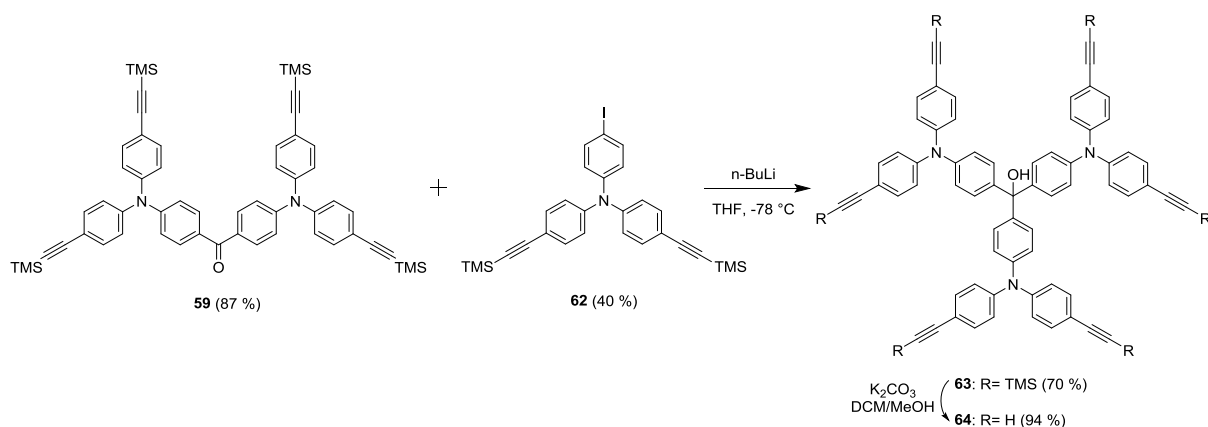
Table 5: Selected IR ($\text{cm}^{-1} \pm 2$) signatures for the ferrocenyl compounds

At this stage, a similar addition reaction between the tetra-iodo ketone **57** and a di-iodo lithiated triaryl amine **60** was also attempted, in order to check if the hexa-iodo species previously targeted (**63**) might be obtained by this new route. This compound was actually obtained and could be characterized by NMR and mass spectroscopy, but its solubility was very low and resulted in low isolated yields (<5%), making this new approach not attractive as a synthetic procedure.

Addition of HBF_4 to a solution of **S2(Fc)^{OH}** in Et_2O gave the corresponding tris-ferrocenyl carbocation **S2(Fc)⁺**. This species, analogous to **O4⁺** (Chapter I), is stable in solution, due to the presence of the peripheral arylamine groups which stabilize the central carbocation much more efficiently than did previously the ethynylferrocenyl groups in **S1(Fc)⁺**.

2.2.3. Metal alkynyl derivatives

The synthesis of the corresponding hexa-yne precursor to the related metal-alkynyl species was achieved in good yields, following a route similar to that used to obtain the ferrocene derivative from the ketone **58**. Thus, a Sonogashira cross-coupling reaction afforded **59** from this compound. Addition of the lithiated species derived from **62** to **59** formed **63**, which could be isolated in good yields after chromatographic purification. The desired hexa-yne **64** was then obtained after removal of trimethylsilyl protecting groups using potassium carbonate.



Scheme 11: Synthesis of the hexayne precursor **64**

Reaction with the ruthenium 5-coordinate precursor complex **45** was attempted first because the resulting Ru(II) alkynyl complexes are usually air-stable, in contrast to their Fe(II) analogues with the $[\text{Fe}(\eta^5\text{-C}_5\text{Me}_5)(\kappa^2\text{-dppe})]$ endgroups, which are much more electron rich. Furthermore, the vinylidene carbinol organoiron derivatives previously synthesized (Chap. II; sect 2.3.) turned out to be more difficult to deprotonate than their ruthenium counterparts and led to unstable mixtures of carbocationic species.

As previously stated with **56** (Scheme 5), this reaction also led to a carbinol/hexavinylidene species which underwent a spontaneous dehydration, leading to the formation of a hexa-ruthenium carbocation with one of its vinylidene groups deprotonated. Subsequent addition of Et_3N cleanly led to formation of the desired dye **S2(Ru)⁺** with a PF_6^- counter anion (Chart 4). The overall transformation could be easily monitored by ^{31}P NMR spectroscopy. Figure 5 shows this unusual behavior upon comparing the spectra of the penta-vinylidene intermediate and the final **S2(Ru)⁺** derivative with a ^{31}P NMR shift of 49.58 ppm, close to the value expected for a classic Ru(II) alkynyl complex, as seen for other derivatives presented in chapter II. Unfortunately, this last derivative turned out to be quite sensitive and slowly decomposed (in the solid state) after these NMR measurements were performed. It will therefore require synthesis again for further characterization. Ruthenium derivatives are usually stable over time, even in air. This slow spontaneous decomposition is unusual and may be linked to charge delocalization taking place on the peripheral amine, activating the acetylide bond toward external nucleophilic attacks or electron-transfer reactions, causing its decomposition upon aerial exposure. Under such conditions and due to time limitations, the related reaction with $[\text{Fe}(\eta^5\text{-C}_5\text{Me}_5)(\kappa^2\text{-dppe})]$ was not attempted.

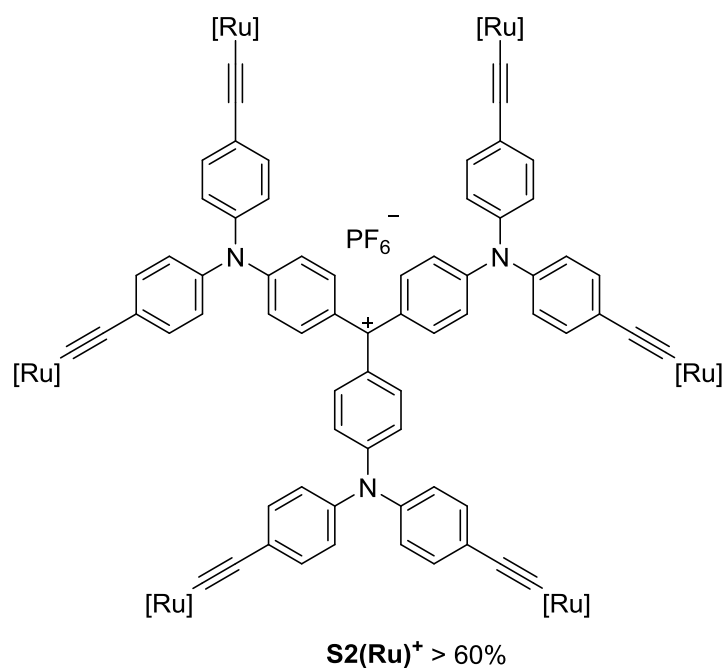


Chart 4: The extended CV⁺ analogue [S2(Ru)⁺][PF₆⁻]

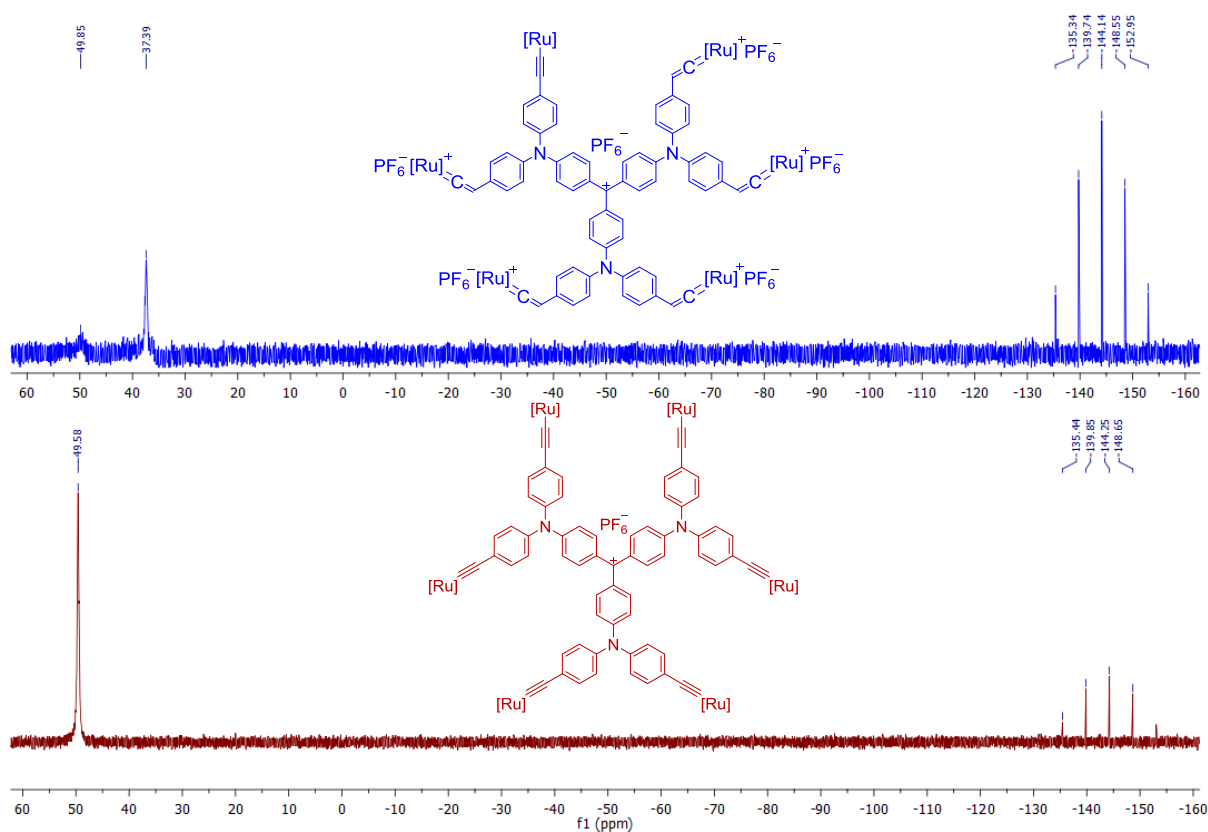


Figure 5: ³¹P NMR spectra of [S2(Ru)⁺][PF₆⁻] and its penta-vinylidene precursor

Characterization of the new precursors was also performed using NMR and IR spectroscopies. They all possess the expected characteristic stretching modes for such compounds,

as shown in the **Table 6**. The X-ray structure of compound **59** has also been solved (**Figure 6**). The bonding parameters are not unusual and can be consulted in the experimental part, and likewise for the other experimental characterizations obtained for these compounds.

Complex	$\nu_{\text{O-H}}$	$\nu_{\text{C}\equiv\text{C}}$	$\nu_{\text{C}\equiv\text{H}}$	$\nu_{\text{Si-Me}}$	$\nu_{\text{C=O}}$
59	-	2159	-	1272	1672
62	-	2154	-	1248	-
63	n.d. ^a	2153	-	1272	-
64	3300	2104	3287	-	-

Table 6: IR ($\text{cm}^{-1} \pm 2$) data for selected Ru(II) alkynyl derivatives and their precursors. a: Too weak to be detected

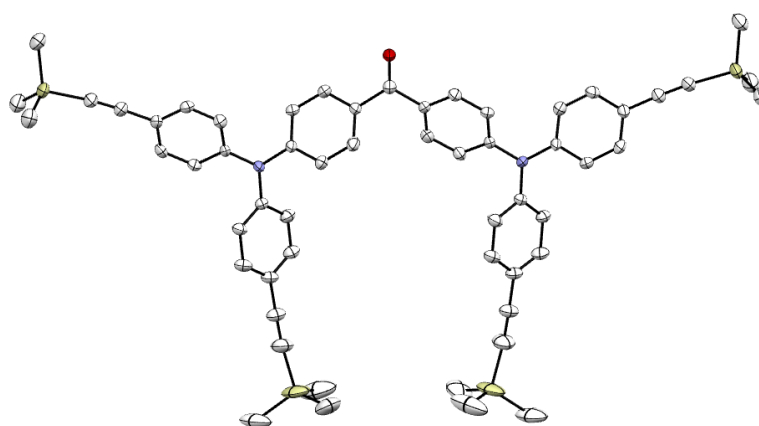


Figure 6: Crystal structure of **59** solved by Dr. Graeme Moxey

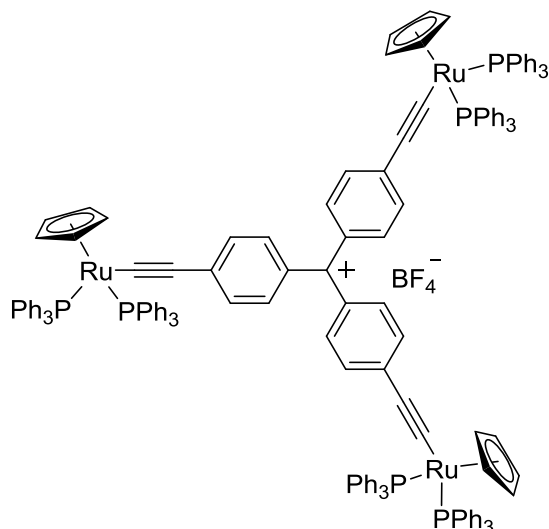
3. Electronic and optical properties

The synthesis of the targeted organometallic CV^+ derivatives S1^+ and S2^+ turned out to be more difficult than expected and stability issues as well as solubility issues were encountered. Some of them were eventually overcome, but only one short S1^+ -type carbocation and one extended S2^+ -type carbocation were isolated: the ruthenium derivative S1(Ru)^+ and the extended ferrocene derivative S2(Fc)^+ . These species were actually stable enough for further characterization. To unravel their electronic and optical properties, these new organometallic TPM dyes were then also characterized by cyclic voltammetry, UV-vis spectroscopy and spectroelectrochemistry.

3.1. UV-Vis spectroscopy

3.1.1. Trimetallic **S1(Ru)**⁺ compound

Figure 9 presents the UV-vis spectra of the Ru(II) alkynyl carbocation **S1(Ru)**⁺ and the key data are summarized in **Table 7**. For this ruthenium tris-alkynyl compound, values very similar to those reported for the derivative **XIX_e** (**Chart 4**) synthesized by Wu *et al.* were found.^[1]



XVII_e: $\lambda_{\text{max}} = 974 \text{ nm}$ ($\epsilon = 1.15 \times 10^5 \text{ L} \cdot \text{mol}^{-1} \cdot \text{cm}^{-1}$)^a

Chart 4: Analogue of **S1(Ru)**⁺ synthesized by Wu *et al.* a: In DCM

The lowest energy absorption found for **S1(Ru)**⁺ is shifted further into the NIR range compared with **XVII_e** ($\Delta\nu = 145 \text{ cm}^{-1}$) (**Figure 7**), probably due to a better d- π -overlap for [Ru(κ^2 -dppe)₂] compared to that of [Ru(η^5 -C₅H₅)(PPh₃)₂], as the electron-richness of these endgroups is similar, at least based on the first oxidation potentials of the bis-chloro complex [Ru(κ^2 -dppe)₂Cl₂] (+0.600 V) and [Ru(η^5 -C₅H₅)(PPh₃)₂Cl] (+0.595 V).^[28] There is an even more significant shift of ~400 nm (4800 cm⁻¹) between these ruthenium derivatives and **CV**⁺ accompanied by a remarkable increase in intensity of the low-energy band. This shift can be explained firstly by the much larger electron-donating power of the ruthenium metal center in the excited state compared to diphenylamine and also (partly) by the increase of the π -system due to the presence of the additional alkynyl bonds. The absorption due to the charge transfer (CT) transition in **CV**⁺ most likely corresponds to a metal-to-ligand charge transfer (MLCT) process in **S1(Ru)**⁺. Unsurprisingly, the latter compound exhibits very similar spectral features such as a shoulder on the high-energy side of the lowest-energy band, a

fairly similar extinction coefficient for this band, and a second set of bands near 620 nm likely attributable to the forbidden A→A band observed near 300 nm in **CV**⁺.

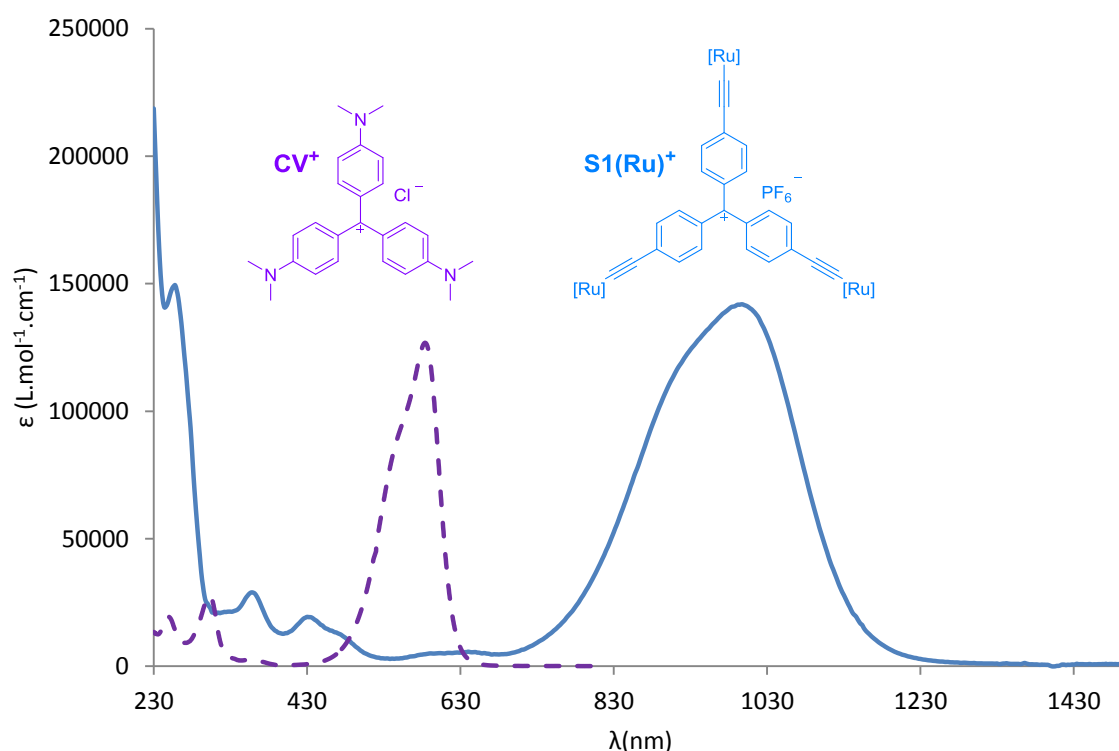


Figure 7: UV-Vis spectra of the ruthenium derivative **[S1(Ru)]⁺[PF₆]⁻** and **[CV]⁺[Cl]⁻**

3.1.2. Hexametallic **S2(Fc)**⁺ compound

The UV-vis spectrum of the hexa-ferrocene derivative **S2(Fc)**⁺ is presented in **Figure 8**, along with that of its carbinol precursor. The spectrum of the all-organic diphenylamino analogue of **CV**⁺ (**O4**⁺) (Chapter I, 2.2) is also given in that figure for comparison. The key electronic absorption data is collected in **Table 7** for these three compounds. Regardless of the presence of the ethynylferrocene endgroups, the carbinol **S2(Fc)**^{OH} has most of its electronic absorptions located at wavelengths shorter than 430 nm, in line with amine- and ferrocene-based transitions (at 340 nm), while the carbocation **S2(Fc)**⁺ presents a band at much lower energy (690 nm), responsible for its deep green color. In spite of the poor influence of the peripheral ferrocenyl groups in the GS evidenced by **CV**⁺, these organometallic substituents seem nevertheless to exert an influence on the first excited state of this dye, since its intense low-energy band in the visible range appears red-shifted (60 nm, 1380 cm⁻¹) when compared to the non-substituted derivative **37**⁺. This significant bathochromic shift possibly results from increased polarizability of the π-manifold induced by these organometallic

electron-releasing groups. The shift (48 nm, 1309 cm^{-1}) between O4^+ and CV^+ largely results from the extension of the π -manifold.

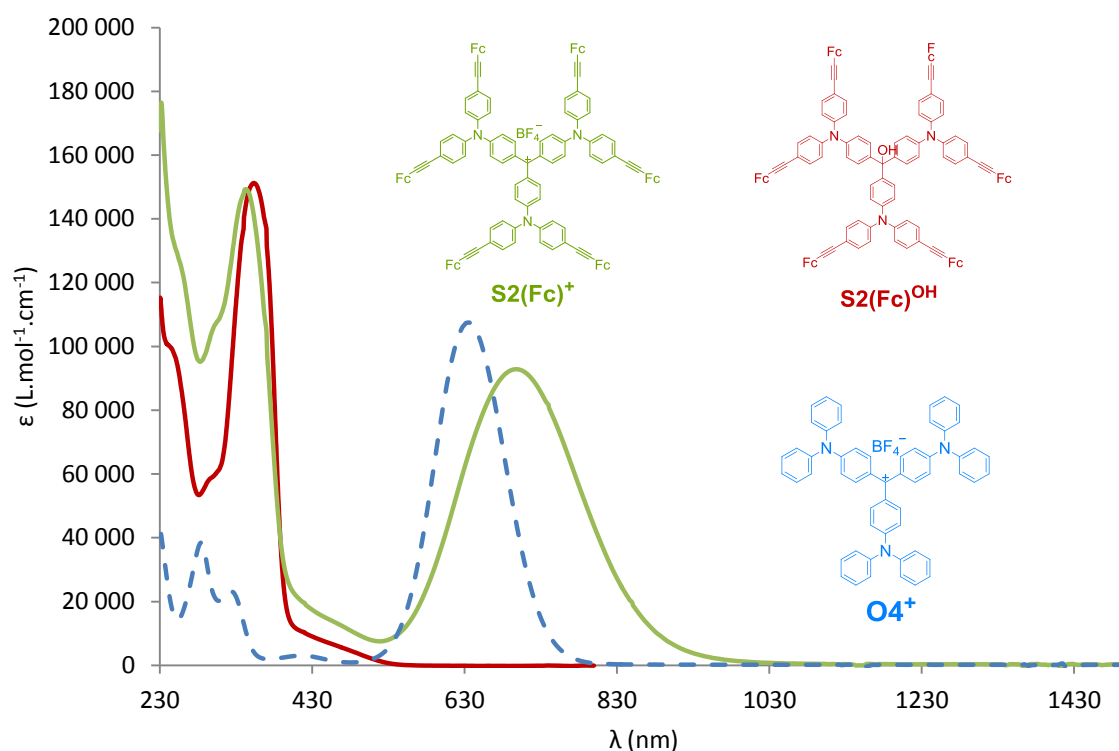


Figure 8: UV-vis spectra of the ferrocene derivatives $\text{S2(Fc)}^{\text{OH}}$, $[\text{S2(Fc)}^+][\text{BF}_4^-]$ and $[\text{O4}^+][\text{BF}_4^-]$ (used as reference)

Complex	O4^+	S2(Fc)^+	CV^+	S1(Ru)^+	Ref
$\lambda_{\text{max}} (\epsilon \cdot 10^5 \cdot \text{M}^{-1} \cdot \text{cm}^{-1})$	630 (1.1)	690 (0.92)	582 (1.26)	988 (1.4)	974 (1.2) ^b
	405 (0.003)	445 (0.001)	360 ^a	627 (0.001)	n.d.
$\Delta E (\text{cm}^{-1})$	8818	7979	10595	5827	-

Table 7: UV-Vis data for ruthenium alkynyl- and ethynylferrocene-based TPM dyes, $[\text{CV}^+][\text{Cl}^-]$ and $[\text{O4}^+][\text{BF}_4^-]$ (used as reference values. a: Not observable. b: ref^[1])

3.1.3. Conclusion

In conclusion, these new organometallic TPM dyes present strong absorptive properties in the visible-NIR range. Their lowest energy bands possess similar extinction coefficients to their organic analogues CV^+ and 37^+ , but are significantly red-shifted, especially in the case of the Ru(II) alkynyl derivatives, for which direct conjugation with the carbocationic center is possible. These

observations suggest that large absorptive third-order NLO effects might be observed, located deep in the NIR range, prompting us to undertake the Z-scan measurements for the organometallic octupoles. To assign the absorptions observed at higher energy for these organometallic dyes or to draw additional conclusions on the effect of the metal centers on their linear optical absorption spectra, some TD-DFT calculations are needed. We will now investigate the redox properties of these new derivatives.

3.2. Cyclic voltammetry

3.2.1. Trimetallic **S1(Ru)⁺** compound

In the case of the ruthenium tris-alkynyl derivative **S1(Ru)⁺**, an interesting situation is encountered: upon reduction, there is a one-electron irreversible reduction of the central carbocation, and upon oxidation, a reversible oxidation process takes place at 0.66 V, followed by another quasi-reversible event at higher potentials (1.09 V). When compared to the oxidation potential of the corresponding phenylacetylene analogue ($E_{1/2} = 0.41$ V under these conditions, *i.e.* $\Delta E_{1/2} = 0.25$ V)^[29], the first oxidation occurs at 0.25 V more positive potential (**Table 8**). This potential shift is likely due to the positive charge. Notably, this oxidation potential is also higher than those previously found for the related **MG⁺**-based dyes in the previous chapter (**Table 8**), indicating that part of the cationic charge was efficiently delocalized on the two amino-substituents in these monometallic derivatives. Thus, **M3(Ru)⁺** and **M4(Ru)⁺** (**Chart 2**) undergo metal-centred oxidation at 0.58 V and 0.54 V, respectively. Furthermore, integration reveals that this oxidation is a two-electron process with the oxidation of two ruthenium centers probably leading to a di-radical compound such as that represented in **Figure 9**, with the remaining arm stabilizing the cationic charge. As such, the resulting trication should have a less symmetrical structure than **CV⁺**, closer to that of **MG⁺** derivatives. This trication can actually be considered as an allenylidene complex with two weakly π -attracting substituents in the *para*-positions on the terminal rings. Also, due to the much lower electron-releasing power of these endgroups, it will exhibit an increased chemical reactivity in solution, resembling that of non-stabilized TPM carbocations. According to the cyclic voltammogram, the third ruthenium-containing endgroup can also be oxidized at even higher potentials but this oxidation is not fully chemically reversible this time. Based on DPV experiments (**Table 8**), only the first oxidized state **S1(Ru)³⁺** might exhibit sufficient stability in solution for electrochemical generation by electrolysis.

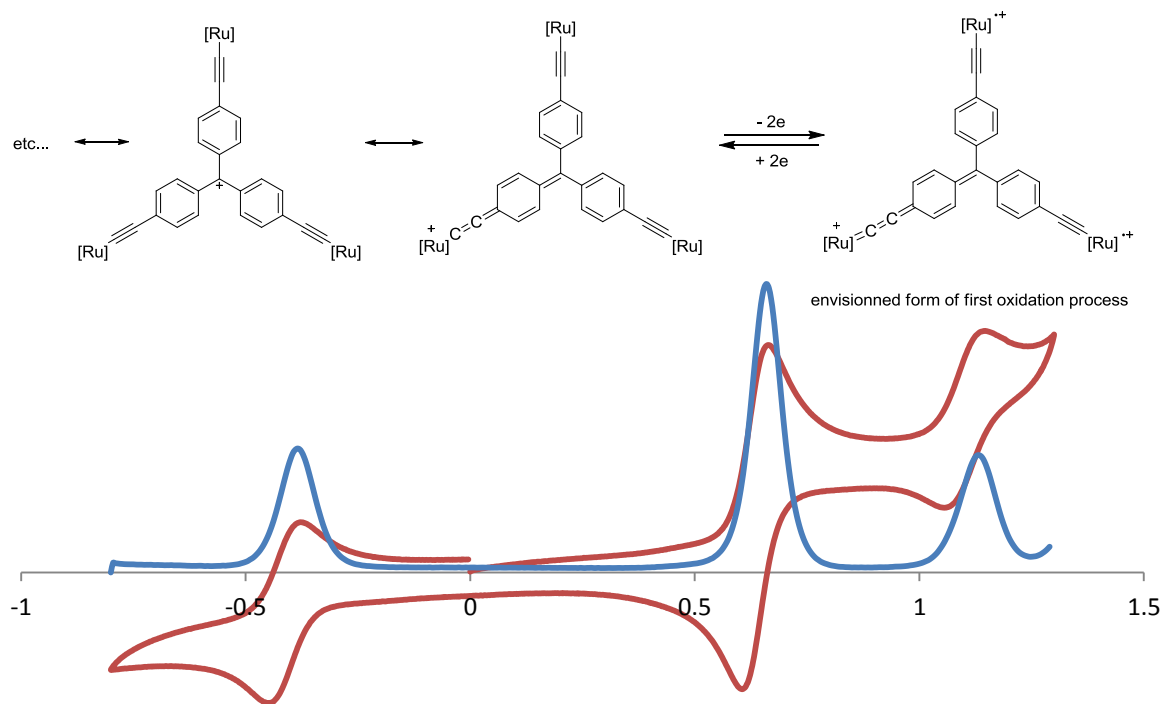


Figure 9: Cyclic voltammetry and DPV data for Ru derivative $[S1(Ru)^+][PF_6^-]$ in DCM containing 0.10 M $[n-Bu_4N][PF_6]$ ($E_{1/2}$, $\Delta E_{1/2}$ and ΔE_p in V vs. SCE)

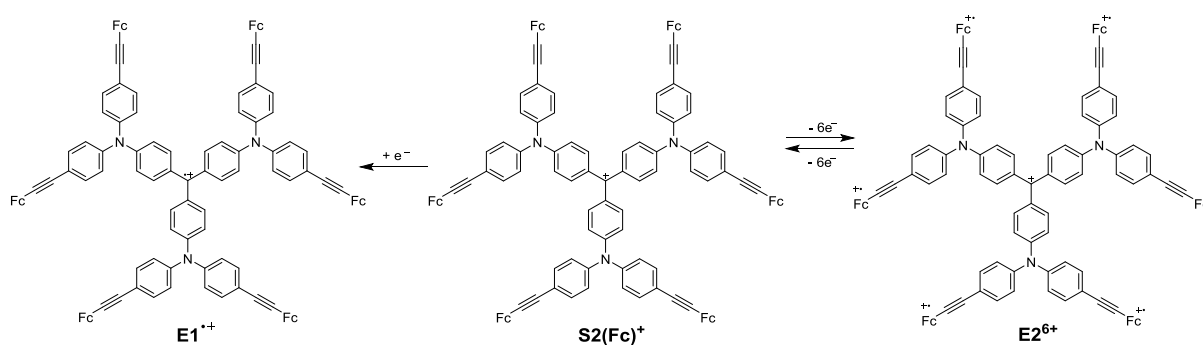
complex	$E_{1/2}$	ΔE_p	i_{pc}/i_{pa}	integration
$[Ru]-C\equiv C-Ph$	0.44	-	-	-
$M3(Ru)^+$	0.58	0.04	1.0	1
$M4(Ru)^+$	0.54	0.04	1.0	1
$S1(Ru)^+$ (redI)	-0.41	0.04	0.83	1
$S1(Ru)^+$ (oxI-oxII)	0.66	0.04	1.0	2
$S1(Ru)^+$ (oxIII)	1.09	0.07	0.64	1

Table 8: Cyclic voltammetric and DPV data for Ru derivatives in DCM containing 0.10 M $[n-Bu_4N][PF_6]$ ($E_{1/2}$, $\Delta E_{1/2}$ and ΔE_p in V vs. SCE)

3.2.2. Hexametallic $S2(Fc)^+$ compound

The extended $S2(Fc)^+$ derivative and of its carbinol precursor $S2(Fc)^{OH}$ reveal quite similar voltammograms, similar to those obtained for previously isolated ethynylferrocene derivatives such as $M3(Fe)^+$ or $M4(Fc)^+$ (Chapter II-3.5. and **Figure 10** and **Table 9**). In line with previous data, this indicates that there is not much electronic interaction between the carbocationic TPM core and the

peripheral ethynylferrocene groups. This lack of interaction is emphasized for the extended **CV**⁺-based derivative **S2(Fc)**⁺ for which the metallic center is spatially even further away from the central carbon atom. The absence of interaction between the ferrocenyl groups and the cationic core is more pronounced in this derivative due to the presence of the nitrogen atoms at intermediate distances which stabilize the central charge without any strong involvement of the terminal metal centers. One single wave integrating for six simultaneous oxidations is thus found when compared to the one-electron reduction process of the central carbocation. This quasi-reversible reduction is clearly linked to the carbocation as the carbinols do not possess this reduction wave. Thus, this compound featuring six equivalent redox-active ferrocenyl groups possesses only three distinct redox states; the monocationic state corresponding to the starting compound, the mono-reduced state, corresponding to the carbon radical and the heptacationic state corresponding to the cation with all ferrocene moieties oxidized (**Scheme 12**). Relative to **E2**⁶⁺, **E1**⁺ possesses limited stability in solution, based on DPV experiments (**Table 9**).



Scheme 12: Oxidation states of **S2(Fc)**⁺

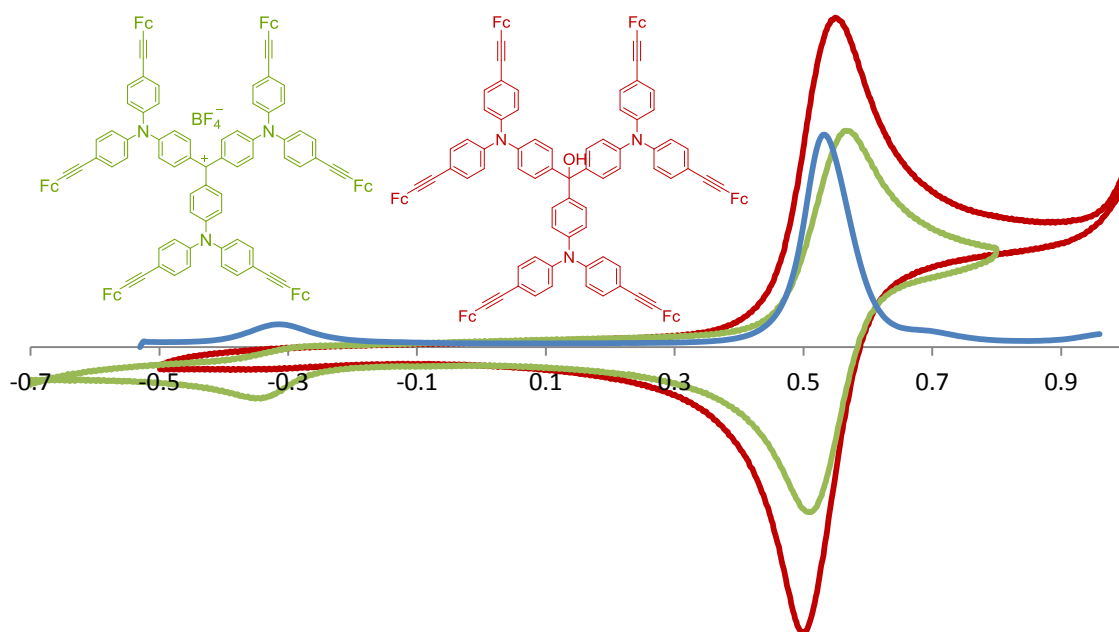


Figure 10: Cyclic voltammetry scans of $\text{S2(Fc)}^{\text{OH}}$ and $[\text{S2(Fc)}]^+[\text{BF}_4]^-$ along with corresponding DPV trace

Complex	$E_{1/2}$	ΔE_p	i_{pc}/i_{pa}	integration
$\text{S2(Fc)}^{\text{OH}}$	0.52	0.05	0.98	-
S1(Fc)^+	0.53	0.05	0.99	6

Table 9: Cyclic voltammetric data for ferrocene derivatives in DCM containing 0.10 M $[n\text{-Bu}_4\text{N}][\text{PF}_6]$ ($E_{1/2}$, $\Delta E_{1/2}$ and ΔE_p given in V vs. SCE)

3.2.3. Conclusion

This electrochemical behavior of S2(Fc)^+ contrasts with that exhibited by the trinuclear ruthenium cation S1(Ru)^+ , for which the three rutheniums strongly interact through the cationic TPM core, leading to the reversible and simultaneous oxidation of two ruthenium centers first followed by a third irreversible oxidation of the third ruthenium (**Figure 9**). Both S1(Ru)^+ and S2(Fc)^+ possess seemingly stable redox states at accessible oxidation potentials which should give different linear optical properties, provided that these multiply-charged species are sufficiently stable in solution. As we shall see in the next (spectroelectrochemical) part, only the first oxidation of these organometallic dyes did actually allow a practical electrochemical access to another stable redox isomer by electrolysis.

3.3. Spectroelectrochemistry

3.3.1. Trimetallic **S1(Ru)**⁺ compound

The spectroelectrochemistry of these organometallic dyes has been investigated to delineate the influence of oxidation on their linear absorptive properties and also to ascertain at which particular wavelength they might exhibit the most pronounced third-order nonlinear optical effects regarding the new absorption maxima in the electronic spectra of their oxidized species.^[30–32]

For the trinuclear ruthenium(II) derivative **S1(Ru)**⁺, only the first (tricationic) oxidized state is chemically accessible at the electrode and could be investigated in the spectroelectrochemical cell. The resulting spectral changes are given in **Figure 11**. Curiously, only small spectral changes accompany this two-electron oxidation: a broadening of the absorption band located in the NIR range, along with a slight weakening in intensity. Overall, these changes recall those observed during the oxidation of the related **MG**⁺ derivatives **M3(Ru)**⁺ and **M4(Ru)**⁺, but far less pronounced. The amino substituents that afford very similar linear absorptions for the carbocationic chromophores in the **M3**⁺ and **M4**⁺ dyes, regardless of the oxidation state of the metallic centre, have been replaced by oxidizable metal centers in **S1(Ru)**⁺; based on the VB scheme previously discussed, only dioxidation of **S1(Ru)**⁺ takes place and leads to a redox isomer possessing a symmetry similar to that of **MG**⁺, and hence to the splitting of the low-energy absorption into two bands, possibly at the origin of the spectral broadening observed. Moreover, for this particular trication (**S1(Ru)**³⁺), it seems that the new LMCT bands formed after oxidation of the two metallic termini overlap with the remaining MLCT band originating from the last Ru(II) endgroup, and thus are less differentiated than in the case of **M3(Ru)**⁺ or **M4(Ru)**⁺. More dramatic changes might have been observed in the case of the tetracation **S1(Ru)**⁴⁺ in which all the metallic endgroups are oxidized, but unfortunately this species is insufficiently stable to be cleanly generated in the OTTE cell.

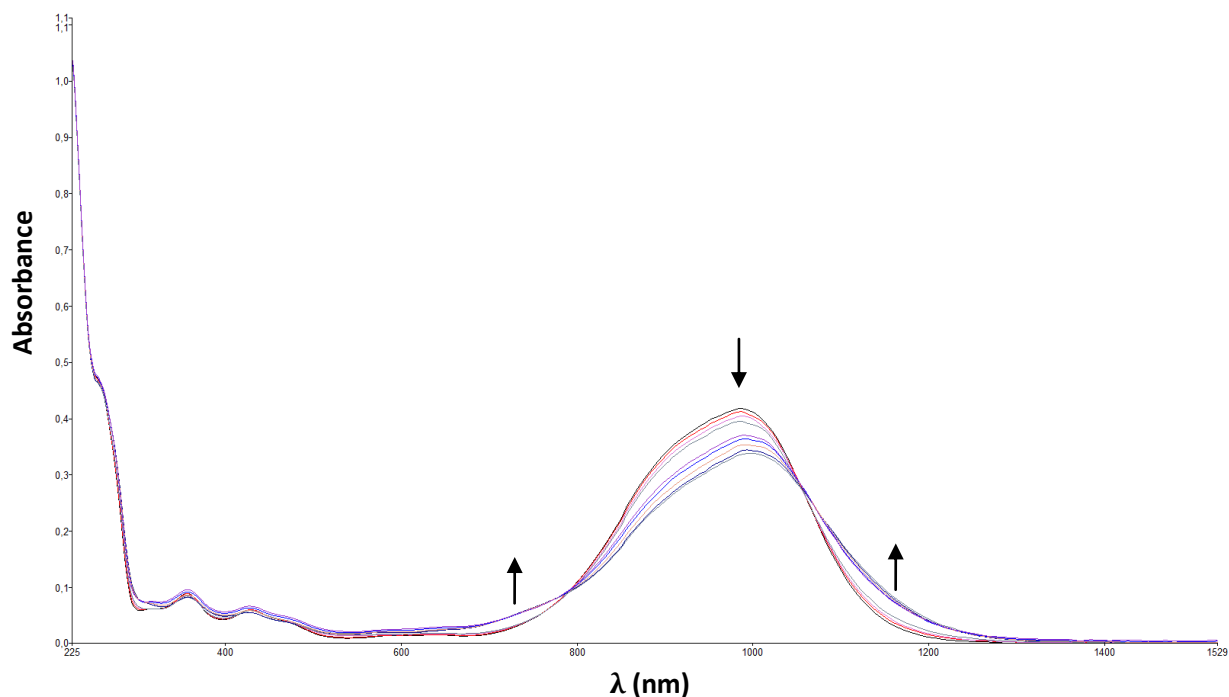


Figure 11: Spectroelectrochemistry of $[S1(Ru)^+][PF_6^-]$

3.3.2. Hexametallic $S2(Fc)^+$ compound

Very weak spectral changes are also seen upon hexa-electronic oxidation of the tris-ferrocene derivative $S2(Fc)^+$ (Figure 9). Because the oxidation was previously demonstrated not to impact the electronic structure of the carbocationic core to an appreciable extent (see section 3.2.2 describing the cyclic voltammetry study) nor to lower the symmetry of this dye (as all ferrocenyl groups are oxidized at the same time), only slight spectral changes were expected. These are consistent with the weak electronic influence of the peripheral ethynylferrocenyl substituents already observed in the linear optical spectrum of $S2(Fc)^+$ relative to that of the organic reference carbocation $O4^+$. Thus the main absorption band undergoes a slight hypsochromic shift of 10 nm (213 cm^{-1}) and new (weak) contributions grow in at ca. 400 and 950 nm. This blue-shift is understandable as oxidation of the ferrocene weakens the donating power of the amine, hence reducing the donor-acceptor character of this CT transition. The latter is very broad and recalls similar bands previously observed during the spectroelectrochemical oxidation of related ethynylferrocene-containing dyes such as $M4(Fc)^+$, although the ferrocenyl groups are interacting more strongly with the carbocationic chromophore in these compounds because they are spatially closer to it.

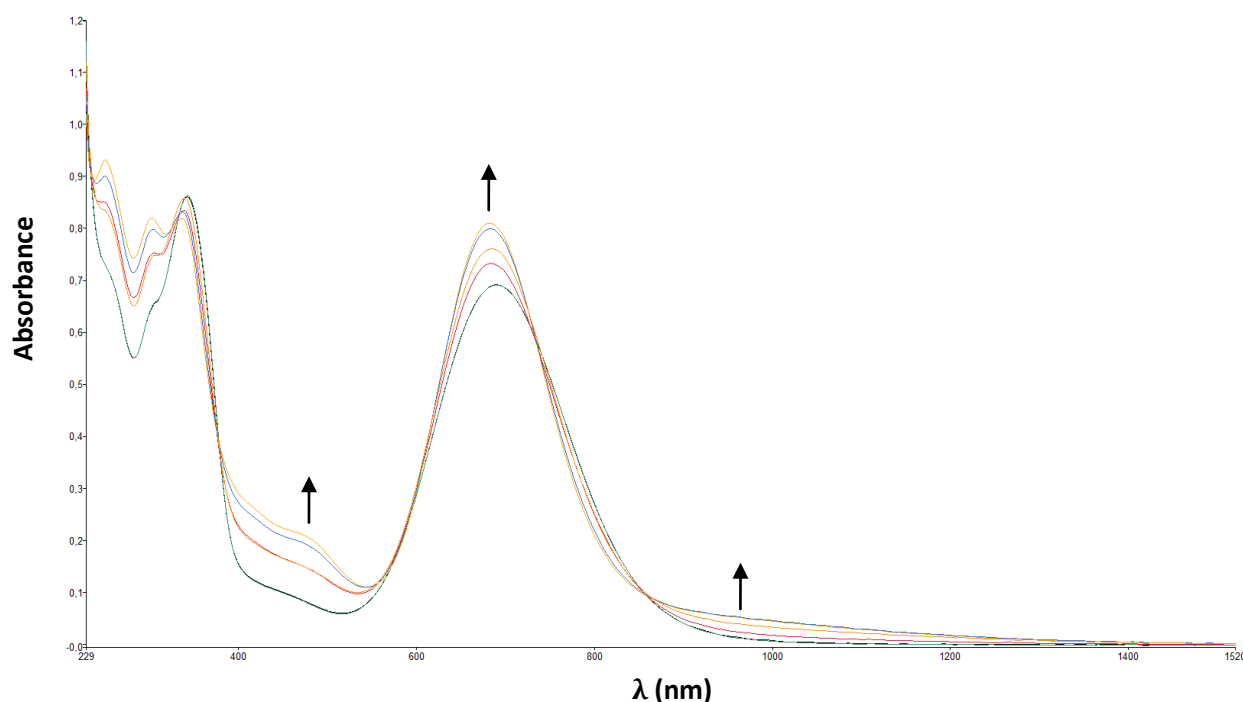


Figure 9: Spectroelectrochemistry of $[S2(Fc)^+][BF_4^-]$

3.3.3. Conclusion

Both star-shaped organometallic dyes $S1(Ru)^+$ and $S2(Fc)^+$ possess similar spectra in their starting (cationic) state and in their first oxidized state. While such a weak linear electrochromism had been anticipated for $S2(Fc)^+$, based on spectroelectrochemical results previously obtained for $M4(Fc)^+$ and on the fact that the ferrocenyl substituents are more remote from the carbocationic center in the extended derivative $S2(Fc)^+$, the weak electrochromism exhibited by $S1(Ru)^+$ was more surprising to us. While several hypotheses have been made to explain this, a deeper understanding of this phenomenon will require a proper assignment of the most intense underlying transitions and of their actual metallic character (*i.e.* MLCT vs. LMCT contribution upon oxidation). This will require TD-DFT calculations to be performed on these derivatives. From the perspective of redox-controlling their third-order NLO properties, the strongest switching effects might be seen for the spectral regions where the largest absorptive changes take place. These are centered either around 750 nm and 1100 nm for $S1(Ru)^+$, and around 500 nm and 900 nm for $S2(Fc)^+$. Overall, based on TPA vs. RSA effects, only moderate changes in their cubic NLO responses are nevertheless anticipated for these TPM dyes upon oxidation.

4. Conclusion

New synthetic routes have been developed to reach the targeted octupolar TPM dyes, with either a small (**S1**⁺) or extended (**S2**⁺) carbocationic core. While several of our targets are unstable in solution, we were nevertheless able to isolate one representative of each kind. Thus the tris-Ru(II) alkynyl derivative **S1(Ru)**⁺ was isolated for the minimal structure **S1**⁺, in which all peripheral amino substituents are replaced by *trans*-[Ru(κ^2 -dppe)₂(Cl)C \equiv C] donor groups, and the hexa-ethynylferrocene derivative **S2(Fc)**⁺ was isolated as a representative structure of **S2**⁺, with an extended core featuring peripheral functionalization of the aminoaryl rings. These two carbocations were extensively characterized and a poor quality crystal structure was determined [**S1(Ru)**⁺][Cl⁻]. In addition, preliminary results also suggest that some of the other targeted organometallic derivatives might be amenable to study after generation *in situ* from the corresponding carbinols. This is the case for the tris-ethynyl ferrocenyl dye [**S1(Fc)**⁺][BF₄⁻], the smaller version of [**S2(Fc)**⁺][BF₄⁻], and the hexa-Ru(II) alkynyl dye [**S2(Ru)**⁺][PF₆⁻], corresponding to the extended version of [**S1(Ru)**⁺][PF₆⁻].

Compared to the corresponding organic analogues, which are Crystal Violet (**CV**⁺) for the shorter derivatives and **O4**⁺ for the larger ones, the introduction of redox-active metal centers led always to the appearance of a new reversible oxidation largely centered on the metal atoms. This opens an opportunity for redox modulation of the optical properties, given that the reduced state (carbon-based radical) of all these dyes is usually not stable at all.

Thus, for the tris-ruthenium(II) alkynyl derivative [**S1(Ru)**⁺][PF₆⁻], cyclic voltammetry reveals a strong electronic interaction in the cationic GS, resulting in a simultaneous and reversible oxidation of two metal centers, the positive charge being probably delocalized on the remaining arm, followed by the quasi-reversible oxidation of the last metallic arm, some 430 mV higher in potential. A very large effect of the metal centers is apparent on the electronic absorption spectrum of this particular carbocation, resulting in a large bathochromic shift of the first allowed transition compared to **CV**⁺, in line with observations made on related organometallic **MG**⁺ derivatives in the previous chapter.

For [**S2(Ru)**⁺][PF₆⁻], the oxidation of all ferrocenyl groups is occurring reversibly at once, in line with a poor conjugation of this metal center with the rest of the system and virtually no metal-metal interactions in the GS. The introduction of metal centers in this carbocation has nevertheless an effect on the energy of the lowest allowed excited state, as revealed by the slight but significant bathochromic shift of its linear absorption band.

To our knowledge $[\mathbf{S1(Ru)^+}][\text{PF}_6^-]$ and $[\mathbf{S2(Ru)^+}][\text{PF}_6^-]$ are the first organometallic derivatives of the TMP dye to be extensively analyzed using these techniques. From this work, one can anticipate a comparatively larger influence from the metal centers in extended derivatives such as $[\mathbf{S1(Ru)^+}][\text{PF}_6^-]$ that could only be partially characterized because of low stability. Such species are certainly worth further studies after being generated *in situ* from their stable carbinol precursors.

As stated for organics, the extension of the π -manifold and also the replacement of electron-releasing substituents by d^6 metal centers lead to bathochromic shifts of the linear absorption at lowest energy. These shifts can be very large as seen for $[\mathbf{S1(Ru)^+}][\text{PF}_6^-]$. The effect on the cubic NLO properties, which should be also important, remains to be probed by Z-scan.

Finally, in relation to the redox switching of these cubic NLO properties, the spectroelectrochemical experiments performed on these derivatives reveal an overall poorer electrochromism upon oxidation than that seen for the organometallic \mathbf{MG}^+ derivatives studied in the previous chapter. Thus, our observations suggest poorly contrasted cubic NLO responses between their cationic resting state and the next oxidized state for these organometallic dyes through much of the visible-NIR region. While largely counter-intuitive with the strong effect on the linear absorption spectra seen upon introduction of the metal centers, which results in a large metallic character for the dominant transitions at low energy, this result requires further investigations. In this respect a precise assignment of the low energy transitions should now be undertaken for each redox state with the help of TD-DFT calculations.

References

- [1] I.-Y. Wu, J. T. Lin, Y. S. Wen, *Organometallics* **1999**, *18*, 320–327.
- [2] F. Paul, C. Lapinte, *Coord. Chem. Rev.* **1998**, *178–180*, 431–509.
- [3] D. Touchard, P. Haquette, S. Guesmi, L. Le Pichon, A. Daridor, L. Toupet, P. H. Dixneuf, *Organometallics* **1997**, *16*, 3640–3648.
- [4] M. A. Fox, J. E. Harris, S. Heider, V. Pérez-Gregorio, M. E. Zakrzewska, J. D. Farmer, D. S. Yufit, J. A. K. Howard, P. J. Low, *J. Organomet. Chem.* **2009**, *694*, 2350–2358.
- [5] J. C. Goeltz, C. P. Kubiak, *Organometallics* **2011**, *30*, 3908–3910.
- [6] H. Plenio, J. Hermann, A. Sehring, *Chem. – Eur. J.* **2000**, *6*, 1820–1829.
- [7] S. Sengupta, S. K. Sadhukhan, *J. Mater. Chem.* **2000**, *10*, 1997–1999.
- [8] S. Sengupta, *Tetrahedron Lett.* **2003**, *44*, 307–310.
- [9] R. Denis, L. Toupet, F. Paul, C. Lapinte, *Organometallics* **2000**, *19*, 4240–4251.
- [10] S. Le Stang, D. Lenz, F. Paul, C. Lapinte, *J. Organomet. Chem.* **1999**, *572*, 189–192.
- [11] S. Le Stang, F. Paul, C. Lapinte, *Inorg. Chim. Acta* **1999**, *291*, 403–425.
- [12] F. de Montigny, G. Argouarch, T. Roisnel, L. Toupet, C. Lapinte, S. C.-F. Lam, C.-H. Tao, V. W.-W. Yam, *Organometallics* **2008**, *27*, 1912–1923.
- [13] S. I. Ghazala, N. Gauthier, F. Paul, L. Toupet, C. Lapinte, *Organometallics* **2007**, *26*, 2308–2317.
- [14] F. Paul, S. Goeb, F. Justaud, G. Argouarch, L. Toupet, R. F. Ziessel, C. Lapinte, *Inorg. Chem.* **2007**, *46*, 9036–9038.
- [15] W. Su, W. Zhong, G. Bian, X. Shi, J. Zhang, *Org. Prep. Proced. Int.* **2004**, *36*, 499–547.
- [16] K. Sonogashira, Y. Tohda, N. Hagihara, *Tetrahedron Lett.* **1975**, *16*, 4467–4470.
- [17] E. Akiyama, S. Nishimura, T. Suzuki, Y. Nagase, *Trans. Mater. Res. Soc. Jpn.* **2012**, *37*, 459–462.
- [18] F. H. Allen, D. G. Watson, L. Brammer, A. G. Orpen, R. Taylor, in *Int. Tables Crystallogr.* (Ed.: E. Prince), International Union of Crystallography, Chester, England, **2006**, pp. 790–811.
- [19] C. Villalonga-Barber, K. Vallianatou, S. Georgakopoulos, B. R. Steele, M. Micha-Screttas, E. Levin, N. Gabriel Lemcoff, *Tetrahedron* **2013**, *69*, 3885–3895.
- [20] C. Villalonga-Barber, B. R. Steele, V. Kovač, M. Micha-Screttas, C. G. Screttas, *J. Organomet. Chem.* **2006**, *691*, 2785–2792.
- [21] O. Plietzsch, A. Schade, A. Hafner, J. Huuskonen, K. Rissanen, M. Nieger, T. Muller, S. Bräse, *Eur. J. Org. Chem.* **2013**, *2013*, 283–299.
- [22] M. I. Bruce, *Chem. Rev.* **1998**, *98*, 2797–2858.
- [23] K. Orito, T. Hatakeyama, M. Takeo, H. Suginome, *Synthesis* **1995**, *1995*, 1273–1277.
- [24] O. P. Varnavski, J. C. Ostrowski, L. Sukhomlinova, R. J. Twieg, G. C. Bazan, T. Goodson, *J. Am. Chem. Soc.* **2002**, *124*, 1736–1743.
- [25] C. Sissa, V. Parthasarathy, D. Drouin-Kucma, M. H. V. Werts, M. Blanchard-Desce, F. Terenziani, *Phys. Chem. Chem. Phys.* **2010**, *12*, 11715–11727.
- [26] P. G. M. Wuts, T. W. Greene, in *Greenes Prot. Groups Org. Synth.*, John Wiley & Sons, Inc., Hoboken, New jersey, **2006**, pp. 16–366.
- [27] G. Koeckelberghs, M. Vangheluwe, I. Picard, L. De Groof, T. Verbiest, A. Persoons, C. Samyn, *Macromolecules* **2004**, *37*, 8530–8537.
- [28] G. J. Perkins, M. I. Bruce, B. W. Skelton, A. H. White, *Inorg. Chim. Acta* **2006**, *359*, 2644–2649.
- [29] N. Gauthier, N. Tchouar, F. Justaud, G. Argouarch, M. P. Cifuentes, L. Toupet, D. Touchard, J.-F. Halet, S. Rigaut, M. G. Humphrey, K. Costuas, F. Paul *Organometallics* **2009**, *28*, 2253–2266.
- [30] G. Grelaud, M. P. Cifuentes, F. Paul, M. G. Humphrey, *J. Organomet. Chem.* **2014**, *751*, 181–200.
- [31] K. A. Green, M. P. Cifuentes, M. Samoc, M. G. Humphrey, *Coord. Chem. Rev.* **2011**, *255*, 2530–2541.
- [32] C. E. Powell, M. P. Cifuentes, J. P. Morrall, R. Stranger, M. G. Humphrey, M. Samoc, B. Luther-Davies, G. A. Heath, *J. Am. Chem. Soc.* **2003**, *125*, 602–610.

General conclusion

General conclusion

Several objectives were defined for the work presented in this thesis: firstly, the preparation of new organic derivatives based on the well-known triphenylmethylium (TPM) dyes **MG⁺** and **CV⁺** in order to confirm their potential as two-photon absorbers; and secondly, the incorporation of redox-active metal centers into these structures in order to enhance their third-order NLO responses and to explore their potential as redox-switchable dyes. The potential of TPM dyes as third-order NLO-phores stems from their architecture: a central carbocation, one of the strongest electron-accepting groups, and peripheral diamino electron-donating groups, in an octupolar or pseudo-octupolar geometry. Moreover, these dyes usually possess intense near-infrared absorptions which should result in two-photon absorptions located in the infrared range, a region interesting for various applications in fields as diverse as medicine or telecommunications.

The first set of organic derivatives is shown in **Chart 1**. The structural modifications at **MG⁺** or **CV⁺** include the extension of the π -manifold with the use of 9-anthracene or 2-fluorene as well as diphenylamino substituents, synthons already known for promoting TPA activity. Rigidification of the system has also been investigated to decrease the non-radiative decay of these chromophores. The series of compounds synthesized possesses the same spectral features as their model compounds, with two main bands for the less symmetric **MG⁺**-based dyes. A bathochromic shift of the characteristic absorptions at low energy is observed. The latter is largely attributable to the extension of the π -system. The rigidified systems **O3⁺** resulted in an even more pronounced shift, the compounds exhibiting absorptions well into the infrared range. Preliminary (open-aperture) Z-scan studies on these compounds have confirmed their potential as two-photon absorbers. Among **MG⁺**-based dyes, the highest two-photon cross-sections being found for molecules combining 2-fluorenyl groups and diphenylamino substituents and among **CV⁺**-based dyes for the octupolar derivative **O4⁺**. Unfortunately, the rigidified fluorenum molecules could not be measured yet and will require further work to evaluate their TPA cross-sections. This study constitutes the first two-photon absorption measurements via Z-scan for a series of triphenylmethane dyes at multiple wavelengths.

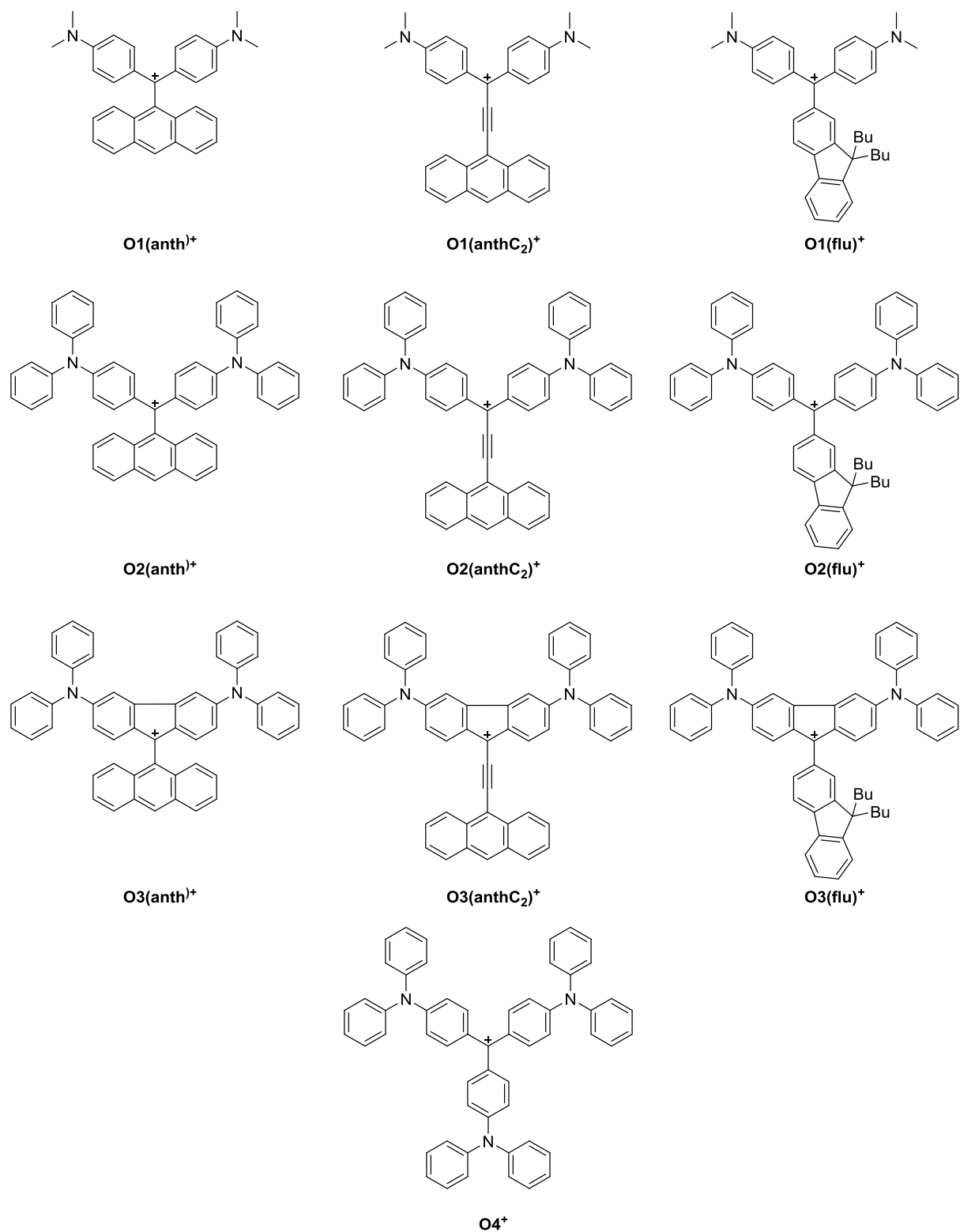


Chart 1: targeted **MG⁺** derivatives

Thanks to these encouraging preliminary results, the organometallic derivatives of **MG⁺** depicted in **Chart 2** were next targeted. These new chromophores feature redox-active endgroups

such as ethynylferrocene, " $\text{Fe}(\eta^5\text{-C}_5\text{Me}_5)(\kappa^2\text{-dppe})\text{-C}\equiv\text{C}-$ " and " $\text{Ru}(\text{Cl})(\kappa^2\text{-dppe})_2\text{-C}\equiv\text{C}-$ " appended at the *para*-position of the phenyl ring, or directly appended to the carbocationic site. The synthesis of these derivatives has revealed some unexpected synthetic difficulties induced by their high reactivity. Thus, some of the targeted " $\text{Fe}(\eta^5\text{-C}_5\text{Me}_5)(\kappa^2\text{-dppe})\text{-C}\equiv\text{C}-$ " alkynyl derivatives could not be obtained. Nonetheless, the new bis-alkynyl species **M5(Ru)₂⁺** (**Chart 2**) was isolated and structurally characterized, along with **M1(M)⁺** (M = Fc, Fe, Ru). The electronic and redox properties of these new compounds were next investigated. Two distinct types of behavior were observed, depending on the organic end-groups. In the case of the ethynylferrocene derivatives, the electronic communication with the carbocationic core is rather weak, and their electronic spectrum is only slightly modified relative to organic reference compounds. In the case of metal alkynyl derivatives, a much larger interaction takes place resulting in a significant cumulenenic character in the GS. In their electronic spectra, large bathochromic shifts also take place for the low-lying transitions, likely originating from their increased MLCT character. Third-order nonlinearities have not been measured yet for these organometallic derivatives, but from the results obtained with the organic derivatives **O2(Flu)⁺** and **O4⁺**, non-negligible two-photon absorption is expected in the NIR range, given that the particular redox-active end-groups present in these dyes are usually known to enhance the third-order NLO properties relative to all-organic derivatives of comparable size and structure.

Evaluation of the redox behavior of these organometallic dyes further confirms the stronger metal-carbocation interaction operative in the metal-alkynyl derivatives, resulting in a significant shift of the metal-centered oxidation potential to higher values and in a corresponding shift of the carbocation reduction potential to lower values. Only the reversible metal-centered redox processes were suitable for electrochemical switching. Spectroelectrochemical investigations were next performed to investigate the linear absorptions of the first oxidized states for each compound. Overall, only minor changes were seen for the ethynylferrocene derivatives, consistent with the weak interaction between the metal center and the carbocationic core previously evidenced. For alkynyl derivatives, the spectral changes between the two redox states are more noticeable, although no dramatic change takes place. While moderate-to-weak bands (believed to correspond to LMCT or d-d bands) appear in the NIR range upon oxidation, the most important bands are only poorly affected. Thus, while a large nonlinear electrochromism cannot be anticipated in the visible range for most of these organometallic dyes, the NIR range is possibly the best spectral range for observing such a behavior with the metal-alkynyl derivatives **M1-M5**.

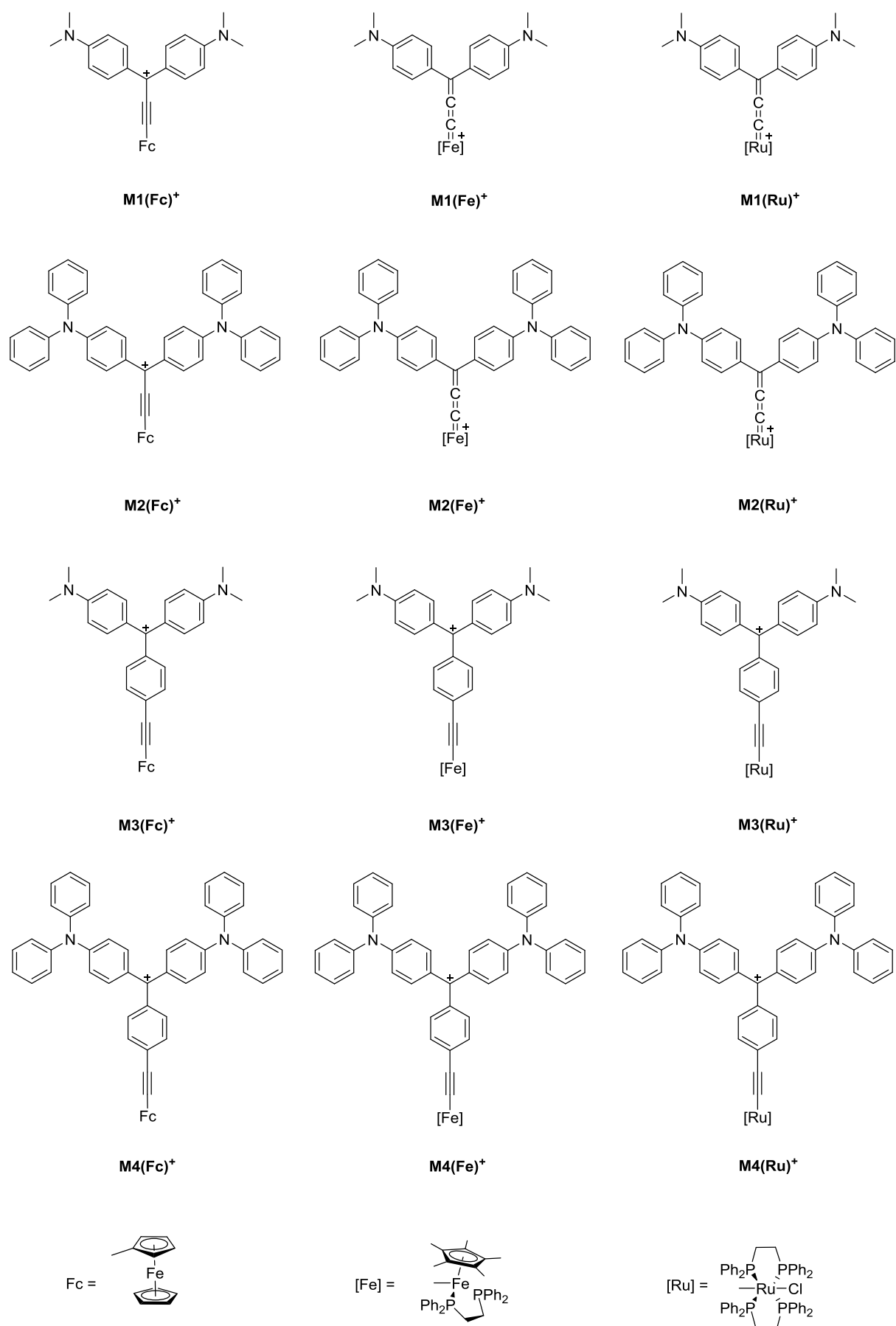


Chart 2: Targeted organometallic derivatives of **MG⁺** salts

Along similar lines, the four octupolar organometallic derivatives of **CV**⁺, **S1(Fc)**⁺-**S2(Ru)**⁺ (**Chart 3**), have been targeted. The kinetic stability of the derivatives **S1(Fc)**⁺ and **S2(Ru)**⁺ was problematic for their full characterization and only **S1(Ru)**⁺ and **S2(Fc)**⁺ could be extensively characterized. These derivatives were investigated by UV-vis spectroscopy, cyclic voltammetry and spectroelectrochemistry. The influence of the organometallic end-group in the extended ethynylferrocenyl derivative **S2(Fc)**⁺ is again weakly felt by the rest of the system and the linear absorptions of this compound are very similar to those of its organic equivalent **O4**⁺. In contrast, the influence of the organometallic end-groups for the shorter ruthenium(II) derivative **S1(Ru)**⁺ is comparatively much more important; the transitions at lowest-energy of **O4**⁺ are shifted deep into the NIR range (near *ca.* 988 nm); the Ru-based redox processes are split into two distinct processes corresponding to the chemically reversible and simultaneous oxidation of two out of three ruthenium centers, followed by the quasi-reversible oxidation of the last metallic center. Again, and unexpectedly in the case of **S1(Ru)**⁺, spectroelectrochemistry reveals that the electrochromism of these new dyes when proceeding to their first oxidized state is rather weak, auguring for weakly contrasted cubic NLO responses. However, the two-photon absorption cross-sections for these octupolar polymetallic dyes in their carbocationic state might be quite important in the NIR and will shortly be measured by Z-scan, as well as their other third-order NLO properties.

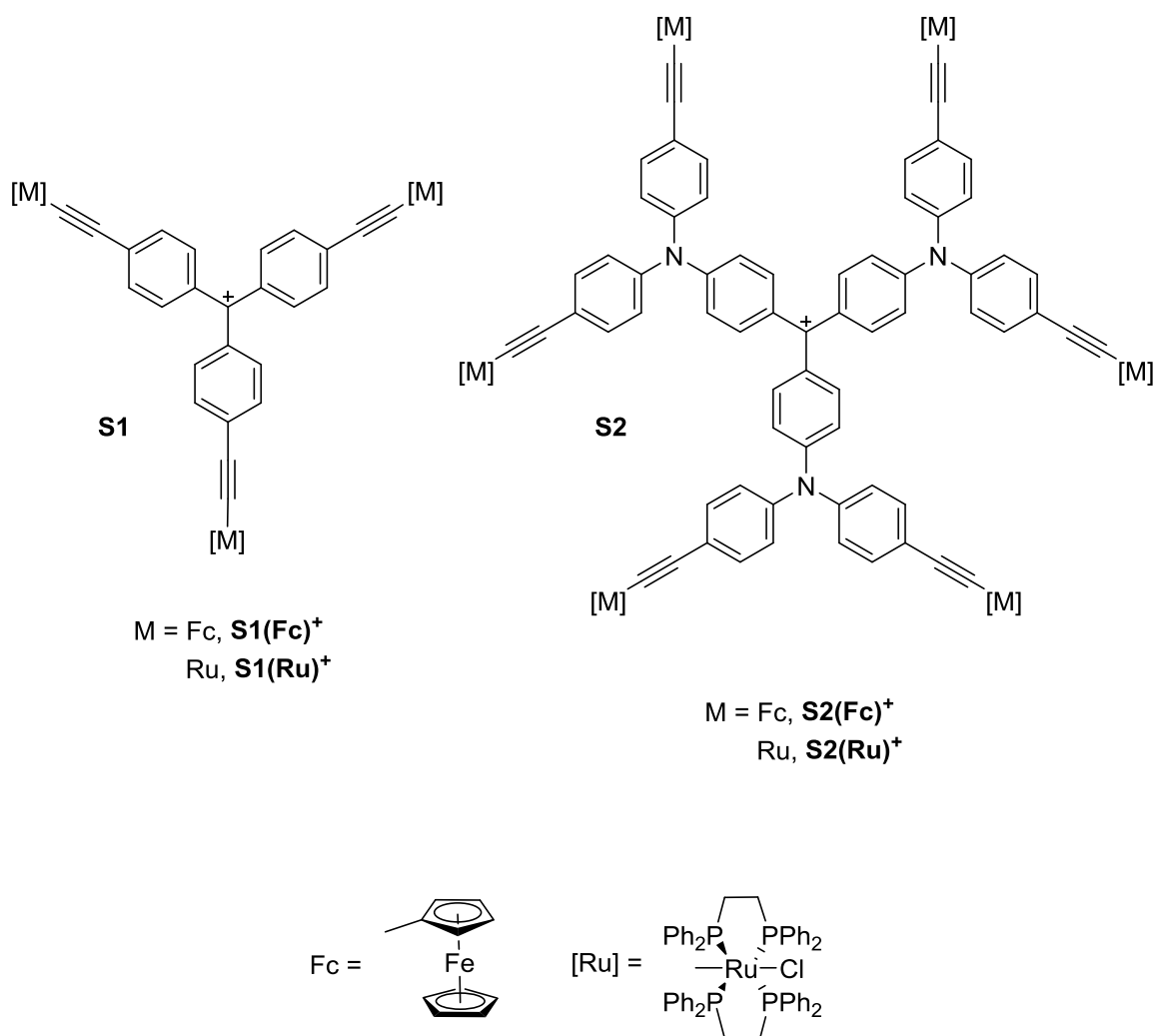


Chart 3: Targeted organometallic derivatives based on CV^+

In conclusion, while purely organic triphenylmethane dyes have confirmed their potential as two-photon absorbing materials, a further enhancement of this property is more than probable thanks to the addition of suitable metal centers. Accordingly, the cubic NLO properties of the redox-active organometallic dyes will now be investigated by Z-scan and, hopefully, a significant nonlinear electrochromism will be evidenced for some of these derivatives in the NIR range. Finally, further attempts at better characterizing $[\text{S1}(\text{Fc})^+][\text{BF}_4^-]$ and $[\text{S2}(\text{Ru})^+][\text{PF}_6^-]$ should be made, as well as isolation of the organoiron analogues of $[\text{M1}(\text{Ru})^+ - \text{M4}(\text{Ru})^+][\text{PF}_6^-]$ and $[\text{S1}(\text{Ru})^+][\text{PF}_6^-]$.

Experimental

Experimental

Contents

1. Instrumentation	200
1.1. Nuclear magnetic resonance spectroscopy.....	200
1.2. Infrared, near infrared and UV-visible spectroscopy	200
1.3. Spectroelectrochemistry	200
1.4. Cyclic voltammetry	201
1.5. Mass spectrometry and elemental analyses.....	201
2. Equipment	201
2.1. Glassware	201
2.2. Temperature control and stirring.....	202
2.3. Chromatography.....	202
3. Chemicals	202
3.1. Solvents	202
3.2. Inert gases	203
3.3. Reagents	203
4. General procedures	204
5. Synthesis of organic derivatives	206
5.1. Organic carbinols.....	206
5.2. Organic carbocations.....	225
6. Synthesis of organometallic derivatives	254
6.1. Ferrocene carbinols.....	254
6.2. Ferrocene carbocations.....	262
6.3. Organometallic precursors.....	270
7. Organometallic derivatives of CV⁺	313
7.1. S1 -type derivatives	313
7.2. S2 -type derivatives	322
8. Z-scan traces	344
References	348

1. Instrumentation

1.1. Nuclear magnetic resonance spectroscopy

Samples were dissolved in CDCl_3 , CD_2Cl_2 or acetone- d_6 , as indicated, filtered, and placed in 5 mm class sample tubes. Spectra were recorded at 298 K.

^1H NMR spectra were acquired on a Bruker Avance I 300 (300 MHz), Varian Gemini-300 FT NMR (300 MHz), a Varian MR-400 FT, Bruker Avance 400-HD or a Chemical 800 MHz Bruker FTNMR spectrometer. Shifts are given in ppm relative to residual non-deuterated solvent signal (CHCl_3 : δ 7.26 ppm, DCM: δ 5.32 ppm, acetone: δ 2.05 ppm).^[1]

^{13}C NMR spectra were acquired on a Bruker DPX200 (50 MHz) or Varian Gemini-300 FT NMR (75 MHz), Bruker Avance I 300 (75 MHz), Varian Inova-500 (125 MHz) or Chemical 800 MHz Bruker FTNMR with total proton decoupling. Chemical shifts are given in ppm relative to residual deuterated solvent signal (CHCl_3 : δ 77.2 ppm, DCM: 53.84, δ acetone: δ 29.8 ppm).^[1]

^{31}P NMR spectra were acquired on a Bruker DPX200 (81 MHz), Bruker Avance I 300 (121 MHz), Varian Gemini-300 (121 MHz) or Bruker Avance-400 HD FTNMR with total proton decoupling and are referenced to external 85% H_3PO_4 (0.0 ppm).

1.2. Infrared, near infrared and UV-Visible spectroscopy

Infrared spectra were obtained as KBr pellets (1 % w/w in 100 – 200 mg of dry spectroscopy grade KBr, pressed under vacuum with a static pressure of 10 tons in a stainless steel pelletizer) with a Bruker IFS28 FT-IR. Near-IR and UV-visible spectra were recorded as DCM solutions using a 1 cm path length quartz cell on a Cary 5 double beam spectrophotometer or a Perkin-Elmer Lambda 950 UV-VIS-NIR spectrophotometer.

1.3. Spectroelectrochemistry

Solution UV-visible / near-IR spectra of the oxidized species were obtained at 298 K or 248 K by electrogeneration on a platinum mesh electrode in a custom 0.05 mm optically transparent thin-layer electrochemical (OTTLE) cell, using a silver wire as pseudo-reference and a platinum wire as counter-electrode. Solutions were made up with 0.30 M $[\text{n-Bu}_4\text{N}][\text{PF}_6]$ in dry and deoxygenated DCM and kept under an atmosphere of pure argon.

1.4. Cyclic voltammetry

Cyclic voltammograms were recorded at 25°C in DCM solutions (containing 0.10 M [n-Bu₄N][PF₆], purged with argon and maintained under inert atmosphere) at 100 mV/s scan rate using an EG&G-PAR model 263 potentiostat / galvanostat (using a Pt disk as working electrode, a Pt wire as counter-electrode and the reference electrode was a saturated calomel electrode) or an e-corder 401 potentiostat system from eDAQ Pty Ltd (using a Pt disk as working electrode, a Pt wire as counter-electrode and the reference electrode was an Ag / AgCl electrode). The FcH / FcH⁺ couple was used as an internal calibrant for the potential measurements (0.46 V vs SCE, 0.56 V vs Ag / AgCl, $\Delta E_p = 0.09$ V; $i_{pa}/i_{pc} = 1$).^[2]

1.5. Mass spectrometry and elemental analyses

Electrospray ionization (ESI) mass spectra were recorded at the Research School of Chemistry, Australian National University, using a LCT-ZMD single quadrupole liquid chromatograph-MS (Waters-Micromass) and high resolution ESI mass spectra were carried out utilizing a LCT Premier XE ESI-TOF instrument (Waters-Micromass), or at the "Centre Régional de Mesures Physiques de l'Ouest", Université de Rennes 1, on a ZAB Spec Q-TOF (Micromass, high resolution), double quadrupole micro TOF-Q 2 (Bruker) and Q-ToF 2 (Waters). All mass spectrometry peaks are reported as m/z. Elemental analyses were performed on an EA1112 (Thermo Finnigan) at "Centre Régional de Mesures Physiques de l'Ouest", Université de Rennes 1 or at London Metropolitan University.

2. Equipment

2.1. Glassware

All glassware (including NMR tubes) was oven-dried or flame-dried, cooled under high-vacuum and conditioned under argon prior to use. Single use polyethylene syringes were conditioned under argon before use. Sintered glass funnels used for filtration were of Buchner type whereas Hirsch type funnels were used for the collection of solids. Both types were fitted with porosities adapted to the compound. A water-jet or diaphragm pump was used as the vacuum source.

2.2. Temperature control and stirring

Unless otherwise indicated, the temperature refers to the temperature of the external heating or cooling bath. Reactions performed above room temperature ($\approx 20^{\circ}\text{C}$) were thermostated ($\pm 1^{\circ}\text{C}$) and heated with stirring in a silicone oil bath. Cooling of reaction mixtures below room temperature was achieved by immersing the reaction flasks into the following cold baths contained in Dewar flasks: melting ice (0°C), acetone/solid CO_2 (-78°C), ethanol/liquid N_2 (-90°C). The temperature of the cold bath was monitored using low temperature alcohol thermometers. Reaction mixtures were magnetically stirred with Teflon coated stir bars, at a rate of 250 – 500 rpm and above (as indicated by “vigorous stirring” and during purification by precipitation).

2.3. Chromatography

Flash column chromatography^[3] was performed using silica (Merck kieselgel 60 or Scharlau 60, 230 – 400 mesh) wet-packed in glass columns of various sizes depending on the quantity of product to purify. Deactivated silica refers to silica previously treated with an equal volume of appropriate eluent (v/v) and 10 % triethylamine packed in the column. The column was then eluted with 1 % triethylamine (v/v) in the eluent or without, depending of the sensitivity of the compound to be purified. Silica columns were performed using a slight over-pressure of air. Thin-layer chromatography was performed using silica. Preparative thin-layer chromatography were carried out on glass plates (20 x 20 cm) coated with silica (Merck 60 GF254, 0.5 mm thick). Unless otherwise stated, R_f values were measured on silica plates visualized using a UV lamp (254 nm, 365 nm for fluorescent compounds) or chemical stains (vanillin or acidic solution) if necessary.

3. Chemicals

3.1. Solvents

All solvents for synthesis (and work-up in the case of air sensitive compounds) were freshly distilled and sparged with inert gas by for at least 15 min before use. Solvents for column chromatography and normal work-up were of technical grade and used as received. Deuterated solvents were used as received but sparged with argon before use for air-sensitive complexes and filtered through dry basic alumina. Solvents were dried and distilled under inert an atmosphere using the following dehydrating agents: $-\text{Et}_2\text{O}$, *n*-pentane, *n*-hexane and reagent grade THF:

sodium/benzophenone - toluene: sodium -DCM: dried over P_2O_5 , distilled over K_2CO_3 or dried and distilled over CaH_2 -MeOH: Mg/I_2 - diisopropylamine and triethylamine: KOH- DMSO: dried and stored over activated 4 Å molecular sieves.^[4]

3.2. Inert gases

All reactions and also workup procedures for air-sensitive compounds were carried out under an atmosphere of dry, high purity argon or nitrogen, using standard Schlenk techniques.^[5] In all cases, an overpressure of inert gas (0.5 bar) was permanently kept in the system during work-up and reaction period involving sensitive compounds. Air-sensitive samples and distilled solvents were stored under positive pressures of inert gases in appropriate flasks.

3.3. Reagents

The following compounds were prepared as described in the literature:

- $PdCl_2(PPh_3)_2$ ^[6]
- 4,4'-diphenylaminobenzophenone (**29**)^[7]
- 9-(2,2-dibromovinyl)anthracene^[8]
- 9-ethynylantracene (**32**)^[9]
- 2-bromo-9,9-dibutyl-9-fluorene (**33**)^[10]
- 1-bromo-4-ferrocenylethynylbenzene (**36**)^[11]
- 4-bromotriphenylamine^[12]
- $(\eta^5-C_5Me_5)(\kappa_2-dppe)FeCl$ (**46**)^[13]
- *cis*-(κ^2 -dppe)Ru(Cl)₂ and *cis*-[(κ^2 -dppe)Ru(Cl)][PF₆] (**45**)^[14]
- tris(*p*-iodophenyl)amine (**60**)^[15]

Modifications to the literature procedures were applied to the preparation of the following compounds, as described here or in their respective experimental procedures:

- 3,6-bis(diphenylamino)-9H-fluoren-9-one (**30**)^[16–19] (the final Buchwald-Hartwig reaction was carried with *in situ* formation of the catalyst Pd(P^tBu₃)₂ from Pd₂dba₃, ^tBu₃PHBF₄ and DiPA; the rest of the reagents were then added in solution)
- acetylferrocene (**34**) and ethynylferrocene (**35**)^[20] (the initial deprotonation was carried out at 0°C rather than -78°C and the suspension of the enolate anion was stirred for 1h at 0°C before electrophilic quenching at 78°C)
- tris(4-((trimethylsilyl)ethynyl)phenyl)methanol (**54**) and tris(4-ethynylphenyl) methanol (**55**)^[21] (the initial reaction was performed with a lithiate equivalent instead of a Grignard reagent)
- ^tBuOK (by solvent extraction with THF)^[22]
- lithium diisopropylamide solutions were prepared from n-BuLi (1.10 equivalent) and diisopropylamine (1.20 equivalent) in THF (1.0 mL per mmol of DiPA at 0 °C)^[23]
- zinc dust was freed of oxides by an HCl wash^[24]
- copper bronze was freed of oxide by iodine solution and HCl washes^[7]
- water present in CBr₄ as stabilizer was removed by stirring over anhydrous MgSO₄ as a DCM solution followed by removal of the solvent by rotary evaporation and drying under high vacuum.

All other chemicals were obtained from commercial sources and used as received after having checked their purity by various analytical methods (TLC, NMR). If necessary, but this was case specific, purification of the needed compound or reagent was performed according to the procedures reported by Armarego and Chai.^[25]

4. General procedures

General procedure for metal/halogen exchange followed by addition of the desired ketone (GP1)

Reaction: In a Schlenk flask under argon, *n*-BuLi was added drop wise to a solution of the desired halogenated or alkynyl compound in dried and distilled THF at -78°C. After stirring for 30 min, the ketone solution in dried and distilled THF was added drop wise to the solution. The cold bath was then removed and the mixture was stirred and allowed to warm to room temperature over 3 h.

Work-up: 20 mL of water were added to the flask and the two phases were separated. The aqueous layer was extracted with Et₂O (3 x 20 mL) and the combined organic phases were washed with water (10 mL) and saturated aqueous NaCl (10 mL). The aqueous phase was then back-extracted with Et₂O (20 mL). The organic phase was dried over Na₂SO₄ and the solvents were removed to give the crude product as a solid.

General procedure for formation of 9-ethynylanthracene lithiate followed by addition on desired ketone (GP2)

Reaction: In a Schlenk flask under argon, *n*-BuLi was added drop wise to a solution of 9-ethynylanthracene in distilled and deoxygenated THF (15 mL) at 0°C. After stirring for 30 min, the ketone in distilled and deoxygenated THF (15 mL) was added drop wise to the solution. The cold bath was then removed and the mixture was stirred and allowed to warm up to room temperature for 3 h.

Work-up: 20 mL of water were added to the flask and the two phases were separated. The aqueous layer was extracted with Et₂O (3 x 20 mL) and the combined organics phases were washed with water (10 mL) and saturated aqueous NaCl (10 mL). The aqueous phase was then back extracted with Et₂O (20 mL). The organic phases were dried over Na₂SO₄ and the solvent was removed to give the expected product as a powdery solid.

General procedure for organic and ethynyl ferrocene carbocations (BF₄ salts) (GP3)

Reaction: In a Schlenk flask under argon, HBF₄·Et₂O was added drop wise to a solution of carbinol in distilled and deoxygenated Et₂O at room temperature. After stirring for 2 h, the precipitate was filtered by cannula.

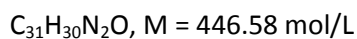
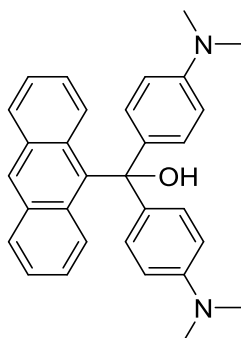
Work-up: The precipitate was washed with distilled and deoxygenated Et₂O (3 x 10 mL) and dried in vacuum. The solid was then dissolved in a minimum of distilled and deoxygenated DCM and precipitated with distilled and deoxygenated Et₂O and washed with distilled pentane. After filtration and drying in *vacuo* the expected compound was obtained as a dark powder.

NB: some of the carbinols are slightly soluble in Et₂O, and hence precipitations were carried out at lower temperatures. (-40 °C or -78 °C)

5. Synthesis of organic derivatives

5.1. Organic carbinols

9-anthracenyl-bis(4-(dimethylamino)phenyl)methanol ($O1(\text{anth})^{\text{OH}}$)



Reagents: 9-bromoanthracene **31** (1.1 eq, 282 mg, 1.1 mmol), Michler's ketone **28** (1 eq, 268 mg, 1 mmol), *n*-BuLi (1.1 eq, 400 μL at 2.5 M in hexane, 1.1 mmol).

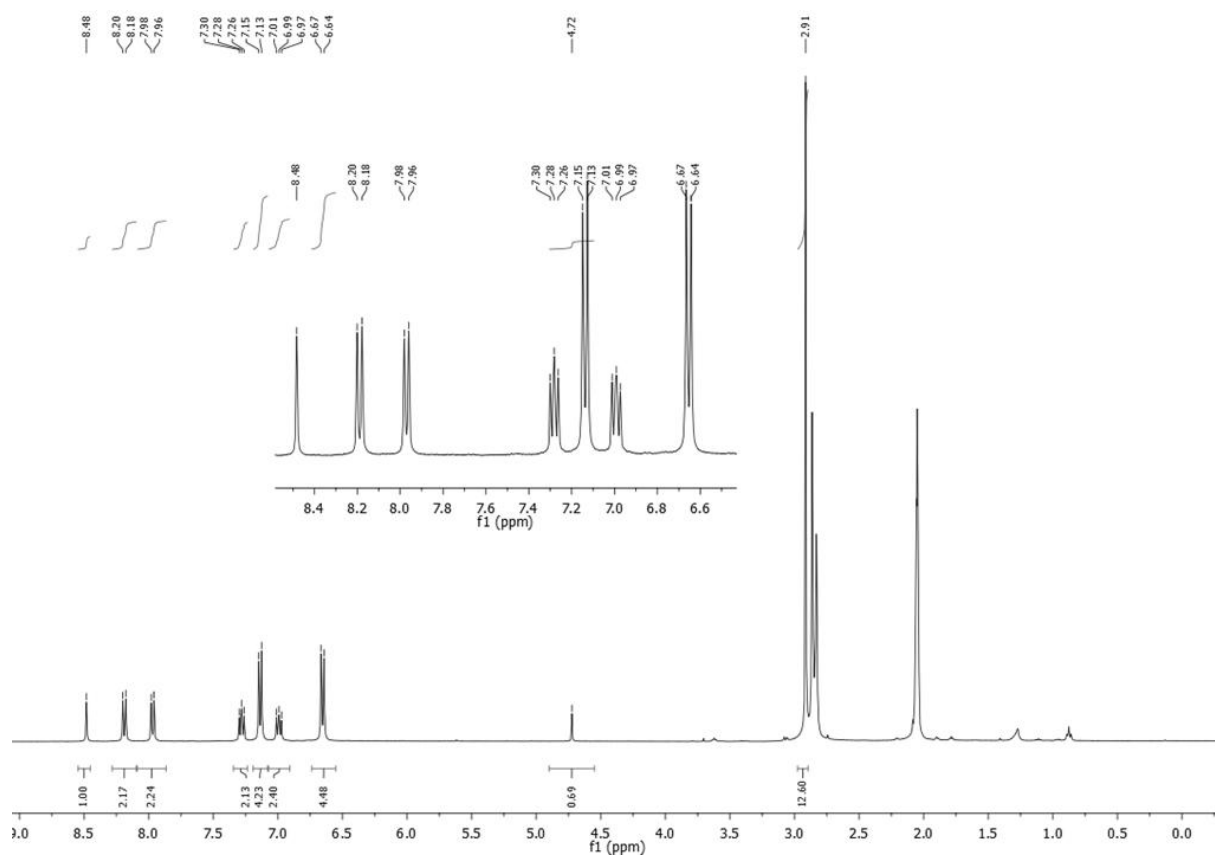
Reaction and work up: Prepared according to **GP1**.

Purification: The crude yellow solid was adsorbed on deactivated silica and purified by column chromatography (neutralized silica gel with 10 % NEt_3 , 15 x 5 cm) eluting with hexane/ Et_2O (2/1) with 1 % NEt_3 to give 9-anthracenylbis(4-(dimethylamino)phenyl)methanol as a white solid which decomposed over time (~2 days).

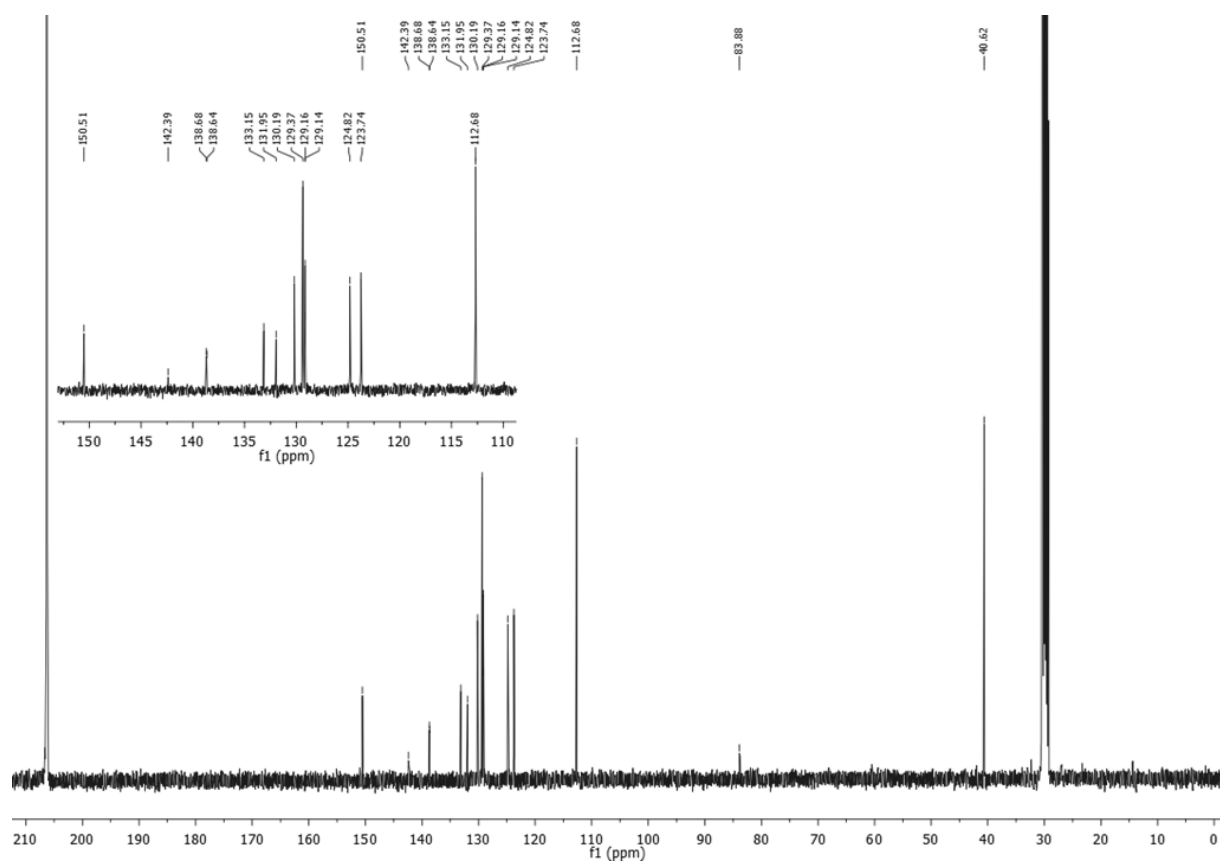
R_f (hexane/ Et_2O , 2/1): 0.43

Yield: 260 mg (58 %)

^1H NMR (400 MHz, $(\text{CD}_3)_2\text{CO}$) δ 8.48 (s, 1H), 8.19 (d, $J = 9.3$ Hz, 2H), 7.97 (d, $J = 8.5$ Hz, 2H), 7.28 (m, 2H), 7.14 (d, $J = 9.1$ Hz, 4H), 6.99 (m, 2H), 6.65 (d, $J = 9.0$ Hz, 4H), 4.72 (s, 1H, -OH), 2.91 (s, 12H, - NMe_2).



¹³C NMR (101 MHz, (CD₃)₂CO) δ 150.51, 142.39, 138.68, 138.64, 133.15, 131.95, 130.19, 129.37, 129.16, 129.14, 124.82, 123.74, 112.68, 83.88 (C-OH), 40.62 (-NMe₂).

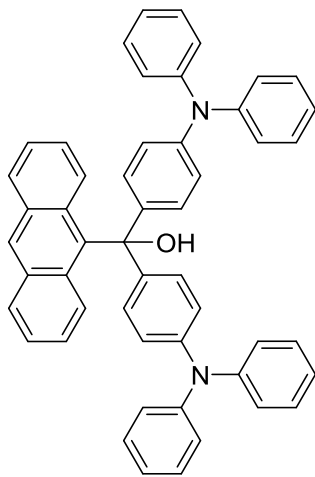


HRMS (ESI): calcd.: 447.2438[M⁺·OH]⁺, 429.2331 M⁺. ; found: 447.2436 [M⁺·OH]⁺, 429.332 M⁺.

IR (cm⁻¹): 3446 (ν_{OH}).

UV-Vis (DCM): λ_{max}, nm (ε, 10⁻⁵·M⁻¹·cm⁻¹): 262 (0.32).

9-anthracenyl-bis(4-(diphenylamino)phenyl)methanol (O2(anth)^{OH})



C₅₁H₃₈N₂O, M = 694.86 g/mol

Reagents: 9-bromoanthracene **31** (1.1 eq, 282 mg, 1.1 mmol), 4, 4'- diphenylaminobenzophenone **29** (1 eq, 516 mg, 1 mmol), *n*-BuLi (1.1 eq, 400 μL at 2.5 M in hexane, 1.1 mmol).

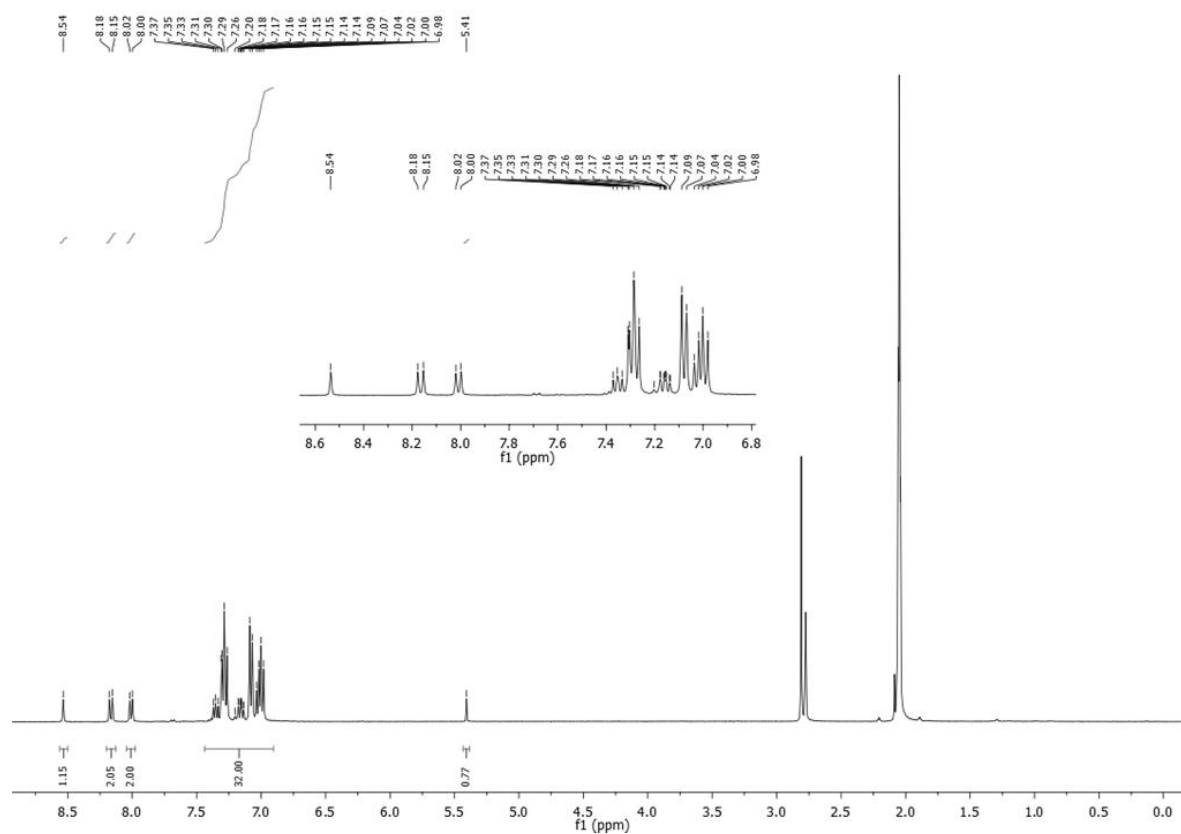
Reaction and work up: Prepared according to **GP1**.

Purification: The crude yellow solid was adsorbed on deactivated silica and purified by column chromatography (neutralized silica gel with 10 % NEt₃, 15 x 5 cm) eluting with hexane/Et₂O (4/1) with 1 % NEt₃ to give 9-anthracenyl-bis(4-(diphenylamino)phenyl)methanol as a yellow solid which decomposed over time (~2 days). The compound was precipitated from acetone/MeOH.

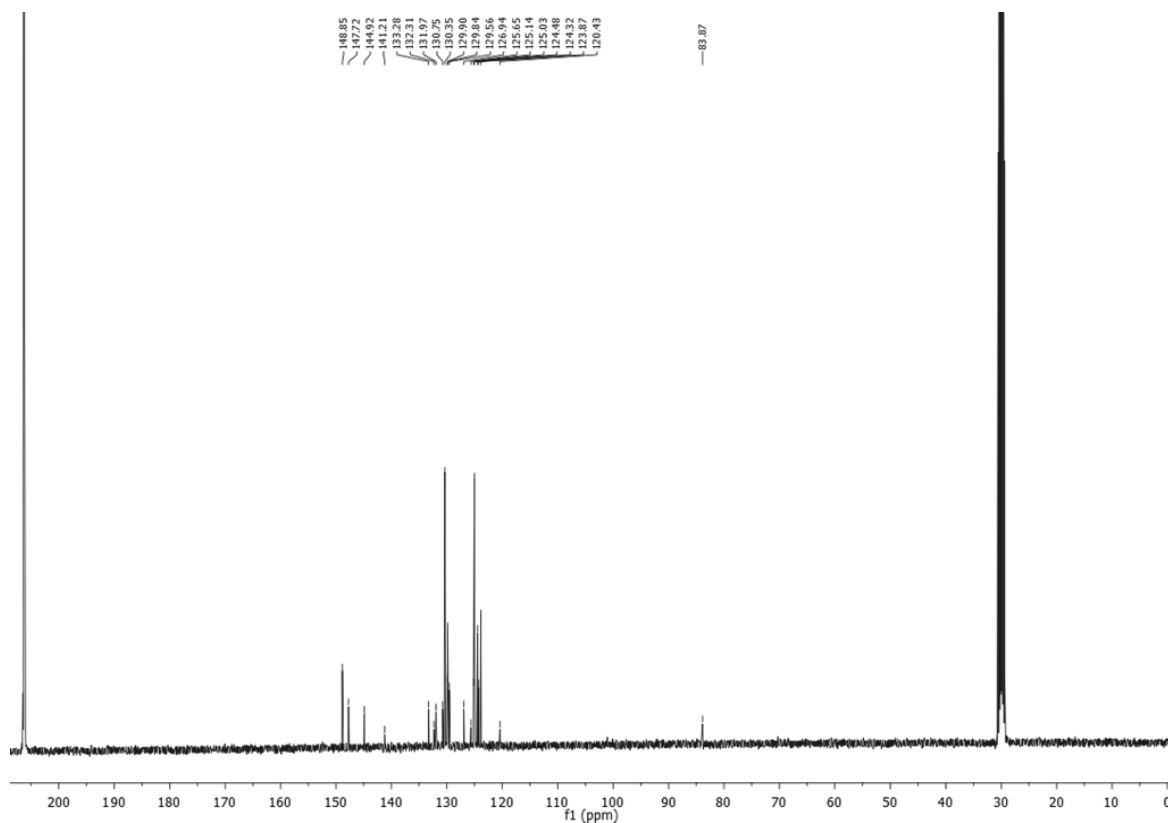
R_f (hexane/Et₂O, 4/1): 0.5

Yield: 560 mg (81%).

¹H NMR (400 MHz, (CD₃)₂CO) δ 8.53 (s, 1H), 8.16 (d, *J* = 9.3 Hz, 2H), 8.01 (d, *J* = 8.5 Hz, 2H), 7.43 – 6.93 (m, 32H), 5.41 (s, 1H, -OH).



¹³C NMR (101 MHz, (CD₃)₂CO) δ 148.85, 147.72, 144.92, 141.21, 133.28, 132.31, 131.97, 130.75, 130.35, 129.90, 129.84, 129.56, 126.94, 125.65, 125.14, 125.03, 124.48, 124.32, 123.87, 120.43, 83.87 (C-OH).

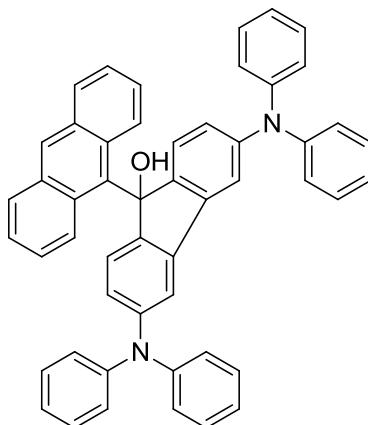


HRMS (ESI): 693.29004 $[M-H]^+$, 694.29786 M^+ , 677.29512 $[M^{\cdot-}\cdot OH]^+$; found 693.2893 $[M-H]^+$, 694.2967 M^+ , 677.2950 $[M^{\cdot-}\cdot OH]^+$.

IR (cm^{-1}): 3530 (ν_{OH}).

UV-Vis (DCM): λ_{max} , nm (ϵ , $10^{-5} \cdot M^{-1} \cdot \text{cm}^{-1}$): 260 (0.50), 304 (0.32).

9-(9-anthracenyl)-3,6-bis(diphenylamino)-9H-fluoren-9-ol (O3(anth)^{OH})



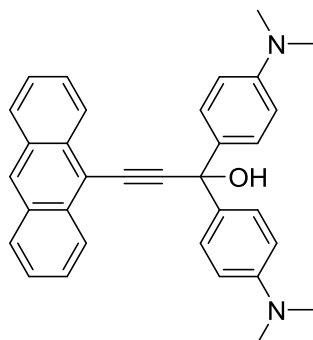
$C_{51}H_{36}N_2O$, $M = 692.84 \text{ g/mol}$

Reagents: 9-bromoanthracene **31** (1.1 eq, 282 mg, 1.1 mmol), 3,6-bis(diphenylamino)-9H-fluoren-9-one **30** (1 eq, 514 mg, 1 mmol), *n*-BuLi (1.1 eq, 400 μL at 2.5 M in hexane, 1.1 mmol).

Reaction and work up: Prepared according to **GP1**.

Purification: Not isolated (not stable in solution or in solid state, crude material was directly used to next step)

3-(9-anthracenyl)-1,1-bis(4-(dimethylamino)phenyl)prop-2-yn-1-ol (O1(anthC₂)^{OH})



$C_{33}H_{30}N_2O$, $M = 470.60 \text{ g/mol}$

Reagents: 9-ethynylantracene **32** (1.1 eq, 222.5 mg, 1.1 mmol), Michler's ketone **28** (1 eq, 268.35 mg, 1 mmol), *n*-BuLi (1.1 eq, 687 μ L at 1.6 M in hexane, 1.1 mmol)

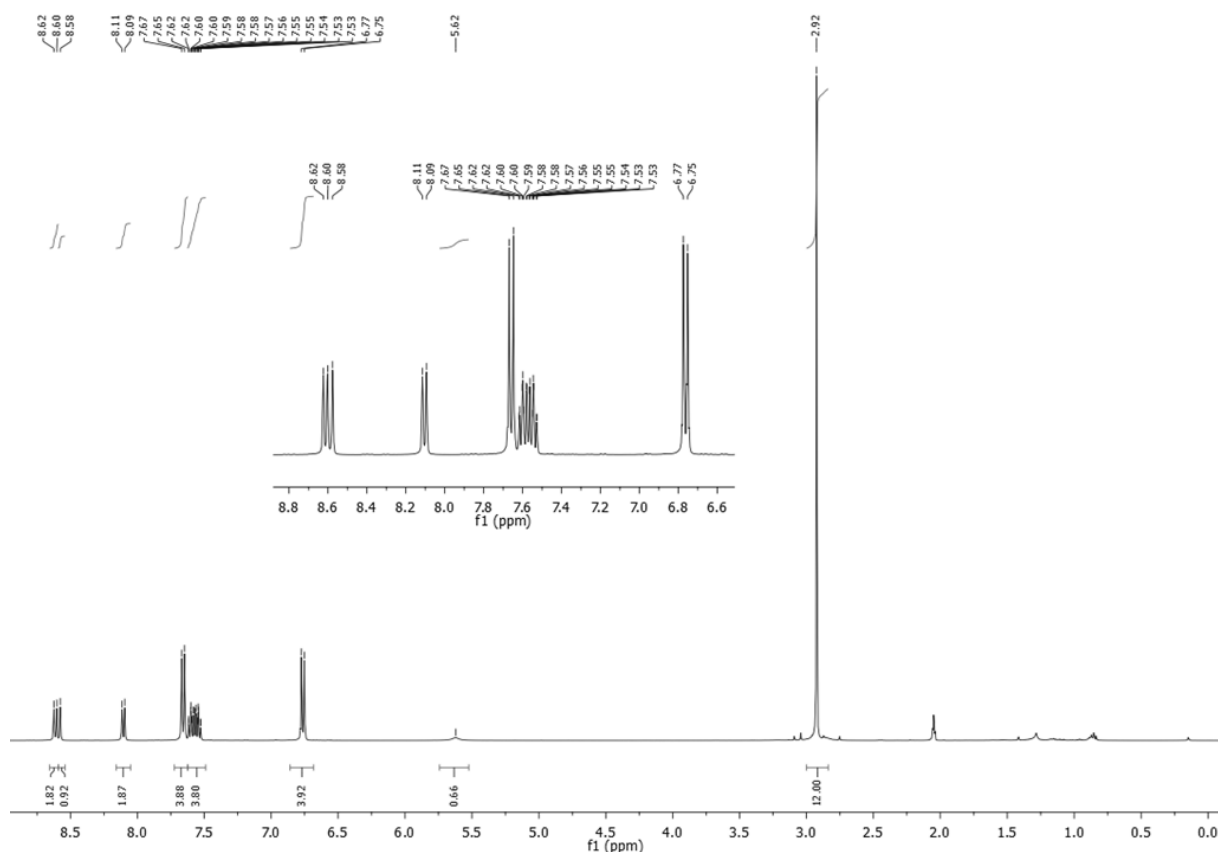
Reaction and work up: Prepared according to **GP2**.

Purification: The crude brown solid was adsorbed on deactivated silica and purified by column chromatography (neutralized silica gel with 10 % NEt₃, 15 x 5 cm) eluting with hexane/Et₂O (1/1) with 1 % NEt₃ to give 3-(9-anthracenyl)-1,1-bis(4-(dimethylamino)phenyl)prop-2-yn-1-ol as a yellow solid.

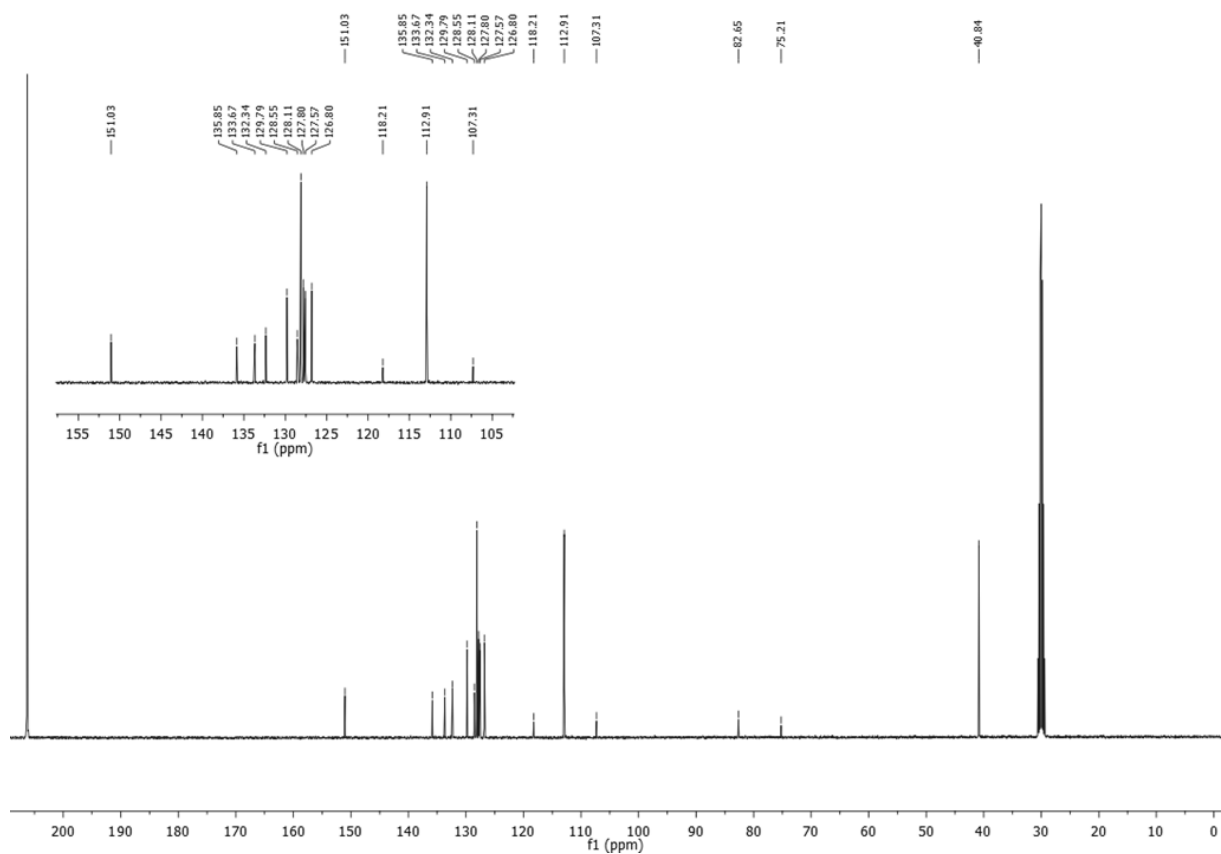
Rf (hexane/Et₂O, 1/1): 0.14

Yield: 450 mg (95 %)

¹H NMR (400 MHz, (CD₃)₂CO) δ 8.61 (d, *J* = 8.7 Hz, 2H), 8.58 (s, 1H), 8.10 (d, *J* = 8.3 Hz, 2H), 7.66 (d, *J* = 8.9 Hz, 4H), 7.57 (m, 4H), 6.76 (d, *J* = 8.9 Hz, 4H), 5.62 (s, 1H, -OH), 2.92 (s, 12H, -NMe₂).



¹³C NMR (101 MHz, (CD₃)₂CO) δ 151.03, 135.85, 133.67, 132.34, 129.79, 128.55, 128.11, 127.80, 127.57, 126.80, 118.21, 112.91, 107.31 (C-OH), 82.65, 75.21, 40.84 (-NMe₂).

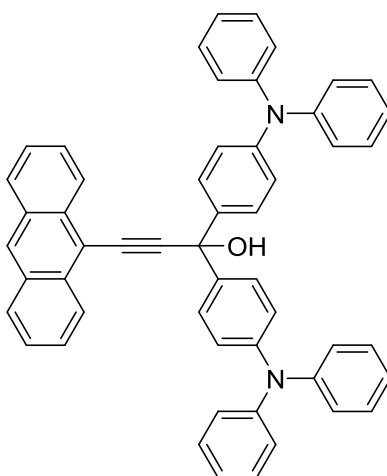


HRMS (ESI): calcd.: 471.2436 $[M-H]^+$, 453.2331 $[M\cdot OH]^+$; found: 471.2437 $[M-H]^+$, 453.2332 $[M\cdot OH]^+$.

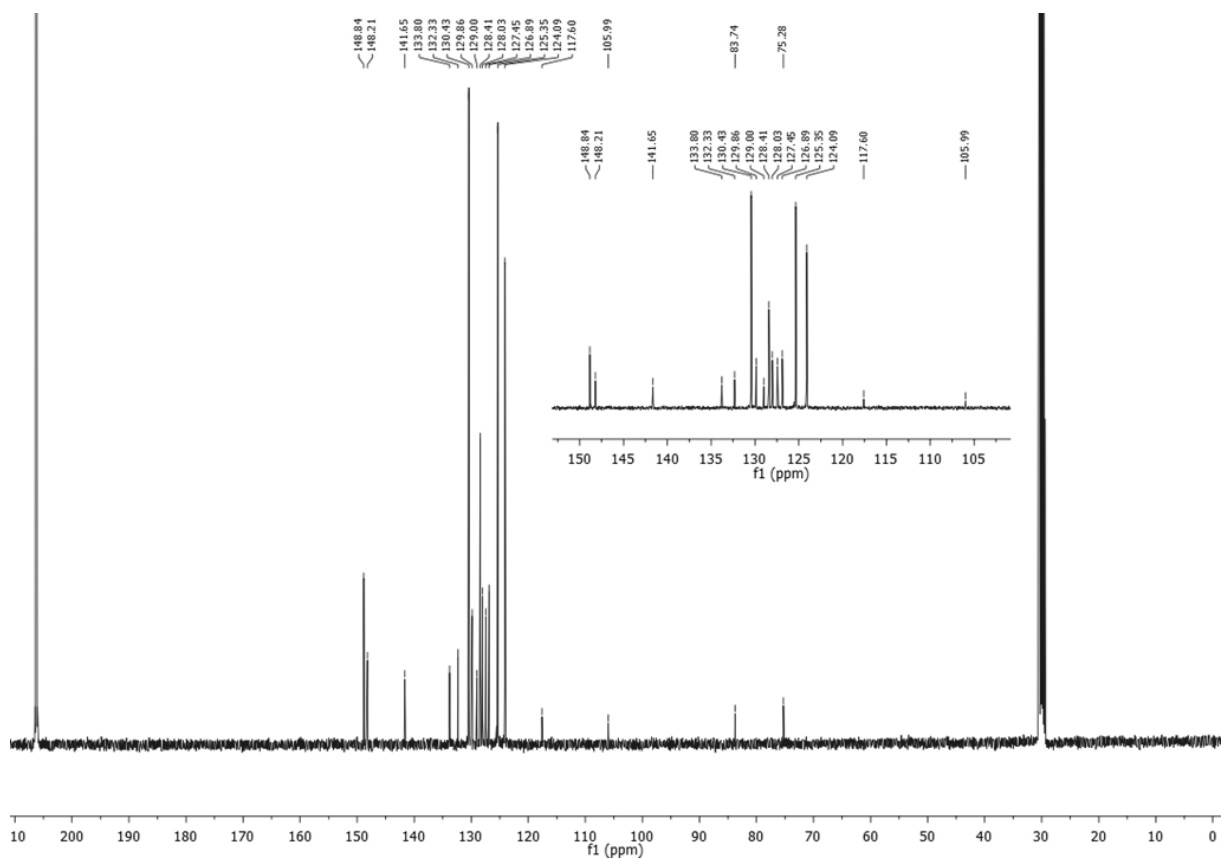
IR (KBr, cm^{-1}): 3046 (ν_{OH}).

UV-Vis (DCM): λ_{max} , nm (ϵ , $10^{-5} \cdot \text{M}^{-1} \cdot \text{cm}^{-1}$): 262 (1.50), 386 (0.19), 412 (0.13).

3-(9-anthracenyl)-1,1-bis(4-(diphenylamino)phenyl)prop-2-yn-1-ol (O2(anthC₂)^{OH})



$\text{C}_{53}\text{H}_{38}\text{N}_2\text{O}$, $M = 718.88 \text{ g/mol}$

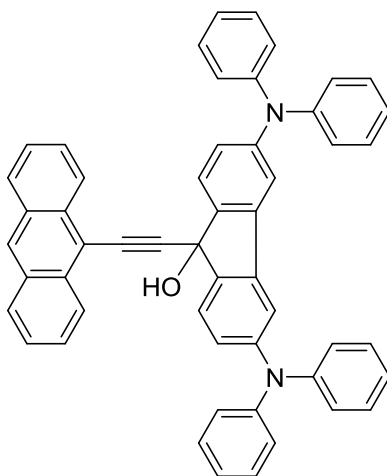


HRMS (ESI): calcd.: 741.28763 $[M+Na]^+$, 757.26157 $[M+K]^+$; found: 741.2870 $[M+Na]^+$, 757.2609 $[M+K]^+$.

IR (KBr, cm^{-1}): 3421 (ν_{OH}).

UV-Vis (DCM): λ_{max} , nm (ϵ , $10^{-5} \cdot \text{M}^{-1} \cdot \text{cm}^{-1}$): 262 (1.80), 304 (0.62), 386 (0.24), 408 (0.24).

9-(9-ethynylantracenyl)-3,6-bis(diphenylamino)-9H-fluoren-9-ol (O3(anthC₂)^{OH})



$\text{C}_{53}\text{H}_{36}\text{N}_2\text{O}$, $M = 716.87 \text{ g/mol}$

Reagents: 9-ethynylantracene **32** (1.1 eq, 222.5 mg, 1.1 mmol), 3,6-bis(diphenylamino)-9H-fluoren-9-one **30** (1 eq, 514 mg, 1 mmol), *n*-BuLi (1.1 eq, 687 μ L at 1.6 M in hexane, 1.1 mmol).

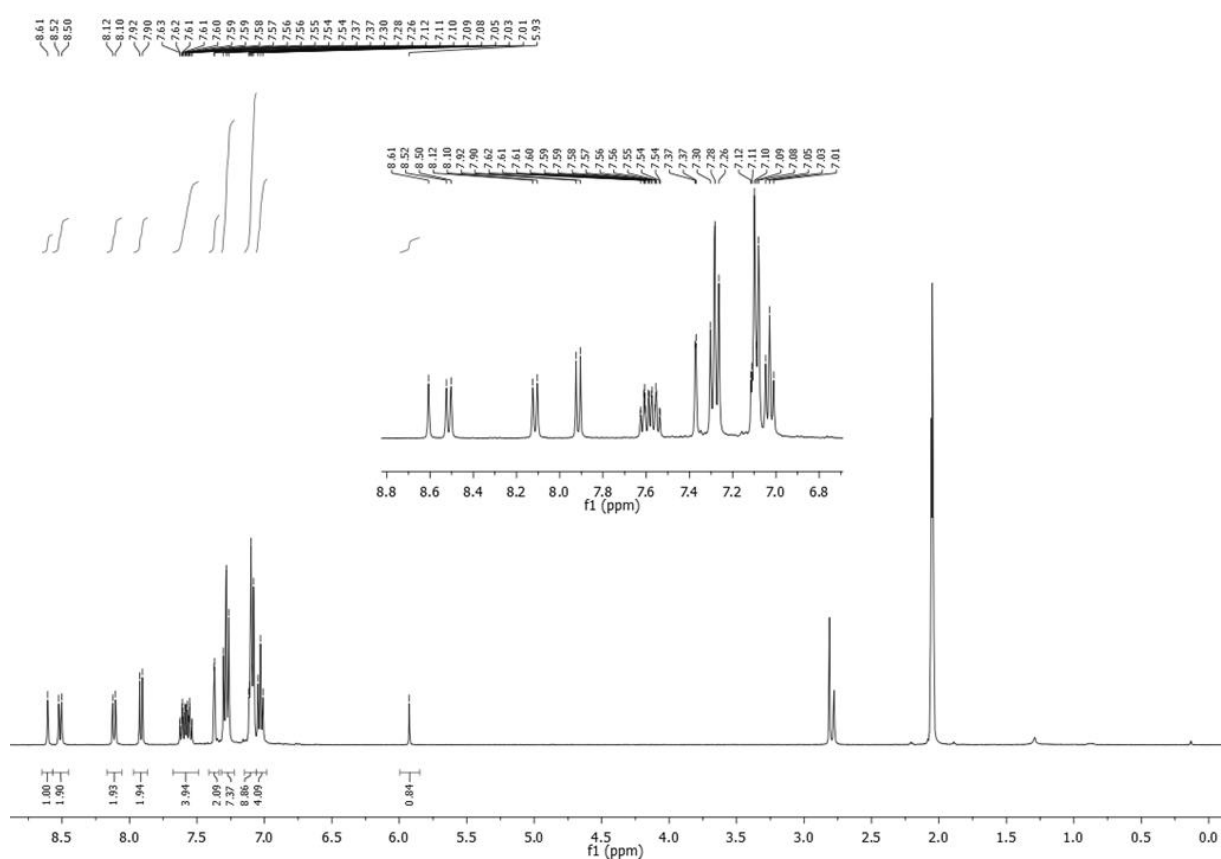
Reaction and work up: Prepared according to **GP2**.

Purification: The crude brown solid was adsorbed on deactivated silica and purified by column chromatography (neutralized silica gel with 10 % NEt_3 , 15 x 5 cm) eluting with a gradient of hexane/ Et_2O from 19/1 to 4/1 with 1 % NEt_3 to give 9-(9-ethynylantraceny)-3,6-bis(diphenylamino)-9H-fluoren-9-ol as an orange solid. The product was precipitated from acetone/MeOH.

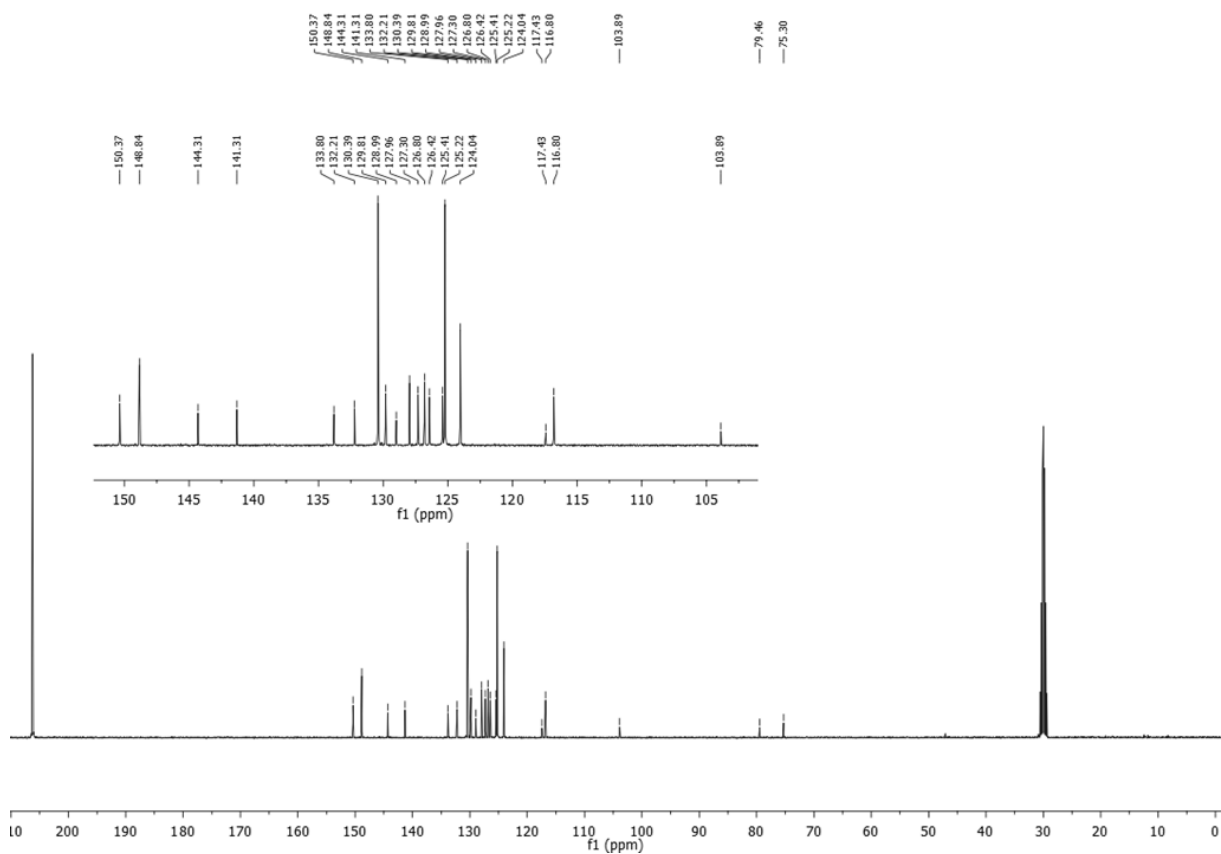
R_f (hexane/ Et_2O , 4/1): 0.2

Yield: 700 mg (96 %)

^1H NMR (400 MHz, $(\text{CD}_3)_2\text{CO}$) δ 8.60 (s, 1H), 8.51 (d, $J = 8.5$ Hz, 2H), 8.11 (d, $J = 8.3$ Hz, 2H), 7.92 (d, $J = 8.2$ Hz, 2H), 7.58 (dt, $J = 14.2, 6.8$ Hz, 4H), 7.37 (d, $J = 1.8$ Hz, 2H), 7.28 (t, $J = 7.8$ Hz, 8H), 7.10 (m, 8H), 7.03 (t, $J = 7.3$ Hz, 4H), 5.93 (s, 1H, -OH).



^{13}C NMR (101 MHz, $(\text{CD}_3)_2\text{CO}$) δ 150.36, 148.84, 144.30, 141.30, 133.79, 132.20, 130.38, 129.80, 128.98, 127.95, 127.30, 126.80, 126.41, 125.40, 125.21, 124.03, 117.42, 116.79, 103.87 (C-OH), 79.44, 75.28.

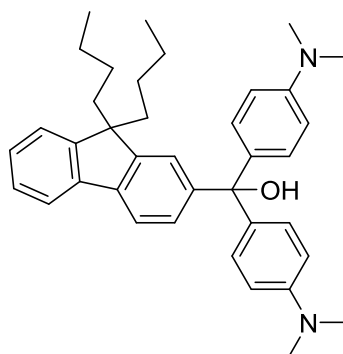


HRMS (ESI): calcd.: 741.28763 $[M+Na]^+$, 757.26157 $[M+K]^+$; found: 741.2870 $[M+Na]^+$, 757.2609 $[M+K]^+$.

IR (cm^{-1}): 3447 (ν_{OH}).

UV-Vis (DCM): λ_{max} , nm (ϵ , $10^{-5} \cdot \text{M}^{-1} \cdot \text{cm}^{-1}$): 262 (1.47), 299 (0.43), 392 (0.19), 415 (0.16).

(9,9-dibutyl-9H-fluoren-2-yl)bis(4-(dimethylamino)phenyl)methanol (O1(Flu)^{OH})



$\text{C}_{38}\text{H}_{46}\text{N}_2\text{O}$, $M = 546.78 \text{ g/mol}$

Reagents: 2-bromo-9,9-dibutyl-9H-fluorene **33** (1.2 eq, 857.6 mg, 2.4 mmol), Michler's ketone **28** (1 eq, 536.7 mg, 2 mmol), *n*-BuLi (1.1 eq, 1.375 mL at 1.6 M in hexane, 2.2 mmol).

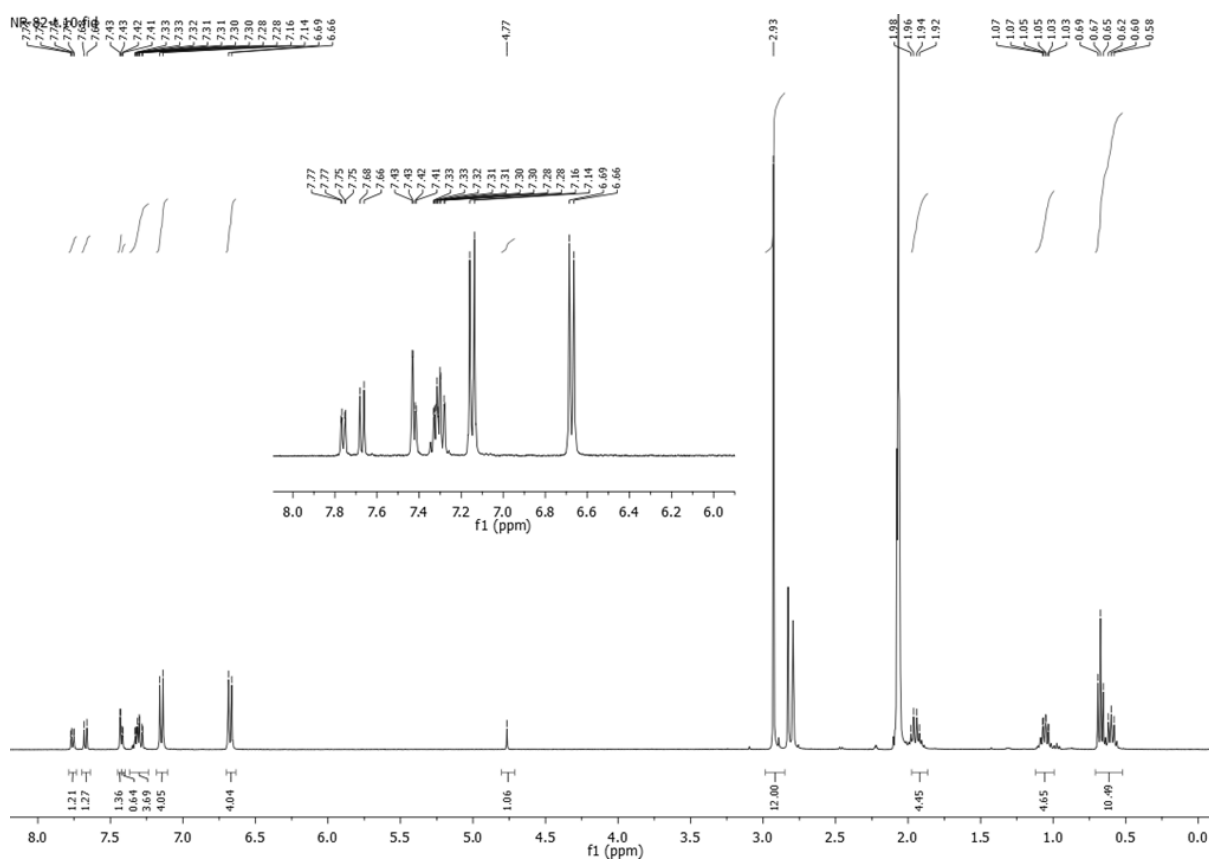
Reaction and work up: Prepared according to **GP1**.

Purification: The crude brown solid was adsorbed on deactivated silica and purified by column chromatography (neutralized silica gel with 10 % NEt₃, 20 x 5 cm) eluting with hexane/Et₂O (1/1) with 1 % NEt₃ to give (9,9-dibutyl-9H-fluoren-2-yl)bis(4-(dimethylamino)phenyl)methanol as a white solid.

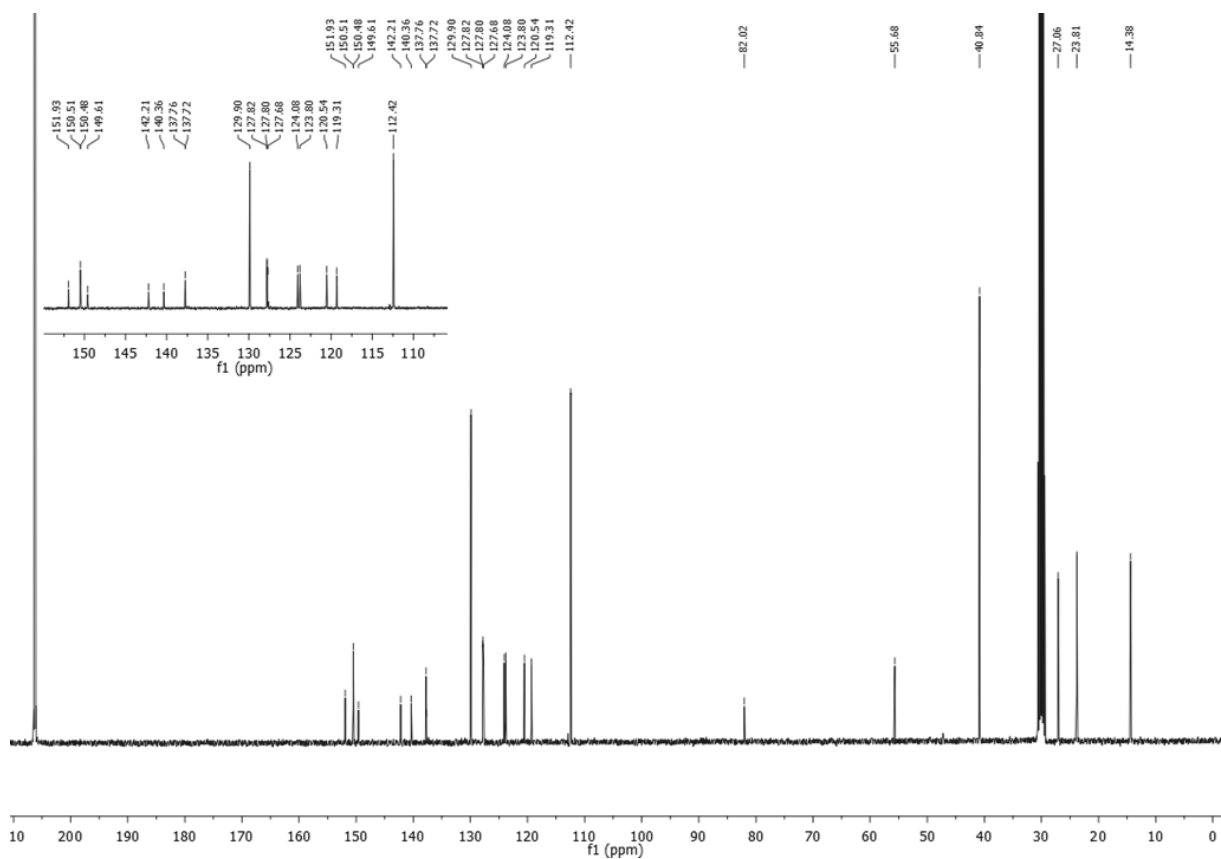
R_f (hexane/Et₂O, 1/1): 0.29

Yield: 1.05 g (96 %)

¹H NMR (400 MHz, (CD₃)₂CO) δ 7.74 (dd, *J* = 6.2, 1.9 Hz, 1H), 7.65 (d, *J* = 7.9 Hz, 1H), 7.41 (dd, *J* = 9.1, 1.5 Hz, 2H), 7.35 – 7.23 (m, 3H), 7.14 (d, *J* = 8.9 Hz, 4H), 6.66 (d, *J* = 8.9 Hz, 4H), 4.74 (s, 1H, OH), 2.91 (s, 12H, -NMe₂), 2.01 – 1.84 (m, 4H), 1.12 – 0.99 (m, 4H), 0.71 – 0.50 (m, 10H).



¹³C NMR (101 MHz, (CD₃)₂CO) δ 151.93, 150.51, 149.61, 142.21, 140.36, 137.76, 137.72, 129.90, 127.82, 127.80, 127.68, 124.08, 123.80, 120.54, 119.31, 112.42, 82.02 (C-OH), 55.68, 40.84 (-NMe₂), 27.06, 23.81, 14.38.

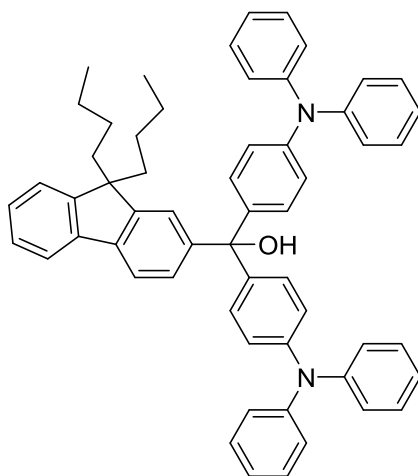


HRMS (ESI): calcd.: 547.36884 $[M+H]^+$, 529.35827 $[M-\cdot OH]^+$; found: 547.3685 $[M+H]^+$, 529.3586 $[M-\cdot OH]^+$.

IR (cm^{-1}): 3455 (ν_{OH}).

UV-Vis (DCM): λ_{max} , nm (ϵ , $10^{-5} \cdot \text{M}^{-1} \cdot \text{cm}^{-1}$): 272 (0.58), 309 (0.26).

(9,9-dibutyl-9H-fluoren-2-yl)bis(4-(diphenylamino)phenyl)methanol (O2(Flu)^{OH})



$\text{C}_{58}\text{H}_{54}\text{N}_2\text{O}$, $M = 795.06 \text{ g/mol}$

Reagents: 2-bromo-9,9-dibutyl-9H-fluorene **33** (1.2 eq, 428.8 mg, 1.2 mmol), 4,4'-diphenylaminobenzophenone **29** (1 eq, 516 mg, 1 mmol), *n*-BuLi (1.1 eq, 687 μ L at 1.6 M in hexane, 1.1 mmol).

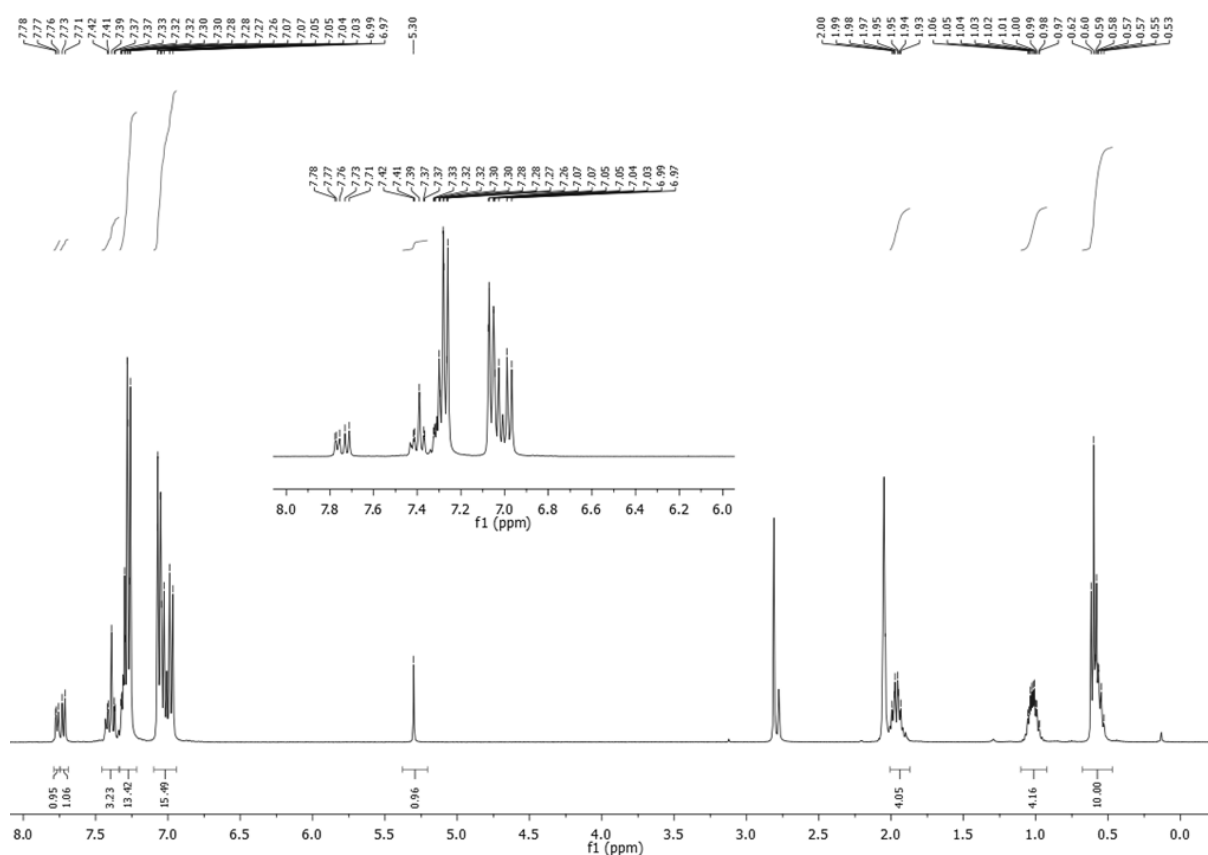
Reaction and work up: Prepared according to **GP1**.

Purification: The crude brown solid was adsorbed on deactivated silica and purified by column chromatography (neutralized silica gel with 10 % NEt₃, 15 x 5 cm) eluting with a gradient of hexane/Et₂O from 2/1 to 1/1 with 1 % NEt₃ to give (9,9-dibutyl-9H-fluoren-2-yl)bis(4-(diphenylamino)phenyl)methanol **O2(Flu)**^{OH} as a white solid. The product was precipitated from acetone/MeOH.

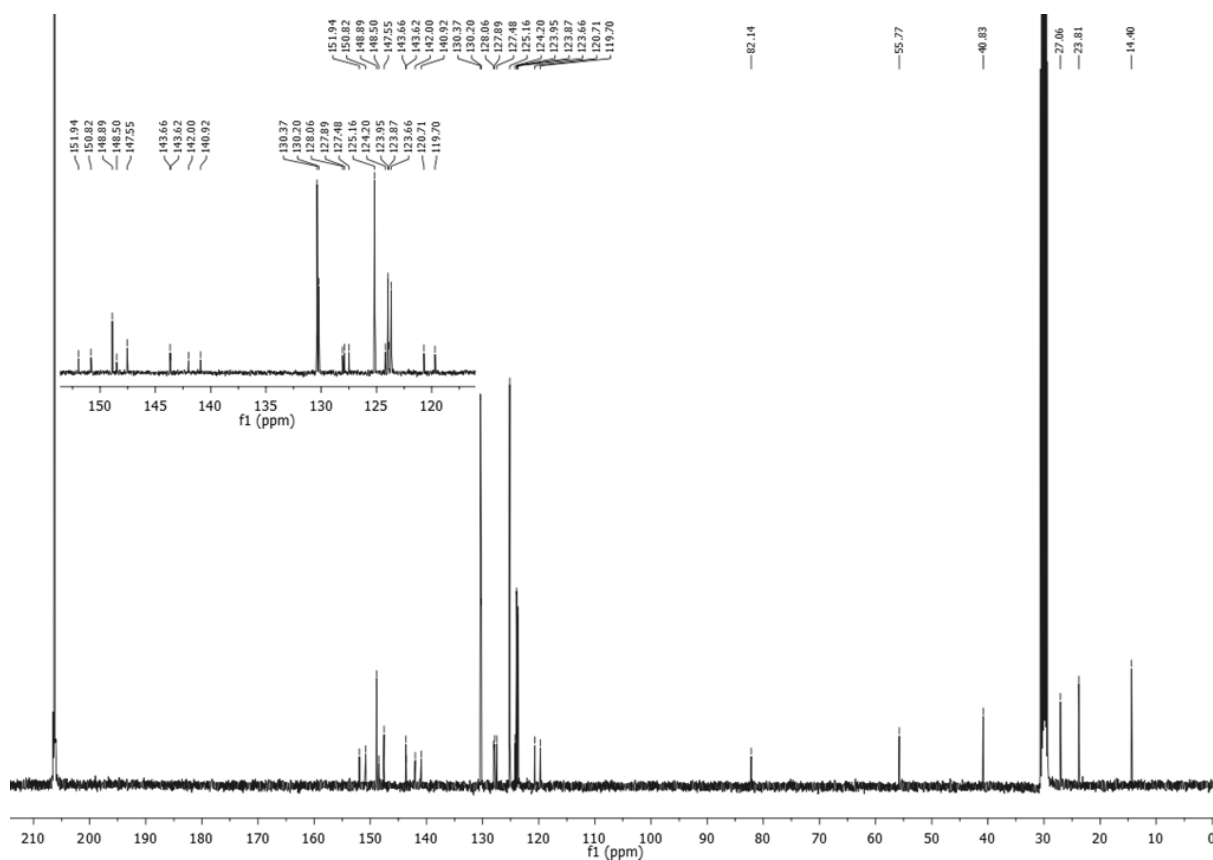
R_f (hexane/Et₂O, 1/1): 0.47

Yield: 750 mg (94 %)

¹H NMR (400 MHz, (CD₃)₂CO) δ 7.78 – 7.74 (m, 1H), 7.71 (d, *J* = 7.9 Hz, 1H), 7.57 – 7.35 (m, 4H), 7.35 – 7.18 (m, 14H), 7.18 – 6.88 (m, 15H), 5.29 (s, 1H, -OH), 2.04 – 1.85 (m, 4H), 1.13 – 0.99 (m, 4H), 0.65 – 0.52 (m, 10H).



^{13}C NMR (101 MHz, $(\text{CD}_3)_2\text{CO}$) δ 151.94, 150.82, 148.89, 148.50, 147.55, 143.66, 142.00, 140.92, 130.37, 130.20, 128.06, 127.89, 127.48, 125.16, 124.20, 123.95, 123.87, 123.66 (*p*-Ph), 120.71, 119.70, 82.14 (C-OH), 55.77, 40.83, 27.06, 23.81, 14.40.

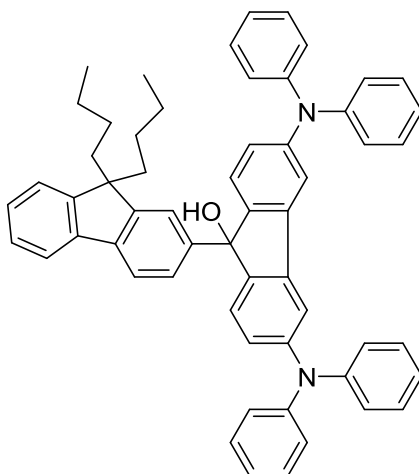


HRMS (ESI): calcd.: 777.42033 $[\text{M}-\text{OH}]^+$, 817.41283 $[\text{M}+\text{Na}]^+$, 501.23252 $[\text{M}-\text{OH}+\text{H}]^+$; found: 777.4211 $[\text{M}-\text{OH}]^+$, 817.4121 $[\text{M}+\text{Na}]^+$, 501.2327 $[\text{M}-\text{OH}+\text{H}]^+$.

IR (cm^{-1}): 3530 (ν_{OH}).

UV-Vis (DCM): λ_{max} , nm (ϵ , $10^{-5} \cdot \text{M}^{-1} \cdot \text{cm}^{-1}$): 312 (0.52).

9,9-dibutyl-3',6'-bis(diphenylamino)-9H,9'H-[2,9'-bifluoren]-9'-ol (O3(Flu)^{OH})



$C_{58}H_{52}N_2O$, $M = 793.05$ g/mol

Reagents: 2-bromo-9,9-dibutyl-9H-fluorene **33** (1.2 eq, 643.2 mg, 1.8 mmol), 3,6-bis(diphenylamino)-9H-fluoren-9-one **30** (1 eq, 771 mg, 1.5 mmol), *n*-BuLi (1.1 eq, 1.03 mL at 1.6 M in hexane, 1.65 mmol).

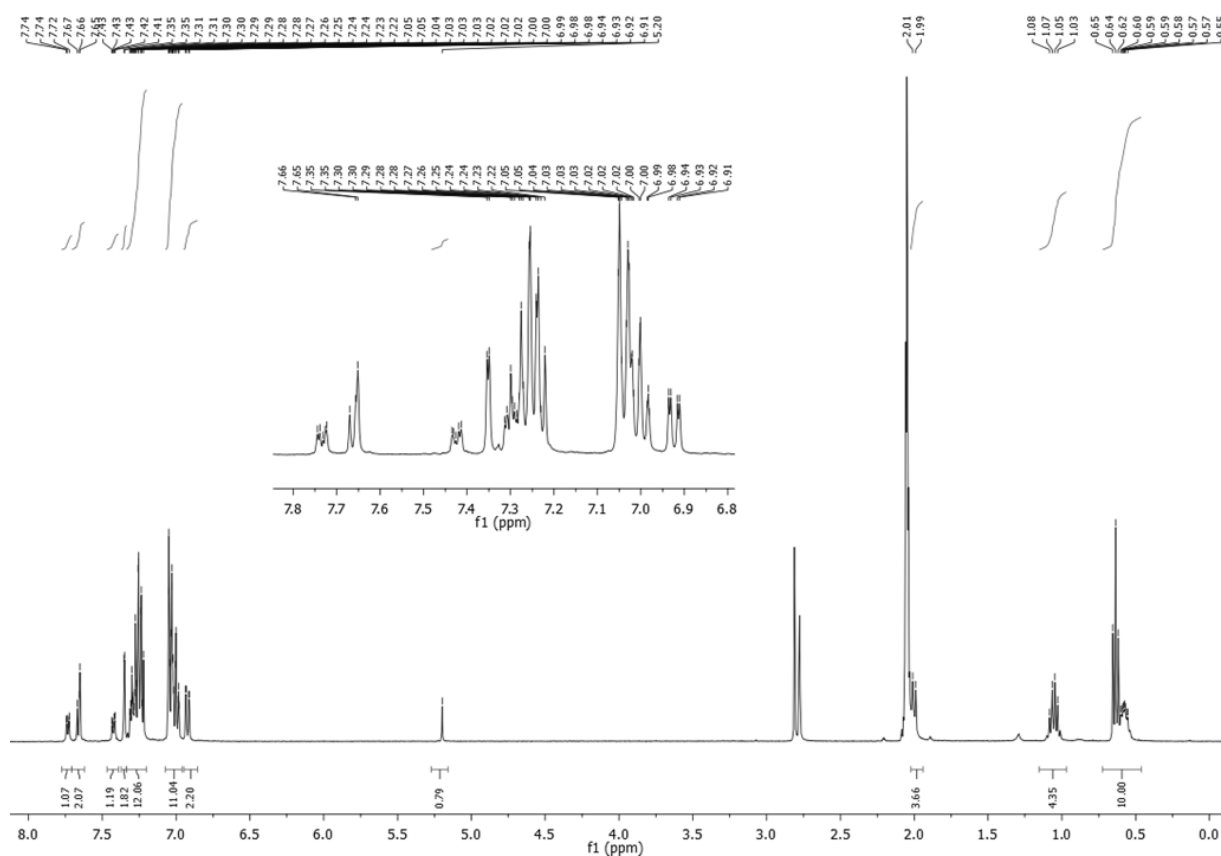
Reaction and work up: Prepared according to **GP1**.

Purification: The crude brown solid was adsorbed on deactivated silica and purified by column chromatography (neutralized silica gel with 10 % NEt₃, 15 x 5 cm) eluting with hexane/Et₂O (4/1) with 1 % NEt₃ to give 9,9-dibutyl-3',6'-bis(diphenylamino)-9H,9'H-[2,9'-bifluoren]-9'-ol **O3(Flu)^{OH}** as an orange solid. The product was precipitated in cold MeOH.

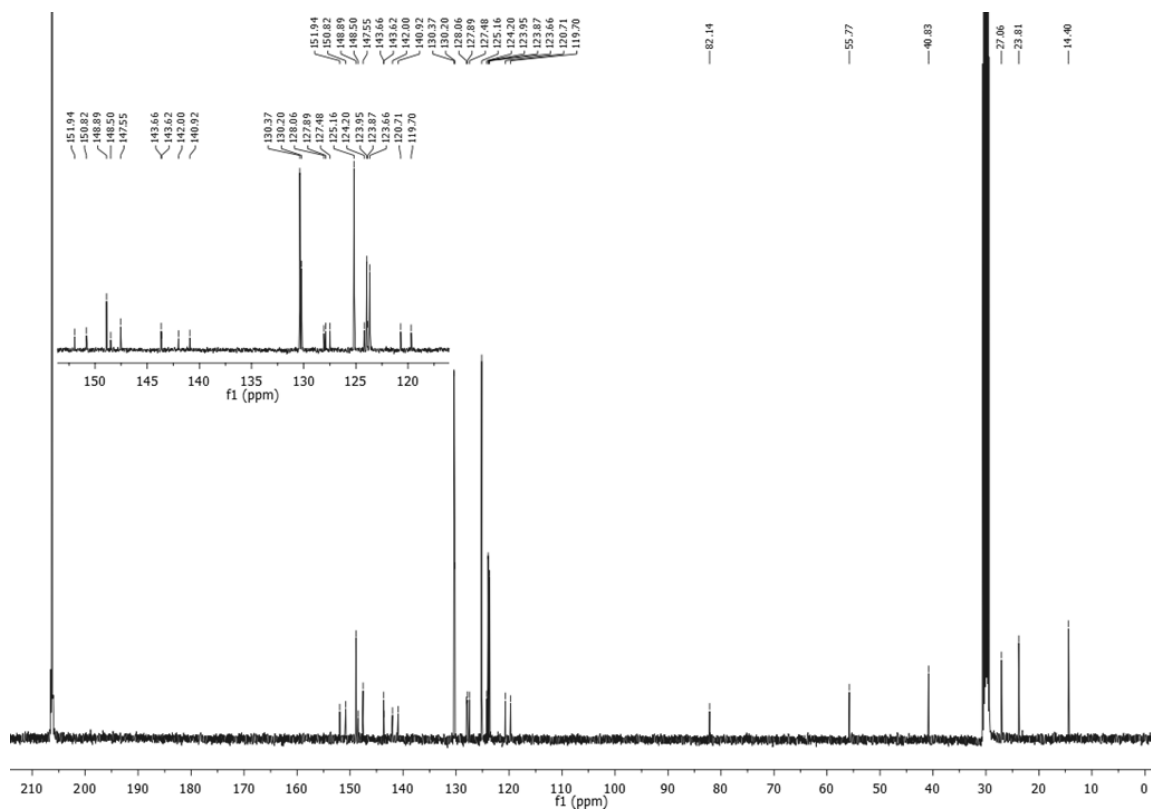
R_f(hexane/Et₂O, 4/1): 0.2

Yield: 1.05 g (88 %)

¹H NMR (400 MHz, (CD₃)₂CO) δ 7.78 – 7.70 (m, 1H), 7.70 – 7.61 (m, $J = 7.6$ Hz, 2H), 7.45 – 7.38 (m, 1H), 7.35 (d, $J = 1.7$ Hz, 2H), 7.34 – 7.14 (m, 13H), 7.12 – 6.95 (m, 12H), 6.92 (dd, $J = 8.2, 1.9$ Hz, 2H), 5.20 (s, 1H, -OH), 2.03 – 1.95 (m, 4H), 1.11 – 1.00 (m, 4H), 0.70 – 0.47 (m, 10H).



¹³C NMR (101 MHz, (CD₃)₂CO) δ 151.81, 151.42, 149.60, 149.01, 148.07, 148.04, 145.41, 142.13, 141.84, 141.00, 130.37, 127.93, 127.86, 126.57, 125.52, 125.14, 124.98, 123.87, 121.48, 120.54, 120.18, 117.05, 83.76 (-OH), 55.82, 40.80, 27.05, 23.80, 14.38.

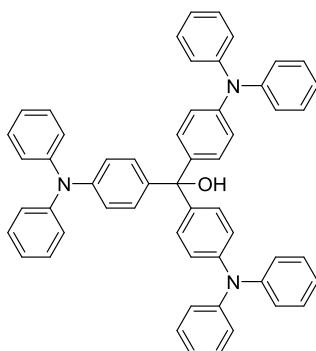


HRMS (ESI): Calcd.: 775.40468 $[M-\text{OH}]^+$, 792.40741 M^+ , 815.39718 $[M+\text{Na}]^+$; found: 775.4047 $[M-\text{OH}]^+$, 792.4065 M^+ , 815.3970 $[M+\text{Na}]^+$.

IR (cm^{-1}): 3447 (ν_{OH}).

UV-Vis (DCM): λ_{max} , nm (ϵ , $10^{-5} \cdot \text{M}^{-1} \cdot \text{cm}^{-1}$): 287 (0.47), 310 (0.43).

tris(4-(diphenylamino)phenyl)methanol (O4^{OH})



$\text{C}_{55}\text{H}_{43}\text{N}_3\text{O}$, $M = 761.97 \text{ g/mol}$

Reagents: 4-bromotriphenylamine (1.5 eq, 729 mg, 2.25 mmol), 4,4'-diphenylaminobenzophenone **29** (1 eq, 774 mg, 1.5 mmol), *n*-BuLi (1.5 eq, 900 μL at 2.5 M in hexane, 2.25 mmol).

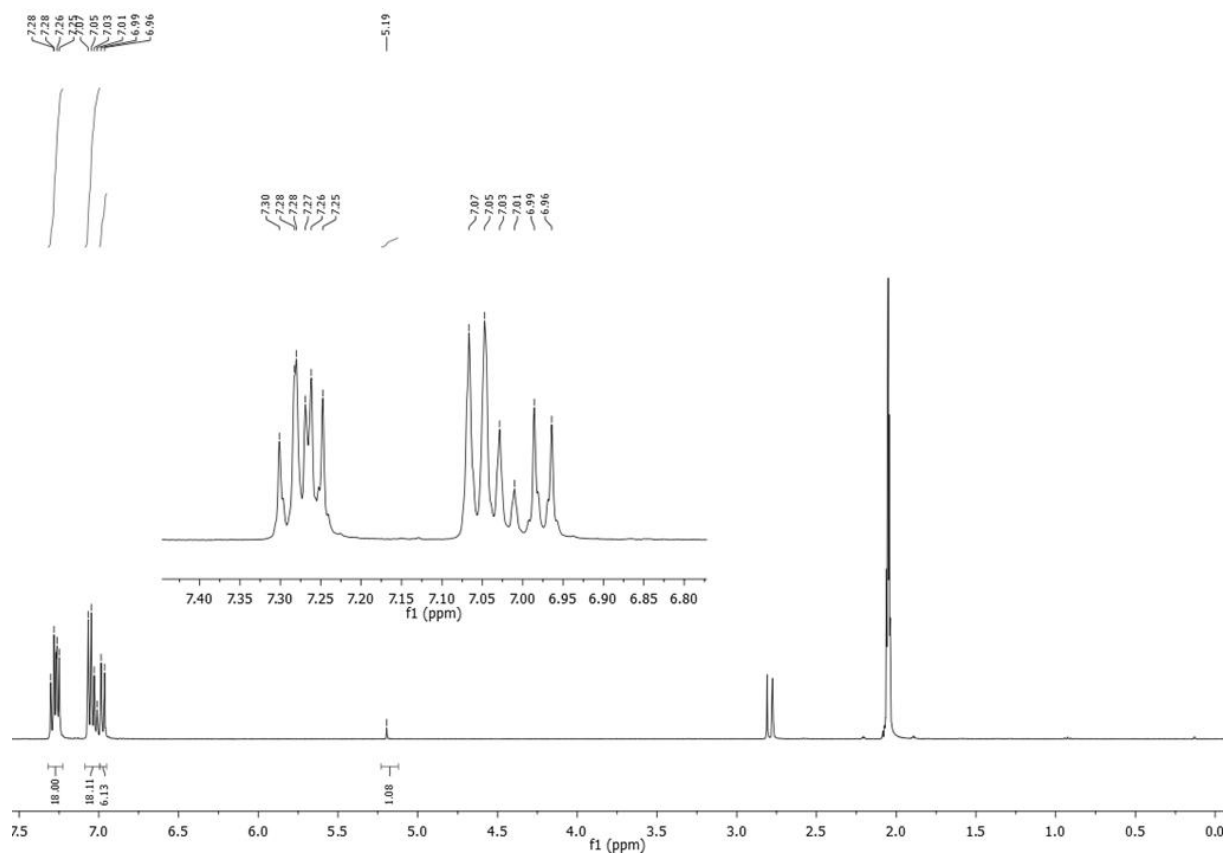
Reaction and work up: Prepared according to **GP1**.

Purification: The crude yellow solid was adsorbed on deactivated silica and purified by column chromatography (neutralized silica gel with 10 % NEt_3 , 20 x 5 cm) eluting with hexane/ Et_2O (4/1) with 1 % NEt_3 to give tris(4-(diphenylamino)phenyl)methanol as a white solid.

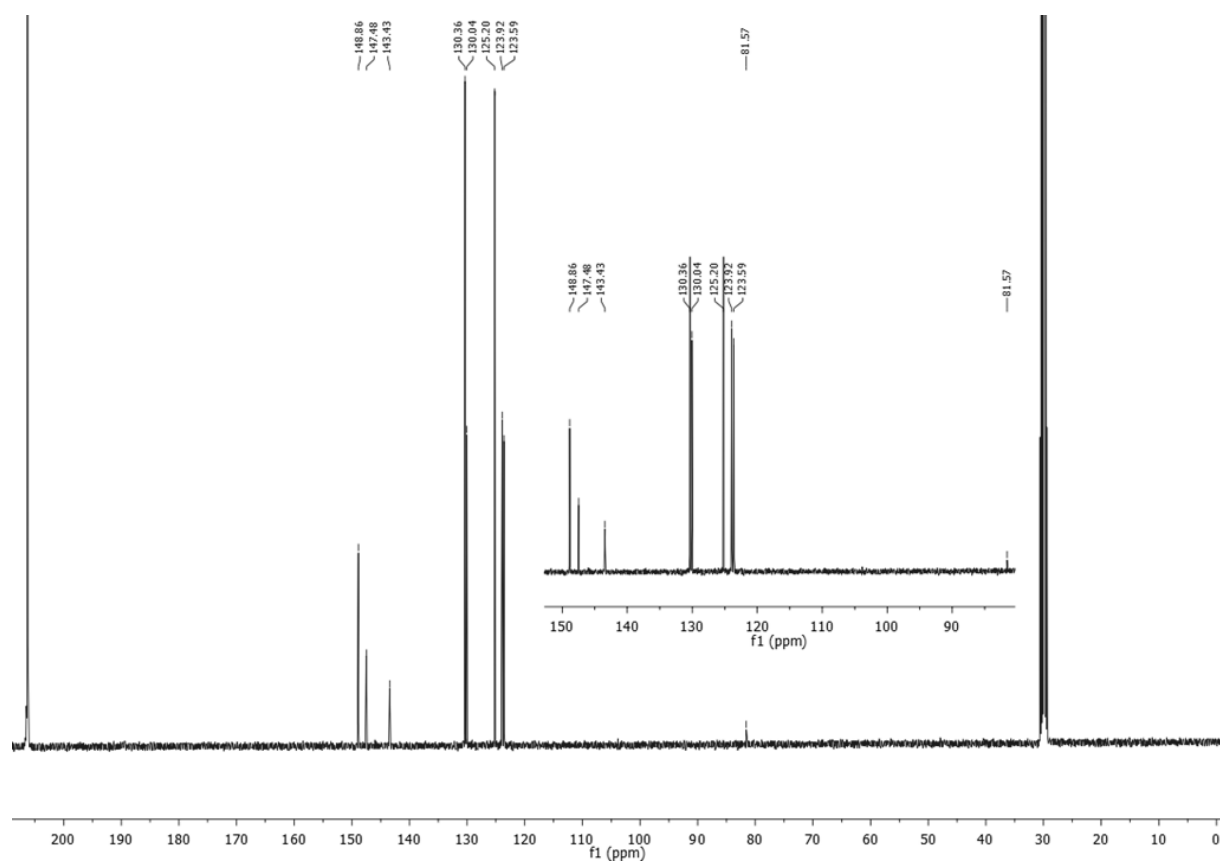
R_f (hexane/ Et_2O , 8/2): 0.29

Yield: 852 mg (75 %)

^1H NMR (400 MHz, $(\text{CD}_3)_2\text{CO}$) δ 7.31 – 7.20 (m, 18H), 7.10 – 6.99 (m, 18H), 6.96 (d, $J = 8.6 \text{ Hz}$, 6H), 5.20 (s, 1H, -OH).



¹³C NMR (101 MHz, (CD₃)₂CO) δ 148.86, 147.48, 143.43, 130.36, 130.04, 125.20, 123.92, 123.59, 81.56 (C-OH).



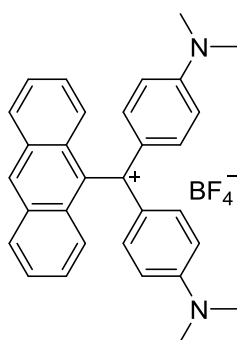
HRMS: calcd: 784.3304 $[M+Na]^+$, found: 784.3304 $[M+Na]^+$

IR (cm^{-1}): 3435 (ν_{OH}).

UV-Vis (DCM): λ_{max} , nm (ϵ , $10^{-5} \cdot \text{M}^{-1} \cdot \text{cm}^{-1}$): 312 (0.69).

5.2. Organic carbocations

9-anthracenyl-bis(4-(dimethylamino)phenyl)methylium tetrafluoroborate ([O1(anth)⁺][BF₄⁻])

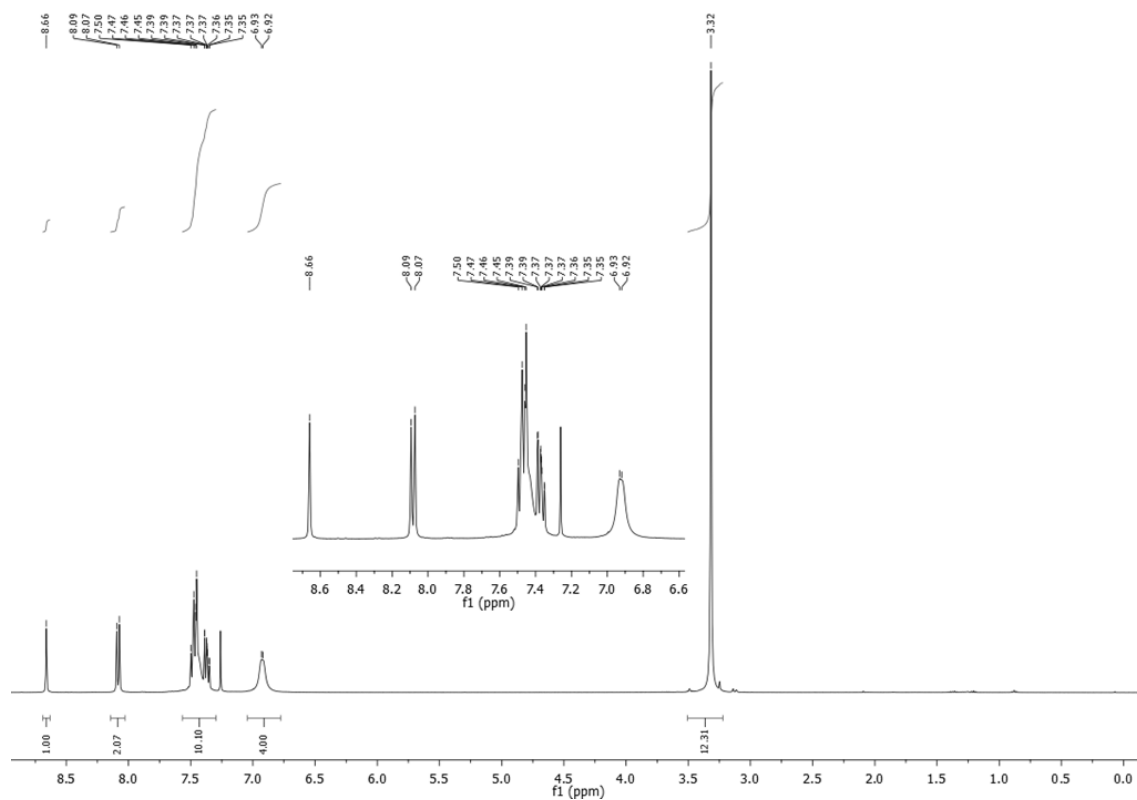


$\text{C}_{31}\text{H}_{29}\text{BF}_4\text{N}_2$, $M = 516.38 \text{ g/mol}$

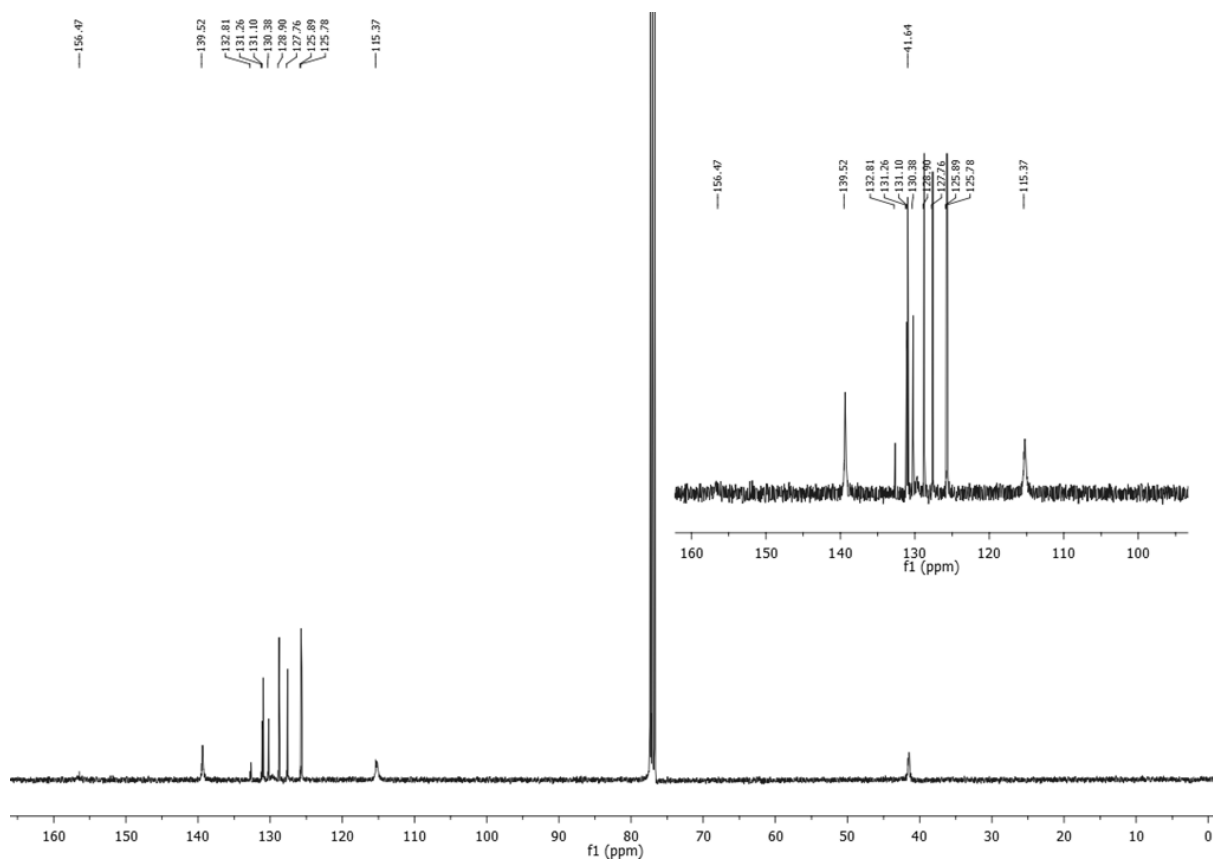
Reagents: 9-anthracenyl-bis(4-(dimethylamino)phenyl)methanol **O1(anth)^{OH}** (1 eq, 115 mg, 0.25 mmol), $\text{HBF}_4 \cdot \text{Et}_2\text{O}$ (1.1 eq, 37 μL , 0.275 mmol).

Reaction and work up: Prepared according to **GP3** to obtain 9-anthracenyl-bis(4-(dimethylamino)phenyl)methylium tetrafluoroborate **O1(anth)⁺** as a violet powder.

¹H NMR (400 MHz, CDCl_3) δ 8.66 (s, 1H), 8.08 (d, $J = 8.4 \text{ Hz}$, 2H), 7.57 – 7.30 (m, 10H), 7.04 – 6.77 (broad d, 4H), 3.32 (s, 12H).



¹³C NMR (101 MHz, CDCl₃) δ 156.69 (C⁺), 139.52, 132.81, 131.26, 131.10, 130.38, 128.90, 127.76, 125.89, 125.78, 115.37, 41.64.

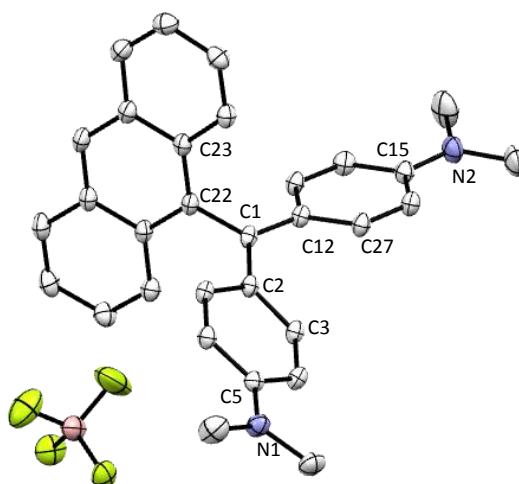


HRMS (ESI): calcd.: 429.2331 [M]⁺; found: 429.331 [M]⁺.

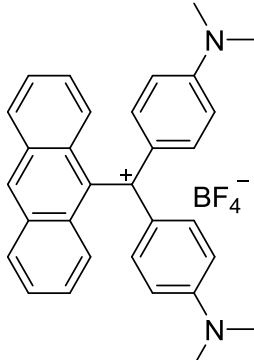
IR (KBr, cm⁻¹): 1056 (ν_{B-F}).

UV-Vis (DCM): λ_{max}, nm (ε, 10⁻⁵·M⁻¹·cm⁻¹): 255 (0.88), 642 (1.02).

X-ray diffraction study:



ORTEP view of [O1(anth)⁺][BF₄⁻] with 50 % thermal ellipsoids solved by Dr. Graeme Moxey

	
Formula	C ₃₁ H ₂₉ BF ₄ N ₂
Molecular weight (g/mol)	516.37
Dark shiny crystals by slow diffusion of Et ₂ O vapor in a DCM solution of the molecule at room temperature.	

Crystal parameters	
Crystal class	Orthorhombic
Space group	P b c a
Cell angles (°)	α= 90
	β= 90
	γ= 90
Cell length (Å)	a= 20.56
	b= 11.65
	c= 21.99
Cell volume (Å ³)	5267.58
Z	Z= 8

Selected bond length (Å)

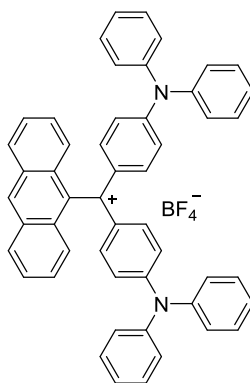
C1 - C22	1.497 (2)	C2 - C3	1.420 (2)
C1 - C2	1.426 (2)	C5 - N1	1.348 (3)
C1 - C12	1.414 (2)	C15 - N2	1.343 (3)
C12 - C17	1.426 (2)		

Selected angles (°)

C22 - C1 - C2	119.04 (1)	C1 - C2/C12 - C13*	25.22 (1)
C plane	0.01 (2)	C1 - C2/C22 - C23*	107.29 (2)

*torsion angle

anthracen-9-ylbis(4-(diphenylamino)phenyl)methylumtetrafluoroborate ([O2(anth)⁺][BF₄⁻])

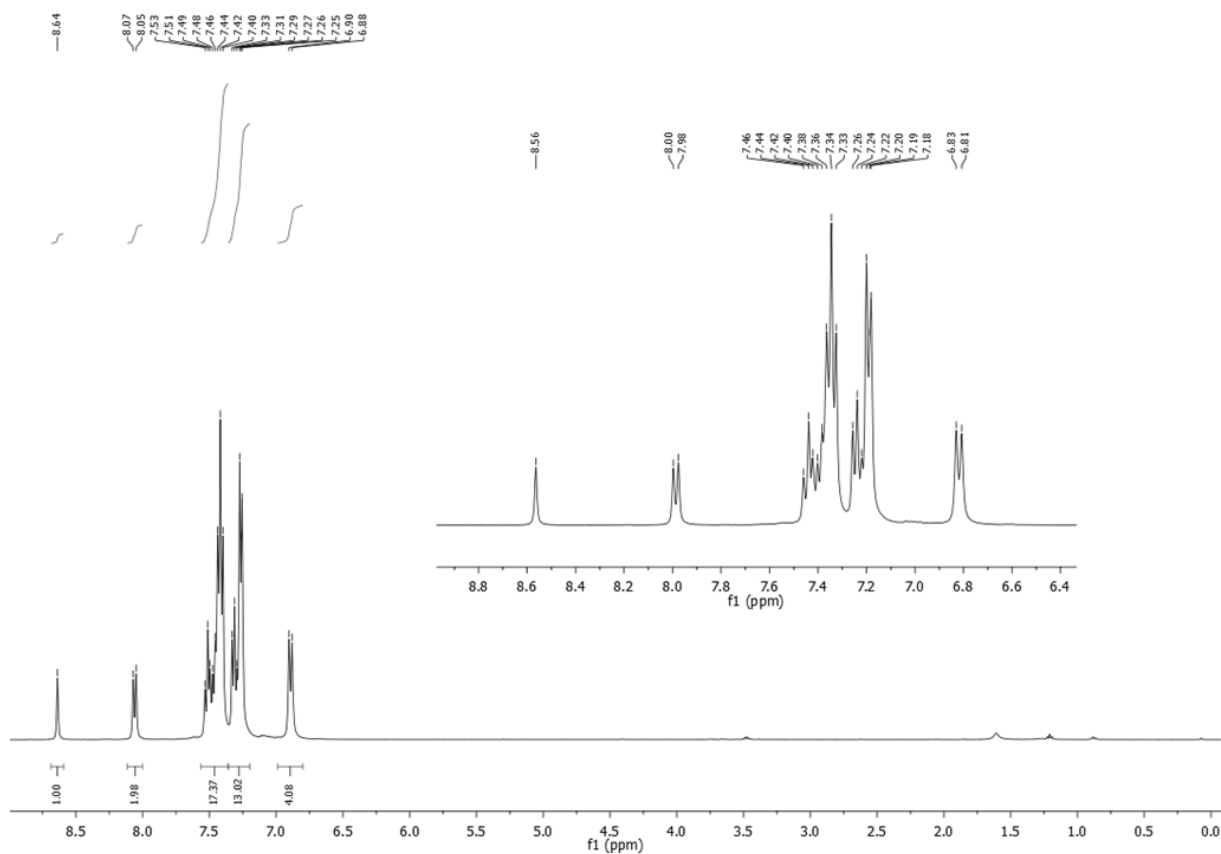


C₅₁H₃₇BF₄N₂, M = 764.66 g/mol

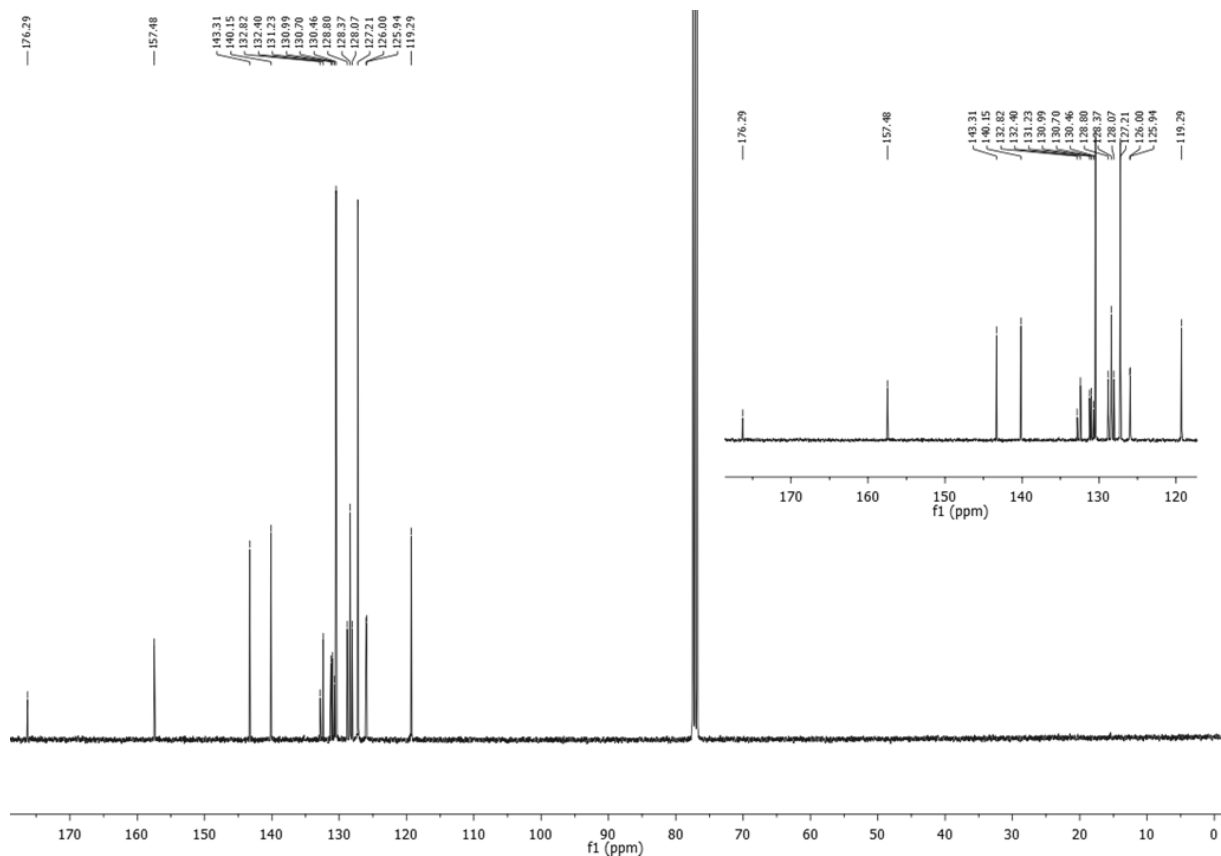
Reagents: 9-anthracenyl-bis(4-(diphenylamino)phenyl)methanol **O2(anth)^{OH}** (1 eq, 191 mg, 0.25 mmol), HBF₄·Et₂O (1.1 eq, 37 µL, 0.275 mmol).

Reaction and work up: Prepared according to **GP3** to obtained 9-anthracenyl-bis(4-(diphenylamino)phenyl)methylum tetrafluoroborate **O2(anth)⁺** as a violet powder.

¹H NMR (400 MHz, CDCl₃) δ 8.64 (s, 1H), 8.06 (d, *J* = 8.3 Hz, 2H), 7.56 – 7.36 (m, 17H), 7.36 – 7.20 (m, 13H), 6.89 (d, *J* = 9.0 Hz, 4H).



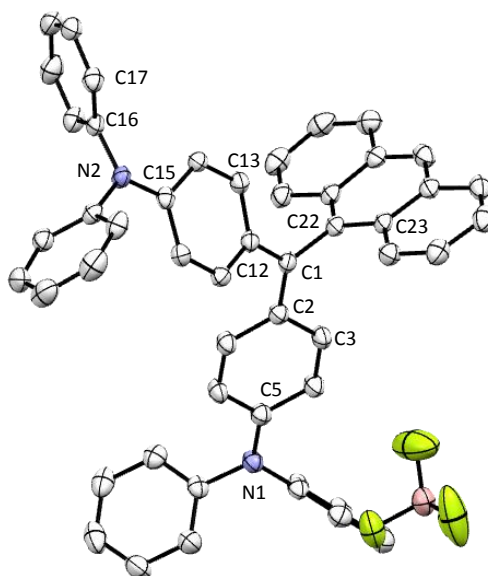
¹³C NMR (101 MHz, CDCl₃) δ 176.29 (C⁺), 157.48, 143.31, 140.15, 132.82, 132.40, 131.23, 130.99, 130.70, 130.46, 128.80, 128.37, 128.07, 127.21, 126.00, 125.94, 119.29.



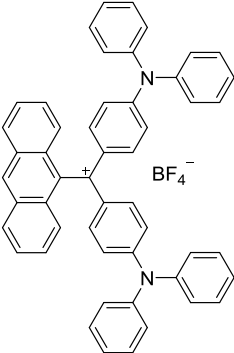
HRMS (ESI): calcd.: 677.29512 $[M]^+$, found: 677.2949 $[M]^+$.

UV-Vis (DCM): λ_{\max} , nm (ϵ , $10^{-5} \cdot M^{-1} \cdot cm^{-1}$): 247 (0.63), 267 (0.33), 702 (0.90).

X-ray diffraction study:



ORTEP view of $[(O2(anth))^+][BF_4^-]$ with 50 % thermal ellipsoids solved by Dr. Thierry Roisnel

	
Formula	$C_{51}H_{37}BF_4N_2$
Molecular weight (g/mol)	764.66
Violet shiny crystals by slow diffusion of Et_2O vapor into a DCM solution of the molecule at room temperature.	

Crystal parameters	
Crystal class	monoclinic
Space group	$P 2_1/n$
Cell angles ($^\circ$)	$\alpha = 90$
	$\beta = 98$
	$\gamma = 90$
Cell length (\AA)	$a = 16.45$
	$b = 13.53$
	$c = 17.78$
Cell volume (\AA^3)	3921.12
Z	$Z = 4$

Selected bond length (Å)

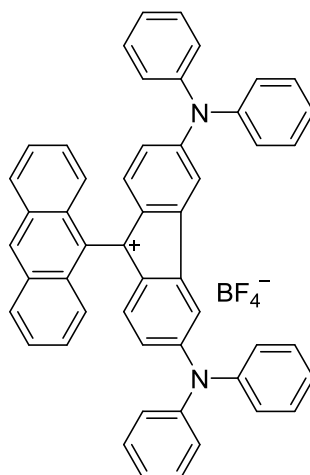
C1 - C2	1.488 (3)	C2 - C17	1.433 (3)
C1 - C12	1.448 (3)	C5 - N1	1.379 (3)
C1 - C22	1.405 (3)	C15 - N2	1.351 (3)
C12 - C13	1.414 (3)		

Selected angles (°)

C1 - C2 - C22	117.02 (2)	C1 - C2/ C22 - C1*	100.03 (3)
C plane	3.69 (2)	C14 - C15/ C16 - C17*	64.96 (3)
C1 - C22/C2 -C3*	32.17 (3)	C15 - N2/ C16 - C17*	70.32 (3)

*torsion angle

9-(9-anthracenyl)-3,6-bis(diphenylamino)-9H-fluoren-9-ylum tetrafluoroborate ([O3(anth)⁺][BF₄⁻])



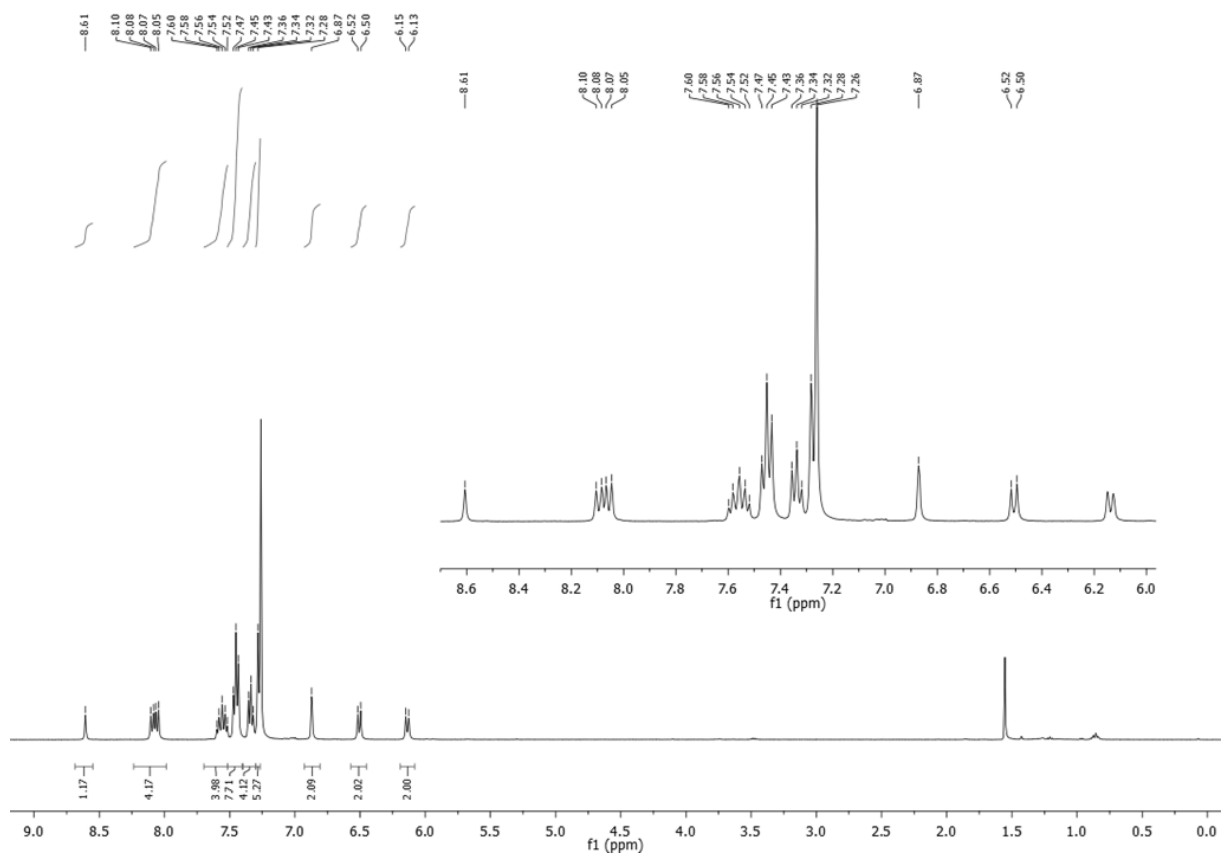
C₅₁H₃₅BF₄N₂, M = 762.64 g/mol

Reagents: directly from the carbinol's reaction **O3(anth)^{OH}**

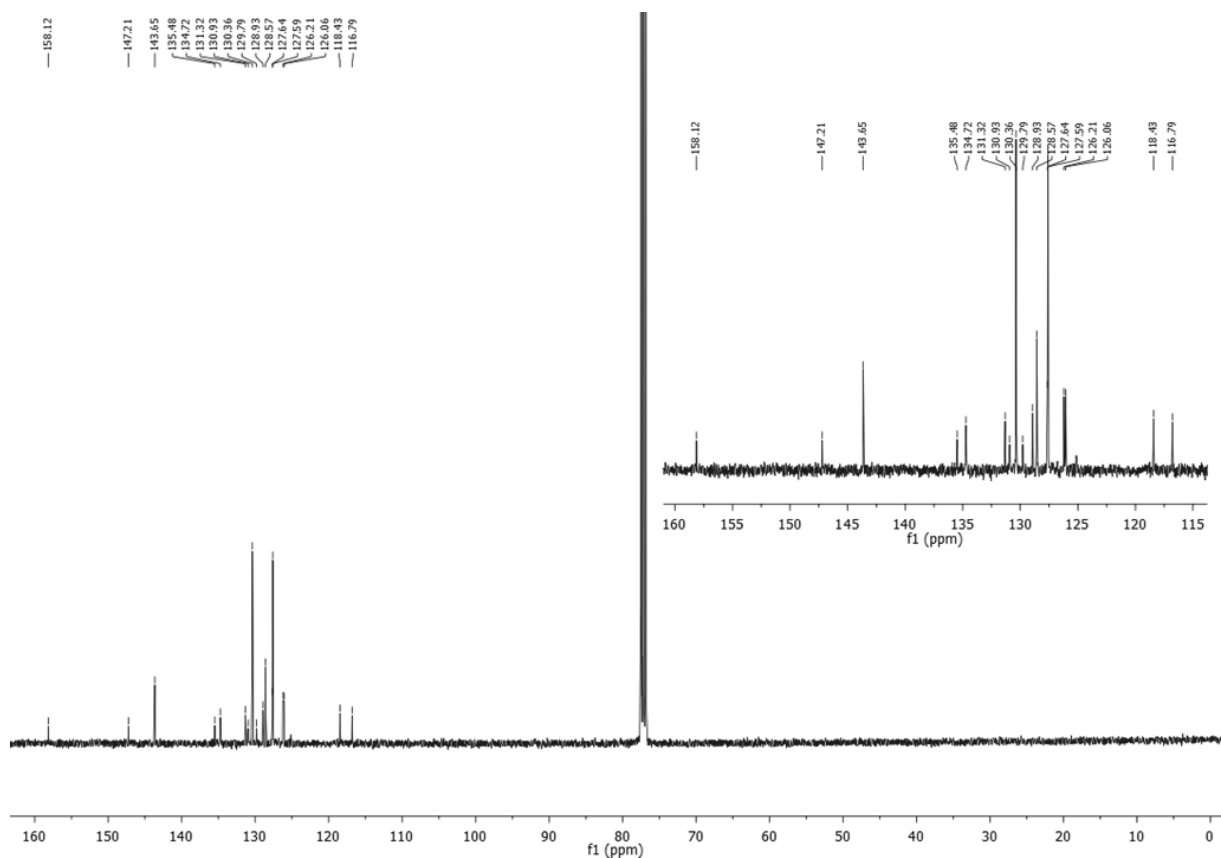
Reaction and work up: Prepared according to **GP3** to obtained 9-(9-anthracenyl)-3,6-bis(diphenylamino)-9H-fluoren-9-ylum tetrafluoroborate ([O3(anth)⁺][BF₄⁻]) as a violet powder.

Overall yield= 21 %.

¹H NMR (400 MHz, CDCl₃) δ 8.61 (s, 1H), 8.08 (dd, *J* = 15.2, 8.3 Hz, 4H), 7.56 (dt, *J* = 15.2, 6.6 Hz, 4H), 7.45 (t, *J* = 7.6 Hz, 8H), 7.34 (t, *J* = 7.4 Hz, 4H), 7.28 (s, 5H), 6.87 (s, 2H), 6.51 (d, *J* = 8.9 Hz, 2H), 6.14 (d, *J* = 8.7 Hz, 2H).



¹³C NMR (101 MHz, CDCl₃) δ 158.12 (C⁺), 147.21, 143.65, 135.48, 134.72, 131.32, 130.93, 130.36, 129.79, 128.93, 128.57, 127.64, 127.59, 126.21, 126.06, 118.43, 116.79.

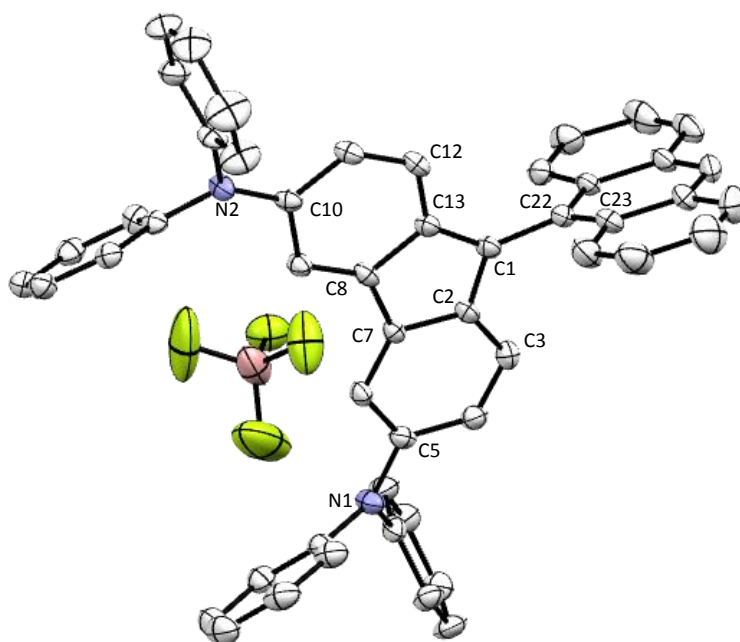


UV-Vis (DCM): λ_{\max} , nm (ϵ , $10^{-5} \cdot \text{M}^{-1} \cdot \text{cm}^{-1}$): 510 (0.13), 1068 (0.25).

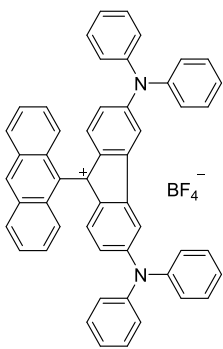
HRMS (ESI): calcd.: 675.280, $[\text{M}]^+$; found: 675.2800, $[\text{M}]^+$.

IR (KBr, cm^{-1}): 1257 ($\nu_{\text{B-F}}$)

X-ray diffraction study:



ORTEP view of $[\text{O3(anth)}^+][\text{BF}_4^-]$ with 50 % thermal ellipsoids solved by Dr. Graeme Moxey

	
Formula	$\text{C}_{51}\text{H}_{35}\text{BF}_4\text{N}_2$
Molecular weight (g/mol)	762.64
Dark shiny crystals by slow diffusion of Et_2O vapor in a DCM solution of the molecule at room temperature.	

Crystal parameters	
Crystal class	monoclinic
Space group	$P 2_1/c$
Cell angles ($^\circ$)	$\alpha = 90$
	$\beta = 96$
	$\gamma = 90$
Cell length (\AA)	$a = 29.27$
	$b = 25.71$
	$c = 10.31$
Cell volume (\AA^3)	7717.87
Z	$Z = 8$

Selected bond length (Å)

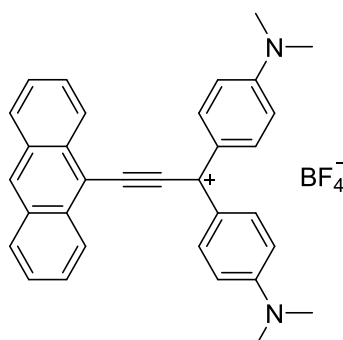
C1 - C22	1.477 (5)	C13 - C12	1.409 (5)
C1 - C2	1.450 (5)	C2 - C3	1.391 (5)
C13 - C8	1.437 (5)	C10 - N2	1.371 (5)
C2 - C7	1.415 (5)	C5 - N1	1.396 (5)

Selected angles (°)

C plane	2.89 (2)	C6 - C5/N1 -C47*	27.81 (5)
C13 - C1/C22 - C23	70.37 (2)	C6 - C5/ C47 - C48*	63.42 (4)

*torsion angle

3-(9-anthracenyl)-1,1-bis(4-(dimethylamino)phenyl)prop-2-yn-1-ylum tetrafluoroborate
([O1(anthC₂)⁺][BF₄⁻])



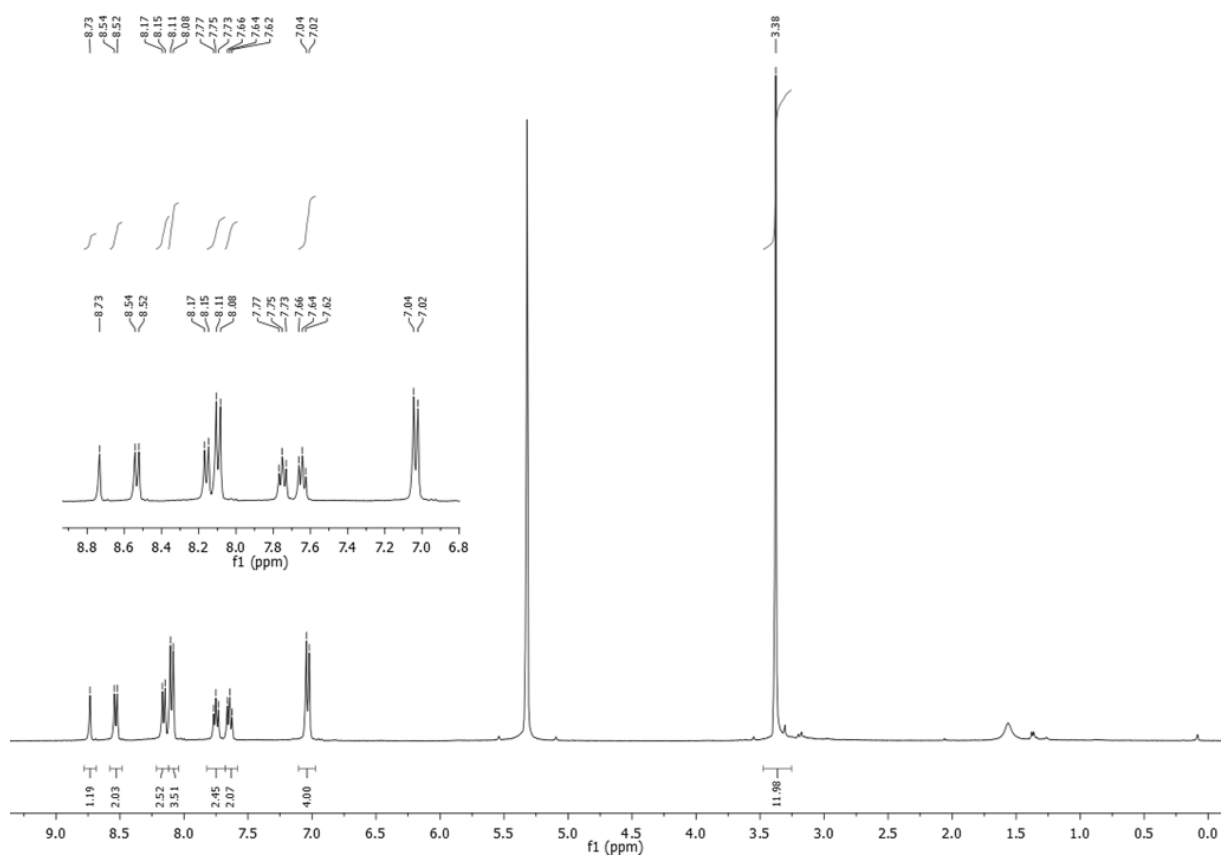
C₃₃H₂₉BF₄N₂, M = 540.40 g/mol

Reagents: 3-(9-anthracenyl)-1,1-bis(4-(dimethylamino)phenyl)prop-2-yn-1-ol **O1(anthC₂)^{OH}** (1 eq, 470.5 mg, 1 mmol), HBF₄·Et₂O (1.1 eq, 150 µL, 1.1 mmol).

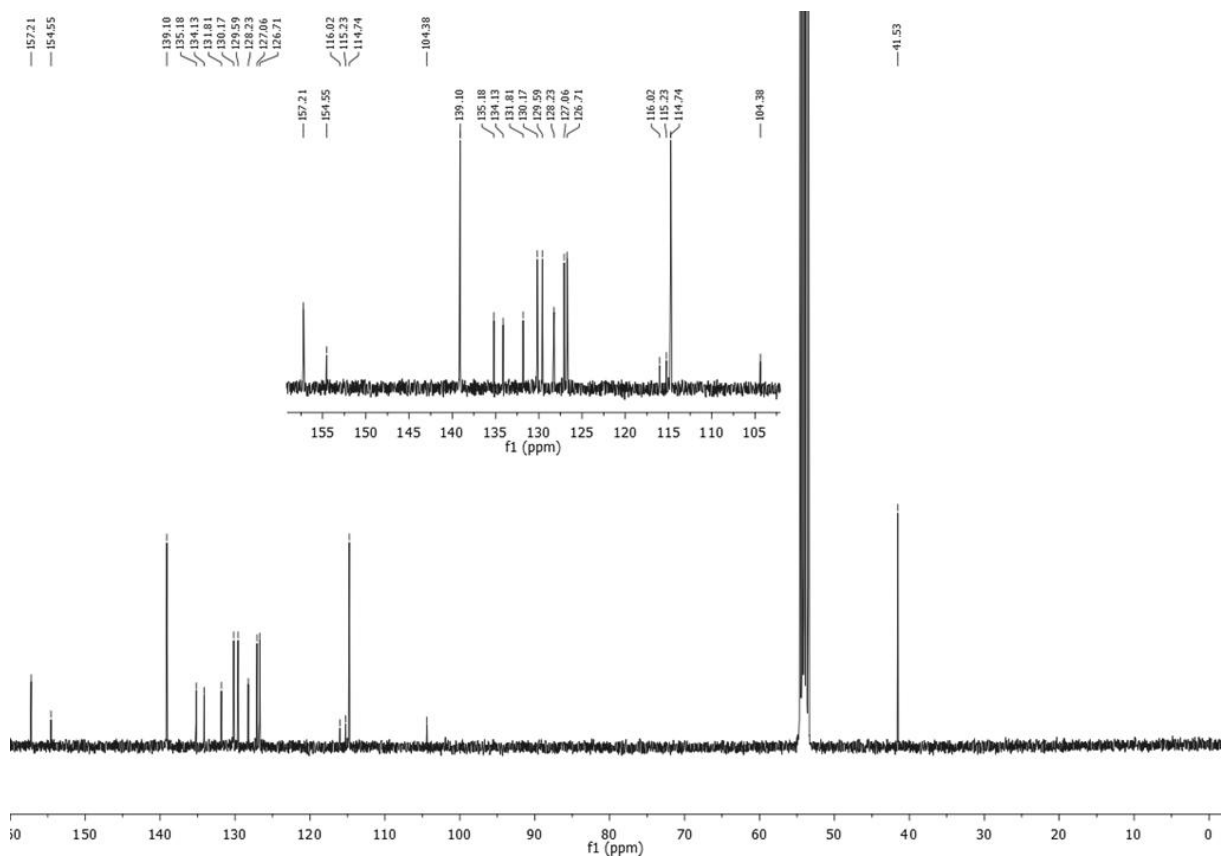
Reaction and work up: Prepared according to **GP3** to obtained 3-(9-anthracenyl)-1,1-bis(4-(dimethylamino)phenyl)prop-2-yn-1-ylum tetrafluoroborate **O1(anthC₂)⁺** as a green powder.

Yield: 480 mg (89 %)

¹H NMR (400 MHz, CD₂Cl₂) δ 8.73 (s, 1H), 8.53 (d, *J* = 8.6 Hz, 2H), 8.16 (d, *J* = 8.4 Hz, 3H), 8.09 (d, *J* = 9.3 Hz, 4H), 7.82 – 7.68 (m, 2H), 7.68 – 7.58 (m, 2H), 7.03 (d, *J* = 9.2 Hz, 4H), 3.38 (s, 12H).



¹³C NMR (101 MHz, CD₂Cl₂) δ 157.21, 154.55 (C⁺), 139.10, 135.18, 134.13, 131.81, 130.17, 129.59, 128.23, 127.06, 126.71, 116.02, 115.23, 114.74, 104.38, 41.53.

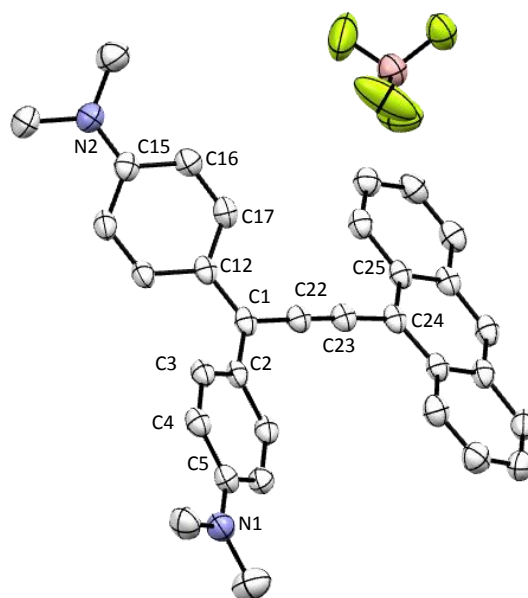


HRMS (ESI): calcd.: 453.23307 [M]⁺; found: 453.2334 [M]⁺.

IR (KBr, cm⁻¹): 2140 (ν_{C≡C}) and 1162 (ν_{B-F}).

UV-Vis (DCM): λ_{max}, nm (ε, 10⁻⁵·M⁻¹·cm⁻¹): 263 (1.16), 317 (0.25), 704 (1.09).

X-ray diffraction study:



ORTEP view of ([O1(anthC₂)⁺][BF₄⁻]) with 50 % thermal ellipsoids solved by Dr. Graeme Moxey

Formula	C ₃₃ H ₂₉ BF ₄ N ₂
Molecular weight (g/mol)	540.40
Dark shiny crystals by slow diffusion of Et ₂ O vapor into a DCM solution of the molecule at room temperature.	

Crystal parameters	
Crystal class	monoclinic
Space group	P 2 ₁ /n
Cell angles (°)	α= 90
	β= 97
	γ= 90
Cell length (Å)	a= 16.41
	b= 7.29
	c= 22.75
Cell volume (Å ³)	2697.62
Z	Z= 4

Selected bond length (Å)

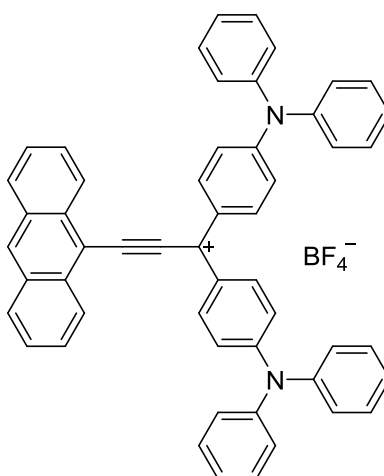
C1 - C22	1.423 (2)	C3 - C4	1.363 (3)
C1 - C2	1.426 (3)	C12 - C17	1.420 (3)
C1 - C12	1.433 (3)	C16 - C17	1.361 (3)
C22 - C23	1.203 (3)	C15 - N2	1.348 (3)
C1 - C3	1.422 (3)	C5 - N1	1.341 (3)

Selected angles (°)

C plan	1.40 (2)	C1 - C22 - C23	179.20 (3)
C2-C1/C12 - C13*	23.61 (3)	C1 - C12/C24 - C25*	12.84 (3)

*torsion angle

3-(9-anthracenyl)-1,1-bis(4-(diphenylamino)phenyl)prop-2-yn-1-ylum tetrafluoroborate
([O2(anthC₂)⁺][BF₄⁻])



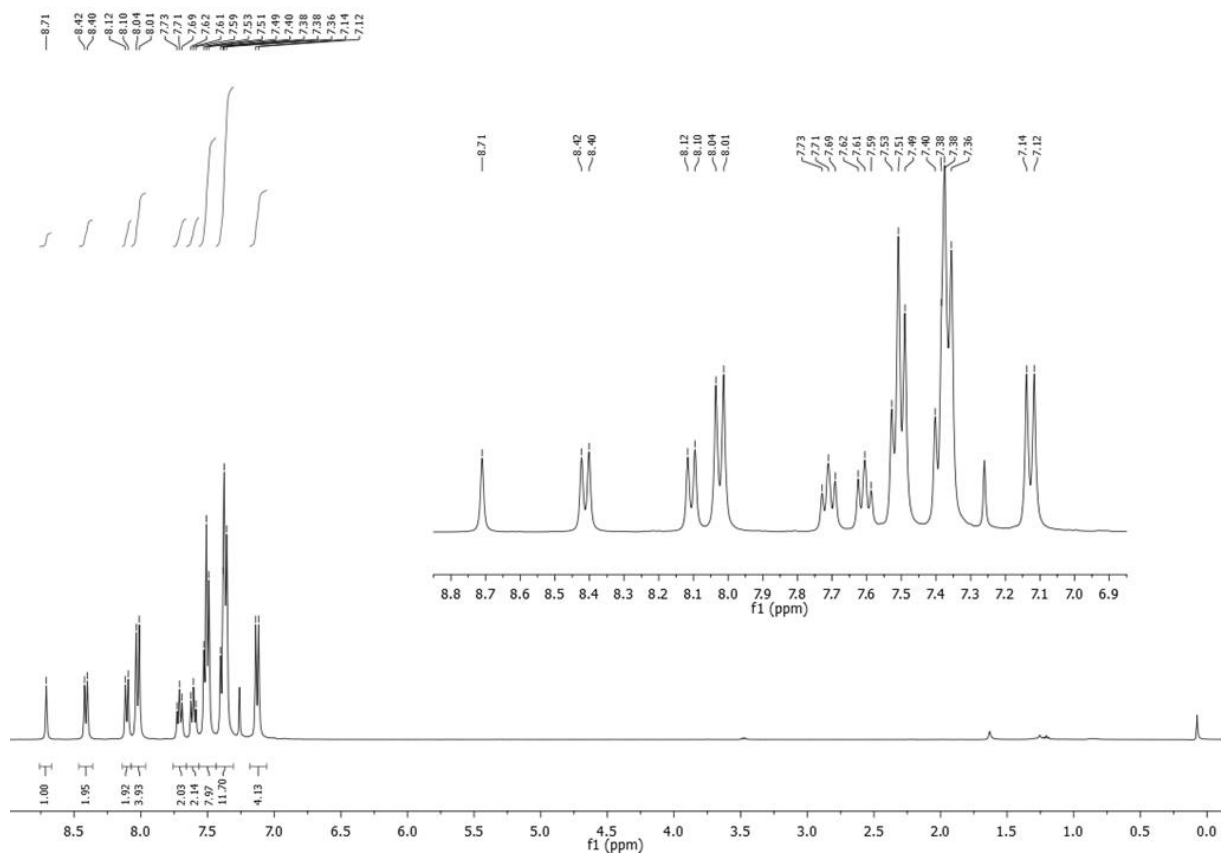
C₅₃H₃₇BF₄N₂, M = 788.68 g/mol

Reagents: 3-(9-anthracenyl)-1,1-bis(4-(diphenylamino)phenyl)prop-2-yn-1-ol **O2(anthC₂)^{OH}** (1 eq, 360 mg, 0.5 mmol), HBF₄·Et₂O (1.1 eq, 75 μL, 0.55 mmol).

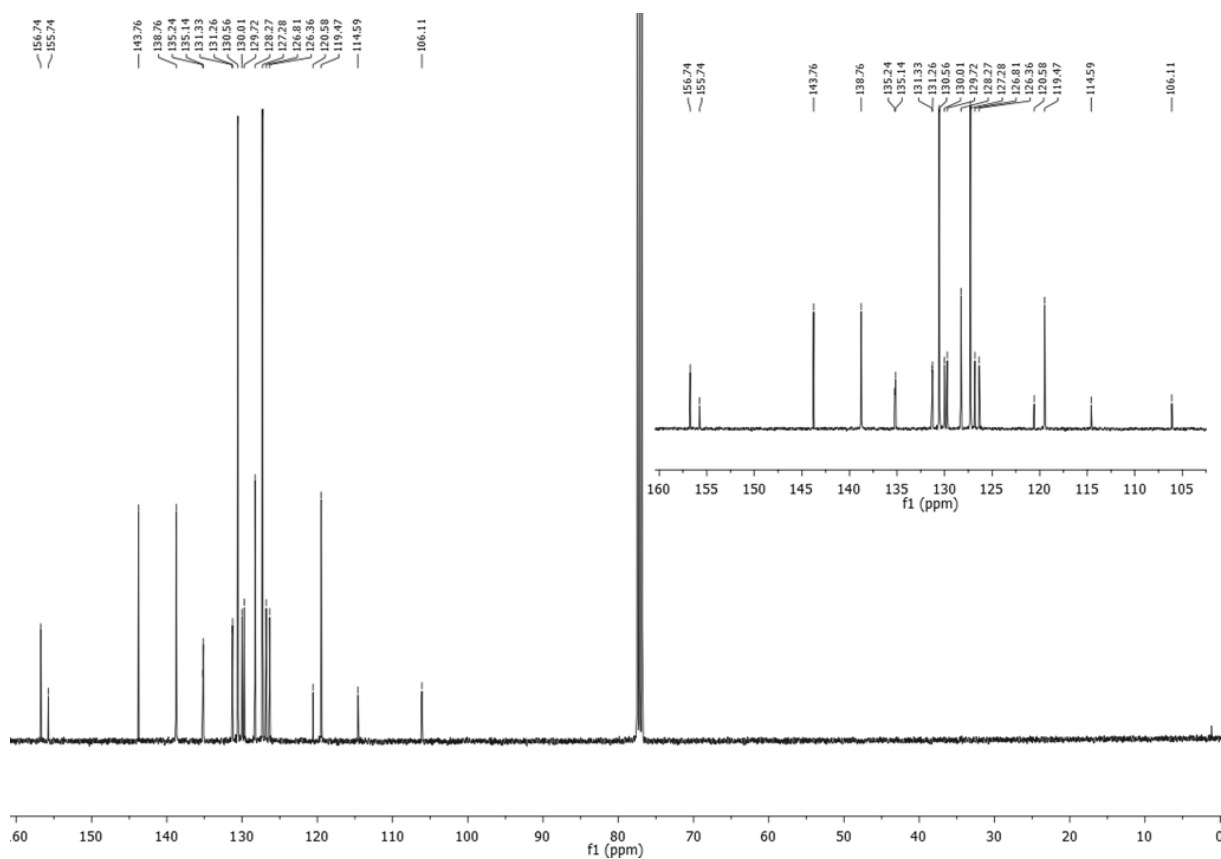
Reaction and work up: Prepared according to **GP3** to obtained 3-(9-anthracenyl)-1,1-bis(4-(diphenylamino)phenyl)prop-2-yn-1-ylum tetrafluoroborate **([O2(anthC₂)⁺][BF₄⁻])** as a green powder.

Yield: 350 mg (88 %)

^1H NMR (400 MHz, CDCl_3) δ 8.71 (s, 1H), 8.41 (d, $J = 8.6$ Hz, 2H), 8.11 (d, $J = 8.4$ Hz, 2H), 8.02 (d, $J = 9.0$ Hz, 4H), 7.71 (t, $J = 7.6$ Hz, 2H), 7.61 (t, $J = 7.6$ Hz, 2H), 7.51 (t, $J = 7.7$ Hz, 8H), 7.37 (t, $J = 5.7$ Hz, 12H), 7.13 (d, $J = 8.9$ Hz, 4H).



^{13}C NMR (101 MHz, CDCl_3) δ 156.74, 155.74 (C^+), 143.76, 138.76, 135.24, 135.14, 131.33, 131.26, 130.56, 130.01, 129.72, 128.27, 127.28, 126.81, 126.36, 120.58, 119.47, 114.59, 106.11.

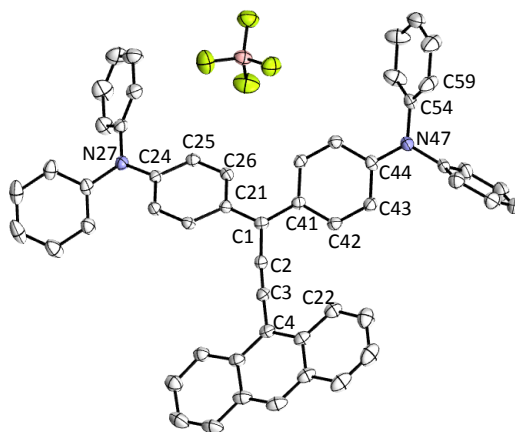


HRMS (ESI): calcd.: 701.29512 $[M]^+$; found: 701.2949 $[M]^+$.

IR (KBr, cm^{-1}): 2135 ($\nu_{\text{C}\equiv\text{C}}$) and 1249 ($\nu_{\text{B-F}}$).

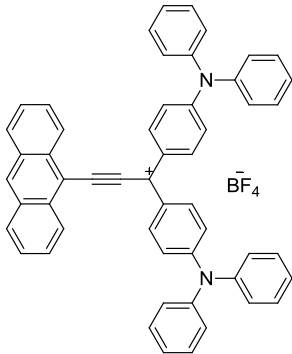
UV-Vis (DCM): λ_{max} , nm (ϵ , $10^{-5} \cdot \text{M}^{-1} \cdot \text{cm}^{-1}$): 261 (1.11), 736 (1.26).

X-ray diffraction study:



ORTEP view of $[(\text{O2}(\text{anthC}_2))^+][\text{BF}_4]^-$ with 50 % thermal ellipsoids solved by Dr. Thierry Roisnel.

Molecule of DCM omitted for clarity.

	
Formula	C ₅₃ H ₃₇ BF ₄ N ₂
Molecular weight (g/mol)	788.68
Dark shiny crystals by slow diffusion of Et ₂ O vapor into a DCM solution of the molecule at room temperature.	

Crystal parameters	
Crystal class	monoclinic
Space group	P 2 ₁ /c
Cell angles (°)	α= 90
	β= 92.40
	γ= 90
Cell length (Å)	a= 9.195
	b= 15.24
	c= 31.65
Cell volume (Å ³)	4431.76
Z	Z= 4

Selected bond length (Å)

C1 - C2	1.412 (5)	C41 - C42	1.418 (3)
C2 - C3	1.210 (3)	C26 - C25	1.367 (3)
C1 - C21	1.437 (3)	C42 - C43	1.366 (3)
C1 - C41	1.436 (3)	C24- N27	1.360 (3)
C21 - C26	1.418 (3)	C44 - N47	1.379 (3)

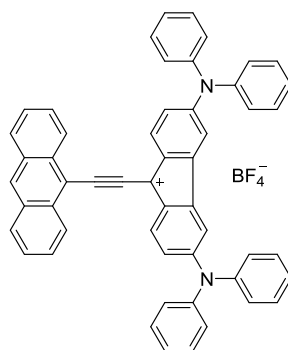
Selected angles (°)

C plan	0.44 (2)	C1 - C41/C4 - C17*	12.55 (3)
C21-C1/C41 - C46*	21.92 (2)	C44 - N47/C54 - C59*	50.86 (2)
C1 - C22 - C23	173.39 (2)	C45 - C44/ C54 - 59*	54.87 (3)

*torsion angle

9-(9-ethynylantracenyl)-3,6-bis(diphenylamino)-9H-fluoren-9-ylum
([O3(anthC₂)⁺][BF₄⁻])

tetrafluoroborate



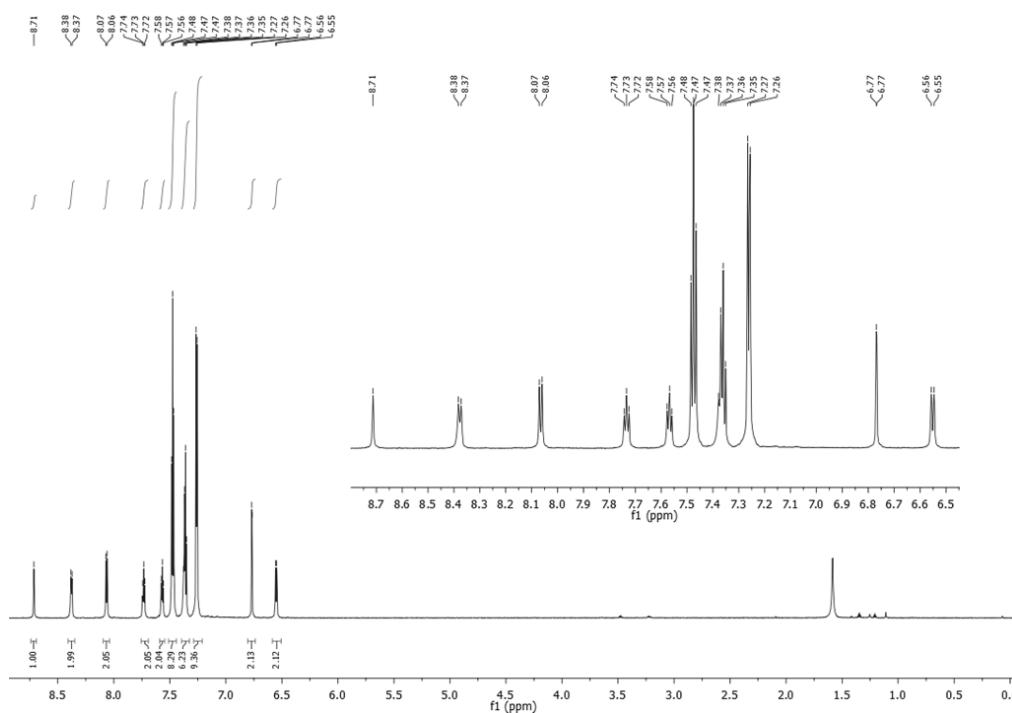
C₅₃H₃₅BF₄N₂, M = 786.66 g/mol

Reagents: 9-(9-anthracenylethynyl)-3,6-bis(diphenylamino)-9H-fluoren-9-ol **O3(anthC₂)^{OH}** (1 eq, 358.4 mg, 0.5 mmol), HBF₄·Et₂O (1.1 eq, 75 μL, 0.55 mmol).

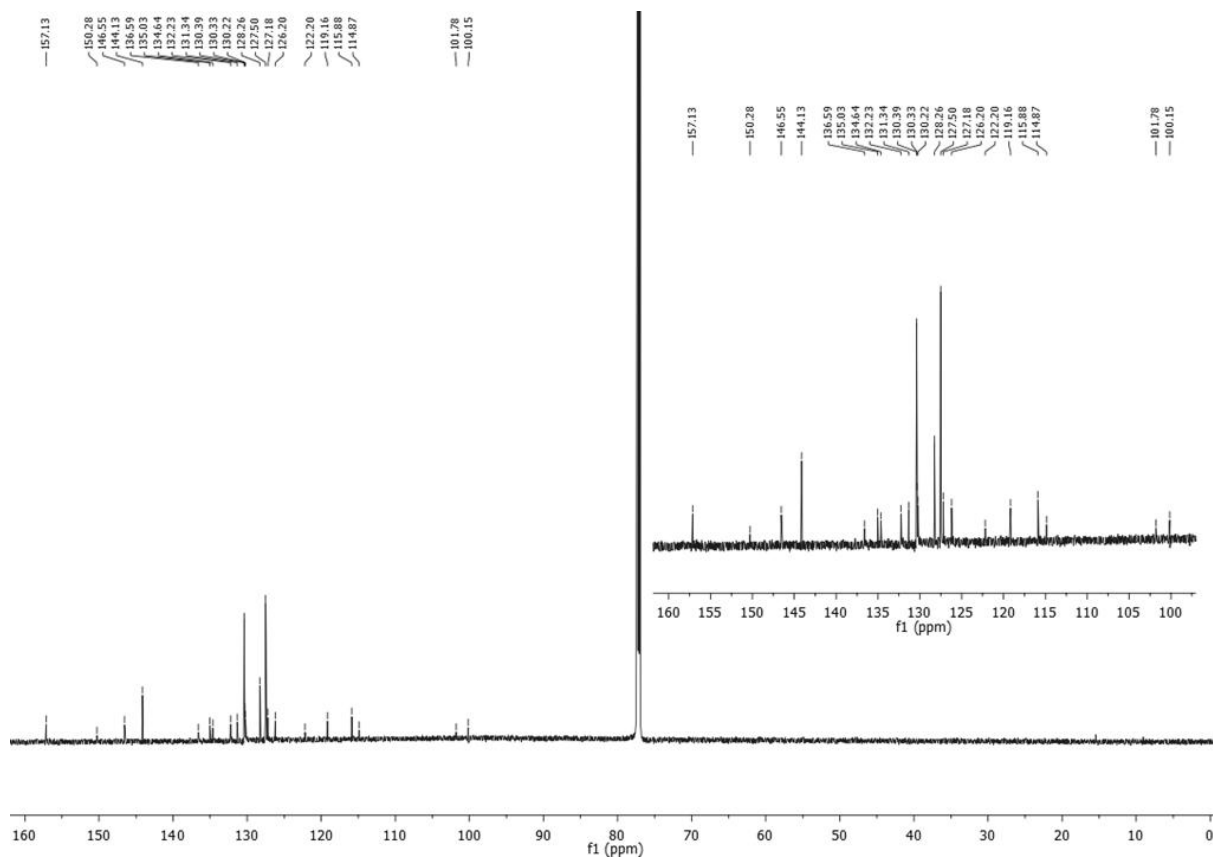
Reaction and work up: Prepared according to **GP3** to obtained 9-(anthracen-9-ylethynyl)-3,6-bis(diphenylamino)-9H-fluoren-9-ylum tetrafluoroborate (**[O3(anthC₂)⁺][BF₄⁻]**) as a violet powder.

Yield: 380 mg (96 %)

¹H NMR (800 MHz, CDCl₃) δ 8.71 (s, 1H), 8.38 (d, *J* = 8.5 Hz, 2H), 8.06 (d, *J* = 8.3 Hz, 2H), 7.73 (t, *J* = 7.6 Hz, 2H), 7.57 (t, *J* = 7.4 Hz, 2H), 7.47 (t, *J* = 7.9 Hz, 8H), 7.36 (q, *J* = 7.4 Hz, 6H), 7.26 (d, *J* = 7.6 Hz, 9H), 6.80 – 6.74 (m, 2H), 6.55 (d, *J* = 8.5 Hz, 2H).



^{13}C NMR (201 MHz, CDCl_3) δ 157.13, 150.28 (C^+), 146.55, 144.13, 136.59, 135.03, 134.64, 132.23, 131.34, 130.39, 130.33, 130.22, 128.26, 127.50, 127.18, 126.20, 122.20, 119.16, 115.88, 114.87, 101.78, 100.15.

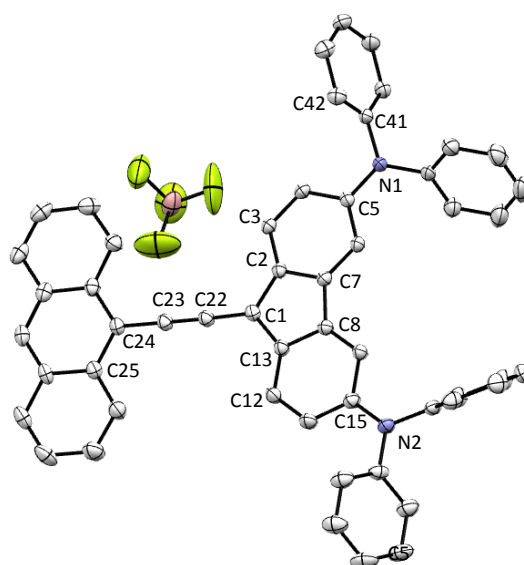


HRMS (ESI): calcd.: 699.27947 $[\text{M}]^+$; found: 699.2789 $[\text{M}]^+$.

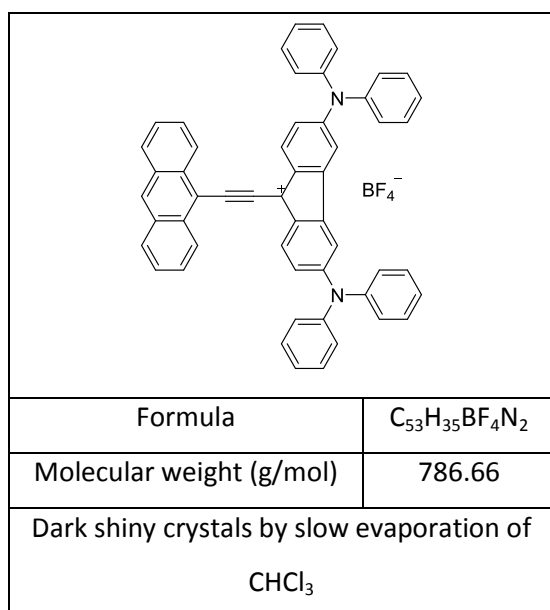
IR (KBr, cm^{-1}): 2132 ($\nu_{\text{C}\equiv\text{C}}$) and 1169 ($\nu_{\text{B-F}}$).

UV-Vis (DCM): λ_{max} , nm (ϵ , $10^{-5} \cdot \text{M}^{-1} \cdot \text{cm}^{-1}$): 257 (0.81), 794 (0.22), 1136 (0.1).

X-ray diffraction study:



ORTEP view of ([O3(anthC₂)⁺][BF₄⁻]) with 50 % thermal ellipsoids solved by Dr. Graeme Moxey



Crystal parameters	
Crystal class	triclinic
Space group	P - 1
Cell angles (°)	$\alpha = 66.92$
	$\beta = 86.09$
	$\gamma = 69.21$
Cell length (Å)	a= 11.99
	b= 13.74
	c= 17.45
Cell volume (Å ³)	2466.53
Z	Z= 2

Selected bond length (Å)

C1 - C22	1.392 (3)	C13 - C12	1.404 (3)
C1 - C13	1.425 (3)	C2- C3	1.397 (4)
C1 - C2	1.430 (3)	C10- N2	1.364 (3)
C13 - C8	1.424 (4)	C5 - N1	1.374 (3)
C2 - C7	1.425 (3)	C8 - C7	1.472 (3)

Selected angles (°)

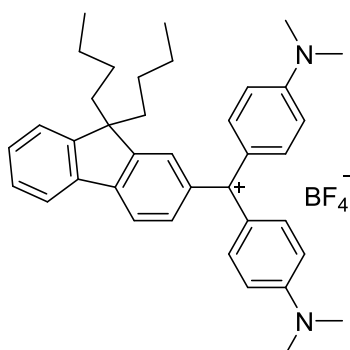
C plan	1.84 (2)	C5- N1/C41 -C42*	62.45 (4)
C1 - C22 - C23	176.45 (3)	C5 - C4/ C41 - C42*	69.11 (3)
C13 - C1/C24 - C25	2.24 (3)		

*torsion angle

(9,9-dibutyl-9H-fluoren-2-yl)bis(4-(dimethylamino)phenyl)methylium

tetrafluoroborate

[[O1(Flu)⁺][BF₄⁻]]



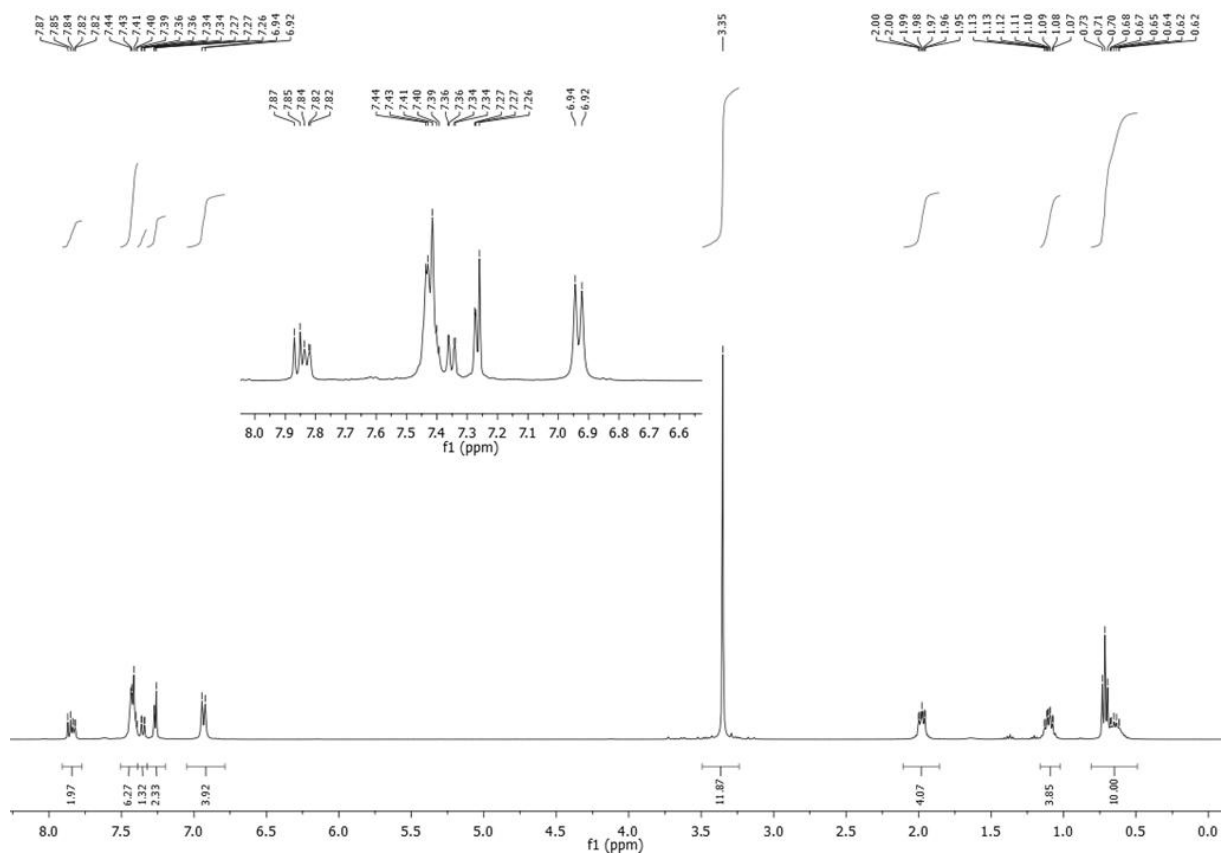
$C_{38}H_{45}BF_4N_2$, $M = 616.58$ g/mol

Reagents: (9,9-dibutyl-9H-fluoren-2-yl)bis(4-(dimethylamino)phenyl)methanol **O3(flu)^{OH}** (1 eq, 273.4 mg, 0.5 mmol), HBF₄·Et₂O (1.1 eq, 75 μL, 0.55 mmol).

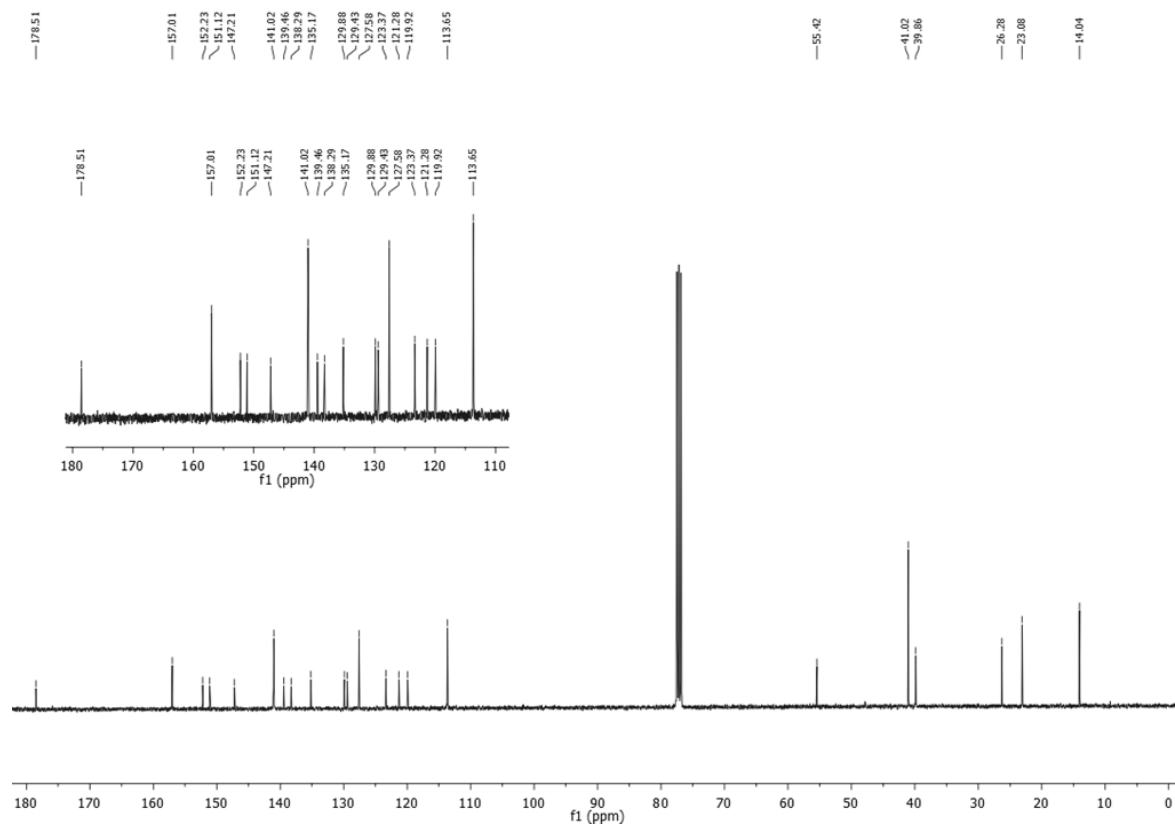
Reaction and work up: Prepared according to **GP3** to obtained (9,9-dibutyl-9H-fluoren-2-yl)bis(4-(dimethylamino)phenyl)methylium tetrafluoroborate **[[O1(Flu)⁺][BF₄⁻]]** as a black powder.

Yield: 277mg (90 %)

¹H NMR (400 MHz, CDCl₃) δ 7.86 (d, $J = 7.9$ Hz, 1H), 7.83 (d, $J = 6.9$ Hz, 1H), 7.42 (m, 7H), 7.35 (d, $J = 7.9$ Hz, 1H), 7.27 (1H under CDCl₃), 6.93 (d, $J = 8.9$ Hz, 4H), 3.35 (s, 12H, -NMe₂), 2.02 – 1.93 (m, 4H), 1.17 – 1.03 (m, 4H), 0.75 – 0.57 (m, 10H).



¹³C NMR (101 MHz, CDCl₃) δ 178.52 (C⁺), 157.02, 152.24, 151.13, 147.22, 141.03, 139.46, 138.29, 135.17, 129.89, 129.43, 127.59, 123.37, 121.29, 119.92, 113.65, 55.42, 41.02 (-NMe₂), 39.85, 26.27, 23.07, 14.03.

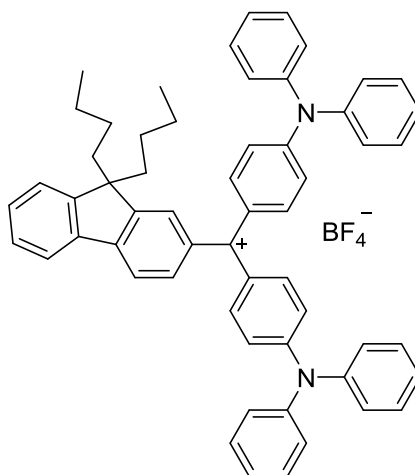


HRMS (ESI): calcd.: 529.35827 [M]⁺; found: 529.3577 [M]⁺.

IR (cm⁻¹): 1168 (ν_{B-F})

UV-Vis (DCM): λ_{max}, nm (ε, 10⁻⁵·M⁻¹·cm⁻¹): 313 (0.22), 489 (0.47), 624 (1.26).

(9,9-dibutyl-9H-fluoren-2-yl)bis(4-(diphenylamino)phenyl)methylium **tetrafluoroborate**
[[O2(flu)]⁺][BF₄⁻]



C₅₈H₅₃BF₄N₂, M = 864.86 g/mol

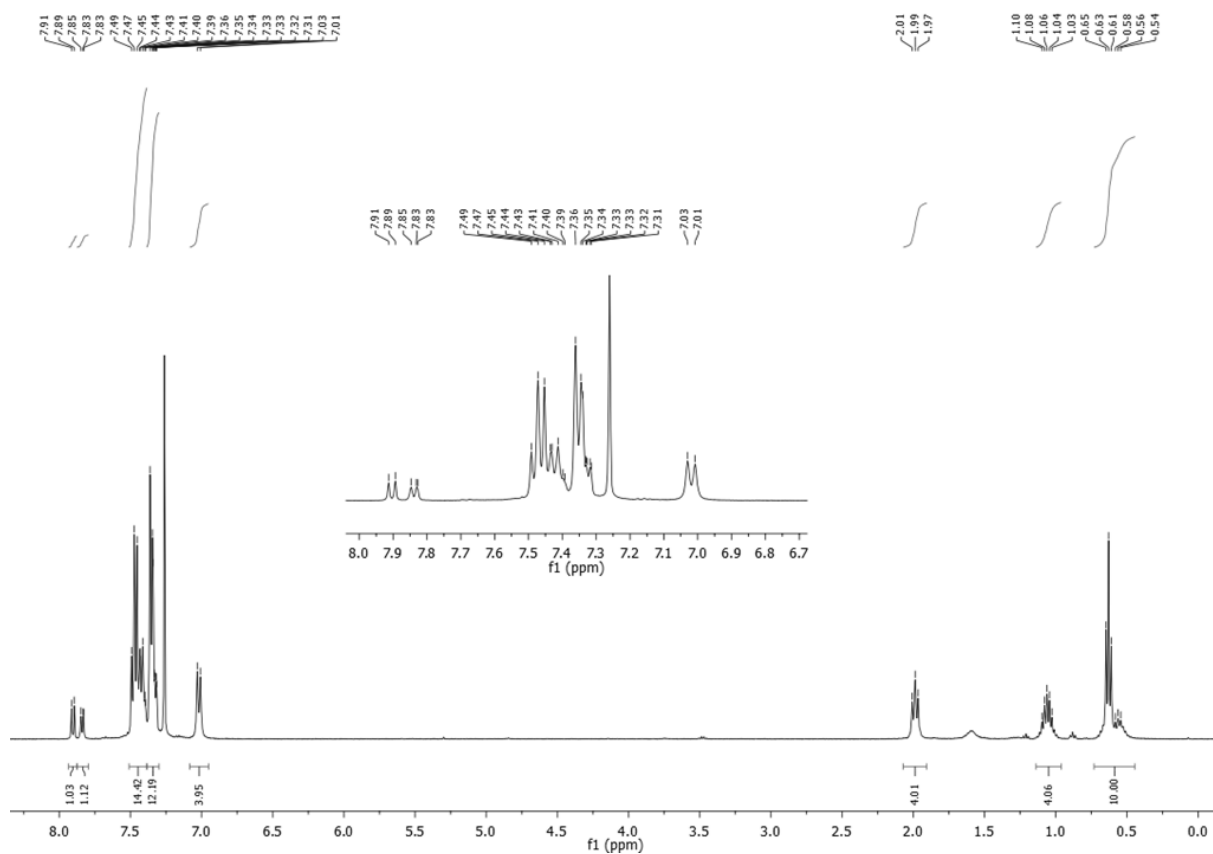
Reagents: (9,9-dibutyl-9H-fluoren-2-yl)bis(4-(diphenylamino)phenyl)methanol **O3(flu)**^{OH} (1 eq, 425.6 mg, 0.5 mmol), HBF₄·Et₂O (1.1 eq, 75 μL, 0.55 mmol).

Reaction and work up: Prepared according to **GP3** to obtained (9,9-dibutyl-9H-fluoren-2-yl)bis(4-(diphenylamino)phenyl)methylium tetrafluoroborate **[[O2(flu)]⁺][BF₄⁻]** as a violet powder.

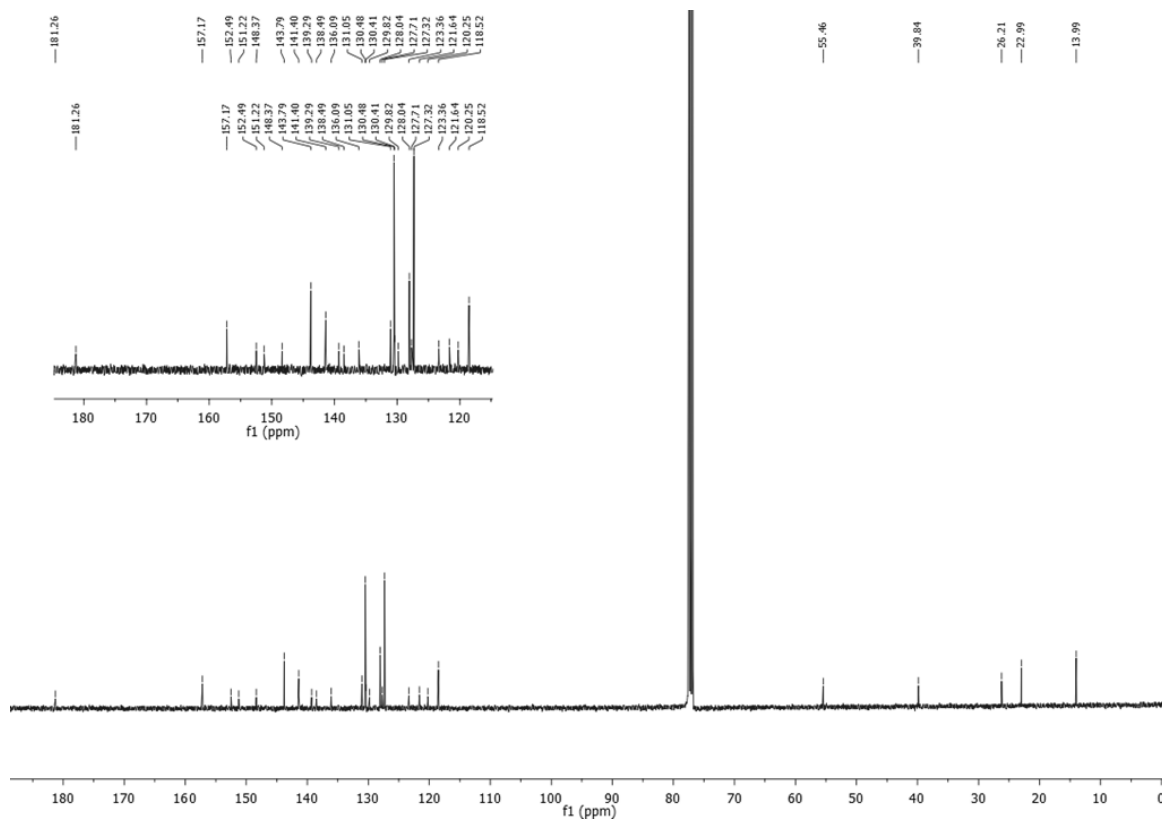
Yield: 296mg (70 %)

nb: quantitative but loss of product during washes, partially soluble in Et₂O.

¹H NMR (400 MHz, (CD₃)₂CO) δ 8.13 (d, J = 7.9 Hz, 1H), 8.02 (d, J = 7.3 Hz, 1H), 7.61 – 7.42 (m, 29H), 7.06 (d, J = 8.9 Hz, 4H), 2.18 – 2.07 (m, 4H), 1.13 – 1.07 (m, 4H), 0.69 – 0.58 (m, 10H).



¹³C NMR (101 MHz, CDCl₃) δ 181.12 (C⁺), 157.03, 152.35, 151.08, 148.23, 143.65, 141.26, 139.15, 138.35, 135.94, 130.91, 130.34, 129.67, 127.90, 127.57, 127.18, 123.22, 121.50, 120.11, 118.37, 55.31, 39.69, 26.06, 22.83, 13.83.

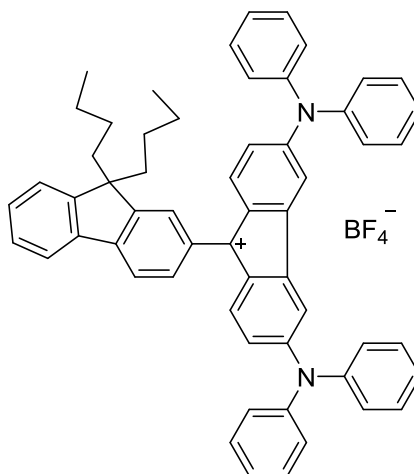


HRMS (ESI): calcd.: 777.42033 [M]⁺; found: 777.4204 [M]⁺.

IR (cm⁻¹): 1167 (ν_{B-F}).

UV-Vis (DCM): λ_{max}, nm (ε, 10⁻⁵·M⁻¹·cm⁻¹): 284 (0.35), 532(0.48), 666 (0.89).

9,9-dibutyl-3',6'-bis(diphenylamino)-9H-[2,9'-bifluoren]-9'-ylium tetrafluoroborate ([O3(flu)]⁺)[BF₄⁻]



C₅₈H₅₁BF₄N₂, M = 862.84 g/mol

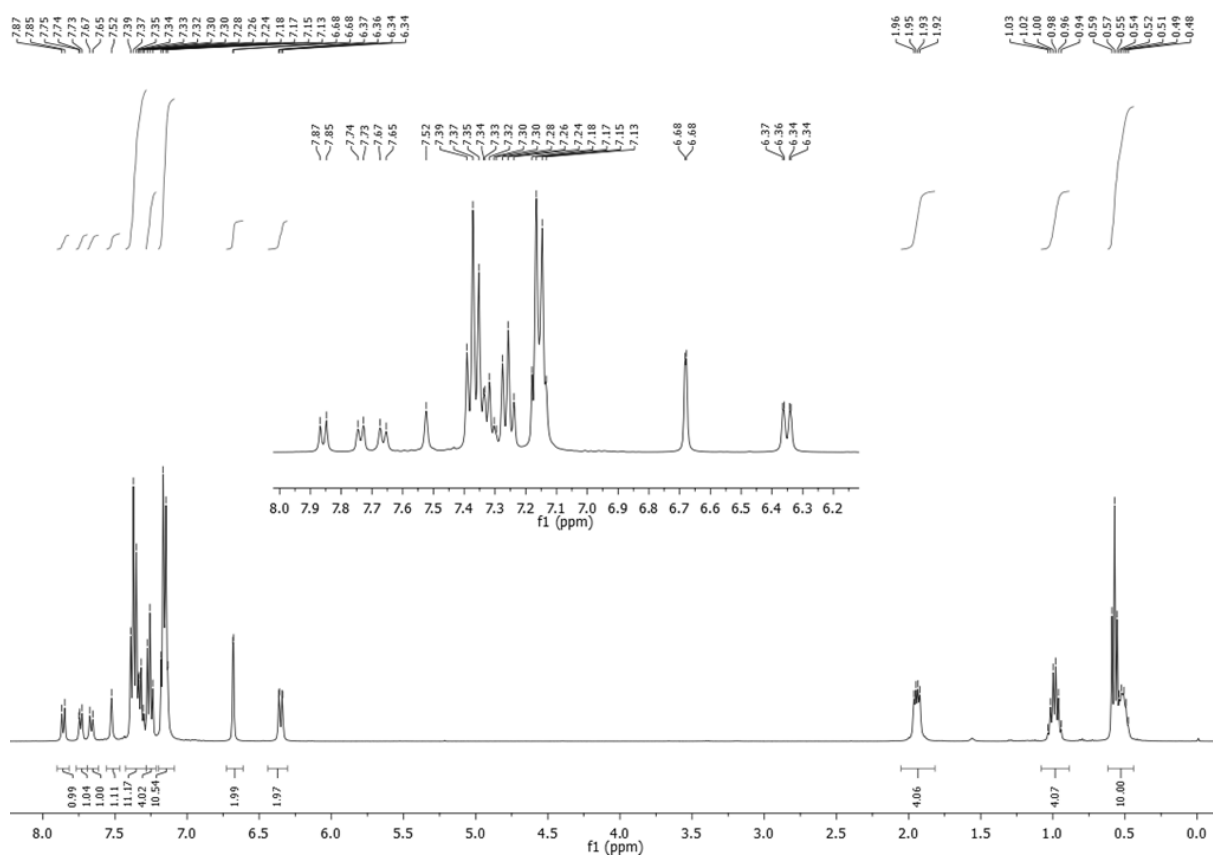
Reagents: 9,9-dibutyl-3',6'-bis(diphenylamino)-9H,9'H-[2,9'-bifluoren]-9'-ol **O3(flu)**^{OH} (1 eq, 396.5 mg, 0.5 mmol), HBF₄·Et₂O (1.1 eq, 75 μL, 0.55 mmol).

Reaction and work up: Prepared according to **GP3** to obtained (9,9-dibutyl-9H-fluoren-2-yl)bis(4-(diphenylamino)phenyl)methyl cation tetrafluoroborate (**[O3(flu)]⁺**)[BF₄⁻] as a violet powder.

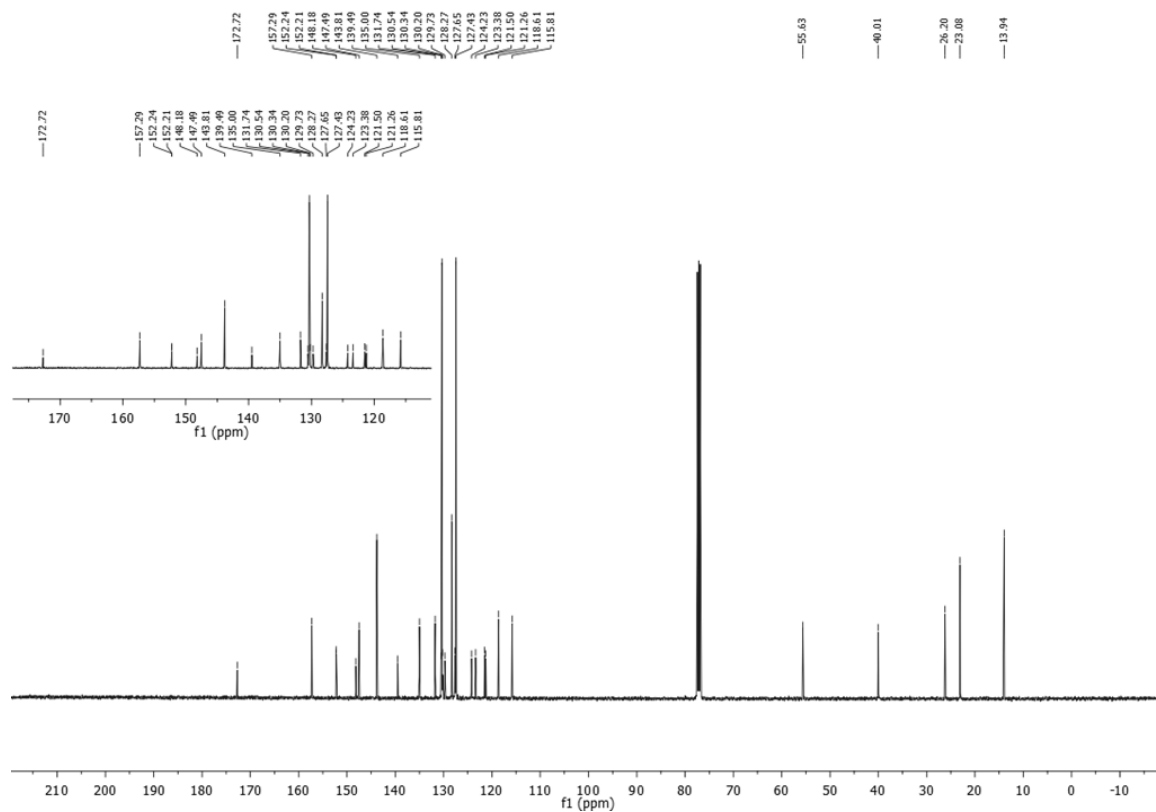
Yield: 350 mg (81 %)

nb: quantitative but loss of product during washes, partially soluble in ether.

¹H NMR (400 MHz, CDCl₃) δ 7.94 (d, *J* = 7.9 Hz, 1H), 7.82 (d, *J* = 7.0 Hz, 1H), 7.74 (d, *J* = 7.8 Hz, 1H), 7.60 (s, 1H), 7.42 (m, 11H), 7.34 (t, *J* = 7.4 Hz, 4H), 7.24 (m, 10H), 6.76 (d, *J* = 1.8 Hz, 2H), 6.43 (d, *J* = 8.7 Hz, 2H), 2.02 (m, 4H), 1.07 (m, 4H), 0.74 – 0.50 (m, 10H).



¹³C NMR (101 MHz, CDCl₃) δ 172.73 (C⁺), 157.30, 152.24, 152.22, 148.18, 147.50, 143.81, 139.49, 135.01, 131.74, 130.55, 130.35, 130.20, 129.73, 128.27, 127.66, 127.43, 124.23, 123.38, 121.51, 121.26, 118.61, 115.82, 55.63, 40.01, 26.20, 23.08, 13.94.

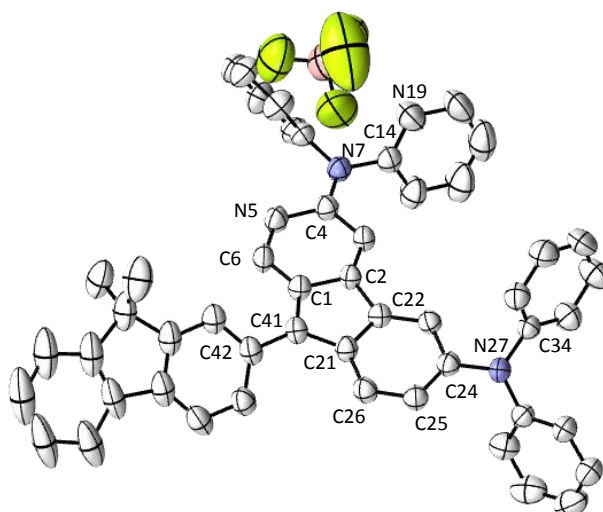


HRMS (ESI): calcd.: 775.4068 [M]⁺; found: 775.4050 [M]⁺.

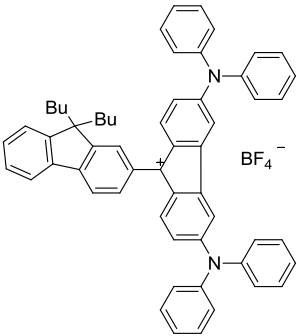
IR (cm⁻¹): 1279 (ν_{B-F}).

UV-Vis (DCM): λ_{max}, nm (ε, 10⁻⁵·M⁻¹·cm⁻¹): 275 (0.64), 379 (0.25), 637 (0.53), 923 (0.23), 1048 (0.32).

X-ray diffraction study:



ORTEP view of ([O3(flu)]⁺)[BF₄⁻] with 50 % thermal ellipsoids solved by Dr. Thierry Roisnel. Molecule of H₂O and butyl chains not displayed for visibility.

	
Formula	C ₅₈ H ₅₁ BF ₄ N ₂
Molecular weight (g/mol)	862.84
Dark shiny crystals by slow diffusion of Et ₂ O vapor into a DCM solution of the molecule at room temperature.	

Crystal parameters	
Crystal class	monoclinic
Space group	P 2 ₁ /c
Cell angles (°)	α= 90
	β= 111.35
	γ= 90
Cell length (Å)	a= 21.09
	b= 9.35
	c= 26.28
Cell volume (Å ³)	4827.99
Z	Z= 4

Selected bond length (Å)

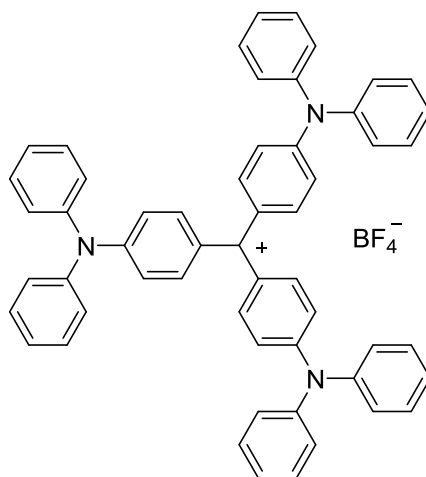
C41 - C42	1.465 (4)	C21 - C22	1.485 (6)
C41 - C1	1.404 (4)	C1 - C2	1.440 (5)
C41 - C21	1.466 (5)	C22 - C2	1.471 (5)
C26 - C25	1.387 (5)	C24 - N27	1.408 (4)
C6 - C5	1.353 (4)	C4 - N7	1.348 (4)

Selected angles (°)

C5 - C4/ C14 - C19*	62.16 (3)	C47 - C42/C41 - C1*	35.25 (3)
C5 - C4/ N7 - C14*	7.49 (5)	C23 - 24/ N27 - C34*	38.37 (4)

*torsion angle

4,4',4''-methyliumtriyltris(N,N-diphenylaniline) tetrafluoroborate ([O4⁺][BF₄⁻])



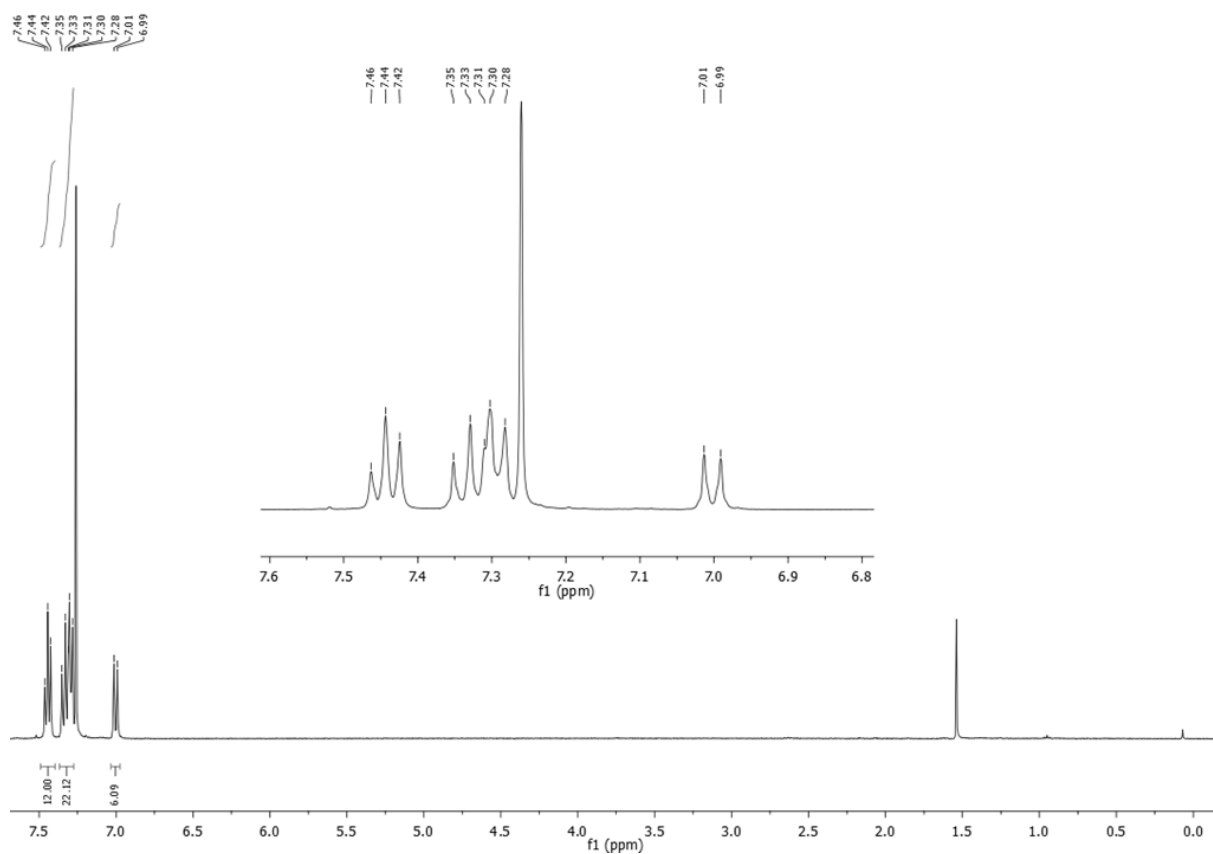
C₅₅H₄₃BF₄N₃, M = 832.75 g/mol

Reagents: tris(4-(diphenylamino)phenyl)methanol **O4^{OH}** (1 eq, 190.5 mg, 0.25 mmol), HBF₄·Et₂O (1.1 eq, 37 µL, 0.275 mmol).

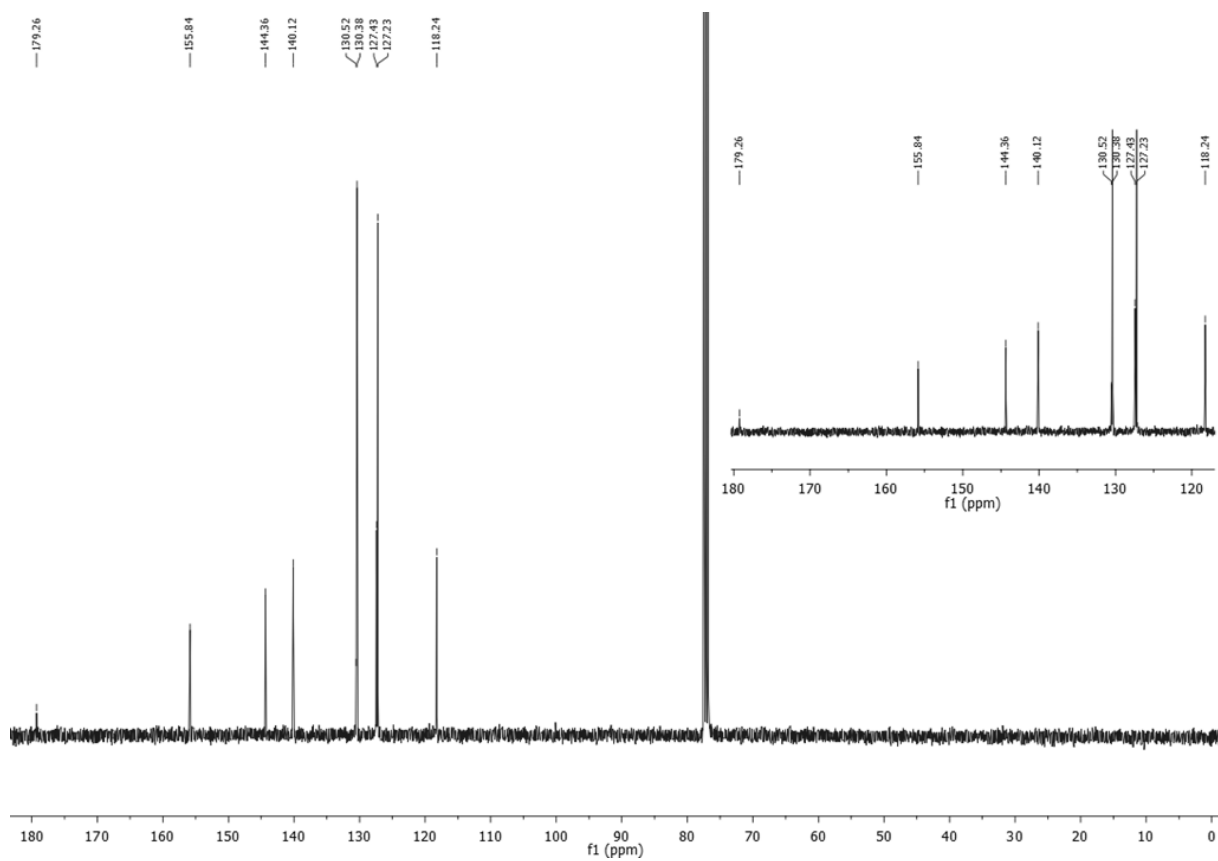
Reaction and work up: Prepared according to **GP3** to obtain the desired product tris(4-(diphenylamino)phenyl)methanol **([O4⁺][BF₄⁻])** as a blue powder.

Yield: quant.

¹H NMR (400 MHz, CDCl₃) δ 7.44 (t, *J* = 7.7 Hz, 12H), 7.37 – 7.28 (m, 22H), 7.00 (d, *J* = 9.0 Hz, 6H).



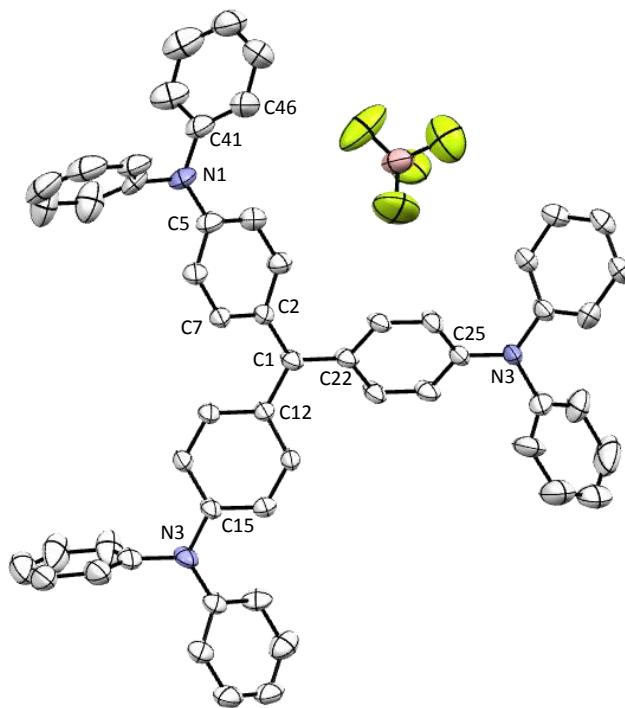
¹³C NMR (101 MHz, CDCl₃) δ 179.26 (C⁺), 155.84, 144.36, 140.12, 130.52, 130.38, 127.43, 127.23, 118.24.



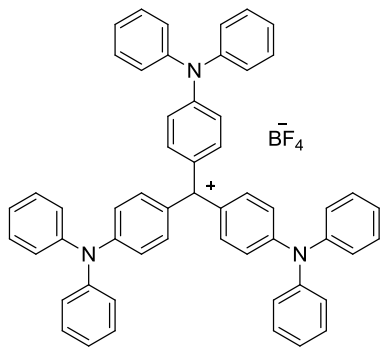
UV-Vis (DCM): λ_{\max} , nm (ϵ , $10^{-5} \cdot \text{M}^{-1} \cdot \text{cm}^{-1}$): 289 (0.35), 644 (1.05).

HRMS: calcd.: 744.3379 $[\text{M}]^+$, found: 744.3400 $[\text{M}]^+$.

X-ray diffraction study:



ORTEP view of $[(\text{O}4^+)](\text{BF}_4^-)$ with 50 % thermal ellipsoids solved by Dr. Graeme Moxey

	
Formula	$\text{C}_{55}\text{H}_{43}\text{BF}_4\text{N}_3$
Molecular weight (g/mol)	832.75
Dark shiny crystals by slow diffusion of Et_2O vapor in a DCM solution of the molecule at room temperature	

Crystal parameters	
Crystal class	triclinic
Space group	$P 3_1$
Cell angles ($^\circ$)	$\alpha = 90$
	$\beta = 90$
	$\gamma = 120$
Cell length (\AA)	$a = 18.21$
	$b = 18.21$
	$c = 45.57$
Cell volume (\AA^3)	13085.7
Z	$Z = 12$

Selected bond length (Å)

C1 - C2	1.417 (10)	C1 - C22	1.437 (8)
C1 - C12	1.450 (10)	N1 - C5	1.379 (9)
C15-N2	1.367 (10)	C25-N3	1.370 (8)

Selected angles (°)

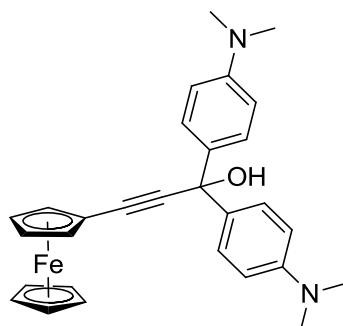
C plan	3.29 (1)	C5 - N1/C41 - C46*	83.63 (7)
C1 - C12 / C2 - C7*	30.13 (7)		

*torsion angle

6. Synthesis of organometallic derivatives

6.1. Ferrocene carbinols

Ferrocene-[3,3-[4-(dimethylamino)phenyl]-3-hydroxy-1-propenyl] (**M1(Fc)^{OH}**)



$C_{29}H_{30}FeN_2O$, $M = 478.41$ g/mol

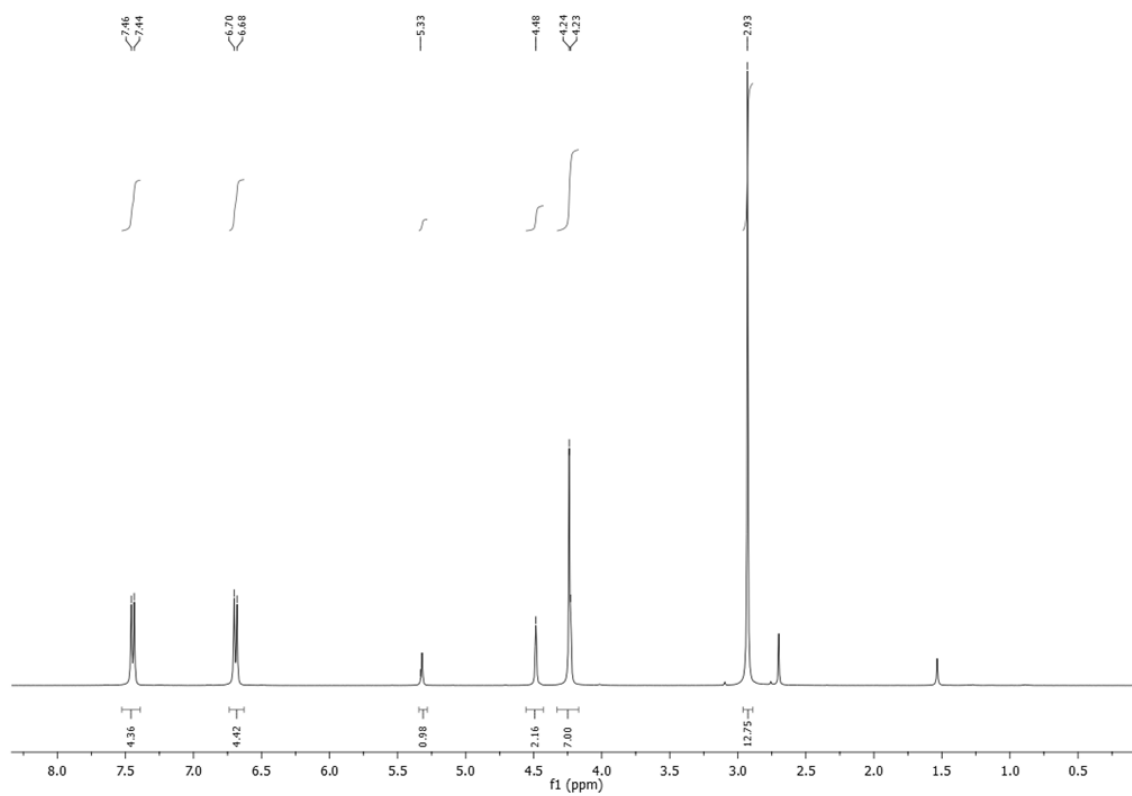
Reagents: Ethynylferrocene **35** (1.1 eq, 682 mg, 3.2 mmol), *n*-BuLi (1.1 eq, 2 mL at 1.6 M in hexane, 3.2 mmol), Michler's ketone **28** (1 eq, 805 mg, 3 mmol).

Reaction and work up: Prepared according to **GP1**.

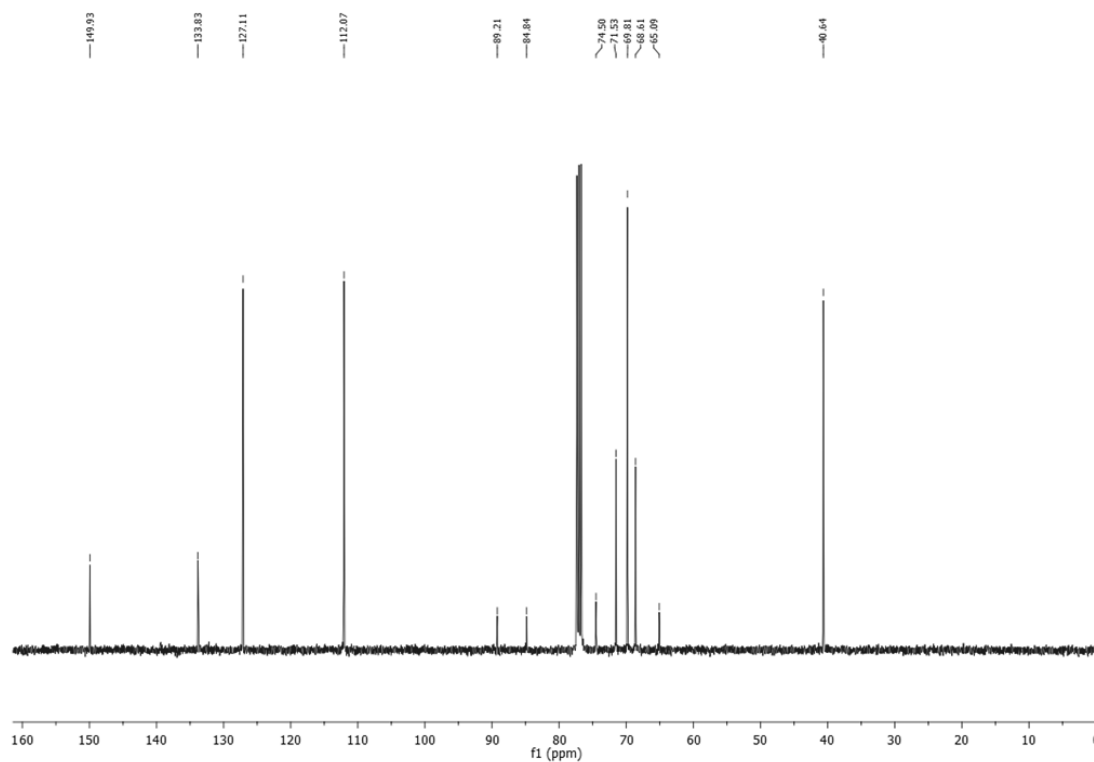
Purification: The crude was dissolved in DCM and precipitated in hexane two times to give the desired ferrocene-[3,3-[4-(dimethylamino)phenyl]-3-hydroxy-1-propenyl] **M1(Fc)^{OH}** as an orange solid.

Yield: 810 mg (56 %).

^1H NMR (400 MHz, CD_2Cl_2) δ 7.45 (d, $J = 8.7$ Hz, 4H), 6.69 (d, $J = 8.7$ Hz, 4H), 5.33 (s, 1H, -OH), 4.48 (s, 2H), 4.24 (s, 7H, Cp), 2.93 (s, 12H, -NMe₂).



^{13}C NMR (101 MHz, CDCl_3) δ 150.04, 133.95, 127.22, 112.19, 89.33, 84.96, 74.62 (C-OH), 71.65, 69.93, 68.72, 65.21, 40.76.



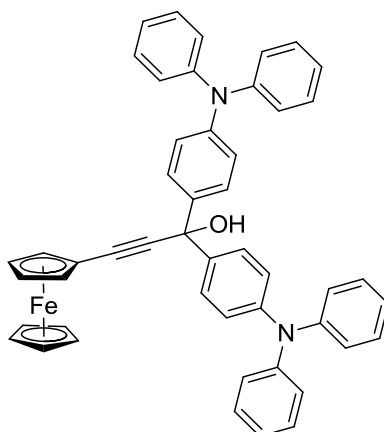
HRMS: Calcd: 461.16801 [M-OH]⁺, 479.17858 [M+H]⁺, 478.17075 [M]⁺; found: 461.1675 [M-OH]⁺, 479.1797 [M+H]⁺, 478.1733 [M]⁺.

IR (KBr, cm⁻¹): 3191 (ν_{O-H}), 2222 (ν_{C≡C}), 820 (δ_{C-H} Fc).

UV-Vis: (DCM): λ_{max}, nm (ε, 10⁻⁵·M⁻¹·cm⁻¹): 270 (0.40).

CV (DCM, 0.10 M [*n*-Bu₄N][PF₆], V vs SCE): M^{III}/M^{II}: E_{1/2}: 0.55 (ΔE_p = 0.06 V; *i*_{pc}/*i*_{pa} = 0.98), amine oxidation: E_{pc} (V): 0.83V.

[3,3-[4-(diphenylamino)phenyl]-3-hydroxy-1-propenyl]ferrocene (M2(Fc)^{OH})



C₄₉H₃₈FeN₂O, M = 726.23 g/mol

Reagents: Ethynylferrocene **35** (1.1 eq, 231 mg, 1 mmol), *n*-BuLi (1.1 eq, 687.5 μL at 1.6 M in hexane, 1.1 mmol), 4,4'-bis(diphenylaminobenzophenone) **29** (1 eq, 516 mg, 1 mmol).

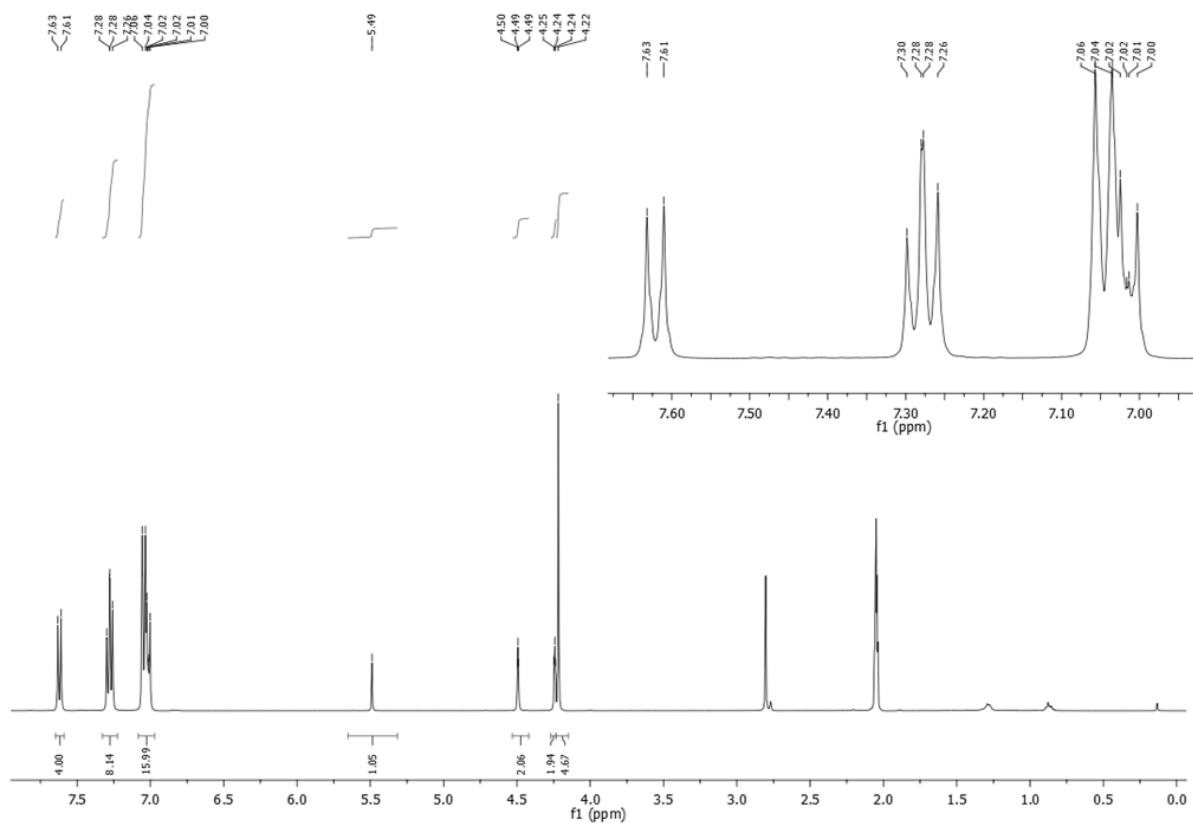
Reaction and work up: Prepared according to **GP1**.

Purification: The crude orange solid was adsorbed on deactivated silica and purified by column chromatography (neutralized silica gel with 10 % NEt₃, 20 x 5 cm) eluting with hexane/Et₂O (4/1) with 1 % NEt₃ to give [3,3-[4-(diphenylamino)phenyl]-3-hydroxy -1-propenyl]ferrocene **M2(Fc)^{OH}** as an orange solid.

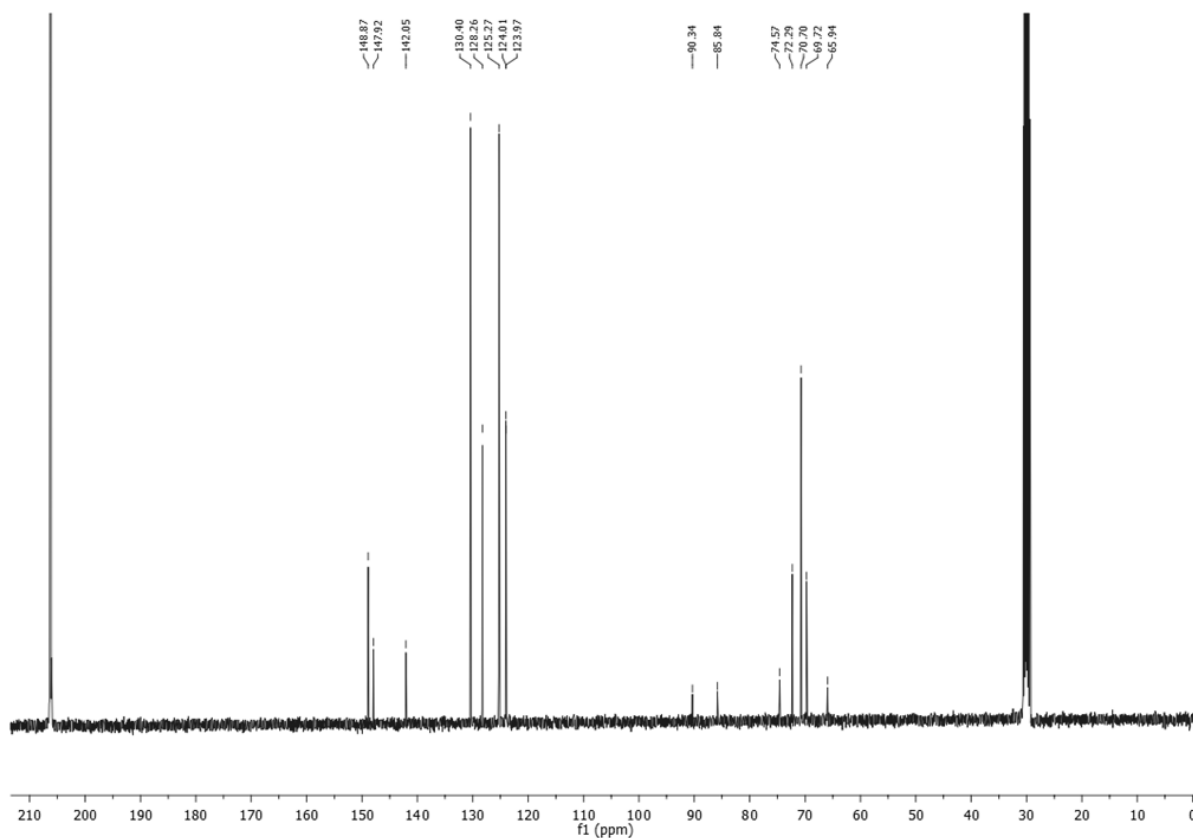
R_f(hexane/Et₂O, 4/1): 0.4

Yield: 480 mg (64 %)

¹H NMR (400 MHz, (CD₃)₂CO) δ 7.62 (d, *J* = 8.7 Hz, 4H), 7.28 (m, *J* = 8.4, 7.4 Hz, 8H), 7.08 – 6.97 (m, 16H), 5.49 (s, 1H, -OH), 4.49 (t, *J* = 1.8 Hz, 2H), 4.27 – 4.23 (t, *J* = 1.8 Hz, 2H), 4.22 (s, 5H, Cp).



¹³C NMR (101 MHz, (CD₃)₂CO) δ 148.87, 147.92, 142.05, 130.40, 128.26, 125.27, 124.01, 123.97, 90.34, 85.84, 74.57 (C-OH), 72.29, 70.70, 69.72, 65.94.



HRMS(ESI): calcd.: 709.23006[M-.OH]⁺, 749.22257[M+Na]⁺, 765.19651[M+K]⁺; found :709.2299[M-.OH]⁺,749.2225[M+Na]⁺, 765.1975[M+K]⁺.

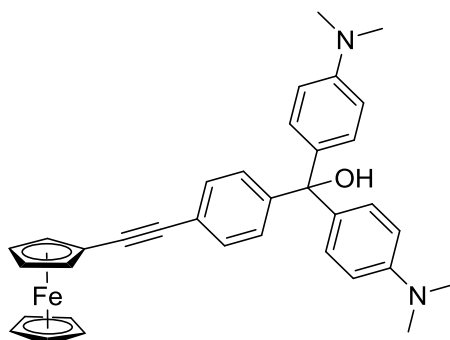
IR (KBr.cm⁻¹): 3574.67 (ν_{O-H}), 2224.61 (ν_{C≡C}), 821.63 (s, δ_{C-H} Fc).

EA: calcd. for C₄₉H₃₈FeN₂O: C = 80.99; H= 5.27; Fe= 7.68; N= 3.85; O= 2.20, found: C = 80.81; H= 5.19; N= 3.78.

UV-Vis: (DCM): λ_{max}, nm (ε, 10⁻⁵·M⁻¹·cm⁻¹): 302 (0.58).

CV: (DCM, 0.10 M [*n*-Bu₄N][PF₆], V vs SCE): M^{III}/M^{II}: E_{1/2}: 0.56 (ΔE_p = 0.02 V, *i*_{pc}/*i*_{pa}= 1.0), amine oxidation: E_{pc} (V): 0.94.

4-ethynylferrocene-[3,3-[4-(dimethylamino)phenyl]-3-hydroxy-1-benzene] (M3(Fc)^{OH})



C₃₅H₃₄FeN₂O, M = 554.50 g/mol

Reagents: *p*-bromo(ferrocenylethynyl)benzene **36** (1.2 eq, 438 mg, 1.2 mmol), *n*-BuLi (1.1 eq, 687.5 μL at 1.6 M in hexane, 1.1 mmol), Michler'sketone **28** (1 eq, 268.3 mg, 1 mmol).

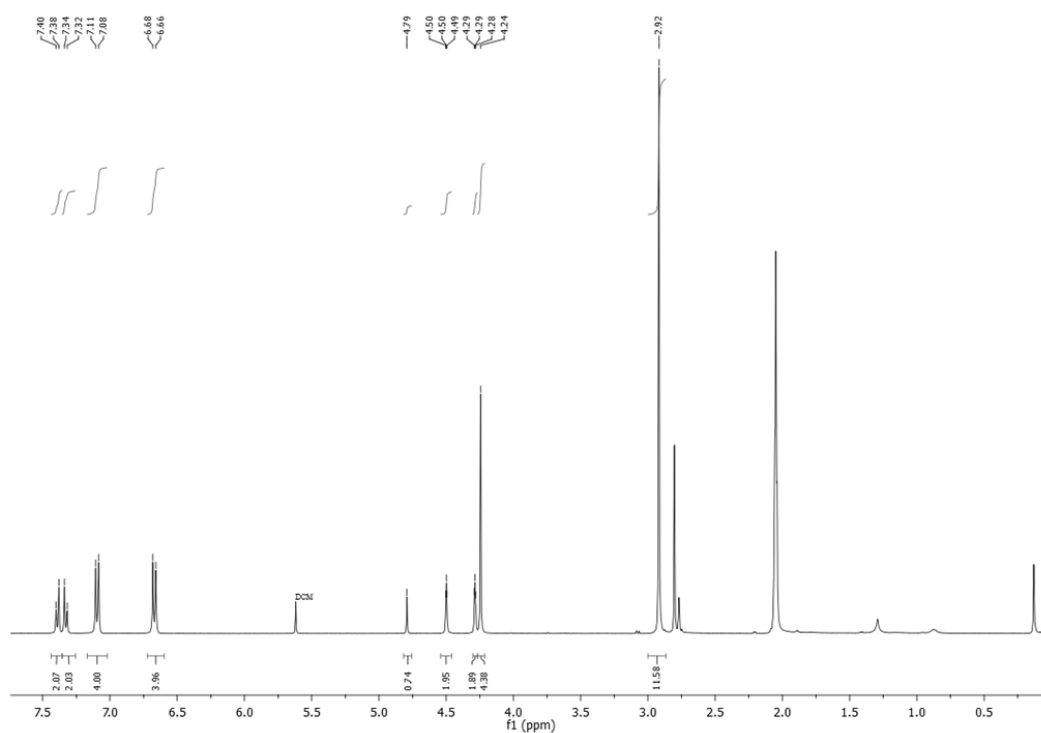
Reaction and work up: Prepared according to **GP1**.

Purification: The crude brown solid was adsorbed on deactivated silica and purified by column chromatography (neutralized silica gel with 10 % NEt₃, 15 x 5 cm) eluting with a gradient of hexane/Et₂O (9/1) to (1/1) with 1 % NEt₃ to obtain 4-ethynylferrocene-[3,3-[4-(dimethylamino)phenyl]-3-hydroxy-1-benzene] **M3(Fc)^{OH}** as an orange solid. A final precipitation from acetone/H₂O carried out to purify the product.

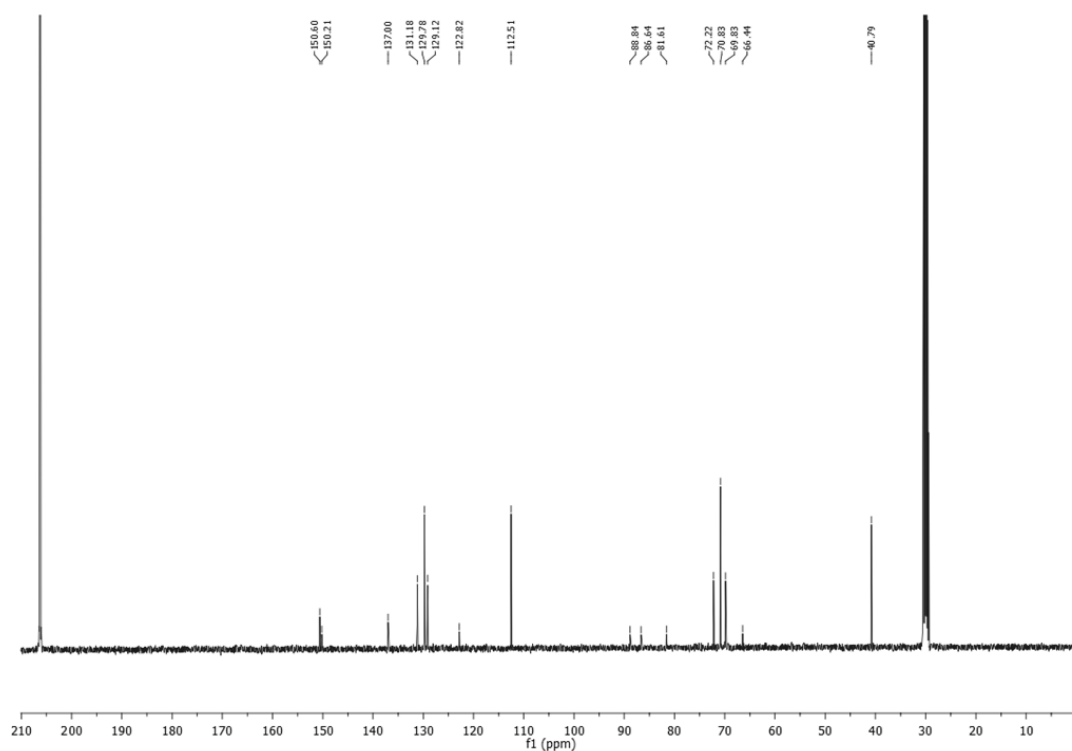
R_f (hexane): 0.2

Yield: (290 mg) 52 %

^1H NMR (400 MHz, $(\text{CD}_3)_2\text{CO}$) δ 7.39 (d, J = 8.5 Hz, 2H), 7.33 (d, J = 8.4 Hz, 2H), 7.10 (d, J = 8.9 Hz, 4H), 6.67 (d, J = 8.9 Hz, 4H), 4.79 (s, 1H, -OH), 4.54 – 4.46 (m, 2H), 4.30 – 4.27 (m, 2H), 4.24 (s, 5H, Cp), 2.92 (s, 12H).



^{13}C NMR (101 MHz, $(\text{CD}_3)_2\text{CO}$) δ 150.60, 150.21, 137.00, 131.18, 129.78, 129.12, 122.82, 112.51, 88.84, 86.64, 81.61 (C-OH), 72.22, 70.83, 69.83, 66.44, 40.79 ($-\text{NMe}_2$).



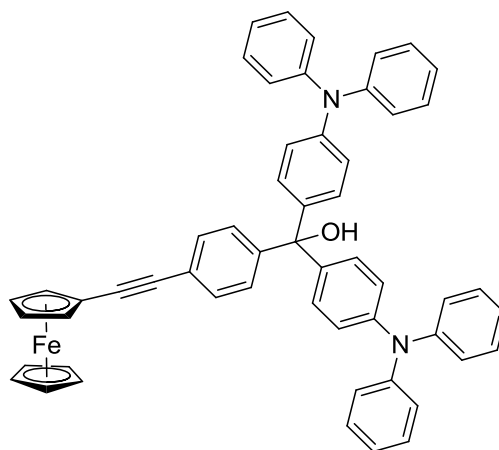
HRMS (ESI): calcd. : 554.20205 $[M]^+$, 537.19931 $[M-.OH]^+$; found: 554.2020 $[M]^+$, 537.20 $[M-.OH]^+$.

IR (KBr. cm^{-1}): 3205 ($\nu_{\text{O-H}}$), 2206 ($\nu_{\text{C}\equiv\text{C}}$), 820 (s, $\delta_{\text{C-H Fc}}$).

UV-VIS: (DCM): λ_{max} , nm (ϵ , $10^{-5}\cdot\text{M}^{-1}\cdot\text{cm}^{-1}$): 263 (0.60), 292 (0.32).

CV: (DCM, 0.10 M $[n\text{-Bu}_4\text{N}][\text{PF}_6]$, V vs SCE): $\text{M}^{\text{III}}/\text{M}^{\text{II}}$: $E_{1/2}$: 0.52 ($\Delta E_p = 0.08$ V, $i_{pc}/i_{pa} = 0.98$), amine oxidation: E_{pc} (V): 0.74 V.

4-ethynylferrocene-[3,3-[4-(diphenylamino)phenyl]-3-hydroxy-1-benzene] ($\text{M4}(\text{Fc})^{\text{OH}}$)



$\text{C}_{55}\text{H}_{42}\text{FeN}_2\text{O}$, $M = 802.78$ g/mol

Reagents: *p*-bromo(ferrocenylethynyl)benzene **36** (1.2 eq, 219 mg, 0.6 mmol), *n*-BuLi (1.1 eq, 344 μL at 1.6 M in hexane, 0.55 mmol), 4,4'-bis(diphenylaminobenzophenone (1 eq, 258 mg, 0.5 mmol).

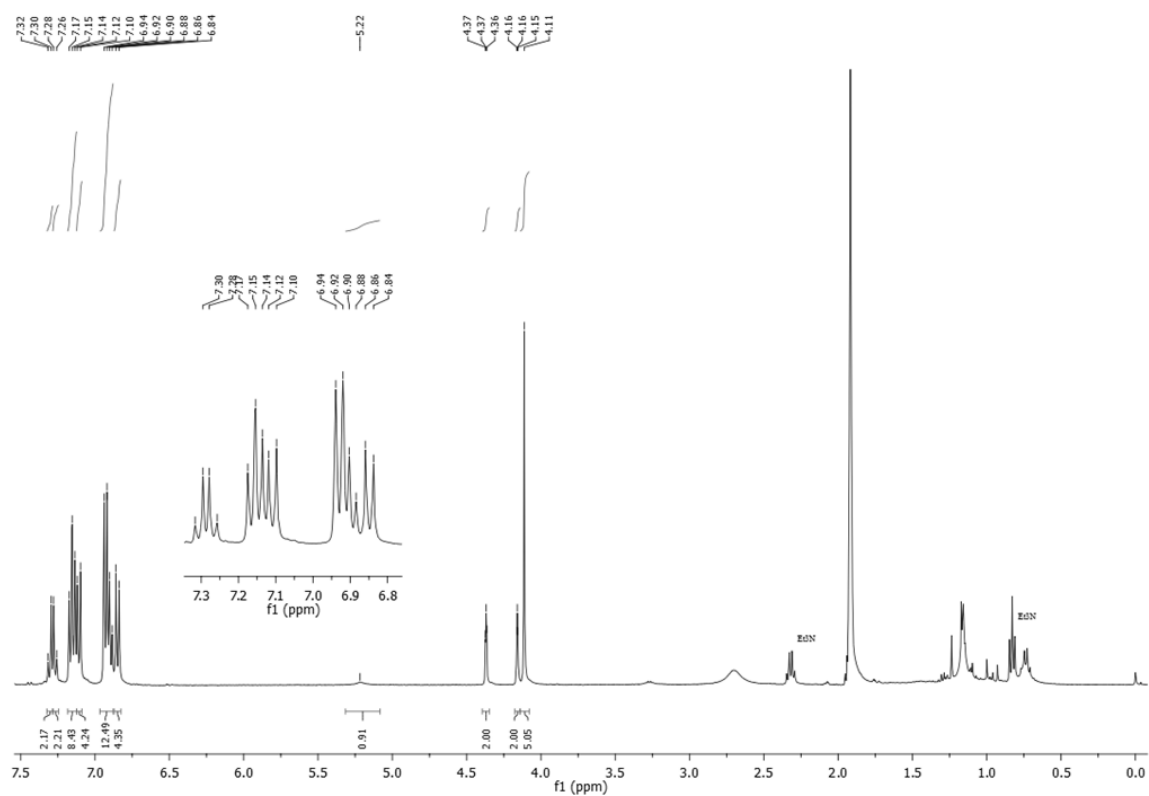
Reaction and work up: Prepared according to **GP1**.

Purification: The crude orange solid was adsorbed on deactivated silica and purified by column chromatography (neutralized silica gel with 10 % NEt_3 , 15 x 5 cm) eluting with hexane/ Et_2O (9/1) with 1 % NEt_3 to give 4-ethynylferrocene-[3,3-[4-(diphenylamino)phenyl]-3-hydroxy-1-benzene] **M4(Fc)^{OH}** as an orange solid.

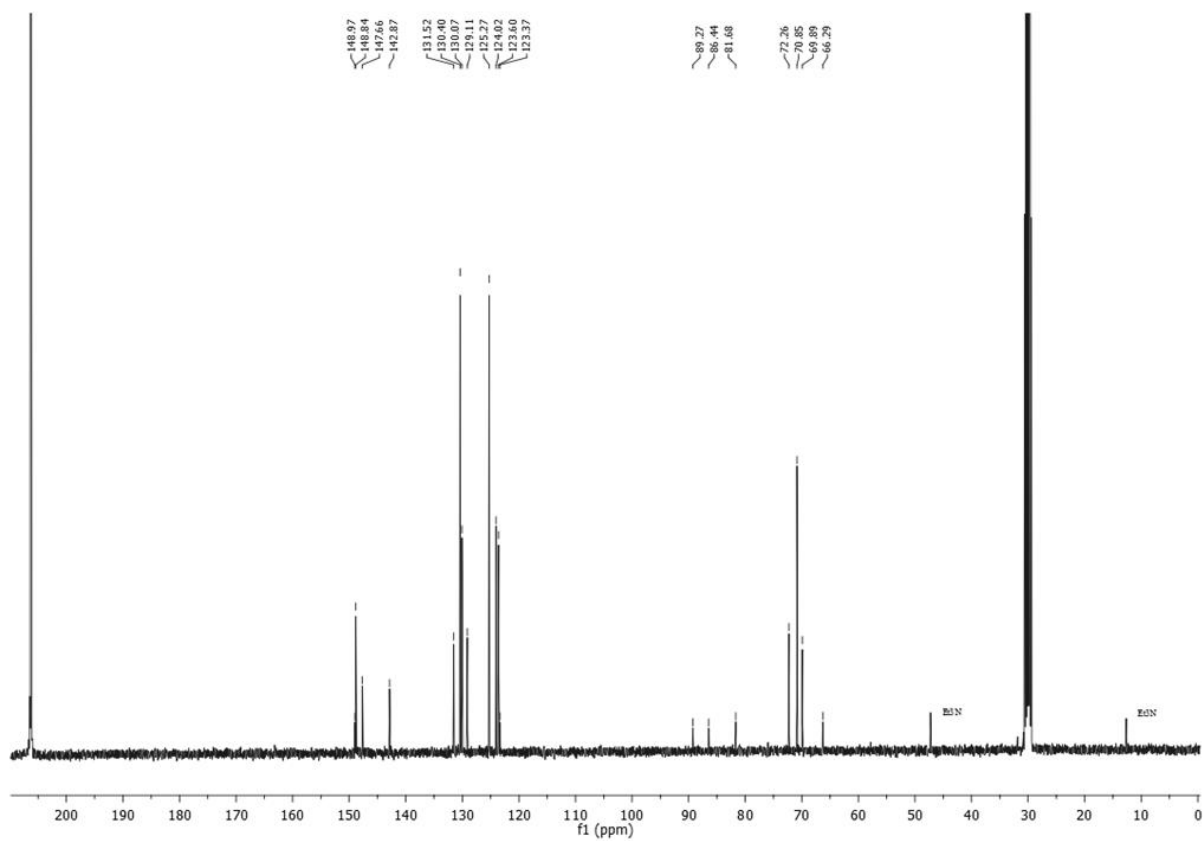
R_f (hexane/ Et_2O , 19/1): 0.34

Yield: 380 mg (94%)

^1H NMR (400 MHz, $(\text{CD}_3)_2\text{CO}$) δ 7.31 (d, $J = 8.5$ Hz, 2H), 7.27 (d, $J = 8.6$ Hz, 2H), 7.15 (t, $J = 7.9$ Hz, 8H), 7.11 (d, $J = 8.7$ Hz, 4H), 6.91 (m, 12H), 6.85 (d, $J = 8.7$ Hz, 4H), 5.22 (s, 1H, -OH), 4.39 – 4.35 (m, 2H), 4.17 – 4.14 (m, 2H), 4.11 (s, 5H, Cp).



¹³C NMR (101 MHz, (CD₃)₂CO) δ 148.97, 148.84, 147.66, 142.87, 131.52, 130.40, 130.07, 129.11, 125.27, 124.02, 123.60, 123.37, 89.27, 86.44, 81.68 (C-OH), 72.26, 70.85, 69.89, 66.29.



HRMS (ESI): calcd. : 802.2641[M]⁺, 785.26136 [M-.OH]⁺; found: 802.2640 [M]⁺, 785.2610 [M-.OH]⁺.

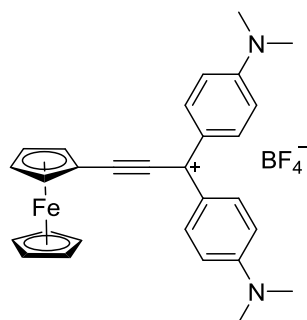
IR (KBr, cm⁻¹): 3446 (ν_{O-H}), 2206 (ν_{C≡C}), 825 (s, δ_{C-H} Fc).

UV-VIS: (DCM): λ_{max}, nm (ε, 10⁻⁵·M⁻¹·cm⁻¹): 305 (0.62).

CV: (DCM, 0.10 M [*n*-Bu₄N][PF₆], V vs SCE): M^{III}/M^{II}: E_{1/2}: 0.56 (ΔE_p = 0.02 V, *i*_{pc}/*i*_{pa} = 1.0), amine oxidation: E_{pc} (V): 0.95 V.

6.2. Ferrocene carbocations

Ferrocene-[bis-3-[4-(dimethylamino)phenyl]-1-propenyl-3-carbenium]tetrafluoroborate
([M1(Fc)⁺][BF₄⁻])



C₂₉H₂₉BF₄FeN₂, M = 548.20 g/mol

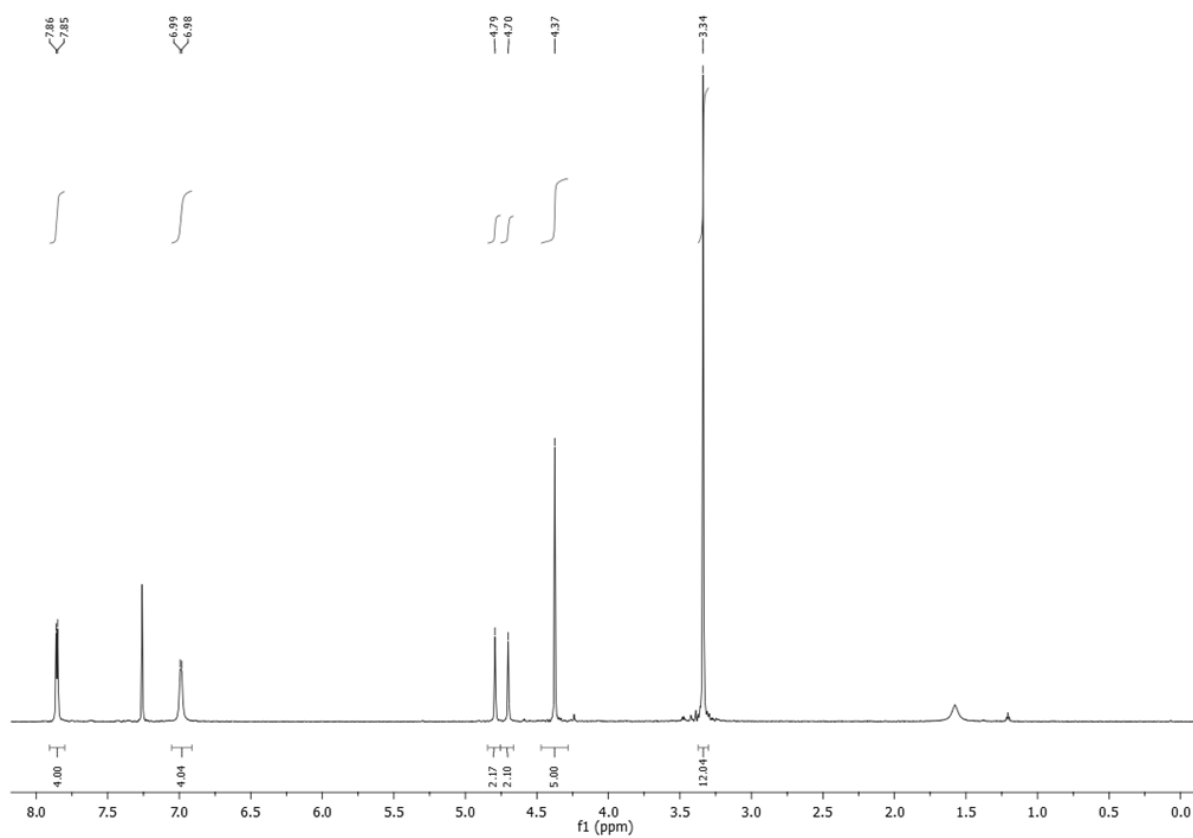
Reagents: [3,3-[4-(dimethylamino)phenyl]-3-hydroxy-1-propenyl]ferrocene **M1(Fc)^{OH}** (1 eq, 548 mg, 1 mmol), HBF₄·Et₂O (1.1 eq, 149 μL, 1.1 mmol)

Reaction and work up: Prepared according to **GP3**.

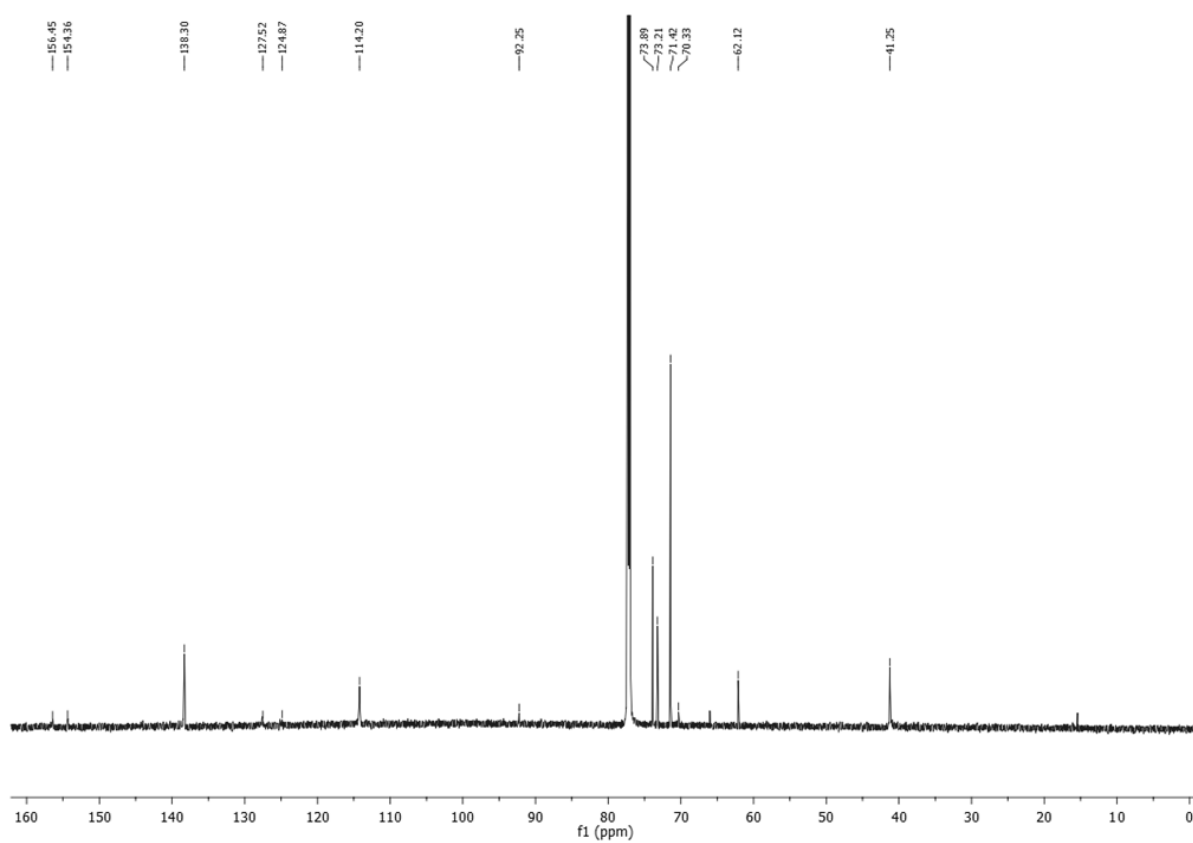
Work up and purification: The formed precipitate was cannula filtered and washed with dry and distilled Et₂O (3x10 mL). The dark green solid was then precipitated from DCM/pentane and filtered to obtain a green fine powder.

Yield: quant.

¹H NMR (800 MHz, CDCl₃) δ 7.86 (d, *J* = 8.7 Hz, 4H), 6.99 (d, *J* = 7.1 Hz, 4H), 4.79 (s, 2H), 4.70 (s, 2H), 4.37 (s, 5H, Cp), 3.34 (s, 12H, -NMe₂).



¹³C NMR (201 MHz, CDCl₃) δ 156.45 (C⁺), 154.36, 138.30, 127.52, 124.87, 114.20, 92.25, 73.89, 73.21, 71.42, 70.33, 62.12, 41.25.

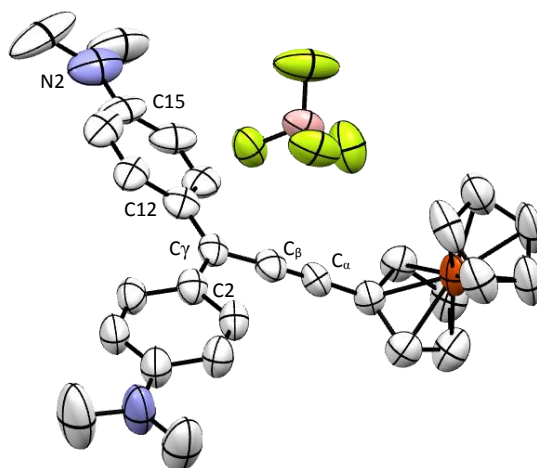


IR (cm^{-1}): 2143.89 ($\nu_{\text{C}\equiv\text{C}}$), 1167.73 ($\nu_{\text{B-F}}$), 827.27 (s, $\delta_{\text{C-H}}$ Fc).

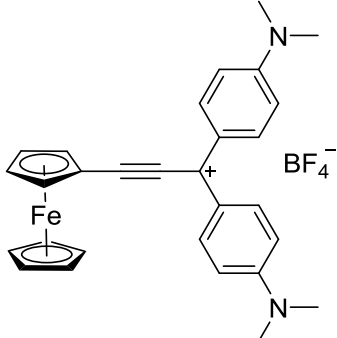
UV-VIS: (DCM): λ_{max} , nm (ϵ , $10^{-5} \cdot \text{M}^{-1} \cdot \text{cm}^{-1}$): 486 (0.15), 625 (0.23), 667 (0.59)

CV (DCM, 0.10 M [*n*-Bu₄N][PF₆], V vs Ag⁺/Ag): C⁺/C⁺: -0.35; M^{III}/M^{II}: E_{1/2}: 0.59 V ($\Delta E_p = 0.04$ V, $i_{\text{pc}}/i_{\text{pa}}=1.0$), amine oxidation : E_{pc} : 1.02 V

X-ray diffraction study:



ORTEP view of **([M1(Fc)⁺][BF₄⁻])** with 50 % thermal ellipsoids solved by Dr. Thierry Roisnel

	
Formula	2(C ₂₉ H ₂₉ FeN), 2(BF ₄), CH ₂ Cl ₂
Molecular weight (g/mol)	832.75
Copper-like shiny crystals by slow diffusion of pentane vapor into a DCM solution of the molecule at room temperature	

Crystal parameters	
Crystal class	monoclinic
Space group	P 21/c
Cell angles (°)	α= 90
	β= 95.10
	γ= 90
Cell length (Å)	a= 8.52
	b= 29.18
	c= 22.01
Cell volume (Å ³)	5453.96
Z	Z= 4

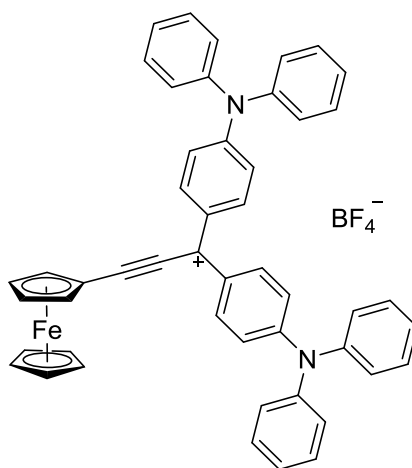
Selected bond length (Å)

C_γ-C2	1.419 (9)	C5-N1	1.339 (10)
C_γ-C12	1.446 (9)	C15-N2	1.388 (10)
C_β-C_γ	1.435 (9)	C2-C3	1.425 (10)
C_α-C_β	1.185 (9)	C3-C4	1.458 (10)
M/Fc-C_α	1.444 (9)		

Selected angles (°)

C plan	3.32 (4)	C2-C3/ C3-C4	33.74 (5)
--------	----------	---------------------	-----------

Ferrocene-[3,3-[4-(diphenylamino)phenyl]-1-propenyl-3-carbenium] ([M2(Fc)⁺][BF₄⁻])



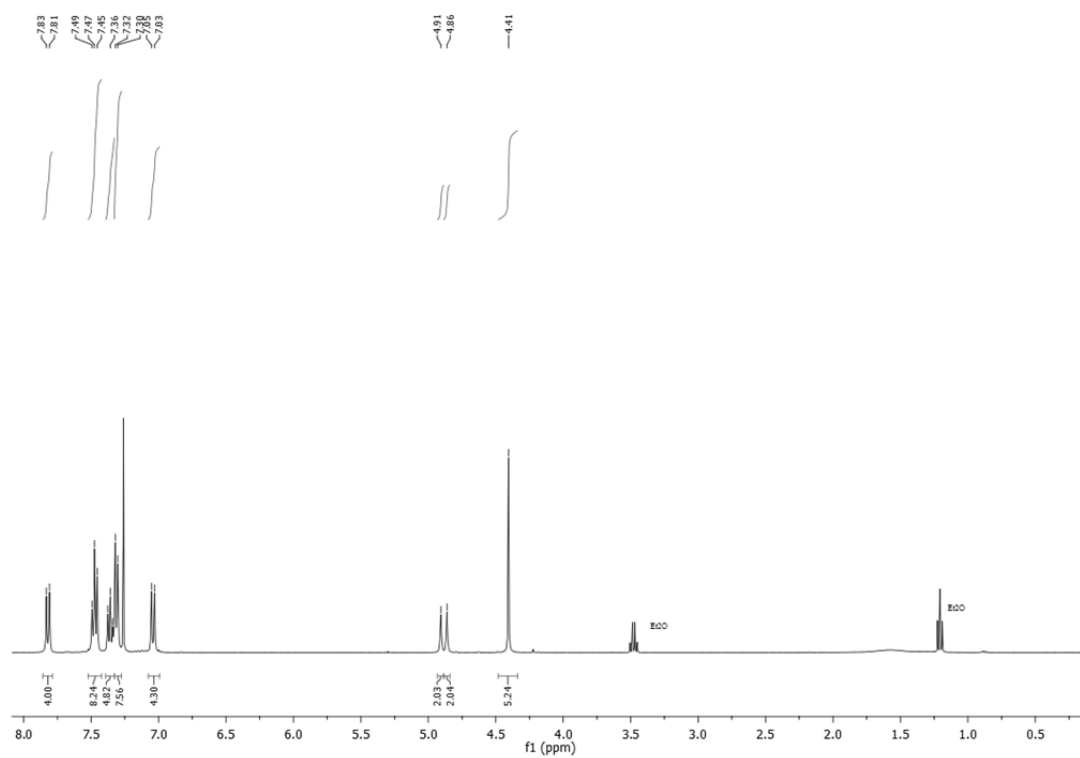
C₄₉H₃₇BF₄FeN₂O, M = 796.23 g/mol

Reagents: [3,3-[4-(diphenylamino)phenyl]-3-hydroxy-1-propenyl]-ferrocene **M2(Fc)^{OH}** (1 eq, 72 mg, 0.1 mmol), HBF₄·Et₂O (1.1 eq, 14 μL, 0.11 mmol)

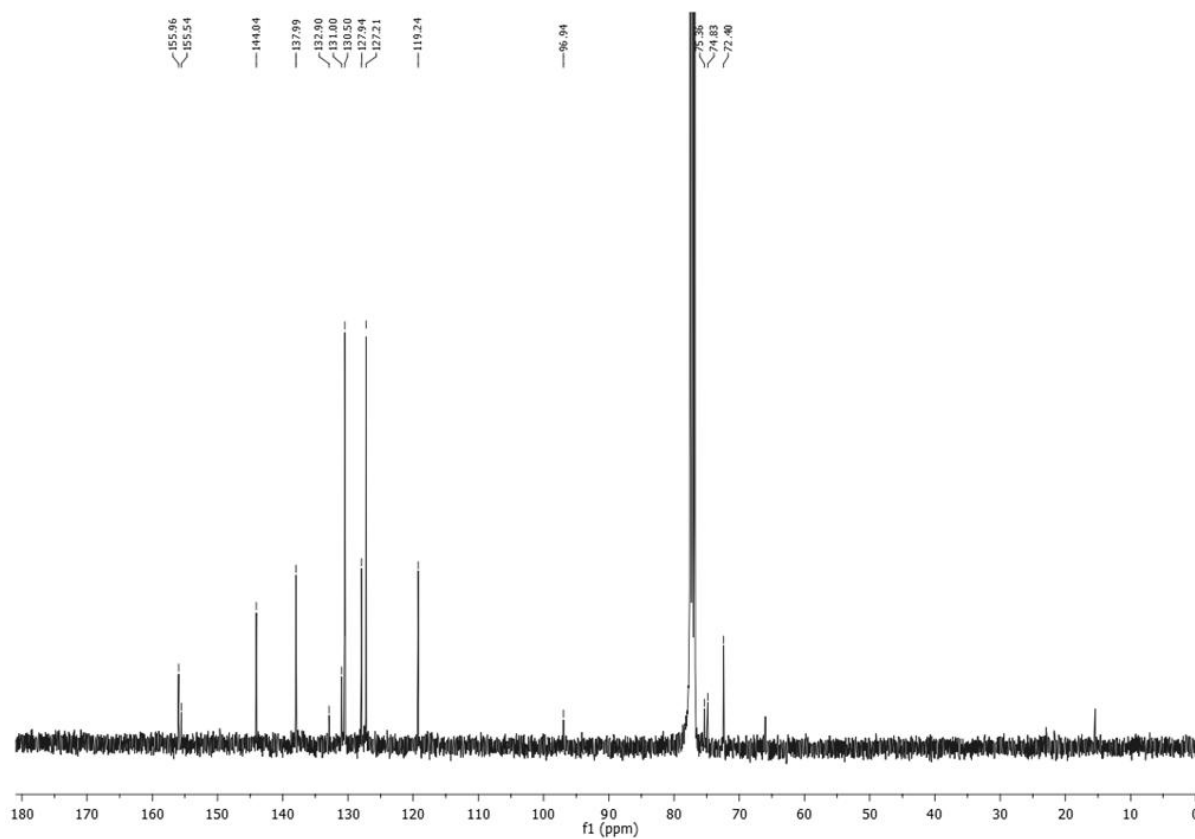
Reaction and work up: Prepared according to **GP3** and [3,3-[4-(diphenylamino)phenyl]-3-hydroxy-1-propenyl]-ferrocene (**[M2(Fc)⁺][BF₄⁻]**) was obtained as a green powder.

Yield: quant.

¹H NMR (400 MHz, CDCl₃) δ 7.82 (d, *J* = 9.2 Hz, 4H), 7.47 (t, *J* = 7.7 Hz, 8H), 7.36 (t, *J* = 7.4 Hz, 4H), 7.31 (d, *J* = 7.5 Hz, 8H), 7.04 (d, *J* = 9.2 Hz, 4H), 4.91 (s, 2H), 4.86 (s, 2H), 4.41 (s, 5H, Cp).



¹³C NMR (101 MHz, CDCl₃) δ 155.96, 155.54 (C⁺), 144.04, 137.99, 132.90, 131.00, 130.50, 127.94, 127.21, 119.24, 96.94, 75.36, 74.83, 72.40.



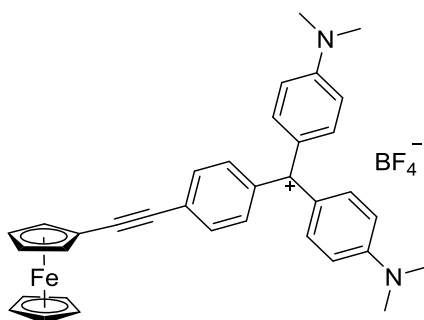
HRMS (ESI): calcd.: 709.23006 [M]⁺; found: 709.2299 [M]⁺.

IR (cm⁻¹): 2136 (ν_{C≡C}), 1172 (ν_{B-F}), 837 (s, δ_{C-H} Fc).

UV-VIS: (DCM): λ_{max}, nm (ε, 10⁻⁵·M⁻¹·cm⁻¹): 280 (0.25), 524 (0.20), 720 (0.65)

CV: (DCM, 0.10 M [*n*-Bu₄N][PF₆], V vs SCE): C⁺/C⁺: -0.06; E_{1/2}: 0.56 V (ΔE_p = 0.04 V, *i*_{pc}/*i*_{pa} = 0.98); amine oxidation: 1.10 V.

4-ethynylferrocene-[3,3-[4-(dimethylamino)phenyl]-1-phenyl-3-carbenium] ([M3(Fc)⁺][BF₄⁻])



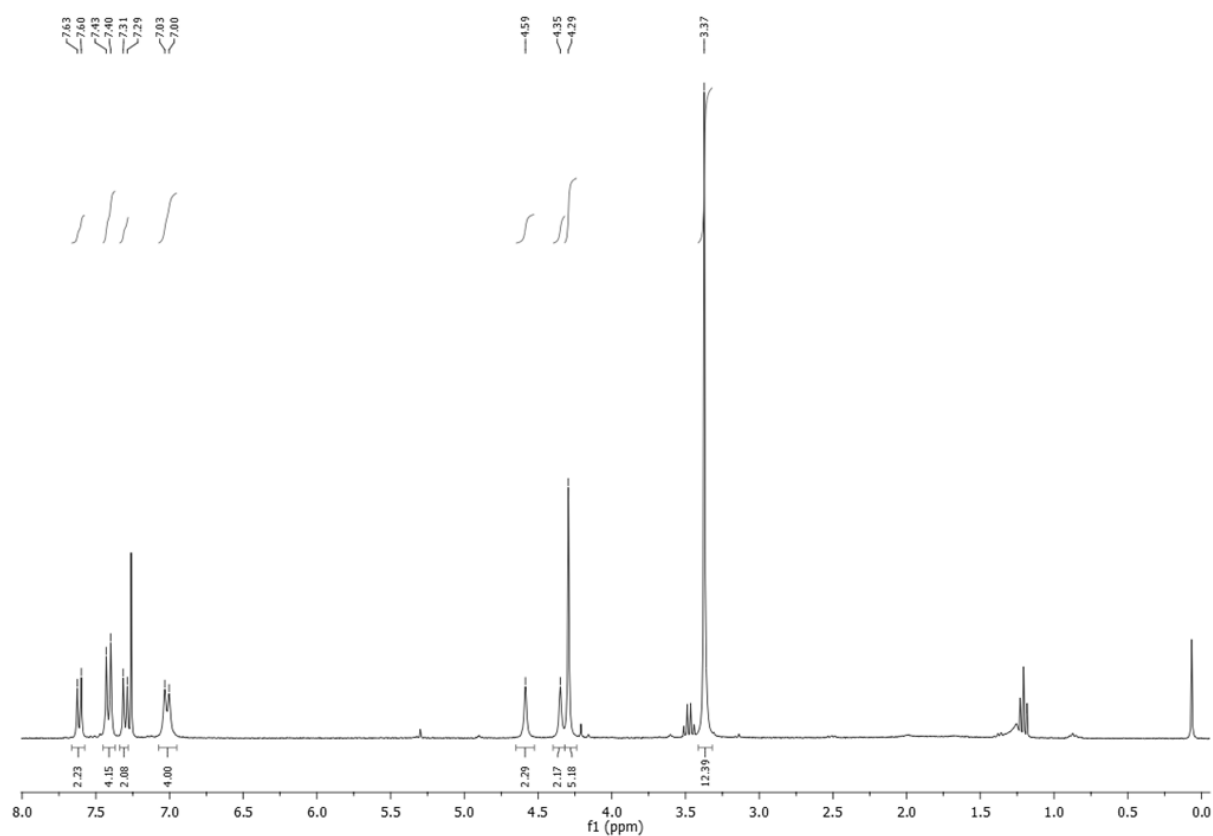
C₃₅H₃₃FeBF₄N₂O, M = 624.30.50 g/mol

Reagents: [3,3-[4-(diphenylamino)phenyl]-3-hydroxy-1-propenyl]ferrocene (1 eq, 55 mg, 0.1 mmol), HBF₄·Et₂O (1.1 eq, 14 μL, 0.11 mmol)

Reaction and work up: Prepared according to **GP3** with obtention of 4-ethynylferrocene-[3,3-[4-(dimethylamino)phenyl]-1-phenyl-3-carbenium] ([M3(Fc)⁺][BF₄⁻]) as a green powder.

Yield: quant.

¹H NMR (300 MHz, CDCl₃) δ 7.61 (d, *J* = 8.3 Hz, 2H), 7.41 (d, *J* = 9.2 Hz, 4H), 7.30 (d, *J* = 8.3 Hz, 2H), 7.02 (d, *J* = 8.9 Hz, 4H), 4.59 (s, 2H), 4.35 (s, 2H), 4.29 (s, 5H, Cp), 3.37 (s, 12H, -NMe₂).

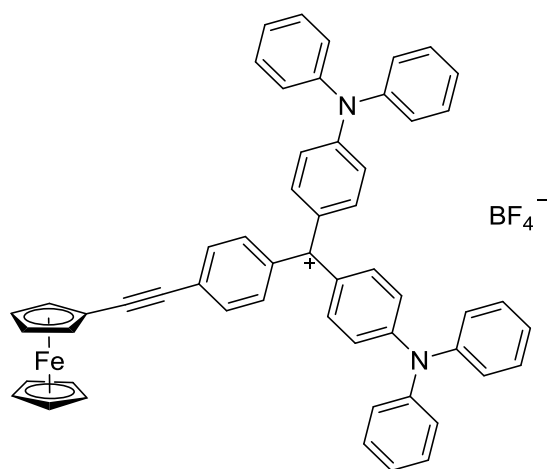


IR (KBr, cm^{-1}): 2198 ($\nu_{\text{C}\equiv\text{C}}$), 1171 ($\nu_{\text{B-F}}$), 830 ($\delta_{\text{C-H}}$ Fc).

UV-VIS (DCM): λ_{max} , nm (ϵ , $10^{-5} \cdot \text{M}^{-1} \cdot \text{cm}^{-1}$): 306 (0.20), 450 (0.22), 626 (0.94).

CV (DCM, 0.10 M [*n*-Bu₄N][PF₆], V vs SCE): C⁺/C⁺: -0.40 V; E_{1/2}: 0.6 ($\Delta E_p = 0.04$ V, $i_{pc}/i_{pa} = 0.90$); amine oxidation: 1.28 V.

4-ethynylferrocene-[3,3-[4-(diphenylamino)phenyl]-1-phenyl-3-carbenium] ([M4(Fc)⁺][BF₄⁻])



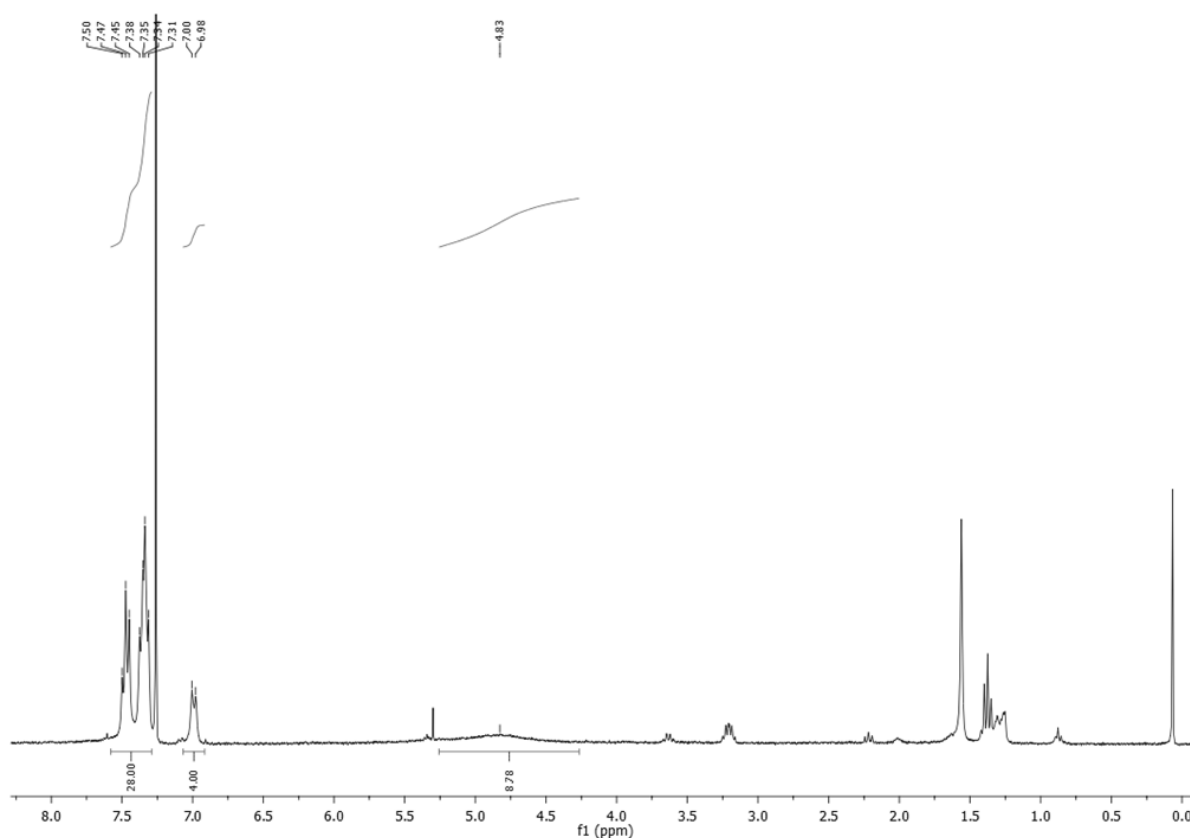
$\text{C}_{55}\text{H}_{41}\text{BF}_4\text{FeN}_2$, $M = 872.58$

Reagents: $\text{M4}(\text{Fc})^{\text{OH}}$ (1 eq, 436 mg, 0.5 mmol), $\text{HBF}_4 \cdot \text{Et}_2\text{O}$ (1.1 eq, 70 μL , 0.55 mmol)

Reaction and work up: Prepared according to **GP3** with obtention of $([\text{M4}(\text{Fc})^+][\text{BF}_4^-])$ as a green powder.

Yield: quant.

^1H NMR (300 MHz, CDCl_3) δ 7.58 – 7.29 (m, 6H), 6.99 (d, $J = 7.9$ Hz, 1H), 4.83 (broad s, 9H, Fc).



^{13}C NMR was insufficiently resolved. It may be due to the presence of some oxidized compound or aggregation.

HRMS (ESI): calcd.: 785.26136 $[\text{M}]^+$; found: 785.2608 $[\text{M}]^+$.

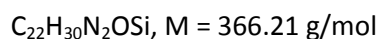
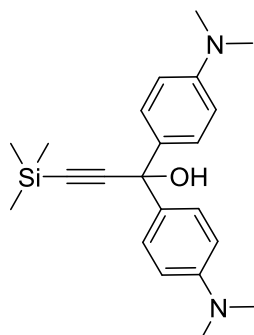
IR (KBr, cm^{-1}): 2196 ($\nu_{\text{C}\equiv\text{C}}$), 1173 ($\nu_{\text{B-F}}$), 833 ($\delta_{\text{C-H Fc}}$).

CV: (DCM, 0.10 M $[\text{n-Bu}_4\text{N}][\text{PF}_6]$, V vs SCE): $\text{C}^+/\text{C}^{\cdot+}$: -0.23 V; $\text{M}^{\text{II}}/\text{M}^{\text{III}}$: $E_{1/2}$: 0.73 ($\Delta E_p = 0.02$ V, $i_{pc}/i_{pa} = 0.84$), amine oxidation: 1.31 V.

UV-VIS (DCM): λ_{max} , nm (ϵ , $10^{-5} \cdot \text{M}^{-1} \cdot \text{cm}^{-1}$): 277 (0.33), 481 (0.19), 681 (0.66).

6.3. Organometallic precursors

1,1-bis(4-(dimethylamino)phenyl)-3-(trimethylsilyl)prop-2-yn-1-ol (**37**)



Reagents: TMSA (1.5 eq, 622 μL , 4.5 mmol), *n*-BuLi (1.5 eq, 2.81 mL at 1.6 M in hexane, 4.5mmol), Michler's ketone **28** (1 eq, 805 mg, 3 mmol).

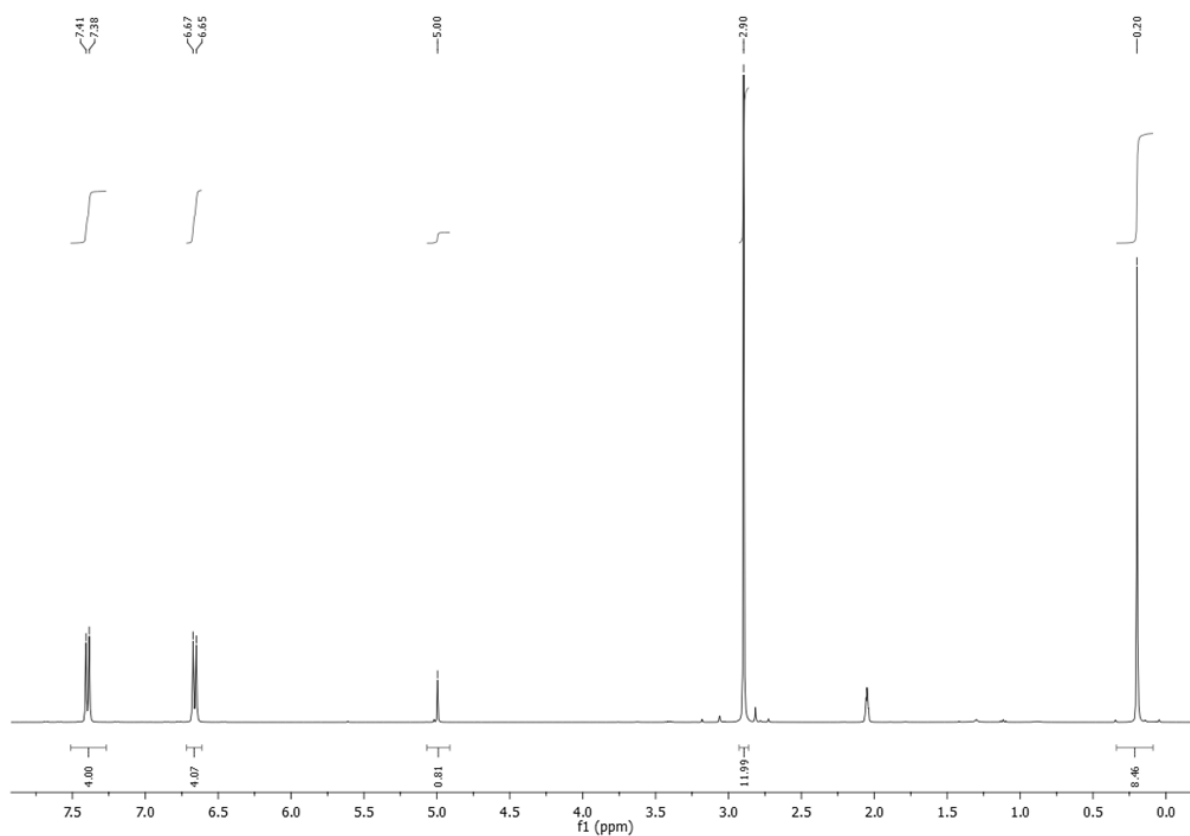
Reaction: In a Schlenk flask under argon, *n*-BuLi was added drop wise to a solution of TMSA in 25 mL of dried and distilled THF at 0°C. After stirring for 15 min, the ketone in 15 ml of dried and distilled THF was added drop wise to the solution. The cold bath was then removed and the mixture was stirred and allowed to warm to room temperature for 3h.

Work up: 20 mL of water were added to the flask and the two phases were separated. The aqueous layer was extracted with Et₂O (3 x 20 mL) and the combined organic phases were washed with water (10 mL) and saturated aqueous NaCl (10 mL). The aqueous phase was then back extracted with Et₂O (20 mL). The organic phase was dried over Na₂SO₄ and the solvents were removed to give the crude product as a grayish solid.

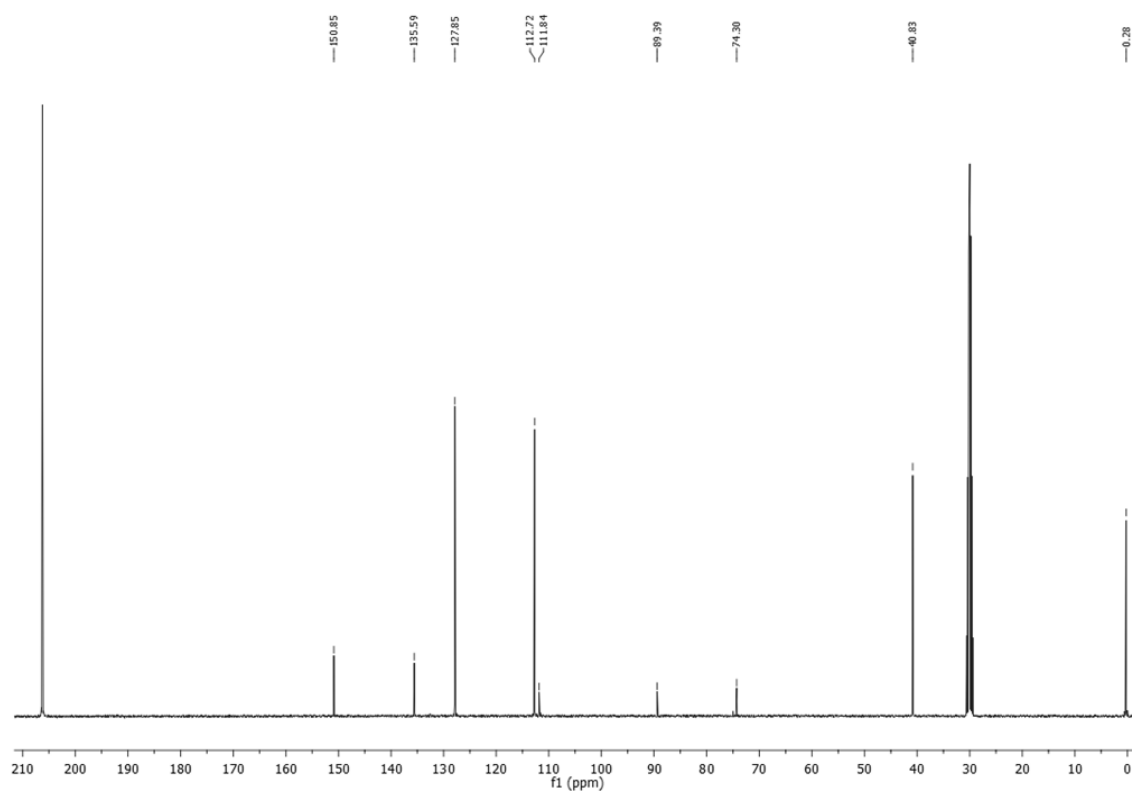
Purification: The crude was crystallized from DCM/hexane to give the desired compound as a white crystalline solid.

Yield: 830 mg (76 %)

¹H NMR (400 MHz, (CD₃)₂CO) δ 7.40 (d, *J* = 8.8 Hz, 4H), 6.66 (d, *J* = 8.9 Hz, 4H), 5.00 (s, 1H, -OH), 2.90 (s, 12H, -NMe₂), 0.20 (s, 9H, -CH₃).



¹³C NMR (101 MHz, (CD₃)₂CO) δ 150.85, 135.59, 127.85, 112.72, 111.84 (C-OH), 89.39, 74.30, 40.83, 0.28.

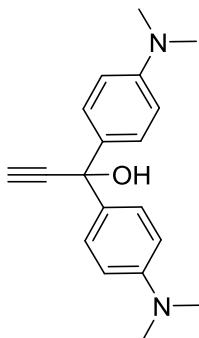


HRMS(ESI): calcd: 366.21274 $[M]^+$, 349.21000 $[M-OH]^+$; found: 336.2131 $[M]^+$, 349.2115 $[M-OH]^+$.

IR (KBr, cm^{-1}): 3310 ($\nu_{\text{O-H}}$), 2166 ($\nu_{\text{C}\equiv\text{C}}$).

EA: calcd : C: 72.08, H: 8.25, N: 7.64, found : C: 72.38, H: 8.15, N: 7.62.

1,1-bis(4-(dimethylamino)phenyl)prop-2-yn-1-ol (41)



$\text{C}_{19}\text{H}_{22}\text{N}_2\text{O}$, $M = 294.17 \text{ g/mol}$

Reagents: 1,1-bis(4-(dimethylamino)phenyl)-3-(trimethylsilyl)prop-2-yn-1-ol **37** (1 eq, 478 mg, 1.3 mmol), K_2CO_3 (1.5 eq, 270 mg, 1.95 mmol)

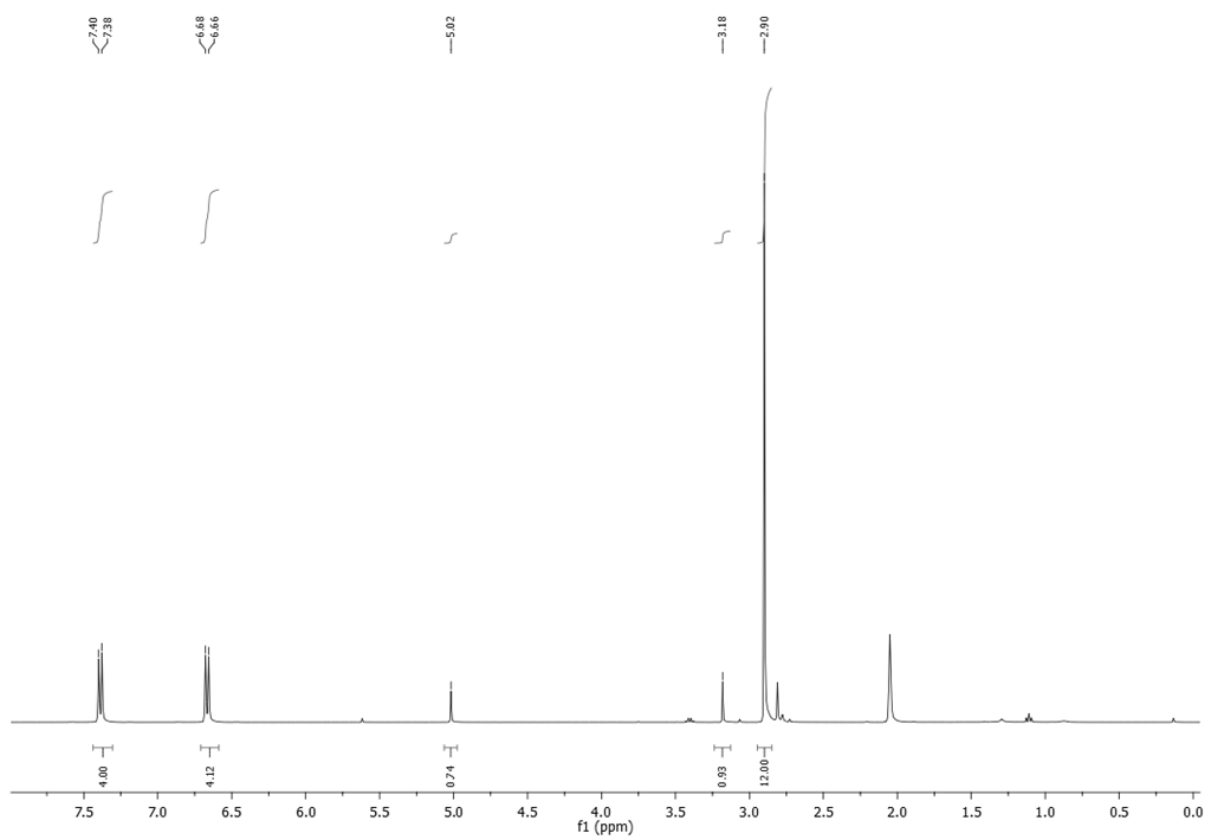
Reaction: In a round-bottom flask, 1,1-bis(4-(dimethylamino)phenyl)-3-(trimethylsilyl)prop-2-yn-1-ol **37** and K_2CO_3 were stirred in a mixture of MeOH (15 mL) and DCM (15 mL) for 6 h at room temperature.

Work-up: Solvents were removed and the residue was treated with water (20 mL) and Et_2O (20 mL). The two layers were separated and the aqueous layer was extracted with Et_2O (3x20 mL). The combined organic layers were washed with water (3x10mL) and saturated aqueous NaCl (10 mL). The aqueous layer was then back-extracted with Et_2O (20 mL). The combined organic layers were dried over Na_2SO_4 and evaporated under reduced pressure to give a white solid.

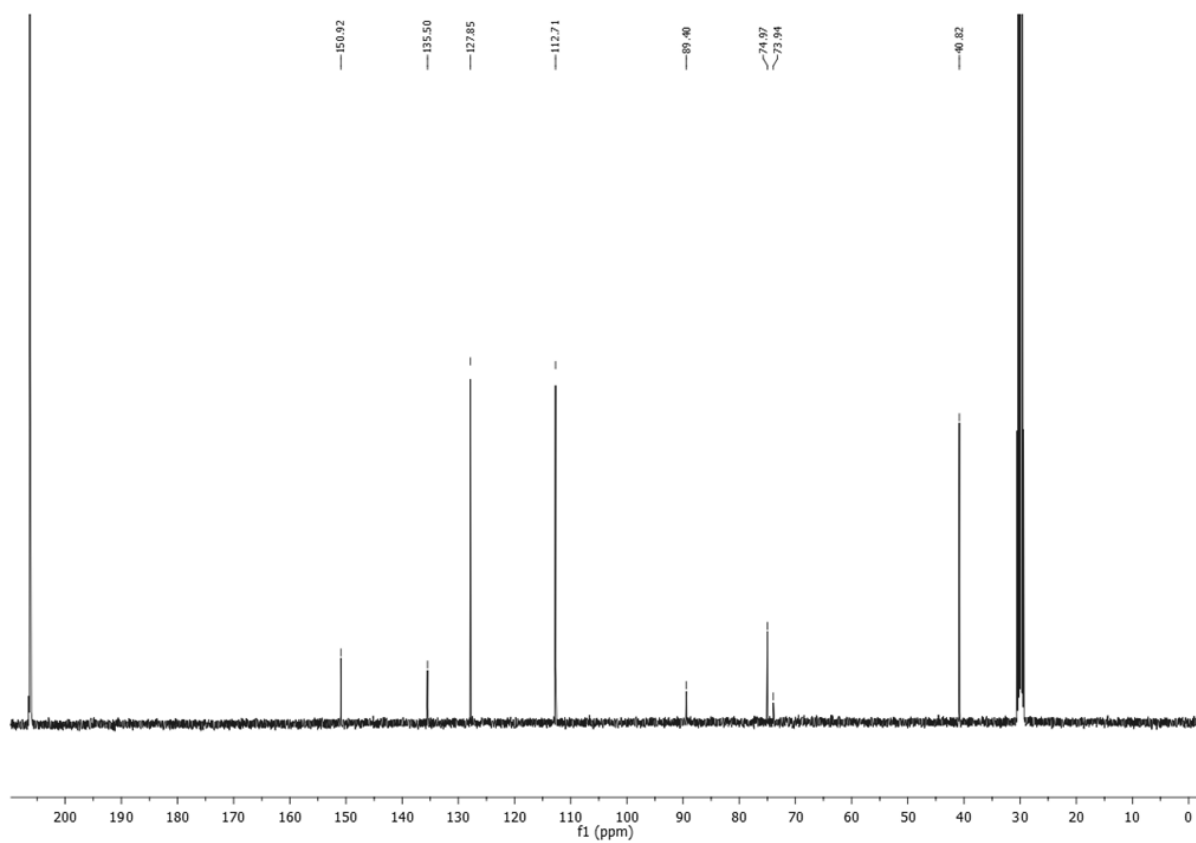
Purification: The solid residue was then recrystallized from DCM/hexane to give the desired compound as white crystals.

Yield: 310 mg (81 %).

^1H NMR (400 MHz, $(\text{CD}_3)_2\text{CO}$) δ 7.39 (d, $J = 8.8 \text{ Hz}$, 4H), 6.67 (d, $J = 8.9 \text{ Hz}$, 4H), 5.02 (s, 1H, -OH), 3.18 (s, 1H), 2.90 (s, 12H, - NMe_2).



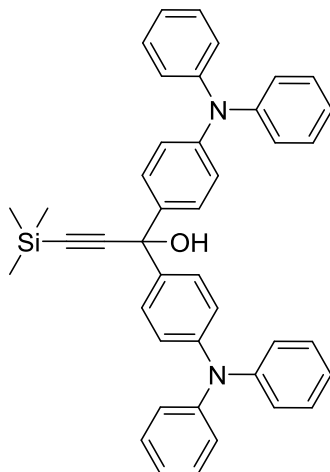
¹³C NMR (101 MHz, (CD₃)₂CO) δ 150.92, 135.50, 127.85, 112.71, 89.40, 74.97, 73.94 (C-OH), 40.82.



HRMS (ESI): calcd.: 317.16298 $[M+Na]^+$, 277.17047 $[M-\cdot OH]^+$, 295.18104 $[M+H]^+$; found: 317.1629 $[M+Na]^+$, 277.1704 $[M-\cdot OH]^+$, 295.1810 $[M+H]^+$.

IR (KBr, cm^{-1}): 3400 (ν_{OH}), 3274 (ν_{CH}), 2105 ($\nu_{C\equiv C}$).

1,1-bis(4-(diphenylamino)phenyl)-3-(trimethylsilyl)prop-2-yn-1-ol (38)



$C_{42}H_{38}N_2OSi$, $M = 614.85$ g/mol

Reagents: TMSA (1.5 eq, 207 μ L, 1.5 mmol), *n*-BuLi (1.5 eq, 937 μ L at 1.6 M in hexane, 1.5 mmol), 4,4'-diphenylaminebenzophenone **29** (1 eq, 517 mg, 1 mmol).

Reaction: In a Schlenk flask under argon, *n*-BuLi was added drop wise to a solution of TMSA in 25 mL of dried and distilled THF at 0°C. After stirring for 15 min, the ketone in 15 mL of dried and distilled THF was added drop wise to the solution. The cold bath was then removed and the mixture was stirred and allowed to warm to room temperature for 3h.

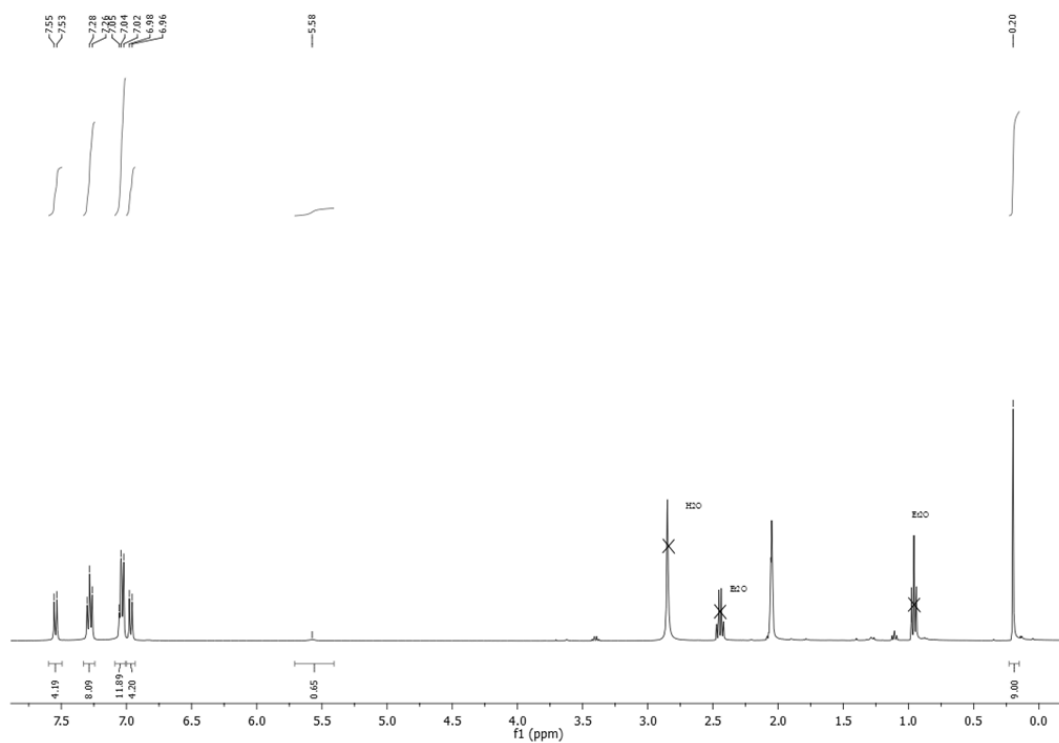
Work up: 20 mL of water were added to the flask and the two phases were separated. The aqueous layer was extracted with Et₂O (3 x 20 mL) and the combined organic phases were washed with water (3 x 10 mL) and saturated aqueous NaCl (10 mL). The aqueous phase was then back extracted with Et₂O (20 mL). The organic phase was dried over Na₂SO₄ and the solvents were removed.

Purification: The crude product was adsorbed onto deactivated silica and purified by column chromatography (neutralized silica gel with 10 % NEt₃, 20 x 3 cm) eluting with hexane/EA (3/1) with 1 % NEt₃ to give the desired product as a pale yellow solid.

R_f (hexane/EA, 3/1): 0.3.

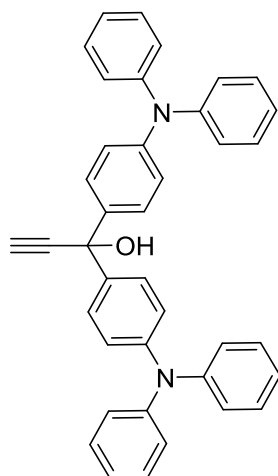
Yield: 600 mg (94 %).

^1H NMR (400 MHz, $(\text{CD}_3)_2\text{CO}$) δ 7.46 (d, $J = 8.7$ Hz, 4H), 7.26 – 7.19 (m, 8H), 7.13 – 7.05 (m, 8H), 7.05 – 6.97 (m, 8H), 2.96 (s, 1H), 0.22 (s, 9H).



IR (KBr, cm^{-1}): 3532 (ν_{OH}), 2167 ($\nu_{\text{C}\equiv\text{C}}$).

1,1-bis(4-(diphenylamino)phenyl)prop-2-yn-1-ol (42)



$\text{C}_{39}\text{H}_{30}\text{N}_2\text{O}$, $M = 542.67$ g/mol

Reagents: 1,1-bis(4-(diphenylamino)phenyl)-3-(trimethylsilyl)prop-2-yn-1-ol **38** (1 eq, 600 mg, 0.8 mmol), K_2CO_3 (1.5 eq, 207.3 mg, 1.2 mmol)

Reaction: In a round bottom flask, 1,1-bis(4-(diphenylamino)phenyl)-3-(trimethylsilyl)prop-2-yn-1-ol **38** and K_2CO_3 were stirred in a mixture of MeOH (15 mL) and DCM (15 mL) for 6 h at room temperature.

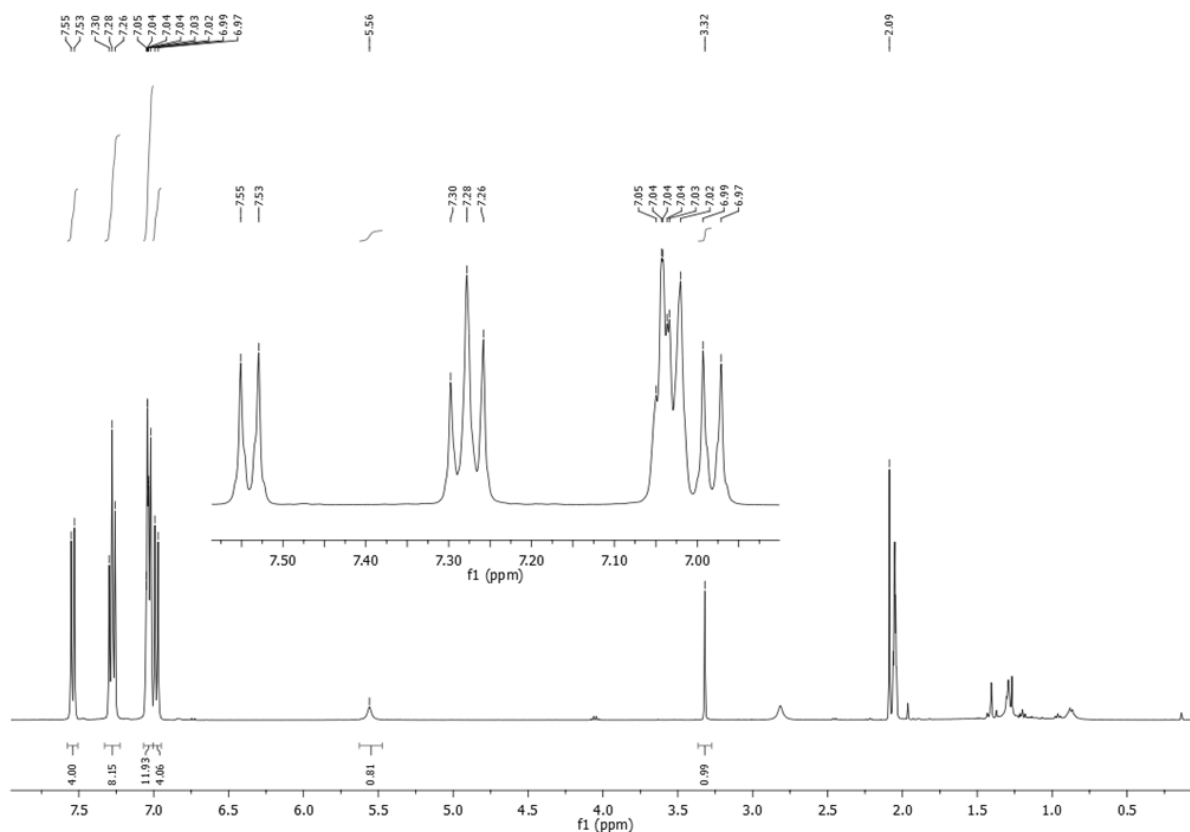
Work-up: Solvents were removed and the residue was treated with water (20 mL) and Et_2O (20 mL). The two layers were separated and the aqueous layer was extracted with Et_2O (3 x 20 mL). The combined organic layers were washed with water (3 x 10 mL) and saturated aqueous NaCl (10 mL). The aqueous layer was then back extracted with Et_2O (20 mL). The combined organic layers were dried over Na_2SO_4 and evaporated under reduced pressure to give a white solid.

Purification: The crude solid was adsorbed onto deactivated silica and purified by column chromatography (neutralized silica gel with 10 % NEt_3 , 20 x 3 cm) eluting with hexane/EA (2/1) with 1 % NEt_3 to give the desired product as a white solid.

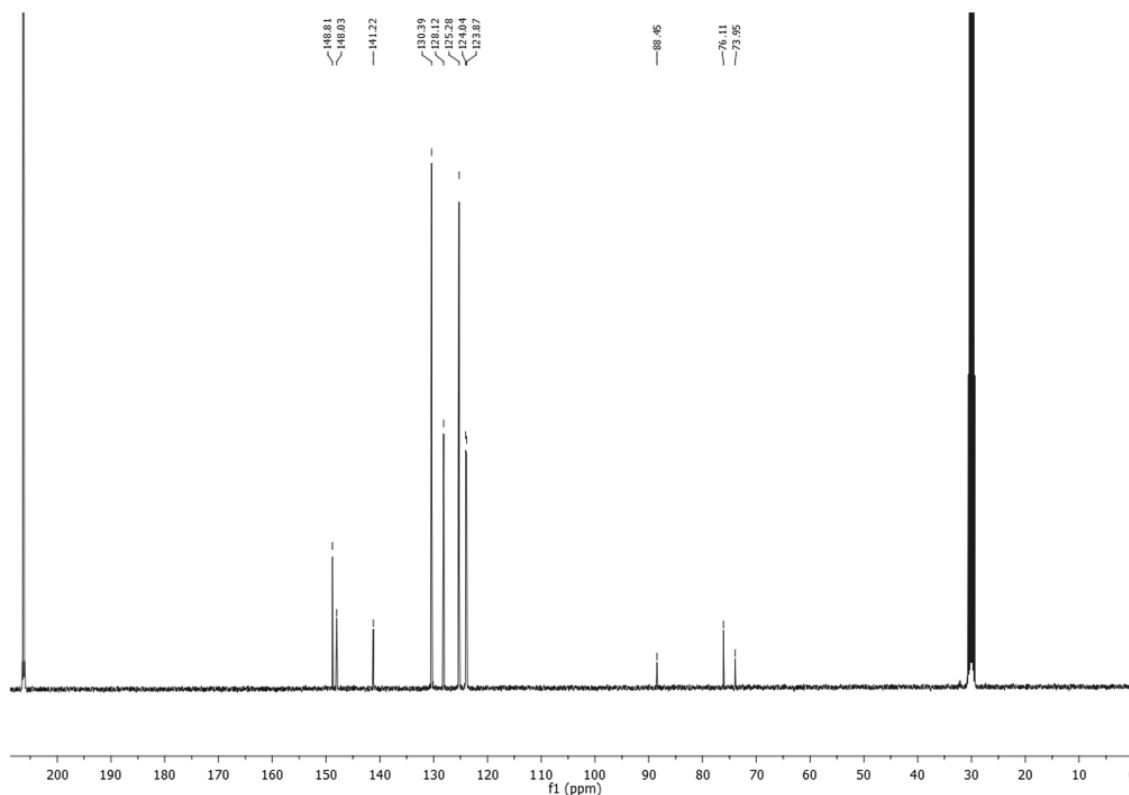
R_f (hexane/EA, 2/1): 0.4.

Yield: 385mg (94 %).

1H NMR (400 MHz, $(CD_3)_2CO$) δ 7.54 (d, J = 8.7 Hz, 4H), 7.28 (t, J = 7.9 Hz, 8H), 7.07 – 7.00 (m, 12H), 6.98 (d, J = 8.7 Hz, 4H), 5.56 (s, 1H, -OH), 3.32 (s, 1H, $C\equiv C-H$).



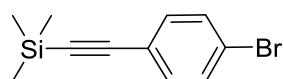
^{13}C NMR (101 MHz, $(\text{CD}_3)_2\text{CO}$) δ 148.81, 148.03, 141.22, 130.39, 128.12, 125.28, 124.04, 123.87, 88.45, 76.11 (C-OH), 73.95.



HRMS (ESI): calcd.: 525.23307 $[\text{M}-\text{OH}]^+$, 543.24309 $[\text{M}+\text{H}]^+$, 541.22744 $[\text{M}-\text{H}]^+$; found: 317.1629 $[\text{M}+\text{Na}]^+$, 525.2324 $[\text{M}-\text{OH}]^+$, 543.2428 $[\text{M}+\text{H}]^+$, 541.2273 $[\text{M}-\text{H}]^+$.

IR (KBr, cm^{-1}): 3535 (ν_{OH}), 3278 ($\nu_{\text{C}\equiv\text{CH}}$), 2107 ($\nu_{\text{C}\equiv\text{C}}$).

((4-bromophenyl)ethynyl)trimethylsilane



$\text{C}_{11}\text{H}_{13}\text{BrSi}$, $M = 253.21 \text{ g/mol}$

Reagents: *p*-bromiodobenzene (1.2 eq, 2.23 g, 7.88 mmol), TMSa (1 eq, 1.09 mL, 7.64 mmol), $\text{PdCl}_2(\text{PPh}_3)_2$ (0.02 eq, 10 mg, 0.014 mmol), CuI (0.04 eq, 6 mg, 0.03 mmol).

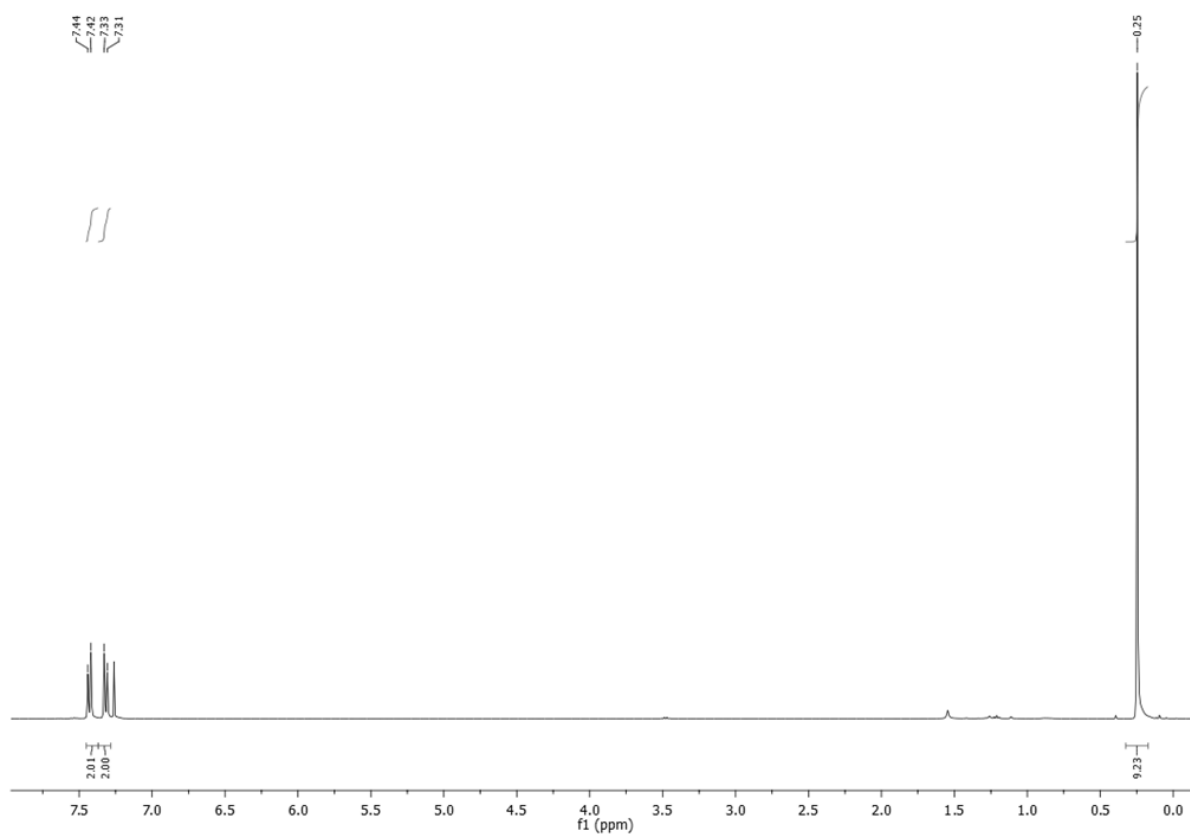
Reaction: In a Schlenk tube under argon, *p*-bromiodobenzene, $\text{PdCl}_2(\text{PPh}_3)_2$ and CuI were dissolved in NEt_3 (20 mL). TMSa was added and the resulting black solution was heated at RT for 3 h.

Work-up: After evaporation of the solvents by cryoscopic transfer, the residue was extracted with Et₂O and filtered to remove ammonium salts. The extract was washed with a saturated aqueous solution of NH₄Cl (10 mL), water (3 x 10 mL) and saturated aqueous NaCl (10 mL). the aqueous layer was then back extracted with Et₂O (20 mL). The combined organic layers were dried over MgSO₄ and evaporated under reduced pressure to give a brown solid.

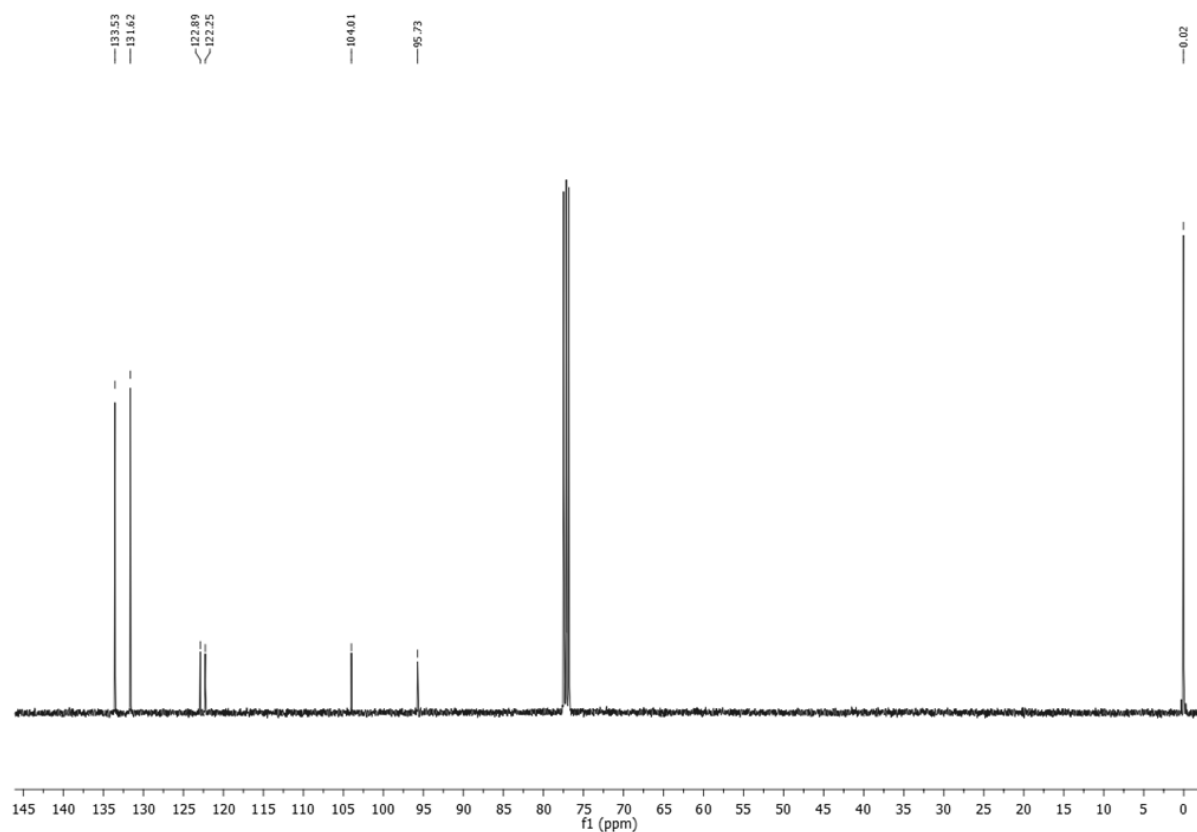
Purification: The crude was carefully filtered through a small pad of silica (10 cm) with hexane to give a white solid that was dried in *vacuo*.

Yield: 1.90 g (98 %).

¹H NMR (400 MHz, CDCl₃) δ 7.43 (d, *J* = 8.5 Hz, 2H), 7.32 (d, *J* = 8.5 Hz, 2H), 0.25 (s, 9H, -CH₃).



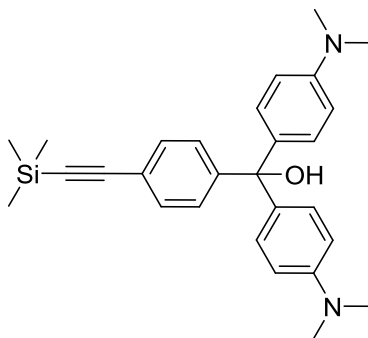
¹³C NMR (101 MHz, CDCl₃) δ 133.53, 131.62, 122.89, 122.25, 104.01, 95.73, 0.02 (CH₃).



HRMS (ESI): calcd.: 251.99699 $[M]^+$; found: 251.9969 $[M]^+$.

IR (KBr, cm^{-1}): 2155 ($\nu_{\text{C}\equiv\text{C}}$).

bis(4-(dimethylamino)phenyl)(4-((trimethylsilyl)ethynyl)phenyl)methanol (39)



$\text{C}_{28}\text{H}_{34}\text{N}_2\text{OSi}$, $M = 442.67 \text{ g/mol}$

Reagents: ((4-bromophenyl)ethynyl)trimethylsilane (1.2 eq, 456 mg, 1.8 mmol), *n*-BuLi (1.1 eq, 968 μL at 1.6 M in hexane, 1.55 mmol), Michler's ketone **28** (1 eq, 402 mg, 1.5 mmol).

Reaction: In a Schlenk flask under argon, *n*-BuLi was added drop wise to a solution of ((4-bromophenyl)ethynyl)trimethylsilane in 20 mL of dried and distilled THF at -78°C . After stirring for 30

min, the ketone in 15 mL of dried and distilled THF was added drop wise to the solution. The cold bath was then removed and the mixture was stirred and allowed to warm to room temperature for 2h.

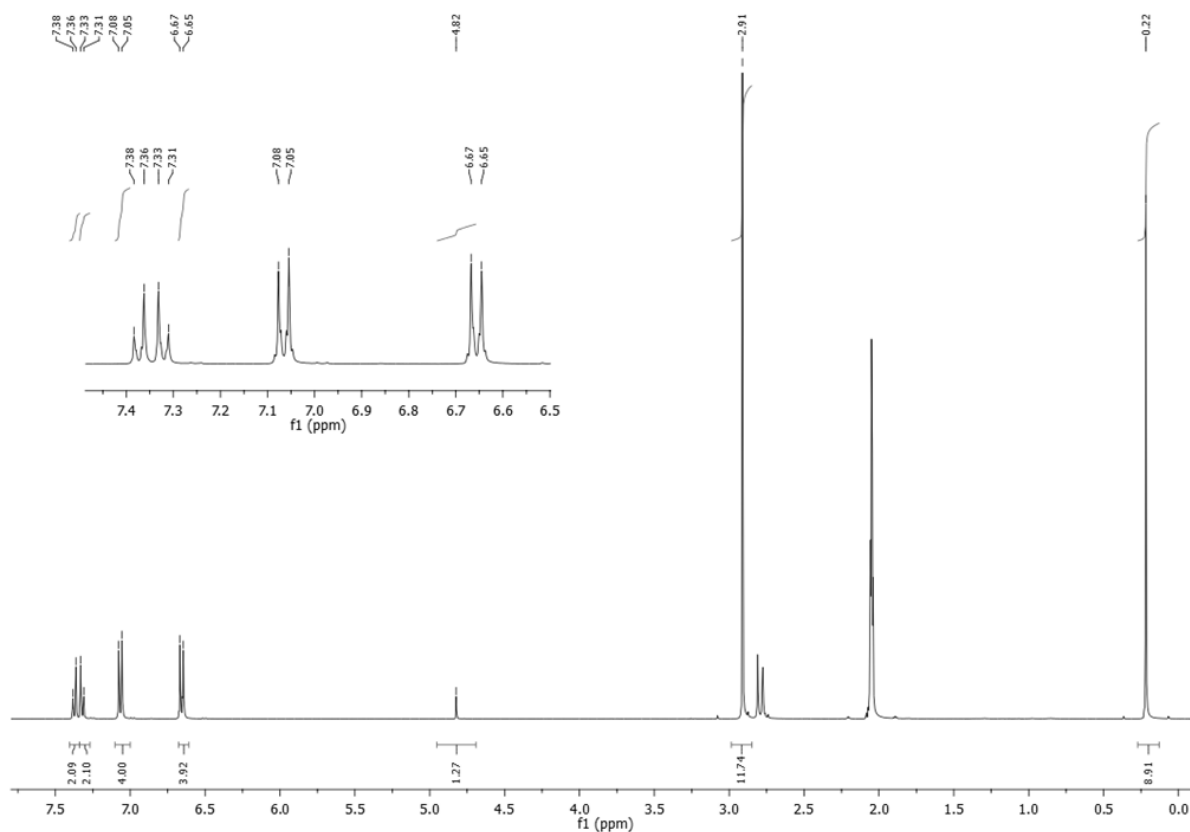
Work up: 20 mL of water were added to the flask and the two phases were separated. The aqueous layer was extracted with Et₂O (3 x 20 mL) and the combined organic phases were washed with water (3 x 10 mL) and saturated aqueous NaCl (10 mL). The aqueous phase was then back-extracted with Et₂O (20 mL). The organic phase was dried over Na₂SO₄ and the solvents were removed to give the expected product as a white solid.

Purification: The crude product was adsorbed onto deactivated silica and purified by column chromatography (neutralized silica gel with 10 % NEt₃, 15 x 3 cm) eluting with hexane/EA (6/1) with 1 % NEt₃ to give the desired product as a light white solid.

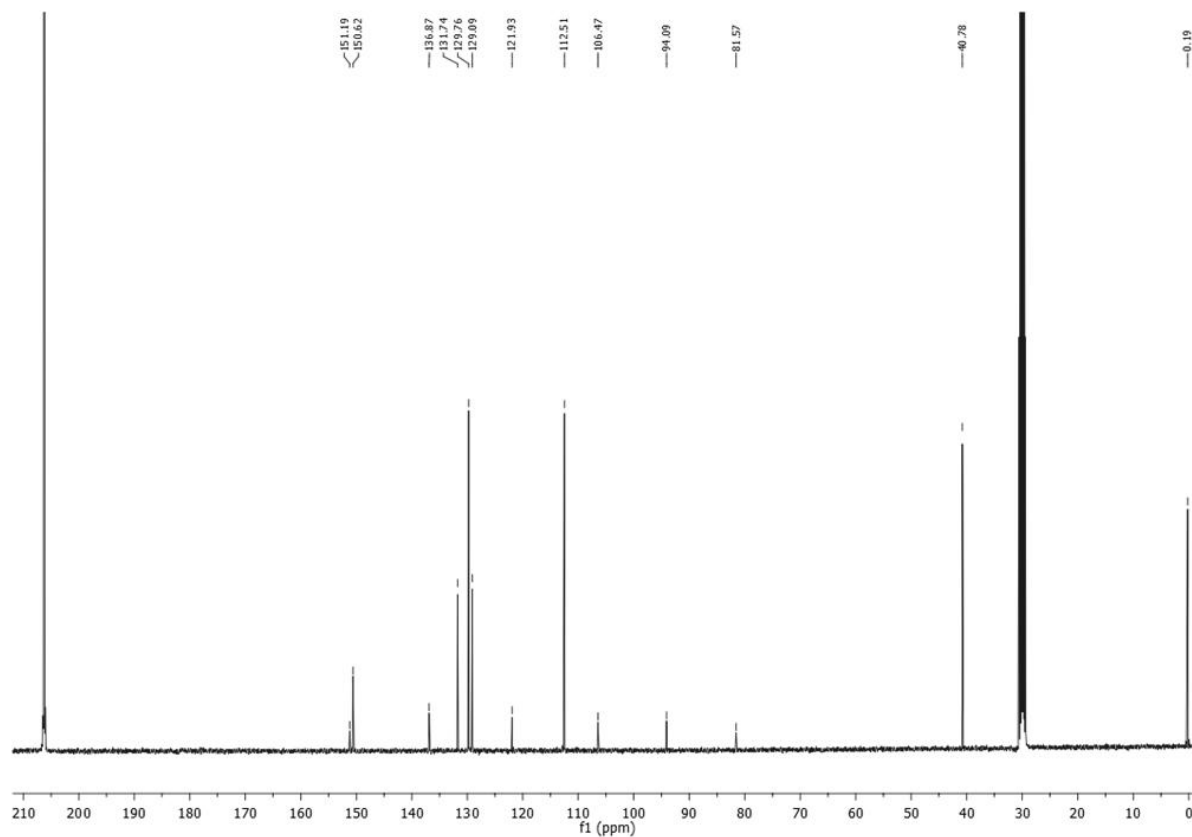
R_f(hexane/EA, 6/1): 0.28

Yield: 620 mg (93 %).

¹H NMR (400 MHz, (CD₃)₂CO) δ 7.37 (d, *J* = 8.5 Hz, 2H), 7.32 (d, *J* = 8.5 Hz, 2H), 7.07 (d, *J* = 8.9 Hz, 4H), 6.66 (d, *J* = 8.9 Hz, 4H), 4.81 (s, 1H, -OH), 2.91 (s, 12H, -NMe₂), 0.22 (s, 9H, CH₃).



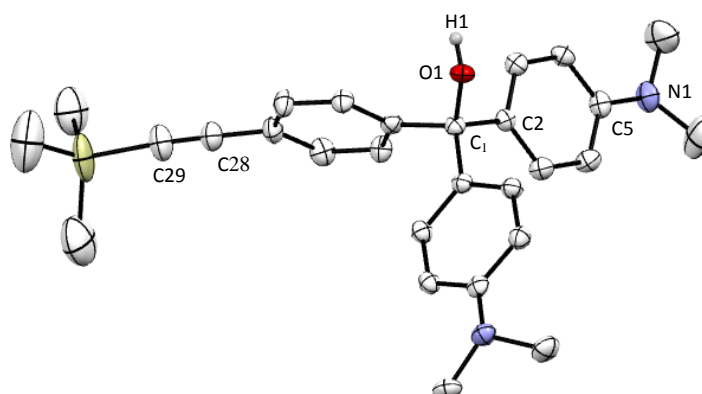
^{13}C NMR (101 MHz, $(\text{CD}_3)_2\text{CO}$) δ 151.19, 150.62, 136.88, 136.85, 131.75, 129.77, 129.10, 121.94, 112.52, 106.48 (C-OH), 94.10, 81.59, 40.80 (-NMe₂), 0.22 (-CH₃).



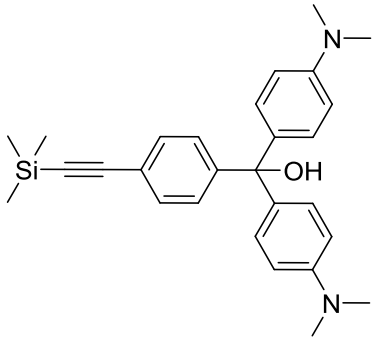
HRMS(ESI): calcd: 443.25132 $[\text{M}+\text{H}]^+$, 222.1293 $[\text{M}+2\text{H}]^{2+}$, 425.24075 $[\text{M}-\text{OH}]^+$; found : 443.2512 $[\text{M}+\text{H}]^+$, 222.1292 $[\text{M}+2\text{H}]^{2+}$, 425.2407 $[\text{M}-\text{OH}]^+$.

IR (cm^{-1}): 3400 (ν_{OH}), 2155 ($\nu_{\text{C}\equiv\text{C}}$).

X-ray diffraction study:



ORTEP view of **39** with 50 % thermal ellipsoids solved by Dr. Graeme Moxey

	
Formula	C ₂₈ H ₃₄ N ₂ OSi
Molecular weight (g/mol)	442.67
white crystals by slow diffusion of hexane vapor into a DCM solution of the molecule at room temperature	

Crystal parameters	
Crystal class	orthorhombic
Space group	P c a 2 ₁
Cell angles (°)	α= 90
	β= 90
	γ= 90
Cell length (Å)	a= 18.42
	b= 13.89
	c= 10.42
Cell volume (Å ³)	2667.88
Z	Z= 4

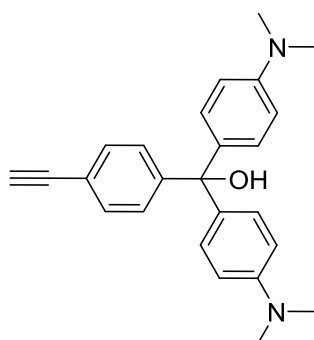
Selected bond length (Å)

O1-C1	1.444 (4)	C2-C7	1.386 (5)
C1-C2	1.540 (5)	C28-C29	1.186 (6)
C5-N1	1.412 (5)		

Selected angles (°)

O1-C1-C2	105.61 (3)
-----------------	------------

bis(4-(dimethylamino)phenyl)(4-ethynylphenyl)methanol (43)



C₂₅H₂₆N₂O, M = 370.49 g/mol

Reagents: bis(4-(dimethylamino)phenyl)(4-((trimethylsilyl)ethynyl)phenyl)methanol **39** (1 eq, 486 mg, 1.1 mmol), K₂CO₃ (2 eq, 276 mg, 2.2 mmol).

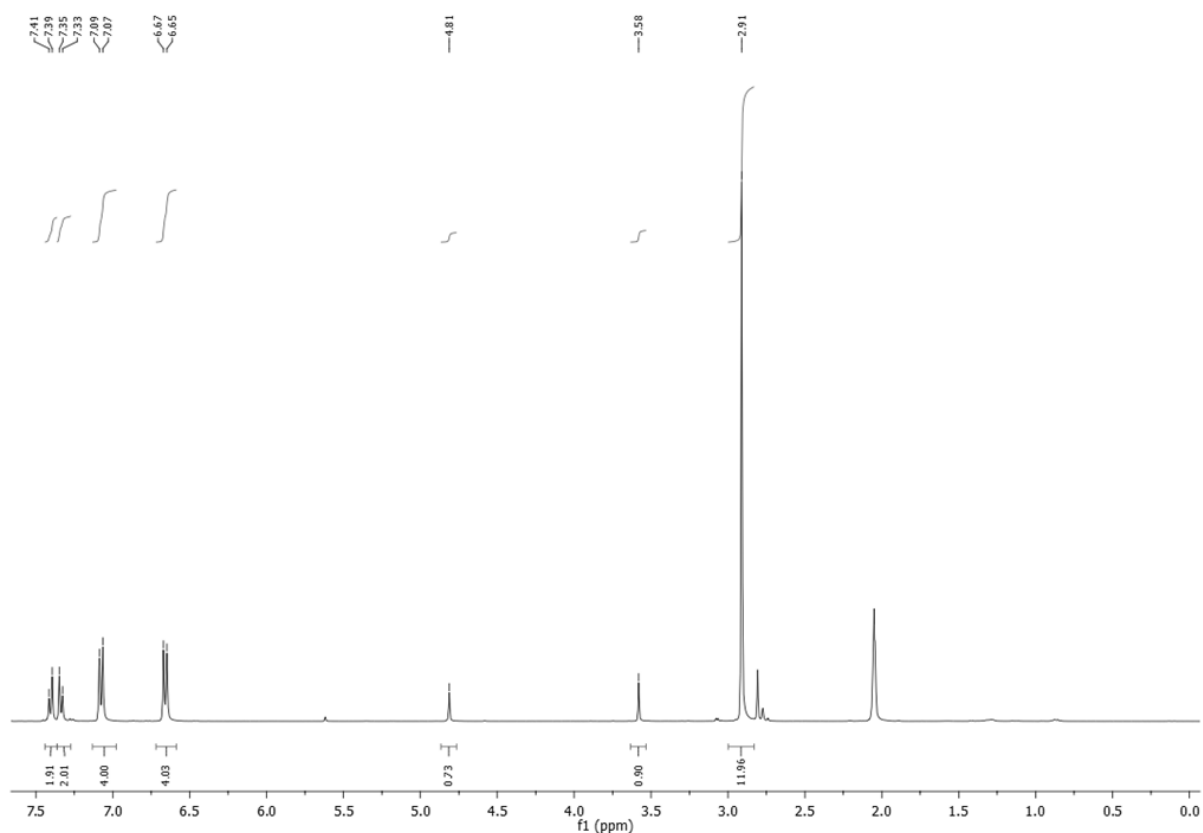
Reaction: In a round bottom flask, 1,1-bis(4-(diphenylamino)phenyl)-3-(trimethylsilyl)prop-2-yn-1-ol and K₂CO₃ were stirred in a mixture of MeOH (20 mL) and DCM (20 mL) for 6 h at room temperature.

Work-up: Solvents were removed and the residue was treated with water (20 mL) and Et₂O (20 mL). The two layers were separated and the aqueous layer was extracted with Et₂O (3 x 20 mL). The combined organic layer was washed with water (3 x 10 mL) and saturated aqueous NaCl (10 mL). The aqueous layer was then back-extracted with Et₂O (20 mL). The combined organic layers were dried over Na₂SO₄ and evaporated under reduced pressure to give a white solid.

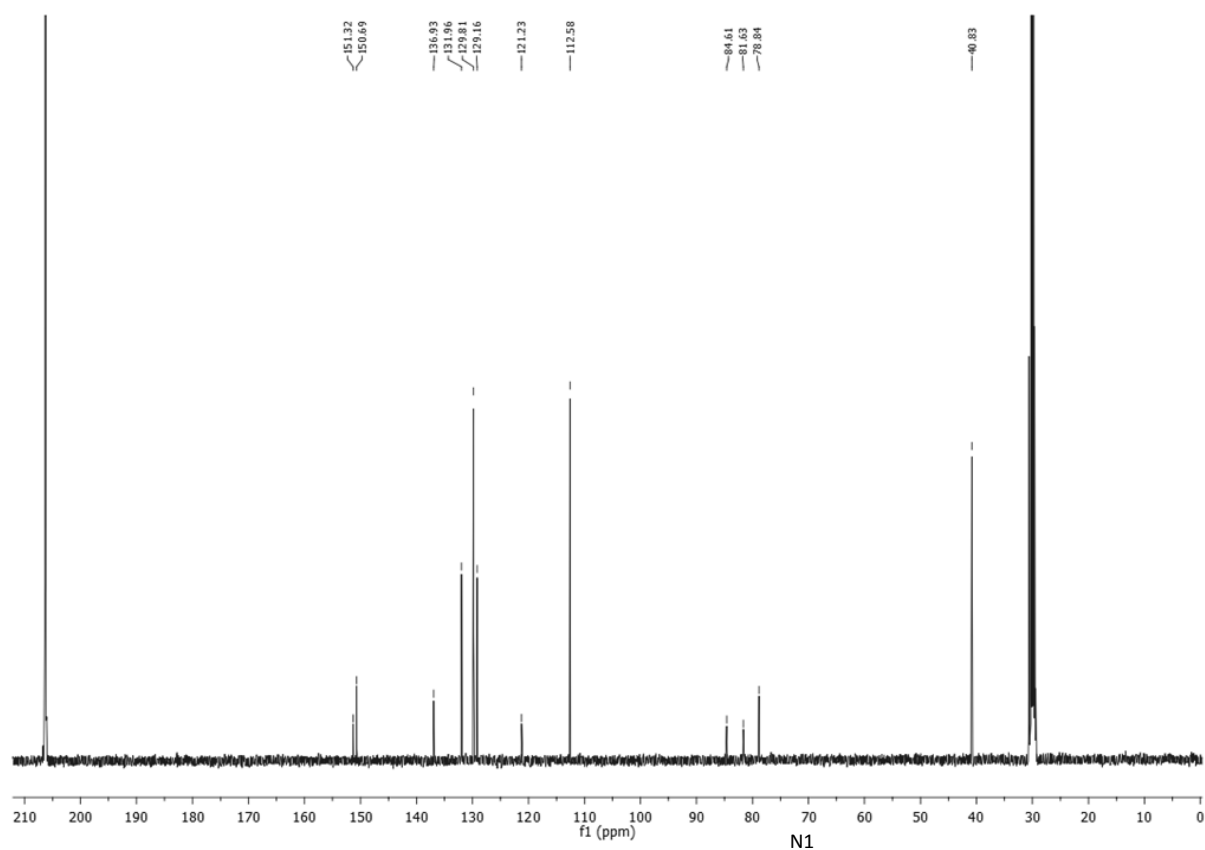
Purification: Crystallization from DCM/hexane to obtain white needles.

Yield: 320mg (79 %).

¹H NMR (400 MHz, (CD₃)₂CO) δ 7.40 (d, *J* = 8.3 Hz, 2H), 7.34 (d, *J* = 8.4 Hz, 2H), 7.08 (d, *J* = 8.9 Hz, 4H), 6.66 (d, *J* = 8.9 Hz, 4H), 4.81 (s, 1H, -OH), 3.58 (s, 1H, C≡C-H), 2.91 (s, 12H, -NMe₂).



¹³C NMR (101 MHz, (CD₃)₂C) δ 151.32, 150.69, 136.93, 131.96, 129.81, 129.16, 121.23, 112.58, 84.61 (C-OH), 81.63, 78.84, 40.83.

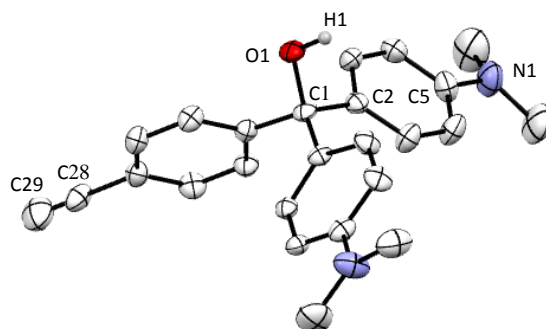


HRMS (ESI): calcd: 371.21234 $[M+H]^+$, 353.20177 $[M-\cdot OH]^+$; found : 371.2121 $[M+H]^+$, 353.2021 $[M-\cdot OH]^+$.

IR (cm^{-1}): 3453 (ν_{OH}), 3529 ($\nu_{\text{C}\equiv\text{C-H}}$), $\nu_{\text{C}\equiv\text{C}}$ too weak to be observable

RX: slow diffusion of hexane in a saturated solution of DCM

X-ray diffraction study:



ORTEP view of **39** with 50 % thermal ellipsoids solved by Dr. Thierry Roisnel

Formula	C ₂₅ H ₂₆ N ₂ O
Molecular weight (g/mol)	370.49
white crystals by slow diffusion of hexane vapor in a DCM solution of the molecule at room temperature	

Crystal parameters	
Crystal class	orthorhombic
Space group	P c a 2 ₁
Cell angles (°)	α= 90
	β= 90
	γ= 90
Cell length (Å)	a= 10.75
	b= 17.45
	c= 21.80
Cell volume (Å ³)	4095.57
Z	Z= 4

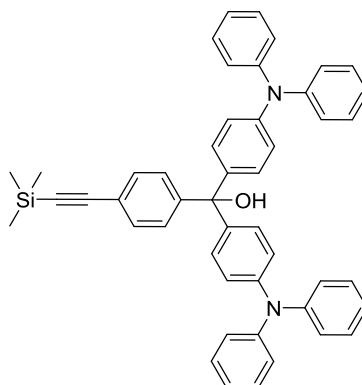
Selected bond length (Å)

O1-C1	1.469 (4)	C2-C7	1.378 (6)
C1-C2	1.529 (5)	C28-C29	1.048 (8)
C5-N1	1.397 (6)		

Selected angles (°)

O1-C1-C2	107.12 (3)
-----------------	------------

bis(4-(diphenylamino)phenyl)(4-((trimethylsilyl)ethynyl)phenyl)methanol (**40**)



C₄₈H₄₂N₂OSi, M = 690.95 g/mol

Reagents: ((4-bromophenyl)ethynyl)trimethylsilane (1.5 eq, 456 mg, 1.8 mmol), *n*-BuLi (1.1 eq, 968 μL at 1.6 M in hexane, 1.55 mmol), 4,4'-bis(diphenylamino)benzophenone **29** (1 eq, 794 mg, 1.5mmol).

Reaction: In a Schlenk flask under argon, *n*-BuLi was added drop wise to a solution of ((4-bromophenyl)ethynyl)trimethylsilane in 25 mL of dried and distilled THF at -78°C. After stirring for 15 min, the ketone in 15 mL of dried and distilled THF was added drop wise to the solution. The cold bath was then removed and the mixture was stirred and allowed to warm to room temperature over 3 h.

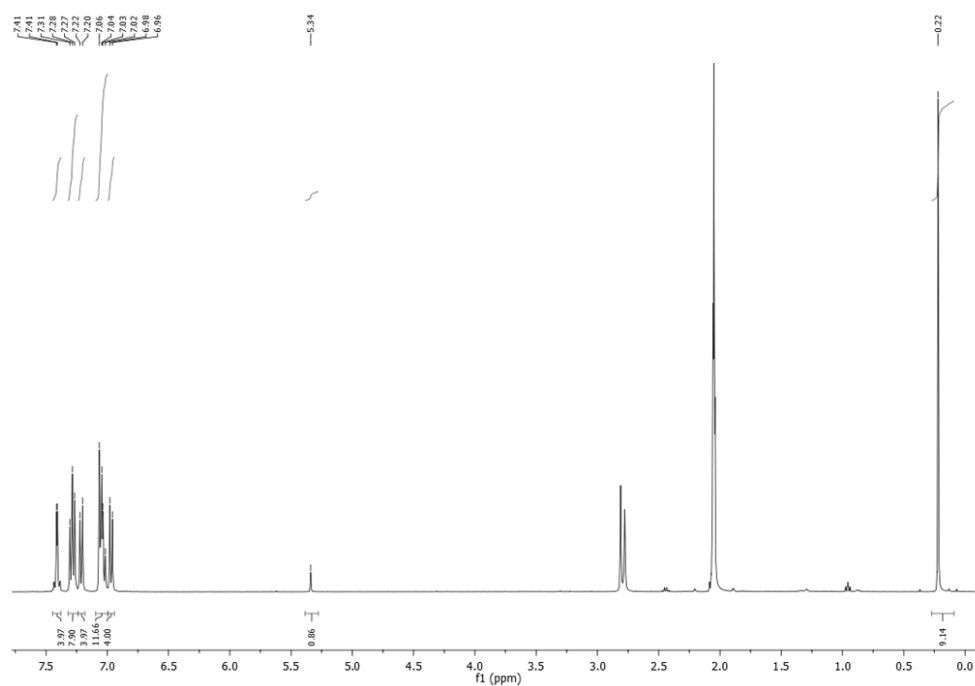
Work up: 20 mL of water were added to the flask and the two phases were separated. The aqueous layer was extracted with Et₂O (3 x 20 mL) and the combined organics phases were washed with water (3 x 10 mL) and saturated aqueous NaCl (10 mL). The aqueous phase was then back-extracted with Et₂O (20 mL). The organic phase was dried over Na₂SO₄ and the solvents were removed to give the expected product as a light yellow solid.

Purification: The crude was adsorbed on deactivated silica and purified by column chromatography (neutralized silica gel with 10 % NEt₃, 15 x 3 cm) eluting with hexane/AE (9/1) with 1 % NEt₃ to give the desired product as a light yellow solid.

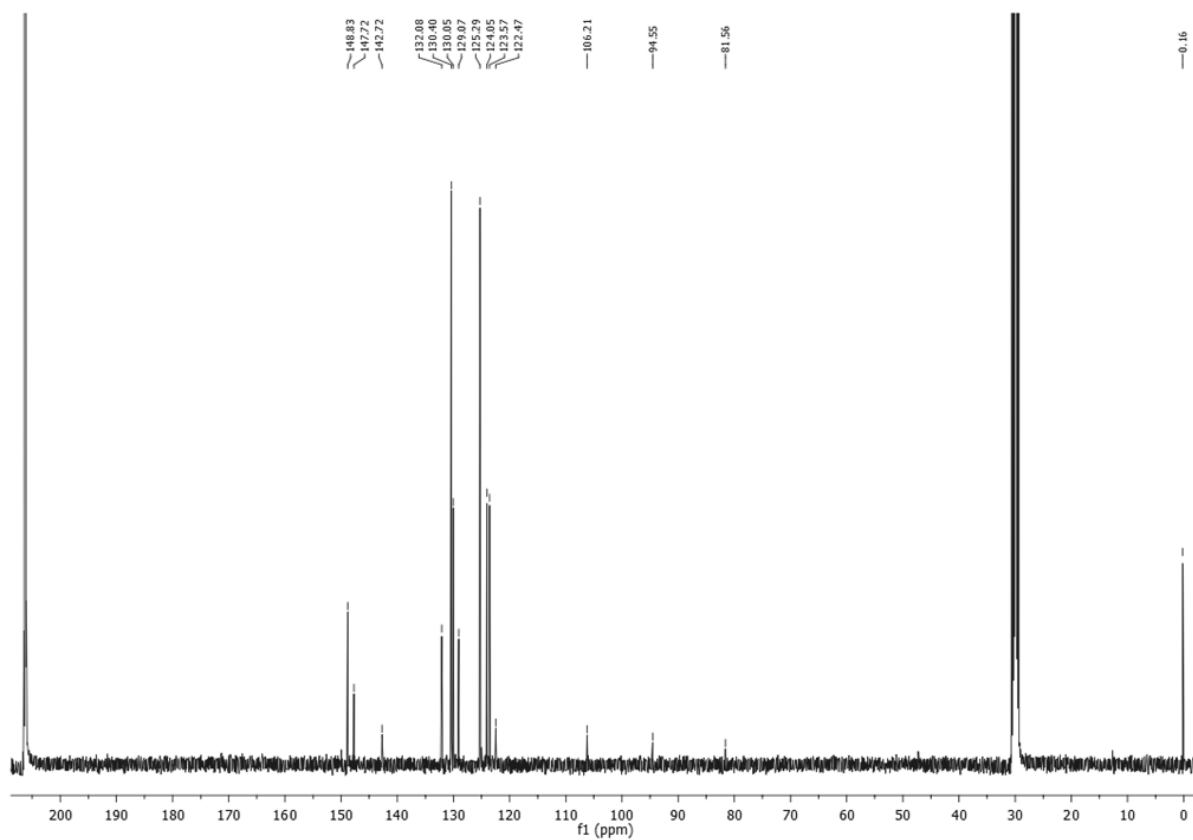
R_f(hexane/AE, 9/1): 0.33

Yield: 940 mg (91 %).

¹H NMR (400 MHz, (CD₃)₂CO) δ 7.41 (s, 4H), 7.28 (t, *J* = 7.8 Hz, 8H), 7.21 (d, *J* = 8.5 Hz, 4H), 7.08 – 7.00 (m, 12H), 6.96 (d, *J* = 8.5 Hz, 4H), 5.33 (s, 1H, -OH), 0.22 (s, 9H, CH₃).



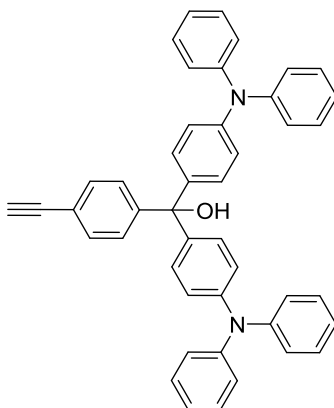
^{13}C NMR (101 MHz, $(\text{CD}_3)_2\text{CO}$) δ 148.83, 147.72, 142.72, 132.08, 130.40, 130.05, 129.07, 129.29, 125.29, 123.57, 122.47, 106.21 (C-OH), 94.55, 81.56, 0.16.



HRMS (ASAP): calcd: 691.31392 $[\text{M}+\text{H}]^+$, 690.30609 M^+ , 690.30609 $[\text{M}-\text{OH}]^+$; found : 691.3135 $[\text{M}+\text{H}]^+$, 690.3060 M^+ , 690.3060 $[\text{M}-\text{OH}]^+$.

IR ($\text{KBr}, \text{cm}^{-1}$): 3450 (ν_{OH}), 2157 ($\nu_{\text{C}\equiv\text{C}}$).

bis(4-(diphenylamino)phenyl)(4-ethynylphenyl)methanol (44)



$\text{C}_{45}\text{H}_{34}\text{N}_2\text{O}$, $M = 618.76 \text{ g/mol}$

Reagents: bis(4-(dimethylamino)phenyl)(4-((trimethylsilyl)ethynyl)phenyl)methanol **40** (1 eq, 759 mg, 1.1 mmol), K₂CO₃ (2 eq, 276 mg, 2.2 mmol).

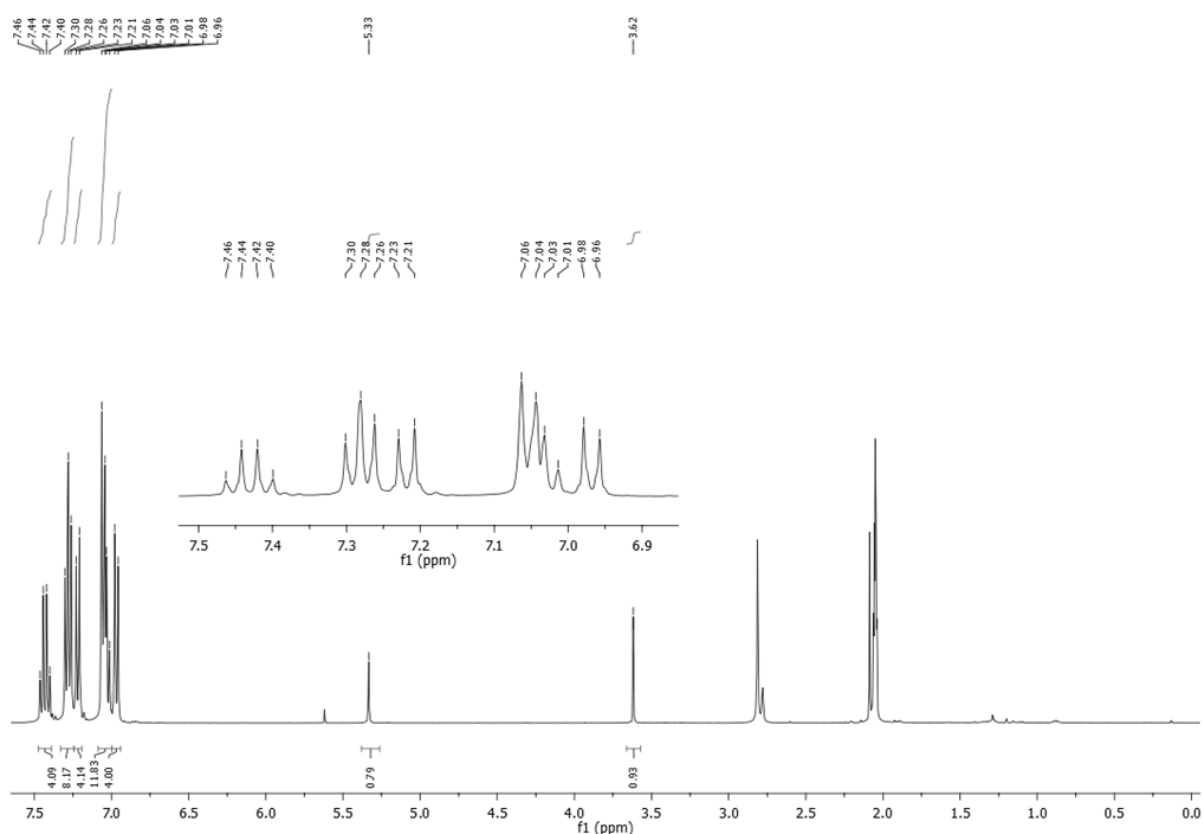
Reaction: In a round bottom flask, 1,1-bis(4-(diphenylamino)phenyl)-3-(trimethylsilyl)prop-2-yn-1-ol **40** and K₂CO₃ were stirred in a mixture of MeOH (20 mL) and DCM (20 mL) for 6 h at room temperature.

Work-up: Solvents were removed and the residue was treated with water (20 mL) and Et₂O (20 mL). The two layers were separated and the aqueous layer was extracted with Et₂O (3 x 20 mL). The combined organic layers were washed with water (3 x 10 mL) and saturated aqueous NaCl (10 mL). The aqueous layer was then back extracted with Et₂O (20 mL). The combined organic layers were dried over Na₂SO₄ and evaporated under reduced pressure to give a yellow solid.

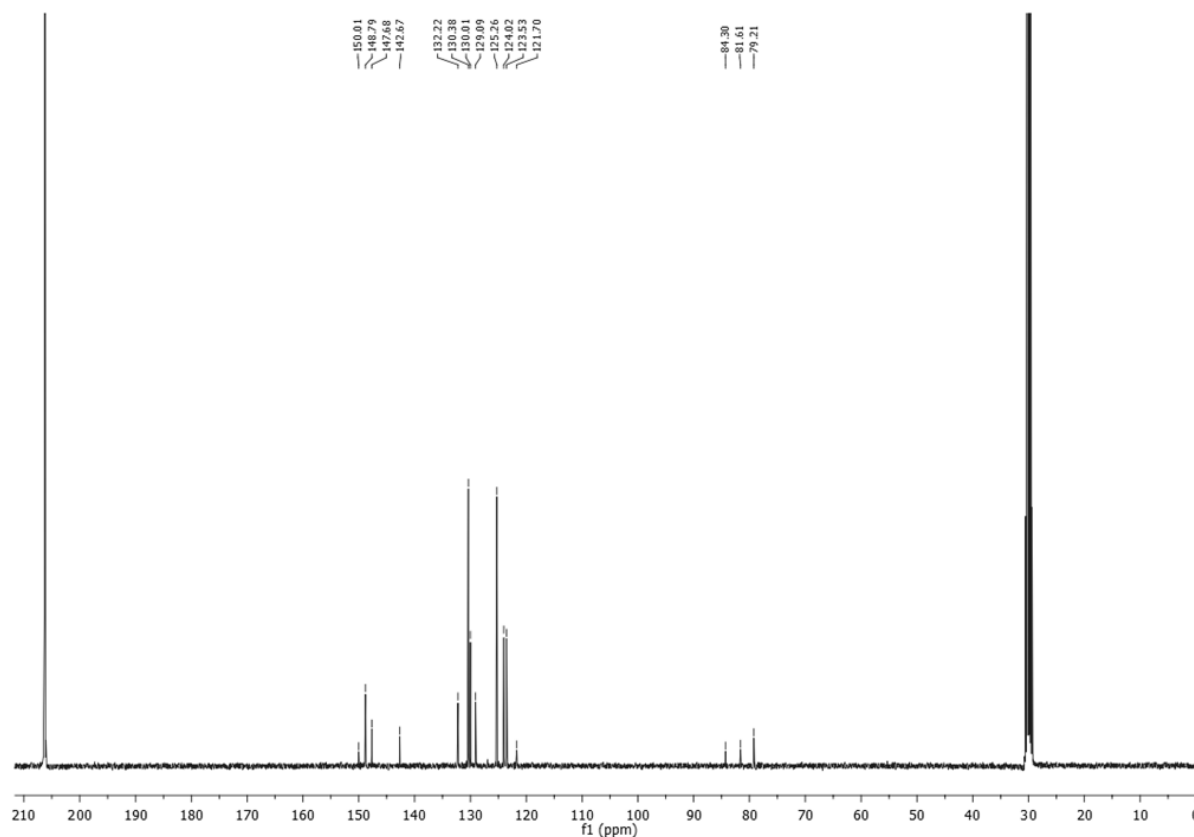
Purification: The solid residue was then precipitated with DCM/hexane three times to give the desired compound as a yellow powder.

Yield: 560 mg (82 %).

¹H NMR (400 MHz, (CD₃)₂CO) δ 7.43 (q, *J* = 8.3 Hz, 4H), 7.28 (t, *J* = 7.8 Hz, 8H), 7.22 (d, *J* = 8.6 Hz, 4H), 7.04 (m, 12H), 6.97 (d, *J* = 8.6 Hz, 4H), 5.32 (s, 1H, -OH), 3.61 (s, 1H, C≡C-H).



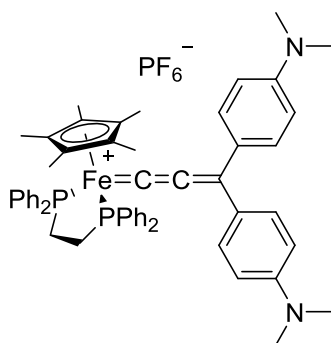
^{13}C NMR (101 MHz, $(\text{CD}_3)_2\text{CO}$) δ 150.10, 148.90, 147.79, 142.77, 132.30, 130.45, 130.10, 129.17, 125.36, 124.11, 123.63, 121.80, 84.39 (C-OH), 81.72, 79.23.



HRMS (ASAP): calcd: 619.27439 $[\text{M}+\text{H}]^+$, 618.26656 $[\text{M}]^+$, 601.26382 $[\text{M}-\text{OH}]^+$; found : 619.2746 $[\text{M}+\text{H}]^+$, 618.2670 $[\text{M}]^+$, 601.2643 $[\text{M}-\text{OH}]^+$.

IR (cm^{-1}): 3550 (ν_{OH}), 3279 ($\nu_{\text{C}\equiv\text{C}-\text{H}}$), $\nu_{\text{C}\equiv\text{C}}$ too weak to be observable.

Fe ($\eta^5\text{-C}_5\text{Me}_5$)($\kappa^2\text{-dppe}$)= $\text{C}=\text{C}=\text{C}$ (4-(dimethylamino)phenyl) $_2$ hexafluorophosphate ($[\text{M1}(\text{Fe})^+][\text{PF}_6^-]$)



$\text{C}_{53}\text{H}_{59}\text{F}_6\text{FeN}_2\text{P}_3$, $M = 986.81$ g/mol

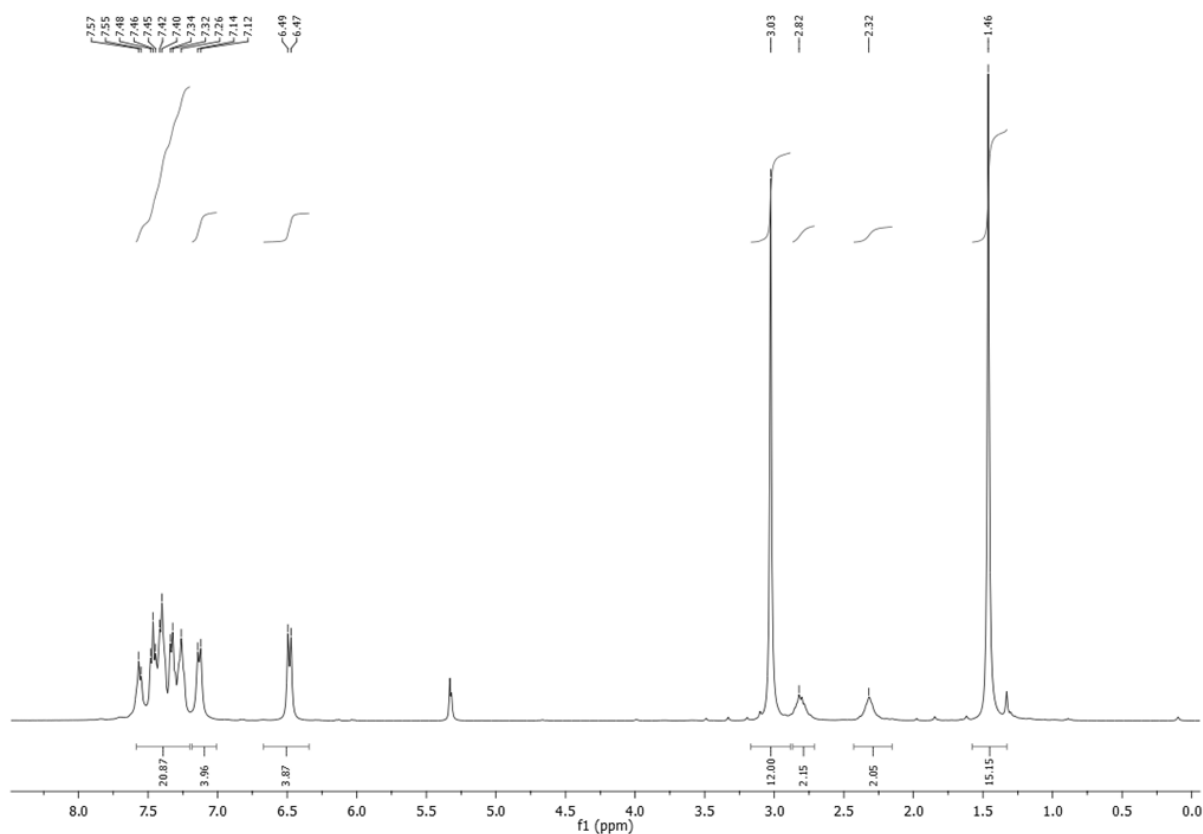
Reagents: (η^5 -C₅Me₅)(κ^2 -dppe)Fe(Cl) (1.1 eq, 562 mg, 0.9 mmol), KPF₆ (1.1eq, 165 mg, 0.9 mmol), 4,4'-(dimethylamino)phenyl)prop-2-yn-1-ol **41** (1 eq, 250 mg, 0.8 mmol).

Reaction: In a Schlenk tube under argon, (η^5 -C₅Me₅)(κ^2 -dppe)Fe(Cl), KPF₆ and 1,1-bis(4-(dimethylamino)phenyl)prop-2-yn-1-ol **41** were dissolved in 15 mL of dry and deoxygenated MeOH. The resulting solution was stirred at 40°C for 16h.

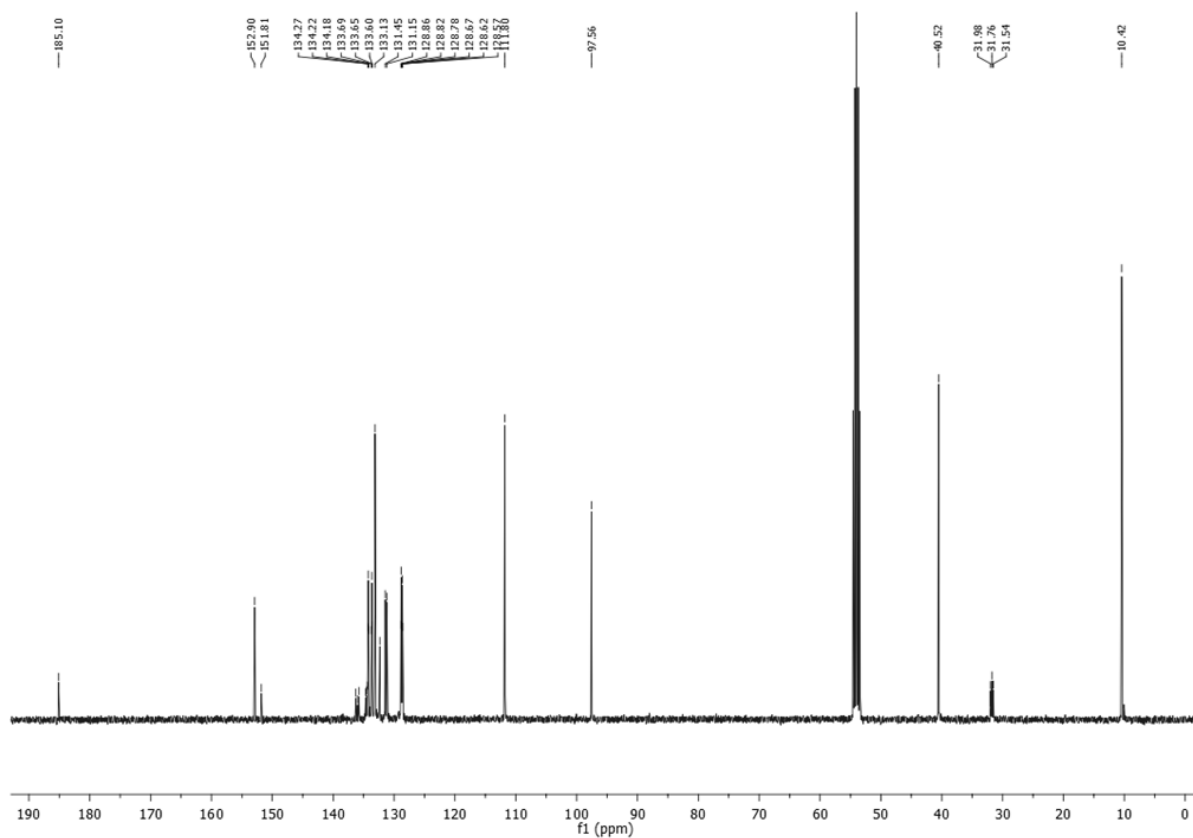
Work-up and purification: After evaporation of the solvent by cryoscopic transfer, the residue was extracted with DCM (3 x 10 mL). The resulting solid was then precipitated from DCM/Et₂O and washed with pentane to give the desired compound, after filtration, as a violet powder.

Yield: 740 g (91 %).

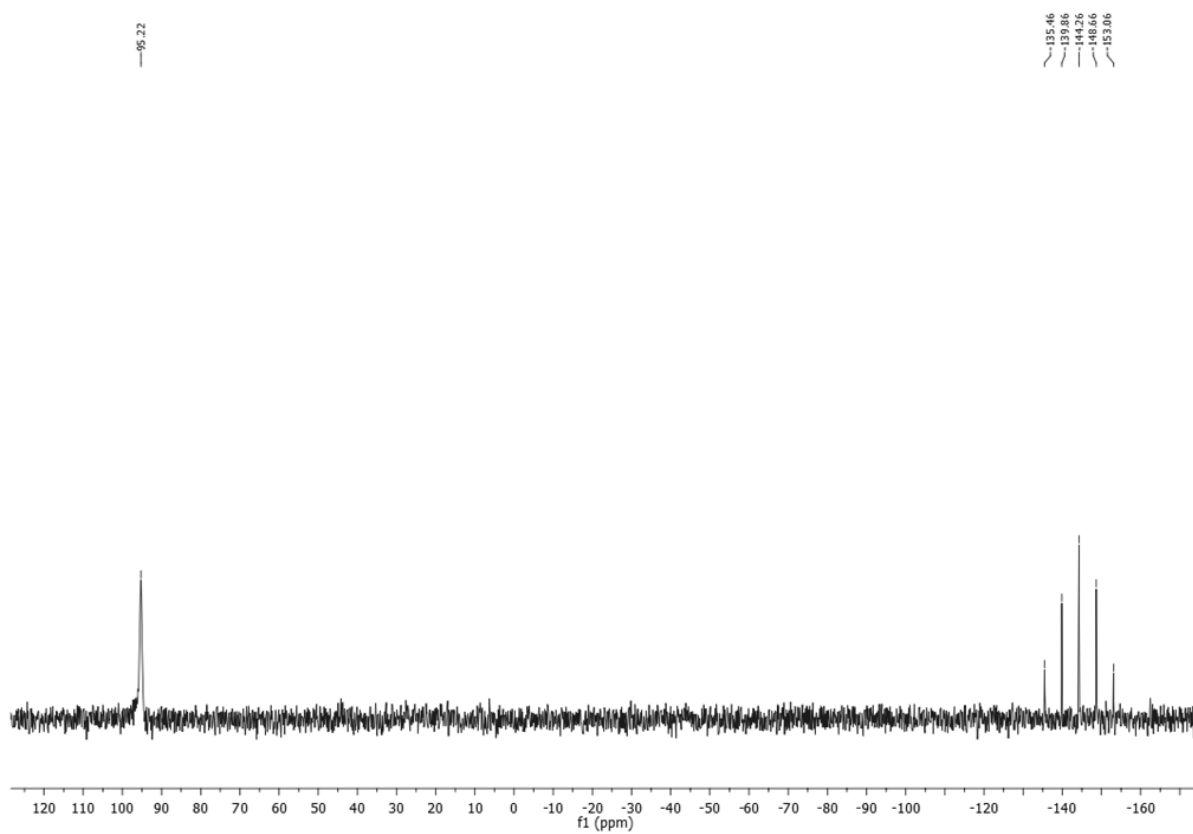
¹H NMR (400 MHz, CD₂Cl₂) δ 7.58 – 7.20 (m, 20H), 7.13 (d, J = 7.9 Hz, 4H), 6.48 (d, J = 8.5 Hz, 4H), 3.03 (s, 12H, -NMe₂), 2.82 (s, 2H, H-CH₂ dppe), 2.32 (s, 2H, H-CH₂ dppe), 1.46 (s, 15H, Cp*).



¹³C NMR (101 MHz, CD₂Cl₂) δ 185.10, 152.90, 151.81, 136.02, 134.52, 134.22, 133.65, 133.13, 132.33, 131.45, 131.15, 128.86-128.57 (m), 111.80, 97.56, 40.52 (-NMe₂), 31.76 (m, CH₂ dppe), 10.42 (s, CH₃ Cp*).



³¹P NMR (162 MHz, CD₂Cl₂) δ 95.22, -144.48(q).

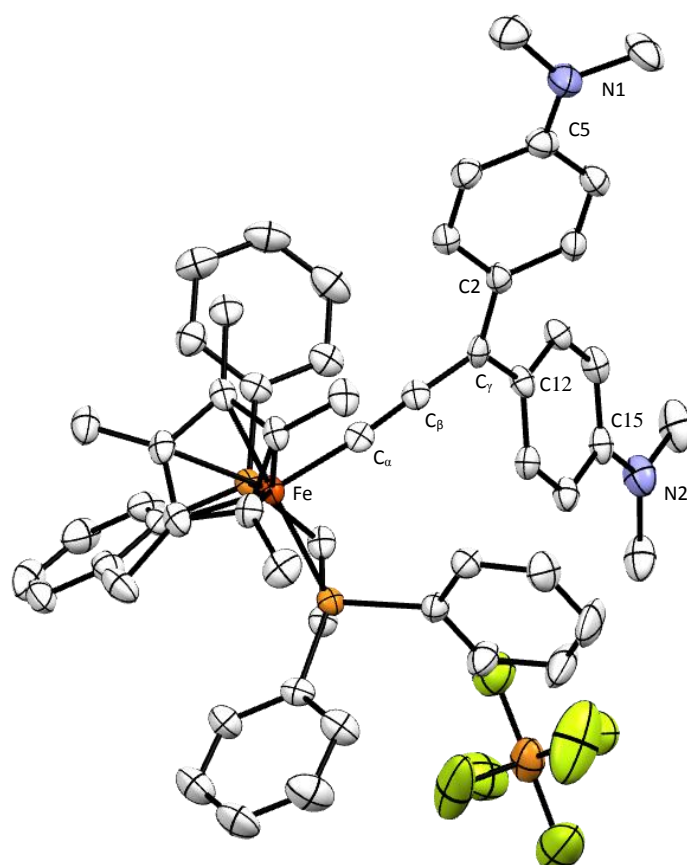


IR (cm^{-1}): 1926 ($\nu_{\text{C}\equiv\text{C}}$), 841 ($\nu_{\text{P-F}}$).

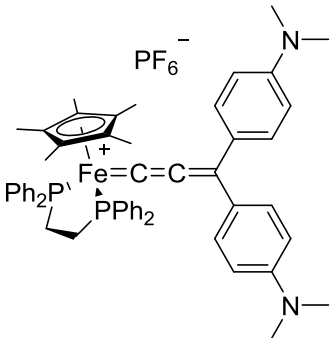
UV-Vis (DCM): λ_{max} , nm (ϵ , $10^{-5} \cdot \text{M}^{-1} \cdot \text{cm}^{-1}$): 405 (0.07), 516 (0.45), 660 (0.36).

CV: (DCM, 0.10 M $[n\text{-Bu}_4\text{N}][\text{PF}_6]$, V vs Ag/Ag^+): $E_{1/2} \text{C}^+/\text{C}^{\cdot+}$: -1.27 V; $E_{1/2}$: 0.34 V ($\Delta E_p = 0.05$ V, $i_{pc}/i_{pa} = 1.05$).

X-ray diffraction study:



ORTEP view of $([\text{M1}(\text{Fe})^+][\text{PF}_6^-])$ with 50 % thermal ellipsoids solved by Dr. Thierry Roisnel

	
Formula	2(C ₅₅ H ₅₉ FeN ₂ P ₂), 2(F ₆ P)
Molecular weight (g/mol)	1973.62
Violet crystals by slow diffusion of pentane vapor into a DCM solution of the molecule at room temperature	

Crystal parameters	
Crystal class	monoclinic
Space group	P 2 _{1/n}
Cell angles (°)	α= 90
	β= 92.13
	γ= 90
Cell length (Å)	a= 23.70
	b= 17.07
	c= 27.75
Cell volume (Å ³)	11228
Z	Z= 4

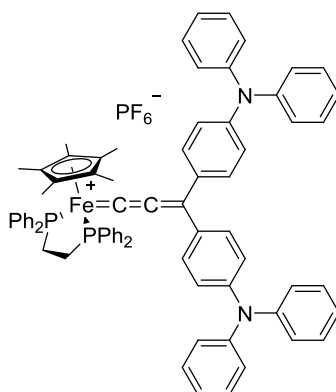
Selected bond length (Å)

C_γ-C2	1.438 (6)	C15-N2	1.375 (4)
C_γ-C12	1.460 (5)	C5-N1	1.375 (3)
C_β -C_γ	1.389 (5)	C3-C4	1.415 (6)
C_α-C_β	1.239 (5)	C2-C3	1.370 (7)
Fe-C_α	1.826 (3)		

Selected angles (°)

Phenyl torsion	21.88 (2)	C plane	0.26 (2)
-----------------------	-----------	----------------	----------

Fe (η⁵-C₅Me₅)(κ²-dppe)=C=C=C(4-(diphenylamino)phenyl)₂ hexafluorophosphate ([M2(Fe)⁺][PF₆⁻])



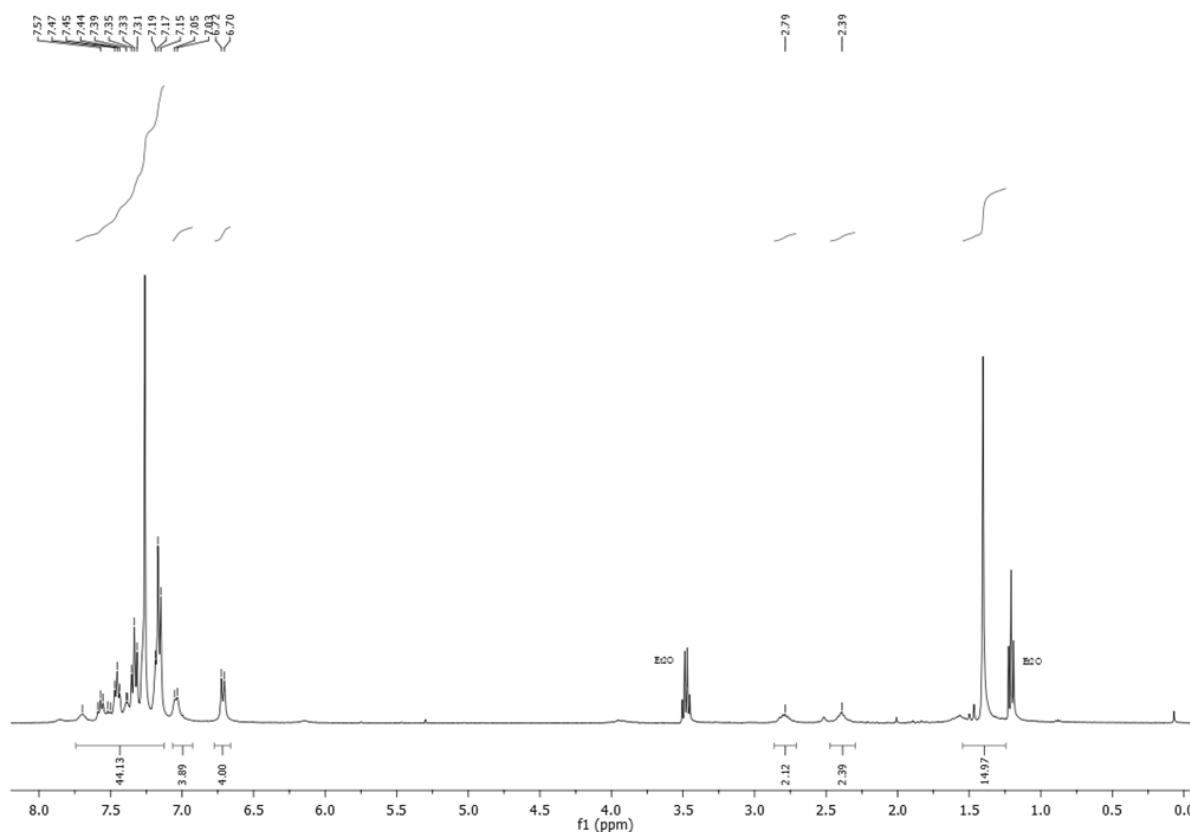
C₇₃H₆₇F₆FeN₂P₃, M = 1235,08 g/mol

Reagents: (η^5 -C₅Me₅)(κ^2 -dppe)Fe(Cl) (1.1 eq, 68.7 mg, 0.11 mmol), KPF₆ (1.1 eq, 20.2 mg, 0.11mmol), 1,1-bis(4-(diphenylamino)phenyl)prop-2-yn-1-ol **42** (1 eq, 61.8 mg, 0.1 mmol).

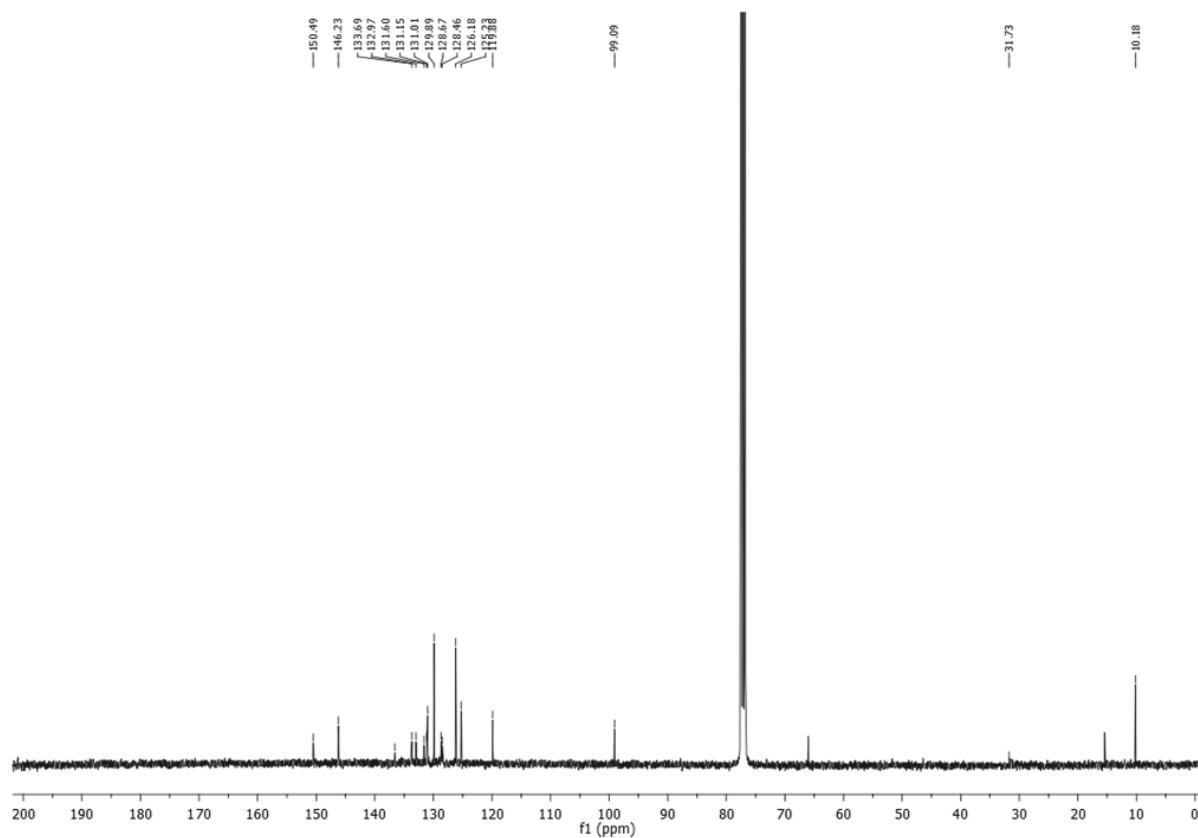
Reaction: In a Schlenk tube under argon, (η^5 -C₅Me₅)(κ^2 -dppe)Fe(Cl), KPF₆ and 1,1-bis(4-(diphenylamino)phenyl)prop-2-yn-1-ol **42** were dissolved in 15 mL of dry and deoxygenated MeOH. The resulting solution was stirred at room temperature for 16 h.

Work-up and purification: After evaporation of the solvent by cryoscopic transfer, the residue was extracted with DCM (3 x 10 mL). The resulting solid was then precipitated with DCM/pentane to give the desired compound, after filtration, as a violet powder.

¹H NMR (400 MHz, CD₂Cl₂) δ 7.62 – 7.10 (m, 40H), 7.07 (d, J = 7.6 Hz, 4H), 6.73 (d, J = 8.6 Hz, 4H), 2.82 (s, 2H, CH₂ dppe), 2.40 (s, 2H, CH₂ dppe), 1.40 (s, 15H, CH₃ Cp*).

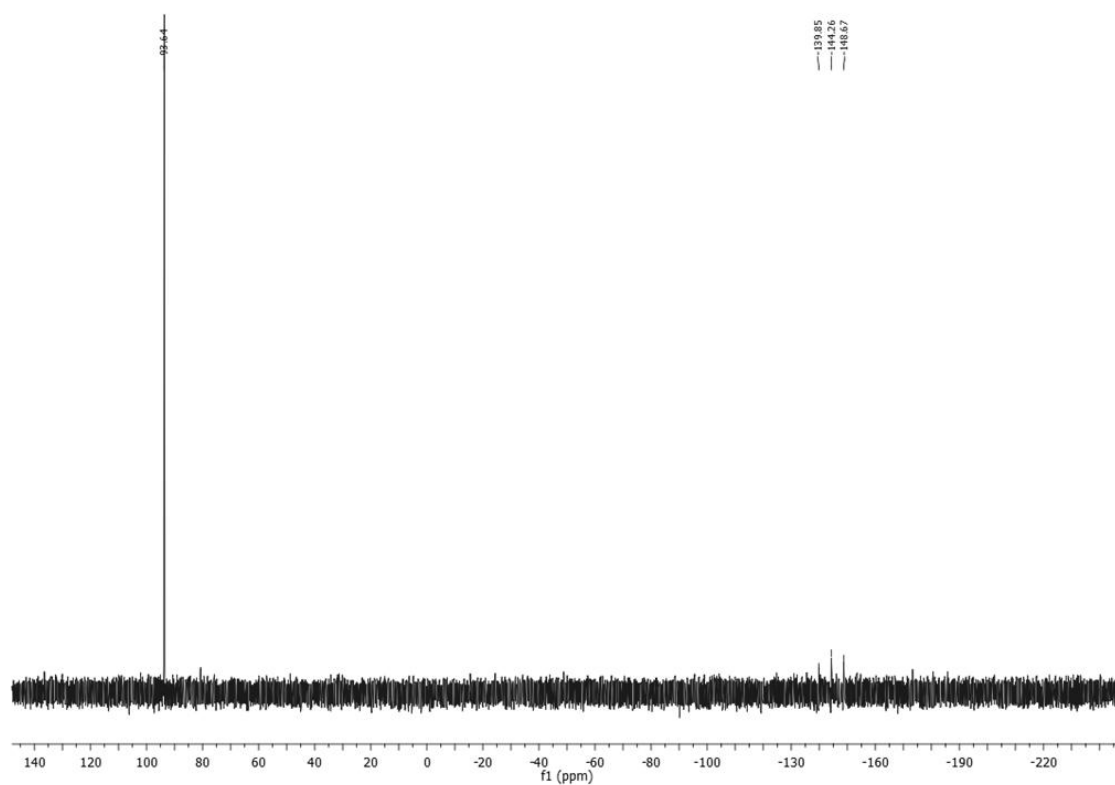


¹³C NMR (101 MHz, CDCl₃) δ 150.49, 146.23, 136.58, 133.69, 132.97, 131.60, 131.15, 131.01, 129.89, 128.67, 128.46, 126.18, 125.23, 119.88, 99.09, 31.73 (dppe), 10.18 (CH₃ Cp*).



³¹P NMR (162 MHz, CD₂Cl₂) δ 93.64, -144.26 (q).

NB: regarding the intensity of the PF₆ peak, anionic metathesis may have happened.

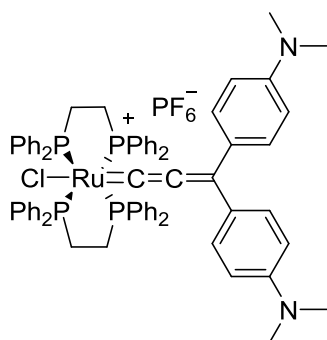


IR (cm⁻¹): 1911 (ν_{C≡C}), 836 (ν_{P-F}).

UV-Vis (DCM): λ_{max}, nm (ε, 10⁻⁵·M⁻¹·cm⁻¹): 274 (0.49), 432 (0.04), 546 (0.32), 655 (0.3).

CV: (DCM, 0.10 M [*n*-Bu₄N][PF₆], V vs SCE): C⁺/C^{·+} E_{1/2}: -0.75 V; E_{1/2}: 0.48 V (ΔE_p = 0.05 V, *i*_{pc}/*i*_{pa} = 1.02).

Ru(Cl)(κ²-dppe)₂=C=C=C(4-(dimethylamino)phenyl)₂ hexafluorophosphate ([M1(Ru)⁺][PF₆⁻])



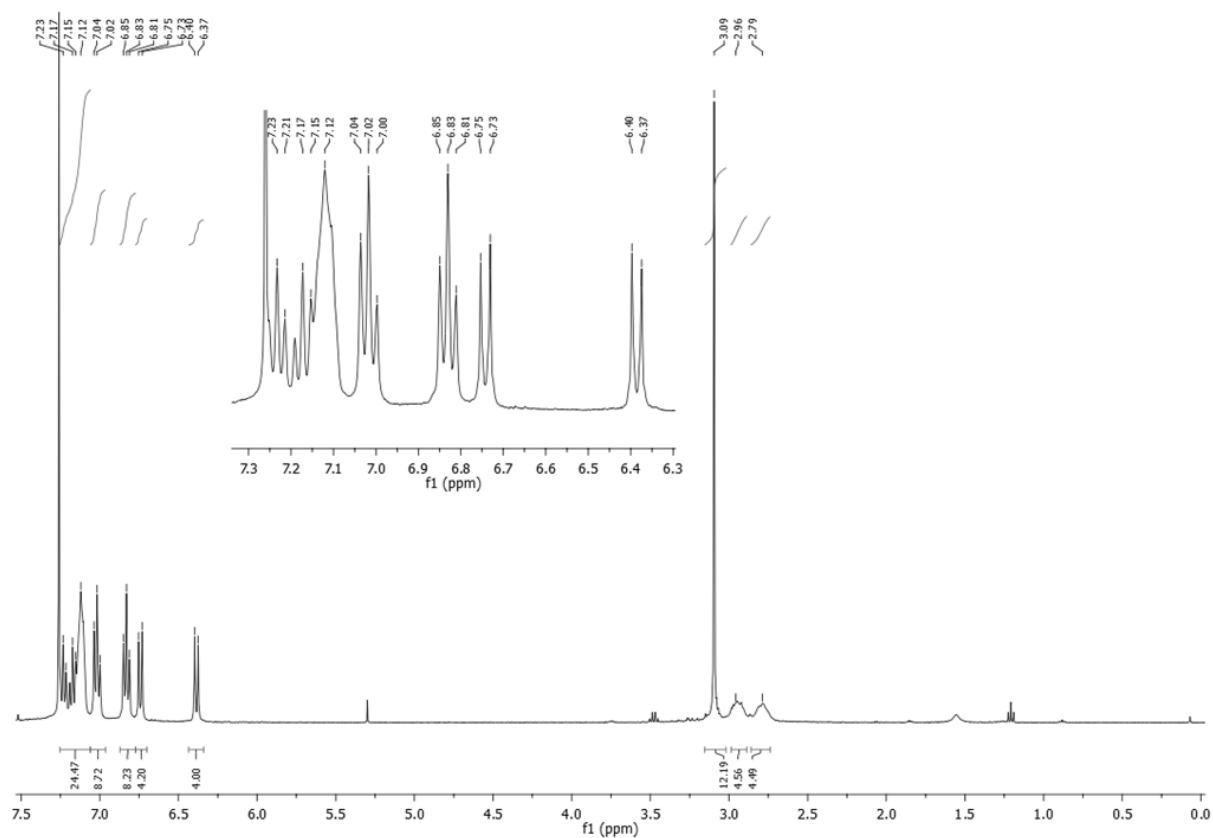
C₇₁H₆₈F₆N₂P₅Ru, M = 1319.24 g/mol

Reagents: 1,1-bis(4-(dimethylamino)phenyl)prop-2-yn-1-ol **41** (1 eq, 92.6 mg, 0.25 mmol), [RuCl(dppe)₂PF₆] (0.8 eq, 211 mg, 0.2 mmol).

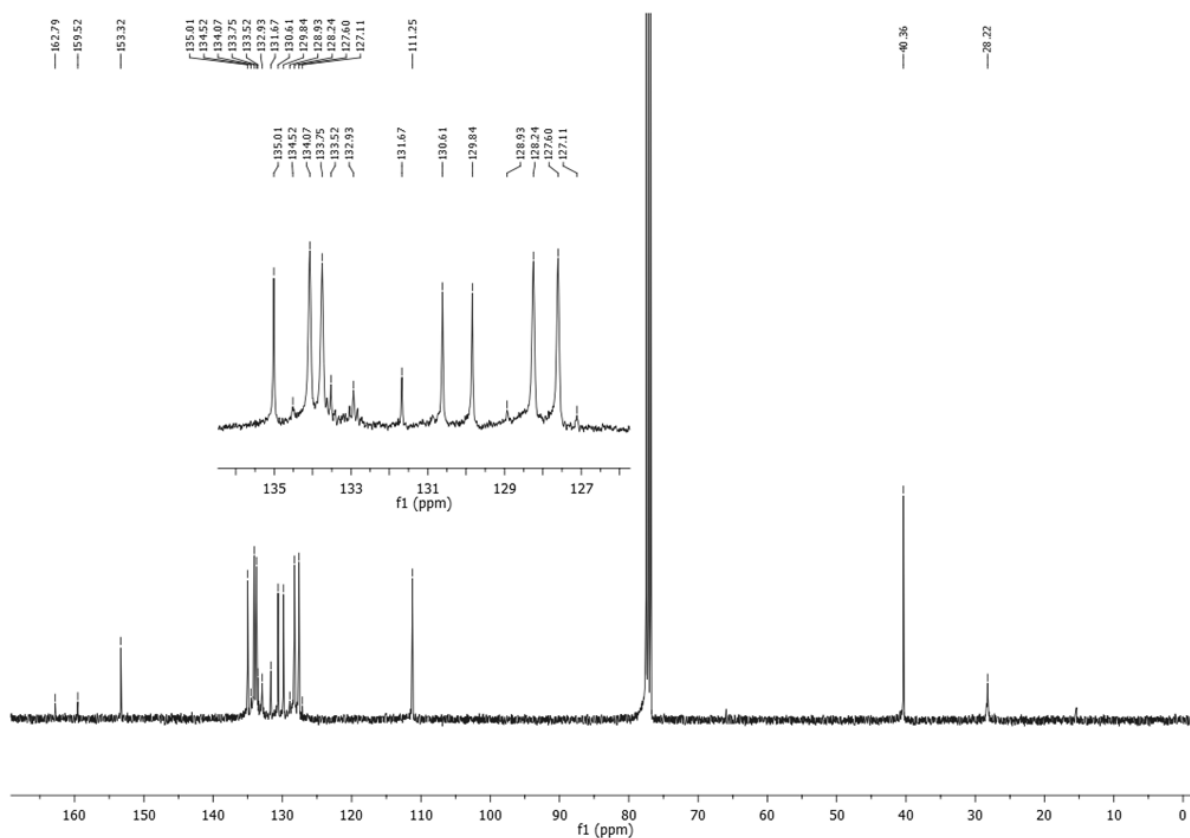
Reaction: In a Schlenk flask under argon, 10 mL of distilled and deoxygenated DCM were added to 1,1-bis(4-(dimethylamino)phenyl)prop-2-yn-1-ol and [RuCl(dppe)₂PF₆]. The resulting mixture was stirred for 24h at room temperature.

Work-up: The volume was reduced to a minimum and the desired product was precipitated from Et₂O and washed with dried and deoxygenated pentane to give a violet powder.

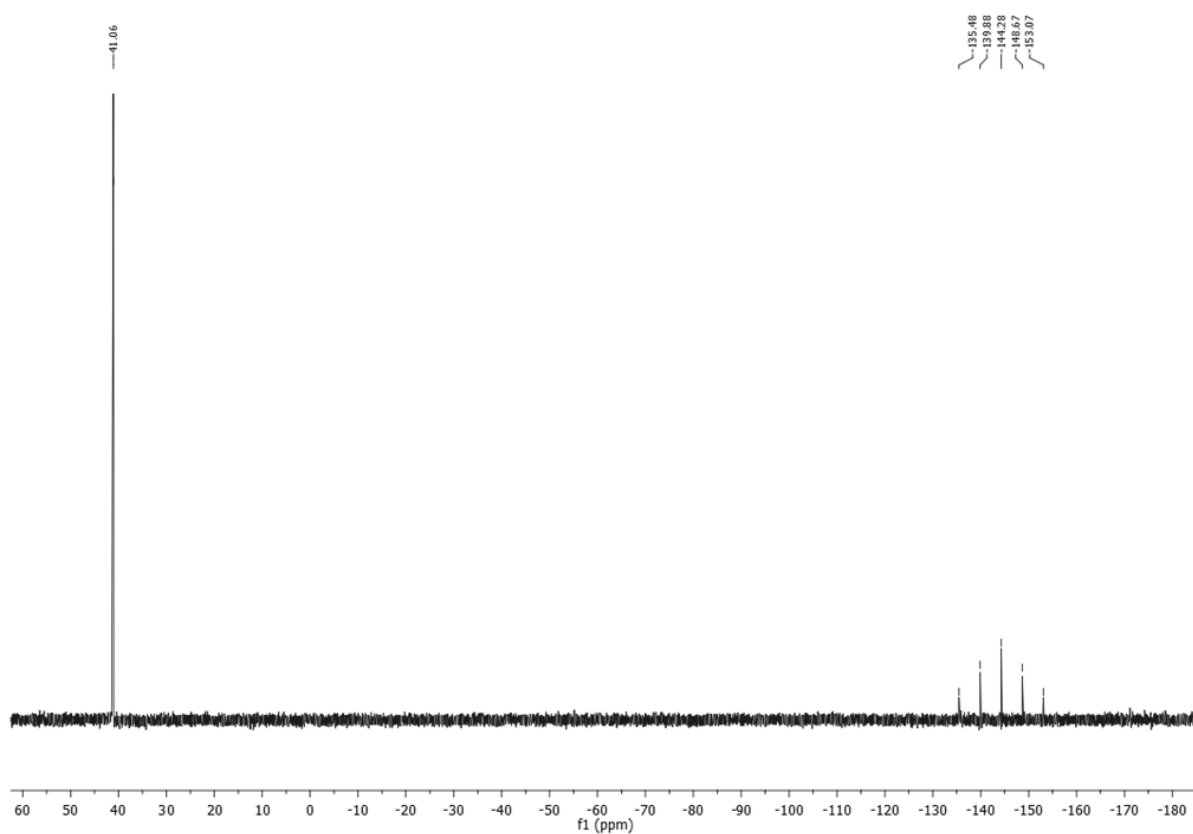
¹H NMR (400 MHz, CDCl₃) δ 7.30 – 7.07 (m, 24H + CDCl₃), 7.02 (t, *J* = 7.6 Hz, 8H), 6.83 (t, *J* = 7.6 Hz, 8H), 6.74 (d, *J* = 8.8 Hz, 4H), 6.39 (d, *J* = 8.8 Hz, 4H), 3.09 (s, 12H, -NMe₂), 2.95 (s, 4H, CH₂ dppe), 2.80 (s, 4H, CH₂ dppe).



¹³C NMR (101 MHz, CDCl₃) δ 162.78, 159.52, 153.32, 135.00, 134.07, 133.75, 133.52, 132.93, 131.67, 130.61, 129.83, 128.24, 127.60, 111.24, 40.36 (-NMe₂), 28.22 (CH₂ dppe).



^{31}P NMR (162 MHz, CDCl_3) δ 41.06 (s), -144.27 (sept).



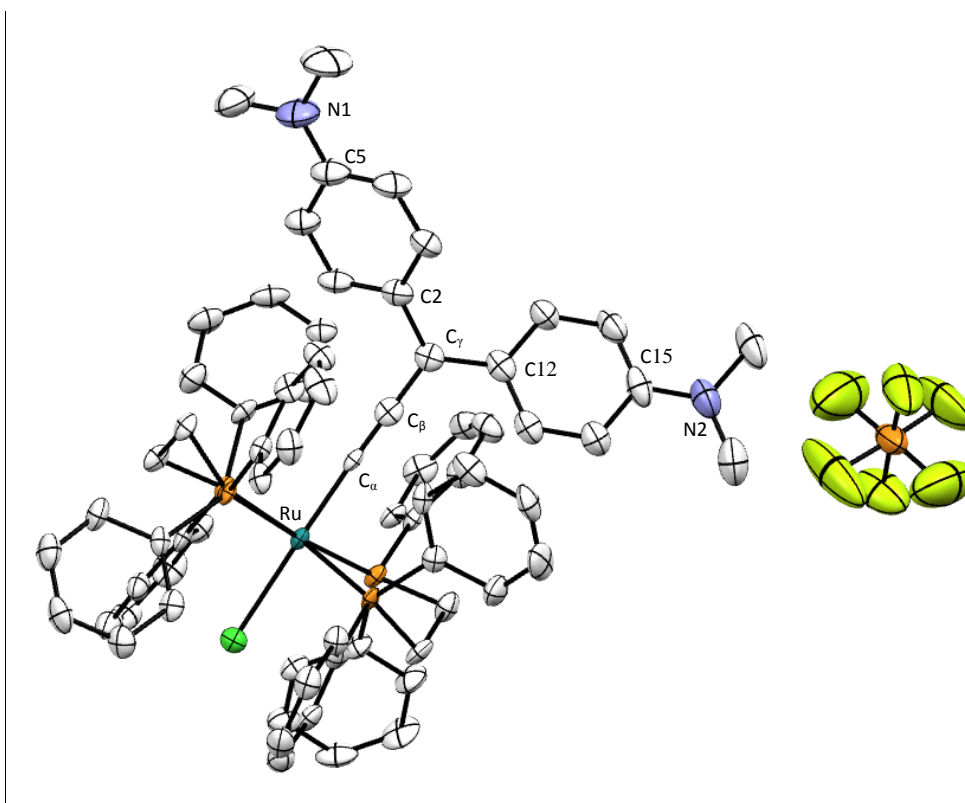
HRMS (ESI): calcd.: 1209.3065 $[\text{M}]^+$; found: 1209.3065 $[\text{M}]^+$.

IR (cm^{-1}): 1942 ($\nu_{\text{C}\equiv\text{C}}$), 842 ($\nu_{\text{P-F}}$).

CV: (DCM, 0.10 M $[\text{n-Bu}_4\text{N}][\text{PF}_6]$, V vs SCE): $\text{C}^+/\text{C}^\bullet$, $E_{1/2}$: -0.98 V; $\text{M}^{\text{III}}/\text{M}^{\text{II}}$, $E_{1/2}$: 0.92 V ($\Delta E_p = 0.04$ V, $i_{\text{pc}}/i_{\text{pa}} = 0.98$).

UV-VIS: λ_{max} , nm (ϵ , $10^{-5} \cdot \text{M}^{-1} \cdot \text{cm}^{-1}$): 261(0.61), 540 (0.51), 597 (0.59), 692 (0.5).

X-ray diffraction study:



ORTEP view of $[(M1(Ru))^+][PF_6^-]$ with 50 % thermal ellipsoids solved by Dr. Graeme Moxey

Formula	$C_{71}H_{68}ClN_2P_4Ru, F_6P$
Molecular weight (g/mol)	1319.24
Violet crystals by slow evaporation of a saturated DCM solution of the molecule at room temperature	

Crystal parameters	
Crystal class	monoclinic
Space group	$P 2_1/c$
Cell angles ($^\circ$)	$\alpha = 90$
	$\beta = 107.92$
	$\gamma = 90$
Cell length (\AA)	$a = 12.28$
	$b = 35.94$
	$c = 18.66$
Cell volume (\AA^3)	7842.67
Z	$Z = 4$

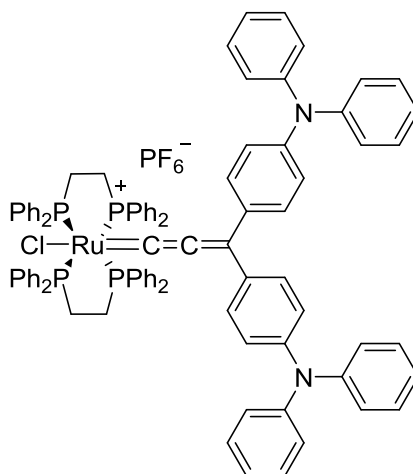
Selected bond length (Å)

C_γ-C2	1.460 (10)	C15-N2	1.379 (10)
C_γ-C12	1.476 (10)	C5-N1	1.364 (10)
C_β-C_γ	1.387 (5)	C3-C4	1.394 (10)
C_α-C_β	1.220 (5)	C2-C3	1.364 (10)
Ru-C_α	1.941 (6)		

Selected angles (°)

Phenyl torsion	28.70 (3)	C plane	1.50 (5)
-----------------------	-----------	----------------	----------

Ru(Cl)(κ²-dppe)₂=C=C=C(4-(diphenylamino)phenyl)₂ hexafluorophosphate ([M²(Ru)⁺][PF₆⁻])



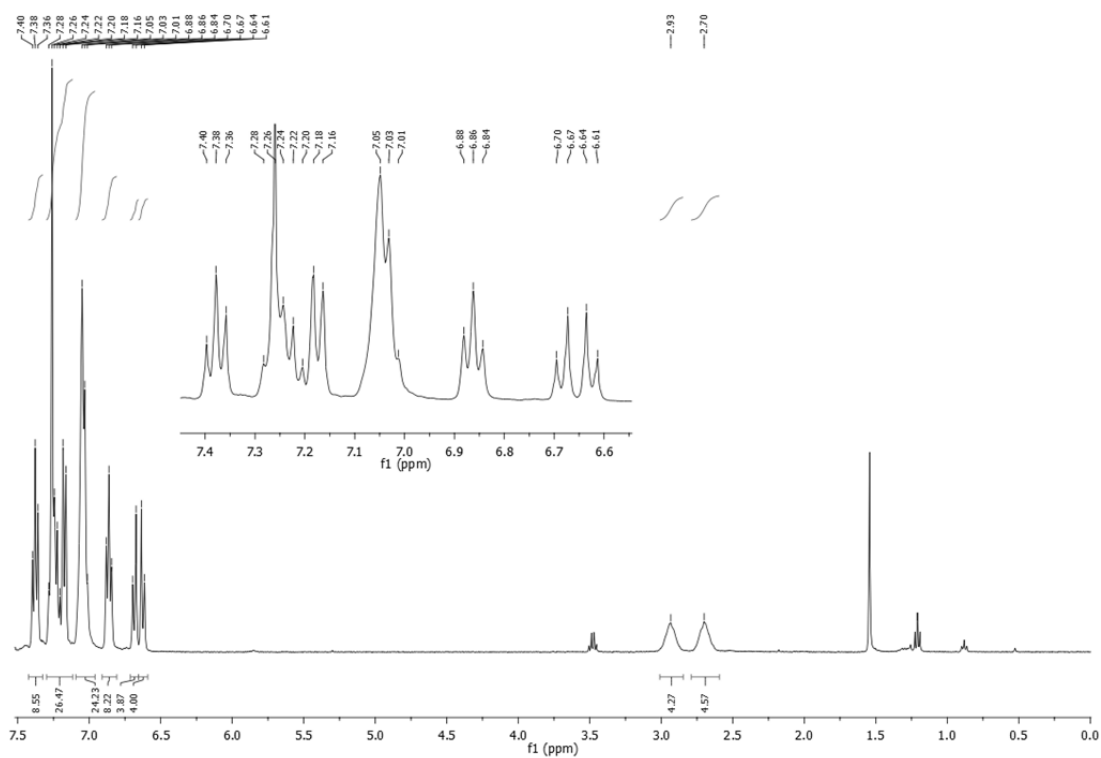
C₉₁H₇₆ClF₆N₂P₅Ru, M = 1603.00 g/mol

Reagents: 1,1-bis(4-(diphenylamino)phenyl)prop-2-yn-1-ol **42** (1 eq, 154.6 mg, 0.25 mmol), [RuCl(dppe)₂](PF₆) (1.05 eq, 285.7 mg, 0.625 mmol).

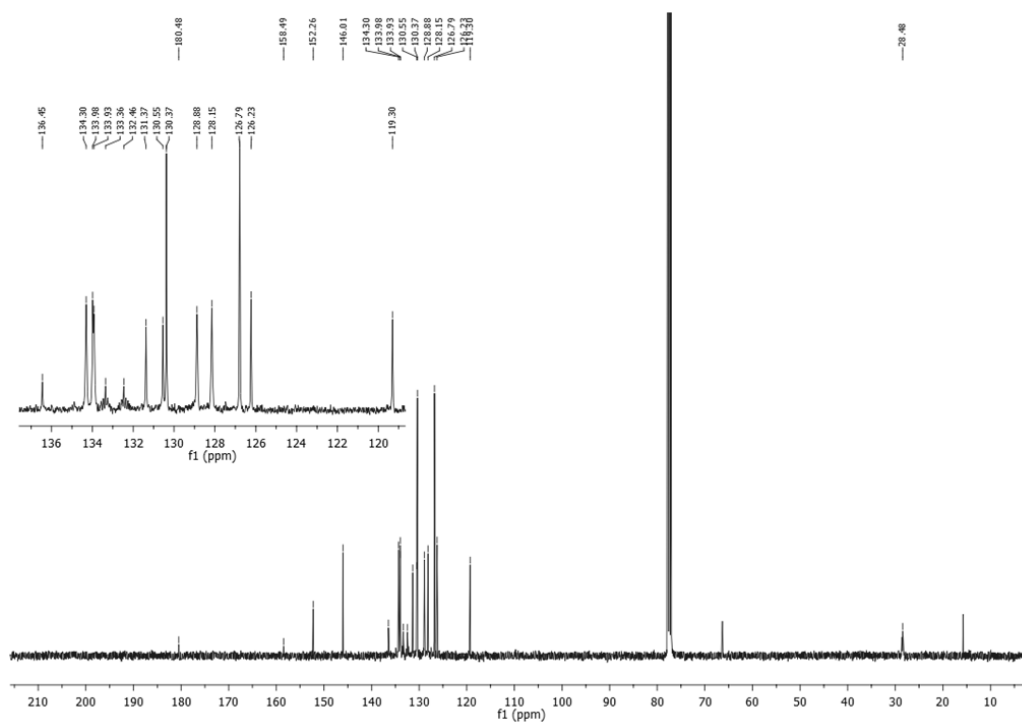
Reaction: In a Schlenk flask under argon, 20 mL of distilled and deoxygenated DCM were added to 1,1-bis(4-(diphenylamino)phenyl)prop-2-yn-1-ol **42** and [RuCl(dppe)₂](PF₆). The resulting mixture was stirred for 72h at room temperature.

Work-up: The volume was reduced to a minimum and the desired product was precipitated with Et₂O at - 40 °C and washed with dried and deoxygenated pentane to give a violet powder.

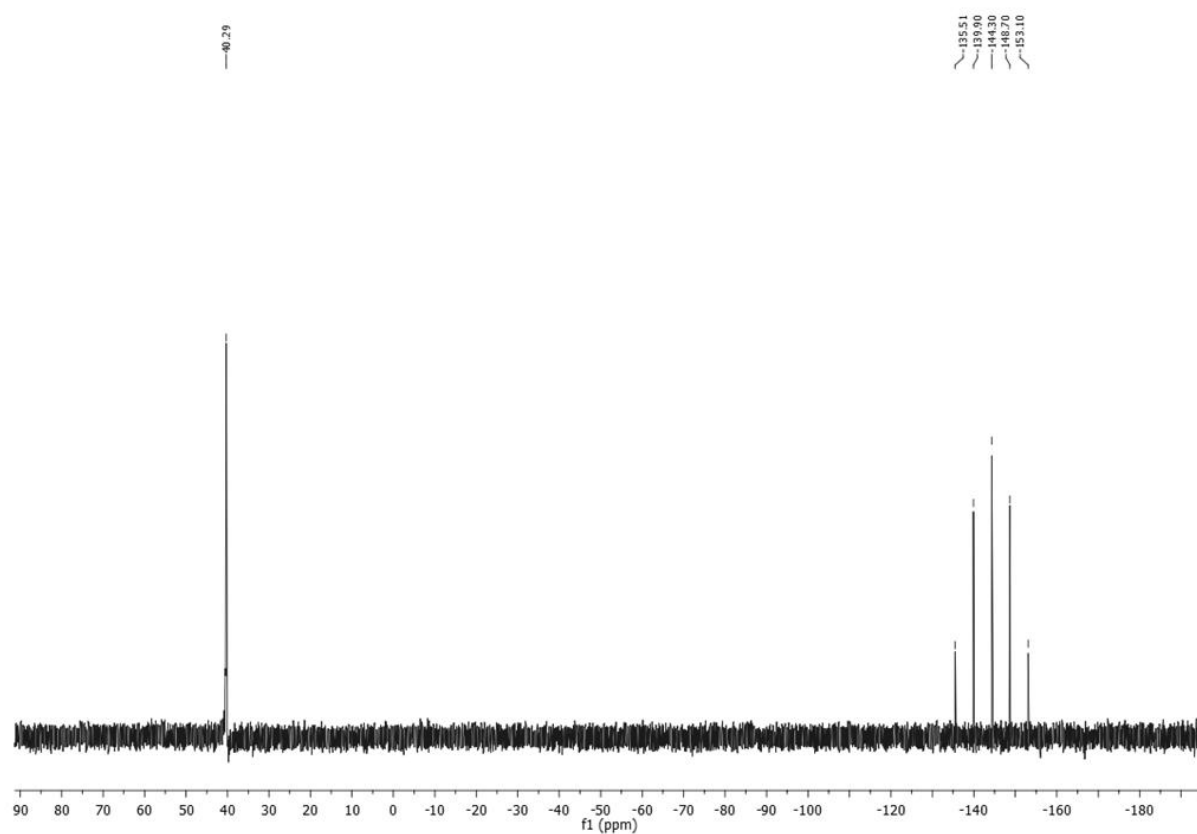
^1H NMR (400 MHz, CDCl_3) δ 7.38 (t, $J = 7.8$ Hz, 8H), 7.30 – 7.12 (m, 12H), 7.09 – 6.96 (m, 24H), 6.86 (t, $J = 7.6$ Hz, 8H), 6.68 (d, $J = 9.0$ Hz, 4H), 6.62 (d, $J = 9.0$ Hz, 4H), 2.93 (s, 4H, CH_2 dppe), 2.70 (s, 4H, CH_2 dppe).



^{13}C NMR (101 MHz, CDCl_3) δ 180.48, 158.49, 152.26, 146.01, 136.45, 134.30, 133.98, 133.93, 133.36, 132.46, 131.37, 130.55, 130.37, 128.88, 128.15, 126.79, 126.23, 119.30, 28.48 (dppe).



^{31}P NMR (162 MHz, CDCl_3) δ 40.29, -144.31 (sept).

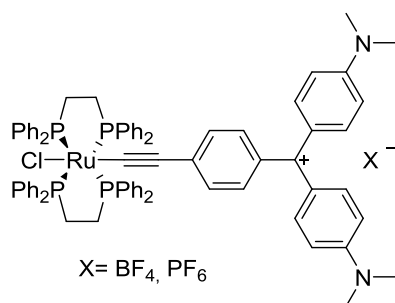


IR (cm^{-1}): 1921 ($\nu_{\text{C}\equiv\text{C}}$), 836 ($\nu_{\text{P-F}}$).

UV-Vis (DCM): λ_{max} , nm (ϵ , $10^{-5} \cdot \text{M}^{-1} \cdot \text{cm}^{-1}$): 265 (1.4), 574 (0.65), 621 (0.76).

CV: (DCM, 0.10 M [*n*-Bu₄N][PF₆], V vs Ag⁺/Ag): C⁺/C⁺ $E_{1/2}$: -0.75 V; M^{III}/M^{II} $E_{1/2}$: 1.06 V ($\Delta E_p = 0.06$ V, $i_{\text{pc}}/i_{\text{pa}} = 0.82$).

Ru(Cl)(κ^2 -dppe)₂-C \equiv C-(*p*-C₆H₄)-C(4-(dimethylamino)phenyl)₂ tetrafluoroborate / hexafluorophosphate ([M³(Ru)]⁺)[BF₄⁻/PF₆⁻])



X = BF₄, C₇₇H₇₂BClF₄N₂P₄Ru, M = 1372.66 g/mol

X = PF₆, C₇₇H₇₂ClF₆N₂P₅Ru, M = 1430.82 g/mol

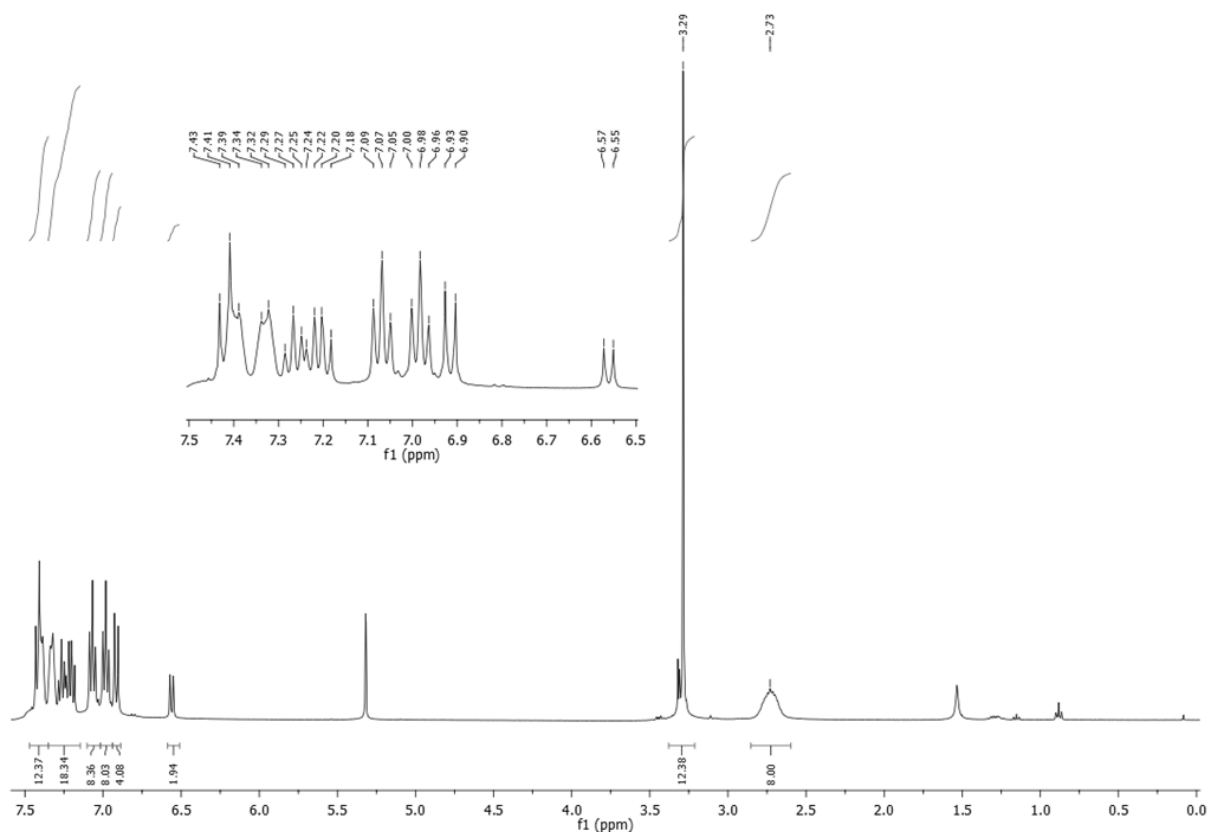
X= PF₆:

Reagents: 1,1-bis(4-(dimethylamino)phenyl)prop-2-yn-1-ol **43** (1 eq, 185 mg, 0.25 mmol), [RuCl(dppe)₂]PF₆ (1.05 eq, 285.7 mg, 0.265 mmol).

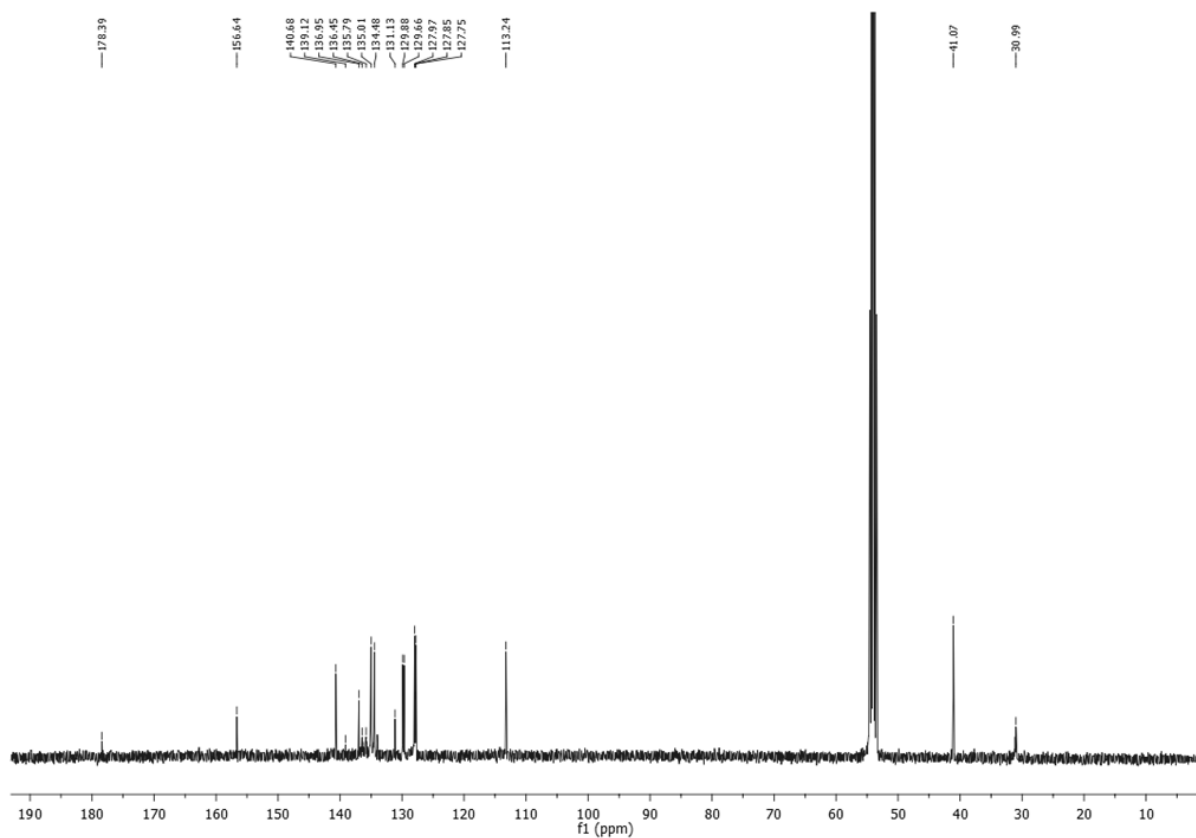
Reaction: In a Schlenk flask under argon, 20 mL of distilled and deoxygenated DCM were added to 1,1-bis(4-(dimethylamino)phenyl)prop-2-yn-1-ol and [RuCl(dppe)₂]PF₆. The resulting mixture was stirred overnight at room temperature.

Work-up and purification: The volume was reduced to a minimum and the desired product was precipitated with Et₂O, filtered and washed with Et₂O and pentane to obtain a dark powder. The obtained mixture of product was then dissolved in CHCl₃ and the bis-substituted product (**M5(Ru)**²⁺) was crystallized at -20°C. The crystals were then filtered with a cannula. The same operation was repeated until the bis-coupled product was removed. (3 or 4 times).

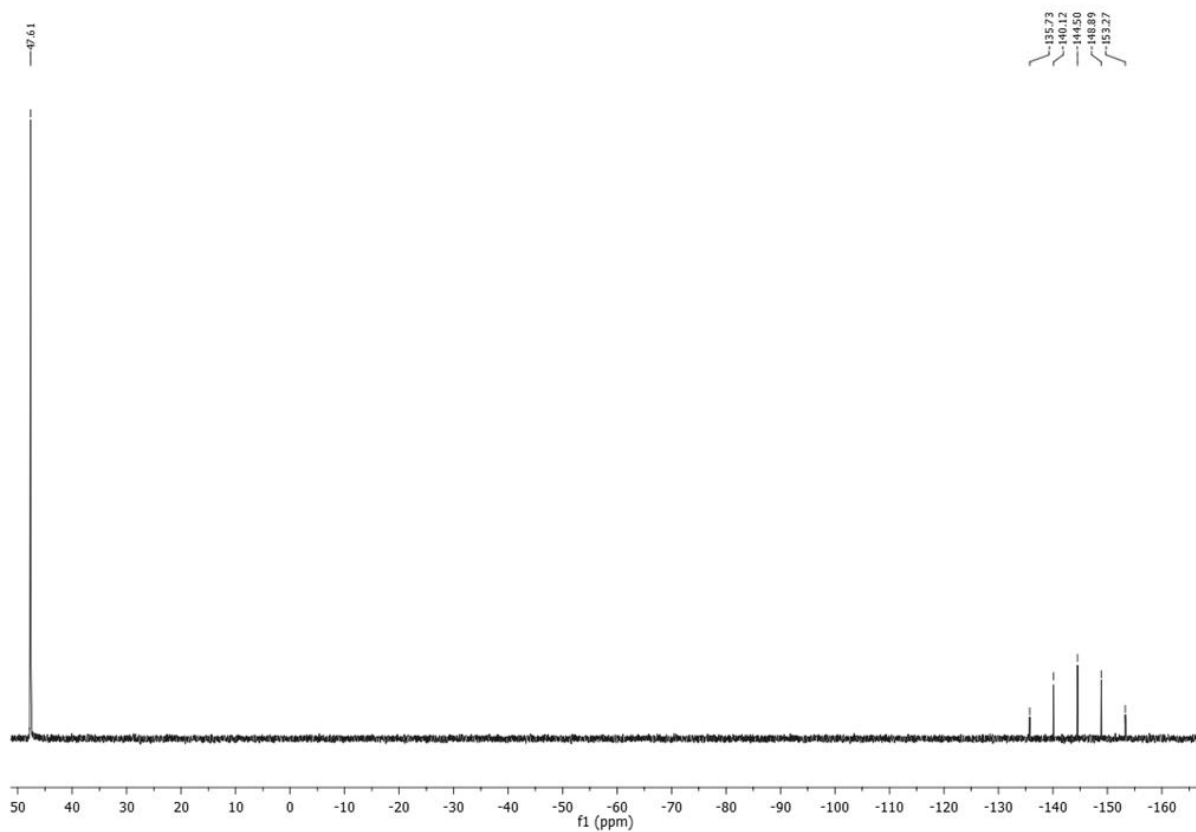
¹H NMR (400 MHz, CD₂Cl₂) δ 7.47 – 7.35 (m, 12H), 7.35 – 7.15 (m, 18H), 7.10 – 7.02 (m, 8H), 6.97 (m, 8H), 6.92 (d, *J* = 9.3 Hz, 4H), 6.56 (d, *J* = 8.5 Hz, 2H), 3.29 (s, 12H, -NMe₂), 2.73 (s, 8H, CH₂ dppe).



¹³C NMR (101 MHz, CD₂Cl₂) δ 178.39, 156.64, 140.68, 139.12, 136.95, 136.45, 135.79, 135.01, 134.48, 131.13, 129.88, 129.66, 127.97, 127.85, 127.75, 113.24, 41.07 (-NMe₂), 30.99 (dppe).



³¹P NMR (162 MHz, CD₂Cl₂) δ 47.61 (s), -144.50 (sept).



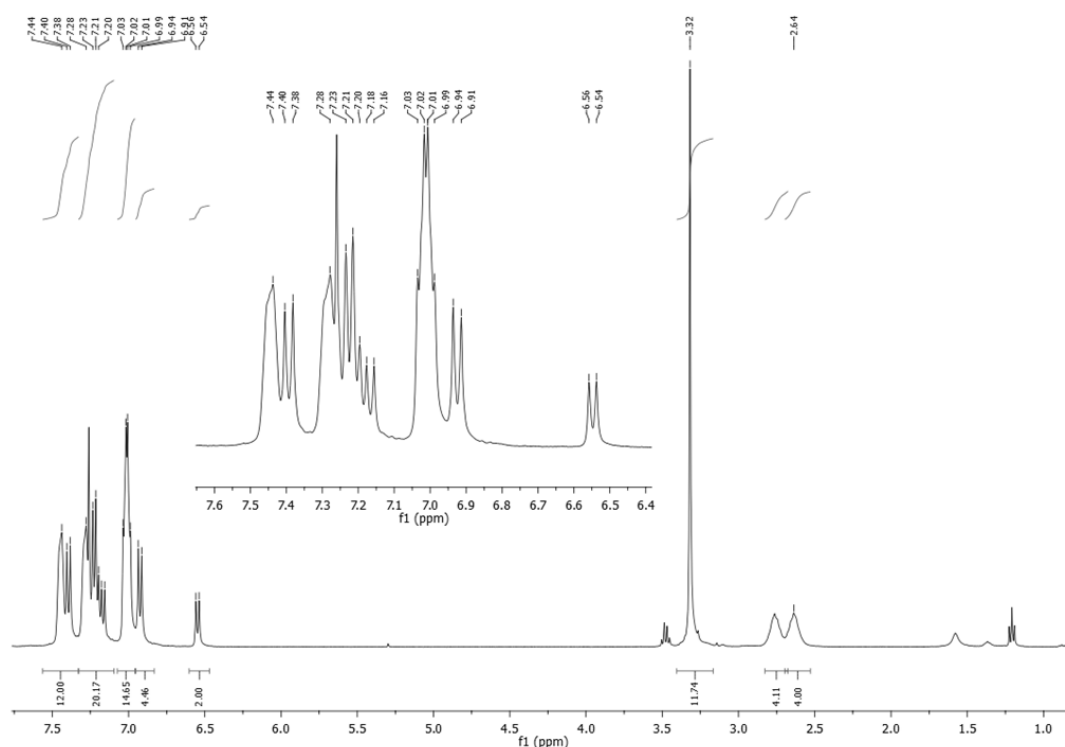
X= BF₄:

Reagents: 1,1-bis(4-(dimethylamino)phenyl)prop-2-yn-1-ol **43** (1 eq, 37 mg, 0.15 mmol), HBF₄·Et₂O (1.05 eq, 14.4 μL, 0.265 mmol), [RuCl(dppe)₂]PF₆ (1 eq, 107.8 mg, 0.15 mmol), Et₃N (3 eq, 8.3 μL, 0.35 mmol).

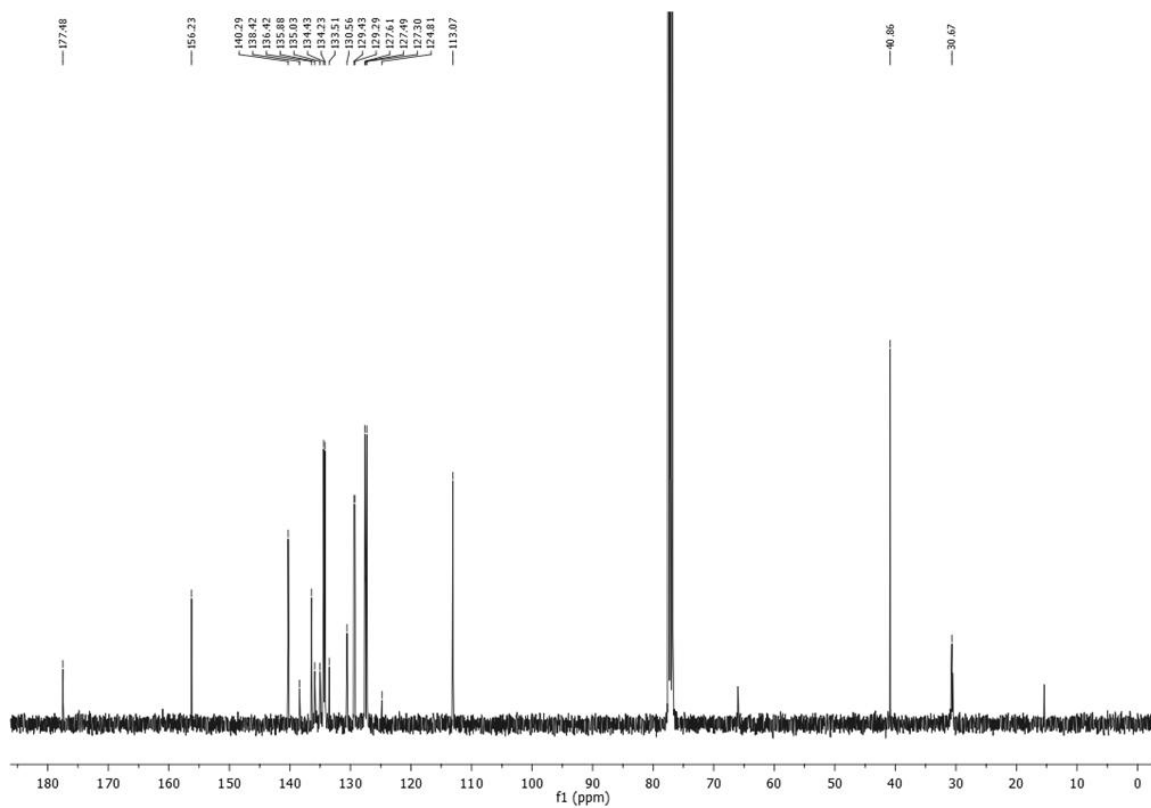
Reaction and work up: In a Schlenk flask under argon, to a solution of 1,1-bis(4-(dimethylamino)phenyl)prop-2-yn-1-ol in 20 mL of distilled and deoxygenated Et₂O at 0°C were added HBF₄·Et₂O. After stirring for 15 min, the formed precipitate was filtered off and washed with Et₂O three times. [RuCl(dppe)₂]PF₆ and 5 mL of DCM were added to the obtained solid and the resulting mixture was stirred overnight at room temperature. The obtained vinylidene solution was reduced to a minimum and the product precipitated with Et₂O, filtered and washed with Et₂O and pentane to obtain a green powder.

The vinylidene was dissolved in dried and deoxygenated DCM and Et₃N was added to the solution and stirred for 10 min at room temperature. The dark green solution was reduced and again precipitated with Et₂O, filtered and washed with Et₂O and pentane to obtain the desired acetylide as a green powder.

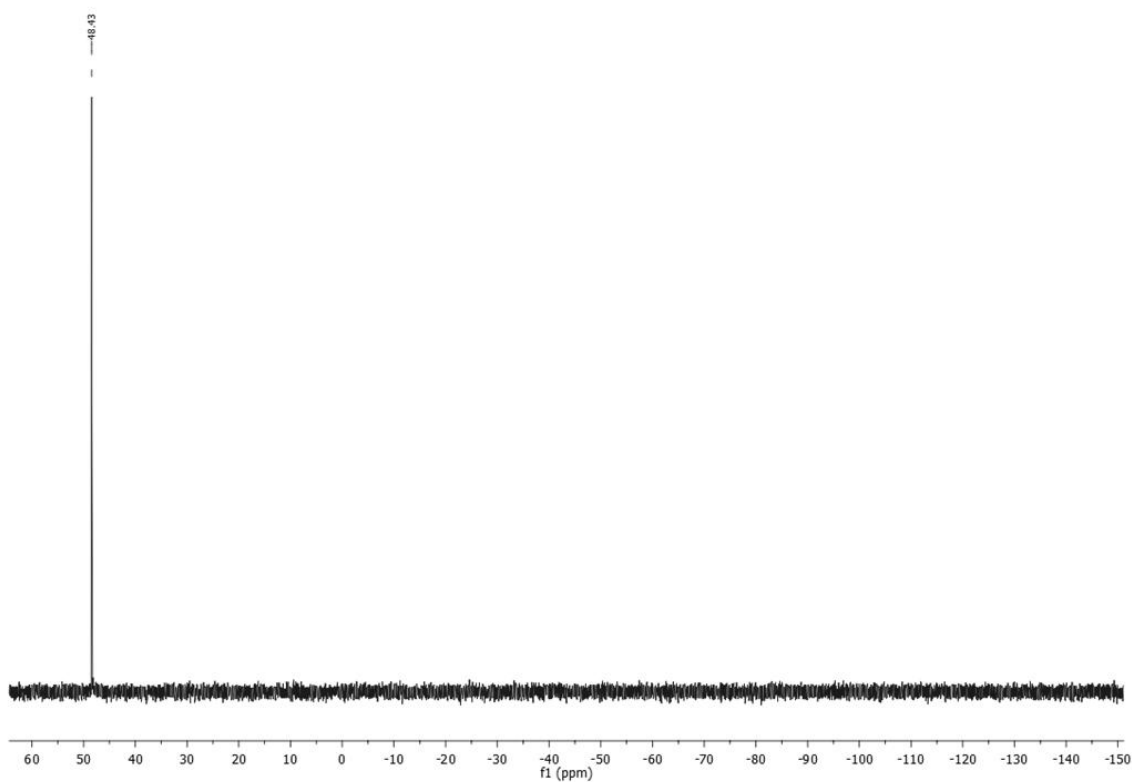
¹H NMR (400 MHz, CDCl₃) δ 7.56 – 7.33 (m, 12H), 7.33 – 7.09 (m, 20H + CDCl₃), 7.01 (m, 14H), 6.92 (d, *J* = 9.1 Hz, 4H), 6.55 (d, *J* = 8.3 Hz, 2H), 3.32 (s, 12H, -NMe₂), 2.72 (s, 4H, CH₂ dppe), 2.64 (s, 4H, CH₂ dppe).



^{13}C NMR (101 MHz, CDCl_3) δ 177.48, 156.23, 140.29, 138.42, 136.42, 135.88, 135.03, 134.43, 134.23, 133.51, 130.56, 129.43, 129.29, 127.61, 127.49, 127.30, 124.81, 113.07, 40.86 ($-\text{NMe}_2$), 30.67 (dppe).



^{31}P NMR (162 MHz, CDCl_3) δ 48.43 (s).



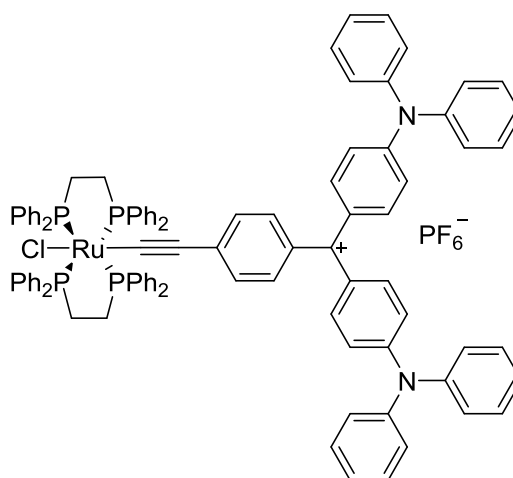
IR (cm⁻¹): 2013 (ν_{C≡C}), 839 (ν_{P-F})/833 (ν_{B-F}).

UV-Vis (DCM): λ_{max}, nm (ε, 10⁻⁵·M⁻¹·cm⁻¹): X= BF₄: 268 (0.85), 440 (0.14) 600 (1.02), 748 (0.56); X= PF₆: 268 (1.1), 440 (0.20) 600 (1.04), 748 (0.59)

HRMS (ESI): calcd.: 1285.3378 [M]⁺, found: 1285.3384 [M]⁺.

CV: DCM, 0.10 M [*n*-Bu₄N][PF₆], V vs Ag⁺/Ag: C⁺/C⁺ E_{1/2}: -0.66 V; M^{III}/M^{II} E_{1/2}: 0.58 (ΔE_p = 0.04 V, *i*_{pc}/*i*_{pa} = 1.0).

Ru(Cl)(κ²-dppe)₂-C≡C-(*p*-C₆H₄)-C(4-(diphenylamino)phenyl)₂ hexafluorophosphate ([M4(Ru)]⁺)[PF₆⁻]



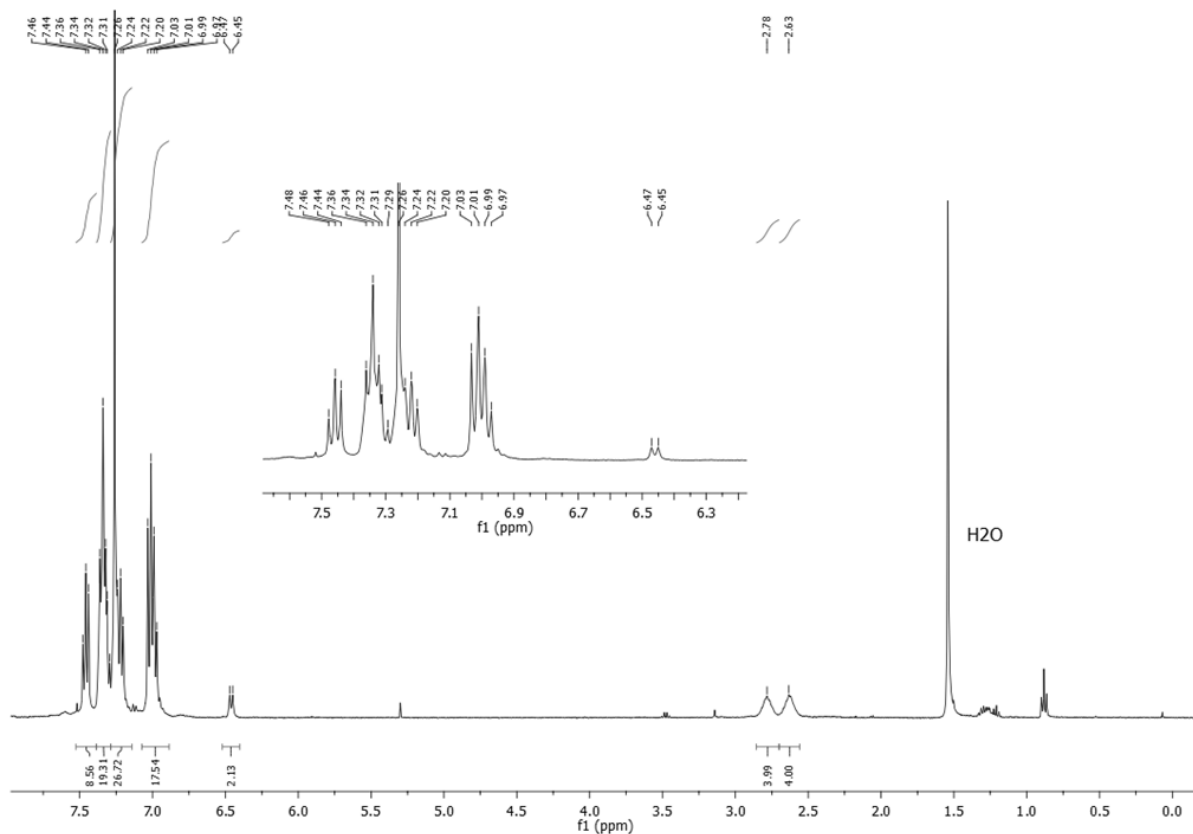
C₉₇H₈₀ClF₆N₂P₅Ru, 1679.10 g/mol

Reagents: bis(4-(diphenylamino)phenyl)(4-ethynylphenyl)methanol **44** (1 eq, 77 mg, 0.125 mmol), [RuCl(dppe)₂](PF₆) (1.05 eq, 141.5 mg, 0.13 mmol).

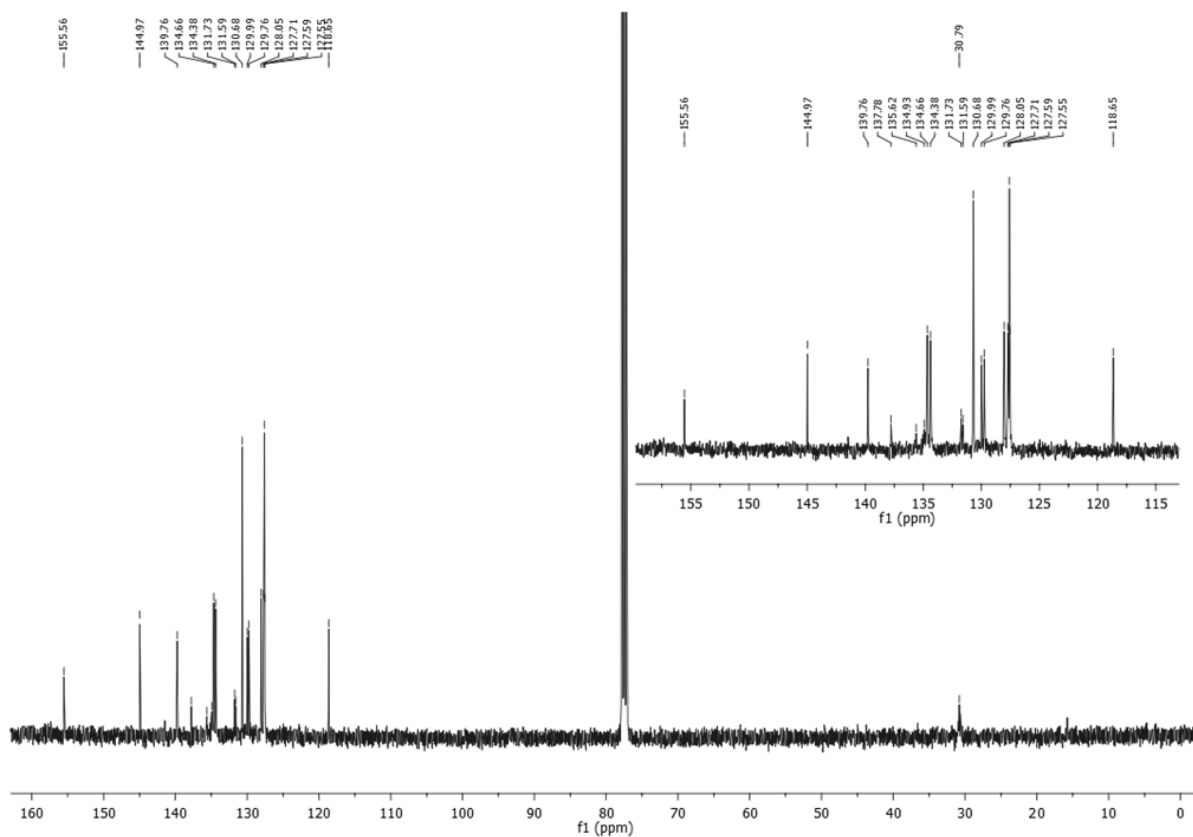
Reaction: In a Schlenk flask under argon, 10 mL of distilled and deoxygenated DCM were added to bis(4-(diphenylamino)phenyl)(4-ethynylphenyl)methanol **44** and [RuCl(dppe)₂](PF₆). The resulting mixture was stirred for 72h at room temperature.

Work-up and purification: The solvent was evaporated. The crude product was taken up in a minimum of dried and deoxygenated DCM and precipitated with dried and distilled Et₂O to give the product as a violet powder.

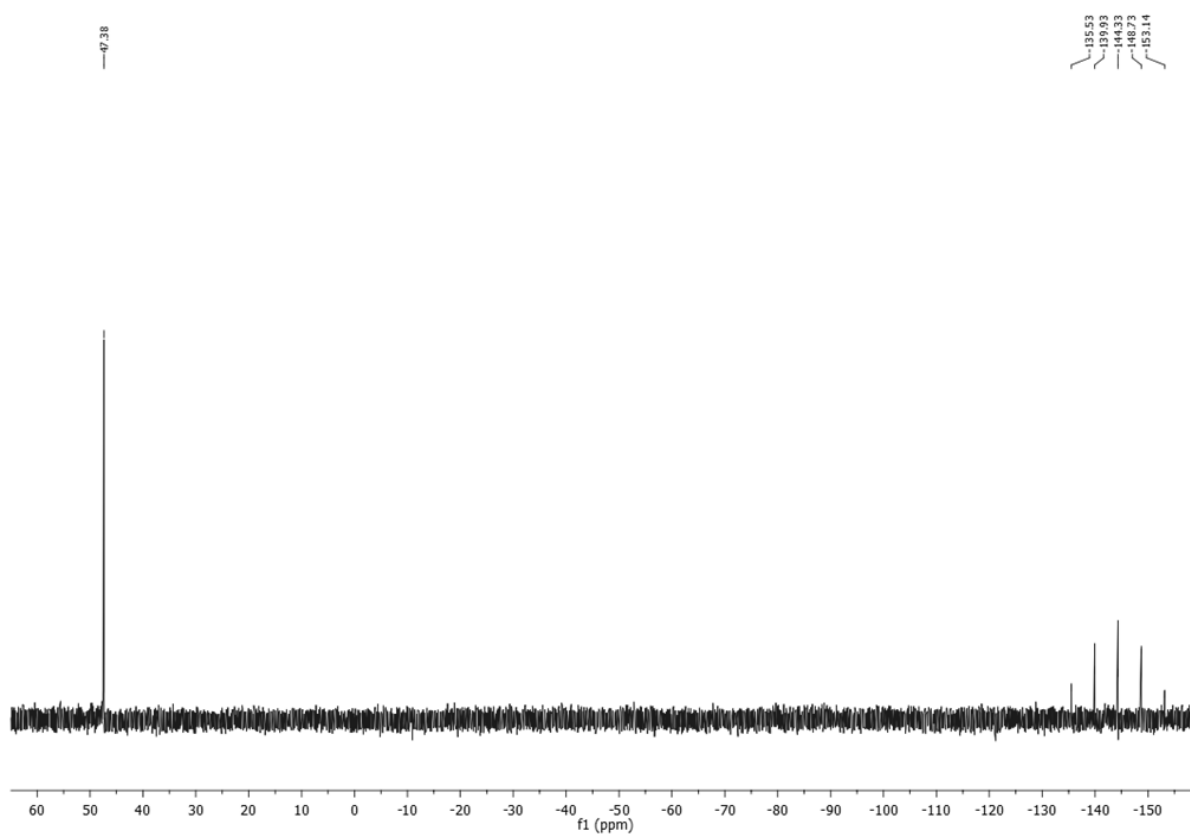
¹H NMR (400 MHz, CDCl₃) δ 7.50 – 7.42 (m, 8H), 7.40 – 7.30 (m, 20H), 7.29-7.20 (m, 22H + CDCl₃), 7.03-7.97 (m, 20H), 6.46 (d, *J* = 8.3 Hz, 2H), 2.78 (s, 4H, CH₂ dppe), 2.63 (s, 4H, CH₂ dppe).



¹³C NMR (101 MHz, CDCl₃) δ 155.56, 144.97, 139.76, 137.78, 135.62, 134.93, 134.66, 134.38, 131.73, 131.59, 130.68, 129.99, 129.76, 128.05, 127.71, 127.59, 127.55, 118.65, 30.79 (dppe).



^{31}P NMR (162 MHz, CDCl_3) δ 47.38 (s), -144.34 (sept).



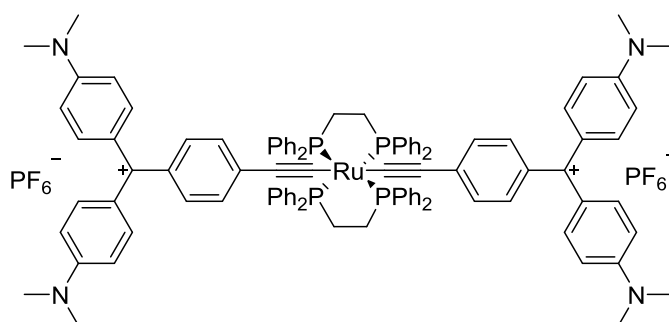
IR (cm^{-1}): 1985 ($\nu_{\text{C}\equiv\text{C}}$), 836 ($\nu_{\text{P-F}}$).

UV-Vis (DCM) λ_{max} , nm (ϵ , $10^{-5} \cdot \text{M}^{-1} \cdot \text{cm}^{-1}$): 4.98 (0.18), 634 (0.54), 854 (0.60).

HRMS (ESI): calcd: 1533.4005 $[\text{M}]^+$; found: 1533.4004 $[\text{M}]^+$.

CV: DCM, 0.10 M $[\text{n-Bu}_4\text{N}][\text{PF}_6]$, V vs Ag^+/Ag : $\text{C}^+/\text{C}^{\cdot+}$ $E_{1/2}$: -0.57 V; $\text{M}^{\text{III}}/\text{M}^{\text{II}}$ $E_{1/2}$: 0.54 ($\Delta E_p = 0.04$ V, $i_{\text{pc}}/i_{\text{pa}} = 1.0$).

***trans*-Ru(κ^2 -dppe) $_2$ [-C \equiv C-(*p*-C $_6$ H $_4$)-C(4-(dimethylamino)phenyl) $_2$] $_2$ bis-hexafluorophosphate
([M $^{\text{V}}$ (Ru) $^{2+}$][PF $_6^-$] $_2$)**

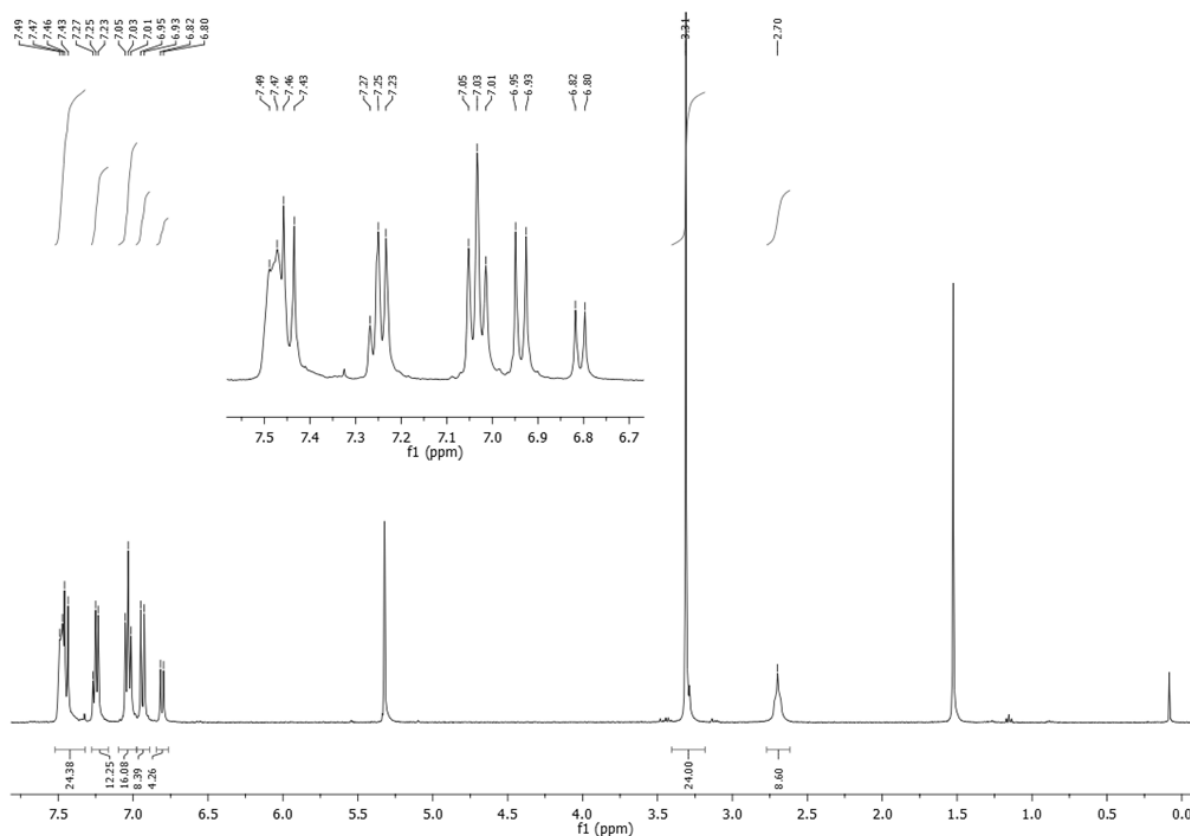


$\text{C}_{102}\text{H}_{96}\text{F}_{12}\text{N}_4\text{P}_6\text{Ru}$, $M = 1892.81$ g/mol

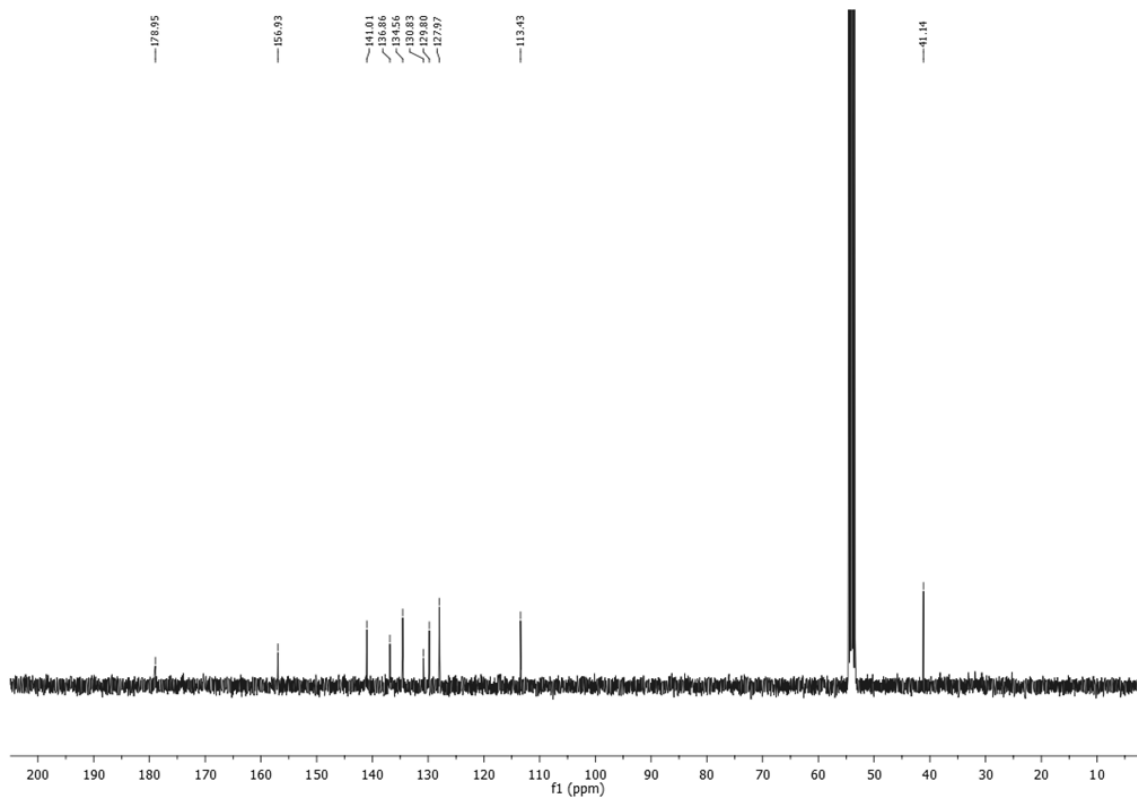
Reaction and reagents: Same procedure as **M4(Ru)⁺**, the mono-substituted product, is followed and the desired bis-acetylide is obtained as a crystalline powder.

Purification: The compounds is dissolved in dried and deoxygenated DCM and precipitated with dry and distilled Et₂O to give the product as a dark purple powder.

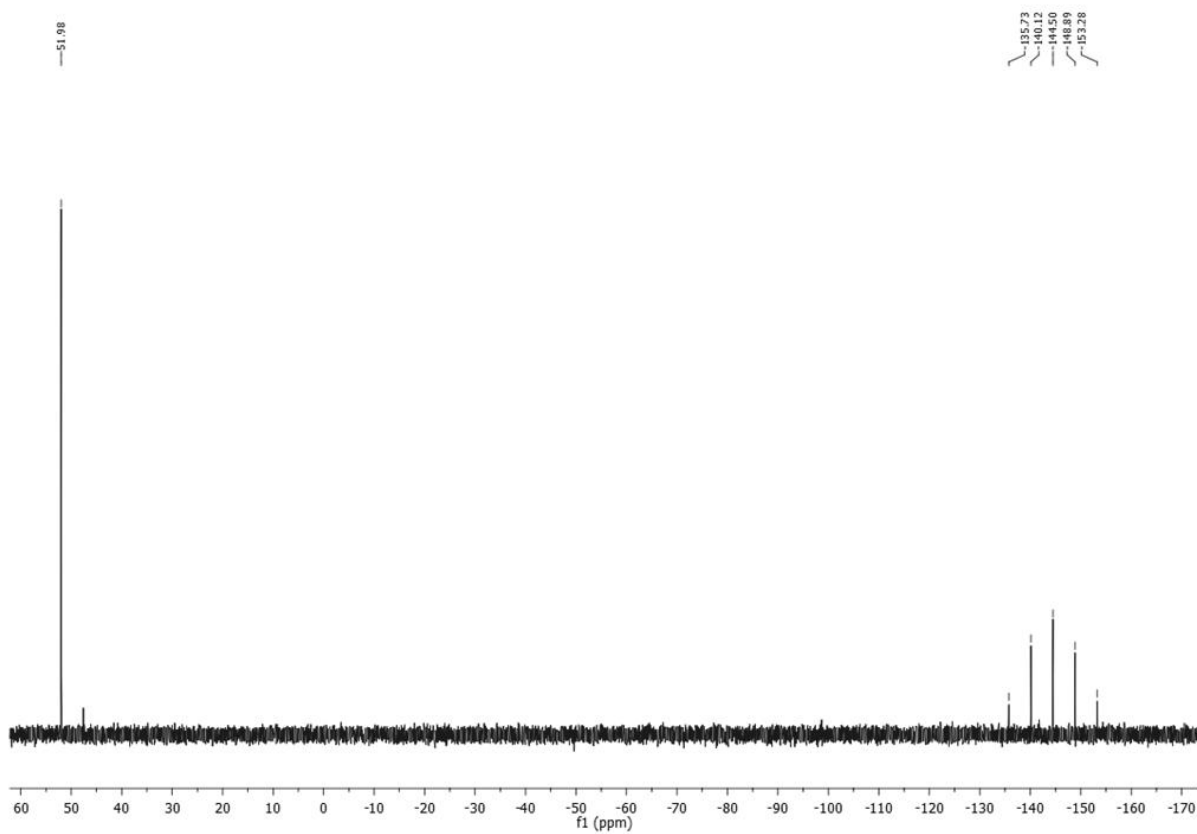
¹H NMR (400 MHz, CD₂Cl₂) δ 7.49 - 7.43 (m, 24H), 7.29 – 7.19 (m, 12H), 7.05 - 7.01 (m, 16H), 6.94 (d, *J* = 9.3 Hz, 8H), 6.81 (d, *J* = 8.4 Hz, 4H), 3.31 (s, 24H, -NMe₂), 2.70 (s, 8H, CH₂ dppe).



¹³C NMR (101 MHz, CD₂Cl₂) δ 178.95, 156.93, 141.01, 136.86, 134.56, 130.83, 129.80, 127.97, 113.43, 41.14. (solubility problems)



^{31}P NMR (162 MHz, CD_2Cl_2) δ 51.98 (s), -144.50 (sept).

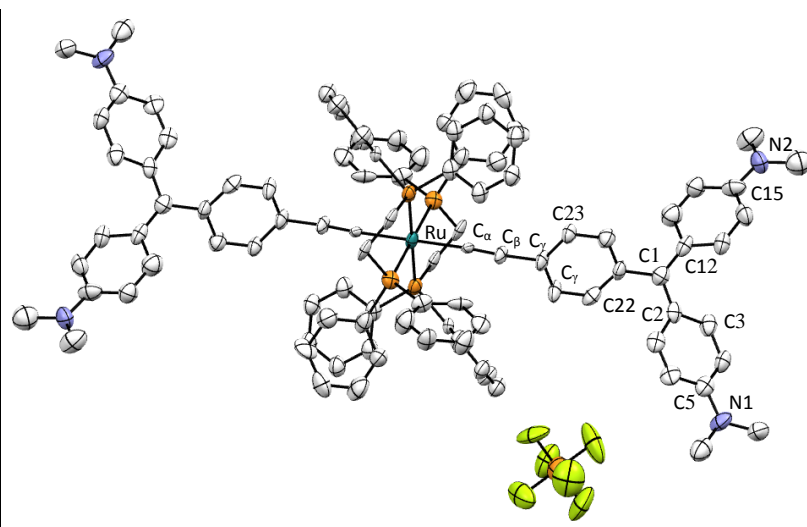


IR (cm^{-1}): 2034 and 2007 ($\nu_{\text{C}\equiv\text{C}}$), 839 ($\nu_{\text{P-F}}$).

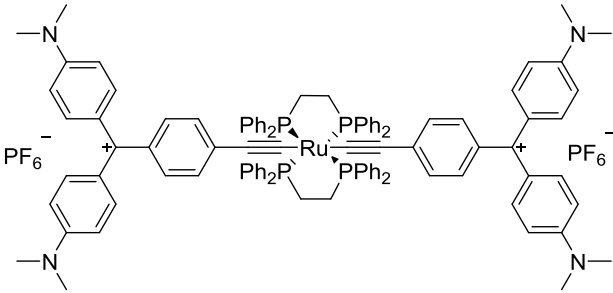
UV-Vis (DCM): λ_{\max} , nm (ϵ , $10^{-5} \cdot \text{M}^{-1} \cdot \text{cm}^{-1}$): 606 (2.20), 752 (1.03)

CV: DCM, 0.10 M [*n*-Bu₄N][PF₆], V vs Ag): C⁺/C⁺ E_{1/2}: -0.90 V; M^{III}/M^{II} E_{1/2}: 0.66 ($\Delta E_p = 0.03$ V, $i_{pc}/i_{pa} = 1.0$).

X-ray diffraction study:



ORTEP view of ([M1(Ru)⁺][PF₆⁻]₂) with 50 % thermal ellipsoids solved by Dr. Graeme Moxey

	
Formula	C ₁₀₂ H ₉₆ N ₄ P ₄ Ru, 2(F ₆ P), 4(CHCl ₃)
Molecular weight (g/mol)	1892.81
Crystals obtained by slow evaporation/cooling of a saturated CHCl ₃ solution of the molecule	

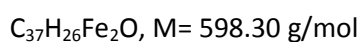
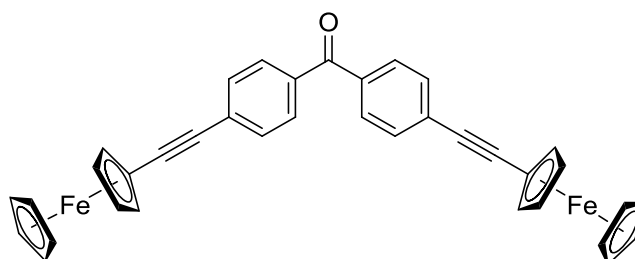
Crystal parameters	
Crystal class	triclinic
Space group	P -1
Cell angles (°)	α= 81.91
	β= 78.84
	γ= 83.25
Cell length (Å)	a= 11.15
	b= 14.26
	c= 17.85
Cell volume (Å ³)	2750.09
Z	Z= 1

Selected bond length (Å)

C1-C2	1.391 (2)	C5-N1	1.397 (2)
C1-C12	1.391 (2)	C15-N2	1.403 (3)
C_β-C_γ	1.494 (2)	C1-C22	1.487 (2)
C_α-C_β	1.202 (2)	C_γ-C23	1.405 (2)
Ru-C_α	2.020 (2)		

Selected angles (°)

Phenyl torsion	34.89 (7)	C plane	1.60 (3)
-----------------------	-----------	----------------	----------

7. Organometallic derivatives of CV⁺**7.1. S1-type derivatives****4,4'-bis-ethynylferrocene benzophenone (47)**

Reagents: ethynylferrocene (3 eq, 316 mg, 1.5 mmol), *p*-dibromobenzophenone **52** (1 eq, 170 mg, 0.5 mmol), PdCl₂(PPh₃)₂ (0.04 eq, 14 mg, 0.06 mmol), CuI (0.08 eq, 12 mg, 0.12 mmol).

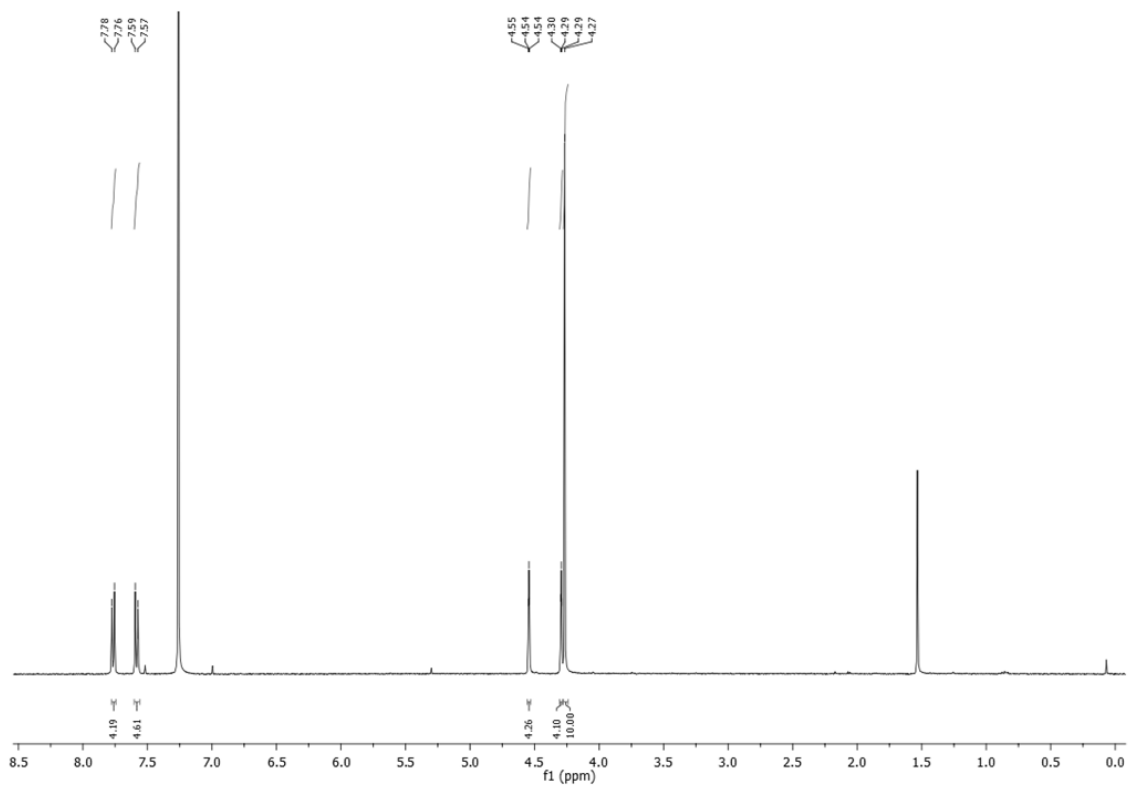
Reaction: A Schlenk tube under argon, **52**, PdCl₂(PPh₃)₂ and CuI were dissolved in distilled and deoxygenated NEt₃ (20 mL) and toluene (20 mL). Ethynylferrocene was added and the resulting red solution was heated at 80°C overnight.

Work-up: After evaporation of the solvents by cryoscopic transfer, the residue was extracted with DCM and filtered to remove ammonium salts. The extract was washed with a saturated and aqueous solution of NH₄Cl (10 mL), water (3 x 10 mL) and saturated aqueous NaCl (10 mL), the aqueous layer was then back extracted with DCM (20 mL). The combined organic layers were dried over MgSO₄ and evaporated under reduced pressure to give a red solid.

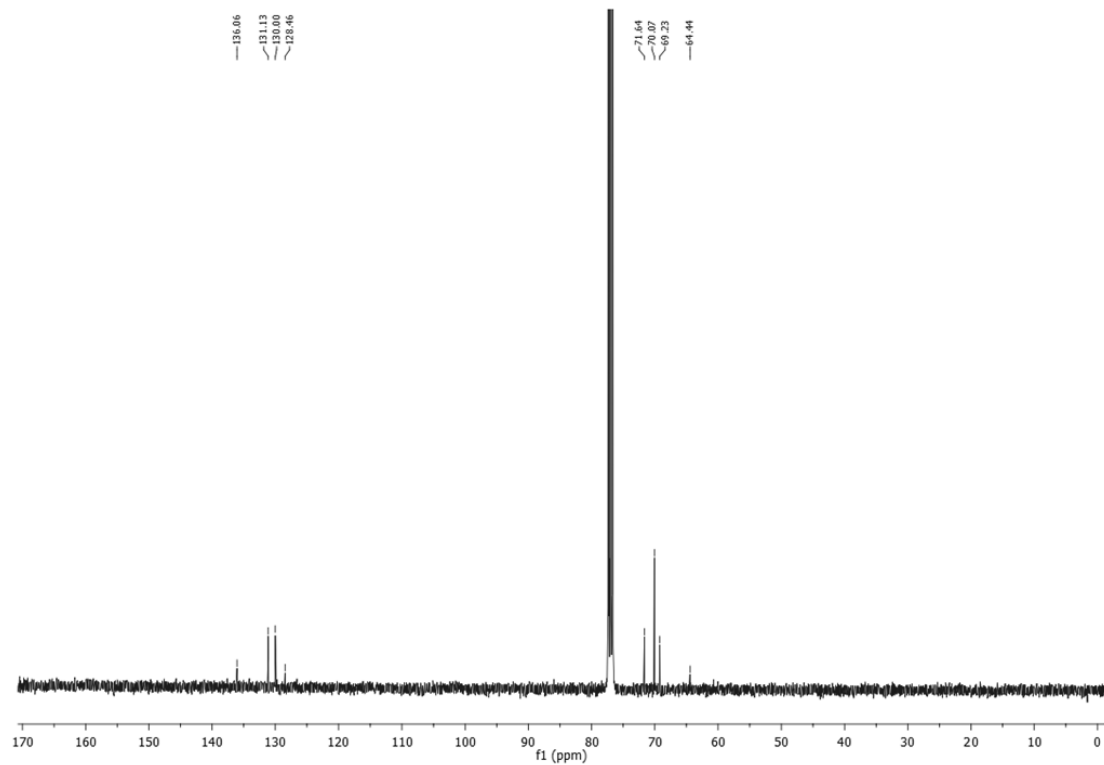
Purification: The desired product was recrystallized from DCM/hexane.

Yield: 280 mg (90 %).

^1H NMR (400 MHz, CDCl_3) δ 7.77 (d, $J = 8.3$ Hz, 4H), 7.58 (d, $J = 8.3$ Hz, 4H), 4.54 (t, $J = 1.8$ Hz, 4H), 4.32 – 4.27 (t, $J = 1.8$ Hz, 4H), 4.27 (s, 10H, Cp).



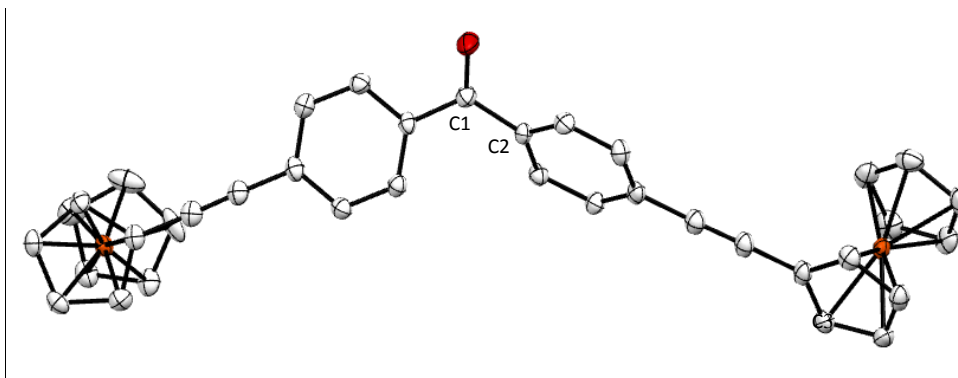
^{13}C NMR (101 MHz, CDCl_3) δ 136.06, 131.13, 130.00, 128.46, 71.64, 70.07, 69.23, 64.44.



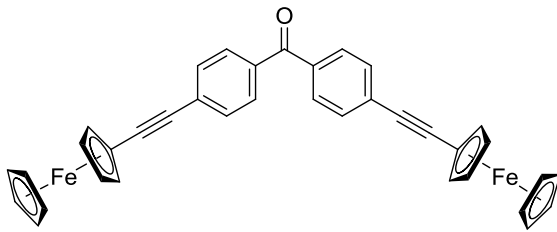
IR (cm⁻¹): 2198 ($\nu_{C\equiv C}$), 1640 ($\nu_{C=O}$), 856-813 (δ_{C-H} Fc).

HRMS (ESI): calc. 599.0761 [M]⁺; found: 599.0746 [M]⁺

X-ray diffraction study:



ORTEP view of **47** with 50 % thermal ellipsoids solved by Dr. Graeme Moxey

	
Formula	C ₃₇ H ₂₆ Fe ₂ O
Molecular weight (g/mol)	598.30
Red crystals obtained by slow evaporation/cooling of a saturated DCM solution of the molecule	

Crystal parameters	
Crystal class	monoclinic
Space group	P 2 _{1/c}
Cell angles (°)	α = 90
	β = 91.07
	γ = 90
Cell length (Å)	a= 5.86
	b= 19.24
	c= 22.92
Cell volume (Å ³)	2588.68
Z	Z= 4

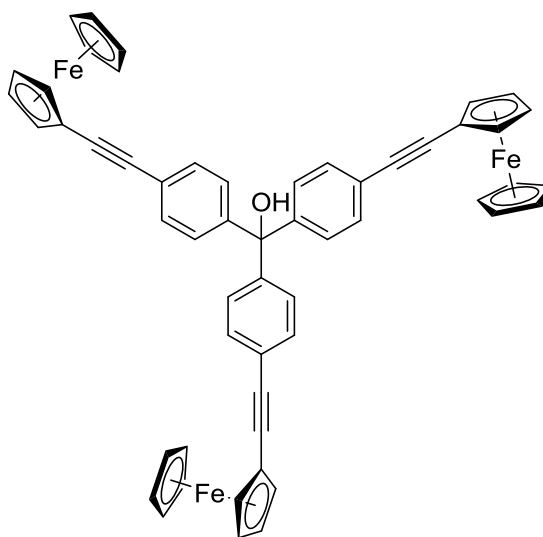
Selected bond length (Å)

C≡C	1.198 (3)	C1-C2	1.493 (3)
C=O	1.222 (3)		

Selected angles (°)

Phenyl torsion	19.52 (3)
----------------	-----------

tris(4-ethynylferrocenebenzene) methanol ($S1(Fe)^{OH}$)



$C_{55}H_{40}Fe_3O$, $M = 884.46$ g/mol

Reagents: 4,4'-bis-ethynylferrocene benzophenone **47** (1 eq, 300 mg, 0.5 mmol), 1-bromo-4-ferrocenylethynylbenzene **48** (1.2 eq, 219 mg, 0.6 mmol), *n*-BuLi (1.1 eq, 343 μ L at 1.6 M).

Reaction: In a Schlenk flask under argon, *n*-BuLi was added drop wise to a solution of **48** in dried and distilled THF at -78°C . After stirring for 30 min, a solution of **47** in dried and distilled THF was added drop wise to the solution. The mixture was stirred and allowed to warm to room temperature for 16h.

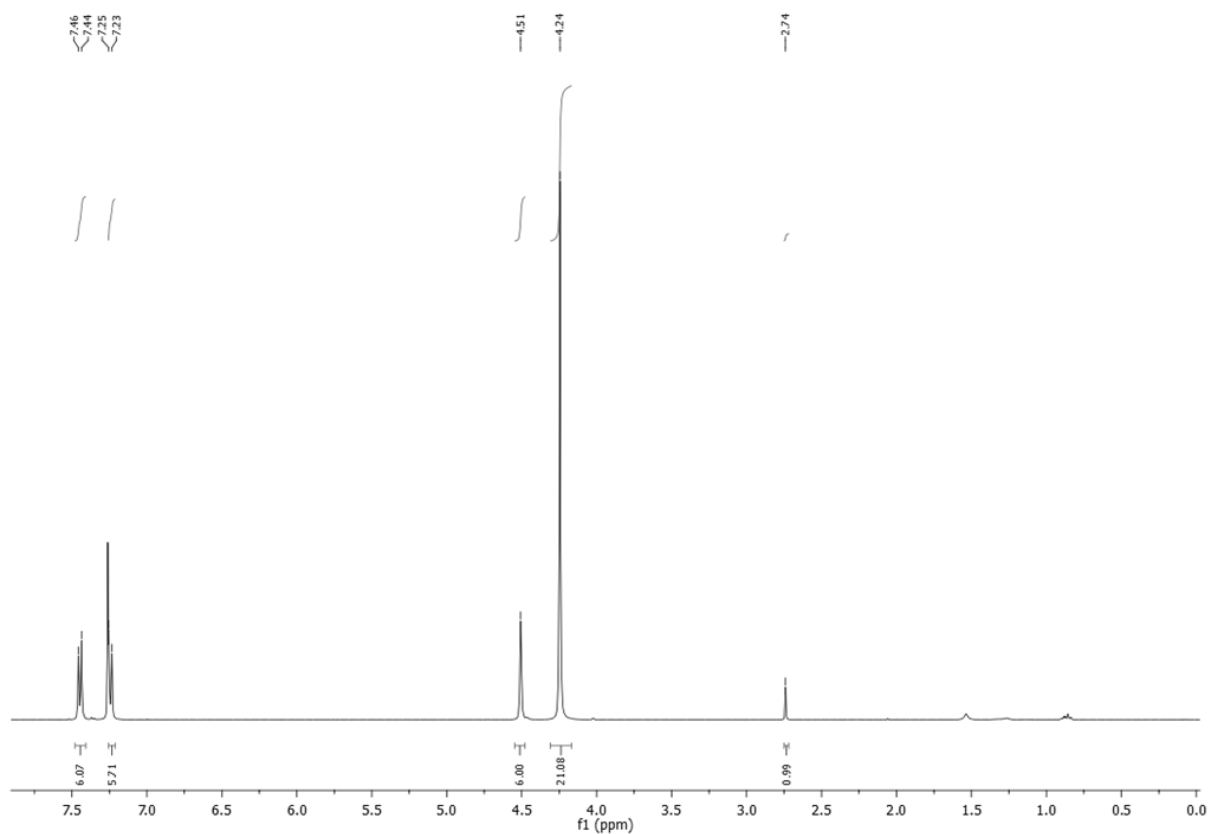
Work-up: 20 mL of water were added to the flask and the two phases were separated. The aqueous layer was extracted with DCM (3 x 20 mL) and the combined organic phases were washed with water (10 mL) and saturated aqueous NaCl (10 mL). The aqueous phase was then back-extracted with DCM (20 mL). The organic phase was dried over $MgSO_4$ and the solvents were removed to give the crude product as a solid.

Purification: The product was then separated by preparative chromatography with toluene/hexane (4/1) as eluent. The desired product was then recrystallized from DCM/hexane.

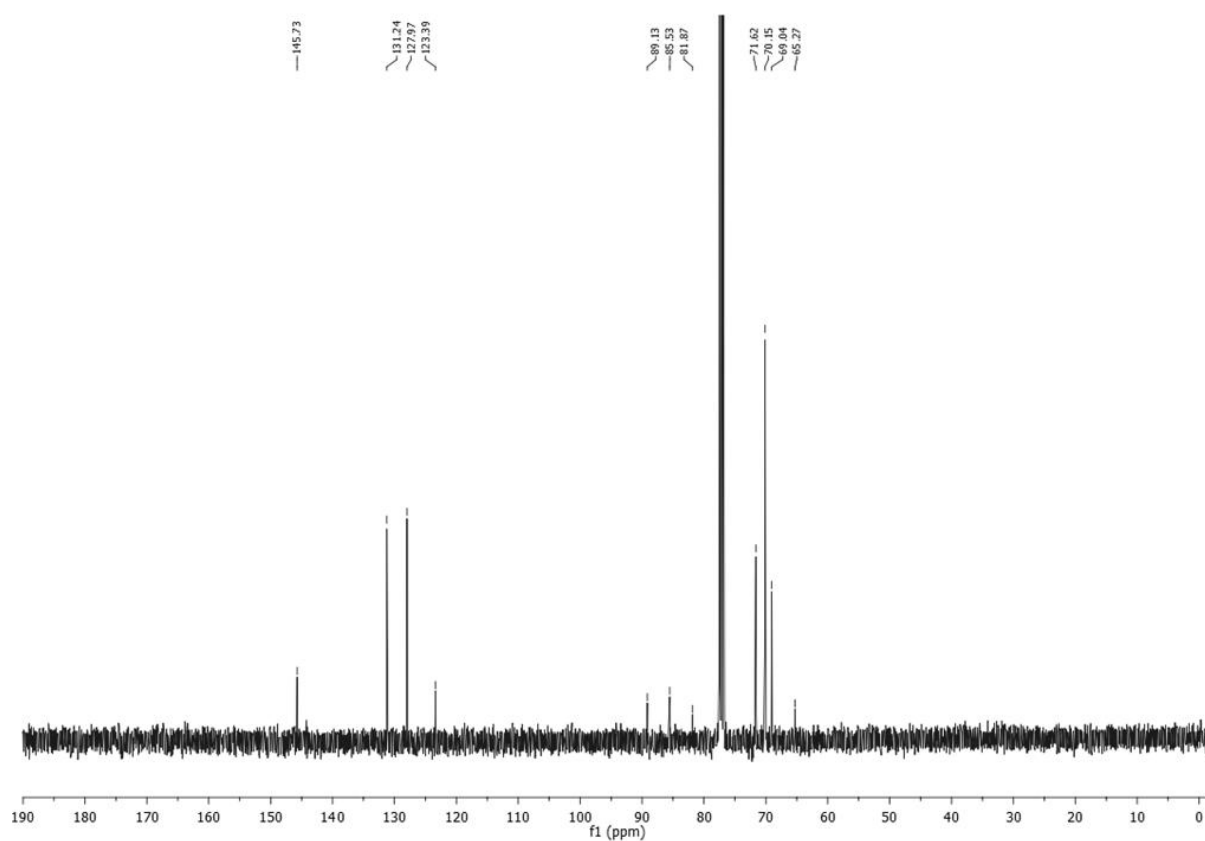
R_f (tol/hexane, 4/1): 0.3

Yield: 40 mg (20 %).

$^1\text{H NMR}$ (400 MHz, $CDCl_3$) δ 7.45 (d, $J = 8.4$ Hz, 6H), 7.24 (d, $J = 8.5$ Hz, 6H + $CDCl_3$), 4.51 (s, 6H), 4.24 (s, 21H, Cp) 2.74 (s, 1H, -OH).



¹³C NMR (101 MHz, CDCl₃) δ 145.73, 131.24, 127.97, 123.39, 89.13, 85.53, 81.87, 71.62, 70.15, 69.04, 65.27.

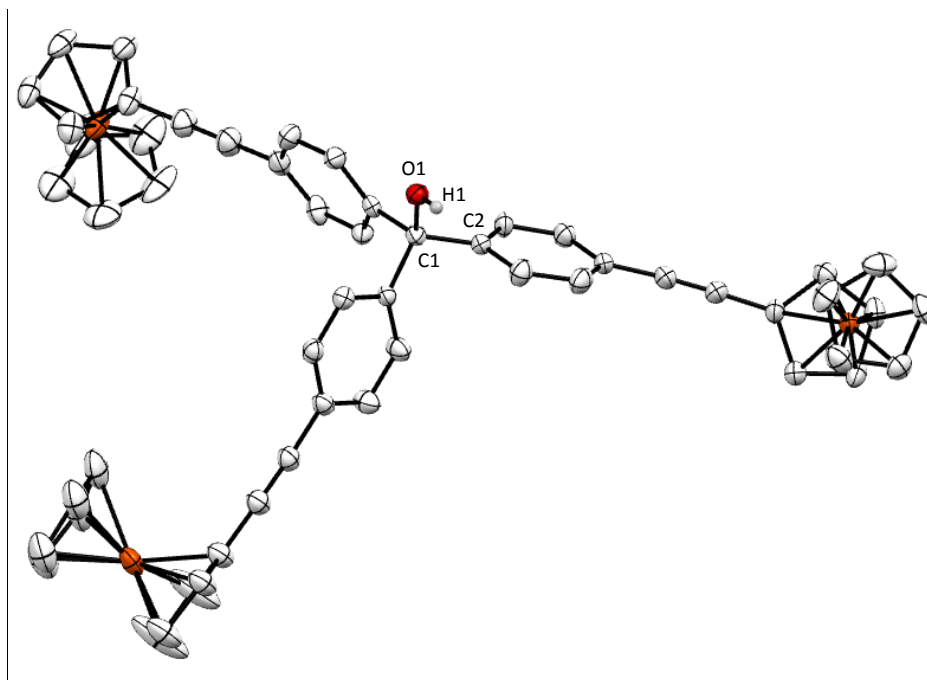


IR(cm⁻¹): 3538 ($\nu_{\text{O-H}}$), 2205 ($\nu_{\text{C}\equiv\text{C}}$), 825 ($\delta_{\text{C-H}}$ Fc).

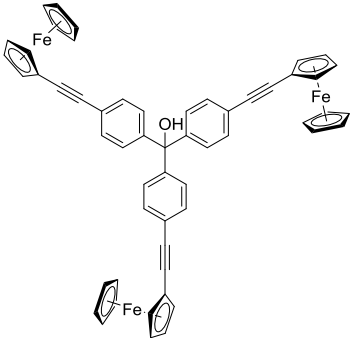
HRMS: calc. 884.1127 [M]⁺; found: 884.1127 [M]⁺.

EA: calc. C: 74.69 ,H: 4.56; found: C: 74.56, H: 4.47.

X-ray diffraction study:



ORTEP view of **47** with 50 % thermal ellipsoids solved by Dr. Graeme Moxey

	
Formula	C ₅₅ H ₄₀ Fe ₃ O
Molecular weight (g/mol)	884.46
Orange crystals obtained by slow diffusion of hexane into a DCM solution of the molecule at room temperature	

Crystal parameters	
Crystal class	monoclinic
Space group	P 2 ₁ /c
Cell angles (°)	α = 90
	β = 109.59
	γ = 90
Cell length (Å)	a= 11.85
	b= 36.92
	c= 10.23
Cell volume (Å ³)	4218.82
Z	Z= 4

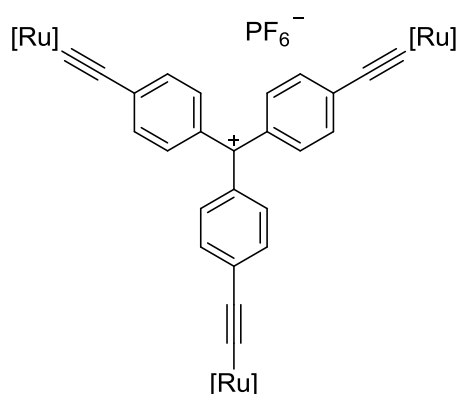
Selected bond length (Å)

C≡C	1.194 (9)	C1-C2	1.533 (7)
C-O	1.442 (5)		

Selected angles (°)

O1-C1-C2	108.5 (3)
-----------------	-----------

tris[*trans*-Ru(κ^2 -dppe)₂]-C≡C-(*p*-C₆H₄)-]C⁺ hexafluorophosphate ([S1(Ru)⁺][PF₆⁻])



C₁₈₁H₁₅₆Cl₃F₆P₁₃Ru₃, M: 3257.45 g/mol

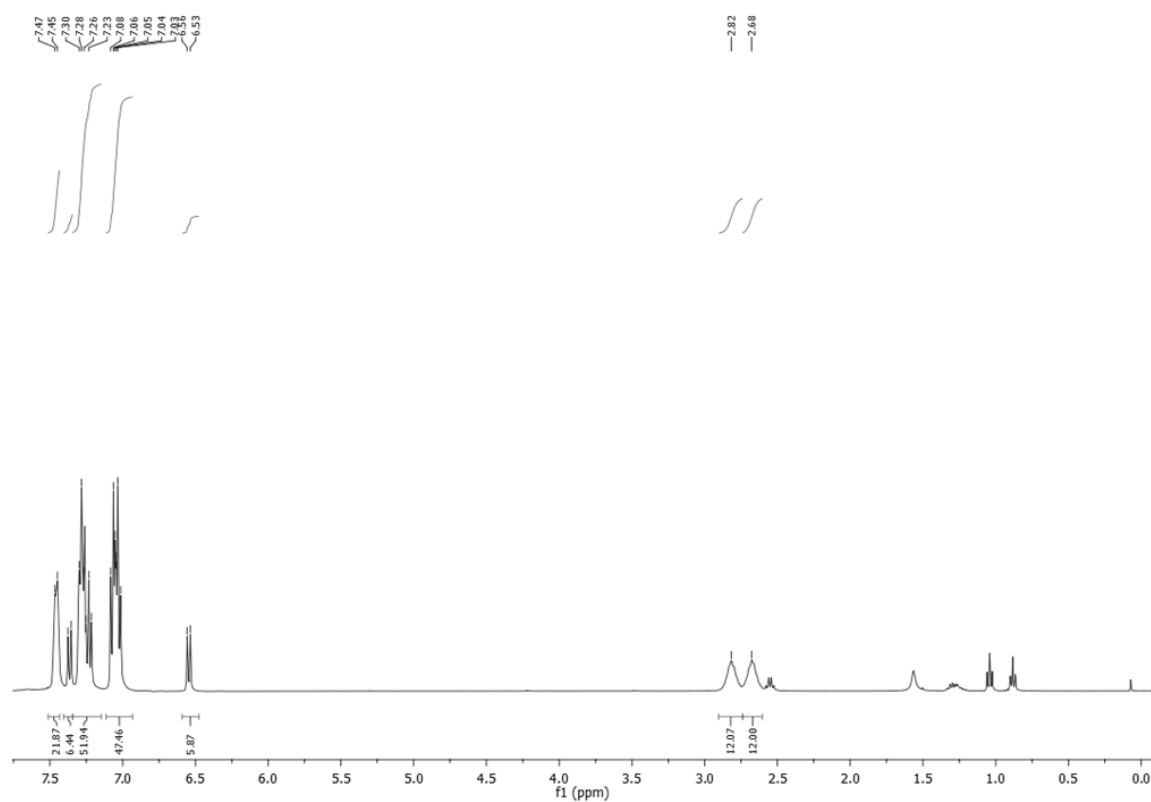
Reagents: tris(4-ethynylphenyl) methanol **55** (1 eq, 33 mg, 0.1 mmol), [RuCl(dppe)₂]PF₆ **46** (5 eq, 540 mg, 0.5 mmol), Et₃N (30 eq., 50 μ L).

Reaction: In a Schlenk flask under argon, 10 mL of distilled and deoxygenated DCM were added to **55** and RuCl(dppe)₂PF₆ **46**. The resulting blue mixture was stirred for 24h at room temperature. The crude product was reduced to a minimum of solvent and cannula filtered into a new Schlenk flask under argon and precipitated with dried and distilled MeOH to give the product as a green powder. The same procedure was repeated until total removal of the 5-coordinate ruthenium complex in which was in excess (clear solution). The resulting powder was then washed with distilled and deoxygenated Et₂O. 10 mL of distilled and deoxygenated DCM was then added to the resulting solid followed by addition of Et₃N. The solution was stirred for 10 min and precipitated with distilled and deoxygenated Et₂O, and washed with pentane.

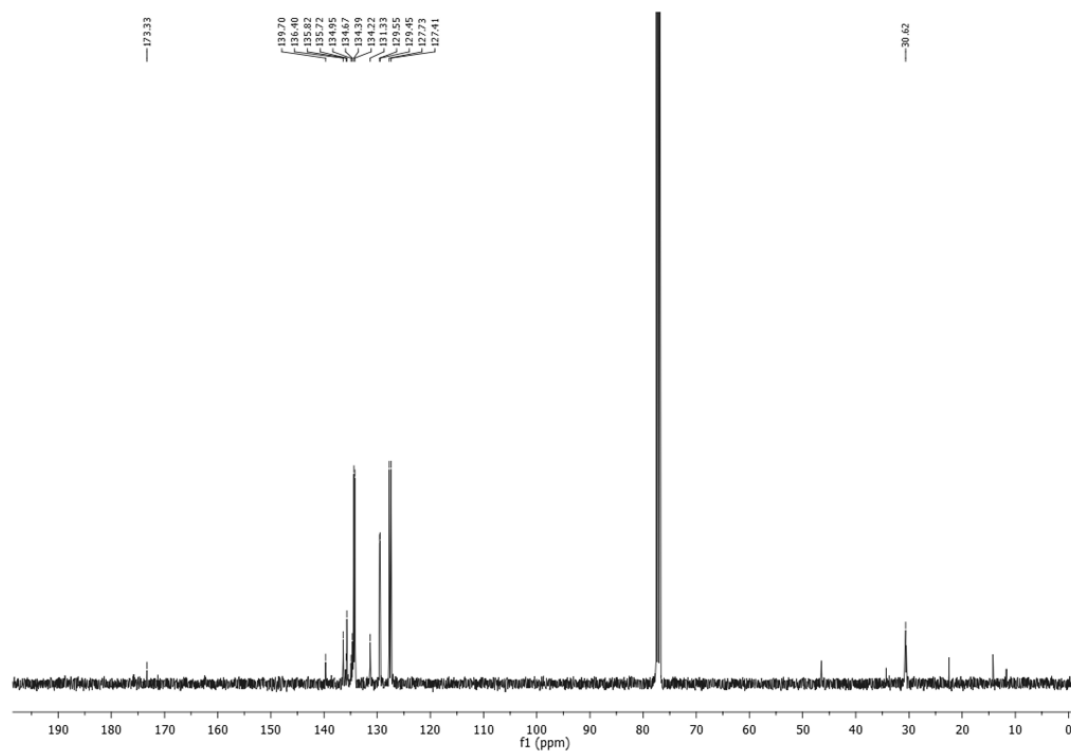
Purification: The resulting green powder was precipitated from DCM/Et₂O to afford small green crystals.

Yield: >70 %.

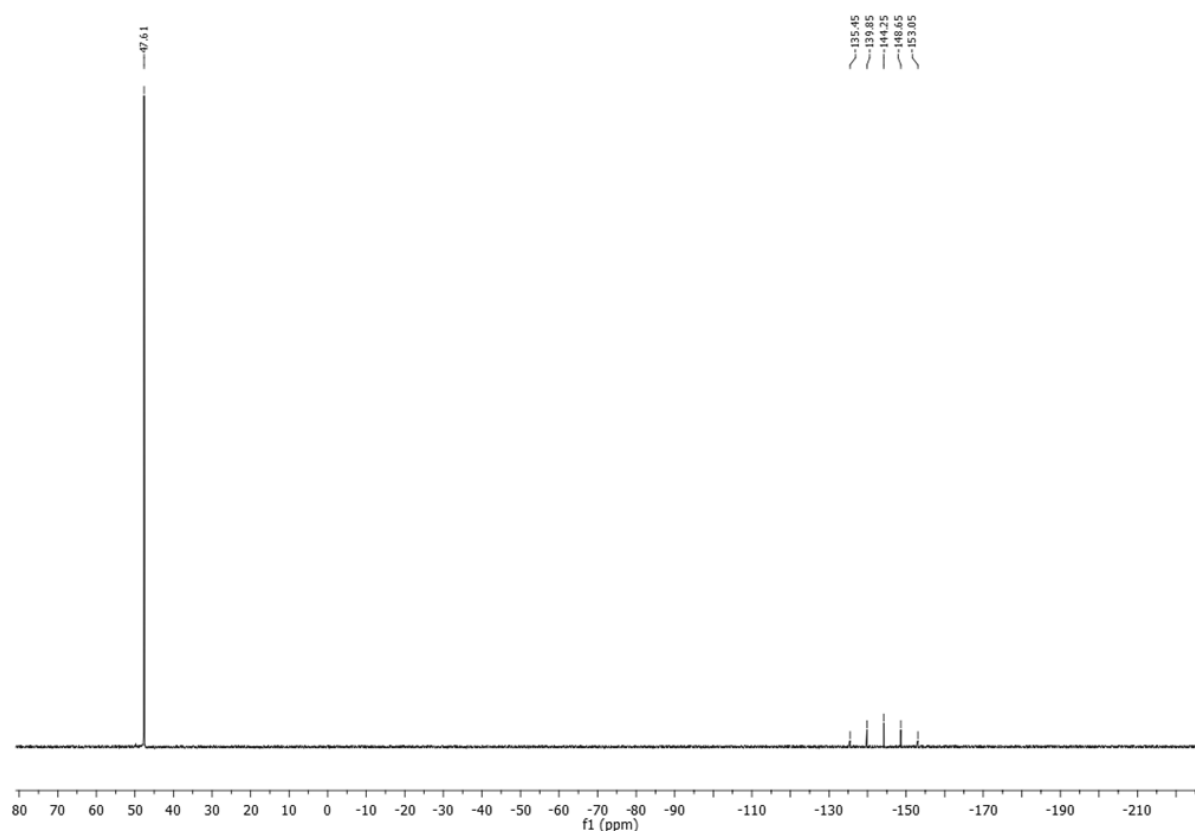
^1H NMR (400 MHz, CDCl_3) δ 7.47-7.45 (m, 22H), 7.36 (d, $J = 8.6$ Hz, 22H), 7.30-7.23 (m, 50H + CDCl_3), 7.08-7.03 (m, 48H), 6.55 (d, $J = 8.5$ Hz, 6H), 2.82 (s, 12H, CH_2 dppe), 2.68 (s, 12H, CH_2 dppe).



^{13}C NMR (101 MHz, CDCl_3) δ 173.33 (C^+), 139.70, 136.40, 135.82, 135.72, 134.95, 134.67, 134.39, 134.22, 131.33, 129.55, 129.45, 127.73, 127.41, 30.62 (CH_2 dppe).



^{31}P NMR (162 MHz, CDCl_3) δ 47.61 (s), -144.25 (sept).



IR (cm^{-1}): 1958 ($\nu_{\text{C}\equiv\text{C}}$), 690 ($\nu_{\text{P-F}}$).

HRMS (ESI): calcd.: 3111.52 $[\text{M}]^+$, found: 3111.63 $[\text{M}]^+$.

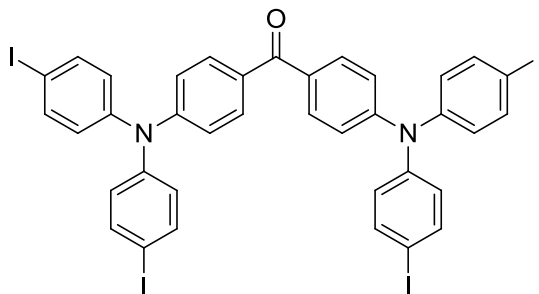
UV-VIS: DCM λ_{max} , nm (ϵ , $10^{-5} \cdot \text{M}^{-1} \cdot \text{cm}^{-1}$): 627 (0.01), 988 (14.1).

CV: DCM, 0.10 M $[\text{n-Bu}_4\text{N}][\text{PF}_6]$, V vs Ag): $\text{C}^+/\text{C}^{\cdot+}$ $E_{1/2}$: -0.41 V ($\Delta E_p = 0.04$ V, $i_{\text{pc}}/i_{\text{pa}} = 0.83$); $\text{M}^{\text{III}}/\text{M}^{\text{II}}$ $E_{1/2}$: 0.66 V ($\Delta E_p = 0.04$ V, $i_{\text{pc}}/i_{\text{pa}} = 1.0$); $E_{1/2}$: 1.09 V ($\Delta E_p = 0.07$ V, $i_{\text{pc}}/i_{\text{pa}} = 0.64$).

X-ray diffraction study: (connectivity only). Crystals obtained from slow diffusion of Et_2O vapor into a DCM solution of the molecule at room temperature.

7.2. S2-type derivatives

bis(4-(bis(4-iodophenyl)amino)phenyl)methanone (57)



$C_{37}H_{24}I_4N_2O$, $M = 1020.23$ g/mol

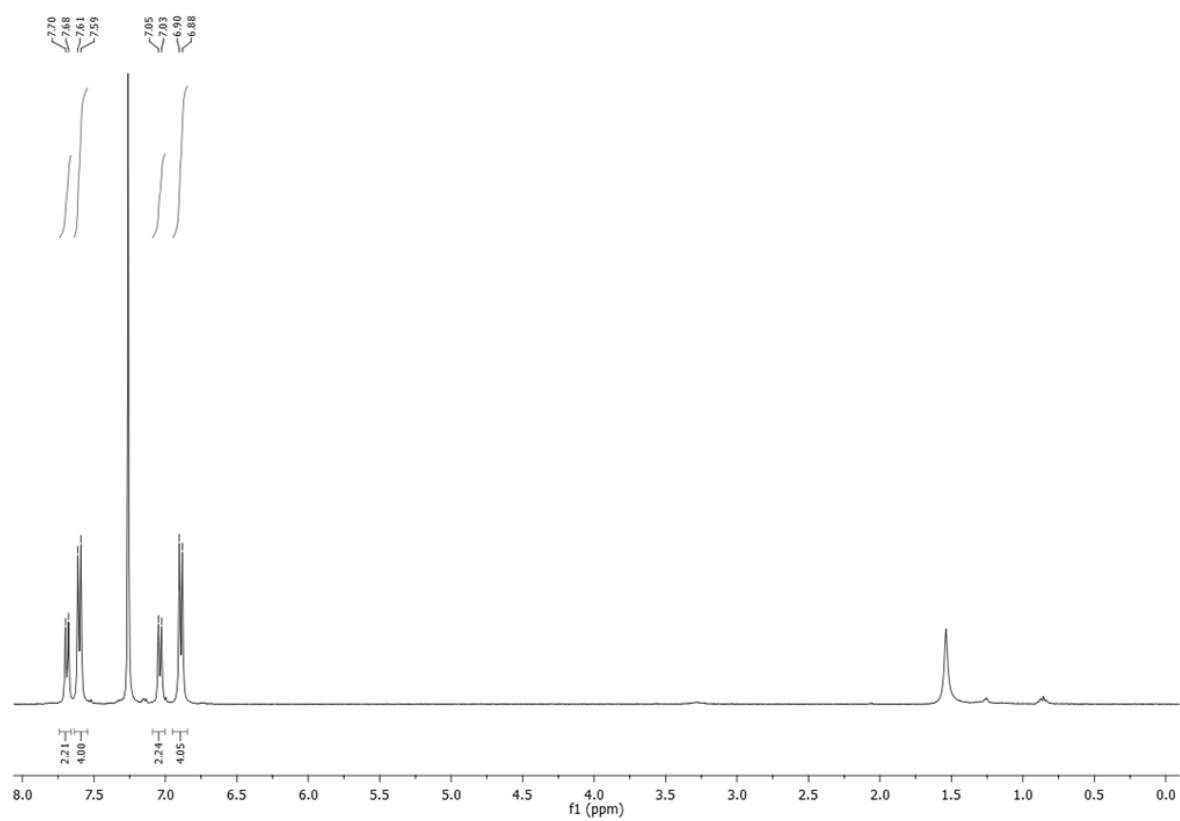
Reagents: 4 4'-diphenylaminobenzophenone (1 eq, 516 mg, 1 mmol), KI (11 eq, 1.826 g, 11 mmol), KIO_3 (16.5 eq, 3.53 g, 16.5 mmol), AcOH(30 mL).

Reaction: In a round-bottom flask, glacial AcOH was added to 4, 4'-diphenylaminobenzophenone, KI and KIO_3 . The resulting mixture was heated at 75°C for two days.

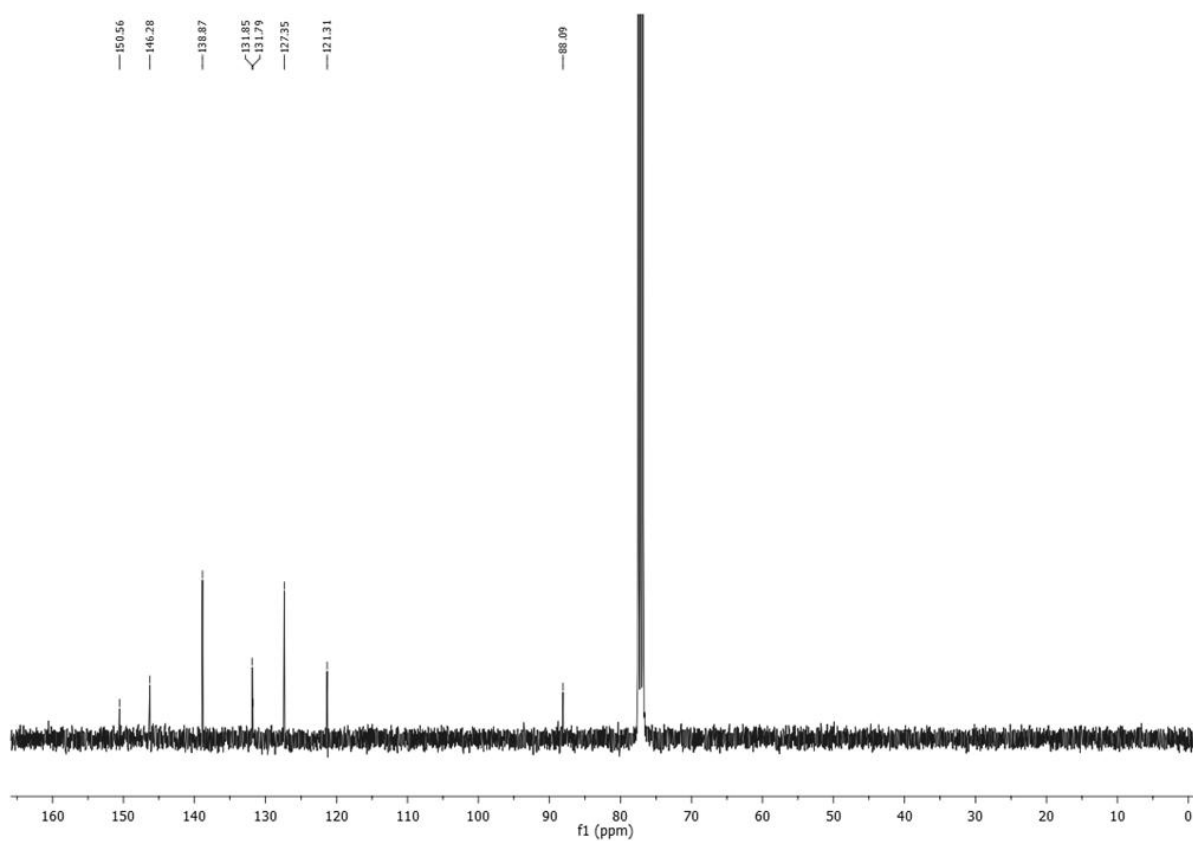
Work-up and purification: After cooling to room temperature, the iodine excess was neutralized upon addition of $NaHSO_3$. The acid was then neutralized by slow addition of an aqueous solution of NH_3 to achieve a pH ~ 9 . The obtained yellow suspension was then filtrated and the solid was dissolved in hot toluene and precipitated and washed with cold toluene.

Yield: 850 g (83 %)

1H NMR (400 MHz, $CDCl_3$) δ 7.69 (d, $J = 8.2$ Hz, 4H), 7.60 (d, $J = 8.1$ Hz, 8H), 7.03 (d, $J = 8.3$ Hz, 4H), 6.88 (d, $J = 8.2$ Hz, 8H).



¹³C NMR (101 MHz, CDCl₃) δ 150.56, 146.28, 138.87, 131.85, 131.79, 127.35, 121.31, 88.09. (not soluble enough to see ketonic carbon)

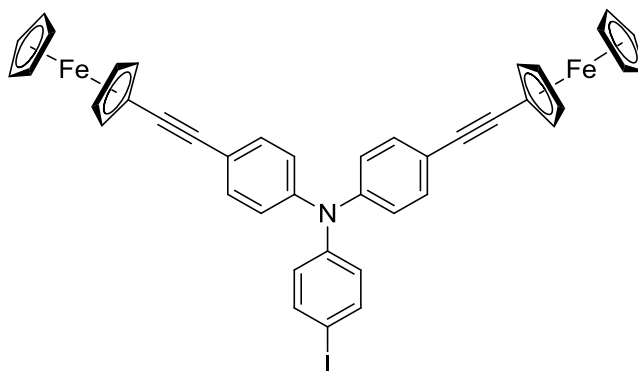


HRMS (ASAP): calcd.: 1020.81405 $[M+H]^+$, 1019.80622 $[M]^+$, 893.90957 $[M-I+H]^+$; found : 1020.8150 $[M+H]^+$, 1019.8070 $[M]^+$, 893.9098 $[M-I+H]^+$.

EA: calcd.: C = 43.56; H = 2.37; N = 2.75; O, 1.57; found: C = 43.61; H = 2.35, N = 2.58.

IR(KBr, cm^{-1}): 1704 ($\nu_{\text{C=O}}$), 515 ($\nu_{\text{C-I}}$).

4-iodo-N,N-bis(4-(ethynylferrocene)phenyl)aniline (61)



$\text{C}_{42}\text{H}_{26}\text{Fe}_2\text{IN}$, 783.26 g/mol

Reagents: tri(4-iodophenyl)amine (1 eq, 623 mg, 1 mmol), ethynyl ferrocene (2 eq, 420 mg, 2 mmol), $\text{PdCl}_2(\text{PPh}_3)_2$ (0.04 eq, 28 mg, 0.04 mmol), CuI (0.08 eq, 15 mg, 0.08 mmol).

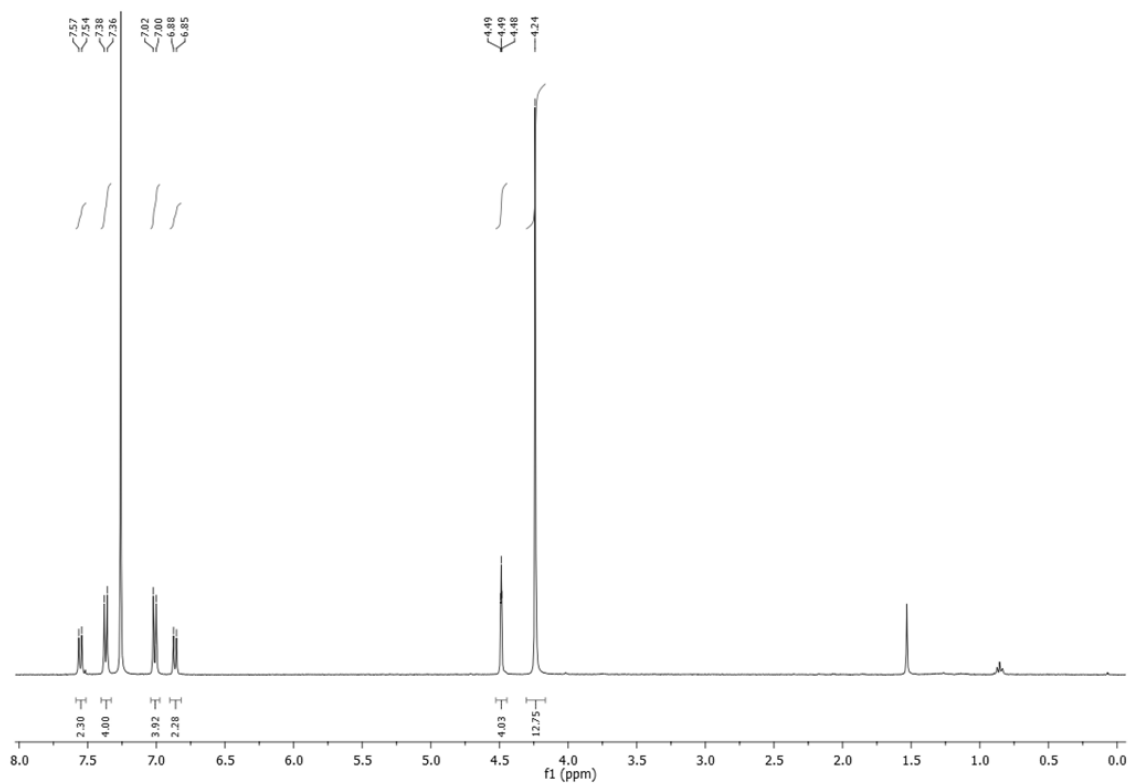
Reaction: In a Schlenk tube under argon $\text{PdCl}_2(\text{PPh}_3)_2$ and CuI were dissolved in a mixture of toluene (10 mL) and Et_3N (10 mL). Ethynyl ferrocene was added and the resulting red solution was stirred at room temperature for 16 h.

Work-up: After evaporation of the solvents by cryoscopic transfer, the residue was dissolved in Et_2O and filtered on a plug of celite to remove salts. The crude extract was washed with water (3 x 10 mL) and saturated aqueous NaCl (10 mL); the aqueous layer was then back-extracted with Et_2O (20 mL). The combined organic layers were dried over MgSO_4 and evaporated under reduced pressure to give an orange solid.

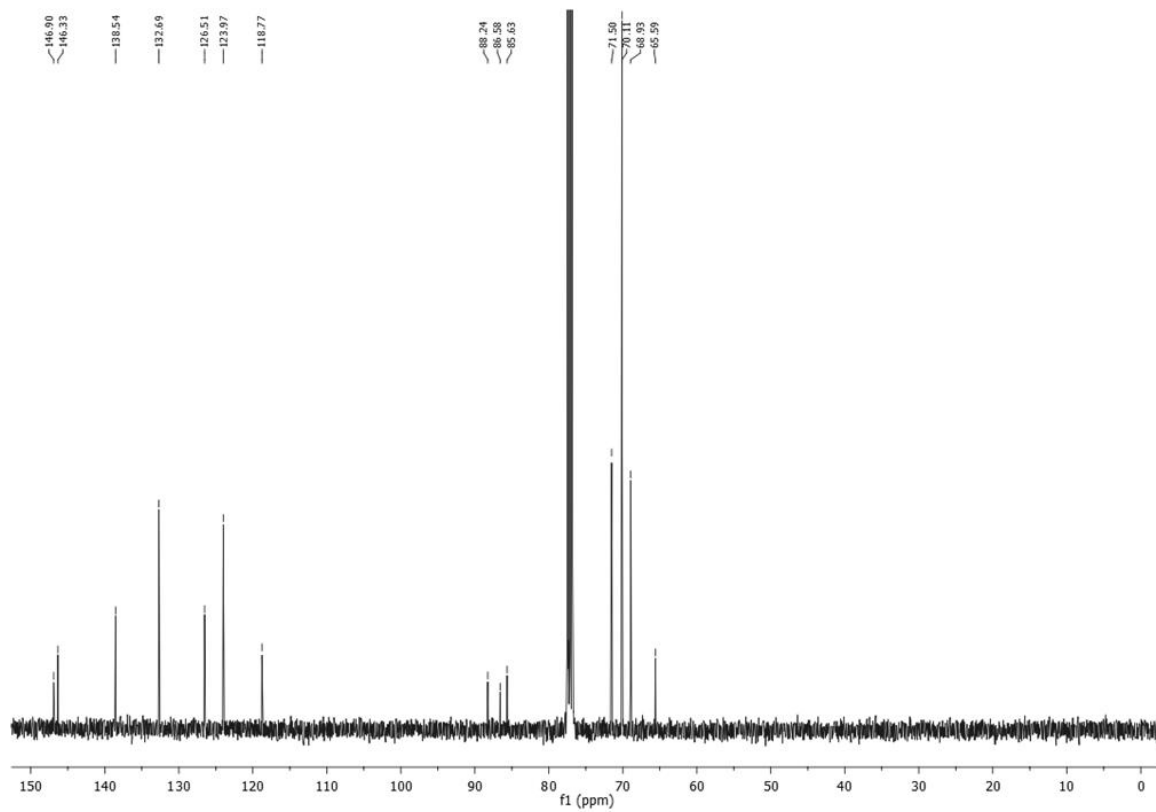
Purification: The obtained solid was then adsorbed onto silica and loaded on the top of a chromatographic column and eluted with a gradient of hexane/ Et_2O from 9/1 to 4/1. The second fraction was collected and solvents were removed under reduced pressure.

Yield: m= 340 mg (43 %)

^1H NMR (400 MHz, CDCl_3) δ 7.55 (d, J = 8.7 Hz, 2H), 7.37 (d, J = 8.6 Hz, 4H), 7.01 (d, J = 8.6 Hz, 4H), 6.86 (d, J = 8.7 Hz, 2H), 4.53 – 4.44 (m, 4H), 4.24 (s, 14H, Cp).



¹³C NMR (101 MHz, CDCl₃) δ 146.90, 146.33, 138.54, 132.69, 126.51, 123.97, 118.77, 88.24, 86.58, 85.63, 71.50, 70.11, 68.93, 65.59.

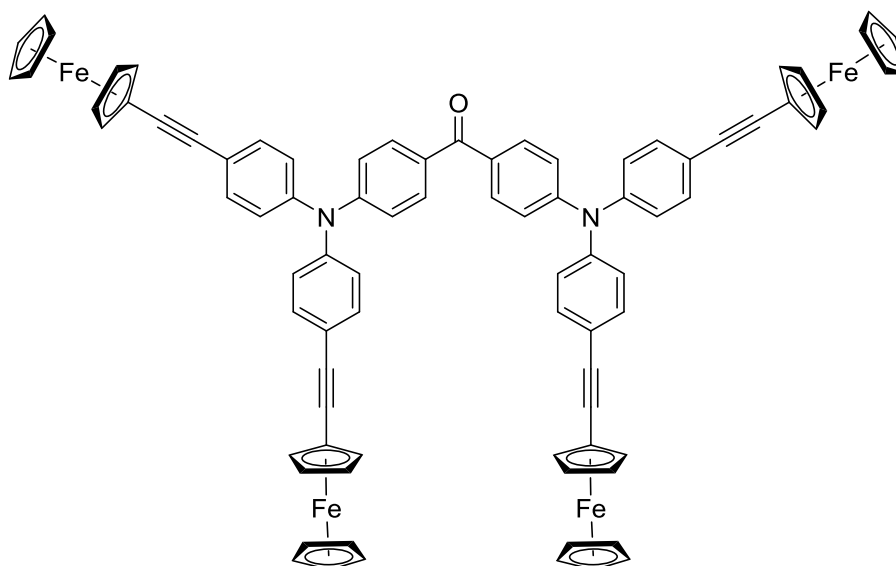


HRMS: (ESI) calcd.: 787.01218 [M]⁺; found : 787.0121 [M]⁺.

EA: calcd.: C = 64.07, H = 3.84, N = 1.78; found: C = 64.00, H = 4.02, N = 1.57.

IR(cm⁻¹): 2209 (ν_{C≡C}), 816 (δ_{C-H} Fc), 535 (ν_{C-I}).

bis(4-(bis(4-(ethynylferrocene)phenyl)amino)phenyl)methanone (58)



C₈₅H₆₀Fe₄N₂O, M = 1348.81 g/mol

Reagents: bis(4-(bis(4-iodophenyl)amino)phenyl)methanone **57** (1 eq, 2 g, 2 mmol), ethynyl ferrocene (1.05 eq, 1.76 g, 8.4 mmol), PdCl₂(PPh₃)₂ (0.08 eq, 112.32 mg, 0.16 mmol), CuI (0.16 eq, 61 mg, 0.32 mmol).

Reaction: In a Schlenk tube under argon, **57**, PdCl₂(PPh₃)₂ and CuI were dissolved in distilled and deoxygenated NEt₃ (20 mL). Ethynylferrocene was added and the resulting red solution was heated at 80°C for 16h.

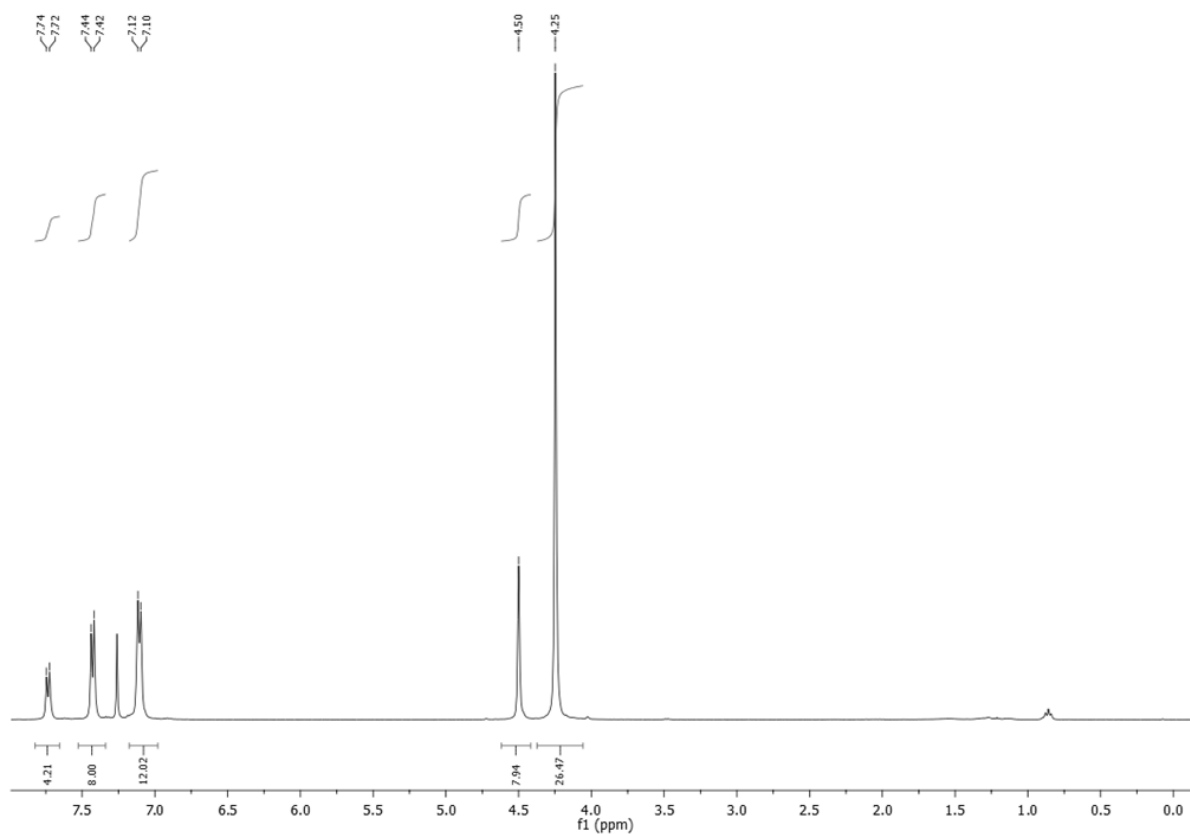
Work-up: After evaporation of the solvents by cryoscopic transfer, the residue was extracted with DCM (3 x 10 mL) and filtered to remove ammonium salts. The extract was washed with water (3 x 10 mL), saturated aqueous NH₄Cl (10 mL) and aqueous NaCl (10 mL); the aqueous layer was then back-extracted with DCM (10 mL). The combined organic layers were dried over MgSO₄ and evaporated under reduced pressure to give a red solid.

Purification: The obtained solid was absorbed onto silica and loaded on the top of a chromatographic column. The orange fraction, eluted with a gradient of hexane/DCM from 3/1 to 1/1, was collected

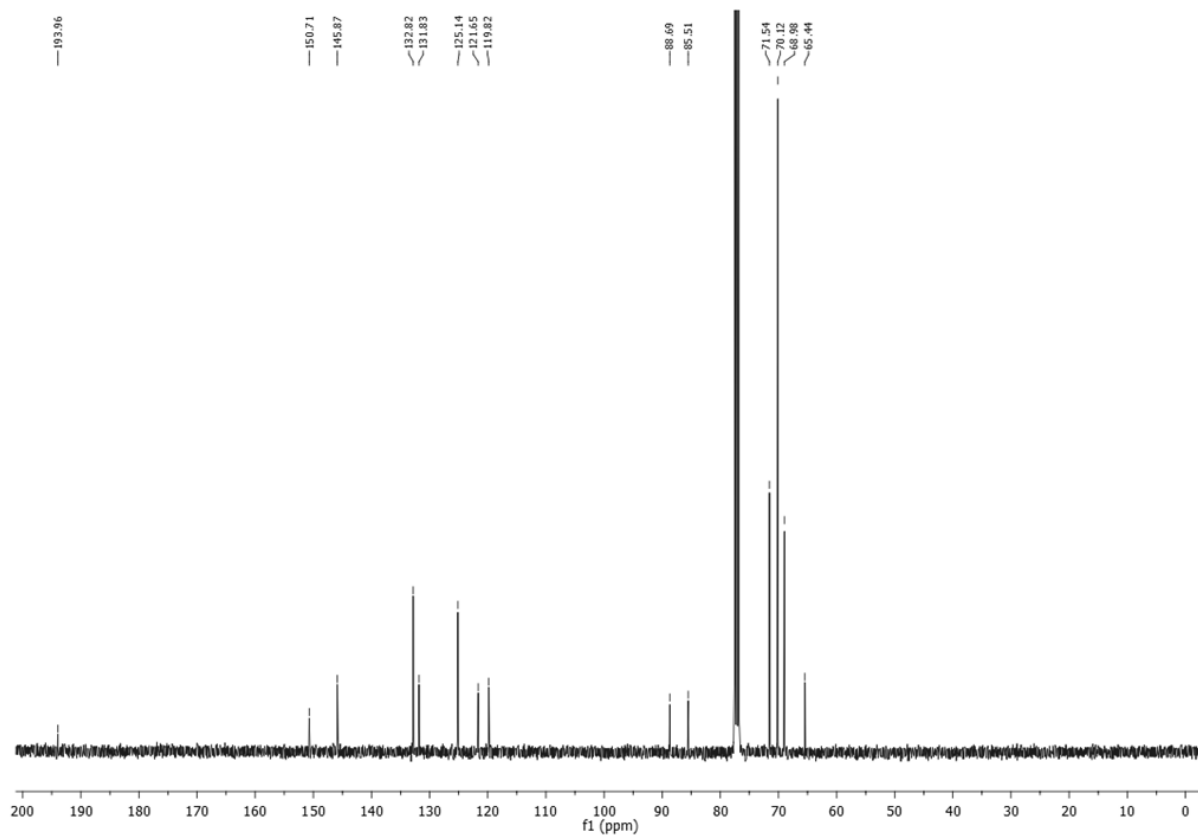
and solvents were removed under reduced pressure. The product was then precipitated from DCM/Et₂O.

Yield: m= 1.990 g (75 %).

¹H NMR (400 MHz, CDCl₃) δ 7.73 (d, *J* = 8.4 Hz, 4H), 7.43 (d, *J* = 8.3 Hz, 8H), 7.12 - 7.10 (m, 12H), 4.50 (s, 8 H, Cp), 4.25 (s, 28H, Cp).



¹³C NMR (101 MHz, CDCl₃) δ 193.96 (C=O), 150.71, 145.87, 132.82, 131.83, 125.14, 121.65, 119.82, 88.69, 85.51, 71.54, 70.12, 68.98, 65.44.

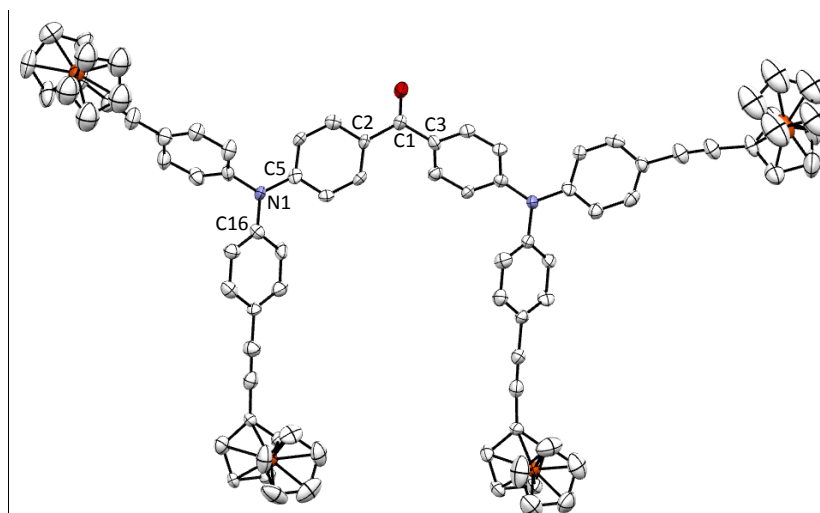


HRMS (ESI): calcd.: 1348.20977 $[M]^+$; found: 1348.2116 $[M]^+$.

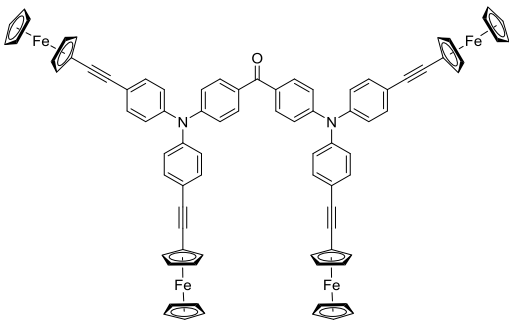
EA: calcd.: C = 75.69, H = 4.48, N = 2.08; found: C = 75.55, H = 4.54, N = 2.19.

IR(cm⁻¹): 2204 ($\nu_{C\equiv C}$), 1645 ($\nu_{C=O}$), 821 (δ_{C-H} Fc).

X-ray diffraction study:



ORTEP view of **58** with 50 % thermal ellipsoids solved by Dr. Thierry Roisnel

	
Formula	C ₈₅ H ₅₉ Fe ₄ N ₂ O
Molecular weight (g/mol)	1348.81
Orange crystals obtained by slow diffusion of hexane into a DCM solution of the molecule at room temperature	

Crystal parameters	
Crystal class	triclinic
Space group	P -1
Cell angles (°)	α= 103.70
	β= 95.25
	γ= 99.83
Cell length (Å)	a= 7.18
	b= 16.31
	c= 28.52
Cell volume (Å ³)	3169.33
Z	Z= 2

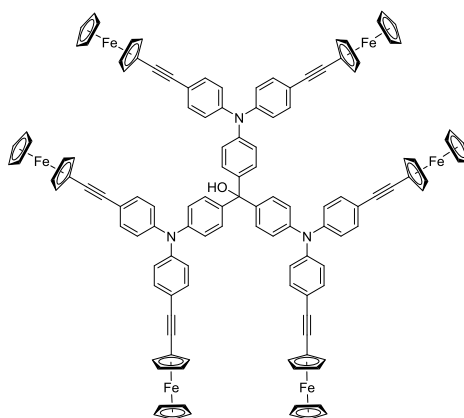
Selected bond length (Å)

C≡C	1.167 (1)	C1-C2	1.481 (1)
C-O	1.229 (1)		

Selected angles (°)

C3-C1-C2	27.38 (5)	C5-N1-C16	43.00 (5)
-----------------	-----------	------------------	-----------

tris(4-(bis(4-((ethynylferrocene)phenyl)amino)phenyl)methanol (S2(Fc)^{OH})



C₁₂₇H₉₁Fe₆N₃O, M = 2010.21 g/mol

Reagents: bis(4-(bis(4-(ethynylferrocene)phenyl)amino)phenyl)methanone **58** (1 eq, 428 mg, 0.317 mmol), 4-iodo-N,N-bis(4-(ethynylferrocene)phenyl)aniline **61** (1.2 eq, 250 mg, 0.381 mmol), *n*-BuLi (1.1 eq, 182 μ L (1.6 M)).

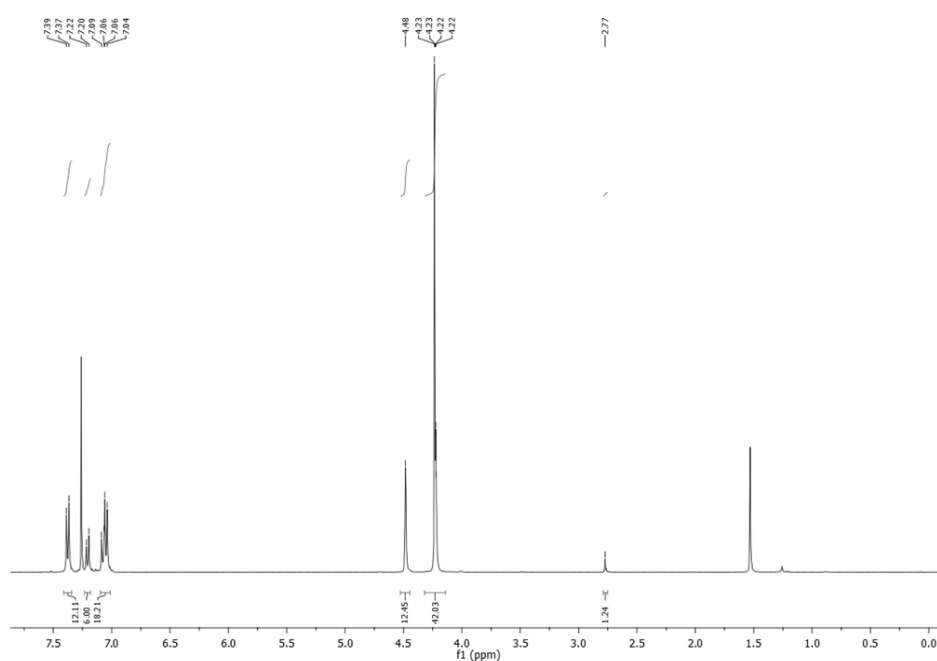
Reaction: In a Schlenk flask under argon, *n*-BuLi was added drop-wise to a solution of **61** in dry and distilled THF at -78°C . After stirring for 30 min, a solution of **58** in dry and distilled THF was added drop wise to the solution. The mixture was stirred and allowed to warm to room temperature for 16 h.

Work-up: 20 mL of water were added to the flask and the two phases were separated. The aqueous layer was extracted with DCM (3 x 20 mL) and the combined organics phases were washed with water (10 mL) and saturated aqueous NaCl (10 mL). The aqueous phase was then back extracted with DCM (20 mL). The organic phases were dried over MgSO_4 and the solvents were removed to give the crude product as a solid.

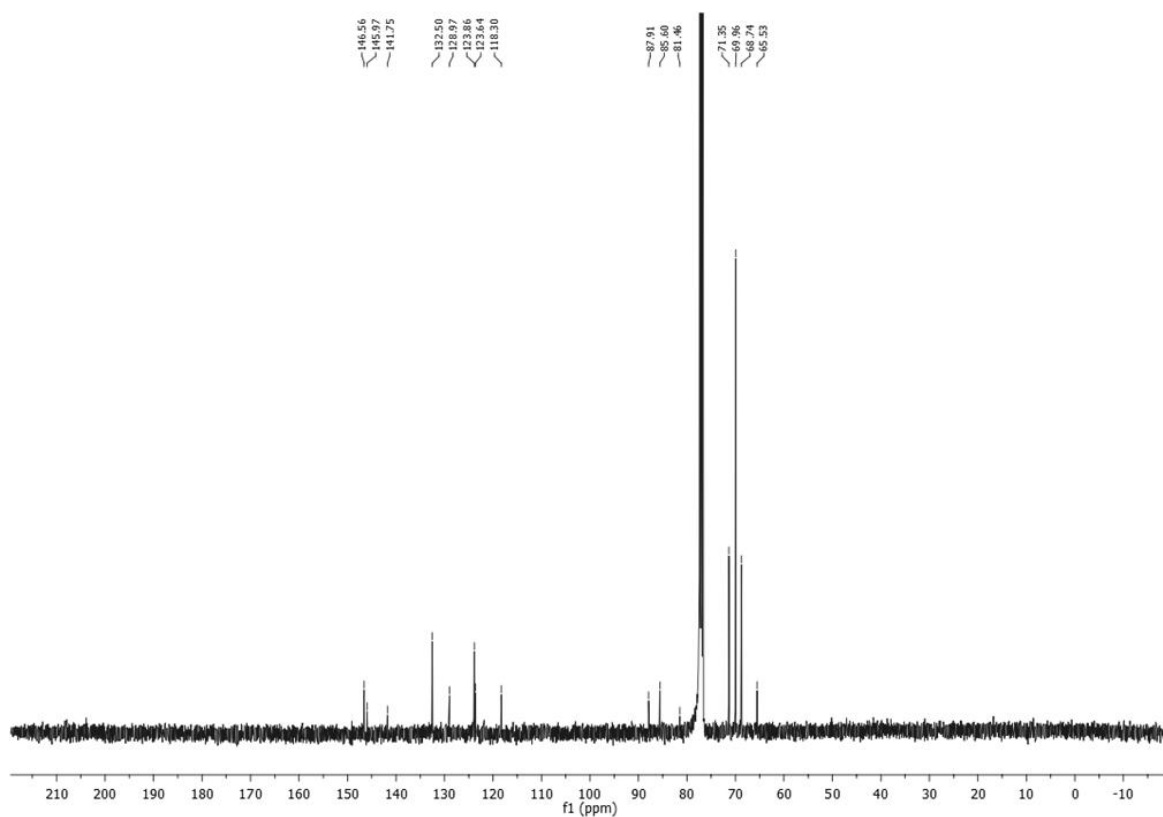
Purification: The obtained solid was absorbed onto deactivated silica and loaded on the top of a chromatographic column. The orange fraction, eluted with toluene/hexane (7/3) + 1% Et_3N , was collected and solvents were removed under reduced pressure. The product was then precipitated from DCM/ Et_2O .

Yield: m = 200 mg (32 %).

^1H NMR (400 MHz, CDCl_3) δ 7.38 (d, J = 8.6 Hz, 12H), 7.21 (d, J = 8.7 Hz, 6H), 7.09 - 7.04 (m, 18H), 4.48 (s, 12H), 4.32 – 4.14 (m, 42H, Cp), 2.77 (s, 1H, -OH).



^{13}C NMR (101 MHz, CDCl_3) δ 146.56, 145.97, 141.75, 132.50, 128.97, 123.86, 123.64, 118.30, 87.91, 85.60, 81.46, 71.35, 69.96, 68.74, 65.53.



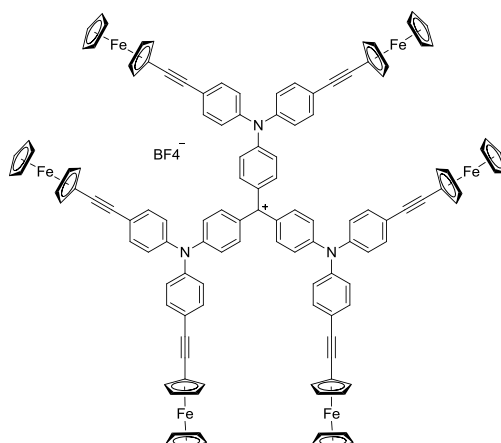
HRMS (ESI) calcd.: 1004.66238 $[\text{M}]^{2+}$, 669.77473 $[\text{M}]^{3+}$, 2009.3253 $[\text{M}]^{+}$, 1992.32256 $[\text{M}-\text{OH}]^{+}$;
found: 1004.6629 $[\text{M}]^{2+}$, 669.7755 $[\text{M}]^{3+}$, 2009.3219 $[\text{M}]^{+}$, 1992.3193 $[\text{M}-\text{OH}]^{+}$

IR: (cm^{-1}): 3563 ($\nu_{\text{O-H}}$), 2206 ($\nu_{\text{C}\equiv\text{C}}$), 819 ($\delta_{\text{C-H}}$ Fc).

UV-Vis (DCM): λ_{max} , nm (ϵ , $10^{-5} \cdot \text{M}^{-1} \cdot \text{cm}^{-1}$): 349 (1.5).

CV: DCM, 0.10 M $[\text{n-Bu}_4\text{N}][\text{PF}_6]$, V vs ECS): $\text{M}^{\text{III}}/\text{M}^{\text{II}}$ $E_{1/2}$: 0.52 V ($\Delta E_p = 0.05$ V, $i_{\text{pc}}/i_{\text{pa}} = 0.98$) (six ferrocenes at the same time)

tris(4-(bis(4-((ethynylferrocene)phenyl)amino)phenyl)methyl)methylium tetrafluoroborate ([S2(Fc)⁺][BF₄⁻])



C₁₂₇H₉₀BF₄Fe₆N₃, M = 2080.01 g/mol

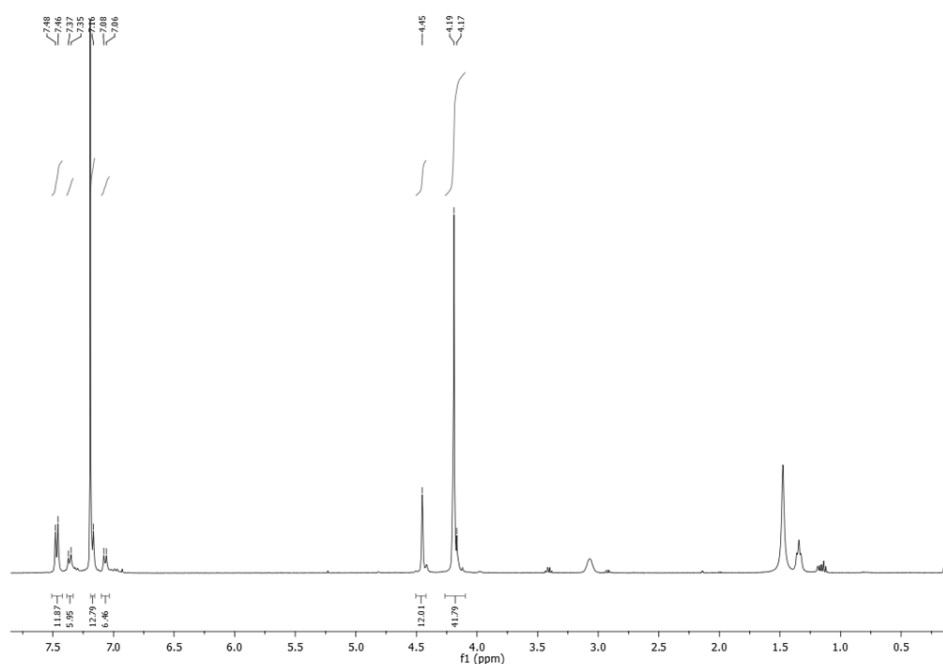
Reagents: S2(Fc)^{OH} (1 eq, 100 mg, 0.05 mmol), HBF₄·Et₂O (1.1 eq, 8 μL, 1.1 mmol)

Reaction and work up: Prepared according to GP3.

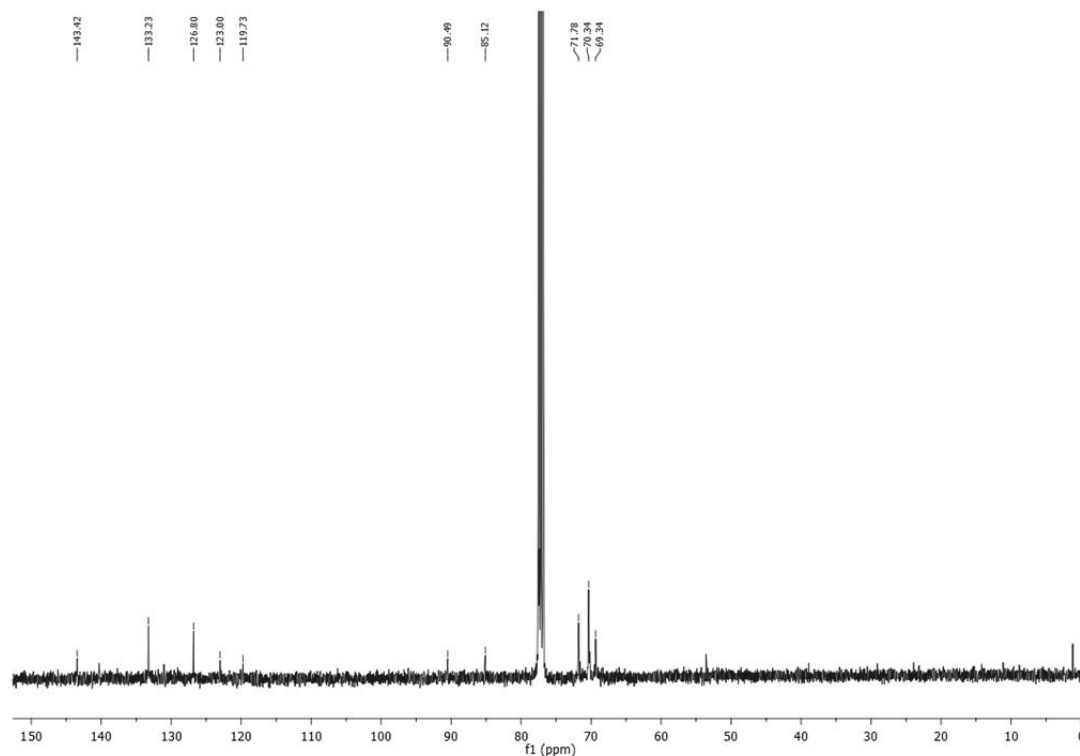
Work up and purification: The green precipitate was washed with dry and distilled Et₂O (3x10 mL). The dark green solid was then precipitated from DCM/pentane and filtered to obtain a green fine powder.

Yield: quant.

¹H NMR (400 MHz, CDCl₃) δ 7.47 (d, J = 8.3 Hz, 12H), 7.36 (d, J = 8.7 Hz, 6H), 7.16 (d, 12H + CDCl₃), 7.07 (d, J = 8.6 Hz, 6H), 4.45 (s, 12H, Cp), 4.18 (d, J = 9.1 Hz, 42H, Cp).



^{13}C NMR (101 MHz, CDCl_3) δ 143.42, 133.23, 126.80, 123.00, 119.73, 90.49, 85.12, 71.78, 70.34, 69.34.

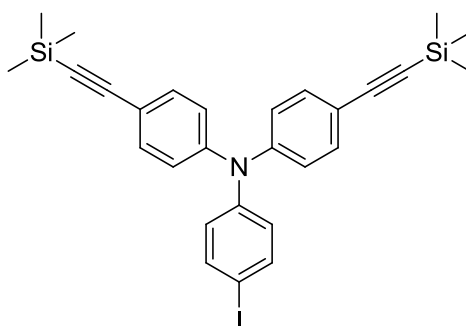


IR: (cm^{-1}): 2204 ($\nu_{\text{C}\equiv\text{C}}$), 820 ($\delta_{\text{C-H}}$ Fc), 1172 ($\nu_{\text{B-F}}$).

UV-Vis: (DCM): λ_{max} , nm (ϵ , $10^{-5} \cdot \text{M}^{-1} \cdot \text{cm}^{-1}$): 341 (1.49), 689 (0.92).

CV: DCM, 0.10 M [$n\text{-Bu}_4\text{N}$][PF_6], V vs ECS): C^+/C^+ : E_{pc} : -0.35 V, $\text{M}^{\text{III}}/\text{M}^{\text{II}}$: $E_{1/2}$: 0.53 V ($\Delta E_p = 0.05$ V, $i_{\text{pc}}/i_{\text{pa}} = 0.99$) (six ferrocenes at the same time)

4-iodo-N,N-bis(4-((trimethylsilyl)ethynyl)phenyl)aniline (62)



$\text{C}_{28}\text{H}_{30}\text{I}\text{NSi}_2$, $M = 563.63$ g/mol

Reagents: tris(4-iodophenyl)amine (1 eq, 3.115 g, 5 mmol), TMSA (10 eq, 1.413 mL, 10 mmol), $\text{PdCl}_2(\text{PPh}_3)_2$ (0.04 eq, 140 mg, 0.2 mmol), CuI (0.08 eq, 75 mg, 0.4 mmol).

Reaction: A Schlenk tube under argon, tri(4-iodophenyl)amine, $\text{PdCl}_2(\text{PPh}_3)_2$ and CuI were dissolved in a mixture of toluene (50 mL) and Et_3N (50 mL). TMSA was added and the resulting yellow solution was stirred at room temperature for 6 h.

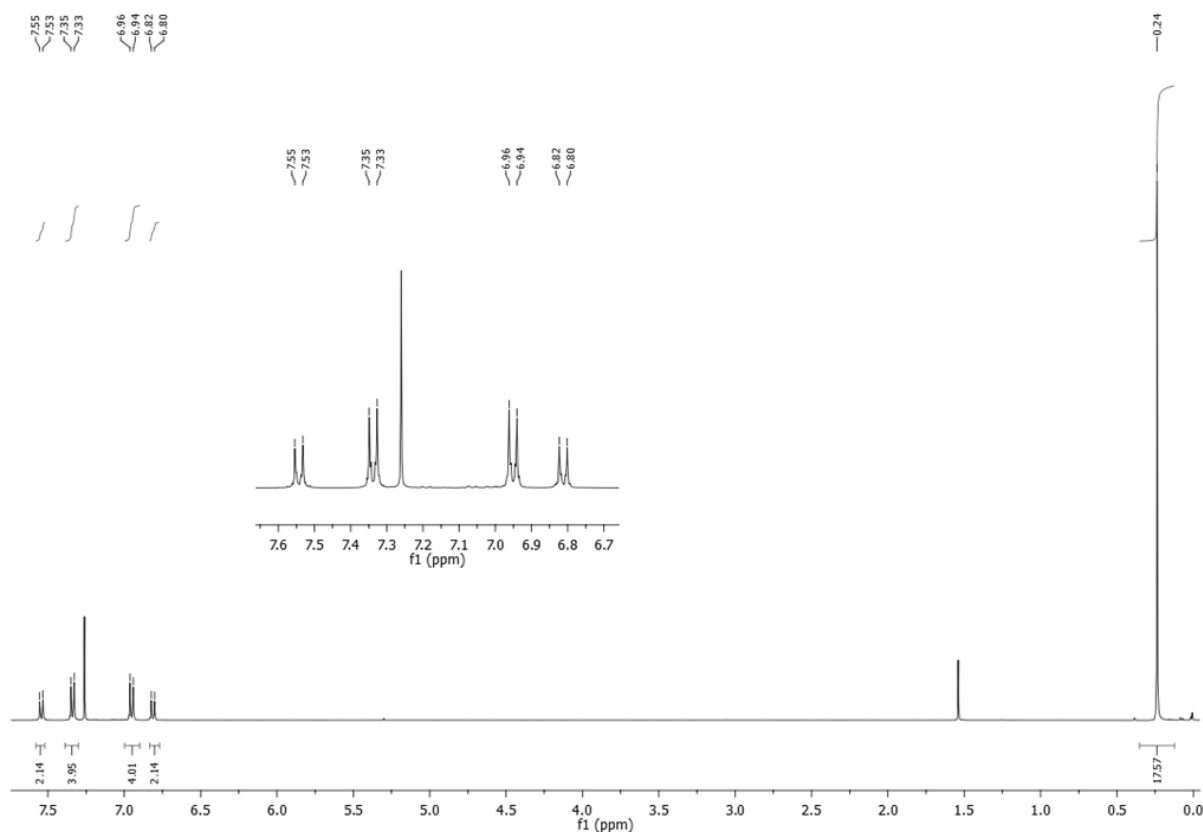
Work-up: After evaporation of the solvents by cryoscopic transfer, a saturated aqueous solution of NH_4Cl (30 mL) and DCM (30 mL) was added to the residue. The aqueous layer was extracted with DCM (3 x 25 mL). The combined organic phases were washed with water (10 mL) and saturated aqueous NaCl (10 mL), and the aqueous layer was then back-extracted with DCM (25 mL). The combined organic layers were dried over MgSO_4 and evaporated under reduced pressure to give a light yellow solid.

Purification: The obtained solid was absorbed onto silica and loaded on the top of a chromatographic column and eluted with hexane. The product was precipitated from DCM/MeOH.

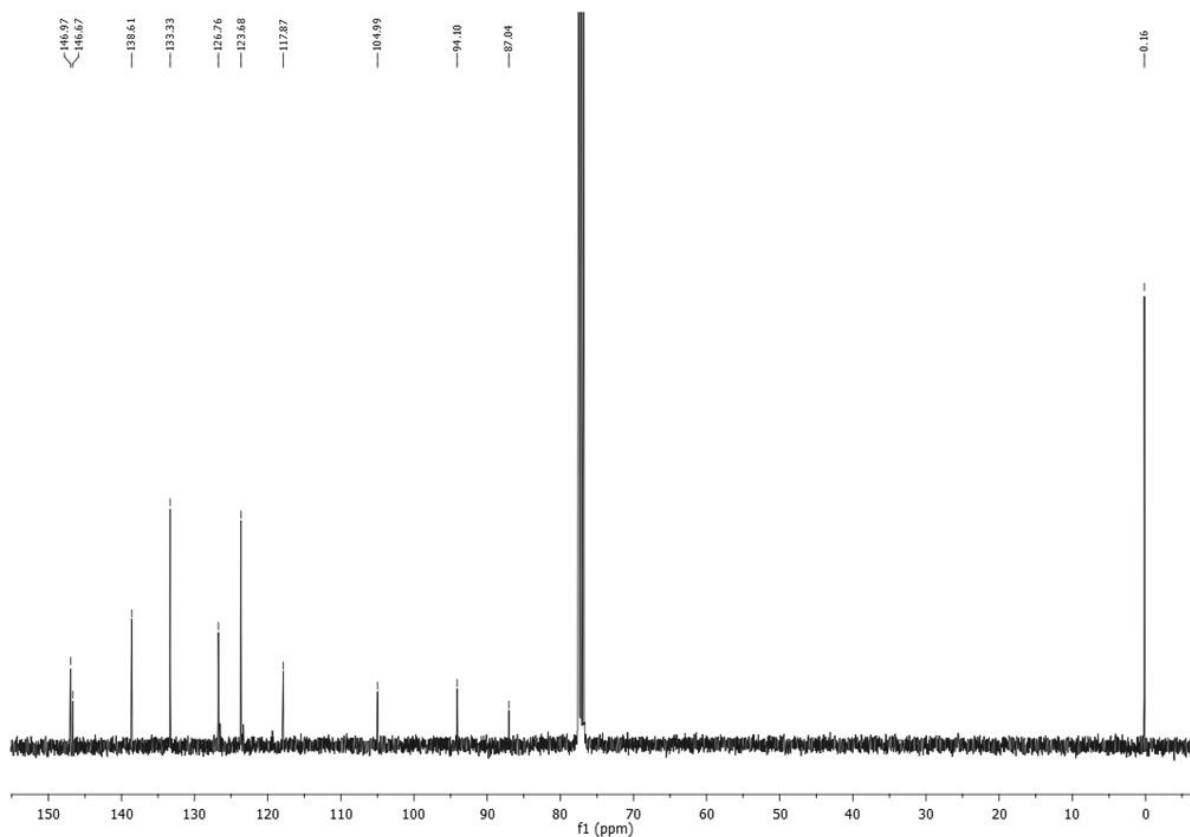
R_f(hexane) = 0.16

Yield: m= 229 mg (40 %)

^1H NMR (400 MHz, CDCl_3) δ 7.54 (d, J = 8.7 Hz, 2H), 7.34 (d, J = 8.7 Hz, 4H), 6.95 (d, J = 8.6 Hz, 4H), 6.81 (d, J = 8.7 Hz, 2H), 0.24 (s, 18H, CH_3 Si).



^{13}C NMR (101 MHz, CDCl_3) δ 146.96, 146.66, 138.60, 133.33, 126.75, 123.68, 117.86, 104.99, 94.10, 87.04, 87.04, 0.16 (CH_3 Si).

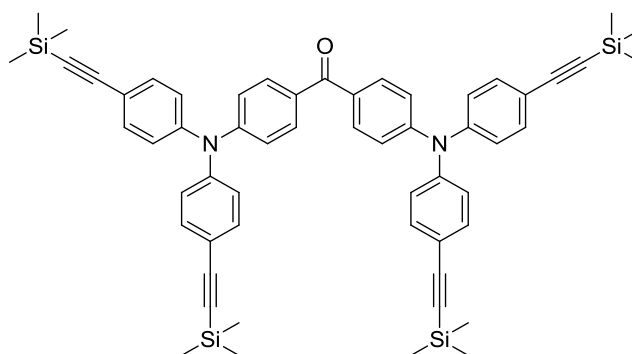


HRMS (ESI) calcd.: 564.1040 $[\text{M}+\text{H}]^+$; found: 564.1042 $[\text{M}+\text{H}]^+$

IR: 2154.55 ($\nu_{\text{C}\equiv\text{C}}$), 544 ($\nu_{\text{C-I}}$).

EA: calcd.: C: 59.67, H: 5.37, N: 2.49, found: C: 59.57, H: 5.31, N: 2.58.

bis(4-(bis(4-((trimethylsilyl)ethynyl)phenyl)amino)phenyl)methanone (59)



$\text{C}_{57}\text{H}_{60}\text{N}_2\text{OSi}_4$, $M=901.46$

Reagents: bis(4-(bis(4-iodophenyl)amino)phenyl)methanone **57** (1 eq, 1.02 g, 1 mmol), TMSa (9 eq, 1.27 mL, 9 mmol), $\text{PdCl}_2(\text{PPh}_3)_2$ (0.16 eq, 112 mg, 0.16 mmol), CuI (0.32 eq, 75 mg, 0.32 mmol).

Reaction: A Schlenk tube under argon, **57**, $\text{PdCl}_2(\text{PPh}_3)_2$ and CuI were dissolved in a mixture of toluene (25 mL) and Et_3N (25 mL). TMSa was added and the resulting yellow solution was stirred at 40°C for 6 h.

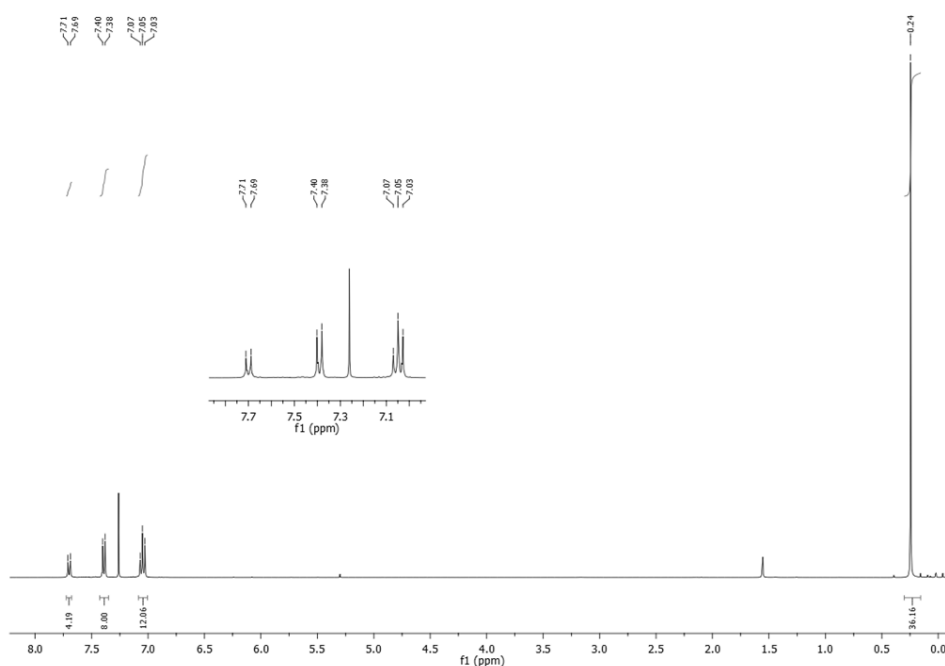
Work-up: After evaporation of the solvents by cryoscopic transfer, a saturated aqueous solution of NH_4Cl (30 mL) and DCM (30 mL) was added to the residue. The aqueous layer was extracted with DCM (3 x 25 mL). The combined organic phases were washed with water (10 mL) and saturated aqueous NaCl (10 mL); the aqueous layer was then back-extracted with DCM (25 mL). The combined organic layers were dried over MgSO_4 and evaporated under reduced pressure to give a light yellow solid.

Purification: The obtained solid was absorbed onto silica and loaded on the top of a chromatographic column and eluted with a gradient of hexane/DCM from 8/2 to 1/1. Precipitation from DCM/MeOH afforded the desired compound as a yellow crystalline powder.

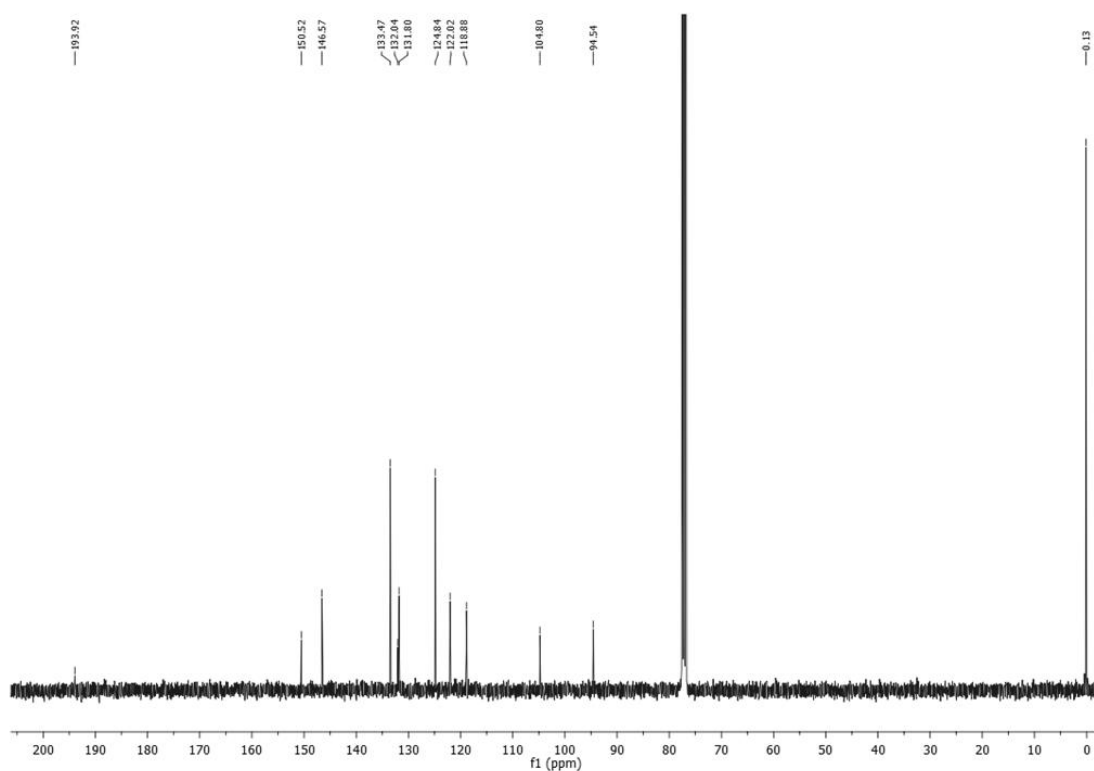
$R_f(\text{hexane/DCM}) = 0.36$.

Yield: m= 790 mg (87 %).

$^1\text{H NMR}$ (400 MHz, CDCl_3) δ 7.70 (d, $J = 8.8$ Hz, 4H), 7.39 (d, $J = 8.7$ Hz, 8H), 7.07-7.03 (m, 12H), 0.24 (s, 36H).



^{13}C NMR (101 MHz, CDCl_3) δ 193.92 (C=O), 150.52, 146.57, 133.47, 132.04, 131.80, 124.84, 122.02, 118.88, 104.80, 94.54, 0.13 (CH_3Si).

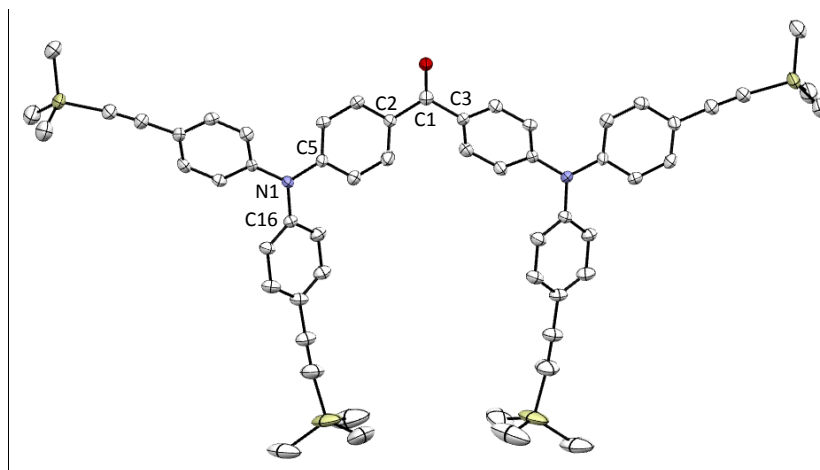


IR (cm^{-1}): 1672 ($\nu_{\text{C=O}}$), 2159 ($\nu_{\text{C}\equiv\text{C}}$), 1272 ($\nu_{\text{Si-Me}}$).

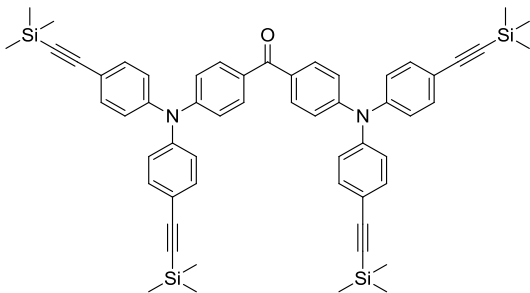
HRMS (ESI): calcd.: 923.3680 $[\text{M}+\text{Na}]^+$; found: 923.3681 $[\text{M}+\text{Na}]^+$

EA: calcd.: C: 75.95, H: 6.71, N: 3.11, found: C: 75.88, H: 6.65, N: 3.19.

X-ray diffraction study:



ORTEP view of **58** with 50 % thermal ellipsoids solved by Dr. Graeme Moxey

	
Formula	C ₅₇ H ₆₀ N ₂ OSi ₄
Molecular weight (g/mol)	1348.81
Orange crystals obtained by slow diffusion of MeOH into a DCM solution of the molecule at room temperature	

Crystal parameters	
Crystal class	orthorhombic
Space group	P 2 ₁ 2 ₁ 2
Cell angles (°)	α= 90
	β= 90
	γ= 90
Cell length (Å)	a= 8.03
	b= 46.79
	c= 15.47
Cell volume (Å ³)	5823.2
Z	Z= 4

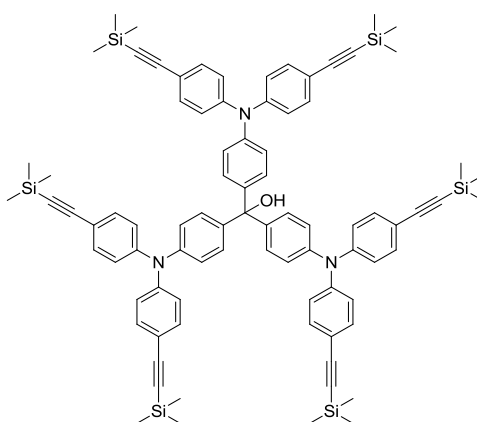
Selected bond length (Å)

C≡C	1.194 (9)	C1-C2	1.516 (9)
C-O	1.229 (9)		

Selected angles (°)

C3-C1-C2	33.14 (4)	C5-N1-C16	32.06 (4)
-----------------	-----------	------------------	-----------

tris(4-(bis(4-((trimethylsilyl)ethynyl)phenyl)amino)phenyl)methanol (63)



C₈₅H₉₁N₃OSi₆, M= 1339.19 g/mol

Reagents: bis(4-(bis(4-((trimethylsilyl)ethynyl)phenyl)amino)phenyl)methanone **59** (1 eq, 350 mg, 0.4 mmol), 4-iodo-N,N-bis(4-((trimethylsilyl)ethynyl)phenyl)aniline **62** (1.5 eq, 327 mg, 0.582 mmol), *n*-BuLi (1.1 eq, 312 μ L (1.6 M)).

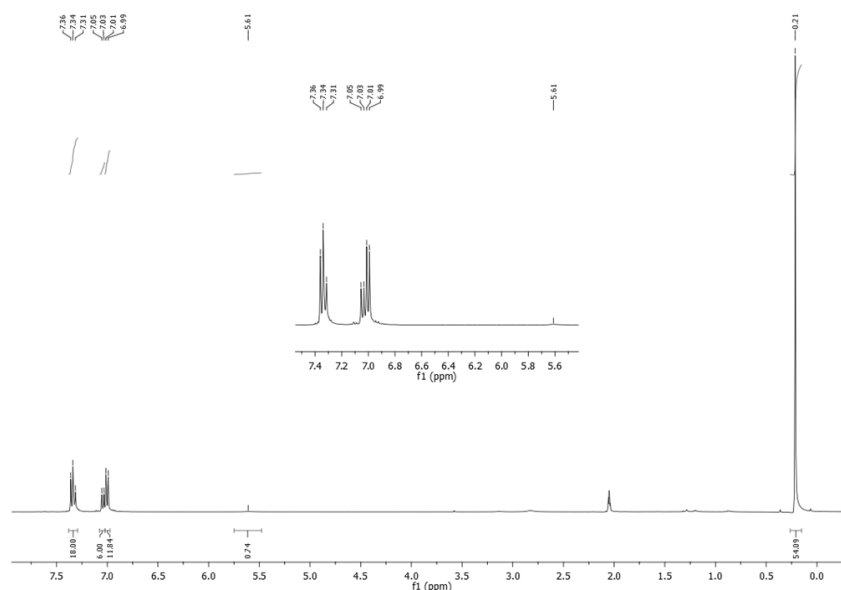
Reaction: In a Schlenk flask under argon, *n*-BuLi was added drop-wise to a solution of **62** in dried and distilled THF at -78°C. After stirring for 30 min, a solution of **59** in dried and distilled THF was added drop-wise to the solution. The mixture was stirred at -78°C for 16 h and allowed to warm up to room temperature.

Work-up: 20 mL of water were added to the flask and the two phases were separated. The aqueous layer was extracted with DCM (3 x 20 mL) and the combined organic phases were washed with water (10 mL) and saturated aqueous NaCl (10 mL). The aqueous phase was then back extracted with DCM (20 mL). The organic phase was dried over Na₂SO₄ and the solvents were removed to give the crude product as a solid.

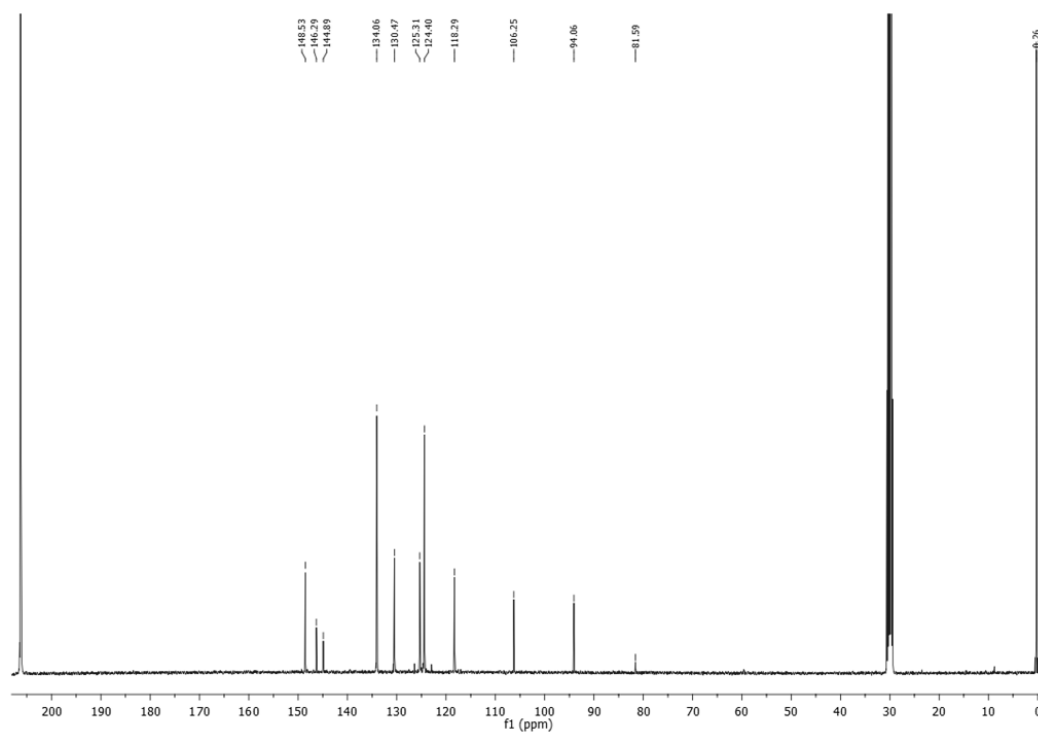
Purification: The obtained solid was absorbed onto silica and loaded on the top of a chromatographic column. The yellow fraction was eluted with a gradient of hexane/Et₂O (7/3) + 1% Et₃N (with the gradient ranging from pure hexane to 4/1 hexane/Et₂O), and was collected and solvents were removed under reduced pressure. The product was then precipitated from DCM/MeOH to afford a light yellow solid.

Yield: m= 380 mg (70 %).

¹H NMR (400 MHz, (CD₃)₂CO) δ 7.38 – 7.29 (m, 18H), 7.08 – 7.02 (d, *J* = 8.7 Hz, 6H), 7.00 (d, *J* = 8.6 Hz, 12H), 5.61 (s, 1H, OH), 0.21 (s, 54H, CH₃ Si).



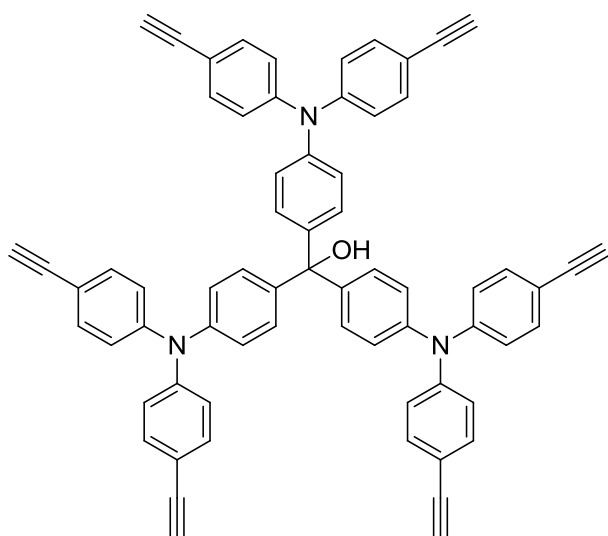
^{13}C NMR (101 MHz, $(\text{CD}_3)_2\text{CO}$) δ 148.53, 146.29, 144.89, 134.06, 130.47, 125.31, 124.40, 118.29, 106.25, 94.06, 81.59 (C-OH), 0.26 (CH_3 Si).



IR (cm^{-1}) 2153 ($\nu_{\text{C}\equiv\text{C}}$), 1272 ($\nu_{\text{C-Si}}$), ν_{OH} too weak to be detected.

HRMS (ESI): calc. 1320.5750 $[\text{M-OH}]^+$, found: 1320.5751 $[\text{M-OH}]^+$

tris(4-(bis(4-ethynylphenyl)amino)phenyl)methanol (64)



$\text{C}_{67}\text{H}_{43}\text{N}_3\text{O}$, Mw= 906.10 g/Mol

Reagents: tris(4-(bis(4-((trimethylsilyl)ethynyl)phenyl)amino)phenyl)methanol **63** (1 eq, 300 mg, 0.224 mmol), K₂CO₃ (9 eq, 185 mg, 1.3 mmol).

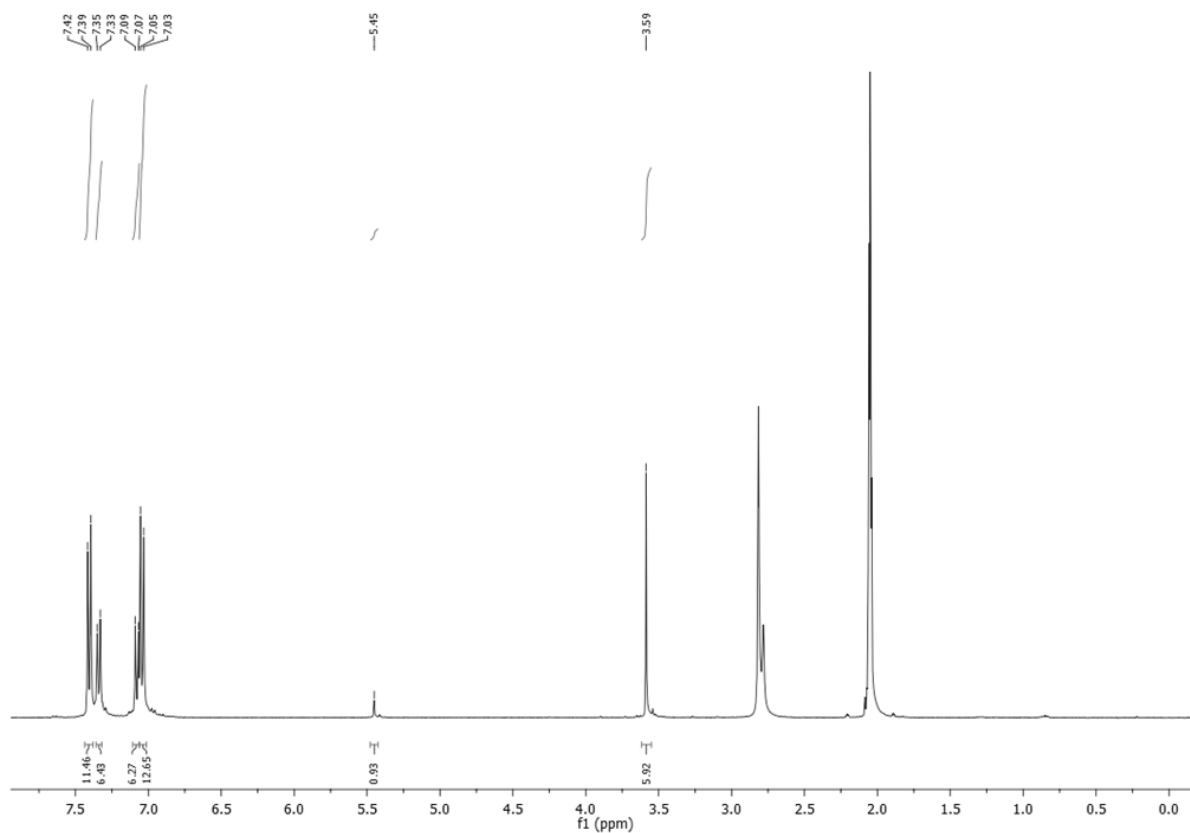
Reaction: In a round bottom flask **63** and K₂CO₃ were stirred in a mixture of MeOH (20 mL) and DCM (20 mL) for 16 h at room temperature.

Work-up: Solvents were removed and the residue was treated with water (20 mL) and DCM (20 mL). The two layers were separated and the aqueous layer was extracted with DCM (3 x 20 mL). The combined organic layers were washed with water (3 x 10mL) and saturated aqueous NaCl (10 mL). The aqueous layer was then back-extracted with DCM (20 mL). The combined organic layers were dried over Na₂SO₄ and evaporated under reduced pressure to give a yellow solid.

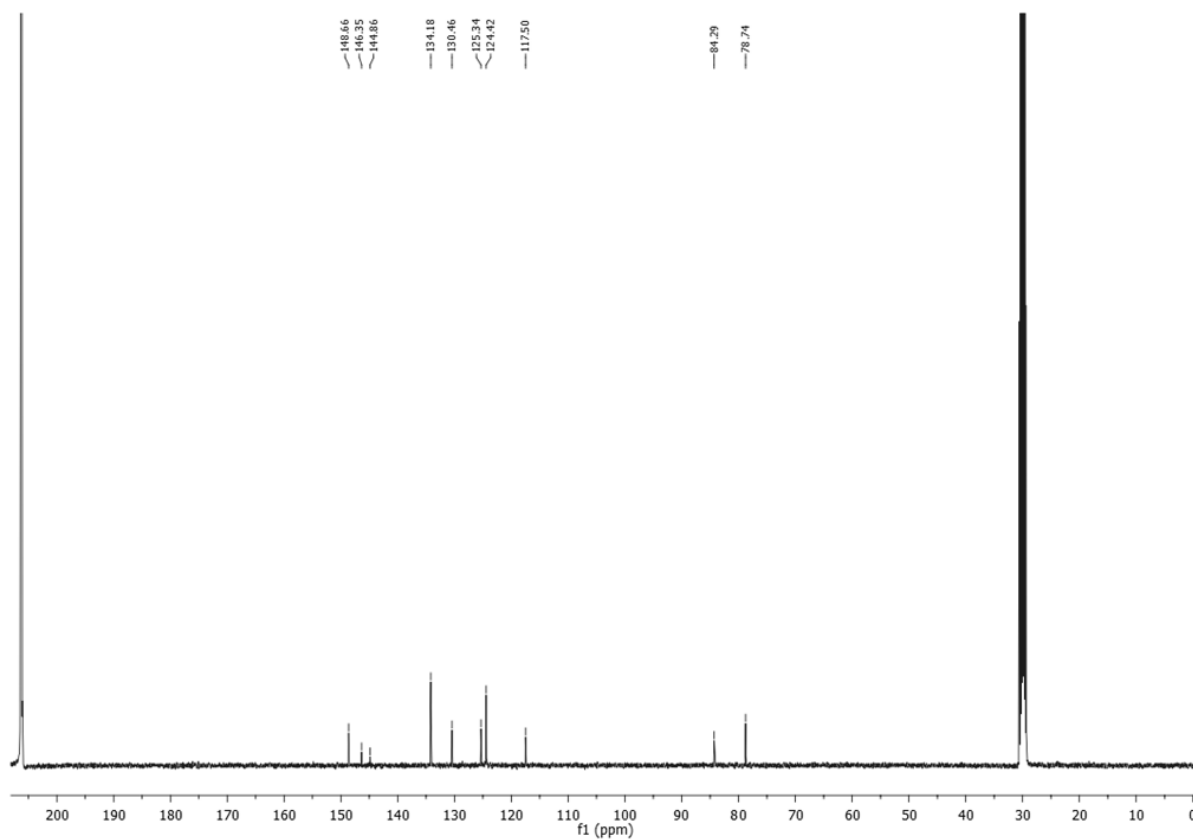
Purification: The solid residue was then precipitated from DCM/MeOH as a yellow powder.

Yield: m= 180 mg (94 %).

¹H NMR (400 MHz, CDCl₃) δ 7.40 (d, *J* = 8.6 Hz, 12H), 7.34 (d, *J* = 8.6 Hz, 16H), 7.08 (d, *J* = 8.6 Hz, 6H), 7.04 (d, *J* = 8.6 Hz, 12H), 5.45 (s, 1H, OH), 3.59 (s, 6H, C≡C-H).



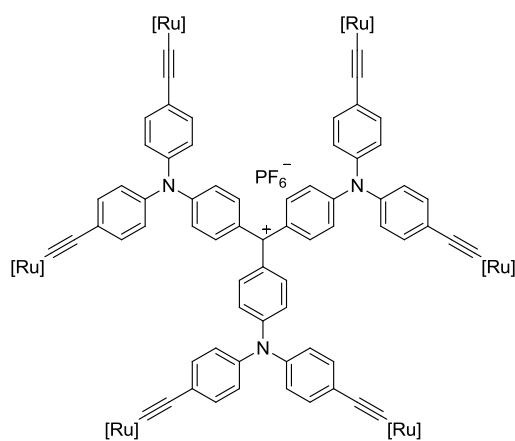
^{13}C NMR (101 MHz, CDCl_3) δ 148.66, 146.35, 144.86, 134.18, 130.46, 125.34, 124.42, 117.50, 84.29 (C-OH), 78.74 (C \equiv C-H).



IR (cm^{-1}): 3300 ($\nu_{\text{O-H}}$), 3287 ($\nu_{\text{C}\equiv\text{CH}}$), 2104 ($\nu_{\text{C}\equiv\text{C}}$).

HRMS (ESI): calc. 888.3379 $[\text{M-OH}]^+$, found: 888.3373 $[\text{M-OH}]^+$

$[\text{S2}(\text{Ru})^+][\text{PF}_6^-]$



$\text{C}_{379}\text{H}_{324}\text{Cl}_6\text{F}_6\text{N}_3\text{P}_{25}\text{Ru}_6$, $M = 6628.24$ g/mol

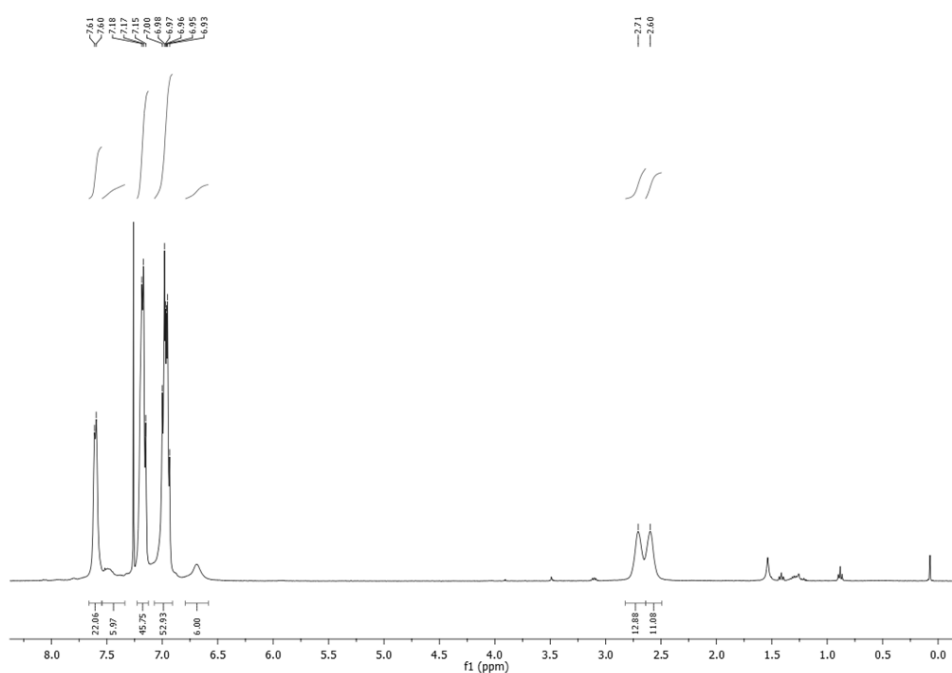
Reagents: tris(4-(bis(4-ethynylphenyl)amino)phenyl)methanol **64** (1 eq, 50 mg, 0.055 mmol), $[\text{RuCl}(\text{dppe})_2]\text{PF}_6$ **46** (9 eq, 533 mg, 0.5 mmol), Et_3N (60 eq., 56 μL).

Reaction: In a Schlenk flask under argon, 5 mL of distilled and deoxygenated DCM were added to **64** and $[\text{RuCl}(\text{dppe})_2]\text{PF}_6$ **46**. The resulting green mixture was stirred for 24h at room temperature. The crude product was reduced to a minimum of solvent and cannula filtered into a clean Schlenk flask under argon and precipitated with dried and distilled MeOH to give the product as a green powder. The same procedure was repeated until total removal of the 5-coordinate complex that was present in excess (affording a clear solution). The resulting powder was then washed with distilled and deoxygenated Et_2O . 10 mL of distilled and deoxygenated DCM was then added to the resulting solid followed by addition of Et_3N . The solution is stirred for 10 min and precipitated with distilled and deoxygenated Et_2O , and washed with pentane.

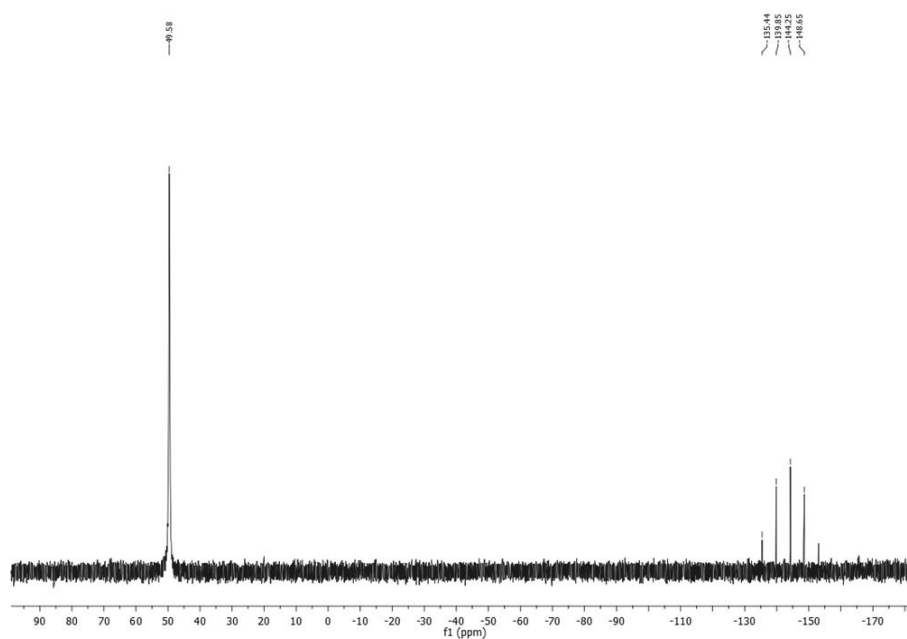
Purification: The resulting purple powder was precipitated from DCM/ Et_2O to afford a fine purple powder.

Yield: >60 %.

^1H NMR (400 MHz, CDCl_3) δ 7.60 (d, $J = 6.3$ Hz, 22H), 7.50 (s, 6H), 7.23 – 7.13 (m, 46H), 7.00-6.93 (m, 54H), 6.69 (s, 6H), 2.71 (s, 2H, CH_2 dppe), 2.60 (s, 12H, CH_2 dppe).

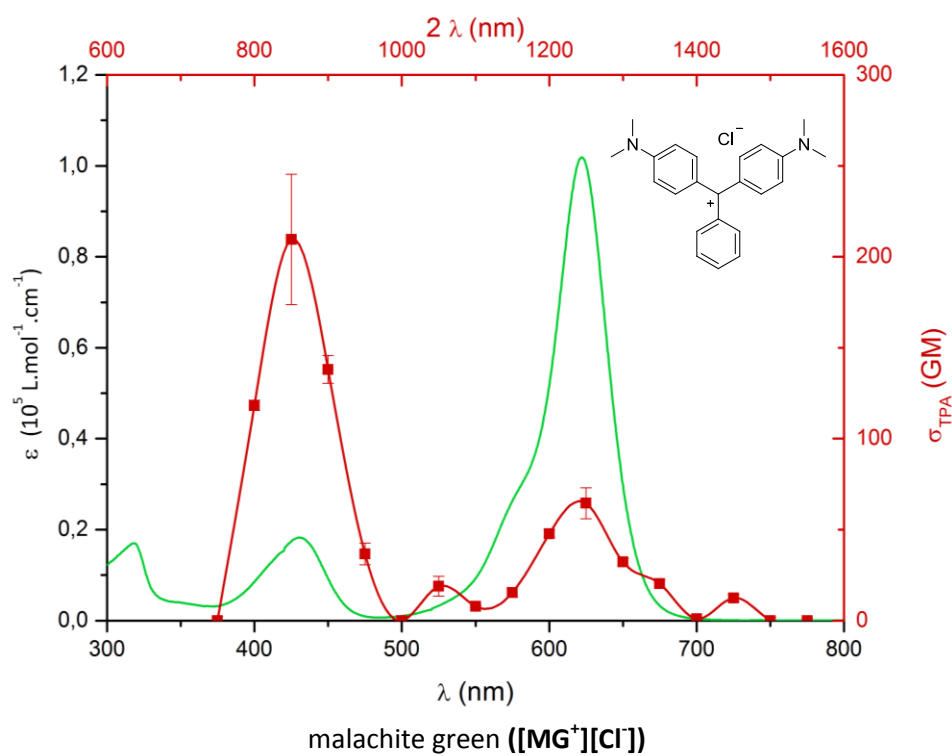


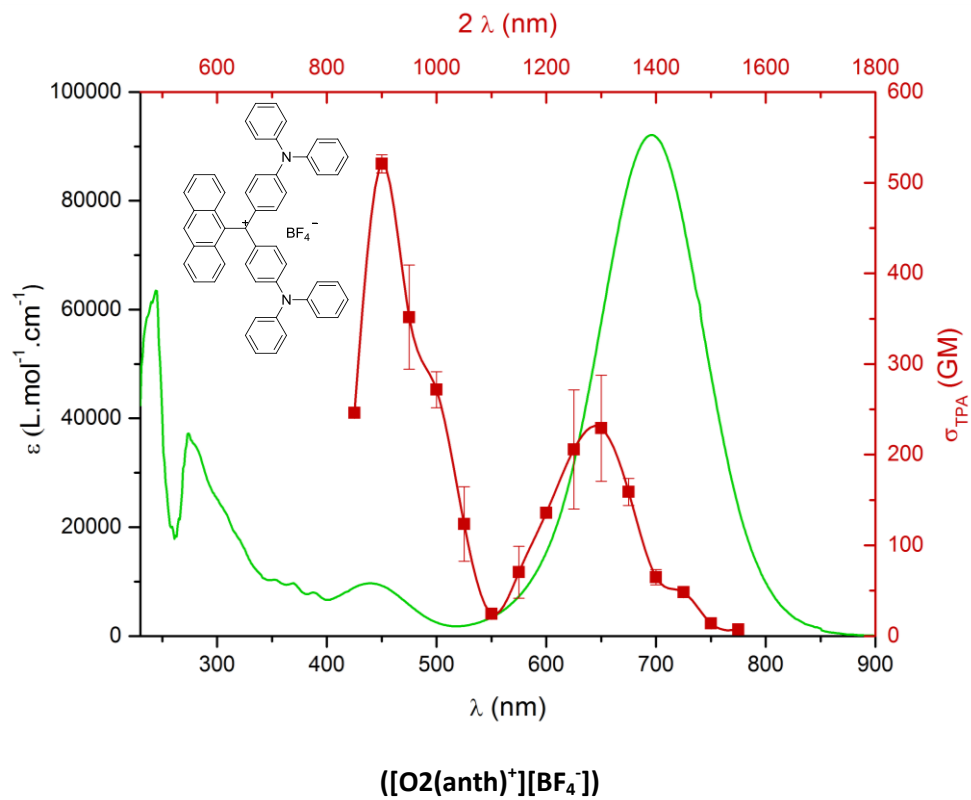
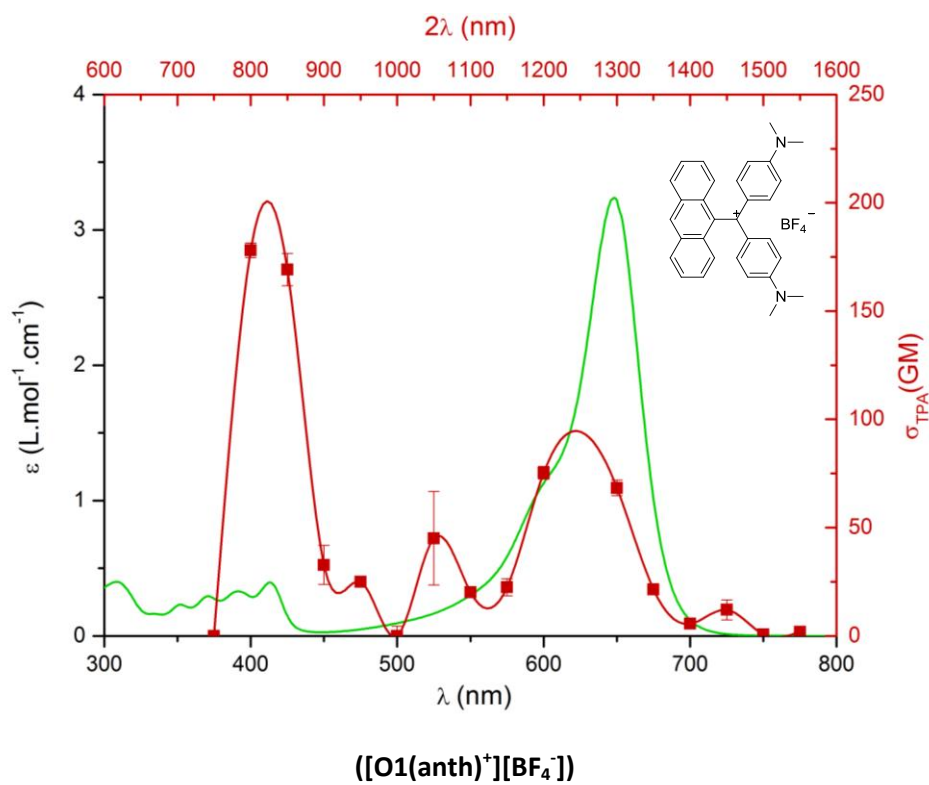
^{31}P NMR (162 MHz, CDCl_3) δ 49.58 (s), -144.25 (sept).

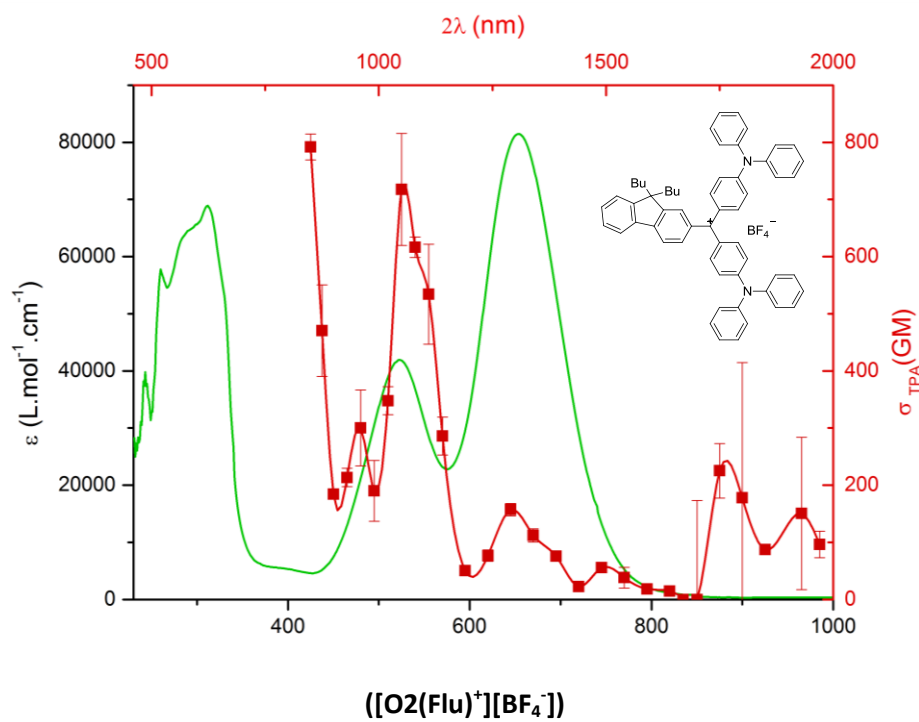
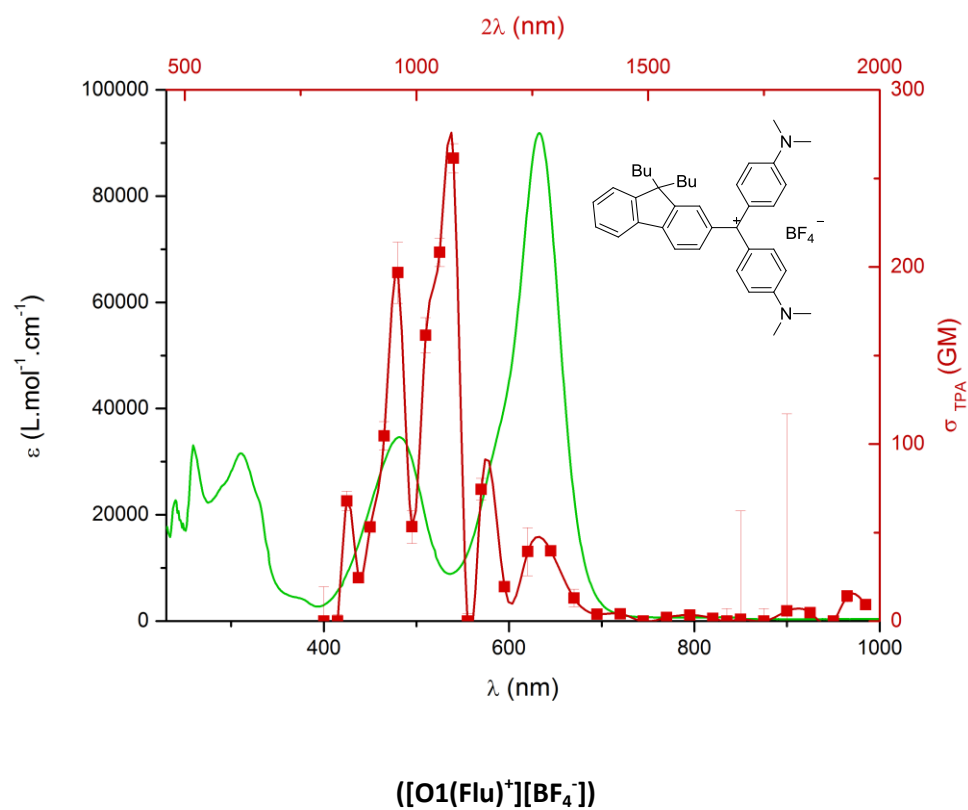


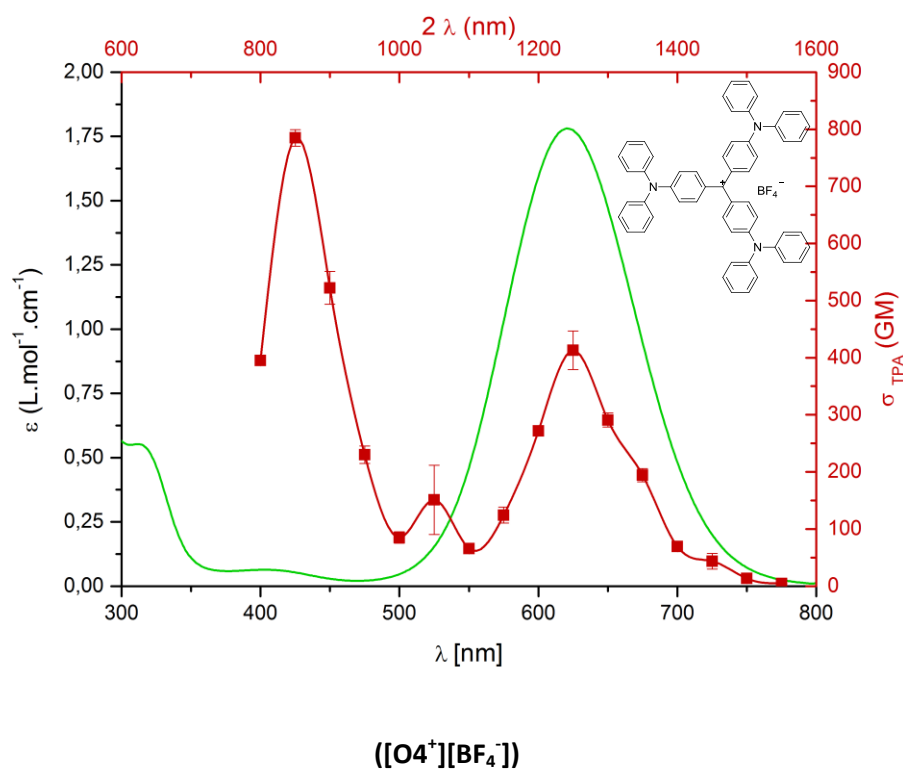
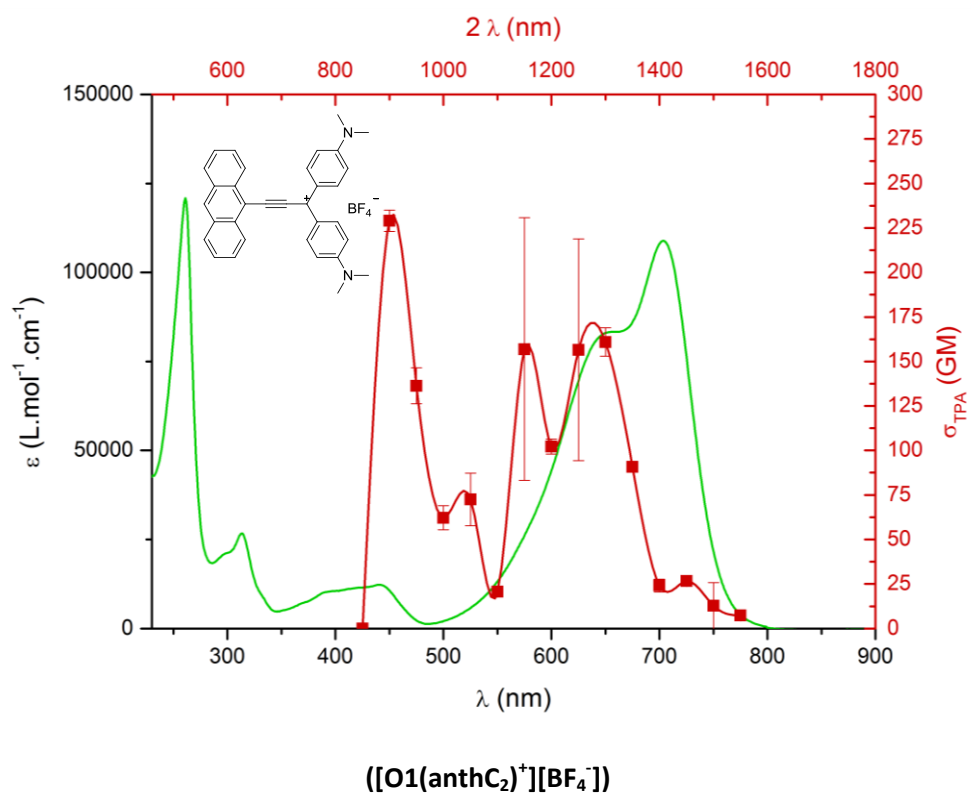
8. Z-scan traces

Green traces correspond to the linear absorptions and red plot to the two photon spectra. Error is represented by the bars on the dots.









References

- [1] G. R. Fulmer, A. J. M. Miller, N. H. Sherden, H. E. Gottlieb, A. Nudelman, B. M. Stoltz, J. E. Bercaw, K. I. Goldberg, *Organometallics* **2010**, *29*, 2176–2179.
- [2] N. G. Connelly, W. E. Geiger, *Chem. Rev.* **1996**, *96*, 877–910.
- [3] W. C. Still, M. Kahn, A. Mitra, *J. Org. Chem.* **1978**, *43*, 2923–2925.
- [4] A. I. Vogel, B. S. Furniss, *Vogel's Textbook of Practical Organic Chemistry*, Longman, **1989**.
- [5] D. F. Shriver, M. A. Drezdson, *The Manipulation of Air-Sensitive Compounds*, 2nd Edition, Wiley, **1986**.
- [6] S. Komiya, *Synthesis of Organometallic Compounds: A Practical Guide*, Wiley, **1997**.
- [7] J. N. Moorthy, A. L. Koner, S. Samanta, A. Roy, W. M. Nau, *Chem. – Eur. J.* **2009**, *15*, 4289–4300.
- [8] T. R. Kelly, J. P. Sestelo, I. Tellitu, *J. Org. Chem.* **1998**, *63*, 3655–3665.
- [9] A. Nierth, A. Y. Kobitski, G. U. Nienhaus, A. Jäschke, *J. Am. Chem. Soc.* **2010**, *132*, 2646–2654.
- [10] M. Chandrasekharam, G. Rajkumar, C. S. Rao, T. Suresh, P. Y. Reddy, J.-H. Yum, M. K. Nazeeruddin, M. Graetzel, *Adv. Nat. Sci. Nanosci. Nanotechnol.* **2011**, *2*, 035016.
- [11] V. N. Okulov, M. A. Dyadchenko, A. V. Churakov, E. V. Polunin, D. A. Lemenovskii, H. Yu, L. Wang, V. P. Dyadchenko, *Mendeleev Commun.* **2015**, *25*, 171–173.
- [12] L. Shi, C. He, D. Zhu, Q. He, Y. Li, Y. Chen, Y. Sun, Y. Fu, D. Wen, H. Cao, et al., *J. Mater. Chem.* **2012**, *22*, 11629–11635.
- [13] C. Roger, P. Hamon, L. Toupet, H. Rabaa, J. Y. Saillard, J. R. Hamon, C. Lapinte, *Organometallics* **1991**, *10*, 1045–1054.
- [14] K. A. Green, M. P. Cifuentes, T. C. Corkery, M. Samoc, M. G. Humphrey, *Angew. Chem. Int. Ed.* **2009**, *48*, 7867–7870.
- [15] C. Sissa, V. Parthasarathy, D. Drouin-Kucma, M. H. V. Werts, M. Blanchard-Desce, F. Terenziani, *Phys. Chem. Chem. Phys.* **2010**, *12*, 11715–11727.
- [16] J. Ipaktschi, R. Hosseinzadeh, P. Schlaf, E. Dreiseidler, R. Goddard, *Helv. Chim. Acta* **1998**, *81*, 1821–1834.
- [17] B. Kobin, L. Grubert, S. Blumstengel, F. Henneberger, S. Hecht, *J. Mater. Chem.* **2012**, *22*, 4383–4390.
- [18] Z. Q. Gao, P. F. Xia, P. K. Lo, B. X. Mi, H. L. Tam, M. S. Wong, K. W. Cheah, C. H. Chen, *Org. Electron.* **2009**, *10*, 666–673.
- [19] M. R. Netherton, G. C. Fu, *Org. Lett.* **2001**, *3*, 4295–4298.
- [20] G. Doisneau, G. Balavoine, T. Fillebeen-Khan, *J. Organomet. Chem.* **1992**, *425*, 113–117.
- [21] O. Plietzsch, A. Schade, A. Hafner, J. Huuskonen, K. Rissanen, M. Nieger, T. Muller, S. Bräse, *Eur. J. Org. Chem.* **2013**, *2013*, 283–299.
- [22] T. Glinka, *Aldrichimica Acta*, **1987**, *20*, 34.
- [23] A. P. Smith, J. J. S. Lamba, C. L. Fraser, *Org. Synth.* **2002**, *78*, 82–87.
- [24] F. Wagenknecht, R. Juza, in *Handb. Prep. Inorg. Chem. Second Ed.* (Ed.: G. Brauer), Academic Press, **1965**, pp. 1067–1124.
- [25] W. L. F. Armarego, C. L. L. Chai, in *Purification of Laboratory Chemicals Sixth Ed.* (Ed.: W.L.F.A.L.L. Chai), Butterworth-Heinemann, Oxford, **2009**, pp. xii–xiii.

Résumé

Au cours de cette thèse, de nouveaux dérivés organométalliques basés sur une structure triphénylméthylum ont été synthétisés. Ces composés, notamment grâce à leur structure multipolaire, sont pressentis pour avoir des propriétés remarquables en optique non linéaire (ONL) et pourraient donner lieu à des applications dans plusieurs domaines. Ces caractéristiques, et plus précisément leur absorption biphotonique (A2P), en font des composés particulièrement intéressants pour l'industrie de pointe (microfabrication, imagerie, dispositifs optiques, etc.). Cependant, ces propriétés d'ONL et d'absorption biphotonique n'ont été jusqu'alors que peu étudiées, malgré leur potentiel prometteur.

Dans un premier temps, une famille de nouveaux composés organiques présentant cette structure particulière a été synthétisée afin de confirmer le potentiel d'absorption à deux photons de ces chromophores, notamment par des mesures Z-scan. Dans un second temps, la synthèse d'analogues organométalliques ayant des groupes donneurs tels que « $\text{Fe}(\eta^5\text{-C}_5\text{Me}_5)(\kappa^2\text{-dppe})\text{C}\equiv\text{C}-$ », « $\text{Ru}(\text{Cl})(\kappa^2\text{-dppe})_2\text{C}\equiv\text{C}-$ » ou ethynylferrocène a été réalisée, ainsi que leur caractérisation complète. Ces dérivés organométalliques devraient présenter des sections efficaces d'A2P (ainsi que des réponses ONL de troisième ordre) dans le proche-IR bien supérieures à celles de leurs analogues organiques. De plus, les groupements métalliques redox-actifs utilisés devraient permettre d'obtenir des chromophores électro-commutables. Les études déjà réalisées sur ces composés, et celles à venir sur leur propriétés ONL de troisième ordre, permettront de mieux comprendre les phénomènes électroniques sous-jacents à ces propriétés ainsi que le rôle joué par les parties organiques et organométalliques de leur structure.

Mots clés: Optique Nonlinéaire - Absorption Biphotonique - Vert Malachite - Cristal Violet - Organofer - Organoruthénium - Ferrocène - Commutation Redox.

Abstract

During this PhD, new organic and organometallic triphenylmethylium dyes were synthesized. Due to their multipolar structure, these compounds have been anticipated to possess strong nonlinear optical (NLO) properties which could be of interest in many fields. These characteristics, and more precisely their two-photon absorption (TPA) properties, make them attractive for the design of high technology materials (microfabrication, imaging, optical devices, etc.). However, their multiphoton absorption properties and other related nonlinear optical (NLO) effects have not been thoroughly investigated to date, in spite of their promising potential.

In this respect, a family of organic derivatives has been synthesized to confirm their potential as two-photon absorbers, which was established thanks to Z-scan measurements. Organometallic compounds bearing electron-releasing groups such as « $\text{Fe}(\eta^5\text{-C}_5\text{Me}_5)(\kappa^2\text{-dppe})\text{C}\equiv\text{C}-$ », « $\text{Ru}(\text{Cl})(\kappa^2\text{-dppe})_2\text{C}\equiv\text{C}-$ » or ethynylferrocene were then synthesized and fully characterized. These organometallic dyes should possess larger TPA cross-sections (and also larger third-order NLO properties) in the NIR range than their organic counterparts. Furthermore, these redox-active metal centers permit access to electro-switchable molecules. In this respect, along with the data already gathered on these derivatives, the study of their cubic NLO properties in their different redox states will now contribute to a better understanding of the underlying electronic phenomena and the role played by the organic and organometallic moieties in such architectures.